




Proceedings of the 11th Italian Conference

# Sensors and Microsystems

P Siciliano | S Capone | C Di Natale | A D'Amico

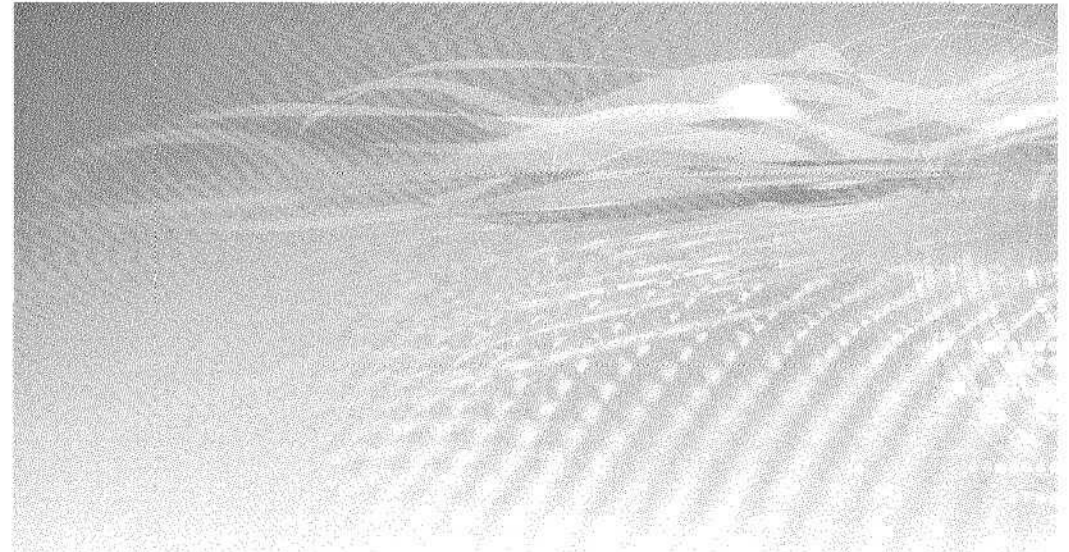
Editors

 World Scientific

Proceedings of the 11th Italian Conference

# **Sensors** and **Microsystems**

**This page intentionally left blank**



Proceedings of the 11th Italian Conference

# Sensors and Microsystems

Lecce, Italy

8 – 10 February 2006

Editors

**P Siciliano**

CNR-IMM, Italy

**S Capone**

CNR-IMM, Italy

**C Di Natale**

University of Rome "Tor Vergata", Italy

**A D'Amico**

University of Rome "Tor Vergata", Italy

 **World Scientific**

NEW JERSEY • LONDON • SINGAPORE • BEIJING • SHANGHAI • HONG KONG • TAIPEI • CHENNAI



*Published by*

World Scientific Publishing Co. Pte. Ltd.

5 Toh Tuck Link, Singapore 596224

*USA office:* 27 Warren Street, Suite 401-402, Hackensack, NJ 07601

*UK office:* 57 Shelton Street, Covent Garden, London WC2H 9HE

**British Library Cataloguing-in-Publication Data**

A catalogue record for this book is available from the British Library.

**SENSORS AND MICROSYSTEMS**

**Proceedings of the 11th Italian Conference**

Copyright © 2008 by World Scientific Publishing Co. Pte. Ltd.

*All rights reserved. This book, or parts thereof, may not be reproduced in any form or by any means, electronic or mechanical, including photocopying, recording or any information storage and retrieval system now known or to be invented, without written permission from the Publisher.*

For photocopying of material in this volume, please pay a copying fee through the Copyright Clearance Center, Inc., 222 Rosewood Drive, Danvers, MA 01923, USA. In this case permission to photocopy is not required from the publisher.

ISBN-13 978-981-279-338-6

ISBN-10 981-279-338-0

## Foreword

This book contains a selection of the contributions presented and discussed during the 11<sup>th</sup> AISEM (Associazione Italiana Sensori e Microsistemi) National Conference on Sensors and Microsystems, held in Lecce, Italy, on February 8-10, 2006.

The Conference has been organized by the Institute for Microelectronics and Microsystems (IMM-CNR) of the National Council of Research. In comparison with the other editions this one has been organized having in mind the idea to emphasize the scientific talent of the young researchers, who are considered to be the future resources of the Science, in general, and of Sensors and Microsystems area, in particular. To this aim, the poster and oral presentations, included invited, after an evaluation and selection based on the scientific contents, were strongly recommended by young researchers. Even if this edition of the Conference could be remembered with the slogan “AISEM for Younger”, it will anyway provide, as usual, a strong opportunity for the presentation of updates results to both theoretical and applied research in the field of Sensors and Microsystems bringing together scientists from academic institutions and industry.

We would like to thank all the people who gave their contributions for the successful organisation of the Conference, in particular the members of the Steering and Scientific Committees of AISEM and mainly the members of the Local Scientific and Organising Committees belonging to the Sensors and Microsystems staff of IMM-CNR in Lecce.

Particularly thanks are due to the various institutions and companies, which sponsors the event giving their support for the organisation of the Conference.

Pietro Siciliano  
Simonetta Capone  
Corrado Di Natale  
Arnaldo D'Amico

**This page intentionally left blank**



## THE 11<sup>TH</sup> NATIONAL CONFERENCE ON SENSORS AND MICROSISTEMI

Lecce, Italy  
8-10 February, 2006

### Conference chair

Pietro Siciliano, IMM-CNR, Lecce

### STEERING COMMITTEE

A. D'Amico *Univ. Roma "Tor Vergata"*  
L. Campanella *Univ. Roma "La Sapienza"*  
P. De Gasperis *CNR-IMM, Roma*  
C. Mari *Univ. Milano*  
G. Martinelli *Univ. Ferrara*  
U. Mastromatteo *ST Microelectronics*  
A.G. Mignani *CNR-IFAC, Firenze*  
M. Prudenziati *Univ. Modena*  
G. Sberveglieri *Univ. Brescia*  
P. Siciliano *CNR-IMM, Lecce*  
G. Soncini *Univ. Trento*

### SCIENTIFIC COMMITTEE

F. Davide *Telecom Italia*  
A. Diligenti *Univ. Pisa*  
C. Di Natale *Univ. Roma "Tor Vergata"*  
L. Dori *CNR-IMM, Bologna*  
G. Faglia *Univ. Brescia*  
C. Malvicino *CRFIAT, Orbassano (TO)*  
M. Mascini *Univ. Firenze*  
B. Morten *Univ. Modena*  
G. Palleschi *Univ. Roma "Tor Vergata"*  
F. Villa *ST Microelectronics*  
M. Zen *ITC-IRST, Trento*

### LOCAL ORGANISATION

#### Local scientific committee

Simonetta Capone  
Cosimo Distante  
Mauro Epifani  
Roberto Rella  
Andrea Baschirottto

#### Local Organisation committee

Francesco Buccolieri  
Angiola Forleo  
Luca Francioso  
Alessandro Leone  
Maria Grazia Manera  
Jolanda Spadavecchia  
Antonella M. Taurino  
Dominique S. Presicce  
Marzia Zuppa



**This page intentionally left blank**

## CONTENTS

### CHEMICALS SENSORS

- F. D'amato, P. Mazzinghi, S. Viciani, P.W. Werle*  
Tunable Diode Laser Spectrometers (TDLS's) as Airborne In-situ Sensors for Stratospheric Trace Gases.....1
- D. Monti, G. Ercolani, R. Paolesse, M. Scarselli, P. Castrucci, M. De Crescenzi*  
Self-Organization of Tetrphenylporphyrin on HOPG. Unprecedented Double-Layer Pattern Driven by Adsorption Compression. ....6
- A. Bonavita, G.Neri, G. Micali, G. Rizzo, N. Pinna, M. Niederberger*  
A Room Temperature Pt/In<sub>2</sub>O<sub>3</sub>-based Oxygen Sensor.....13
- E. Sgreccia, A. Macagnano, E. Dalcanale, C. Di Natale, R. Paolesse*  
A Study of Mass Effect in a Cavitand Supramolecular Sensor .....18
- A. Cusano, A. Iadicicco, P. Pilla, L. Contessa, A. Cutolo, S. Campopiano, M. Giordano*  
Polymer Coated Long Period Gratings: New Perspectives as High Sensitivity Chemical Sensors.....23
- M. Consales, A. Cutolo, A. Cusano, S. Campopiano, M. Penza, P. Aversa, G. Cassano, M. Giordano*  
Optical Fiber Sensors for Hydrogen Detection at Cryogenic Temperatures .....28
- G. Barillaro, A. Diligenti, L. M. Strambini*  
Silicon  $p^+n$  Mesa Junction with a Porous Layer as Sensing Element.....33
- A. De Girolamo Del Mauro, L. Quercia, F. Loffredo, G. Di Francia*  
Influence of Solvent on Thin Film Composite Morphologies and Sensing Properties .....38
- G. Neri, A. Bonavita, G. Micali, F. A. Deorsola, I. Amato, B. De Benedetti*  
Gas Sensing Properties of Nanostructured Titania: A Comparative Study of Different Preparation Methods .....43

<i>S. Kandasamy, A. Trinchi, W. Wlodarsky, E. Comini, G. Sberveglieri, L. Pandolfi, S. Kaciulis</i> Hydrocarbon Sensing Device Based on Binary Metal Oxides.....	48
<i>A. Iadicicco, D. Paladino, A. Cutolo, A. Cusano, S. Campopiano, M. Giordano</i> Multi-Cavity Structured FBGs: Towards Advanced Chemical Sensing Devices .....	53
<i>A.G. Mignani, L. Ciaccheri</i> Belgian Beer Mapping and Digital Fingerprinting using Color and Turbidity Assessment.....	58
<i>C. Cucci, A.G. Mignani, C. Dall'Asta, G. Galaverna, A. Dossena, R. Marchelli, R. Pela</i> A Portable Fluorometer for the Rapid Screening of M1 Aflatoxin in Milk .....	63
<i>A.G. Mignani, L. Ciaccheri, A.A. Mencaglia, R. Paolesse, C. Di Natale, A. Del Nobile, R. Benedetto, A. Mentana</i> Quality Monitoring of Extra-virgin Olive Oil using an Optical Sensor .....	68
<i>R. Bernini, F. Mottola, A. Minardo, L. Zeni</i> Spectral Interrogation of Optical Metal-Cladding Waveguides for Chemical Sensing.....	73
<i>M. Buzzolani, M. Butturi, C. Malagù, G. Martinelli, B. Vendemmiati</i> Application of Quality Standard for the Planning, Design and Realisation of Thick Film Gas Sensors.....	78
<i>M. Pisco, M. Consales, A. Cutolo, A. Cusano, S. Campopiano, M. Giordano, M. Penza, P. Aversa, G. Cassano</i> A Photonic Bandgap Fiber Sensor Based on Single Walled Carbon Nanotubes as Sensing Material .....	81
<i>L. Longo, G. Vasapollo, R. A. Picca, C. Malitesta</i> Synthesis and Selective Nucleoside Recognition of a New Substituted Zinc-phthalocyanine.....	86
<i>V. Biagiotti, F. Valentini, D. Moscone, G. Palleschi</i> Synthesis and Characterization of Nanomaterial as Sensitive Platform to Assemble Selective Chemical Sensors for NO <sub>2</sub> Detection.....	91

<i>S. Capone, P. Siciliano, A.M. Taurino, I. Hotovy, V. Rehacek</i> Modified p-type NiO Thin Films using Pt- and Au-overlayers for H <sub>2</sub> Sensing...	97
<i>V. Marotta, S. Orlando, B. Mitu</i> Multilayered Metal Oxide Thin Film Gas Sensors Obtained by Conventional and RF Plasma-assisted Laser Ablation .....	102
<i>M. Tonezzer, A. Quaranta, G. Della Mea, G. Maggioni, S. Carturan</i> A New Competitive Technique for the Production of Porphyrin Thin Films: The Glow Discharge Induced Sublimation (GDS).....	107
<i>S. Carturan, M. Bonafini, G. Maggioni, A. Quaranta, M. Tonezzer, G. Della Mea, G. Mattei, C. de Julián Fernandez, P. Mazzoldi</i> Optical Sensing to Organic Vapors of Fluorinated Polyimide Nanocomposites containing Silver Nanoclusters .....	112

## PHYSICAL SENSORS

<i>P. Bruschi, N. Nizza, M. Piotto, M. Schipani</i> Solid State Directional Anemometer for Harsh Environments .....	117
<i>C. Calaza, N. Viarani, G. Pedretti, M. Gottardi, V. Zanini, A. Simoni</i> A Focal Plane Array based on CMOS Uncooled Thermoelectric Infrared Detectors .....	122
<i>A. Baschiroto, E. Melissano, P. Siciliano, E. Dallago, P. Malcovati, M. Marchesi, G. Venchi</i> A 2-D Planar Microfluxgate with Sputtered Core.....	127
<i>L. Ciccarelli, M. Medugno</i> An Optical Probe for RF Electric Field .....	132
<i>S. D'Addio, A. Cusano, A. Tutolo, S. Campopiano, M. Giordano, M. Balbi, S. Balzarini</i> Coated Fiber Bragg Grating As High Sensitivity Hydrophone .....	137
<i>M. A. Ferrara, L. Sirleto, G. Messina, M. G. Donato, L. Rotiroti, I. Rendina</i> Strain Measurements in Porous Silicon by Raman Scattering .....	142



<i>C. Ambrosino, P. Capoluongo, D. Davino, C. Visone, A. Cutolo, A. Cusano, S. Campopiano, M. Giordano</i> Fiber Bragg Gratings and Magnetic Shape Memory Alloys: A Novel High Sensitivity Magnetic Sensor.....	147
<i>F. Mancarella, A. Roncaglia, M. Passini, G. C. Cardinali, M. Severi</i> A Computationally Efficient Model for Thermal Sensors Simulation .....	152
<i>L. Rossi, G. Breglio, A. Irace, P. Spirito</i> Characterization of a Point-Wise Close Electric Field Sampling System Exploiting the Electro-Optic Effect .....	157
<i>D. Caputo, G. de Cesare, A. Nascetti, R. Scipinotti</i> On The Realization of Chromium Silicide Stress Sensor.....	162

## BIOSENSORS

<i>F. Olimpico, M. Pighini, S. Bernardi, A. Scarpa and S. Greco</i> Nanogravimetric Immunodetection of Gliadin by $\mu$ Libra Balance.....	167
<i>R. Bernini, E. De Nuccio, A. Minardo, L. Zeni, P. M. Sarro</i> Integrated Silicon Micro Flow Cytometer based on Hollow Arrow Waveguides.....	172
<i>S. Kaciulis, A. Mezzi, A. Galdikas, V. Bukauskas, A. Mironas, A. Šetkus, V. Laurinavičius, R. Meškys, J. Razumienė</i> Properties of Heme c Containing Enzyme Layer Self-assembled on Planar Metallic Electrodes .....	177
<i>D. Caputo, G. de Cesare, A. Nascetti, R. Scipinotti, R. Negri, A. Tarquini</i> Detection of Labelled DNA Based on Amorphous Silicon Devices.....	182
<i>L. Campanella, E. Martini, D. Lelo, M. Tomassetti</i> Carbamate, Triazinic and Benzotriazinic Pesticide Analysis using an Inhibition Tyrosinase Organic Phase Enzyme Sensor.....	187
<i>D. Dell'Atti, M. Minunni, S. Tombelli, M. Mascini, A. Cavazzana, M. Zavaglia, G. Bevilacqua</i> DNA-based Piezoelectric Biosensor for Human Papilloma Virus (HPV) Detection.....	193

<i>M. Del Carlo, M. Mascini, D. Compagnone, A. Visconti</i> User Friendly Electrochemical Hand-Held Device for Durum Wheat Safety.....	198
--	-----

<i>L. Campanella, E. Martini, M. Tomassetti</i> Determination of Immunoglobulin G in Human Serum by Means of an Immunosensor fitted with an Enzymatic Probe as Detector and a Clark Electrode as Transducer.....	203
---	-----

<i>M.G. Manera, J. Spadavecchia, R. Rella, A. Leone, D. Dell'Atti, M. Minunni, M. Mascini</i> SPR Imaging Technique: A Study on DNA-DNA Biological Interactions.....	209
---	-----

## **MICRO- AND NANO-TECHNOLOGY: MATERIALS AND PROCESS**

<i>R. Aina, G. Barlocchi, M. Cattaneo, P. Corona, A. Fischetti, M. Marchi, U. Mastromatteo, M. Palmieri, M. Pesaturo, F. Villa, A. Vinay</i> Lab-on-chip Integrated Genetic Analysis.....	217
--	-----

<i>S. Zampolli, I. Elmi, G.C. Cardinali, M. Severi, E. Dalcanale, P. Betti</i> Use of Cavitands as Selective Adsorbing Materials in GC-like Air Quality Monitoring Microsystems .....	222
---	-----

<i>L. De Stefano, I. Rea, L. Rotiroti, K. Malecki, I. Rendina, L. Moretti, F. G. Della Corte</i> Fast Optical Detection of Chemical Substances in Integrated Silicon-glass Chip .....	227
---	-----

<i>M. Scandiuzzo, D. Stoppa, A. Simoni, L. Pancheri, G.-F. Dalla Betta</i> CMOS Single Photon Avalanche Diode for Imaging Applications .....	232
---	-----

<i>M. Bellei, R. Gaddi, A. Gnudi</i> Design of a MEMS Test-Structure for Stress Characterization by Capacitive Read-out.....	237
--	-----

<i>A. Castaldo, E. Massera, L. Quercia, G. Di Francia</i> Controlling Sensing Properties of Composite Polymers using Different Conductive Nanoparticles.....	242
--	-----

<i>W. Vastarella, M. De Leo, J. Maly, A. Masci, L.M. Moretto, R. Pilloton</i> Biosensors Based on Nano Electrode Ensemble and Screen Printed Substrates .....	247
<i>G. Barillaro, A. Nannini</i> Buried Microchannels by Electrochemical Etching of Silicon.....	252
<i>F. Siviero, N. Coppedè, L. Aversa, M. Nardi, A. Pallaoro, T. Toccoli, R. Verucchi, S. Iannotta</i> Gas Sensing Properties of Metal-oxide/Organic Hybrid Materials Grown by Supersonic Beam Deposition .....	257
<i>V. La Ferrara, I. Nasti, E. Massera, B. Alfano, G. Di Francia</i> Focused Ion Beam in Gas Sensor Technology.....	262
<i>F. Mancarella, A. Roncaglia, S. Cristiani, G.C. Cardinali, M. Severi</i> Process Dependence of Doped Polysilicon Thermal Conductivity for Thermal MEMS Applications.....	267
<i>M. Grassi, P. Malcovati, S. Capone, L. Francioso, P. Siciliano, A. Baschiroto</i> Gas Sensing System Consisting in MOX-based Microsensors Interfaced to a Novel Integrated 5-decade Dynamic Range Front-end .....	272
<i>V. La Ferrara, I. Nasti, E. Massera, G. Di Francia</i> Polymeric Replicas from Porous Silicon Template (and Its Response to Vapour).....	278
<i>C. Bonomo, L. Fortuna, P. Giannone, S. Graziani, S. Strazzeri</i> A Software Tool for the Simulation of IPMC Actuators and Sensors.....	282
<i>R. A. Picca, C. Malitesta, D. Manno</i> Synthesis and Characterization of Imprinted TiO <sub>2</sub> Nanoparticles. Preliminary results .....	287
<i>M. Schipani, T. Ungaretti, P. Bruschi, N. Nizza</i> A Single Chip General Purpose Circuit for Sensor Interfacing and Characterization.....	292
<i>F. Dalena, G. Roselli, P. Flora</i> A Three-Axis Low-g Ultracompact Linear Accelerometer .....	297

<i>F. Lo Castro, A. D'Amico, G. Brambilla</i> Vehicle Health and Comfort Level Measurement: A Preliminary Study .....	302
<i>F. Lo Castro, P. Bisegna</i> Forced Damping Vibration of a Cantilever Beam.....	307
<i>W. Vastarella, M. Ilie, L. Nardi, A. Masci, R. Pilloton, E. Cianci, S. Quaresima, A. Coppa, V. Foglietti</i> Improved Capillaries Connection to a Continuous Flow Glass Micromachined Micro-cell .....	312

## SENSOR ARRAY AND MULTISENSORIAL SYSTEMS

<i>S. Centi, S. Laschi, I. Palchetti, M. Mascini</i> Simultaneous Detection of Polychlorinated Biphenyls (PCBS) by Means of an Electrochemical Disposable Multiarray Sensor .....	317
<i>G. Pioggia, F. Di Francesco, G. Campobello, G. Cannatà, N. Donato, A. Bonavita, G. Micali, G. Neri</i> Integrated Microgravimetric Set-up for Chemical Sensing.....	322
<i>S. De Vito, E. Massera, L. Quercia, G. Di Francia</i> In-Situ Monitoring of Volcanic Gases at Solfatara Crater with Hybrid e-nose.....	328
<i>M.C. Carotta, E. Ferrari, S. Gherardi, C. Malagù, M. Piga, G. Martinelli, A. Rosignoli</i> Monitoring of Airborne Fine Particles and NO <sub>x</sub> Beside a Major Road.....	334
<i>G. Ferri, V. Stornelli, F. Ruscitti, C. Falconi, A. D'Amico</i> A Dynamic-element Matched CCII for Smart Sensors .....	339
<i>C. Moriconi, M. Santoro</i> Multisensor Layout for Robots in Hostile Environments.....	344

## SENSOR NETWORK AND DATA ANALYSIS FOR SENSORS

<i>D. Blasi, V. Cacace, L. Casone, M. Rizzello</i> Wireless Sensor Networks Overview, Looking at the ZIGBEE Architecture...	349
--	-----



<i>M. Conti, E. Gregari, G. Valente, G. Anastasi, C. Spagoni</i> Motes Sensor Networks in Dynamic Scenarios: A Performance Study for Pervasive Applications in Urban Environments.....	354
<i>M. Rizzello, A. Gentile, F. Versori</i> Portable Software Tools for Configuring a IEEE 802.15.4 WSN with Mobile Devices .....	359
<i>M. Cicioni, A. Scorzoni, F. Alimenti, P. Placidi, L. Roselli, S. Zampolli, I. Elmi, G.C. Cardinali, M. Severi, S. Marco, J.M. Gómez, F. Palacio, B. Mazzolai, A. Mondini, V. Raffa, V. Mattoli, P. Dario, R. Ingles Bort, J. L. Ramirez, E. Llobet, E. Abad, T. Becker</i> Low-Power Sensor Front-End Electronics With RFID Communication Capabilities For Food Logistic Datalogging Applications .....	364
<i>M. Medugno</i> A Neural Spectral Classifier for Optical Sensors .....	369
<i>G. Barillaro, P. Bruschi, R.G. Garroppo, S. Giordano, A. Molfese, F. Pieri</i> Design of a Wireless Sensor Network for Urban Pollution Monitoring .....	374
<i>M. Zuppa, A.M. Taurino, C. Distante, D. Presicce, S. Capone, L. Francioso, P. Siciliano</i> Application of Multi-sensor Miniaturized System for Olive Oil Evaluation.....	379
<i>G. Ferri, V. Stornelli, A. De Marcellis F. Mancini</i> Low Voltage Low Power Improved CCII Based Interface for the Measure and Heating Control of Resistive Sensors.....	384

# TUNABLE DIODE LASER SPECTROMETERS (TDLS'S) AS AIRBORNE IN-SITU SENSORS FOR STRATOSPHERIC TRACE GASES

F. D'AMATO, P. MAZZINGHI, S. VICIANI, P.W. WERLE  
*CNR – Istituto Nazionale di Ottica Applicata, L.go E. Fermi 6  
50125 Firenze, Italy*

In this paper two spectrometers will be described, based on tunable diode lasers, suitable for operation on board of a stratospheric aircraft. These instruments are used to carry out measurements about production, transformation and transportation of atmospheric constituents. The principles of operation, the environmental constraints, the technological solutions and some results will be shown.

## 1. Introduction

The knowledge of our atmosphere is a fundamental issue for both understanding some important phenomena, like greenhouse effect, ozone depletion, climate changes, and adopting the necessary countermeasures. While most of the antropogenic emissions occur close to the ground, some natural important productions of gaseous species are distributed all along the height of the troposphere: volcanic emissions of HCl and HF, nitrogen oxides from lightening, etc. A major role in the distribution of the gaseous species in the atmosphere is played by the tropopause, the thermal inversion layer which divides the troposphere from the stratosphere. There is presently one aircraft only, which can carry a payload of 1500 kg up to a height of 21000 m. It's the Myasishev M55 "Geophysica", a Russian plane built for military purposes, and then transferred to a private company and equipped to host several instruments, based on different principles, which can measure different atmospheric parameters (dust, water content, ozone, NO<sub>x</sub>, CFC's, etc.). There are many constraints for devices to be mounted on board of such an aircraft:

1. The power supply on board is either 28 VDC or 110 VAC, 400 Hz. There are limitations on the available power, whose stability is not the same as in one's laboratory.
2. Pressure ranges from 1000 to 50 mBar, temperature from -70 to +50 °C.
3. All instruments must pass the EMI test suitable for this kind of platform.

4. Mechanical design must keep into account vibrations, and instruments must pass severe vibration tests.

## 2. The instruments

Both instruments are based on the Beer-Lambert law:

$$I_{out} = I_{in} \cdot e^{-\alpha L}, \quad (1)$$

where  $I_{out}$ ,  $I_{in}$  are the powers of the light beam respectively at the exit and at the entrance of the sample,  $L$  is the length of the sample and:

$$\alpha = S \cdot g(\nu) \cdot n. \quad (2)$$

In (2)  $S$  is the strength of the absorption,  $g$  is the absorption profile vs frequency and  $n$  is the density of the absorbing molecules. Once  $\nu$  and  $L$  are fixed, the density  $n$  can be retrieved from the absorption measurements, provided that temperature and pressure are known. The optical pathlength should be maximized, but a compromise must be found with the transmission and the dimensions of the multipass cell. When the absorption is of the order of 1%, the detection technique of direct absorption can be easily employed, when the absorbance is lower than this value it is usual to adopt more effective detection techniques, in order to enhance the S/N ratio. Now we enter into the details of the two instruments, for which two quite different layouts have been selected.

### 2.1. Measurement of CO

The starting point for the measurement of CO is the analysis of its infrared absorption spectrum. This species has its fundamental absorption band around  $2140 \text{ cm}^{-1}$  ( $4.67 \text{ }\mu\text{m}$ ). In this region lead salts diode lasers are available, and the main interferences come from water, carbon dioxide and nitrogen oxide ( $\text{N}_2\text{O}$ ). The use of lead salts lasers results in a serious constraint to the experimental apparatus. This sources require cryogenic temperatures for operation, and the same holds for the detectors in the middle infrared. The simplest solution is a Dewar, filled with liquid nitrogen, containing both laser and detector. In order to ensure the stability of the boiling point of nitrogen, the Dewar must be pressurized. The optics layout of this instrument is shown in Figure 1 [1]. The white disk in the center of Fig. 1 is the cover of the Dewar. The laser beam exits from the upper left side. Part of the beam is reflected by a beam splitter.

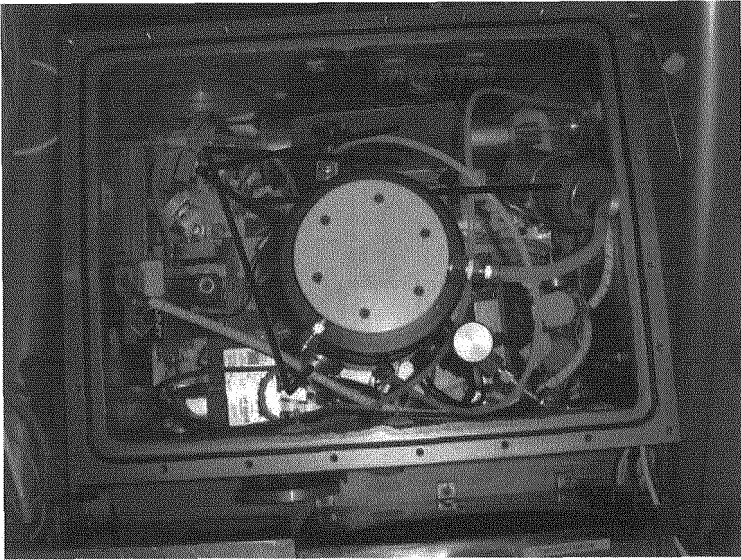


Figure 1. Photo of the optical layout of the CO analyzer.

This beam reaches a reference detector at room temperature, after passing across a cell filled with pure CO and a ZnSe etalon, for relative frequency reference. The main part of the beam enters a multipass cell (36 m pathlength), and then is focused onto a detector, placed in the same Dewar. The air flow through the multipass cell is driven by a small pump, which operates only at altitudes greater than 5000 m, in order to avoid blowing dust or raindrops into the cell.

The detection technique is direct absorption. The laser frequency is scanned across an absorption line at 1 kHz repetition frequency. The signals from the two detectors are digitized with 12 bit vertical resolution, and averaged over 2000 scans. The data processing is carried out off-line, after landing.

A typical result, obtained during a measurement campaign in Brazil in January/February 2005, is shown in Fig. 2. Such results are related to those coming from other instruments, detecting ozone, NO<sub>x</sub>, etc.

### 3. Measurement of methane

The instrument for methane detection has been designed [2] by keeping into account some specific constraints: the volume and the shape of the available space, the maximum weight and power consumption.



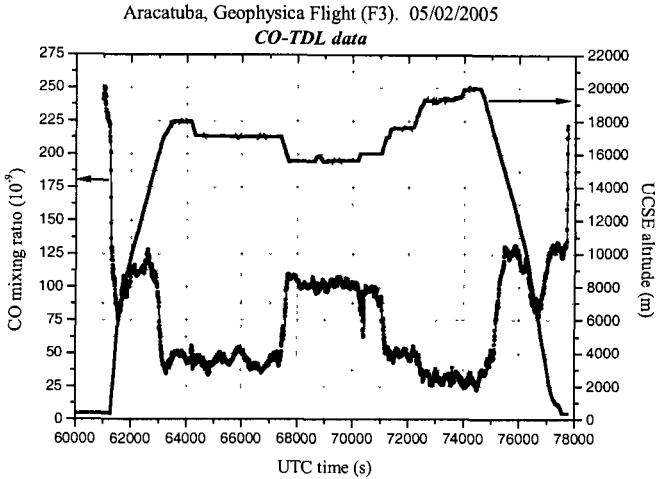


Figure 2a. CO mixing ratio vs time during a flight in Araçatuba (BR) in February 2005.

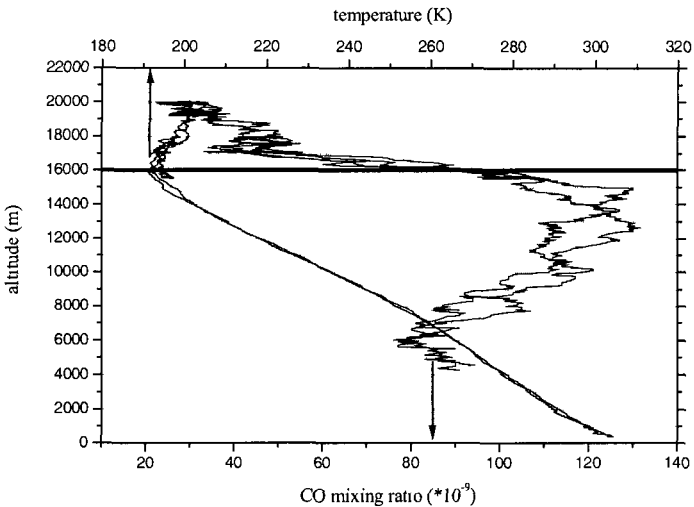


Figure 2b. Profiles of CO mixing ratio and temperature with height. The horizontal line corresponds to the tropopause.

For the limitations above it was not possible to have a pressurized vessel and to use liquid nitrogen, so that a room temperature diode laser had to be employed. The optical setup is very similar to that of the CO analyzer but, due to the low strength of the absorption lines in the near infrared, a more effective

detection technique, the so called two-tone frequency modulation [3], had to be adopted. A typical result is shown in Fig. 3.

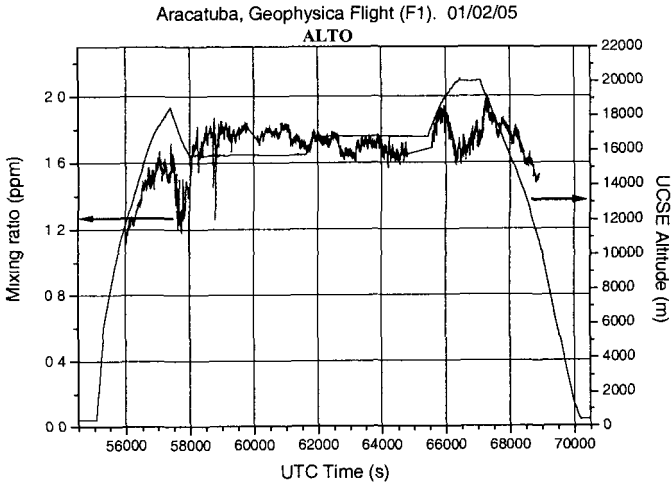


Figure 3 CH<sub>4</sub> mixing ratio vs time during a flight in Araçatuba (BR) in February 2005.

#### 4. Conclusions

Diode laser based analyzer have proved to be useful for fast and sensitive detection of trace gases in the lower stratosphere. The data obtained during the measurement campaigns are being used for environmental analysis.

#### 5. Acknowledgments

This activity has been supported by the European Community through contract TROCCINOX.

#### 6. References

1. G. Toci, P. Mazzinghi, B. Mielke and L. Stefanutti: "An Airborne Diode Laser Spectrometer for the Simultaneous Measurement of H<sub>2</sub>O and HNO<sub>3</sub> Content of Stratospheric Cirrus Clouds", *Opt. & Las. in Eng.* 37, pp. 459-480 (2002)
2. F. D'Amato, P. Mazzinghi and F. Castagnoli: "Methane analyzer based on TDL's for measurements in the lower stratosphere: design and laboratory tests", *Appl. Phys. B* 75, 195-202 (2002)
3. G.R. Janik, C.B. Carlisle, and T.F. Gallagher: "Two-tone frequency-modulation spectroscopy", *J. Opt. Soc. Am.* B3, pp.1070-1074 (1986)

# Self-Organization of Tetraphenylporphyrin on HOPG. Unprecedented Double-Layer Pattern Driven by Adsorption Compression

Donato Monti, Gianfranco Ercolani, Roberto Paolesse

*Dipartimento di Scienze e Tecnologie Chimiche, Università di Tor Vergata, Via della Ricerca Scientifica, Roma, Italy. E-mail: [monti@stc.uniroma2.it](mailto:monti@stc.uniroma2.it)*

Manuela Scarselli, Paola Castrucci, Maurizio De Crescenzi

*Dipartimento di Fisica, Università di Tor Vergata, Via della Ricerca Scientifica, Roma, Italy.*

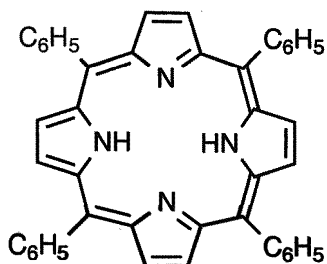
## Summary

Combined Scanning Tunneling Microscopy (STM), X-Ray photoelectron spectroscopy (XPS), Reflection Electron Energy Loss Spectroscopy (REELS) studies have been performed *in situ* under ultra high vacuum condition (UHV), on tetraphenylporphyrin (H<sub>2</sub>TPP) molecules sublimated on highly oriented pyrolytic graphite (HOPG). The results obtained indicate the formation of a well-ordered two-layer structure of H<sub>2</sub>TPP molecules. The first adlayer appears as a densely packed uniform background and closely bound to the substrate as indicated by XPS and REELS measurements. STM images of the second layer, lying above the first one, consists of H<sub>2</sub>TPP molecules arranged according to a quasi-hexagonal lattice with a periodicity of 3.0 nm. This loose unusual arrangement has been investigated by molecular mechanics modeling of the system (MMFF94 force field). The computational results suggest that the second layer, lacking the driving force provided by the interaction with the substrate, would be less densely packed. In particular, each molecule of the second layer, with respect to the arrangement of the first layer, would have its nearest neighbors missing so as to avoid adsorption compression. Accordingly the periodicity of the second layer would be twice that calculated for the first layer. The MMFF94 calculations match perfectly with the observed periodicity lending support to the title hypothesis.

## 1 Introduction

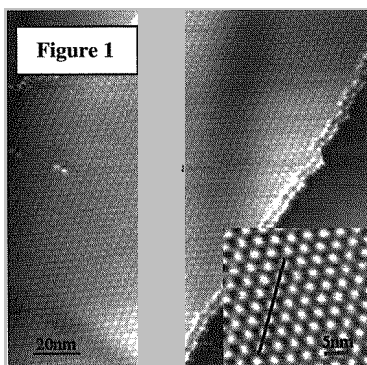
The quest for morphologically defined molecular assemblies, with controlled size and shape, onto solid surfaces, is a mandatory issue not only for fundamental advancements in materials science [1] but also for the development of molecule-based nano-devices and electronics [2]. In this respect porphyrin derivatives and related congeners are playing an increasingly important role as molecular components of optical devices [3], chemical sensors [4], and functional supramolecular materials [5]. Several strategies can be followed for the deposition of porphyrins on solid surfaces with controlled features; mostly important are self-assembly of monolayers on gold [6], Langmuir-Blodgett or Langmuir-Schaefer techniques [7], liquid-

phase deposition [8] and vacuum sublimation [9]. Scanning tunneling microscopy (STM) is one of the preferred experimental techniques to directly investigate the adlayers, as it allows direct assessing of the position, the orientation and the packing arrangement of single or complex molecules deposited on solid substrates and the correlation of the morphological information with their electronic properties [10]. To the best of our knowledge, previous studies dealing with porphyrin adlayers, involved either simple metalloporphyrins] or free-base porphyrin derivatives bearing ad-hoc functional groups, such as peripheral alkyl chains [8,11], or carboxylic substituents, which exert stabilization and ordering by Van der Waals forces or hydrogen bonding, respectively. We focused on the study of the simple 5,10,15,20-tetraphenyl-21*H*,23*H*-porphine (i.e. tetraphenylporphyrin, H<sub>2</sub>TPP hereafter), sublimated under UHV conditions on HOPG, through *in situ* STM, X-ray photoelectron spectroscopy (XPS), and Reflection Electron Energy Loss Spectroscopy (REELS). The results, reported here, are discussed in the light of molecular modeling calculations that nicely agree with the information obtained from STM images.



## 2 Results and Discussion

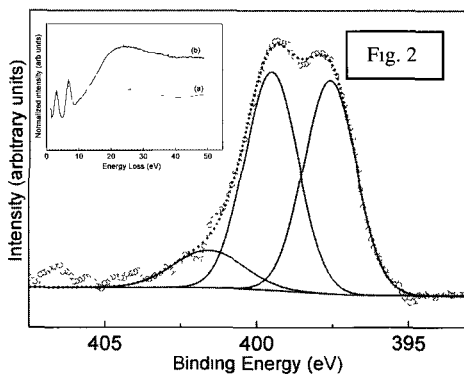
Porphyrin molecules deposited on HOPG by UHV sublimation have been initially studied by STM to investigate spatial arrangement. At very low exposure time, only isolated molecules have been imaged. By increasing the quantity of deposited H<sub>2</sub>TPPs extended areas on the graphite surface result modified by the presence of ordered molecular adlayers extending over areas of hundreds of squared nanometers (STM image in Figure 1). The mean diameter (1.8 nm) and height (0.35 nm)



of each bright spot have been evaluated by averaging the values obtained from profile plots like that reported in Figure 1. The spot diameter matches perfectly the distance of 1.77 nm separating the hydrogens in the *para* positions of opposite phenyl rings of the H<sub>2</sub>TPP structure, as obtained by hybrid density-functional theory geometry optimization carried out at the B3LYP/6-31G(d) level of theory [12,13]. The periodicity of the molecules in

the adlayer turns out to be 3.0 nm, indicating that the Van der Waals surface of each molecule does not come into close contact with those of its nearest neighbors, the minimum separation distance being larger than about 1 nm.

XPS investigation after H<sub>2</sub>TTP sublimation was mainly focused on the binding energy of 1s core level of nitrogen, as reported in Figure 2, evidences two main features at 399.5 eV and 397.6 eV, for the pyrrole type nitrogens and for the imine-type ones, respectively, as previously reported for similar free-base porphyrin derivatives [14]. The energy difference between the N1s

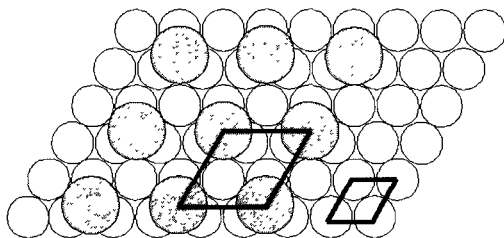


pyrrole type and imine-type energies is about 1.9 eV. An additional structure has been detected at 401.6 eV that can be associated to a strong interaction between carbon atoms of the graphite surface and the H<sub>2</sub>TTP molecule. This assumption can be supported by comparing the reflection energy loss spectra obtained from clean and modified graphite, as reported in Figure 3-Inset. The most significant  $\pi^*$  and  $\sigma^*$  transitions of graphitic carbon result significantly modified after molecules deposition [15]. In particular the original energy position of the two transitions located at about 5.8 eV and 23.9 eV in the HOPG spectrum are shifted at 6.7 eV and 19.6 eV, respectively. The REELS spectrum of the graphite after H<sub>2</sub>TTP deposition shows an additional  $\pi$ - $\pi^*$  feature located at around 3.0 eV (Figure 2, Inset). This new contribution, which is strongly related to the transition involving HOMO and LUMO molecular states of the porphyrins, can be associated to the optical absorption, usually referred as Soret band, that for these molecules occurs at around 2.8 eV. In summary these results indicate the formation of a well-ordered two-layer structure of H<sub>2</sub>TTP molecules on the HOPG surface. The first layer that appears as a uniform background in the STM experiments, about 0.5 nm thick, would be closely bound to the substrate. Although STM failed to give any structural detail of this layer, it showed the ordering of the second layer. In particular it showed that the constituent H<sub>2</sub>TTP molecules are arranged according to a quasi-hexagonal lattice with a periodicity of 3.0 nm indicating that a minimum distance of about 1 nm separates molecules.

These findings, that to the best of our knowledge has not precedents in the porphyrin literature, is surprising; it poses the question of how molecules that do not come in close contact can form such a regular two-dimensional lattice. In order to rationalize the observed results we modelled the system by molecular

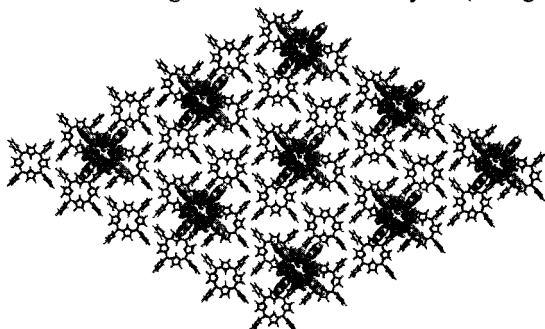
mechanics (MM) calculations by using the Merck Molecular Force Field (MMFF94) developed by Halgren [16]. Our working hypothesis was based on the following reasoning: close-packing of the first layer of  $H_2TPP$  molecules on the graphite surface must be driven primarily by molecule-substrate interactions (adsorption energy) and secondarily by molecule-molecule interactions (two-dimensional crystallization energy). One would normally expect that both interactions are attractive, however if attractions of the molecules to the surface is very strong, molecules are forced to pack to reach greater densities despite this would lead to repulsive forces among them (adsorption compression). This arrangement would affect the packing of the second layer. If attractions of the molecules to the first layer are not as strong as those to the substrate, molecules would lack the driving force to form a second layer as compressed as the first one. This would result in a second layer having the same pattern of the first one, in which, however, the nearest neighbours of each molecule are missing so as to avoid compression (Figure 3).

We first modelled the adsorption of one  $H_2TPP$  molecule on a graphene sheet of the shape of a rhombus consisting of  $30 \times 30$  fused benzenic rings by the MMFF94 force field. The calculated MMFF94 binding energy is  $-33.2 \text{ kcal mol}^{-1}$ .



This value, which is significantly large, could be even underestimated. Indeed MMFF94 evaluates intermolecular interactions by Van der Waals and electrostatic interactions [16], ignoring, as all the MM methods, possible orbital interactions between molecules, which would provide an additional stabilization. In fact XPS and REELS measurements have shown that significant orbital interactions occur between adsorbed  $H_2TPP$  and graphite, indicating an additional electronic stabilization. Considering that the adsorption energy of an isolated molecule is  $-33.2 \text{ kcal mol}^{-1}$ , the two-dimensional crystallization energy of the four molecules is about  $-10 \text{ kcal mol}^{-1}$ , showing favourable attractive interactions among them. Of course such a model is devoid of adsorption compression because the surface available to the molecules was in no way limited. Successively we modelled the absorption of one molecule of  $H_2TPP$  above the compressed unit cell. We carried out a constrained optimization in which the positions of the atoms constituting the compressed unit cell and the graphene layer were frozen, whereas the  $H_2TPP$  molecule constituting the second layer was free to vary its geometry and position [12]. The calculated binding energy of the  $H_2TPP$  molecule constituting the second layer is  $-26.8 \text{ kcal mol}^{-1}$ , which is, as expected, smaller than that of a molecule of the first layer ( $-33.2 \text{ kcal}$

$\text{mol}^{-1}$ ). Apart from the obvious limitations of molecular mechanics, the accordance between the calculated periodicity of the assembly and that measured on the STM images is exceptionally good. Indeed the distance between the porphyrins of the second layer, calculated as twice the distance separating the porphyrins in the compressed layer below, is 3.02 nm to be compared with the experimental distance of *ca.* 3.0 nm. This accordance strongly supports the hypothesis of adsorption compression of the first layer of  $\text{H}_2\text{TPP}$  molecules as the ultimate reason for the observed ordering of the second layer. The calculated vertical distance of the second layer from the graphene sheet is 0.94 nm which is in fair accordance with the average thick of the two layers (background + spot



height) of *ca.* 0.85 nm obtained from STM profile plots (Figure 1). The optimized final structure of the system is shown in Figure 4.

*Fig. 4. Optimised structure of the first layer (tube) and the second layer (space filling) of  $\text{H}_2\text{TPP}$  molecules adsorbed on graphite (not shown for clarity).*

### 3 Experimental

**STM Studies.** Freshly cleaved highly oriented pyrolytic graphite has been introduced in the UHV chamber (base pressure low  $10^{-10}$  Torr) and vacuum sublimation has been performed by heating a tungsten filament previously dipped in a 1%  $\text{H}_2\text{TPP}$  chloroform solution. During the sublimation cycles, the base pressure was kept as low as  $10^{-7}$  Torr and the  $\text{H}_2\text{TPPs}$  deposition rate was estimated from the exposure time and partial pressure, calibrated during preliminary experiments. The sample was characterized *in situ* by X-Ray photoelectron spectroscopy (XPS), Reflection Electron Energy Loss Spectroscopy (REELS) and scanning tunneling microscopy (STM). Scanning tunneling microscopy imaging was performed at room temperature by using an Omicron-STM system. Electrochemically etched tungsten tips were employed for the experiments. STM calibration was done by comparing

images of molecular adsorbates with atomically resolved ones of graphite. All STM images were unfiltered apart from rigid plane subtraction.

**Molecular Modeling Calculations.** The Merck Molecular Force Field (MMFF94) developed by Halgren was the method of choice as its efficiency in modeling porphyrin systems had already been remarked in the literature [17]. MMFF94 calculations were run *in vacuo*, with default parameters and convergence criteria as implemented in the Spartan molecular modeling package (Wavefunction, Inc., Irvine, CA), at the B3LYP/6-31G(d) level of theory [13,18]. Graphite was modeled by a graphene sheet of the shape of a rhombus consisting of 30x30 fused benzenic rings with dangling bonds terminated by hydrogen atoms (formula C<sub>1920</sub>H<sub>122</sub>). Two-dimensional lattices were built with the program GaussView 3.09 (Gaussian, Inc., Pittsburgh, PA). Hybrid density-functional calculations were carried out with the Gaussian 03 program [18].

## References

1. C. F. J. Faul, M. Antonietti, *Adv. Mater.*, 2003, **15**, 673.
2. J. M. Tour, *Acc. Chem. Res.*, 2000, **33**, 791; (b) C. Joachim, J. K. Gimzewski, A. Aviram, *Nature*, 2000, **408**, 541.
3. M. P. Debreczeny, W. A. Svec, M. R. Wasielewski, *Science*, 1996, **274**, 584.
4. R. Paolesse, F. Mandoj, A. Marini, C. Di Natale, *Porphyrin-Based Chemical Sensors* in Encyclopedia of Nanoscience and Nanotechnology, Nalwa, H.S., Ed., American Scientific Publishers CA, 2004, **9**, 21.
5. C. F. Van Nostrum, R. J. M. Nolte, *Chem. Commun.*, 1996, 2385.
6. (a) I. Goldberg, *Chem. Commun.*, 2005, 1243; (b) J.-M. Lehn, *Science*, 2002, **295**, 2400; (c) D. N. Reinhoudt, M. C. Crego-Calama, *Science*, 2002, **295**, 2403.
7. A. Ulmann, *An Introduction of Ultrathin Organic Films, from Langmuir-Blodgett Films to Self-Assembly*, Academic Press, San Diego, CA, 1991.
8. X. Qui, C. Wang, Q. Zeng, B. Xu, S. Yin, H. Wang, S. Xu, C. Bai, *J. Am. Chem. Soc.*, 2000, **122**, 5550.
9. T. Yokoyama, S. Yokoyama, T. Kamidado, Y. Okuno, S. Mashiko, *Nature* 2001, **413**, 619.
10. Wiesendanger (Ed.), *Scanning Probe Microscopy and Spectroscopy*, Cambridge University Press, Cambridge, 1994.
11. S. De Feyter and F. C. De Schryver *J. Phys. Chem. B* 2005, **109**, 4290.
12. A. D. Becke, *J. Chem. Phys.* 1993, **98**, 5648.
13. G. Polzonetti, A. Ferri, M. V. Russo, G. Lucci, S. Licoccia, R. Paolesse, *J. Vac. Sci. Technol. A* 1999, **17**, 832.
14. A. Hoffman, G.L.Nyberg, J. Liesegang, *Phys. Rev. B* 1992, **45**, 567.
15. M. Gouterman, *The Porphyrins*, 1978, **3**, 1, Dolphin D., Ed., Academic, N.Y.



16. T. A. Halgren, *J. Comput. Chem.* 1996, **17**, 490.
17. a) X. Huang, N. Fujioka, G. Pescitelli, F. E. Koehn, T. R. Williamson, K. Nakanishi, N. Berova, *J. Am. Chem. Soc.* 2002, **124**, 10320. (b) G. Pescitelli, S. Gabriel, Y. Wang, J. Fleischhauer, R. W. Woody, N. Berova, *J. Am. Chem. Soc.* 2003, **125**, 7613.
18. Gaussian 03, Revision B.01, Gaussian, Inc., Wallingford CT, 2004.

### **Acknowledgments**

The Authors wish to thank MIUR-FISR “Sensori Ottici ed Elettroottici per Applicazioni Industriali ed Ambientali” (Project SAIA 2003), and MIUR-FIRB (Project No: RBNE01KZZM) for funding.

# A room temperature Pt/In<sub>2</sub>O<sub>3</sub>-based oxygen sensor

A. Bonavita, G. Neri, G. Micali, G. Rizzo

*Dept of Industrial Chemistry and Materials Engineering, University of Messina,  
C/da di Dio, Vill. S. Agata,  
98166 Messina, Italy  
[neri@ingegneria.unime.it](mailto:neri@ingegneria.unime.it)*

N. Pinna

*Martin-Luther-Universität Halle-Wittenberg, Institut für Anorganische Chemie,  
Kurt-Mothes-Strasse 2  
06120 Halle (Saale), Germany*

M. Niederberger

*Max-Planck-Institute of Colloids and Interfaces, 14424 Potsdam, Germany*

## Summary

In this work the effects of Pt-doping and thermal treatments on nanostructured In<sub>2</sub>O<sub>3</sub> powders obtained via nonaqueous sol-gel method were studied with the aim to promote the room temperature sensing characteristics towards oxygen of resistive sensors based on thick films of Pt-doped nanostructured indium oxide powders.

The tested devices have shown very promising sensing characteristics for the O<sub>2</sub> monitoring at room temperature. A synergic effect between the small grain size of In<sub>2</sub>O<sub>3</sub> and the presence of Pt as dopant, opportunely activated via a thermal treatment, is likely at the origin of the behaviour observed.

## 1 Introduction

Oxygen sensing in the low temperature range find its main applicative fields on medical-diagnostic and waste managements. In despite of the obvious advantages given by the use of resistive devices at low working temperature, principally represented by low costs, simple use and assembly and longer lifetimes, few works are reported in literature concerning the application of semiconductor-based devices for application at near room temperature [1-3].

In this work we present a study on the room temperature response towards oxygen of sensing devices based on Pt-doped nanostructured indium oxide. In<sub>2</sub>O<sub>3</sub> is reported to be sensitive to many gases. It is a wide band-gap material, Eg~3.70 eV, whose microstructural, electrical and sensing characteristics have been well studied [4-7]. When prepared in oxygen-deficient form, it reaches n-type doping level due to oxygen vacancies. Further, in order to enhance the sensitivity and get lower operating temperature, In<sub>2</sub>O<sub>3</sub> can be opportunely

prepared in a nanostructured form and/or doped with suitable metallic promoters [8]. The promoting effects on gas sensing characteristics obtainable by reducing the grain size in the nanometric order of magnitude and by doping with noble metal are, in facts, well known. Here we report a study focused on indium oxide nanopowders prepared via a nonaqueous sol-gel method and successively doped with Pt by impregnation, focusing our attention on the effect of metal doping and thermal treatments.

## 2 Experimental

$\text{In}_2\text{O}_3$  nanopowders were synthesised via a nonaqueous sol-gel method involving the solvothermal reaction of indium (III) isopropoxide with benzyl alcohol [8]. The dopant, Pt, has been dispersed on the surface of the semiconducting metal oxide by wetness impregnation, contacting the  $\text{In}_2\text{O}_3$  nanopowders with the proper amount of an aqueous solution of  $\text{H}_2\text{PtCl}_6$ . The preparative and doping routes are schematically reported in Figure 1 .

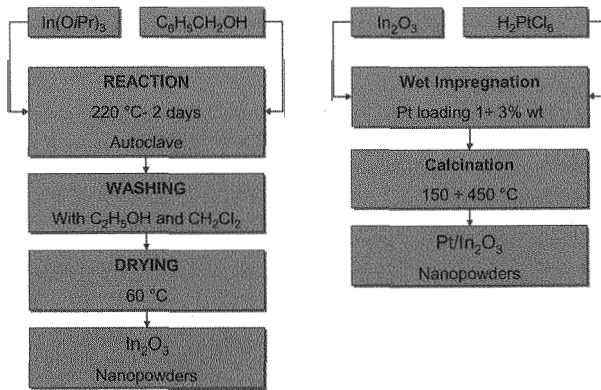


*Fig.1 Preparation and doping routes of  $\text{In}_2\text{O}_3$  nanopowders.*

The nanopowders have been finally dried and fired at controlled temperature (between 150 and 450 °C) in air.

XRD and HRTEM characterization of the synthesized powders were carried out by a Italtstructure diffractometer mod. APD2000 and a Jeol JEM 2010 microscope.

Sensing tests were performed on devices obtained by mixing  $\text{In}_2\text{O}_3$  or Pt-doped  $\text{In}_2\text{O}_3$  powders with water to create a paste which was successively screen-printed on standard alumina substrates ( $3 \times 6 \text{mm}^2$ ) supplied with comb-like electrodes and a Pt-heater. The devices were dried and then treated in air for one hour in order to stabilize the film texture and microstructure.

Resistance measurements were carried out by a Agilent 34970A data acquisition switch unit computer linked, maintaining the sensors under controlled stream of dry nitrogen, and pulsing different O<sub>2</sub> concentrations ranging from 2.5 to 20%.

### 3 Results and discussions

Previous results of microstructural characterization showed a narrow grain size distribution for the In<sub>2</sub>O<sub>3</sub> powders synthesized via the nonaqueous sol-gel method. The mean grain size, calculated by the Sherrer equation and confirmed by TEM analysis (Fig. 2), resulted around 25 nm. The successive impregnation and thermal treatments don't modified the In<sub>2</sub>O<sub>3</sub> microstructure. After the thermal treatment at 350 °C also occurred the decomposition of the Pt precursor salt on the surface of the semiconductor oxide:  $\text{H}_2\text{PtCl}_6 \rightarrow \text{Pt} + \text{H}_2 + 3\text{Cl}_2$ , as well visible in the TEM micrograph.

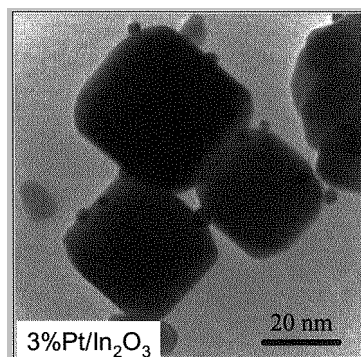


*Fig.2 TEM image of the 3%Pt- In<sub>2</sub>O<sub>3</sub> powder calcined at 350 °C.*

Sensing tests have shown that at room temperature pure In<sub>2</sub>O<sub>3</sub> is not sensitive to oxygen, and Pt addition is necessary to promote the response to O<sub>2</sub>. Figure 3 shows the response dynamic and the calibration curve relative to tests carried out at room temperature with the Pt-doped sensor. Response and recovery times are around 15 min.

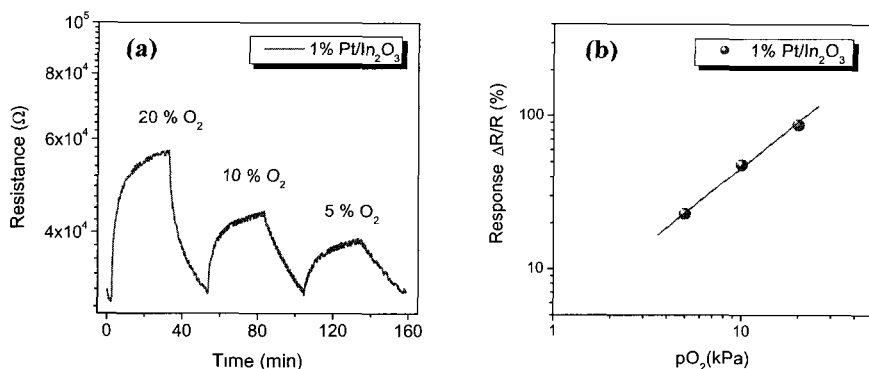


**Fig.3** Transient response at room temperature (a) and calibration curve (b) of the Pt In<sub>2</sub>O<sub>3</sub>-based sensor

Sensing tests have also shown that the pretreatment temperature strongly influence the sensor response. Sensitivity towards oxygen at room temperature has shown a maximum on the sensors treated at 350 °C (Fig. 4). On the basis of characterization results this was directly related to the formation on the surface of the indium oxide grains of small metallic platinum particles.

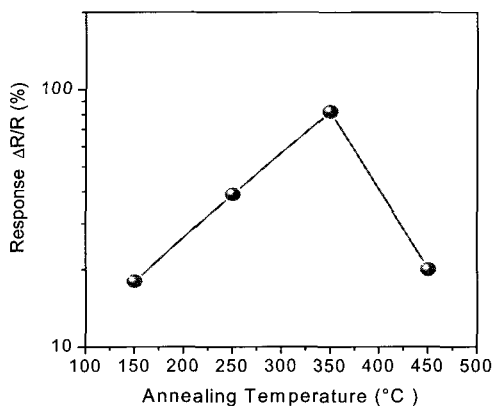


**Fig.4** Effect of the annealing temperature of the Pt/In<sub>2</sub>O<sub>3</sub> film on the response to 20% of O<sub>2</sub>.

## Conclusions

Nanostructured  $\text{In}_2\text{O}_3$  prepared via a non aqueous sol-gel method is a promising material for low temperature  $\text{O}_2$  monitoring. However to promote the response at room temperature doping with Pt is necessary. The annealing temperature at which occurs the decomposition of the Pt precursor influences strongly the sensing performances of Pt/  $\text{In}_2\text{O}_3$ . Therefore an oxygen sensing device operating at room temperature with better performances respect to the existing ones has been fabricated by using  $\text{In}_2\text{O}_3$  nanopowders opportunely activated with Pt.

## References

- [1] F. Chaabouni, M. Abaab, B. Rezig, *Sensors and Actuators B* 100 (2004) 200–204
- [2] Y. Hu, O. K. Tan, J. S. Pan, X. Yao, *J. Phys. Chem. B* 108 (2004) 11214–11218.
- [3] Y. Hu, O. K. Tan, W. Cao, W. Zhu, *Ceram. Int.* 30 (2004) 1819–1822.
- [4] M. Bender, N. Katsarakis, E. Gagaoudakis, E. Hourdakakis, E. Douloufakis, V. Cimalla and G. Kiriakidis *J. Appl. Phys.* 90 (2001) 5382.
- [5] A. Gurlo, M. Ivanovskaya, N. Barsan, M. Schweizer-Berberich, U. Weimar, W. Gopel, A. Dieguez, *Sens. Actuators B* 44 (1997) 327.
- [6] E. Comini, M. Ferroni, V. Guidi, G. Faglia, G. Martinelli and G. Sberveglieri, *Sens. Actuators B* 84 (2002) 26.
- [7] K. Zakrzewska, *Thin Solid Film* 391 (2001) 229; G. Korotcenkov, A. Cerneavski, V. Brinzari, A. Cornet, J. Morante, A. Cabot, J. Arbiol, *Sens. Actuators B* 84 (2002) 37.
- [8] M.I. Baraton in *Nanostructured Materials: Science and Technology*, Nato Advanced Study Institute, Kluwer Academic Publisher, Dordrecht, (1998), 303
- [9] N. Pinna, G. Neri, M. Antonietti, M. Niederberger, *Angew. Chem. Int. Ed.* 43 (2004) 4345.

## Acknowledgments

The authors gratefully acknowledge the financial support for this work by MIUR under the framework of the FIRB-SQuARE project.

## **A study of mass effect in a cavitand supramolecular sensor**

E. Sgreccia, A. Macagnano

*Istituto per la Microelettronica e Microsistemi-Roma, CNR, Via Fosso del  
Cavaliere 100, 00133, Roma*  
[a.macagnano@psm.rm.cnr.it](mailto:a.macagnano@psm.rm.cnr.it)

E. Dalcanale

*Dipartimento di Chimica Organica ed Industriale, Università di Parma, Parco  
Area delle Scienze 17 A, 43100, Parma*

C. Di Natale

*Dipartimento di Ingegneria Elettronica, Università Tor Vergata, Via del  
Politecnico 1, 00133, Roma*

R. Paolesse

*Dipartimento di Scienze e Tecnologie Chimiche, Università Tor Vergata, Via  
della Ricerca Scientifica, 00133, Roma*

### **Summary**

The sensing properties of functionalized cavitand have been studied by thin-films coating TSMRs by measuring their responses towards analytes having different functional groups. We have studied sensing features in term of sensitivity and selectivity and the contribute of viscoelasticity to responses by two growing thickness layers

### **1 Introduction**

In the last few years a great variety of absorbent materials have been synthesized and investigated to improve chemical sensors performances and to develop someone new in order to monitoring specific environments. The structure of a generic chemical sensor can ideally be divided in two subunits: the sensing material and the transducer. The sensing material interacts with the chemical species present in the environment by changing some of its physicochemical properties, while the transducer transforms these variations into a readable signal, generally an electrical signal. The sensor sensitivity, reproducibility and selectivity strictly depend on sensing materials properties.

Advances in supramolecular chemistry offer many opportunities to design and prepare molecules endowed with binding site where multiple interactions can

cooperate to selectively bind a given class of substances; in particular cavitands are molecules where multiple binding interactions are encoded in a single cavitand receptor.

In previous work [1], resorcinarene framework was functionalized, introducing alkyl chains at the lower rim and phosphate or phosphonate substituents at the upper rim, and was used as sensitive film. High selectivity towards short-chain linear alcohols was obtained for molecules having an H-bond acceptor P=O group, oriented inward with respect to the cavity, as a bringing unit at the upper rim of receptor. The purpose of the present work has been to study the sensing features, especially the selectivity towards alcohols, of resorcinarene molecule having four P=O groups oriented inward increasing the film thickness.

Sometimes mass sensors responses is due not only to the mass effect, but also to the viscoelastic properties. In fact mass sensors response is due not only to the mass effect, but also to the film viscoelastic properties. Viscoelastic materials respond to external forces in intermediate manner between elastic solids and viscous liquids, so an acoustic wave that travels in a coated device penetrates into the adjacent (sensitive) film and translates and deforms the film. TSMR reacts to sensitive film deformation as a frequency shift, so it is not yet possible to distinguish between mass and viscoelastic effect [3]. However, electrical parameters analysis can help us to know sensitive film elastic characteristics, especially the plot of the phase of electrical impedance.

## 2 Experimental

The molecular structure of the compound used as sensing material is reported in Figure 1. Resorcinarene molecules were functionalized by introducing alkyl chains at the lower rim and four P=O groups, oriented inward with respect to the cavity, at the upper rim of receptor.

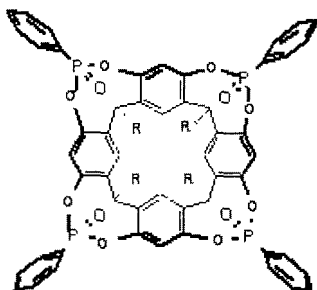


*Fig.1 Resorcinarene molecule functionalized by four P=O groups, oriented inward with respect to the cavity*



Sensors were fabricated using AT-cut quartzes (Electroquarz, Milano) having fundamental frequency of 20 MHz. Two amount of sensitive films (10 kHz and 60 kHz frequency variation) were deposited by spray casting on both sides of QMBs from  $10^{-3}$  M  $\text{CHCl}_3$  solution. In this way mass transducers sensors have been obtained, where the frequency shift is linearly correlated to the mass loading according to the Sauerbrey equation [2]:

$$\Delta f = -k_q \delta m$$

The sensors have been exposed to alcohols (ethanol and isopropanol), aromatics (benzene and toluene), amines (triethylamine) and hydrocarbons (hexane) (reagent grade Aldrich).

### 3 Results and Discussion

Exposure to ethanol vapours shows (Figure 2 (a)) a Langmuir-like responses; the shape of the curves is the result of a complexation between the analyte and the cavitand receptor. The interaction between the film and the analyte doesn't change with the mass increasing but enhance responses and sensitivity (Figure 2 (b)). Sensitivity ( $S = (\partial(\Delta f)/\partial c)$ ) has been calculated, at 50 ppm concentration, fitting the response curves by the Freundlich model:

$$\Delta f = k_q \frac{MW}{N_A} \Gamma c^n$$

(where  $k_q$  is the Sauerbrey constant of the quartz,  $MW$  is the molecular weight,  $N_A$  is the Avogadro number,  $c$  is the concentration,  $G$  and  $n$  are the Freundlich parameters).

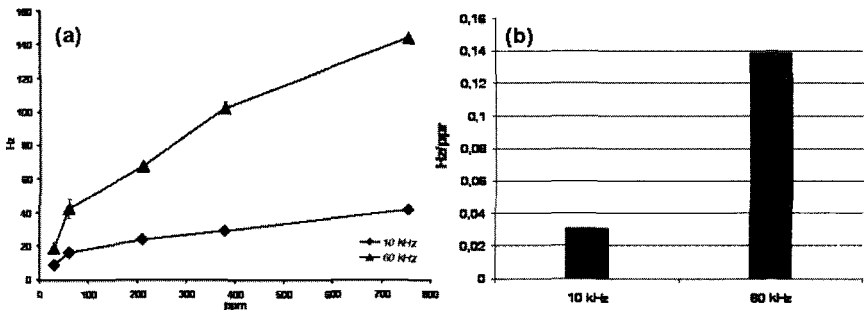


Fig.2 (a) Sensors responses versus increasing ethanol concentration; (b) Sensitivity of different thick layers to ethanol calculated at 50 ppm concentration

Experimental results show a strong contribute of the mass effect for other volatiles too (Figure 3 and Figure 4): higher responses have been obtained not

only to alcohols, but also to aromatics, hydrocarbons and amines (Figure 3). Responses to amines are very high respect to ones other volatiles and sensitivity normalized to molecular weight (1), calculated at 500 ppm concentration, to amines is comparable to one short-chain alcohols (ethanol). Mass increasing doesn't change sensitivity pattern (Figure 4), but increases its value; so the mass increasing of sensitive film improves sensors performances.

$$(1) \quad S = \frac{\partial \left( \frac{\Delta f}{MW} \right)}{\partial c} = \frac{k_q}{N_A} \Gamma n c^{n-1}$$

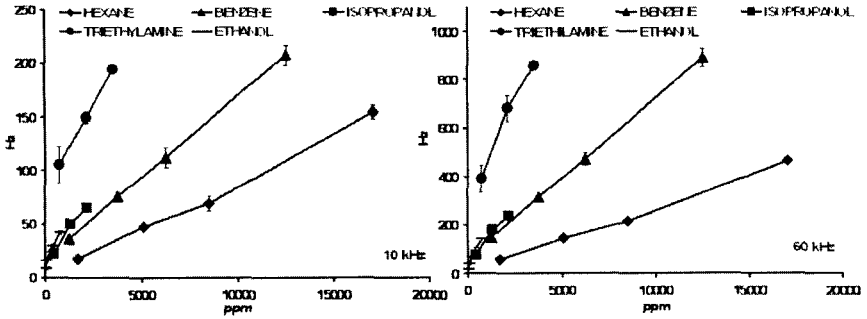


Fig.3 Response curves of 10 kHz and 60 kHz mass deposited versus volatiles

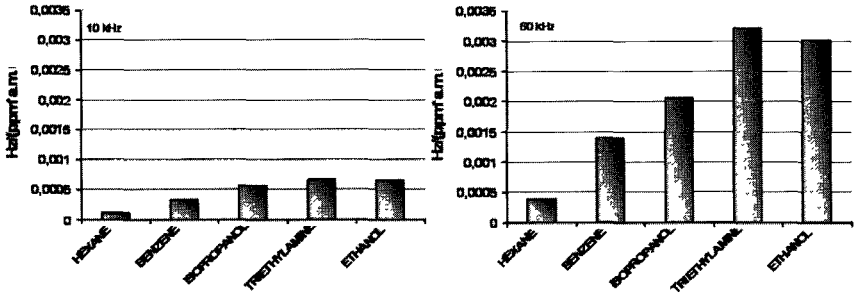


Fig.4 Sensitivity (normalized to molecular weight) at 500 ppm concentration

Sensitive film viscoelastic properties have been investigated by HP8753A Network Analyzer, measuring reflection coefficient. Reflection coefficient ( $S_{11}$ ) is related to electrical impedance by

$$Z = Z_0 \frac{1 + S_{11}}{1 - S_{11}}$$

where  $Z_0$  is  $50 \Omega$ .

Figure 5 shows the phase of the electrical impedance; the shape of this parameter doesn't change with the mass loading and the maximum value doesn't change too. The increasing of the mass loading slightly reduces the width of the resonance, probably it's due to the deposition technique. However mass loading doesn't introduces viscoelastic effect, so the responses observed in previous figures are due only to interactions between cavitands and vapours.

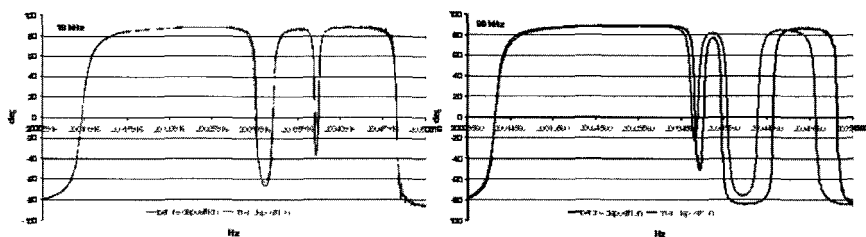


*Fig.5 Phase of electrical impedance before and after sensitive film deposition*

#### 4 Conclusions

The introduction of four P=O group at the upper rim of resorcinarene framework have been enhanced responses to alcohols, especially to linear short-chain alcohols. In the same time, the modification of the molecule introduced a worse selectivity: sensitivity to amines are comparable to ones alcohols.

The growing of thickness of the sensitive film doesn't introduce the increasing of dispersion interactions, so the shape of curves doesn't change, but the responses are enhanced for every volatile examined. For this reason the sensitivity values are increased, while the pattern of its doesn't change.

The increasing of the thickness doesn't introduce viscoelastic effects; in fact electrical parameters and electrical impedance are slightly diminished, so the results obtained are due only to the interactions between sensitive film receptors and volatiles.

#### References

- [1] R. Paolesse, C. Di Natale, S. Nardis, A. Macagnano, A. D'Amico, R. Piali, E. Dalcaneale, *Chemistry – A European Journal*, 9 (2003), 5388
- [2] F. Sauerbrey, *Zeitschrift fur Physik*, 155 (1959), 206
- [3] R. Lucklum, P. Hauptmann, *Sensors and Actuators B*, 70 (2000), 30
- [4] R. Lucklum, C. Behling, P. Hauptmann, *Sensors and Actuators B*, 65 (2000), 277

# **Polymer Coated Long Period Gratings: New Perspectives as High Sensitivity Chemical Sensors**

A. Cusano, A. Iadicicco, P. Pilla, L. Contessa, A. Cutolo  
*Engineering Department, University of Sannio, Benevento Italy*  
[a.cusano@unisannio.it](mailto:a.cusano@unisannio.it)

S. Campopiano  
*Department for Technologies, University of Naples Parthenope, Napoli, Italy*

M. Giordano  
*Institute of Composite Biomedical Materials, National Research Council,  
Napoli, Italy*

## **Summary**

In this work, long period gratings coated with polymeric high refractive index (HRI) thin layers are proposed as high sensitive opto-chemical sensors with tailored sensitivity profile. The deposition of thin coatings with high refractive index (compared to the cladding one) induces strong changes in the field distribution related to the cladding modes. The main effect is a significant change in the sensitivity characteristic to surrounding refractive index (SRI) and to overlay refractive index. Differently from the standard LPG, where the sensitivity to SRI exhibits an exponential form, in HRI coated LPG the sensitivity shows a resonant-like profile. Since the resonant-peak can be centered around the selected SRI by acting on the overlay features (refractive index and thickness), this effect can be efficiently used to realize high performance opto-chemical sensors. In order to investigate the sensor performances the SRI sensitivity of attenuation bands related to different cladding modes have been experimentally tested. Here  $\delta$ -form Syndiotactic Polystyrene (sPS) was selected as nanoscale HRI polymeric layer.

## **1 Introduction**

In-fiber long period gratings (LPGs) which couple light from the core mode to cladding modes have been widely studied for applications in fiber-optic communications such as band rejection filters [1]. On the other side, their high sensitivity to temperature and strain and surrounding refractive index (SRI) has led to the development of LPG-based sensors [2-3].

Although a great effort has been carried out to improve the sensitivity to SRI of the LPG by several researcher groups, the LPG sensor exhibits a monotonic behaviour reaching the maximum value as SRI approaches the silica index [4]. In the last years, new configurations, based on LPGs coated with nano-size overlay with refractive index higher than the fiber one have been widely investigated [5-7]. As an HRI overlay is cast along a standard LPG, a lowering of the modes bounding factor is induced, leading to strong changes in the field

distribution related to the cladding modes. In particular, for a proper combination of the HRI overlay features (thickness and refractive index) and SRI the lowest order cladding mode ( $LP_{02}$ ) becomes guided within the overlay and a re-organization of all the cladding modes occurs. As matter of fact, the HRI coated LPG exhibits a new spectral behaviour, in terms of sensitivity profile, depending on the overlay features (thickness and refractive index) and SRI. For fixed overlay features, the SRI sensitivity exhibits a resonant-like shape versus the SRI. In addition the resonant-peak can be tuned around the desired SRI range by acting on the overlay refractive index or thickness. On the other side, a similar behaviour can be achieved with regards to overlay features when SRI is fixed. In this paper an exhaustive experimental characterization of the changes in sensitivity profile versus SRI as direct consequence of the HRI coating, is presented. The new sensitivity characteristics make the HRI coated LPG an attractive structure to realize high sensitivity chemical-sensor.

## 2 Theoretical approach

As well known, the transmission spectrum of a standard LPG consists of a series of attenuation bands related to the power coupling of the several cladding modes. Since the cladding modes are bounded by the cladding surrounding medium interface, the LPG exhibits high sensitivity to SRI. In addition, in standard LPG the sensitivity increases as the SRI approaches the silica index and as the cladding mode order increases.

When azimuthally symmetric nano-scale HRI coatings are deposited along LPGs, changes in the distribution of cladding modes occur, depending on the layer features (refractive index and thickness) and on the SRI. For a fixed overlay thickness and refractive index, the effective refractive indices of the cladding modes increase with the SRI [7] until a critical value is reached, where the  $n_{\text{eff}}$  related to the lowest order cladding mode ( $LP_{02}$ ) overcomes the refractive index of the cladding. Successive increase of the SRI leads the  $LP_{02}$  mode to be guided in the overlay area exhibiting an evanescent behaviour in the core and cladding area. As direct consequence a re-organization of the other cladding modes aimed to recovery the original field distribution in the fiber occurs. This means that the effective index of the  $i^{\text{th}}$  mode shifts to match the index of the  $(i-1)^{\text{th}}$  mode.

As matter of fact, the effect in the transmitted spectrum is the total weakening of the attenuation band related to the  $LP_{02}$  cladding mode and a quasi simultaneous shift of the attenuation bands due to higher order cladding modes: the peak loss related to cladding mode  $LP_{03}$  shifts to spectral position of the attenuation band associated to  $LP_{02}$  before the mode transition and so on.

Since high shift in the attenuation band are achieved in small SRI range, strong changes in the sensitivity profile are expected. In particular, the sensitivity characteristic of every attenuation bands exhibits a resonant-profile

centered on the SRI responsible of the  $LP_{02}$  transition, leading to a high sensitivity gain.

The key feature of the HRI coated LPG relies on the possibility to tune the SRI range where the transition occurs by acting on the overlay thickness. In fact, since a thicker overlay induces an increase of the effective refractive indices of every cladding mode, the transition region is reached for lower SRI.

From these considerations, a properly coated LPG can be the base structure to realize high performance in-fiber chemical sensors.

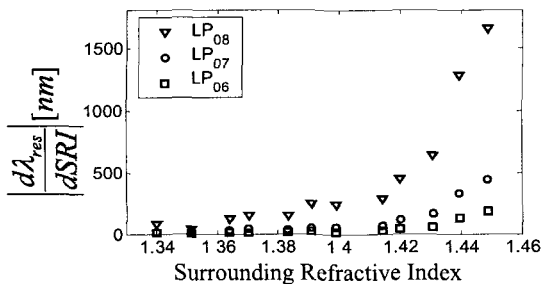


Figure 1 Sensitivity to the SRI of the  $LP_{06}$ ,  $LP_{07}$  and  $LP_{08}$  cladding mode in the bare LPG.

### 3 Experimental results

For the experimental test aimed to prove the sensitivity changes as direct consequence of the HRI coating, a standard LPG with pitch of  $340\mu\text{m}$  was selected. The sensitivity related to the  $LP_{08}$ ,  $LP_{07}$  and  $LP_{06}$  cladding modes are plotted in fig. 1, showing the standard monotonic behaviour versus the SRI where the maximum value is reached for SRI approaching the silica index.

Here, the Syndiotactic Polystyrene (sPS) in  $\delta$ -form, demonstrating a refractive index of 1.58 as proved in previous work [7], is used as HRI coating. To this aim, a simple experimental setup for test and coating deposition, reported in detail elsewhere, was used [6-7].

Fig. 2 shows the transmitted spectra of a 140nm coated LPG for different values of SRI. As observable, the quasi simultaneous transition of the  $LP_{07}$  and  $LP_{06}$  cladding mode is evident. In particular as the SRI reaches the critical value, in this case approximately 1.44, a larger shift in all the attenuation bands central wavelengths modulated by decreasing in the amplitude of the attenuation bands peaks occurs. In addition, after the transition all the attenuation bands exhibits a blue shift able to quasi completely recover the spectral configuration before the transition.

Due to the reorganization of the cladding modes, the sensitivity to SRI of the central wavelengths of the attenuation bands exhibit a totally new shape as shown in fig. 3. As it is observable, the sensitivity of every attenuation bands in the HRI coated LPG exhibit a resonant-like shape centered at SRI where the

transition is reached. The experimental results reveal a sensitivity gain, in the transition region, of 4, 7 and 10 for the LP<sub>08</sub>, LP<sub>07</sub> and LP<sub>06</sub> cladding mode, respectively. To better understand the dependence of the resonant-like sensitivity to the related cladding mode the fig. 4 plots the resonant-peaks and the related SRIs versus the investigated cladding mode.

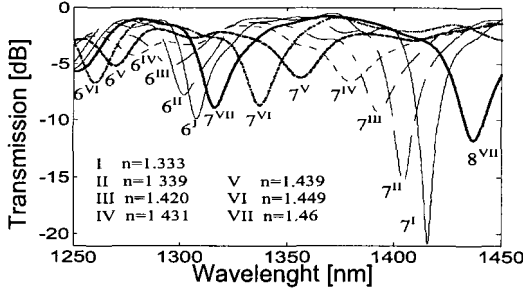


Figure 2. Transmission spectra of a 140nm sPS coated LPG for different values of SRI in the range 1.33-1.472. The LP<sub>0j</sub> cladding modes were marked with JI, JII, ..., JVII where the apices are referred to different SRI.

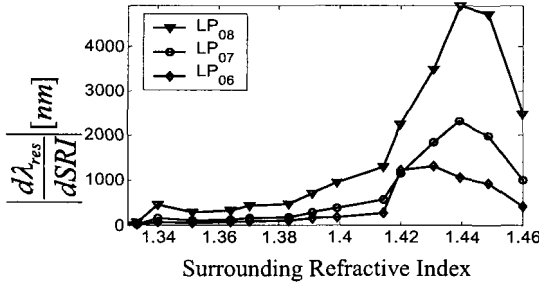


Figure 3 Sensitivity to the SRI of the LP<sub>06</sub>, LP<sub>07</sub> and LP<sub>08</sub> cladding modes in 140 nm HRI coated LPG.

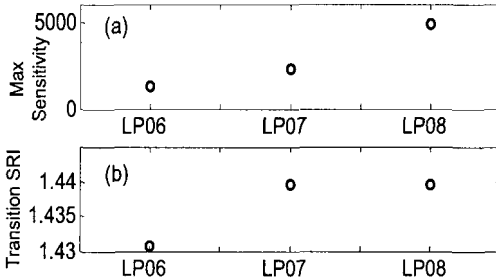


Figure 4 (a): Maximum sensitivity and (b) SRI related to maximum sensitivity versus cladding mode.

As matter of fact the sensitivity strong increases with the cladding mode while the SRI related to the maximum sensitivity slightly changes.

Based on these results the HRI coated LPG could be the base structure for new LPG based chemical sensor. It could be efficiently used to realize high sensitive refractive index measurements in the selected SRI range by a proper chosen of the coating features. On the other side, since high sensitivity to overlay refractive index is achieved in the transition region, as demonstrated in previous work [8-9], this structure can be successfully used for selective chemical sensor as a sensitive material is selected as HRI coating.

## Conclusion

In this work, an experimental characterization of the HRI coated LPG aimed to investigate the changes in the sensitivity has been carried out. The presence of a HRI coating along a standard LPG leads to a new profile of the sensitivity to SRI demonstrating a resonant-like shape. As matter of fact strong sensitivity gain in a selected SRI range can be efficiently achieved by a proper chosen of the overlay features. Based on the attractive sensitivity characteristic this structure can be the base for high performance chemical sensor.

## References

- [1] K. W. Chung, S. Yin, "Analysis of widely tunable long-period grating by use of an ultrathin cladding layer and higher-order cladding mode coupling," *Opt. Lett.* 29, 812-814, 2004.
- [2] V. Bhatia, "Applications of long-period gratings to single and multi-parameter sensing," *Opt. Express* 4, 457-66, 1999.
- [3] C. Y. Lin, L. A. Wang, and G. W. Chern, "Corrugated Long Period Fiber Gratings as Strain, Torsion, and Bending Sensors," *J. Lightwave Technol.* 19, 1159-1168, 2001.
- [4] S.W. James and R.P. Tatam, "Optical fibre long-period grating sensors: characteristics and applications," *Meas.Sci. technol.* 14, R49-R61, 2003.
- [5] I. Del Villar, I.R. Matias, F.J. Arregui and P. Lalanne, "Optimization of sensitivity in Long Period Fiber Gratings with overlay deposition," *Opt. Exp.* 13, 56-69, 2005.
- [6] A. Cusano, A. Iadicicco, P. Pilla, L. Contessa, S. Campopiano, A. Tutolo, M. Giordano, "Cladding Modes Re-Organization in High Refractive Index Coated Long Period Gratings: Effects on The Refractive Index Sensitivity," *Optics Letters*, Vol. 30, No. 19, pp. 2536-2538, October 2005.
- [7] A. Cusano, A. Iadicicco, P. Pilla, L. Contessa, S. Campopiano, A. Cutolo, M. Giordano, " Mode Transition in High Refractive Index Coated Long Period Gratings", *Optics Express* 19, Vol. 14, No. 1, January 2006.
- [8] A. Cusano, P. Pilla, L. Contessa, A. Iadicicco, S. Campopiano, A. Tutolo, M. Giordano, "High Sensitivity Optical Chemo-Sensor Based on Coated Long Period Gratings for Sub ppm Chemical Detection in Water", *Applied Physic Letters*, Vol. 87, 234105, 2005.
- [9] A. Cusano, A. Iadicicco, P. Pilla, L. Contessa, S. Campopiano, A. Cutolo, M. Giordano, G. Guerra, "Coated Long Period Fiber Gratings as High Sensitivity Opto-Chemical Sensors", *IEEE Journal of Lightwave Technology*, Vol. 24, No. 4, April 2006.



# Optical Fiber Sensors For Hydrogen Detection At Cryogenic Temperatures

M. Consales, A. Cutolo, A. Cusano

Optoelectronic Division, Engineering Dept., University of Sannio, Benevento, Italy  
[a.cusano@unisannio.it](mailto:a.cusano@unisannio.it)

S. Campopiano

Department for Technologies, University of Naples Parthenope, Naples, Italy

M. Penza, P. Aversa, G. Cassano

ENEA, C.R. Brindisi, Materials and New Technologies Unit, Brindisi, Italy

M. Giordano

Institute for Composite and Biomedical Materials, CNR, Naples, Italy

## Abstract

In this contribution, preliminary results on the capability of Silica Optical Fiber (SOF) sensors, coated by Single-Walled Carbon Nanotubes (SWCNTs) based sensitive material, to perform hydrogen detection at cryogenic temperatures are presented. The optical configuration exploited is the one of a low finesse Fabry-Perot interferometer, with a thin film of SWCNTs deposited onto the distal end of standard optical fibers [1,2]. Changes in the thickness and complex dielectric constant of the sensitive layer as a consequence of its interaction with the analyte molecules lead to changes in the fiber-film reflectance, indicating the presence of hydrogen in the test ambient. Preliminary results obtained from hydrogen detection testing, carried out at a temperature as low as  $-160^{\circ}\text{C}$  (113 K), demonstrate the excellent potentiality of the proposed configuration to sense very low percentages of gaseous hydrogen (<5%) in air.

## 1 Introduction

The hydrogen detection has been widely studied by the researchers in the last few decades. In 1981 Lundstrom introduced a hydrogen sensor based on thin films of Palladium, deposited on the top of the channel of a MOSFET device [3,4]. Among the big amount of sensing devices, fiber-optic detectors have strongly attracted the attention of the scientific community in this field, especially because of their high sensitivity and lack of sparking possibilities, guaranteed by the removal of all electrical power from the test site. To date several configurations of fiber-optic hydrogen sensors have been proposed, based on different transducing principles and materials [5-9].

Recent reports of high reversible adsorption of molecular hydrogen in carbon nanotubes and graphitic nanofibers [10-11] have stimulated tremendous interests in the research community to exploit the novel carbon materials as ideal candidates for hydrogen storage devices. Due to their hollow structure and high specific surface area, the interactions between carbon nanotubes and gaseous molecules attracted much experimental and theoretical interest.

The integration between SWCNTs as nanoscale sensitive material and optical fiber technologies has already been carried out by the authors for the developing

of SOF sensors capable of Volatile Organic Compounds (VOCs) detection with sub-ppm resolution, good repeatability and fast response [1,2,12].

Here, preliminary results on the capability of SOF sensors, coated by two different kinds of SWCNTs-based sensitive materials, to perform hydrogen detection at cryogenic temperatures are presented. The proposed optical configuration is essentially based on a low finesse Fabry-Perot interferometer, realized by means of the deposition of both Closed-ends (CeSWCNTs) and Opened-ends SWCNTs (OeSWCNTs) on the distal end of a properly prepared single-mode SOF. The sensitive material is transferred upon the optical transducer by means of the well known Langmuir-Blodgett (LB) deposition technique [2,12]. Single wavelength reflectance measurements have been carried out in order to investigate the capability of the proposed SOF sensors to detect low percentages (<5%) of gaseous hydrogen at cryogenic temperature.

Experimental results demonstrated the excellent potentiality of the proposed configuration to sense very low concentrations of hydrogen at the very low temperature of -160°C. Especially CeSWCNTs demonstrated good sensitivity, fast response times together with good recovery and reversibility features.

## 2 Principle of Operation

The key point of a SOF sensor relies on the deposition of a sensing overlay on the distal ends of standard optical fibers. When the light propagating within the fiber encounters the fiber-film interface, the amount of reflected power depends on the optical and geometrical properties of the CNTs-based overlay. Consequently, any change occurring within the sensitive layer is able to induce a corresponding change in the film reflectance ( $\Delta R_{Film}$ ), as expressed in the following equation:

$$\Delta R_{Film} = f(\Delta \varepsilon_{Film}, \Delta d_{Film}) \quad (1)$$

where  $\varepsilon_{Film}$  and  $d_{Film}$  are the complex dielectric constant and the thickness of the CNTs-based film. When the optical probe is exposed to gaseous hydrogen, its molecules are adsorbed within the sensitive layer, changing its complex dielectric function and thus the optical signal reflected at the fiber film interface.

## 3 Sensors Fabrication

Thin films of CeSWCNTs and OeSWCNTs with different thicknesses were transferred upon the distal end of single-mode optical fibers by the molecularly engineered LB deposition technique [12]. Standard silica optical fibers (SMF-28), with core and cladding diameters respectively of 9  $\mu\text{m}$  and 125  $\mu\text{m}$ , have been exploited. The investigation of the capability of the SWCNTs-based SOF sensors to detect gaseous hydrogen at cryogenic temperatures, has been carried out by means of three SOF probes, two coated by 2 and 6 monolayers of CeSWCNTs (called 2\_CeSWCNTs and 6\_CeSWCNTs, respectively) and one coated by 2 monolayers of OeSWCNTs (called 2\_OeSWCNTs).

#### 4 Experimental Set-up

In Fig. 1.a is reported the exploited SOF sensors interrogation system, capable to continuously monitor the fiber-sensitive layer interface reflectance [1,2]. A 2x2 directional coupler redirects the light coming from a Superluminescent Light Emitting Diode (SLED) towards two arms: the first one is directly connected with the photoreceiver<sub>2</sub>, while the second one is connected with the sensor head. The amount of light reflected by the sensitive interface comes back through the same fiber and is collected by the photoreceiver<sub>1</sub>. The optoelectronic sensor output is given by:

$$I = \frac{V_{Signal}}{V_{Source}} = k \cdot R_{Film} \quad (2)$$

where  $k$  is a constant taking into account all the setup parameters,  $V_{Signal}$  is the signal proportional to the source power and to the film reflectance ( $R_{Film}$ ) and  $V_{Source}$  is the signal proportional just to the power emitted by the source. In this configuration, any effect able to modify the complex dielectric function of the sensitive layer changes the normalized output of the optical sensor, and eventual fluctuations of the power emitted by the SLED do not affect the reflectance measurements. In addition, in order to increase the signal to noise ratio, a synchronous detection scheme has been implemented with the light source externally amplitude modulated at 500 Hz and the sensor outputs retrieved by using a dual channel lock-in amplifier. Furthermore, an optical switch has been exploited in order to test all the three realized samples with a Time Division Multiplexing (TDM) approach. The overall set up was properly engineered in order to provide robust, compact and portable equipment.

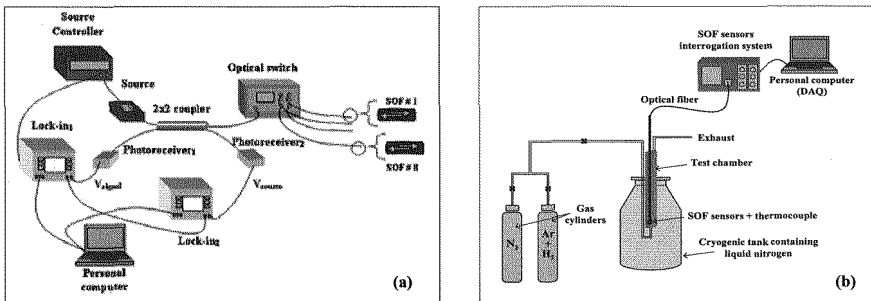


Figure 1. Schematic view of the (a) SOF sensors interrogation system and (b) experimental set-up used for the detection of cryogenic hydrogen.

The hydrogen detection at cryogenic temperatures has been performed by flowing argon gas with hydrogen (5%) in a proper designed cylindrical chamber, where the optical fiber sensors have been located. In order to reach very low temperatures (113 K) the chamber has been inserted in a tank containing liquid nitrogen, as evidenced in Fig 1.b. The temperature monitoring has been carried

out by means of a copper/copper nickel thermocouple located close to the optical sensors heads. Nitrogen gas has been continuously injected in the cylindrical chamber in order to reduce the humidity content before the strong temperature decreasing due to the insertion of the chamber into the cryogenic tank. Nitrogen has also been mixed with the argon and hydrogen gas in order to expose the SOF sensors to an hydrogen concentration lower than 5%.

## 5 Results

Preliminary results obtained from the low temperatures hydrogen detection measurements are shown in Fig. 2, where the responses of the sensors (a) 2\_CeSWCNTs, (b) 6\_CeSWCNTs and (c) 2\_OeSWCNTs, exposed to decreasing concentration pulses of hydrogen at a temperature of 113K are reported.

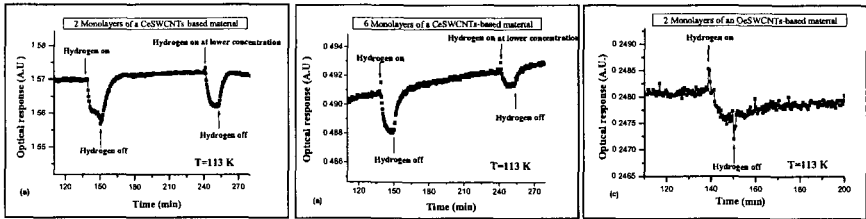


Figure 2. Responses to decreasing concentration pulses of gaseous hydrogen (<5%), at 113 K, of three SOF sensors: (a) 2\_CeSWCNTs, (b) 6\_CeSWCNTs and (c) 2\_OeSWCNTs

As it can be observed from Fig. 3.a, where the normalized reflectance changes  $\Delta R_{\text{Film}}/R_{\text{Film}}$  of the three tested SOF sensors are reported, all the optical probes provides a significant change of the optoelectronic sensor output as a consequence of the adsorption of gaseous hydrogen within the sensitive materials. In addition, good sensitivity and complete recovery of the nitrogen signal after hydrogen concentrations pulses have been observed for the CeSWCNTs sensors, while good sensitivity, but no recovery of the steady-state value has been observed for the OeSWCNTs-based sensor. Furthermore, a study of the sensors response and recovery times reveals that the probes 2\_CeSWCNTs and 6\_CeSWCNTs are characterized by the same response times, which are approx. 3 minutes, but by slightly different recovery times, which are approx. 9 and 11 minutes, respectively (Fig. 3.b). Instead, 2\_OeSWCNTs showed a response time (approx. 5 min.) higher than that obtained with the CeSWCNTs-based material. This could be attributed to the fact that, while in the case of the CeSWCNTs the hydrogen molecules adsorption takes place only on the surface of the single carbon tubes and in the interstitial sites between tubes, in the case of the counterpart OeSWCNTs, the hydrogen molecules adsorption takes place also inside the carbon tubes, requiring, for this reason, more time for the establishment of the equilibrium condition with the external environment.

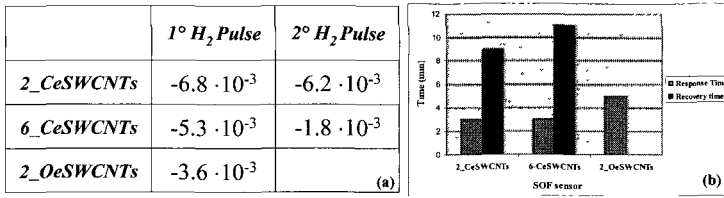


Figure 3. (a) Normalized reflectance changes  $\Delta R_{\text{Film}}/R_{\text{Film}}$  and (b) mean response and recovery times for the three tested SOF sensors.

## 6 Conclusions

In this work have been reported preliminary results on the capability of SOF sensors, coated by thin films of two different types of SWCNTs, Closed-ends SWCNTs (CeSWCNTs) and Opened-ends SWCNTs (OeSWCNTs), to detect very low hydrogen percentages at cryogenic temperatures. The Langmuir-Blodgett technique has been used for the deposition upon the distal end of standard optical fibers of thin film of the aforementioned sensitive materials. The fabricated optical probes have been exposed at cryogenic temperatures to gaseous hydrogen with concentration lower than 5%. Experimental results demonstrated the excellent potentiality of the proposed configuration to sense very low percentages of gaseous hydrogen at cryogenic temperatures as low as 113K (-160°C). As matter of fact, the OeSWCNTs-based sensor is characterized by high sensitivity but no recovery of the steady-state value after the hydrogen adsorption, whereas the CeSWCNTs-based probes exhibited good sensitivity and complete recovery of the nitrogen signal after both hydrogen concentration pulses. Finally, it has been found that the response times of the latter ones are much lower than that of the counterpart OeSWCNTs-based transducer.

## References

- [1] M.Penza et al., 2004, Applied Physics Letters, 85, (12), 2378-2381.
- [2] M.Penza et al., 2005, Sensors and Actuators. B, 111-112, 171-180.
- [3] Lundström et al, 1975, Appl.Phys.Lett, 26,55-57
- [4] Lundstrom, 1981, Sensors and Actuators, 1 403-426.
- [5] M.A.Butler, 1991, J. Electrochem. Soc. 138, L46
- [6] M.A.Butler, 1994, Sensors and Actuators B 22, 155.
- [7] H.Raether, 1988, Springer-Verlag, Berlin, p. 21.
- [8] B.Sutapun et al, 1999. Sensors and Actuators B 60, 27.
- [9] Villatoro et al, 2001, Electr. Lett., 37, 1011.
- [10] AC.Dillon et al., 1997, Nature;386:377-379.
- [11] C.Liu et al., 1999, Science, 286:1127-9.
- [12] M.Penza et al., 2005, Nanotechnology 16, 2536-2547.

# Silicon $p^+n$ mesa junction with a porous layer as sensing element

G. Barillaro, A. Diligenti, L. M. Strambini

*Dipartimento di Ingegneria dell'Informazione: Elettronica, Informatica, Telecomunicazioni, Università di Pisa, via G. Caruso 16, 56126 Pisa-Italy.*  
[g.barillaro@iet.unipi.it](mailto:g.barillaro@iet.unipi.it)

## Summary

The structure of silicon solid-state devices can be modified by locally converting crystalline silicon into porous silicon, so that their  $I$ - $V$  characteristics become sensitive to gases in the surrounding atmosphere. Following this approach, the surface of a  $p^+n$  junction has been provided, by means of electrochemical etching, with a porous layer. The resulting device has been tested as sensor for isopropanol vapours. The fabrication process and the electrical characterization of the device are presented and discussed.

## 1 Introduction

Air monitoring in the environment, industrial installations and hospitals is one of challenges of the modern society. To achieve this goal solid-state sensors, small and low cost, are required. Several materials, such as semiconductor oxides, have been proposed in last years for sensor fabrication; among them, porous silicon (PS) [1] is one of most promising for its high chemical reactivity at room temperature. However, the integration on the same chip of a sensor fully made with PS, along with the necessary conditioning/driving electronic circuitry, is difficult for two reasons: i) the fragility of the material, which limits the use of lithographic processes, and ii) the lack of knowledge on the behaviour of PS/metal contacts.

To avoid these drawbacks, recently a new approach for the integration of PS-based gas sensors using industrial processes has been proposed [2, 3]. In this approach, differently from PS sensors reported in literature, adsorption of molecules into the porous silicon layer is exploited to modify the electrical properties of a crystalline device, such as a FET, for which the PS layer constitutes the sensible part.

In this work, by using the same approach, a crystalline  $p^+n$  silicon diode surrounded by a PS layer (see Fig. 1) is proposed as gas sensor. Adsorption of molecules in the PS layer modifies the electrical properties of the PS and/or of the PS-crystalline silicon (c-Si) interface and in turn the diode current.

## 2. Sensor Fabrication

The fabrication process schematically consists of the following steps: 1) boron implantation on a  $n$ -type wafer ((100) oriented,  $N_D$  about  $10^{15} \text{ cm}^{-3}$ ), and drive-in to form a  $p$  layer,  $2.3 \mu\text{m}$  deep with a surface doping of  $10^{17} \text{ cm}^{-3}$ ; 2) aluminum thermal evaporation and patterning (1<sup>st</sup> mask) to provide the anode contact of the diode. On the same chip several circular contacts with different diameters  $d$  were defined ( $d = 500, 200, 100 \mu\text{m}$ ). 3) Aluminum evaporation on the back of the sample (cathode contact). The cathode is the same for all the diodes. 4) Anode protection by using a patterned photoresist layer (2<sup>nd</sup> mask), hardbaked at  $140 \text{ }^\circ\text{C}$  for 30 minutes; this step is essential in order to make the resist layer able to withstand the electrochemical etching in HF, which is necessary to the PS formation. The final step was the selective anodization of the  $p$  and  $n$  type material through the photoresist-free spaces (fig. 1e) to form the PS layer surrounding the  $p^+n$  diode. The electrochemical process was performed at a current density  $j = 30 \text{ mA/cm}^2$  and for a time of 50 s in a solution HF(48 %): $\text{CH}_3\text{CH}_2\text{OH}/1:1$  under illumination conditions. Finally, the samples were rinsed in acetone, in  $\text{CH}_3\text{CH}_2\text{OH}$  (ethanol) and dried in  $\text{N}_2$  flow.

A schematic drawing of the device at the end of the fabrication sequence is shown in figure 1. In a typical diode the porous film has a thickness of about  $3 \mu\text{m}$ . The whole fabrication process requires only two masks and few technological steps.

## 3. Sensor Characterization in Isopropanol Vapours

In order to investigate the behaviour of the diode as gas sensor, electrical measurements were performed in dry nitrogen and in isopropanol (ISO), the latter properly diluted in  $\text{N}_2$ , used as carrier gas, to obtain a given concentration;

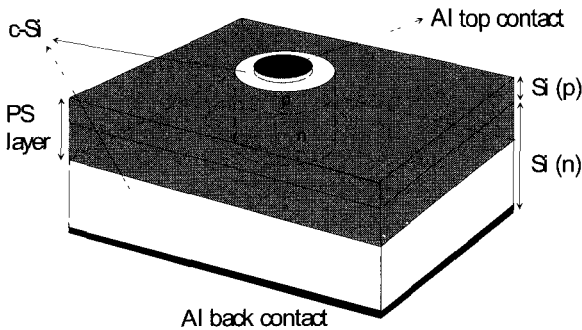


*Fig. 1 Schematic view of the PS surrounded  $p^+n$  diode gas sensor. The cylinder is crystalline silicon*

the experimental set-up is described in ref. [2]. All the measurements were performed at room temperature.

The  $I$ - $V$  DC characteristic in  $N_2$  for a  $p^+n$  junction with a diameter of  $200\ \mu\text{m}$ , is shown in Figure 2.

Since the DC equivalent circuit of the sensor can be represented as a  $pn$  diode and a parallel conductive path, constituted by the PS film, any current variation, at a given bias, induced by the gas adsorption could be ascribed both to the diode and/or the resistor. However, since the variations are sensibly different for forward and reverse polarization at the *same* absolute voltage value, it is reasonable to suppose that the main contribution is given by the diode.

The main sensor features resulting from the characterization are:

- 1) both the forward and the reverse current, respectively  $I_F$  and  $I_R$ , show a noticeable variation when ISO vapours at 10,000 ppm are injected into the test chamber; moreover, the initial current value  $I_0$  (reference current in  $N_2$ ) is completely restored as soon as ISO vapours are removed;
- 2) the transient behaviour is quite fast, some tens of seconds (see Figure 3), and can be related to 1) the time required to fill/empty the test chamber and 2) the diffusion time of molecules toward the diode depletion zone. Because of the volume -  $100\ \text{cm}^3$  - of the test chamber, it is reasonable that the main contribution to the transient time is due to the filling/emptying time; an improvement of the sensor response time is thus expected by reducing the chamber volume.
- 3) the forward current variation  $\Delta I_F = I - I_0$  at a fixed ISO concentration can result  $>0$  or  $<0$ , depending on the forward polarization voltage value;

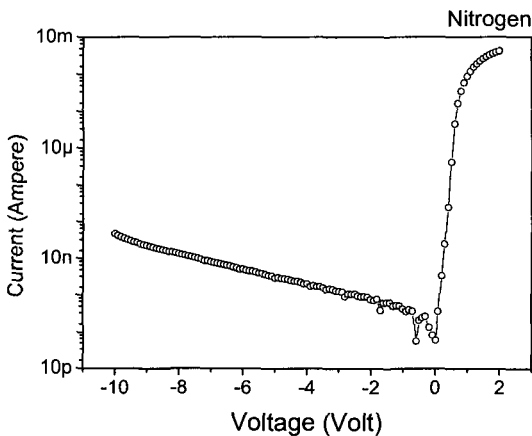


**Fig. 2** Typical  $I$ - $V$  characteristic in nitrogen of a PS surrounded  $p^+n$  diode gas sensor with a diameter of  $200\ \mu\text{m}$ .



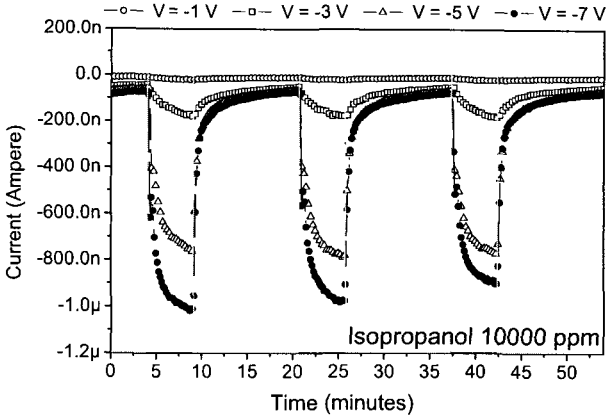


Fig. 3 Transient behaviour of a PS surrounded  $p^+n$  diode gas sensor for different reverse bias values in presence of isopropanol vapours.

- 4) the reverse current variation  $\Delta I_R$  (always  $|\Delta I_R| > 0$ ) at a fixed ISO concentration depends on the reverse bias value and can be as high as several orders of magnitude, when a proper reverse voltage is chosen. In Figure 3 the  $I_R(t)$  behaviour of a diode driven by  $10^4$  ppm ISO pulses is reported for different reverse bias values. It is interesting to note that the current variation noticeably increases as the reverse bias is increased, so that changing the reverse bias value is a feasible way to tune the sensor sensitivity.

The results 1), 3), 4) could be explained if one supposes that the interaction of the adsorbed gas with the localized states on the lateral surface of the diode, changes the surface band structure; the situation is analogous to that of a gate-controlled diode [4], but in this case the gate is floating.

#### 4. Conclusions

The presented device, owing to its high sensitivity and simplicity of fabrication, seems to be suitable for the production of low-cost sensors, and could be integrated along with the necessary control electronics, since the formation of the PS layer occurs at the end of the fabrication process. The approach used, whose validity has been also demonstrated with different devices [2, 3], could be applied to any silicon device, giving rise to a new class of integrable sensors. In this case the test gas was isopropanol, but it is expected, on the basis of results obtained on different sensors, based on the same principle [5], that the diode

results very sensitive for NO<sub>2</sub>, which constitutes a polluting gas of high environmental interest.

### **Acknowledgments**

The authors wish to thank STMicroelectronics (Cornaredo, Milan, Italy) for having supported this work, which was performed in the frame of a cooperation STMicroelectronics/University of Pisa.

### **References**

- [1] M. Tucci, V. La Ferrara , M. Della Noce, E. Massera, L. Quercia, *J. Non-Crystalline Solids* **338-340**, 776 (2004).
- [2] G. Barillaro, A. Nannini, F. Pieri, *Sens. Actuators B* **93**, 263 (2003).
- [3] G. Barillaro, A. Nannini, G. Marola, L. M. Strambini, *Sens. Actuators B* **105**, 278 (2005).
- [4] A. S. Groove, *Physics And Technology of Semiconductor Devices*, John Wiley & Sons, Inc. USA (1967), p. 289.
- [5] G. Barillaro, A. Diligenti, A. Nannini, L. M. Strambini, E. Comini, G. Sberveglieri, *IEEE Sensors Journal* **6**, 19 (2006).

# **Influence of solvent on thin film composite morphologies and sensing properties**

A. De Girolamo Del Mauro, L. Quercia, F. Loffredo, G. Di Francia.  
*Research Centre Portici, ENEA, Naples, Italy*  
quercia@portici.enea.it

## **Summary**

In this work sensors based on thin composite films characterized by different contents of carbon black (5-40% by weight) in polymer matrix (Poly (2 hydroxy-ethyl-metacrylate) are fabricated and characterized. These films are obtained using various organic solvents. We study the samples by dynamic light scattering, optical and scanning electronic microscopy and thermogravimetric analyses. The hypothesis used in order to describe qualitatively the working mechanism of these sensors considers that polymer matrix swells when exposed to organic vapor and the swelling decreases the connectivity between the conductive filler particles. Testing to different VOCs the sensor devices, will show the influence of different morphology on the characteristics of the sensors responses.

## **1. Introduction**

During the past few decades, electrically conductive polymeric composites have found use in a variety of applications. Binary composite systems, comprised of conductive filler (e.g. carbon black (CB), metal powders, graphite fibers, etc.) in a polymer matrix, create a material that is tough, flexible and electrically conductive. These unique materials are ideally suited for antistatic layers [1,2], electromagnetic interference shielding [3], chemical vapor sensors [4-7], and thermal resistors [8].

In previous works we have studied the influence of filler characteristics [9], the thin film morphology and fabrication process [10] on the sensing device performances in order to gain more information on the detailed working mechanism of real devices.

Instead, in present study we have prepared different film polymer composites of poly(2-hydroxy-ethyl-methacrylate) (PHEMA) with CB (PHEMA/CB) using four organic solvents, characterizing the relative sensing devices. PHEMA has been known for its hydrophilic properties and suitability for this kind of sensors [11] and CB is already optimized for applications in conductive polymeric composite. When exposed to vapor phase analytes these conducting composites exhibit good sensitivity through an increase in their resistance. The hypothesis used in order to describe qualitatively the working mechanism of these sensors considers that polymer matrix swells when exposed to organic vapor and the swelling decreases the connectivity between the conductive filler particles [12].

## 2. Experimental part

The sensing films were prepared by dissolving the polymer PHEMA in the suitable solvents and dispersing the filler, in various weight ratios (table 1), in the solution (0.5-0.8% by weight) by ultrasonic bath. All suspensions were deposited by spin coating or casting on different substrates. The four solvents used to prepare the sensors are reported in Table 1.

COMPOSITE	SOLVENTS	PHEMA/CB (mg)
PHEMA/CB	m-cresol (MC)	60/40
	(-)Ethyl L-lactate (ETLAC)	80/20
	ethanol (ETOH)	90/10
	1,1,1,3,3,3 Hexafluoro-2-propanol (HFIP)	95/5

Table 1: Solvents used to prepare the composite films

The thin film polymeric composites obtained have been characterized out by Tencor P10 surface profiler, SEM and optical analysis. To determine the filler contents of the composites, thermogravimetric analyses (TGA) were performed on TA instruments 2950 equipment at a heating rate of  $20^{\circ}\text{C min}^{-1}$  (from  $25^{\circ}\text{C}$  to  $800^{\circ}\text{C}$ ). The sensing devices responses to organic vapors have been studied using a Gas Sensor Characterization System (GSCS) already described [13].

## 3. Results and discussion

Fig.1 shows the optical micrographies of PHEMA/CB composites obtained depositing by spinning on glass substrates different dispersions of CB in PHEMA solution characterized by different solvent but the same initial percent ratio between polymer and filler weights (80/20 weight %).

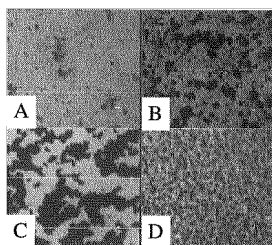


Fig.1: Optical micrographies (100x) of composite films surfaces PHEMA/CB prepared with:  
A) MC; B) ETOH; C) ETLAC; D) HFIP.

The morphologies of the thin film composites result varied depending both on the specific interaction between polymer/CB/solvent in the liquid dispersion and the preparation conditions (spinning parameters and substrate/dispersion interaction).

As expected, HIFP, being a “good” solvent to disperse CB, allows to obtain the most homogeneous thin film composites characterized by the smallest size of the CB agglomerated (fig.1D).

The preparation of thin film composites starting by a biphasic dispersion does not allow to forecast the effective CB content in the thin film. In order to determine experimentally the total filler contents of the composite, we have used thermogravimetric analyses (TGA). In Fig. 2 we compare the results obtained by TGA for composites prepared with ETLAC and HIFP.

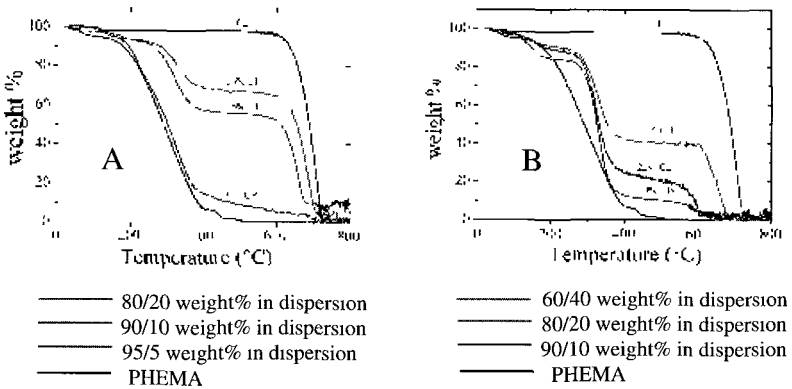


Fig.2: TGA of PHEMA/CB composite films prepared with : A) ETLAC; B) HIFP.  
For composite films, the CB content is indicated on curves

It is interesting to note the CB content in the thin film composite can be up to three times higher than in the dispersion using ETLAC as solvent while it is practically the same using HFIP as solvent. Therefore, it is possible to vary the CB content in the polymeric films only changing the solvent. Furthermore, using HFIP as solvent it has been possible to prepare conducting composite thin films in a wider range of CB content.

All composite thin films, with a CB content ranging from 5% to 40% by weight, have shown a conductivity suited to become sensing elements. The PHEMA/CB sensors are tested to different VOCs type (acetone, methanol, ethanol, acetic acid and humidity). In general we have observed that the sensitivities of devices obtained using different solvents for their preparation does not change as much as we expected considering their morphologies (fig.1) and relative TGA analysis (fig.2). As an example, we show the responses of composite films PHEMA/CB (80/20 weight%), prepared with ETLAC (A) and

HIFP (B), to vapors of ethanol (fig.3). Both devices show comparable sensitivities, however the dynamical responses change strongly especially regarding response times and reversibility. The sensing device obtained using HFIP as solvent, characterized by the more interesting morphology and more controllable preparation conditions, is affected by longer response times and reduced reversibility. This suggests how critical is the choice of the solvent used for the sensing film preparation: morphology, flexibility of preparation conditions and sensing characteristics must be evaluated in order to find the best compromise for the specific application.

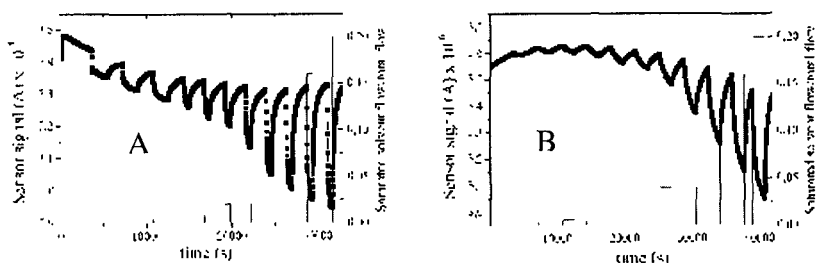


Fig.3. Responses to vapors of ethanol of PHEMA/CB (80/20 weight%) composite films prepared with: A) ETLAC, B) HIFP.

For small relative swelling  $\Delta V/V \ll 1$  (where  $\Delta V$  is the volume increase due to swelling) we have modeled the sensors responses by the equation:

$$\frac{\Delta R}{R} = \frac{t\phi}{(\phi - \phi_c)} - \frac{\Delta V}{V} \quad (1)$$

where  $\phi$  is the volume fraction of CB and  $\phi_c$  is the volume fraction at percolation threshold and  $t$  is the critical exponent as described by G.E.M. equation [13].

We point out that, in principle, are expected little variations of all parameters in equation (1) out of  $\phi$ , the volume fraction, for all PHEMA composite sensors, obtained with different solvents. On the other side, all sensors show similar responses in spite of different total CB content as measured by TGA. This suggests that  $\phi$  is similar for all samples and only a small percentage of CB in the composite films contributes to determine the “effective” value of  $\phi$ .

#### 4. Conclusions

The solvent chosen to prepare the thin film composites has shown a great influence on their morphology. As expected, the more homogeneous

morphology can be obtained by spinning the finest CB/ polymer dispersion (obtained for the PHEMA/CB system with HFIP solvent ).

Thermogravimetric analysis has pointed out that in general carbon black weight percentage vary strongly between the initial liquid dispersion and the resulting composite film.

The composite films obtained using the HFIP as solvent have kept the same carbon black weight percentage of the dispersion. Thank to this it has been possible to prepare sensing devices with a wide and more controlled range of carbon black weight percentage.

Sensitivities to different VOCs of sensing devices prepared with different solvents does not change significantly, as expected by their morphologies and carbon black contents. However, PHEMA/CB composite films obtained with HFIP, characterized by the better homogeneous morphology, are less reversible and show longer response times.

In summary, the choice of better solvent to make sensors based on polymer/carbon black composites films must be related to the application, because it is a compromise between fabrication process and sensor performances requirements.

## References

- [1] Bigg, D. M.; Stutz, D. E. *Polym Comp* 1983, 4, 40.
- [2] Reboul, J. P. in *Carbon Black-Polymer Composites*; Sichel, K., Ed.; Marcel Dekker: New York, 1982, Chapter 3.
- [3] Sau, K. P.; Chaki, T, Chakraborty, A.; Khastgir, D.; *Plast Rubber Comps Process Appl.*; 1997, 26, 291.
- [4] Lundberg, B.; Sundqvist, B.; *J. Appl. Phys.* 1986, 60, 1074.
- [5] Lewis, N. S.; Lonergan, M. C.; Severin, E. J.; Doleman, B. J.; Grubbs, R. H. *SPIE* 1996, 3079, 660.
- [6] Ruschau, G. R.; Newnham, R. E.; Runt, J.; Smith, B.; *Sens. Actuators* 1989, 20, 269.
- [7] Talik, P.; Zabkowska-Waclawek, M.; Waclawek, W.; *J. Mater. Sci.* 1992, 27, 6807.
- [8] Moffat, D. M.; Runt, J. P.; Halliyal, A.; Newnham., R. E. *J. Mater Sci.* 1989, 24, 609.
- [9] Quercia L.; Loffredo F.; Di Francia G.; *Sens. Actuators B* 2005, 109, 153.
- [10] Quercia L.; Loffredo F.; Bombace M.; Nasti I.; Di Francia G.; *Sens. Actuators B* Vol.111-112 (2005), 166-170.
- [11] Chatzandroulis S.; Tegou E.; Goustouridis D.; Polymenakos S.; Tsoukalas D ; *Sensor and Actuators* 2004, 103, 392-396.
- [12] Doleman B. J.; Severin E. J.; Beaver S A.; Grubbs R. H., Lewis N. S.; *Chem. Mater.* 1996, 8, 2298.
- [13] McLachlan D. S.; *Solid State Comm.* 1989, 72, 831.

# Gas sensing properties of nanostructured titania: a comparative study of different preparation methods

G.Neri\*, A. Bonavita, G. Micali

Dept. of Industrial Chemistry and Materials Engineering, University of Messina,  
C/da di Dio, Vill. S.Agata,  
98166 Messina, Italy  
[neri@ingegneria.unime.it](mailto:neri@ingegneria.unime.it)

F. A. Deorsola, I. Amato, B. De Benedetti,

Dept. of Materials Science and Materials Engineering, Corso Duca degli  
Abruzzi, 24, 10129 Torino, Italy

## Summary

This paper reports a study concerning the preparation of nanopowders of titania,  $\text{TiO}_2$ , through two novel processes of synthesis, namely gel-combustion and reactive microemulsion. The microstructural properties of products obtained and their behaviour as  $\lambda$ -sensors for automotive exhaust gas have been evaluated. Titania synthesised by reactive microemulsion has shown the better microstructural (lower grain size, higher surface area) and oxygen sensing properties.

## 1 Introduction

Nanostructured  $\text{TiO}_2$  is a promising material for gas-sensing applications [1]. For example,  $\lambda$  sensors used actually are electrochemical devices based on stabilized zirconia [2]. The lambda factor regulates the air-to-fuel ratio to improve engine combustion and, therefore, optimize the conversion of deleterious combustion products such as CO, hydrocarbons and NOx. The right value of lambda factor for better engines performances is around one, corresponding to partial pressure of oxygen ranging from 0,2kPa to 1kPa. However, planar resistive sensors which use  $\text{TiO}_2$  as sensing element present some advantages and therefore they are actually the subject of numerous investigation [3].

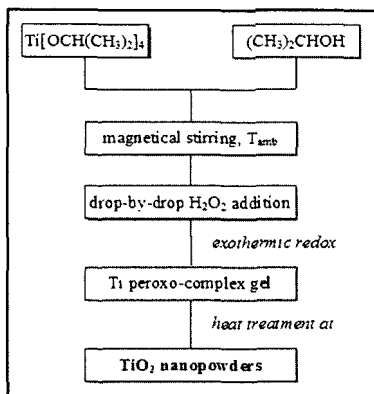
To develop titania with better oxygen sensing characteristics, the process of synthesis is of fundamental importance because it determines the grain size, structure and morphology of the obtained material, all factors affecting strongly the sensing properties. Here, we focused our attention on two novel processes to synthesize  $\text{TiO}_2$  nanopowders: gel-combustion and reactive microemulsion. Gel-combustion is an innovative and low-cost process combining chemical gelation and combustion processes. The synthesis through reactive microemulsion is instead based on the precipitation of particles from a solution,



containing low-cost precursor, previously emulsified in an immiscible liquid. These materials have been tested for oxygen detection as lambda sensor for automotive exhaust gas at high temperature.

## 2 TiO<sub>2</sub> nanopowders synthesis

Flow-charts showing the main paths in the preparation of TiO<sub>2</sub> by gel-combustion and reactive microemulsion are reported in the Schemes 1 and 2, respectively.

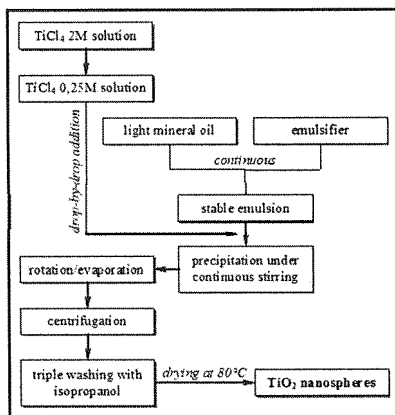


Scheme 1. Flow-chart of the gel-combustion process

TiO<sub>2</sub> gel-combustion nanopowders were synthesized starting from titanium (IV)isopropoxide (Ti(OCH<sub>2</sub>(CH<sub>3</sub>)<sub>2</sub>)<sub>4</sub>), isopropanol and hydrogen peroxide as raw materials. A solution of titanium isopropoxide in isopropanol (50/50 vol) was prepared first. Then, hydrogen peroxide was added drop by drop under continuous stirring. The addition of H<sub>2</sub>O<sub>2</sub> initiated the exothermic reaction, that can be supposed divided in two step: *i*) hydrolysis of titanium isopropoxide forming titanium hydroxide Ti(OH)<sub>4</sub>, and *ii*) oxidation of this product with a significant increase of temperature and gas release [4]. The resulting product obtained is dried at 80°C, ground in a mortar, has the appearance of a highly porous and softly agglomerated nanostructured powder.

In the reactive microemulsion synthesis, an aqueous solution of titanium chloride TiCl<sub>4</sub> was prepared. It was added to a paraffin oil containing a small amount of non ionic emulsifier, creating a water-in-oil emulsion in which each single aqueous droplet contained the TiCl<sub>4</sub> solution. Each individual droplet acted as a reactor, where the precipitation of spherical and nanosized titania powders occurred by means of the thermal instability of the Ti precursor at high temperature [5]. During the precipitation, each particle is coated by an emulsifier

film preventing the agglomeration [6]. Once the process was completed, the precipitate was centrifuged, washed with isopropanol and dried at 80°C.



*Scheme 2. Flow-chart of the microemulsion process*

### 3 Nanopowders characterization

TEM analysis of as synthesized titania through gel-combustion and reactive microemulsion showed particles with very small particle size (Fig. 1). In according, XRD analysis of microemulsion titania showed the formation only of the anatase phase (Fig. 2a), with an average grain size of about 6 nm. Specific surface area was consequently very high (about 280 m<sup>2</sup>/g).

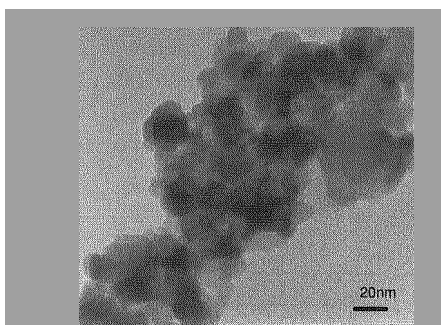


*Fig.1 TEM micrograph of the synthesized TiO<sub>2</sub> nanopowders prepared by reactive microemulsion.*

After treatment at high temperature the rutile phase appeared in the XRD pattern of treated powders (Fig.2b). Moreover a re-crystallization of the

powders also occurred. For example, titania synthesized by reactive microemulsion treated at 600°C, showed an average size of 30 nm and a specific surface of 150 m<sup>2</sup>/g.

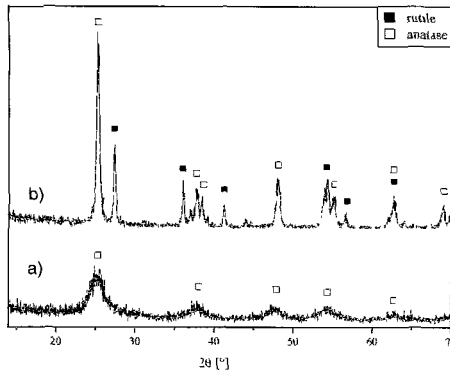


Fig. 2. XRD analysis of TiO<sub>2</sub> nanopowders prepared by reactive microemulsion a) as synthesized; b) treated at 600°C.

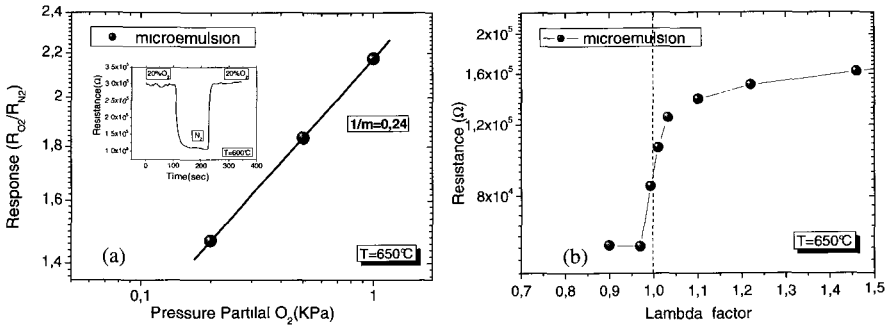
A commercial titania (Aldrich), used as reference, was also characterized. It has a mean particles size of an order of magnitude higher than the gel-combustion and reactive microemulsion synthesized by us.

#### 4 Sensing test

Our synthesised titania samples have shown a higher resistance compared to the commercial TiO<sub>2</sub> at all working temperature. This is related to the smaller particle size of the synthesized samples. In despite of this, titania prepared through the reactive microemulsion was found more effective for detection of low concentrations of O<sub>2</sub> at high temperature, showing a higher response in the range 0,2 -1 kPa of oxygen pressure partial than other samples (Tab. 1).

Lambda factor ( $\lambda$ )	O <sub>2</sub> (kPa)	Gel-combustion Resistance ( $\Omega$ )	Microemulsion Resistance ( $\Omega$ )	Commercial Resistance ( $\Omega$ )
0.99	0.2	$1.0 \cdot 10^5$	$8.4 \cdot 10^4$	$2.0 \cdot 10^3$
1.01	0.5	$1.2 \cdot 10^5$	$1.0 \cdot 10^5$	$2.3 \cdot 10^3$
1.03	1	$1.3 \cdot 10^5$	$1.2 \cdot 10^5$	$2.5 \cdot 10^3$

Tab. 1. Lambda factor, partial pressure and resistive values of titania samples.



Figs. 3(a) Calibration curve at 650°C for low oxygen concentration, (b) Resistance dependence vs lambda factor at 650°C.

Figs. 3a and 3b show the calibration curve at 650°C and the variation of the resistance as a function of the  $\lambda$  factor. Oxygen sensors based on microemulsion titania have shown also a fast dynamic response (see insert in Fig. 3a), a properties highly required for air to fuel regulation of combustion engines.

#### 4 Conclusion

Nanosized titanium oxide powders prepared through gel-combustion and precipitation in reactive microemulsion show promising properties for oxygen detection at high temperature. Particularly, reactive microemulsion give titania with better microstructural (lower grain size, higher surface area) and oxygen sensing properties.

#### References

- [1] J. W. Fergus, J. Mater. Sci. **38**, 4259 (2003).
- [2] J. Riegel, H. Wiedenmann, H. Neumann, Sol. State Ionics **152**, 783 (2002).
- [3] N. Savage, B. Chwieroth, A. Ginwalla, B.R. Patton, S.A. Akbar, P.K. Dutta, Sens. Actuators B **79**, 17(2001).
- [4] M. R. Ayers, A. J. Hunt, Mater. Lett. **34**, 290 (1998).
- [5] H. Herring, R. Hempelmann, Mater. Lett. **27**, 287 (1996).
- [6] R. Zhang, L. Gao, Mater. Res. Bull. **37**, 1659 (2002).

#### Acknowledgments

The authors gratefully acknowledge the financial support for this work by MIUR under the framework of FIRB-SQuARE project.

# Hydrocarbon Sensing Device Based on Binary Metal Oxides

S. Kandasamy<sup>1</sup>, A. Trinchì<sup>2</sup>, W. Wlodarsky<sup>1</sup>.

<sup>1</sup>*School of Electrical and Computer Engineering, RMIT University, GPO Box 2476V, Melbourne, VIC 3001, AUSTRALIA*

<sup>2</sup>*Imbedded Intelligence Team, CSIRO Manufacturing and Infrastructure Technology, Highett, Victoria, AUSTRALIA*

E. Comini<sup>3</sup>, G. Sberveglieri<sup>3</sup>

<sup>3</sup>*CNR-INFN - Sensor Laboratory, Department of Physics and Chemistry for Materials Engineering, University of Brescia, ITALY*

L. Pandolfi<sup>4</sup>, S. Kaciulis<sup>4</sup>

<sup>4</sup>*ISMN-CNR, Monterotondo (RM), ITALY*

## Summary

In this work, chemical and morphological properties of Ti-W-O mixed oxide, employed as material for hydrocarbon sensing devices, has been investigated. The reactive mixed oxide (Ti-W-O) was deposited by r. f. magnetron sputtering from a pure Ti/W target on the polished side of n-type 6H-SiC wafers. For the formation of the Schottky contact, a Pt layer of 100 nm was deposited on top of the oxide layer. The samples before and after thermal treatments were investigated by XPS and FE-SEM techniques.

The changes in the chemical composition and element distribution through the oxide film thickness, caused by thermal treatments, have been revealed. The morphological structure has been also investigated before and after the thermal treatments. The sensing performance of the Pt/(Ti-W-O)/SiC MROSIC device has been investigated as a function of temperature and concentration of propene in synthetic air.

## 1 Introduction

The prevention of the health risks due to the atmospheric pollution is one of the most important challenges in the countries with high industrial production. Nowadays the international rules are imposing the monitoring of hydrogen and hydrocarbons emitted during energy-intensive industrial processes.

Single metal oxides and their various combinations have shown particular sensitivity for H<sub>2</sub> and hydrocarbons. Bulk and surface properties of oxide film, such as band gap, electronic structure, position of Fermi level, etc., are determining its interaction with gases. Therefore, a contemplated choice of the mixed metals enables to obtain a sensing material where one of the above mentioned properties can be emphasized and employed for the gas monitoring.

Moreover, the necessity of direct pollution monitoring frequently requires of the devices working in critical conditions, such as high temperature and corrosive environment. Metal - reactive oxide - silicon carbide (MROSiC) devices have been indicated as one of the solutions for the reliable sensing in industrial environment [1-2].

The Ti-W-O films (as deposited, after annealing at high temperature and after gas sensing test), used in MROSiC sensing devices, were characterized by means of X-ray Photoelectron Spectroscopy (XPS) and Field Emission Scanning Electron Microscopy (SEM-FEG).

## 2 Experimental

Mixed metal oxide films were deposited on the polished side of N-doped (n-type) 6H-SiC wafers. Ohmic contact was formed on the unpolished side of SiC by depositing Ti and Pt, 100 nm each. A layer of Pt with a thickness of 100 nm was deposited on top of the reactive oxide film, forming the Schottky contact (Fig.1).

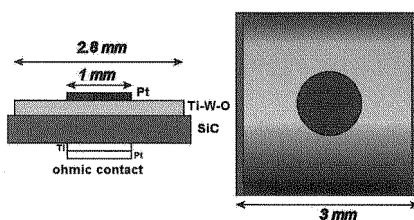


*Fig.1 Schematic of the MROSiC device.*

The mixed oxide was deposited using r. f. magnetron sputtering from a pure Ti/W alloy target (20% and 80% in weight) under reactive atmosphere (Ar : O<sub>2</sub> at  $8 \times 10^{-3}$  mbar). The substrate was kept at 300 °C to promote the formation of the film and to favour the filling of oxygen deficiencies.

For the gas sensing test, the operating temperature was varied between room temperature and 750 °C. Propene (C<sub>3</sub>H<sub>6</sub>) and hydrogen (H<sub>2</sub>), at a constant flow rate of 200 ml/min, were used as analyte gases after the sensor's stabilization in synthetic air. Their concentration was varied in the range of 0.06 to 1%. The response was measured as the voltage change, while the sensors were operated at constant bias current of 10 μA. This voltage shift was recorded by using a HP 33104A multi-meter. The current-voltage (*I-V*) characteristics were obtained using a Tektronix 571 curve tracer.

Selected-area XPS (SAXPS) measurements and Ar<sup>+</sup> ion sputtering have been performed in a VG Escalab MkII spectrometer (5 channeltron detection system; unmonochromatized source of Al Kα). The electrostatic lenses were operated in selected-area mode, providing photoelectrons collection from the sample area of about 0.3 mm<sup>2</sup>. The Ar<sup>+</sup> ion beam of 2.0 keV energy was rastered over an area of 1 x 1 mm<sup>2</sup> and operated at a current density  $j = 3 \mu\text{A}/\text{cm}^2$ .

The morphology of the samples has been investigated by using a LEO 1530 SEM-FEG instrument.

### 3 Results and Discussion

The Schottky contact and the reactive oxide film of the MROSiC gas sensor were investigated after its preparation (as deposited) and after the treatments at 450 °C for 1 h and at 600 °C for 2 h. The XPS depth profiles of two different areas of the as deposited sample are shown in Fig. 2-3.

The depth profile performed on the TiW film (Fig. 2) showed an uniform distribution of both the metals (Ti, W) through the film. The average atomic ratio of W and Ti was about 2.5. The oxygen amount decreased during the profiling due to the well-known effect of preferential sputtering. The rapid decrease of the oxygen and metals concentrations reveals a sharp interface between the oxide film and SiC substrate.

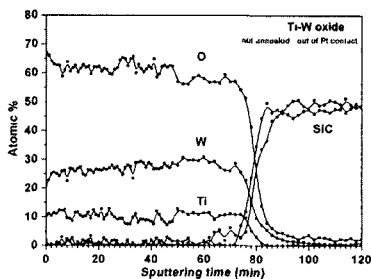


Fig.2 As deposited sample – depth profile out of the Pt contact.

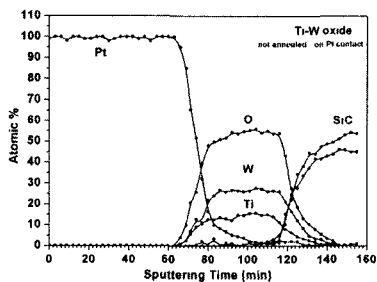


Fig.3 As deposited sample – depth profile on the Pt contact.

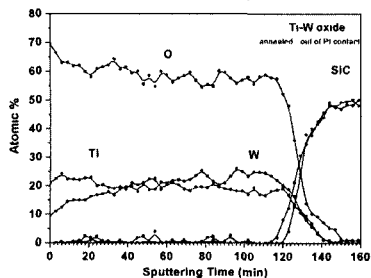


Fig.4 Annealed sample – depth profile out of the Pt contact.

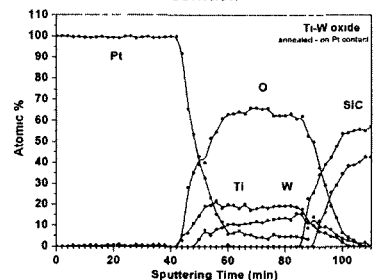


Fig.5 Annealed sample – depth profile on the Pt contact.

The depth profile, performed on the Pt contact, is presented in Fig. 3, where can be seen the multilayer structure of the sample: Pt/Ti-W-O/SiC. Also in this profile was revealed an uniform composition of the layers with steep interfaces.

The depth profiles of the annealed sample are shown in the Fig. 4-5. As it is possible to note, the W distribution through the film's thickness is not uniform. Moreover, the W : Ti ratio varies from 0.5 at the surface to 1.6 at the substrate. It is possible to suppose that the annealing was causing the segregation of W with

its consequent sublimation from the surface. The depth profile, performed on Pt contact, reveals a different picture. Due to the presence of Pt layer, the migration of W is directed not towards the surface but to the substrate. The broader interfaces Pt/oxide and oxide/substrate confirm the thermal diffusion of the metals towards the substrate. The results, obtained for the tested sample, were similar to the ones of the annealed sample. In the depth profile, performed on the Pt contact, the XPS signal of Pt was present until the substrate. The high working temperature caused an intermixing of Pt layer and oxide film.

On the surface of all investigated samples were present the metal ions of  $Ti^{+4}$  and  $W^{+6}$ . In the film's volume, the presence of W sub-oxides was revealed. The decrease of O concentration together with the change of the W chemical state could be attributed to the ion bombardment [3]. However, at the Pt /oxide interface, the W 4f line-shape is different from the one at the oxide/substrate interface. This result indicates that the presence of W sub-oxides is partially caused by the thermal processes in the MORSiC sample during the treatments.

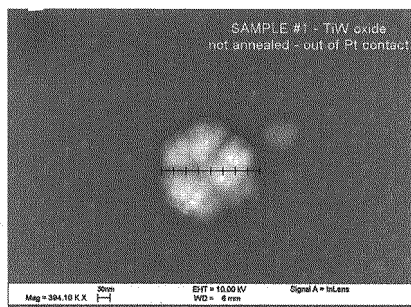


*Fig.6 As deposited sample*

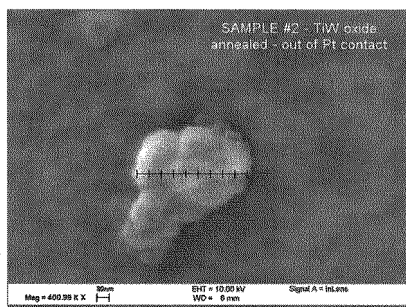


*Fig.7 Annealed sample*

The changes in the sample morphology after the treatment are shown in Fig. 6-7. The as-deposited film consists of amorphous layer with symmetrically shaped nano-crystallites sized of about 200 nm and located on the surface. The heat treatment causes the formation of a nanosized polycrystalline film [2]. The size of the crystallites is increased and their shape becomes asymmetrical.

The gas sensing tests were performed using  $C_3H_6$  and  $H_2$  in air. The sensor presented a maximum voltage shift of 2.52 V when exposed to 1%  $C_3H_6$  at 420 °C. The sensitivity was decreasing with increasing temperature. In the case of 1%  $H_2$ , a maximum shift of 1.15 V was registered at 200 °C, whereas it was only 0.46 V at 420 °C. The response to 1%  $C_3H_6$  is approximately 5 times higher than to the same concentration of  $H_2$ .

Fig. 8 shows the dynamic response-recovery characteristics of the sensor at 420 °C. The voltage shifts of about 2.52 and 0.35V were observed for 1 and 0.06% of  $C_3H_6$ , respectively. The sensor exhibits fast response time (~15 to 20 s), and a longer recovery time (~ 350 s). In the detection of hydrocarbons, the



slow recovery time may not pose a practical problem. The relation between the voltage shift and the  $C_3H_6$  gas concentration is fairly linear, indicating a large operating dynamic range. The  $I-V$  characteristics of the device are shown in Fig. 9. A shift in the  $I-V$  curves was observed when 1% of  $H_2$  and  $C_3H_6$  were introduced into synthetic air. At 420 °C and 10  $\mu A$ , the shifts of 2.6 and 0.46 V were observed for 1%  $C_3H_6$  and  $H_2$ , respectively.

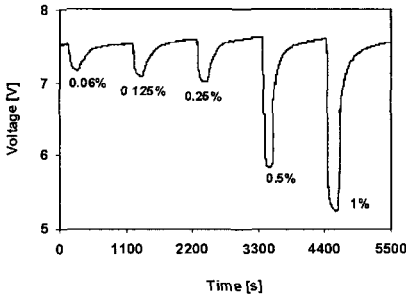


Fig.8 The response-recovery characteristics of the sensor

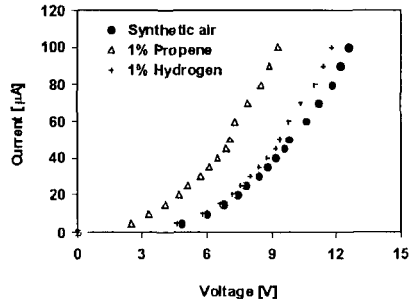


Fig.9 Comparison of the sensor's response to different ambient atmospheres

## 4 Conclusions

The SAXPS investigation has revealed the elemental distribution through the whole thickness of the sensor. Also the changes in the chemical composition and in the morphology of the samples after the thermal treatments have been determined. The results of gas sensing tests and micro-chemical investigations demonstrated the suitability of mixed Ti-W oxide for the application in MORSiC gas sensing devices.

## Acknowledgments

The authors are grateful to Dr. G.M. Ingo (ISMN-CNR) for the acquisition of SEM-FEG images.

## References

- [1] C. V. Gopal Reddy, W. Cao, O. K. Tan, W. Zhu and S. A. Akbar, "Selective detection of ethanol vapor using  $xTiO_2-(1-x)WO_3$  based sensor," *Sens. Actuators B*, vol. 94, pp. 99-102, 2003.
- [2] E. Comini, G. Sberveglieri and V. Guidi, "Ti-W-O sputtered thin film as n- or p-type gas sensors," *Sens. Actuators B*, vol. 70, pp. 108-114, 2000.
- [3] S. Kaciulis, G. Mattogno, "Characterization of thin-film devices for gas sensing" *Surf. Interface Anal.*, vol. 30, pp. 502-506, 2000.

# Multi-Cavity Structured FBGs: Towards Advanced Chemical Sensing Devices

A. Iadicicco, D. Paladino, A. Cutolo, A. Cusano\*  
*Engineering Department, University of Sannio, Benevento, Italy*  
[a.cusano@unisannio.it](mailto:a.cusano@unisannio.it)

S. Campopiano  
*Department for Technologies, University of Naples Parthenope, Napoli, Italy*

M. Giordano  
*Institute of Composite Biomedical Materials, National Research Council,  
Napoli, Italy*

## Summary

This work deals with micro-structured fiber Bragg grating (MSFBG) involving two-defect. Every perturbation consists in a localized stripping of the cladding layer, leading to a distribute phase shift on the guided mode. As consequence one or more defect states are induced inside the original grating bandgap. On the other hand, the spectral features strongly depend on the perturbations features (length and depth), refractive indices surrounding the thinned areas and the geometrical distribution of the perturbations along the structure. Based on the high sensitivity to the external medium refractive index, this structure exhibits attractive features for communication and sensing applications. This work is focused on the possibility to use the two-defect MSFBG for dual-SRI measurements by a single sensing element. This approach could be a suitable solution when a large number of spatial locations have to be monitored.

## 1 Introduction

Recently, the authors proposed and experimentally realized a novel configuration of in-fibre periodic structure employing a localized defect along a standard fiber Bragg grating (FBG) [1-2]. The perturbation consists in a localized stripping of the cladding layer positioned in the centre of the grating. The defect along the periodic structure induces changes in the core propagation [3] and thus a phase-shift on the guided mode [1], leading to the formation of a defect state inside the original bandgap. The length and the depth of the induced perturbation as well as the surrounding refractive index (SRI) define the spectral response of the micro-structured FBG (MSFBG) in terms of position of the defect state inside the band-gap. Differently from standard phase shift grating (PSG) [4], here the spectral position of the defect state is strongly related to the SRI. This effect has been efficiently used for high resolution refractive measurements [2]. Successively the authors report a preliminary study on a two-defect structure, revealing attractive spectral features for sensing and communication applications. In this work, the spectral characteristics of a multi-

defect MSFBG as well as its potentialities for multi-SRI measurement by a single sensing element are numerically investigated.

## 2 Two-Defect structured FBG

According to one-dimensional photonic band-gap [6] and in-fibre phase shift grating (PSG) [4] theories, more perturbations along a periodic structure permit more defect states to be located inside the band-gap. Fig. 1 plots a schematic diagram of a FBG with two cladding stripped regions.  $L_{Th}$  and  $D_{Th}$  are the thinned region length and diameter, respectively, while the subscript 1 and 2 indicate the first and the second perturbation (from left to right). In addition,  $L_1$  and  $L_3$  indicate the left and right unperturbed grating regions lengths while  $L_2$  is the length of the unperturbed region between the thinned areas. As demonstrated in previous work [5], in the multi-defect MSFBG, the spatial distribution of the defects plays a fundamental role on spectral response, in terms of shape and spectral position of the defect states. In particular, the formation of a single defect state with flat band or two defect states is ruled by the ratio of the unperturbed grating length. Here, the geometrical parameters of the investigated structures are selected in order to achieve two-defect state inside the original bandgap.

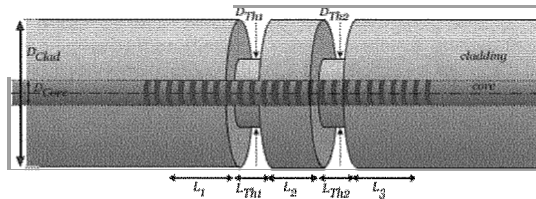


*Fig. 1 Schematic diagram of the two cavities MSFBG (not in scale)*

Numerical analysis based on multilayer approach and doubly cladding fiber model allows an accurate spectral investigation. Here SMF-28 optical fibre features have been used [2]. Fig. 2.a shows the reflected spectra of a MSFBG with two perturbations consisting in totally cladding stripping ( $D_{Th1}=D_{Th2}=D_{Core}$ ) for different SRIs and in case of  $L_1=L_3=2000\mu\text{m}$ ,  $L_{Th1}=L_{Th2}=500\mu\text{m}$  and  $L_2=1000\mu\text{m}$ . Note that the same SRI for both thinned regions has been taken into account. The selected grating exhibits a core refractive index modulation with maximum amplitude  $\Delta n=7\cdot 10^{-4}$ , leading to a central wavelength  $\lambda_B=1550.08\text{nm}$  and a maximum reflectivity of about 99%. As expected, more defect states are induced inside the spectral band-gap. Moreover, SRI changes are able to strongly influence the spectral response of the device, in terms of the defect state shift, leading to the possibility to realize advanced all-fiber devices.

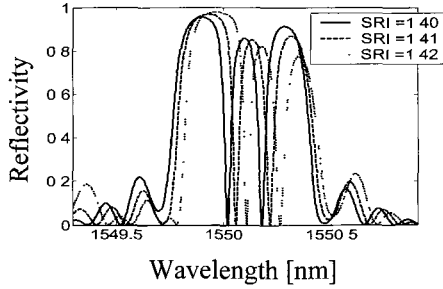


Fig. 2 Spectral response of a two-defect MSFBG for different SRI in case of full etching,  $L_1=L_3=2000\mu\text{m}$ ,  $L_{\text{Th}1}=L_{\text{Th}2}=500\mu\text{m}$  and  $L_2=1000\mu\text{m}$ .

### 3 Sensing Applications

In this section, a preliminary study on the possibility to use a single two-defect MSFBG for dual-SRI measurements, by monitoring the shifts of the central wavelengths of the defect states, is presented. When a large number of spatial locations have to be monitored this approach is the suitable solution.

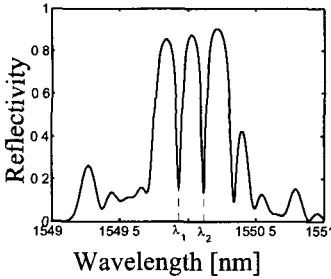


Fig. 3 Spectral response of asymmetric two-defect MSFBG

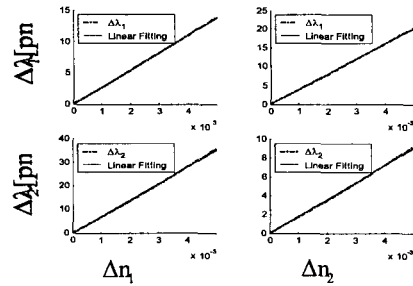


Fig.4 Shifts of the central wavelengths of both defect states versus as  $\Delta n_1$  and  $\Delta n_2$  move in a range of  $5 \cdot 10^{-3}$ .

The investigated structure is characterized by  $L_1=L_3=1650\mu\text{m}$ ,  $L_{\text{Th}1}=L_{\text{Th}2}=950\mu\text{m}$ ,  $L_2=800\mu\text{m}$ ,  $D_{\text{Th}1}=D_{\text{Th}2}=D_{\text{Core}}$ . The SRIs in the two thinned regions move in different ranges: in particular, the SRI in the perturbation 1 moves around 1.42, while the other one around 1.40.  $\Delta n_1$  and  $\Delta n_2$  denote the SRI changes in the perturbation 1 and 2, respectively. Fig. 3 shows the spectral response of the MSFBG in case of unperturbed SRIs. The selected geometrical parameters induce two-defect states inside the spectral band-gap [5], centered at  $\lambda_1=1549.935\text{nm}$  and  $\lambda_2=1550.116\text{nm}$  and ruled by the phase shift of both perturbations. Here, weak defect states are achieved since an asymmetric structure (different SRIs) is taken into account.

The fig. 4 shows that the shifts in the central wavelengths of the two defect states exhibit a quasi linear behaviour versus SRI changes, if  $\Delta n_1$  and  $\Delta n_2$  move in a small range. Based on this result and supposing that the effects of  $\Delta n_1$  and  $\Delta n_2$  can be separated, we can write the wavelength shifts as:

$$\begin{cases} \Delta \lambda_1 \cong k_1 \Delta n_1 + k_2 \Delta n_2 \\ \Delta \lambda_2 \cong k'_1 \Delta n_1 + k'_2 \Delta n_2 \end{cases} \quad (1)$$

where  $\Delta \lambda_1$  and  $\Delta \lambda_2$  are the central wavelength shifts of the left and right defect state, respectively, and  $k_1$ ,  $k_2$ ,  $k'_1$  and  $k'_2$  are constants indicating the sensitivity of the two defect states central wavelengths versus the SRI variations in the two perturbations. Assuming that  $k_1$ ,  $k_2$ ,  $k'_1$  and  $k'_2$  are known, eqs. (1) can be easily solved for  $\Delta n_1$  and  $\Delta n_2$ . From the fig. 4 the following coefficients are estimated:  $k_1=2.753\text{nm}$ ,  $k_2=7.014\text{nm}$ ,  $k'_1=4.037\text{nm}$  and  $k'_2=1.799\text{nm}$ . In case of asymmetric structure, the eqs. (1) form a well-conditioned system, leading to the following solution:

$$\begin{cases} \Delta n_{1S} = \frac{k'_2 \Delta \lambda_1 - k_2 \Delta \lambda_2}{k_1 k'_2 - k'_1 k_2} \\ \Delta n_{2S} = \frac{k_1 \Delta \lambda_2 - k'_1 \Delta \lambda_1}{k_1 k'_2 - k'_1 k_2} \end{cases} \quad (2)$$

where  $\Delta n_{1S}$  and  $\Delta n_{2S}$  are the estimated SRIs variations. They can be slightly different from the  $\Delta n_1$  and  $\Delta n_2$  due to the linear approximation and to the separation of the two perturbations effects proposed by eqs. (1). This means that the residuals  $R_1=\Delta n_{1S}-\Delta n_1$  and  $R_2=\Delta n_{2S}-\Delta n_2$  are strongly dependent on the  $\Delta n_1$  and  $\Delta n_2$  variation ranges, thus the approach advised in eqs. (1) is correct as both  $\Delta n_1$  and  $\Delta n_2$  move in a small range.

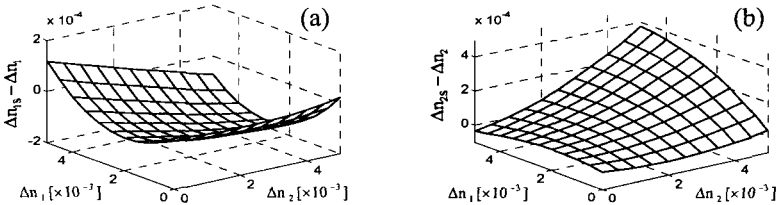


Fig. 5 Residual  $R_1=\Delta n_{1S}-\Delta n_1$  (a) and  $R_2=\Delta n_{2S}-\Delta n_2$  (b) versus  $\Delta n_1$  and  $\Delta n_2$  moving in a range of  $5 \cdot 10^{-3}$  around 1.42 and 1.40, respectively

In order to prove the capability to demodulate the SRI variations in both thinned regions through the linear approximation proposed in eqs. (1), different variations of  $\Delta n_1$  and  $\Delta n_2$  from 0 to  $5 \cdot 10^{-3}$  are taken into account and the induced  $\Delta \lambda_1$  and  $\Delta \lambda_2$  are numerically computed. Then  $\Delta n_{1S}$  and  $\Delta n_{2S}$  are calculated by eq. (2). Figs. 5.a and 5.b report the residuals  $R_1$  and  $R_2$  versus the simultaneous variations of  $\Delta n_1$  and  $\Delta n_2$  in the range  $0 \div 5 \cdot 10^{-3}$  around 1.42 and 1.40

respectively, revealing that the maximum residuals are  $R_{1\max}=1.7\cdot 10^{-4}$  and  $R_{2\max}=3.8\cdot 10^{-4}$ .

As  $\Delta n_1$  and  $\Delta n_2$  move in a range of  $10^{-3}$  around 1.42 and 1.40, respectively, the higher errors strongly decreases to  $R_{1\max}=7.0\cdot 10^{-6}$  and  $R_{2\max}=1.5\cdot 10^{-5}$ . It is obvious that the decrease in the residuals is related to a better linear approximation of the  $\Delta\lambda_1$  and  $\Delta\lambda_2$  as the SRIs move in a smaller range. Based on these results a single multi-defect MSFBG packaged by a properly micro-fluidic holder can be efficiently used for multi-SRI measurements.

#### 4 Conclusions

Based on the obtained results a single multi-defect MSFBG packaged by a properly micro-fluidic holder can be efficiently used for multi-SRI measurements. Note that the small investigated SRI ranges are not limitative for the proposed sensor configuration in case of chemical applications, where low concentration (with the order of ppm) of pollutants needs to be monitored.

The study of MSFBGs with more than two defects is currently under investigation, while, differently from previous works, a new fabrication technique based on UV laser micromachining is actually explored for the first multi-defect MSFBG prototype realization.

#### References

- [1] A. Iadicicco, S. Campopiano, A. Cutolo, M. Giordano, A. Cusano, "Micro-Structured Fiber Bragg Gratings: Analysis and Fabrication", IEE Electronic Letters, Vol. 41, No. 8, April 2005.
- [2] A. Iadicicco, S. Campopiano, A. Cutolo, M. Giordano, A. Cusano, "Refractive Index Sensor Based on Micro-Structured Fiber Bragg Grating", IEEE Photonics Technology Letters Vol. 17, No. 6, June 2005.
- [3] A. Iadicicco, A. Cusano, A. Cutolo, R. Bernini, M. Giordano, "Thinned Fiber Bragg Gratings as High Sensitivity Refractive Index Sensor", IEEE Photonics Technology Letters, Vol. 16, No. 4, 1149-1151, April 2004.
- [4] L. Wei, J.W.Y. Lit, "Phase Shifted Bragg Grating Filters with Symmetrical Structures", Journal of Lightwave Technology, Vol. 15, No. 8, August 1997.
- [5] A. Cusano, A. Iadicicco, S. Campopiano, M. Giordano, A. Cutolo, "Thinned and Micro-Structured Fiber Bragg Gratings: Towards New All Fiber High Sensitivity Chemical Sensors", Journal of Optics A: Pure and Applied Optics Vol. 7, pp. 734-741, 2005.
- [6] I. Del Villar, I. R. Matías, F. J. Arregui, "Fiber-Optic Multiple-Wavelength Filter Based on One-Dimensional Photonic Bandgap Structures With Defects", Journal of Lightwave Technology, Vol. 22, No. 6, June 2004.

# Belgian beer mapping and digital fingerprinting using color and turbidity assessment

A.G. Mignani, L. Ciaccheri  
CNR-IFAC, Sesto Fiorentino (FI), Italy  
[l.ciaccheri@ifac.cnr.it](mailto:l.ciaccheri@ifac.cnr.it)

## Summary

Multi-wavelength and multi-angle absorption spectroscopy performed in the visible spectral range, that is, 'scattered colorimetry', has been used to map a library of 25 diverse and commercially-available Belgian light beers. The resulting map shows four main clusters, relative to blonde, amber, red, and weiss beers, respectively, demonstrating that scattered colorimetry is a valid method for beer authentication and fingerprinting.

## Introduction

Beer is one of the Belgium's greatest specialities. There are more than 100 different breweries producing beers with unusual tastes [1-4]. In addition to having a different taste, each beer has a different and distinctive appearance, which is caused not only by the color but also by the turbidity content. Consequently, the beer's appearance can be considered as a product fingerprint. Suitable methods and technologies for product qualification, authentication, and certification are advisable in order to protect both producers and consumers.

The brewing industry, both the artisan breweries and the large-scale complexes, make use of specially-equipped laboratories for the assessment of beer quality, so that the production process can be optimized. Chemicals responsible for flavor and nutritional aspects, which are of particular interest to beer drinkers are monitored. Other parameters, such as allergens and microbiological organisms, are also measured, in order to guarantee quality and safety during the production process and packaging phase [5, 6].

This paper presents a technique that takes into account the whole content of color and turbidity of beer. Instead of measuring color and/or turbidity only, some indicators are measured that consider the global contribution of both color and turbidity. This is a physical information which can be considered to be complementary with respect to that provided by using standard analytical techniques. The result of this study is the mapping of 25 diverse and commercially-available Belgian light beers. The mapping can be considered as a digital fingerprinting of the beer samples.

## Scattered colorimetry

Multi-wavelength and multi-angle absorption spectroscopy performed in the visible spectral range, which we call ‘scattered colorimetry’ or ‘spectral nephelometry’, is a novel optical method for simultaneously monitoring the whole content of color and turbidity in liquids.

The instrumentation used for scattered colorimetry is an optoelectronic device for measuring the absorption spectra of samples at different angles. It consists of four white-light LEDs spanning the 450-650 nm spectral range, with a miniaturized optical fiber spectrometer that serves as a detector (Figure 1-left). The sources, which can either be fitted to the probe or guided by optical fibers, are located at an angle of  $0^\circ$ ,  $30^\circ$ ,  $60^\circ$ , and  $90^\circ$  with relation to the detector (Figure 1-right) [7, 8]. The LEDs are switched on sequentially in order to measure the transmitted and scattered spectra. Because scattering is a wavelength-dependent phenomenon, the spectrum transmitted in turbid media, which mainly provides information regarding color, is also affected by turbidity. On the other hand, the scattered spectra, which mainly provides information on turbidity, is also affected by color. Given the spectrometer’s spectral resolution, the sample of liquid under test can be characterized by means of a maximum of 184 spectral values coming from the four absorption spectra, each of which consists of 46 wavelengths.

Multivariate data processing is used to achieve a reduction in data dimensionality so as to better extract information significant for sample identification [9-12]. The spectral data are usually processed using principal component analysis (PCA) or linear discriminant analysis (LDA), which provide the coordinates for identifying the samples on two- or three-dimensional maps. When several samples of liquids are analyzed, the maps are populated by point clusters, each of which groups the samples in terms of the similarities in their color and turbidity.

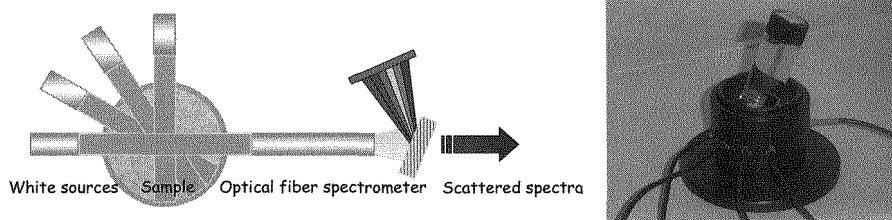


*Figure 1 Working principle of scattered colorimetry (left) and optical probe (right)*



Brand	Type	alc. %	code	Note	PC 1	PC 2
DAS	Hougaardse #1	5,1	DH1	Amber	-4.0	4.2
DAS	Hougaardse #2	5,1	DH2	Amber	-2.4	4.1
Belle-Vue	Gueuze	5,5	BVG	Amber	-3.1	3.9
Dubuisson	Bush	12	DBB	Amber	-4.5	6.1
Pauwel	Kwak	8	PWK	Amber	-8.4	6.9
Palm	Speciale	5,2	PLS	Amber	-2.2	4.2
Hoegaarden	Grand Cru	8,5	HGC	blonde	5.6	0.1
Karmeliet	Triple	8	KTR	blonde	6.9	0.3
Grimbergen	Blonde	6,7	GBB	blonde	5.2	0.2
Kasteel	Blonde	11	KSB	blonde	9.9	-2.8
Brugge	Tripel	8,2	BRT	blonde	1.0	3.5
Leffe	Blonde	6,6	LFB	blonde	3.8	2.0
Caney	Blonde	7	CNB	blonde	5.5	0.1
Duvel	Blonde	8,5	DVB	blonde	11.4	-3.9
Brugse	Straffe Hendrik	6	BSH	blonde	5.9	-0.6
Jupiler	Blonde	5,2	JPB	blonde	9.2	-1.8
Pilaarbijter	Pilaarbijter	7,5	PLB	blonde, fermented in bottle	8.6	-2.7
Brigand	Brigand	9	BRG	blonde, fermented in bottle	4.9	0.6
Timmermans	Peche	4	TMP	blonde, peach taste	2.3	2.3
Corsendonk	Corsendonk	7,5	CRD	Red	-19.5	-2.4
Hoegaarden	Verboden Vrucht	8,5	HGV	Red	-13.2	3.8
Rodenbach	Rodenbach	5	RDB	red, cherry taste	-19.3	-2.1
Belle-Vue	Kriek	5,1	BVK	red, cherry taste	-22.0	-13.9
Hoegaarden	Witbier	4,9	HGW	Weiss	11.1	-7.1
Brugs	Witbier	4,8	BGW	Weiss, orange taste	7.6	-5.2

*Table 1 List and characteristics of Belgian beers measured using the scattered colorimetry technique*

### Beer mapping and fingerprinting

A library of 50 diverse and commercially-available Belgian light beers was considered, as listed in Table 1. These beers differ not only in terms of color and turbidity, but also in their alcoholic content. Brown beers were not considered because of their high absorbance, which results in a poor signal-to-noise ratio. The beer samples were measured using the scattered colorimetry technique, and Figure 2 shows the absorption spectra measured at 0° and 90°. The spectral data

were processed by means of PCA, and Figure 3 shows the beer mapping in the PC1-2 subspace. Figure 3-left shows the mapping according to the symbols that were assigned to the beer types, while Figure 3-right highlights the four main clusters according to type: blonde, amber, red, and weiss. The PC1 and PC2 coordinates, which represent the digital fingerprinting of the measured beers, are listed in Table 1.

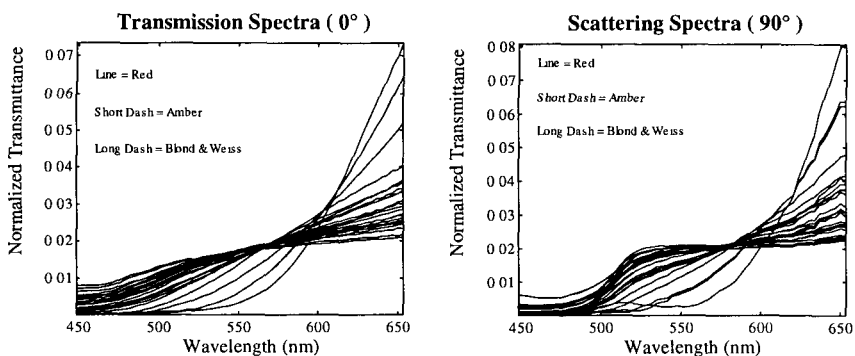


Figure 2 Transmission (left) and  $90^\circ$ -scattering spectra (right) of the blonde, amber, red and weiss Belgian beers

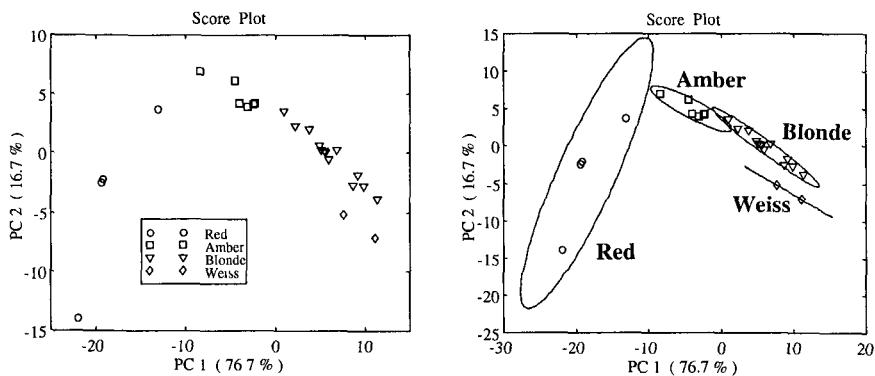


Figure 3 Beer mapping in the PC1-2-3 subspace: according to symbols assigned to the beer types (left), and highlighting the four main clusters according to types: blonde, amber, red, and weiss (right)

## Conclusions

Using scattered colorimetry and PCA data processing, we accurately and non-subjectively mapped different kinds of Belgian beers and grouped them

according to assigned classes. The sharp clustering of blonde, amber, red, and weiss types demonstrates that scattered colorimetry and PCA data mining provide a valid method for beer authentication and fingerprinting. The implementation of an online system to be used in one or more production stages is possible. This could be designed as a multipoint sensing device controlled by a single electrooptic unit. A further implementation of this technique is a multispectral analysis in the UV, near- and mid-infrared spectral regions and the correlation of the spectral data to the most important chemical quantities.

## References

1. M. Jackson's, *Great Beers of Belgium*, Media Marketing Communication SA, Antwerpen, 2001.
2. T. Webb, *Good Beer Guide to Belgium*, Gardners Books, Eastbourne, 2005.
3. B. Dubrulle, *Guide to Belgian Beers*, NeoCity Publishing, Ghent, 2005.
4. <http://belgianstyle.com/mmguide/> .
5. <http://www.ebc-nl.com/> and <http://www.asbcnet.org/> .
6. Y.H. Hui, *Data Sourcebook for Food Scientists and Technologists*, John Wiley&Sons, 1991.
7. A.G. Mignani, L. Ciaccheri, P.R. Smith, A. Cimato, C. Attilio, R. Huertas, M. Melgosa Latorre, A.C. Bertho, B. O'Rourke, N.D. McMillan, 'Scattered colorimetry and multivariate data processing as an objective tool for liquid mapping', *SPIE vol. 5855 17<sup>th</sup> International Conference on Optical Fibre Sensors*, pp. 38-41, 2005.
8. A.G. Mignani, L. Ciaccheri, A. Cimato, C. Attilio, P.R. Smith, 'Spectral nephelometry for the geographic classification of Italian extra virgin olive oils', *Sensors and Actuators B*, vol. 111-112, pp. 363-369, 2005.
9. I.A. Cove, J.W. McNicol, 'The use of principal component in the analysis of the near infrared spectra', *Applied Spectroscopy*, vol. 39, 1985, pp. 257-266.
10. B.G.M. Vandeginste, D.L. Massart, L.C.M. Buydens, S. De Jong, D.J. Lewi, J. Smeyers-Verbeke, *Handbook of Chemometrics and Qualimetrics*, Elsevier Science BV, Amsterdam, 1998.
11. M.J. Adams, *Chemometric in Analytical Spectroscopy*, Royal Society of Chemistry, Cambridge UK, 1995.
12. T.M. Cover, P.E. Hart, 'Nearest neighbor pattern classification', *IEEE Transaction on Information Theory*, vol. IT-13, 1967, pp. 21-27.

# A portable fluorometer for the rapid screening of M1 aflatoxin in milk

C. Cucci, A.G. Mignani  
CNR-IFAC, Sesto Fiorentino (FI), Italy  
[c.cucci@ifac.cnr.it](mailto:c.cucci@ifac.cnr.it)

C. Dall'Asta, G. Galaverna, A. Dossena, R. Marchelli, R. Pela  
*Department of Organic and Industrial Chemistry, University of Parma, Italy*

## Summary

A compact fluorometric sensor equipped with a LED source and a high sensitivity PMT detector has been implemented for the selective detection of native fluorescence of aflatoxin AFM1 in liquid solutions. This compact and easy-to-handle device is addressed to the rapid monitoring of AFM1 in milk, enabling the detection of concentrations up to the legal limit, which is 50 ppt. The system is suitable for preliminary screening at the earlier stages of the industrial process, and makes it possible to discard contaminated milk stocks before their inclusion in the production chain.

## Introduction

Aflatoxins are fungal metabolites produced by widespread moulds (*Aspergillus* species), which can colonise foodstuffs and feed. Among the different aflatoxins identified, four types (aflatoxin B1, B2, G1 and G2) are of main interest, since they have been classified as Group 1 carcinogens by the IARC [1]. Aflatoxin B1 (AFB1), normally predominant in agricultural products, has the highest toxic potential [2, 3]. Its main metabolite is AFM1, also known as 'milk toxin'. AFM1 is indeed found in milk of lactating animals following their ingestion of AFB1-contaminated feed [4, 5]. AFM1 is considered to be a highly hazardous food contaminant, due to the fundamental role of milk in the human diet, especially as infant nourishment.

At international level, the EU has the most rigorous regulations concerning mycotoxins in food [6]. As regards AFM1 in milk, the maximum legal limit is set at 0.05 µg /Kg (50 ppt) for all EU Member States, and guidelines suggest to allowing Member Countries to adopt lower limits (25 ppt) for baby food [7].

Nowadays, different methods, based on HPLC, TLC or immunoassay methods (ELISA), are well-established for detection of AFM1 in milk [8, 9, 10, 11]. These procedures require trained staff and/or expensive equipments, and are not suitable for large-scale screenings. In addition, the routine laboratory controls can be insufficient for coping with sporadic 'aflatoxins emergencies', that are linked to particular environmental/seasonal conditions which favour the fungal

invasion of animal feeds and agricultural products. New low-cost screening methodologies suitable for rapid and large-scale tests on milk are therefore still greatly needed.

In the present work, a prototype of a compact and easy-to-handle device for the rapid detection of AFM1 at concentrations up to the legal limit (50 ppt) is presented. The system is a portable fluorometer based on a LED source and an extremely sensitive PMT detector, which make possible the direct identification of low concentrations of AFM1. This system is intended to be used for quick 'threshold indications' and as an 'early warning system', so as to rapidly single out risk/alarm situations. Three levels of contamination are thus identified: 1) 'alarm' 2) 'alert for baby-food' and 3) 'safe'. Although tested up to now only on synthetic solutions of AFM1, this methodology is highly promising in a perspective of large-scale controls on the milk industrial chain. Indeed, it would make it possible to simply discard contaminated milk stocks before their inclusion in the production chain.

### **The instrumentation**

The instrumentation consisted of a commercially-available compact device for fluorescence analysis [12], which had been specifically re-adapted and optimised for the selective detection of AFM1 in liquid samples.

As shown in Figure 1-left, the instrument made use of a LED source and a highly sensitive PMT detector that made it possible to measure extremely low fluorescence signals. The source and the detector were equipped by means of band pass filters, which provided an optimal optical isolation between the illumination and detection spectral bands. The optical system was PC-driven, and the measurement procedure could be suitably automated by using the specific software. Although the instrument was equipped by means of a quartz cuvette, it could be easily implemented by means of an optical fiber strand, as shown in Figure 1-right.

The optical system consisted of inter-changeable modules, which made the fluorometer highly versatile and adaptable for different applications. In the present work, the LED and the filters of the original instrument have been replaced with new units optimised to match the fluorescence bands of AFM1 aflatoxin [13, 14]. The technical specifications of the optical components used were the following: LED source: Roithner Lasertechnik, UVLED365-10 ( $\lambda=365\text{nm}$ , 1.4 mW at 20 mA,  $10^\circ$ , TO-46 ball lens); Excitation filter: Roithner Lasertechnik, RLT-365-12-A (center band: 365nm); Emission filter: Edmund Optics, Filt. 450nm Broad PO-016746 (center band 450nm); Cell: Quartz ultra-micro cuvette, Hellma 105.251-QS, volume: 45  $\mu\text{l}$ .

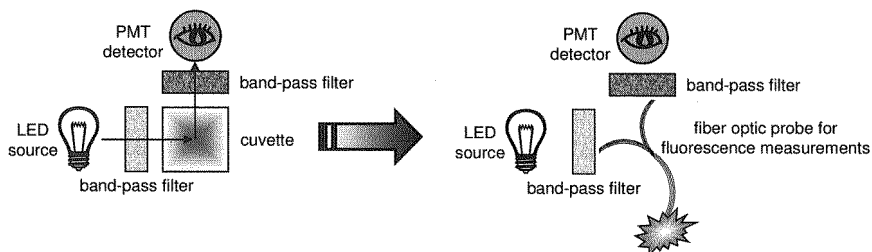


*Figure 1 Schematic diagram of the fluorometer (left) and its possible implementation using fiber optics (right)*

Preliminary tests were performed to check the stability of the system, the entity of the background signal, and the possible noise contributions to the fluorescence signal, under typical measurement conditions. The background signal due to the pure solvent was estimated by using bi-distilled water, ethanol and acetone. With the selected optical configuration, the lowest background signal was obtained using bi-distilled water, which was about  $2800 \pm 100$  counts. Bi-distilled water was therefore the solvent selected for the preparation of AFM1 samples.

## Experimental results

The experimental tests were aimed at measuring the titration curve for the AFM1 aqueous solutions in the 0-125 ppt range, step 25ppt, which is the interval of interest for practical applications. All the samples were prepared by diluting a standard solution of AFM1 (1 ppm; Suppl.: BIOPURE Tulln, Austria). It should be emphasized that the fluorescence signals were directly detected in the solutions prepared at the concentrations reported, without any pre-concentration of the samples, as usually is required in HPLC measurements.

The high sensitivity of the fluorometer had the major drawback of the high susceptibility of the quantitative result to several sources of uncertainty in the measurement and in the sample preparation. In addition to the practical difficulty of obtaining identical replicas of a sample, especially in the case of very low AFM1 concentrations, other sources of uncertainty were present, such as cleanliness of the cell, and impurities or air bubbles in the liquid. Consequently, in order to ensure measurement reproducibility, an experimental protocol was established for: a) sample preparation, b) the method of injecting samples into the cell, aimed at avoiding the formation of micro-air bubbles; c) cell cleaning after measurement; d) check of the cell cleanliness by measuring the reference liquid (pure water).

Six series of samples covering the 0-125 ppt range were prepared and measured in independent sessions. The experimental results, together with the error bars, are shown in Figure 2. Each point of the curve was calculated as mean value over six measurements.

Since the main interest was to develop a reliable screening device able to rapidly single out situations of potential risk, starting from the titration curve three main 'thresholds' were identified:

- level 1 - 'safe', AFM1 < 25 ppt: [2000-2900] photo-counts;
- level 2 - 'alert for baby-food', 25 ppt < AFM1 < 50 ppt: [2900-3770] photo-counts;
- level 3 - 'alarm', AFM1 > 50 ppt: over 3770 photo-counts.

Thus, based on this simplified reference scale, the fluorometer could be used as the starting point for 'tree decisions' when measuring fluorescence of unknown samples: if the result is level 1, the sample is considered 'safe' and the control chain ends at this point; if the fluorescence value falls in level 2, the sample is potentially contaminated, and more thorough analyses are needed; if the result is level 3, the sample belongs to a stock contaminated over the admitted level, and the stock should be discarded.

## Conclusions

A portable fluorometer was proposed for the rapid and straightforward detection of low concentrations of AFM1, without any need of pre-concentration of the sample. The technical features of the fluorometer were presented, with a special focus on its potentialities as an 'early warning system', which makes it possible to distinguish between 'safe' and potentially contaminated samples, according to the legal definition.

Although still limited to tests with synthetic solutions of AFM1, the results obtained encourage us to regard this prototype as the starting point for a new low-cost technology for the rapid screening of AFM1 in milk. Further development could involve a procedure suitable for non-trained users based on low-cost materials, such as disposable plastic cells.

## Acknowledgments

Project MIUR-FIRB #RBNE01KZZM 'Biosens' is gratefully acknowledged for the partial financial support. The authors would like to thank Mr. Franco Cosi for the technical assistance.

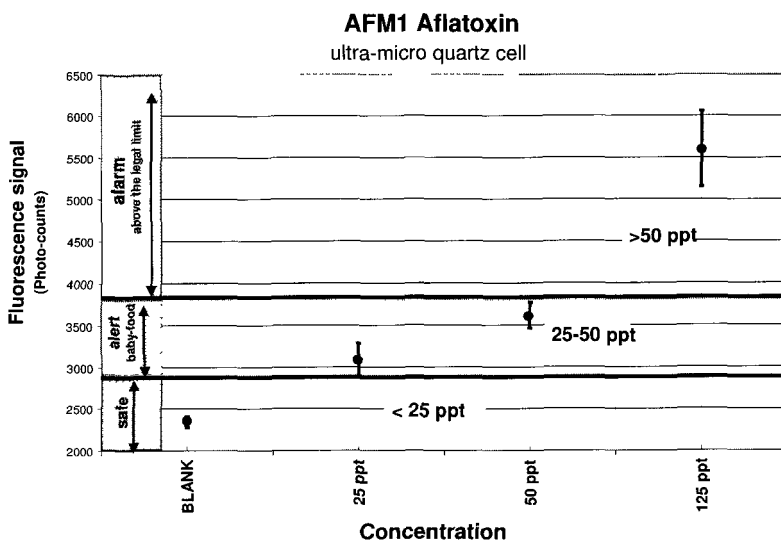


Figure 2 Titration curve for AFM1 aqueous solutions in the 0-125 ppt concentration range

## References

- <sup>1</sup> IARC Monographs on the Evaluation of Carcinogenic Risks to Humans. International Agency for Research on Cancer, Lyon, 56 (1993).
- <sup>2</sup> P.M. Scott, *J. Assoc. Off. Anal. Chem.* **70**, (1987), 276.
- <sup>3</sup> J. Leitao, G. De Saint Balnquat, J. R. Bailly, Ch. Paillas; *J. Chromatogr. A*, **253**, (1998), 229-234.
- <sup>4</sup> R. Alleroft, R. B. A. Carnaghan, *Vet. Rec.* **65**, (1963), 259.
- <sup>5</sup> H.P. Van Egmond, Introduction in Mycotoxins Dairyproducts, Elsevier Applied Science, London 1998.
- <sup>6</sup> FAO, Worldwide regulations for mycotoxins 1995 - A compendium. FAO Food and Nutrition Paper, **64** Rome, ISSN0254-4725 (1997).
- <sup>7</sup> European Committee Regulation No. 1525, Bruxelles, 16 July 1998.
- <sup>8</sup> W.Th. Kok, Th.C.H. van Neer, W.A. Traag, L.G.M.Th Tuinstra; *J. Chromatogr.* **367**, (1986), 231-236.
- <sup>9</sup> M.J. Sheperd, J. Gilbert; *Food Add. Contam.* **1** (1984), 322.
- <sup>10</sup> H. Joshua, *J. Chromatogr. A* **654**, (1993), 247-254.
- <sup>11</sup> O. J. Francis, G.P. Kirschenheuter, G.M. Ware, A.S. Barman, S.S. Kuan, *J. Assoc. Off. Anal. Chem.* **7**, (1988), 725-728.
- <sup>12</sup> PMT-FL fluorometer, Fialab Instruments Inc., Bellevue WA, <http://www.fialab.com/>
- <sup>13</sup> J. Chelkowski, *Photochem. Photobiol.* **20**, (1974), 279-280.
- <sup>14</sup> W.E. Steiner, K. Brunshweiler, E. Leimbacher, R. Schneider; *J. Agric. Food Chem.* **40**, (1992), 2453-2457.



# Quality monitoring of extra-virgin olive oil using an optical sensor

A.G. Mignani, L. Ciaccheri, A.A. Mencaglia  
CNR-IFAC, Sesto Fiorentino (FI), Italy  
[l.ciaccheri@ifac.cnr.it](mailto:l.ciaccheri@ifac.cnr.it)

R. Paolesse, C. Di Natale  
*Università di Roma 'Tor Vergata', Dipartimento di Scienze e Tecnologie  
Chimiche, Dipartimento di Ingegneria Elettronica, Roma, Italy*

A. Del Nobile, R. Benedetto, A. Mentana  
*Università di Foggia, Dipartimento di Scienze degli Alimenti, Foggia, Italy*

## Summary

An optical sensor for the detection of olive oil aroma is presented. It is capable of distinguishing different ageing levels of extra-virgin olive oils, and shows effective potential for achieving a non destructive olfactory perception of oil ageing. The sensor is an optical scanner, fitted with an array of metalloporphyrin-based sensors. The scanner provides exposure of the sensors to the flow of the oil vapor being tested, and their sequential spectral interrogation. Spectral data are then processed using chemometric methodologies.

## Introduction

Extra-virgin olive oil is usually bottled so that a head space is left between the oil surface and the cap. During the oil's shelf life, this head space becomes saturated by oil vapors. These vapors are true indicators of the quality of the oil, since the aroma of the oil changes drastically to rancid because of ageing or improper conservation. Several sensors have been proposed for this purpose, and are usually based on conductive polymers which simulate the olfactory perception [1-3]. A non destructive system would be advisable to detect the state of the oil aroma during its shelf life without opening the bottle.

This work presents preliminary testings of an optical sensor for oil aroma detection that potentially offers the implementation of a 'smart cap', to be used as a non invasive system for oil aroma detection. The sensor presented here makes use of metalloporphyrin-based materials as oil quality indicators. Since these materials change color and, consequently, the absorption spectrum when exposed to oil vapors, absorption spectroscopy was used for the implementation of an optical sensor. An optical scanner fitted with the array of metalloporphyrin-based

sensors was implemented, which provided exposure of the sensors to the flow of the oil vapor being tested and their sequential spectral interrogation. Since metalloporphyrins are highly sensitive to a wide range of volatile compounds, but are lacking in selectivity, the overall array response was processed by means of chemometric methodologies.

This system is capable of distinguishing different ageing levels of extra-virgin olive oils and shows effective potential for achieving a non invasive olfactory perception of oil ageing.

### **The optical scanner**

A fiber optic scanner capable of carrying out absorption spectroscopy was implemented in order to address an array of metalloporphyrin-based sensors operating in the visible spectral range. The scanner consisted of three independent modules (Figure 1) [4]:

- 1) An absorption spectroscopy module for spectral interrogation of the sensor array, which was a custom-made fiber optic spectrophotometer capable of achieving transmission measurements in the 380-780 nm spectral range, with a resolution of 10 nm [5].
- 2) A mechanical module consisting of a gear that housed the sensors and provided them with exposure to the oil vapor being tested, and their sequential interrogation. The gear was a revolving platform rotated by means of a step motor. The revolving platform housed 16 replaceable glass disks arranged around a ring. One disk was taken as a reference for signal normalization. The other 15 disks were the sensors, which were spray-coated by means of metalloporphyrins based on cobalt, iron, copper, manganese, zinc and tin. The platform was fitted into a flow cell suitable for vapor flow. The optical fibers for illumination and detection, which were coupled to the spectrophotometer, were fitted to the mechanical module in a fixed position, so that they could perform transmission measurements of all glass disks while the revolving platform rotated. In practice, the spectral interrogation of the whole sensor array was achieved while the oil vapor flowed through the cell. Gaskets were used in many parts of the cell to provide gas proofing.
- 3) A software module, which was a Labview-driven interface capable of managing the optical and mechanical modules and of recording the spectral response of all the sensors.

The metalloporphyrin-based sensors are highly sensitive to volatile compounds [6], but are lacking in selectivity. Consequently, the overall sensor response was

processed by using chemometric methodologies in order to achieve qualitative information similar to that obtained by means of olfactory perception.

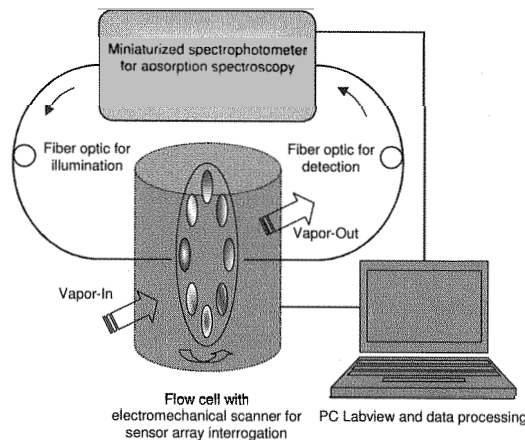


Figure 1 The optical scanner for spectral interrogation of the metalloporphyrin-based sensor-array

## Experimental results

Two types of extra-virgin olive oils from the Italian region of Puglia, Peranzana and Taggiasca, respectively, were artificially aged by exposure to 100°C for 50 hours. The vapors of the original oil and the aged samples were analyzed by means of HPLC measurements, revealing a total content of 45-50 ppm of n-hexaldehyde, octyl-aldehyde, nonanal, and heptaldehyde vapors.

For the optical experiments, a glass vial was used to contain the oil sample being tested: the vial was partially filled with the oil. The vapor generated by the oil in the vial head space was carried to the flow cell containing the optical sensors by means of nitrogen. The metalloporphyrin-based sensor-array was spectrally interrogated when exposed to new and oxidized oils, and PCA processing of sensor-array spectra was computed [7]. The PCA processing linearly combined the spectral data of the 15 sensors characterizing the oil aroma in order to produce new variables or principal components (PCs). High-order PCs had little weight in characterizing the samples, and could be disregarded with little loss of information. In practice, only PCs 1, and 2 were found to be significant for sample identification. Therefore, the two-dimensional map in the PC1-2 subspace was populated by point clusters, each of which grouped the oil samples in terms of the similarities of their aroma. Figure 2 shows the resultant PCA map. 'Oil 0A' and 'Oil 8A' are the Peranzana oil samples, new and aged, respectively. 'Oil 0B' and 'Oil 8B' are the Taggiasca oil samples, new and aged, respectively. This figure shows also that the metalloporphyrin-based sensor array

was capable of distinguishing between new and oxidized oils for both types of oils.

## Conclusions

A metalloporphyrin-based sensor-array has successfully been used to assess the aroma of new and artificially-aged extra-virgin olive oils. When exposed to the vapor of the oil under test, the absorption spectra of the sensor array was measured by means of a fiber optic-based scanner. A chemometric methodology was used in order to achieve qualitative information similar to that obtained by means of olfactory perception. These preliminary results show that it is possible to implement a 'smart cap' capable of revealing the rancidity of the oil contained in a bottle without having to open it. The smart cap should be designed as a suitably sandwiched sensor array which is in contact to the oil vapors on one side, while allowing reflectance spectroscopy measurements on the other. A cap of this type could follow the oil aroma during the bottle's shelf life, thus revealing the onset of rancidity.

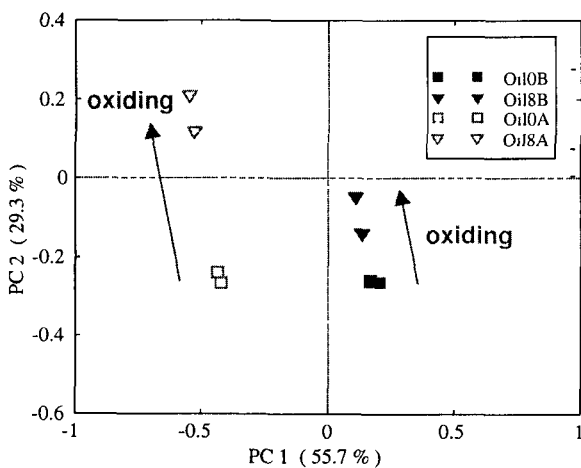


Figure 2 Metalloporphyrin-based sensor-array response: 'Oil 0A' and 'Oil 8A' are the Peranzana oil samples, new and aged, respectively; 'Oil 0B' and 'Oil 8B' are the Taggiasca oil samples new and aged, respectively

## Acknowledgments

Project MIUR-FIRB #RBNE01KZZM 'Biosens' is gratefully acknowledged for the partial financial support. The authors would like to thank Mr. Franco Cosi for the technical assistance.

## References

1. Guadarrama, M.L. Rodríguez-Méndez, J.A. de Saja, J.L. Ríos, J.M. Olías, 'Array of sensors based on conducting polymers for the quality control of the aroma of the virgin olive oil', *Sens. Act. B*, vol. 69, n. 3, 2000, pp. 276- 282.
2. J. Martinez, G. Pioggia, M.L. Rodríguez-Méndez, J.A. De Saja, 'Electronic nose for the quality control of the olive oil aroma discrimination of quality, variety of olive and geographic origin', *Proc. ISOEN02 - 9TH International Symposium Olfaction & Electronic Nose*, Eds. Arnaldo D'Amico, C. Di Natale, ISBN 88-7999-450-6. Aracne Editrice Srl, Roma, 2003, pp. 220-223.
3. S. Buratti, S. Benedetti, M.S. Cosio, 'Evaluation by an electronic nose of olive oil oxidation during storage', *Italian J. Food Sci.*, vol. 17, n. 2, 2005, pp. 203-210.
4. R. Paolesse, C. Di Natale, A. Macagnano, S. Nardis, A. D'Amico, A.A. Mencaglia, P. Bizzarri, A.G. Mignani, 'Fiber optic multimeter for interrogating an array of absorption-based optochemical sensors', *Proc. SPIE vol. 5270 Environmental Monitoring and Remediation III*, 2004, pp. 140-143.
5. A.A. Mencaglia, A.G. Mignani, 'Optical fiber instrumentation for online absorption and reflection spectroscopy', *Proc. SPIE vol. 4763 European Workshop on Smart Structures in Engineering and Technology*, 2003, pp. 248-251.
6. *The Porphyrins*, D. Dolphin Ed., vol. III, Academic Press, New York, 1978.
7. I.A. Cove, J.W. McNicol, 'The use of Principal Component in the analysis of the near infrared spectra', *Appl. Spectr.*, vol. 39, 1985, pp. 257-266.

# Spectral Interrogation of Optical Metal-Cladding Waveguides for Chemical Sensing

R. Bernini

*IREA- CNR, Via Diocleziano 328, 80124 Napoli, Italy*

bernini.r@irea.cnr.it

F. Mottola, A. Minardo, L. Zeni

*Dipartimento di Ingegneria dell'Informazione, Seconda Università di Napoli,*

*via Roma, 29, 81031 Aversa (CE), Italy*

## Summary

An integrated optical sensor, based on a Metal-Cladding Leaky Waveguide is proposed for chemical and biological applications. The proposed sensor permits to measure the refractive index of a liquid placed on its surface by simply monitoring the reflected optical spectrum. The device has been realized by using polymeric materials and the experimental results confirm the numerical simulations. The sensor exhibits sensitivity, calculated for water as the external medium, higher than 2000 nm.

## 1 Introduction

Optical chemical sensors have been widely studied in the past two decades. The interest for optical sensors is due to several advantages provided by optical methods, such as flexibility, high sensitivity, small size, low price, potential of mass production and the absence of electromagnetic interference. Typically, these sensors are based on the interaction of the evanescent part of a guided mode with the sensing medium [1]. In a three-layered waveguide (substrate, guiding layer, external medium), the evanescent field is in contact with the external medium; a change in the external medium leading to a variation of the evanescent field properties. As a result, modal properties change. These changes are translated into a variation of the effective refractive index and/or the losses of the waveguide.

Evanescent field techniques have been employed to detect various particles in water, such as in Reverse Symmetry Waveguide [2], Resonant Mirror [3], and Surface Plasmon Resonance [4].

Also metal-cladding leaky waveguides (MCLWs) have recently attracted a great interest in chemical and biosensing applications, because of their enhanced sensing capabilities with respect to traditional waveguides based on high refractive index guiding films [5]. Enhanced sensitivity comes from the deeper penetration of the evanescent film inside the sensing medium, as the metal film pushes the waveguide mode further into the sensing region.

Typically, MCLWs are interrogated by a monochromatic source, e. g. a laser, measuring the reflected spectrum in function of the angle of incidence. In this work we present a spectral interrogation of MCLW, where the angle of incidence

of the source is kept constant while measuring the reflected intensity as a function of the source wavelength.

## 2 Theoretical background

Optical Metal-cladding leaky waveguides (MCLW) are leaky waveguides in which a metal cladding, inserted between the guiding layer (lower refractive index) and the substrate (higher refractive index), improves the confinement of light in the core region, so that the light lost at each reflection with the metal cladding is reduced.

Metal-cladding waveguide can be used as a chemical sensor, relying on the interaction between the evanescent field of the guided mode, and the analyte. By a suitable design, the penetration depth of the evanescent field in the external medium is large, compared with both conventional dielectric waveguides and surface plasmon resonance [6], resulting in a stronger interaction with the analyte. In Figure 3, a typical modal profile of the fundamental TE mode of a MCLW is shown; as it can be seen the evanescent field of the mode has a quite deep penetration in the sensed medium. This can be useful e.g. in the sensing of particles larger than  $1\mu\text{m}$  diameter, such as bacteria or spores.

Typically, a MCLW sensor is operated in reflection mode, in which the waveguide is illuminated from the bottom side, by means of the Kretschmann configuration, while measuring the reflected intensity as a function of the angle of incidence. This results in a clear dip in the reflected intensity at an angle of incidence that matches the waveguide mode angle [7]. Here we present a novel interrogation method for MCLW based sensors, in which the angle of incidence of light is kept constant while varying the wavelength of the incident light. In this case, the reflectance is measured as a function of wavelength. This configuration presents the advantage of not requiring a high-precision goniometer to evaluate the angle.

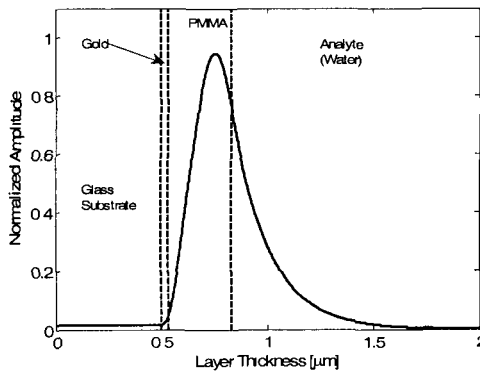


Fig. 3 – Mode profile of a MCLW, evaluated at a wavelength of 633 nm

### 3 Experimental Results

The sensor consists of a glass substrate, whose refractive index is  $n_1=1.51$ , on which a gold thin film ( $n_2=0.12+3.29i$ ,  $d_2=30\text{nm}$ ), acting as a metal-cladding, is sputtered. The guiding layer is deposited by means of the spin coating technique, and consists of a PMMA film ( $n_3=1.49$ ,  $d_3=300\text{nm}$ ). All refractive indices are evaluated at a wavelength of  $633\text{nm}$ .

In Figure 4, the scheme of the experimental setup is shown. Reflection spectrum measurements were carried out by coupling the light at an angle of  $64.5^\circ$  from the substrate, by means of a coupling prism. A white lamp, followed by a collimator and a polarizer, was used as the source, whereas a spectrophotometer was employed for the acquisition of the reflected spectrum.

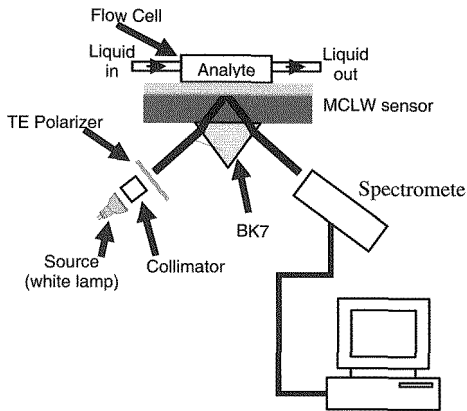


Fig. 4 – Experimental setup

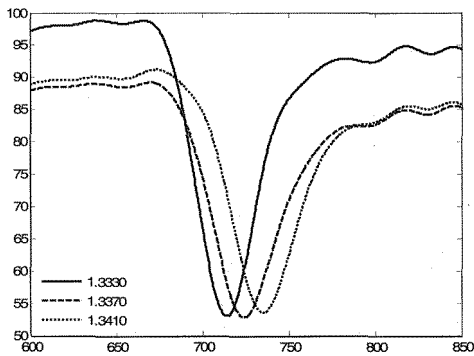


Fig. 5 – Reflected spectra for the MCLW at three different values of the external refractive indexes ( $n_0=1.333$ ;  $1.337$ ;  $1.341$ )



In Fig. 5 the reflected spectra of the MCLW are shown for three different external refractive indexes ( $n_0=1.333$ ;  $1.337$ ;  $1.341$ ).

As the refractive index of the external medium  $n_0$  changes, so does the wavelength at which light is coupled in the waveguide. Hence, the position of the dip of the spectrum is a measurement of the external medium refractive index, within an opportune range. The dip in reflectivity is sharper, compared with surface plasmon resonance. Defining the sensitivity as the ratio between the change in resonant wavelength and the spectral width of the dip, the improvement of MCLW, compared with SPR, can be up to approximatively of a factor of 6 [7].

In Figure 6, the refractive index of the sensed medium  $n_0$ , as a function of the resonant wavelength (i.e. the dip position of the reflected spectrum)  $\lambda_R$  is shown for both theoretical and experimental data. As it can be seen, there is a good agreement. The sensitivity  $S_n = \partial\lambda_R / \partial n_0$  calculated for a refractive index of the external medium  $n_0=1.3330$  is higher than 2000 nm.

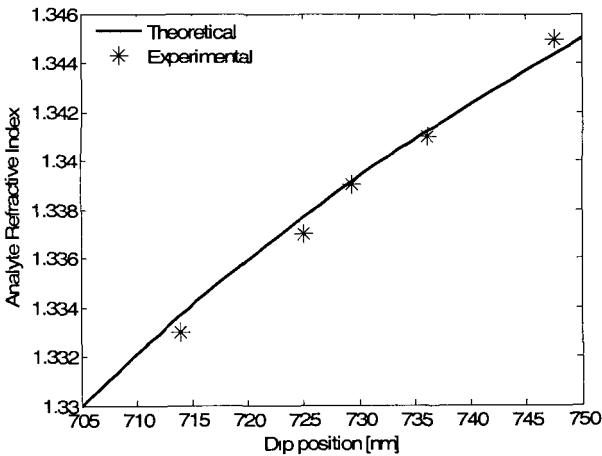


Fig. 6 – Analyte refractive index in function of the resonant wavelength of the MCLW. Comparison between experimental and theoretical data

#### 4 Conclusion

Metal cladding leaky waveguides have been presented as chemical sensors. The sensor is realized using gold as metal-cladding, and PMMA as the guiding layer of the MCLW. The validity of the sensor has been tested by evaluating the spectral response for different refractive indexes of the external medium, and the experimental data are in good agreement with the theoretical ones. The proposed sensor can be used for a number of applications, such as chemical sensing, by

using chemically selective polymers, biological sensing of large particles and cells, and for highly efficient fluorescence detection.

## References

- [1] P. V. Lambeck, *Sens. Act. B* 8, 103–116, 1992.
- [2] R. Horvath, L. R. Lindvold, N. B. Larsen, *Appl. Phys. B* 74, 383–393, 2002
- [3] R. Cush, J. M. Cronin, W. J. Stewart, C. H. Maule, J. O. Molloy, N. J. Goddard, part I-II, *Biosens. Bioelectron.* 8, 347-354, 1993.
- [4] J. Homola, S. S. Yee, G. Gauglitz, *Sens. Act. B* 54, 3-15 1999.
- [5] M. Zourob, N. J. Goddard, *Biosensors and Bioelectronics* 20, 1718-1727, 2005.
  
- [6] M. Zourob, S. Mohr, P. R. Fielden, N. J. Goddard, *Sens. Act. B* 94, 304-312, 2003.
- [7] N. Skivesen, R. Horvath, H. C. Pedersen, *Sens. Act. B* 106, 668-676, 2005.

# **Application of Quality Standard for the planning, design and realisation of thick film gas sensors**

M. Buzzolani\*, M. Butturi,  
C. Malagù, G. Martinelli, B. Vendemiati

*University of Ferrara, Polo Tecnologico – via Saragat, 1 - 44100 Ferrara, Italy  
buzzolani@fe.infn.it*

## **Summary**

The Sensor and Semiconductor Laboratory (SSL) of the Department of Physics of the University of Ferrara has implemented a Quality Management System (QMS) about processes of planning, development and production of thick-film gas sensors and photovoltaic cells. Since March 2006 SSL has also certified the process of managing and monitoring of Project.

The applied International Standard, UNI EN ISO 9001:2000, represents the standard of reference to match the requirements of Quality Management Systems. Especially the documentation (and in particular the Quality Manual) of an organization should be configured in a way that is appropriate to its unique activities.

The management system of the SSL, based on the scheme Plan, Do, Check-Act, allows the monitoring of the laboratory activities to get "continual improvement".

The principles of quality have been applied for the first time to the research activity in the University, and they turned out to be simple but important tools for the success of the system. The international standard applied to SSL is based on four main elements which are: manager responsibility, resource management, design and development (and the management of projects), and measurement and analysis.

## **1. Introduction**

The Project to certify the Sensor and Semiconductor Laboratory according to the Normative Vision 2000, started in 2000. The Top Management chose to improve the Quality Policy through the principles of Customer Satisfaction, Efficiency and Excellence of processes.

The main goal of the SSL has been defining an internal method of working to coordinating the several activities of the teamwork. In particular to promote effectiveness and efficiency to the management of the projects there has been important spread of quality culture and an "approach to goals". To get good results it is necessary to apply a systematic approach to design and development and pay particular attention to the key processes of management and planning

projects. To provide an effective framework for development of activities the Laboratory should plan:

1. Objectives
2. Activities and Processes (of the different projects)
3. Resources
4. Inputs and Outputs
5. Review of design and development of prototypes
6. Monitoring of the projects

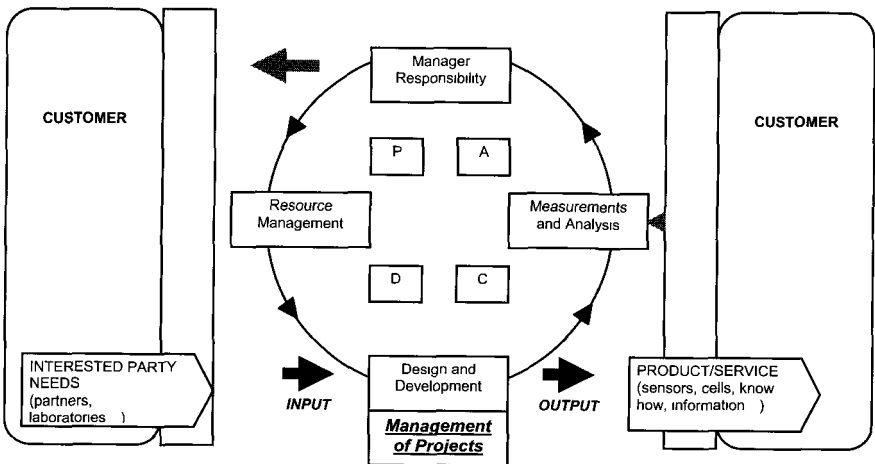


Figure 1. SCHEME "Plan-Do-Check-Act" (PDCA) applied to QMS of SENSOR AND SEMICONDUCTOR LABORATORY

## 2. Application

The SSL has applied the principles of the standard ISO 9001:2000 to the main processes such as management of instruments and facilities, purchasing, management of human resources etc. Particular attention has been paid to the activities of design and manufacturing of thick film gas sensors. The Top Management of the Laboratory decided to apply the ISO 9001:2000 (standard to get the certification) in 2000. Since September 2001 the SSL has certified the processes of design and manufacturing of thick film gas sensors and

photovoltaic cells. The main processes about planning and realization of thick film gas sensors are described in the Quality Manual (QM) [3] and in the procedures of the organization. The QM expresses the policy, the mission and the vision of the Laboratory while the procedures describe the main operational processes (both general and specific). As a consequence there are procedures that describe supporting activities (purchasing, nonconformity, management of human resources etc.) and procedures that specify peculiar processes (sensors planning, sensors development and production etc.).

The process of monitoring of the projects is described in the QM and the main activities are expressed in the “Project Management Procedure”. The structure of this procedure is:

- scope
- application field
- standard references
- modus operandi
- flow-chart
- attachments

Since March 2006 the SSL has certified the process of Managing and Monitoring Projects.

### 3. Conclusions

In a context of scarce resources it is important to realize projects in an effective way to show customers and “working partners” the capacities of the Lab to get the expected goals. So the development of a common working method and a continual monitoring of the activities (from the financial and technical point of view) allows one a simplification of the work and reduces time and risk. Creating a project-management procedure represents an important strategic choice for an organization as a laboratory of research that collaborates with industrial partners and important national and international organization of research.

### References

- [1] ISO 9001:2000 <http://www.iso.org>
- [2] ISO 9000:2000 <http://www.iso.org>
- [3] QM LSS ED. 2005 – University of Ferrara, Department of Physics

# **A Photonic Bandgap Fiber Sensor Based On Single Walled Carbon Nanotubes As Sensing Material**

M.Pisco, M.Consales, A.Cutolo, A.Cusano\*

*Optoelectronic Division - Engineering Department, University of Sannio,  
Corso Garibaldi 107, 82100 Benevento, Italy, a.cusano@unisannio.it*

*S.Campopiano*

*Department for Technologies, University of Naples Parthenope,  
Via Medina 40, 80131 Napoli, Italy*

*M.Giordano*

*Institute of Composite and Biomedical Materials, CNR, 80124, Naples, Italy*

*M.Penza, P.Aversa, G.Cassano*

*ENEA, C.R. Brindisi, Materials and New Technologies Unit, 72100 Brindisi,  
Italy*

## **Summary**

In this work, the feasibility of using Hollow-core Optical Fibers (HOFs) coated by carbon nanotubes for gas detection applications has been investigated. Single Walled Carbon NanoTubes (SWCNTs) overlays have been deposited by the Langmuir-Blodgett technique onto HOFs. The success of the SWCNTs deposition onto the HOF has been confirmed by Scanning Electron Microscope observations carried out on the samples after the deposition procedure. Reflectance characterization of the obtained sensing probes has been carried out in the range 1530-1570nm and an inverse Fourier transform based method has been employed in order to estimate the degree of penetration of the carbon nanotubes inside the hollow structure. Finally the sensing capability of the HOF sensors has been investigated by exposure in a test chamber to Tetrahydrofuran. The preliminary results obtained demonstrate the capability of the novel HOF sensor to perform chemical detection of volatile organic compounds showing a good sensitivity and fast response times.

## **1 Introduction**

Since the first experimental demonstration of Photonic Bandgap (PBG) guidance in Hollow core Optical Fibers (HOFs) in 1998 by Knight et al. [1], the optical properties of such fibers have attracted significant attention in the scientific community and several sensing applications using the HOFs have been developed [2-5]. Furthermore, in the recent years, the sensing properties of the carbon nanotubes deposited onto a singlemode standard optical fiber (SOF) configured in a reflectometric sensor system have been widely investigated [6-8] demonstrating their capability to perform chemical detection of volatile organic compounds (VOCs) at room temperature. As well known, the sensitivity of a refractometric based thin film sensor can be enhanced by increasing the

refractive index mismatch at the interface between the fiber core and the film. Hence, the HOFs, presenting a lower effective refractive index of the propagating mode, can be a promising substitute of the SOF based sensors. In addition, by filling the air holes of the HOF with a sensitive material, an high interaction between the light and the sensing material is expected.

In this work, a novel HOF chemical sensor is presented. The sensor probe is constituted by an HOF covered and partially filled with Single Walled Carbon NanoTubes (SWCNTs) as sensing material. The sensing system principle of operation relies on the measurement of the light intensity reflected at the interface between the fiber and the sensing material. Since the presence of THF *modifies the optical features of the carbon nanotubes, the sensing material dielectric function variations, as well as the losses due to the fiber PBG modification, lead to a reflectance modification of the sensing overlayer.*

## 2 Sensor fabrication and characterization

The Langmuir-Blodgett (LB) technique [6-8] has been chosen to transfer SWCNTs monolayers onto the HOF. Once the HOF end has been properly cut by using a precision cleaver to obtain a planar cross-section, the LB deposition technique has been used in order to deposit twenty monolayers of SWCNTs onto an HOF section with a length of about 9 cm.

After the deposition procedure, the HOF has been spliced at the input end to a singlemode SOF terminated by a fiber connector *in order to improve the coupling efficiency with the source.* The two fibers have been spliced by using a commercial electrical arc splicing system (Fujikura FSM-50S). The fiber ends have been properly cleaved and cleaned, then they have been aligned and pressed against each other using the splicer precision motors. In order to avoid the collapse of air holes, a series of arcs with short duration (100ms) and high power (80bit power) has been forced. The splicing losses were estimated to be about 1dB and are mainly caused by mode field mismatch and light reflection from the silica-air interface. The bonding achieved between the two fibers has been enforced by using an heating protection sleeve.

In order to investigate the spectral features of the sensing probe, the reflectance at the SOF-HOF interface has been measured within the HOF bandwidth. To the aim, a Superluminescent Light Emitting Diode (SLED) with 36nm bandwidth around 1556nm and an optical spectrum analyzer (Ando AQ6315A) were used.

The spectrum of the signal reflected by the HOF sensor probe has been normalized with respect to the reflected spectrum of the same HOF without carbon nanotubes overlayer. The retrieved reflectance is reported in figure 1(a). Several interference fringes have been manifested. In order to determine the

degree of penetration of carbon nanotubes within the hollow structure, the Inverse Fourier Transform (IFT) of the reflectance has been performed.

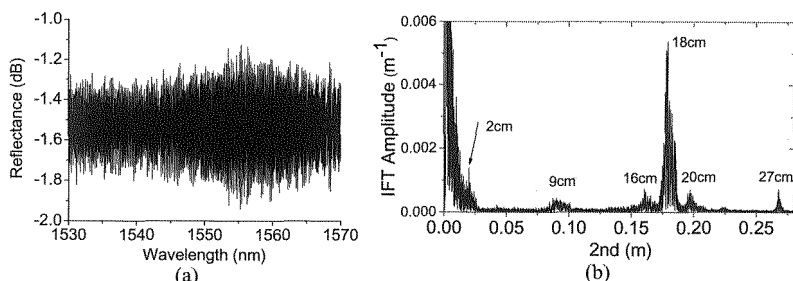


*Fig.1 Reflectance of the HOF coated by 20 monolayers of SWCNTs (a)  
IFT of the HOF sensor reflectance (b)*

In figure 1(b) the result of the IFT on the reflectance of the sensing probe has been reported. The spectrum exhibits several peaks corresponding to the axes coordinates 2cm, 18cm,  $18\pm 2$ cm and  $18\pm 9$ cm. The harmonic components, corresponding to a fixed  $z=2\cdot n\cdot d$ , represent the reflected power contribution due to the power portion going through a path  $2d$  long in a medium with mean refractive index  $n$ . It is worth noting that the harmonic contribution in the low region of the  $z$ -domain has been attributed to the source ripple and to the intermodal interference within the HOF. The peaks at 2cm, 18cm,  $18\pm 2$ cm and 20cm reveal the presence of a double resonant cavity.

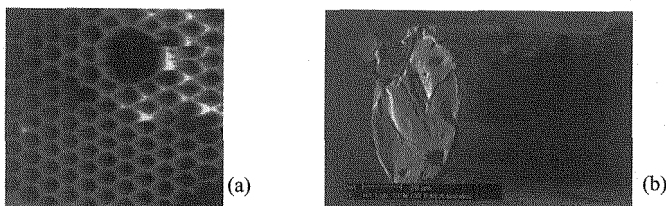


*Fig.2 AFM image of an hollow fiber (a) and  
SEM image of the HOF coated by 10 monolayers of SWCNTs (b)*

The one is composed by the HOF presenting a length of 9cm. The other one, with a 2nd-length of 2cm, represents the resonant cavity constituted by the carbon nanotubes penetrated within the hollow structure during the LB deposition. In spite of the difficulty to offer a reliable estimation of the refractive index of the SWCNTs agglomerate, it is possible to deduce that the sensitive material has been able to adhere on the fiber glass substrate and to penetrate inside the hollow structure along a 0.5-1cm length. The residual peaks,  $18\pm 9$ cm, are attributed to the HOF higher order modes. In order to investigate the morphological characteristic of the fabricated HOF sensor, a SEM have been



used. In figure 2 the AFM image of the HOF before the deposition and the SEM image after the deposition of 10 monolayer of SWCNTs are showed demonstrating the success of the SWCNTs deposition onto the HOF.

### 3 Testing and results

In order to test the sensing performances of the fabricated sensor, reflectance measurements have been carried out by using the interrogation system [8] schematized in Fig. 3 (a). The optoelectronic sensor output, consisting in the ratio between the reflected signal and the one corresponding to the power source monitoring, is proportional to interface reflectance [8].

The optical sensor has been located in a test chamber for THF exposure measurements. Dry air has been used as reference gas and carrier gas to transport the VOCs of THF with different concentration pulses. The test cell containing the sensor had a volume of 1200ml whereas the total flow rate for each exposure has been kept constant at 1000 ml/min. The gas flow rate has been controlled by a mass flowmeter driven by a controller-unit. The VOCs vapors have been generated by the bubbling method with a thermostated flask containing the liquid analyte.

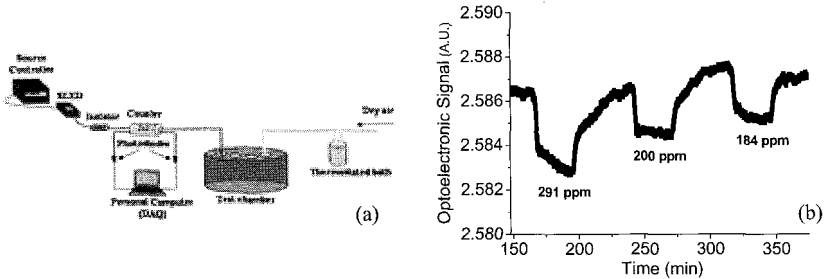


*Fig.3 Experimental setup (a) Time responses of HOF sensor coated by 20 monolayers of SWCNTs, exposed to 3 different concentrations of THF vapors (b)*

The optical response of the SWCNTs-based sensor to 30 minute pulses of THF vapors at three decreasing concentrations is showed in figure 3 (b). The signal decreasing upon exposures to THF vapors can be attributed to a change of the SWCNTs complex refractive index. Moreover, as the carbon nanotubes filled the cladding holes of the HOF, a modification of the mode propagation characteristic occurs and could be responsible for the optical signal decreasing. The revealed sensitivity for low concentrations is  $-1.2 \cdot 10^{-5} \text{ ppm}^{-1}$  and a limit of detection (LOD) of 40ppm with the exploited instrumentations is allowed, whereas, according to the european commission directive 2000/39/EC, the THF permissible exposure limits (PELs) are 50ppm in a long time (8 hours) and 100ppm in a short time (15 minutes) exposure. The time response also

demonstrates a weak drift due to thermal changes occurring in the test chamber during VOC exposure. Finally, good results have been obtained in terms of fast adsorption and desorption kinetics. In particular, response times less than 15 minutes and recovery times less than 30 minutes have been observed.

#### 4 Conclusions

An HOF coated and partially filled with SWCNTs has been used for the first time for VOCs detection. The success of the SWCNTs deposition onto the HOF by LB technique has been confirmed by the SEM image of the sensing probe. Spectral characterization has been carried out in the range 1530-1570nm revealing a degree of penetration of the carbon nanotubes inside the hollow structure of 0.5-1cm. Finally, the fabricated sensor has been located in a test chamber and employed in a refractometric system involving single wavelength reflectance measurements in order to test its sensing performances towards THF vapors. The preliminary results obtained demonstrate the capability of the HOF sensor to perform chemical detection of THF at room temperature with a sensitivity of  $-1.2 \cdot 10^{-5}$  ppm<sup>-1</sup>, a LOD of 40ppm and response times of a few minutes.

#### References

1. Knight, J. C., Birks, T. A., Russell P St, J. and Atkin, D. M., *Opt. Lett.*, 21(19), (1996), pp. 1547-9
2. J. C. Knight, *Nature*, vol. 424, (2003), pp 847-851
3. T. Ritari, J. Tuominen, H. Ludvigsen, J. C. Petersen, T. Sorensen, T.P. Hansen, H.R. Simonsen, *Optic Express*, vol.12, (2004), pp. 4080-4087
4. T.M. Monro, D.J. Richardson and P.J. Bennett, *Electronics Letters*, (1999), Vol. 35, No. 14, pp1188-1189
5. T. T. Larsen, A. Bjarklev, D. S. Hermann, J. Broeng, *Optics Express*, Vol. 11, No. 2, (2003), pp.2589-2596.
6. M. Penza, G. Cassano, P. Aversa, A. Cusano, A. Cutolo, M. Giordano, L. Nicolais, *Nanotechnology*, 16 (2005) 2536-2547.
7. M. Penza, G. Cassano, P. Aversa, F. Antolini, A. Cusano, M. Consales, M. Giordano, L.Nicolais, *Sens. Actuators B* 111-112 (2005) 171-180.
8. M. Penza, G. Cassano, P. Aversa, F. Antolini, A. Cusano, A. Cutolo, M. Giordano, L. Nicolais, *Applied Physics Letters*, vol. 85, n. 12, (2004) pp. 2379-2381

# Synthesis and selective nucleoside recognition of a new substituted zinc-phthalocyanine

Luigia Longo, Giuseppe Vasapollo

*Dept. Ingegneria dell'Innovazione, University of Lecce, Lecce, Italy*  
giuseppe.vasapollo@unile.it

Rosaria Anna Picca, Cosimino Malitesta

*Dept. Scienza dei Materiali, University of Lecce, Lecce, Italy*

## Summary

A new zinc-phthalocyanine peripherally substituted with methacryloyl groups was synthesized to be employed as functional monomer in the formation of molecularly imprinted polymers as nucleoside receptors. The binding affinity and selectivity of the synthesized phthalocyanine towards nucleosides were evaluated by UV-vis titration experiments in CH<sub>2</sub>Cl<sub>2</sub> at 298 K. The binding constant ( $K_a$ ) and Gibbs free energy changes ( $-\Delta G_0$ ) were calculated according to the modified Benesi-Hildebrand equation. Binding experiments showed that  $K_a$  of phthalocyanine with tri-*O*-acetyladenosine (TOAA) is  $1.35 \times 10^4$ , 500 times that of phthalocyanine with tri-*O*-acetyluridine (TOAU), indicating a high selectivity of the synthesized phthalocyanine derivative.

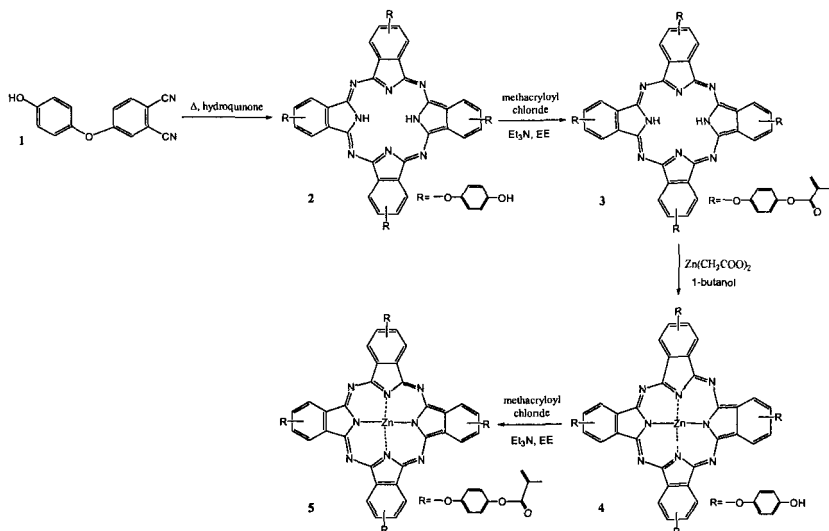
## 1 Introduction

The development of synthetic receptors that recognize nucleotide bases and their derivatives is an important area in chemistry today. The literature provides many examples of artificial molecule receptors for each of the common nucleoside bases [1-7]. Many of these receptors showed selectivity in nucleoside binding based on the positioning of interactive functional groups. A promising approach to design synthetic receptors is the molecular imprinting technique [8]. The procedure involves the formation of a template-monomer complex mediated by specific interactions, followed by polymerization. After the removal of the template, complementary recognition sites remain in the polymer network. Commercially available monomers such as methacrylic acid (MAA) have been widely used, making polymer preparation a simple and facile process. An approach based on cooperative interactions [2] could enable a better control in the formation of high-affinity binding sites for each corresponding template minimizing at the same time the inherent non-specific binding properties common in non-covalent imprinted polymers.

We describe in this work the synthesis and characterization of a new zinc-phthalocyanine peripherally substituted with methacryloyl groups (compound 5, **Scheme 1**) to be employed as functional monomer in the formation of

molecularly imprinted polymers (MIPs) as nucleoside receptors. The synthesis was conducted by using precursors bearing the functional groups required to obtain a three-dimensional binding site on the phthalocyanine plane in cross-linked polymers to which the nucleotide could be specifically bound via coordination by the phthalocyanine metal center and hydrogen bonding/electrostatic interaction by modifiers linked with the phthalocyanine. Cooperative interactions approach in MIP formation, already proposed [2], is for the first time thought out for phthalocyanine compounds.

The binding affinity and selectivity of the synthesized phthalocyanine towards nucleosides were evaluated by UV-vis titration experiments. An organic soluble nucleoside derivative, tri-*O*-acetyladenosine (TOAA), was utilized as prospective template, since it contains the 2-aminopyridine substructure previously found to be important for polymer imprinting with nucleotide derivatives [7]. Tri-*O*-acetyluridine (TOAU), not containing the 2-aminopyridine moiety, was also tested for comparison [7].



*Scheme 1* Synthesis of compound 5

## 2 Experimental Section

**Materials and methods.** All chemicals were obtained commercially and used without further purification.  $^1\text{H}$  and  $^{13}\text{C}$ -NMR spectra were recorded at room temperature on a Bruker Avance 400 instrument operating at 400 MHz with TMS as internal standard. Mass spectra were measured on an Agilent 1100

Series LC/MSD system equipped with an electrospray ionization interface (ESI). FT-IR and UV-vis spectra were obtained with a Jasco FT/IR-660 plus and a Cary 100 Scan UV/vis spectrophotometers, respectively.

**Synthesis of 4-(4-hydroxyphenoxy)phthalonitrile (1).** 1.4 g (0.01 mol) of finely ground anhydrous  $K_2CO_3$  was added gradually (280 mg at intervals of 30 min) under nitrogen atmosphere to a stirred solution of 2 g (0.01 mol) of 4-nitrophthalonitrile and 1.1 g (0.01 mol) of hydroquinone dissolved in 65 ml of dry DMSO. The reaction mixture was stirred for 24 h at room temperature under nitrogen, then it was filtered, added to ca. 50 ml of water, extracted with ethyl ether and dried on anhydrous sodium sulphate. The organic solvent was evaporated under reduced pressure and the crude product was purified by column chromatography (silica, ethyl acetate/petroleum ether 4:6) and recovered in 94 % yield.  $^1H$ -NMR (DMSO- $d_6$ ):  $\delta$  9.64 (s, 1H), 8.04 (d,  $J=9.7$  Hz, 1H), 7.66 (d,  $J=2.4$  Hz, 1H), 7.27 (q,  $J=8.9$  Hz, 1H) 7.02-6.99 (m, 2H), 6.85-6.83 (m, 2H) ppm.  $^{13}C$ -NMR (DMSO- $d_6$ ):  $\delta$  162.6, 155.7, 145.7, 136.6, 122.2, 122.1, 121.3, 117.1, 116.9, 116.4, 115.9, 107.7 ppm. FT-IR (ATR system): 3419, 2233, 1593, 1562, 1505, 1485, 1247, 1195, 1089, 952, 836  $cm^{-1}$ . MS: 53 (79), 63 (50), 76 (29), 81 (100), 88 (13), 100 (78), 109 (67), 115 (10), 127 (70), 236 (18)  $m/z$  (%).

**Synthesis of tetra(4-hydroxyphenoxy)phthalocyanine (2).**

A mixture of 0,6 g (2,54 mmol) of **1** and 0,07 g (0,64 mmol) of hydroquinone was pounded in a mortar and put in a Pyrex tube. The mixture was fused by gentle heating to the melting point without vacuum, cooled, sealed under vacuum and reacted at 180 °C for 20 h. The crude blue-green solid was washed with ethyl ether and then purified by column chromatography (silica, THF/ n-hexane 8:2). The product was recovered in 20% yield. FT-IR (ATR system):  $\nu$  3627, 3291, 2954, 2914, 2871, 1615, 1506, 1473, 1433, 1215, 1150, 1094, 1011, 867  $cm^{-1}$ . UV-vis (THF):  $\lambda_{max}$  286, 339, 606, 638, 667, 703 nm. ESI-MS: calc. M 946, obs.  $[M+1]^+$  947  $m/z$ .

**Synthesis of tetra(4-methacryloyloxyphenoxy)phthalocyanine (3).**

A mixture of 0,3 g (0,32 mmol) of **2**, 0,26 g (2.5 mmol) of triethylamine and 0,26 g (2.5 mmol) of methacryloyl chloride in 15 ml of ethyl ether was stirred for 18 h at room temperature under nitrogen atmosphere. The reaction mixture was added to water, extracted with  $CH_2Cl_2$  and dried on anhydrous sodium sulphate. The crude product, obtained after evaporation of the solvent under reduced pressure, was purified by washing with n-hexane and recovered in 70% yield. FT-IR (ATR system):  $\nu$  2957, 1735, 1616, 1499, 1474, 1320, 1187, 1127, 1012  $cm^{-1}$ . UV-vis ( $CHCl_3$ ):  $\lambda_{max}$  285, 342, 606, 638, 665, 700 nm. ESI-MS: calc. M 1218, obs.  $[M+1]^+$  1219  $m/z$ .

**Synthesis of Zn(II) tetra(4-hydroxyphenoxy)phthalocyanine (4).**

A mixture of 0,15 g (0,123 mmol) of **3** and 0,045 g (0,246 mmol) of zinc(II) acetate in 5 ml of 1-butanol was refluxed for 20 h under nitrogen atmosphere.

After cooling to room temperature the dark green solid product was filtered off, washed with n-hexane and dried under vacuum, giving the pure product in 90% yield. FT-IR (ATR system):  $\nu$  3374, 2955, 2913, 2870, 1608, 1506, 1473, 1395, 1339, 1220, 1084, 1044, 950  $\text{cm}^{-1}$ . UV-vis [(THF):  $\lambda_{\text{max}}$  282, 351, 610, 677 nm. ESI-MS: calc. M 1008, obs.  $[\text{M}+1]^+$  1009  $m/z$ .

**Synthesis of Zn(II) tetra(4-methacryloyloxyphenoxy)phthalocyanine (5).** A mixture of 0,28 g (0,282 mmol) of **4**, 0.24 g (2.26 mmol) of triethylamine and 0.23 g (2.26 mmol) of methacryloyl chloride in 14 ml of ethyl ether was stirred for 18 h at room temperature under nitrogen atmosphere. The reaction mixture was added to water, extracted with  $\text{CH}_2\text{Cl}_2$  and dried on anhydrous sodium sulphate. The crude product, obtained after evaporation of the solvent under reduced pressure, was purified by washing with n-hexane and ethyl ether and recovered in 28% yield. FT-IR (ATR system):  $\nu$  2957, 1735, 1616, 1499, 1239, 1187, 1126, 1044, 947  $\text{cm}^{-1}$ . UV-vis ( $\text{CHCl}_3$ ):  $\lambda_{\text{max}}$  281, 347, 679 nm. ESI-MS: calc. M 1280, obs.  $[\text{M}+1]^+$  1281  $m/z$ .

**UV-Visible titrations.** Small aliquots (10  $\mu\text{l}$ ) of the solution of nucleoside in  $\text{CH}_2\text{Cl}_2$  at 298 K were added to  $5 \times 10^{-5}$  M of **5** in  $\text{CH}_2\text{Cl}_2$  measuring the absorbance at 680 nm until no longer increased. Solutions  $5 \times 10^{-2}$  M of TOAA and 0.5 M of TOAU were utilized. The effect of dilution caused by the addition of nucleoside solutions on the absorption values was taken into account during analysis and corrected.

### 3 Results and Discussion

The metal phthalocyanine **5** was synthesized according to the **Scheme 1**. The analytical characterization confirmed the identity of this compound (see Experimental section). UV-visible titration of phthalocyanine **5** with nucleoside molecules was conducted at 680 nm in  $\text{CH}_2\text{Cl}_2$  at 298 K. The association constants of the complexes of **5** with nucleosides were determined by the modified Benesi-Hildebrand equation, Eq. 1, where  $[\text{H}]_0$  and  $[\text{G}]_0$  refer to the total concentration of **5** and nucleoside, respectively,  $\Delta\epsilon$  is the change in molar extinction coefficient between the free and complexed phthalocyanine, and  $\Delta A$  denotes the absorption changes at 680 nm of the phthalocyanine on addition of nucleoside [9, 10]. For all nucleosides examined, plots of calculated  $[\text{H}]_0[\text{G}]_0/\Delta A$  values as a function of  $[\text{G}]_0$  values gave excellent linear relationships, supporting the 1:1 complex formation. The binding constants ( $K_a$ ) and Gibbs free energy changes ( $-\Delta G_0$ ) of **5** with nucleoside molecules, obtained from usual curve fitting analyses of observed absorbance changes, are summarized in **Table 1**.

$$\frac{[\text{H}]_0[\text{G}]_0}{\Delta A} = \frac{1}{\Delta\epsilon K_a} + \frac{[\text{G}]_0}{\Delta\epsilon} \quad (1)$$

**Table 1** Binding constants ( $K_a$ ) and free energy of complexation ( $-\Delta G_0$ ) for the 1:1 complexes between nucleoside molecules and **5** in  $\text{CH}_2\text{Cl}_2$  at 298 K

nucleoside	$K_a$ ( $\text{dm}^3 \text{mol}^{-1}$ )	$-\Delta G_0$ ( $\text{KJ mol}^{-1}$ )
TOAA	$(1.35 \pm 0.5) \times 10^4$	23.5
TOAU	$27 \pm 2.5$	8.2

#### 4 Conclusion

A new Zn phthalocyanine derivative (compound **5**) to be employed as functional monomer in the formation of molecularly imprinted polymers as nucleoside receptors was prepared. The binding affinity and selectivity of **5** towards different nucleosides (TOAA and TOAU) were evaluated by UV-vis titration experiments, which indicated that phthalocyanine **5** bound TOAA most strongly showing in this way a high selectivity.

#### References

1. K.J. Shea, D.A. Spivak, B. Sellergren, *J. Am. Chem. Soc.*, 115 (1993) 3368
2. J. Matsui, M. Higashi, T. Takeuchi, *J. Am. Chem. Soc.*, 122 (2000) 5218
3. D.A. Spivak, K.J. Shea, *Anal. Chim. Acta*, 435 (2001) 65
4. D. Spivak, M.A. Gilmore, K.J. Shea, *J. Am. Chem. Soc.*, 119 (1997) 4388
5. K. Yano, K. Tanabe, T. Takeuchi, J. Matsui, K. Ikebukuro, I. Karube, *Anal. Chim. Acta*, 363 (1998), 111
6. H. Tsunemori, K. Araki, K. Uezu, M. Goto, S. Furusaki, *Bioseparation*, 10 (2002) 315
7. D.A Spivak, K.J. Shea, *Macromolecules*, 31 (1998) 2160
8. M.J. Syu, J.H. Deng, Y.M. Nian, *Anal. Chim. Acta*, 504 (2004) 167
9. Y. Turgut, E. Sahin, M. Togrul, H. Hosgoren, *Tetra: Asymm.*, 15 (2004) 1583
10. H.A. Benesi, J.H. Hildebrand, *J. Am. Chem. Soc.*, 71 (1949) 2703

#### Acknowledgements

The work was supported by PRIN 2004 – MIUR (N° 2004034021\_003).

# Synthesis and characterization of nanomaterial as sensitive platform to assemble selective chemical sensors for $\text{NO}_2^-$ detection

Vanessa Biagiotti, Federica Valentini, Danila Moscone, Giuseppe Palleschi,  
*Università degli studi di Roma Tor Vergata, Dipartimento di Scienze e  
Tecnologie Chimiche, via della Ricerca Scientifica 1, 00133 Roma (Italy)*  
[vanessa.biagiotti@uniroma2.it](mailto:vanessa.biagiotti@uniroma2.it)

## Summary

Platinum electrodes were modified by electropolymerized polymer nanotubule nets and were applied to nitrite detection in drinking water. Several analytical parameters were investigated such as: different monomers (1,2- 1,3- 1,4-DAB, pyrrole, o-anisidine, 1,8-DAN), permeability toward nitrites and other interferences, permselectivity toward nitrites. The best performances were obtained with a Poly(1,2-DAB) nanotubule net and the assembled sensor was characterized morphologically by scanning electron microscope and electrochemically by cyclic voltammetry and amperometry coupled to flow injection analysis (FIA), in terms of linear range of concentration (10-1000  $\mu\text{M}$ ), limit of detection (2  $\mu\text{M}$ ), reproducibility (RSD%: 1.5) and linear regression ( $y/\mu\text{A}=1.14 \times/\mu\text{M}+2.6$ )

## 1 Introduction

Nitrite is a very interesting analytical substrate because of its prevalence in industrially produced meats as a preserving agent and also appearance builder. But, when ingested it can react with hemoglobin, oxidizing it to methemoglobin and with amines, converting them into nitrosamines, which are well-known carcinogens. The environmental impact from the build-up of high nitrite and nitrate concentrations, owing to their use as fertilizers, and the problems caused by the contamination of water sources used for human consumption, are also important concerns. Nitrites are electroactive species readily oxidized at platinum electrodes polarized at + 900 mV vs Ag/AgCl. Since the potential for nitrite oxidation is high, many other electroactive compounds present in complex media can interfere in the nitrite analysis. To avoid interference effects, platinum electrodes are often covered by membranes or electropolymerized films. In this work platinum electrodes were covered by nanostructured polymeric films: poly(1,2- 1,3- 1,4-diaminobenzene) [poly(1,2- 1,3- 1,4-DAB)], poly(1,8-diaminonaphthalene) [poly(1,8-DAN)], poly(o-anisidine) and poly(pyrrole) were investigated. A study of permeability of electropolymerized films toward nitrites and some common interferences, was performed. For this purpose three target molecules which can be oxidized at the same working potential, were selected: ascorbic acid (AA), phenol (PhOH) and sulfite ( $\text{SO}_3^{2-}$ ).



## 2 Experimental

### 2.1 Electrode polishing

The platinum electrode surfaces were polished with alumina powder ( $\text{Al}_2\text{O}_3$ , Buehler, Evanston, IL) having different particle size: 1, 0.3 and 0.05  $\mu\text{m}$  before use. After rinsing with distilled water, the electrodes were pre-treated by potential cycling in 0.5 M  $\text{H}_2\text{SO}_4$  from  $-0.2$  to  $+1.2$  vs Ag/AgCl at a scan rate of 20 mV/s, until no changes were observed in the cyclic voltammograms [1].

### 2.2 Synthesis of polymeric nanotubule nets

Polymeric nanotubule were produced by the “template synthesis” [2] approach. A metallic Pt foil ( $1\text{ cm}^2$ ) has been used as working electrode. The polycarbonate nanoporous particle track-etched membranes were used as a template membrane for the synthesis of polymer nanostructured nets and they were assembled as working electrode in a conventional one-compartment cell on a platinum foil. The electropolymerization was performed, at room temperature using platinum as counter electrode, and an Ag/AgCl as reference electrode. All the monomers were used at a concentration of 5 mM and dissolved in 0.01 M  $\text{HClO}_4$  + 0.1 M  $\text{NaClO}_4$ , as supporting electrolyte. Solutions were deoxygenated with  $\text{N}_2$  for 15 min just before the electropolymerization experiment. Different potentials were applied for 250 s during the chronocoulometric experiment, depending on the monomer: 0.6 V for the three diaminobenzene isomers, 0.75 V for 1,8-DAN, 0.8 V for pyrrole and o-anisidine. Then, the template was dissolved by dichloromethane and the polymer nanotubules were placed directly on the platinum electrode surface, by drop coating. For the preliminary investigations 50 nm pore of PC template membrane, were used for all the monomers. Then the pore diameter was varied in order to evaluate the size exclusion effect of the nanostructured polymeric film on nitrite ion permeability.

### 2.3 Study of permeability and permselectivity

The permeability toward nitrites and several common interferences such as ascorbic acid, sulfites and phenols, was evaluated by cyclic voltammetry [3]. The potential was cycled between 0.2 V and 1.2 V at scan rate of 20 mV/s. All these analytes were used at a concentration of 40 mM, in 0.1 M acetate buffer pH 4 and the oxidation current peaks of nitrite and interferences were compared.

## 2.4 FIA procedure

For amperometric measurements in a flow injection analysis (FIA) the optimised parameters were found to be: flow-rate 0.6 ml/min, applied potential + 0.9 V vs Ag/AgCl, and 0.1 M acetate buffer, pH 4 as carrier solution. Standard nitrite solutions were prepared in 0.1 M acetate buffer pH 4 and then injected into a 250  $\mu$ l loop, using a six-way injection valve.

## 3 Results and discussion

### 3.1 Study of permeability

The goal of this work is to investigate various polymeric barriers that could be used to assemble a sensor that will be highly permeable to nitrite but exclude as much as possible potential interference. For this purpose, in this work study about permeability toward nitrites and some common interferences, was performed. Film permeability was evaluated measuring the peak current by cyclic voltammetry for each analyte. Then the Permeability (P%) was calculated using the equation 1, as described in [1]:

$$P\% = I_{\text{film}} / I_{\text{bare}} * 100 \quad (1)$$

where  $I_{\text{bare}}$  is the peak current recorded at bare electrode and  $I_{\text{film}}$  is the peak current at the modified platinum electrode. The permeability results obtained for platinum electrodes modified by nanostructured polymeric net are reported on Table 1.

MONOMERS	P% nitrite	P% sulfite	P% PhOH	P% AA
1,2-DAB	4.05	0.790	4.28	0.390
1,3-DAB	34.3	28.3	50.4	25.2
1,4-DAB	65.7	59.1	83.3	20.9
1,8-DAN	17.1	17.7	82.1	14.7
o-anisidine	88.8	65.1	93.9	66.8
pyrrol	19.8	11.7	8.50	19.2

Table 1. Permeability of polymeric nanotubule nets

Almost all of the films exhibit high permeability toward nitrite, but also toward interferences. A better behaviour was obtained using poly(1,2-DAB) nanotubule net, considering that it represented a compromise between good permeability for nitrite with a significant repulsion of interferences.

### 3.2 Study of permselectivity

Since a film that comparably reduces the response to analyte and potential interferences offers no advantages over a bare platinum electrode, the

determination of the permselectivity represents an important factor for evaluation of the sensor performance. It is defined as the ratio between nitrite permeability and interferent permeability, as reported in the equation 2:

$$P = P\%_{\text{nitrites}} / P\%_{\text{interferences}} \quad (2)$$

Fig. 1 shows the results obtained synthesizing polymeric nanostructures using polycarbonate membrane having 50 nm-pore size. The best performances in terms of permselectivity were obtained using poly(1,2-DAB) nanotubule net. The higher permselectivity values are probably related to denser distribution of these structures that is directly related to an easier process of electropolymerization. Infact small pore sizes of template (nanometer cut off) play an important role during the monomer diffusion process making easily 1,2-DAB electropolymerization, because only one amino group is involved. This effect is strictly related to poly(1,2-DAB) molecular structure if compared to the other polymers having complex molecular architectures both in terms of the different substituent positions on the aromatic ring (poly(1,3-DAB) and poly(1,4-DAB)) and a major number of the aromatic rings in the structure (poly(1,8-DAN)). For this purpose, to confirm this hypothesis related to the permselectivity performances of the poly(1,2-DAB) nanotubules and their nanostructured morphology, an additional study was performed using different pore diameters of polycarbonate membrane during the poly(1,2-DAB) nanotubules growth. The best analytical responses were obtained with nanotubules having 30 nm of diameter (Table 2) considering a compromise between a good permeability and a good permselectivity, respectively. This nanometer cut off minimizes the major permeability toward interferences, typical of the largest pore diameter of the template membrane, giving an easier access for the polymer diffusion into the template pores compared to the smaller pore diameter template.

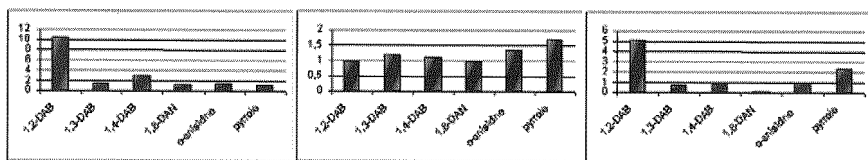


Fig. 1 Permselectivity of polymeric nanotubule nets  
1) Pnit/PAA 2) Pnit/Psulf 3) Pnit/ P PhOH

Pore size diameter (nm)	P nit/ P AA	P nit / P sulfite	P nit/ P PhOH
15	0.88	3.57	1.12
30	10.4	0.95	0.68
50	7.61	3.30	1.46
100	1.55	2.24	1.28

Tab. 2 Study of different pore size PC membrane effect on the permselectivity of Poly(1,2-DAB) nanotubules nets

### 3.3 Morphological characterization

Poly(1,2-DAB) nanotubule nets synthesized by the template method dissolving the membrane in dichloromethane, showed a typical filled cylindrical morphology which was investigated using a field emission type scanning electron microscope (FE-SEM). [4]. This coating provides a large surface area per unit volume, so porous layers were obtained and this is in agreement with high permeability values calculated for these nets.

### 3.4 FIA procedure

Having identified the best nanostructured polymeric film synthesized on the probe surface, it was analytically characterized in a FIA analysis system for the amperometric detection of nitrite. The best nanostructured sensor, assembled using poly(1,2-DAB) nets, showed good linearity over the range 10-1000  $\mu\text{M}$ , a linear regression equation of  $I/\mu\text{A} = 0.20 \times \mu\text{M} + 2.8$  and a detection limit of 2  $\mu\text{M}$  (LOD= 3s/n) The reproducibility in terms of relative standard deviation is 0.09 % on slope values and 1.5 % on bias values for n=3.

## 4 Conclusion

In this work platinum electrodes were modified by polymeric barriers synthesized by "template synthesis" technique to have a selective sensor for nitrite detection. The best resulting sensor was obtained using poly(1,2-DAB) nanotubule nets and it has the sensitivity required for implementation of Italian legal limits for nitrite in drinking water. Further investigations will be carried out using other synthesis approach.

## References

- [1] M. Badea, A. Amine, G. Palleschi, D. Moscone, G. Volpe, A. Curulli, New electrochemical sensors for detection of nitrites and nitrates, Journal of Electroanalytical Chemistry 509 (2001) 66-72
- [2] A. Curulli, F. Valentini, S. Orlanducci, M.L. Terranova, C. Paoletti, G. Palleschi, Electrosynthesis of non conventional-polymer nanotubules: a new nanostructured material for analytical applications, Sensors and Actuators B 100 (2004) 65-71

[3] L.J. Murphy,

Reduction of interference response at a hydrogen peroxide detecting electrode using electropolymerised films of substituted naphthalenes, *Anal. Chem.* 70 (1998) 2928-2935

[4] F.Valentini, A. Salis, A. Curulli, G. Palleschi,

Chemical reversibility and stable low-potential NADH detection with nonconventional conducting polymer nanotubule modified glassy carbon electrodes, *Anal. Chem.* 76 (2004) 3244-3248

### **Acknowledgments**

The authors wish to thank the MIUR target project FIRB 2001 n.RBNEOIMBTC-002 for financial support.

# Modified p-type NiO thin films using Pt- and Au-overlayers for H<sub>2</sub> sensing

S. Capone, P. Siciliano, A.M. Taurino

*Institute of Microelectronics and Microsystems I.M.M.-C.N.R., Sezione di Lecce,  
Via Monteroni, 73100 Lecce, Italy  
[simona.capone@le.imm.cnr.it](mailto:simona.capone@le.imm.cnr.it)*

I. Hotovy, V. Rehacek

*Department of Microelectronics, Slovak University of Technology, Ilkovicova 3,  
812 19 Bratislava, Slovakia*

## Summary

Nanocrystalline NiO thin films were deposited by dc reactive magnetron sputtering in a mixture of oxygen and argon and subsequently coated by Au on a NiO film surface. Very thin Pt and Au overlayers with a thickness of about 1, 5 and 7 nm have been prepared by magnetron sputtering. Then, the surface modified NiO films have been analysed by TEM, EDX and SEM. NiO thin films showed a polycrystalline structure with the size of nanocrystals ranging from a few nanometers to 10 nm. Electrical responses of NiO-based structure towards hydrogen have been measured.

## 1. Introduction

Nickel oxide (NiO), is the metal oxide usually taken as a model for p-type materials. It's is an attractive material well known for its chemical stability as well as for its excellent optical and electrical properties. Indeed, NiO thin films have been studied for applications in electrochromic devices and also as functional layers for solar cells [1,2]. In particular, the field of gas sensing has benefited from the production of prospective materials characterized by a high surface-to-volume ratio. The gas-sensing properties of metal oxides are more or less related to the material surface, to an high porosity and to a nanostructure with small particles. Also, these properties can be essentially improved by doping of the surfaces of the sensing layers by catalytic metals as platinum and gold (Pt and Au) [3,4]. Sputtering is a deposition technology widely used both for the preparation of metal oxide thin films and promoter overlayers. In our previous work, we analysed the influence of the addition of a very thin Pt overlayer on the gas-sensitive properties of sputtered NiO thin films towards H<sub>2</sub> [5]. In this work, we continued this research by comparing the effect of two different metallic overlayers, i.e. platinum and gold (Pt and Au) on the H<sub>2</sub>-sensing properties of sputtered NiO-based gas sensors.

## 2. Experimental

We prepared NiO thin films by dc reactive sputtering from a metallic Ni target in a mixture of oxygen and argon. A sputtering power of 600 W was used. Both the inert argon flow and reactive oxygen flow were controlled by mass flow controllers. The relative partial pressure of oxygen in the reactive mixture O<sub>2</sub>-Ar was 20 %. The total gas pressure was kept at 0.5 Pa. We have successfully prepared nanocrystalline NiO thin films with the mean crystal size of ~10 nm. Next, we modified them with overlayers of metallic promoters. Both Pt and Au thin layers have been sputtered on the surface of the NiO films by varying the sputtering parameters. In particular, the thickness of the catalytic layers were varied by controlling the sputtering time. As measured by AFM, Pt films (1, 5 and 7 nm thick) and Au films (1, 5 and 7 nm thick) resulted. Moreover, a suitable photolithographic mask was used for the deposition of the Pt and Au catalytic layers. The geometry of the photolithographic mask consists in a squared grid by which Pt (or Au) squares, 100 μm × 100 μm sized and ~40μm spaced, have been realized. Gas sensors based on such Pt- and Au-modified NiO films were realized using rough alumina substrates (3 x 3 mm<sup>2</sup> squared) equipped with interdigital capacitor electrode-structure (IDC) and Pt-microheater. In fig.1 a top view of the final structure of the sensor device is shown. The structural features of the films were investigated by means of a Tecnai 20 S-TWIN transmission electron microscope (TEM) operated at 200 kV. It is equipped with energy dispersive Xray (EDX) facility for high resolution chemical analysis. Selected electron diffraction patterns have been recorded together with bright and dark field images of the film structure.

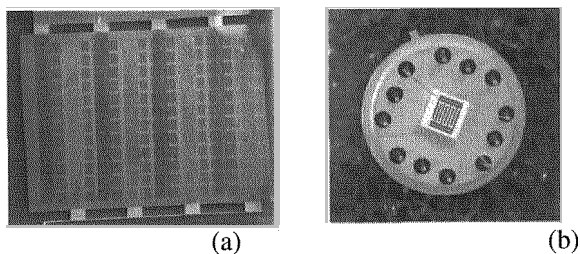
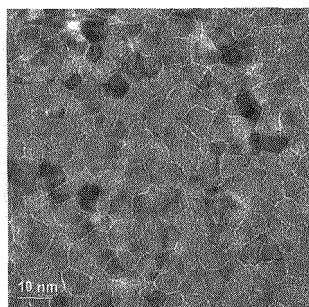


*Fig.1 a) SEM image of the sensor surface and b) image of the device bounded on a standard support.*

## 3. Results and discussion

The structural properties of the NiO thin films have been examined using TEM (fig.2a). Identification of the deposited films was based on the observed electron diffraction patterns. The measured lattice spacings are shown in fig.2b. Comparisons can be made with the tabulated d-spacing for the cubic NiO phase (PDF Number 4-835) and this provides further evidence for the formation of this

oxide. The diffraction pattern was of a continuous ring type indicating a polycrystalline film. The grains were not oriented homogeneously, but into certain prominent directions. TEM observations (fig.2) of unmodified NiO films confirmed that the films were formed by nanocrystals and showed a fine-grained structure. The size of the nanocrystals ranges from a few nanometres to 10 nanometers depending on the position in the film. We can see that the samples contain small grains that are partially bonded into clusters.



(a)

NiO (hkl)	<i>d</i> (nm) expected	pure NiO measured
(111)	0.2410	0.2441
(200)	0.2088	0.2115
(220)	0.1476	0.1489
(311)	0.1259	0.1281
(222)	0.1206	0.1218

(b)

**Fig.2** a) TEM image of the NiO film after deposition, b) results of the diffraction patterns obtained by TEM.

TEM images of the NiO film with Au film is not continuous and close. It does not cover the NiO nanocrystalline surface completely and the Au sputtered atoms create areas of islands and conglomerates. Au nanoparticles tend to form circle shaped closed clusters in diameter of several tens nanometers. The presence of Au was confirmed by EDX analysis recorded during TEM observation. The Au clusters were homogeneously dispersed on the NiO surface [6]. Also Pt film resulted discontinuous and porous, Pt sputtered atoms form areas of islands and conglomerates [5].

The gas-sensing properties of the Pt- and Au-modified NiO films towards hydrogen have been compared. The sensor performances resulted a function both of the catalytic material and the thickness and morphology of promoter layer. As example, in fig.3a the response curve of three NiO based sensors (i.e. unmodified and surface modified with Pt and Au 1 nm thick layer) towards 1000 ppm H<sub>2</sub> in dry air vs. working temperature is reported. Both Pt- and Au-modified NiO sensors showed higher response as compared to unmodified NiO sensor thus confirming the promoting catalytic effect of the metallic layer. At lower temperature the Pt-modified NiO sensor seems to prevail showing a first maximum at ~200 °C, while at higher T the Au-modified sensor showed higher response with an optimum behaviour at ~350 °C. In fig.3b the dynamic response of the above mentioned three sensors at 350 °C is showed.



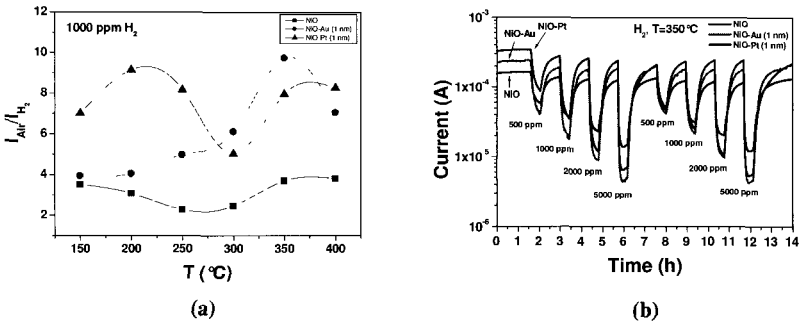


**Fig.3** a) Response to 1000 ppm  $H_2$  for three NiO based sensors (i.e. unmodified and surface modified with Pt and Au 1 nm thick layer); b) corresponding dynamic curve at different  $H_2$  concentrations at  $T=350$  °C.

At increasing the thickness of the Pt and Au overlayers, the response to  $H_2$  resulted still enhanced by the catalytic activity of the Pt and Au films, but some new characteristics appeared due to the higher amount of sputtered metals but also to different morphologies of the two catalytic layers subjected to changes when the sensor working temperature increases (up to 400 °C) (fig.4). This effect was confirmed by SEM analysis (fig.5).

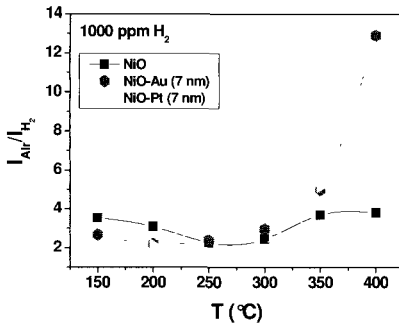


**Fig.4** Response to 1000 ppm  $H_2$  for three NiO based sensors (i.e. unmodified and surface modified with Pt and Au 7 nm thick layer).

**Conclusions**

NiO thin film modified with Au and Pt overlayer (1, 5, 7 nm thick) were deposited by dc reactive magnetron sputtering. Both Pt- and Au-modified NiO sensors (Pt and Au film 1 nm thick) showed higher response as compared to unmodified NiO sensor thus confirming the promoting catalytic effect of the thin metallic overlayer. Both Pt- and Au-modified NiO sensors (Pt and Au film 7 nm thick) showed higher response as compared to unmodified NiO sensor thus confirming the promoting catalytic effect of the thin metallic overlayer. They

showed high responses and sensitivities to medium concentration (500-5000 ppm) of  $H_2$  in air; by taking into account that the lower explosion limit (LEL) range of  $H_2$  is 40,000 ppm, these results make the Au- and Pt-modified NiO sensors promising candidates for implementing hydrogen leak detector.

The  $H_2$  sensing properties have been discussed also with reference to the thickness and the morphology of the Au and Pt thin layers. The sensor response to  $H_2$  resulted to be strongly dependent not only on the grain size of Pt or Au cluster islands but also on the porosity of the catalytic film on the NiO surface. At lower temperature the Pt-modified (1 nm) NiO sensor seems to prevail showing a first maximum at  $\sim 200$  °C, while at higher T the Au-modified sensor showed higher response with an optimum behaviour at  $\sim 350$  °C.

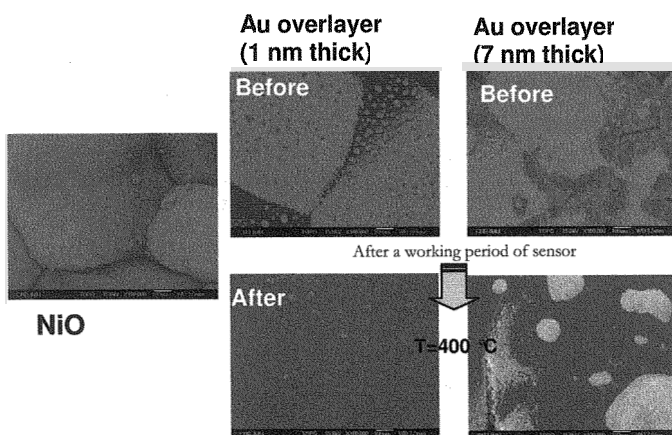


**Fig.4** SEM image of Au-modified (1 and 7 nm thick) NiO surface for a sample (a) as-deposited, (b) a sample after sensor measurement at 400°C (b). The images are compared with the surface of the NiO film on the left.

## References

- [1] Magana C, Acosta D, Martinez A, Ortega J 2006 *Solar Energy* 80 161
- [2] Wang Y, Zhang Y, Liu H, Yu S, Qin Q 2003 *Electrochimica Acta* 48 4253
- [3] Schweizer-Berberich M, Zheng J, Weimar U, Gopel W, Barsan N, Pentia E, Tomescu A 1996, *Sensors and Actuators B* 31 71
- [4] Steffes H, Imawan C, Solzbacher F, Obermeier E 2001 *Sensors and Actuators B* 78 106
- [5] I. Hotovy, J. Huran, P. Siciliano, S. Capone, L. Spiess, V. Rehacek, *Sensors and Actuators B* 103 (2004) 300-311.
- [6] I. Hotovy, D. Donoval, J. Huran, S. Hascik, L. Spiess, M. Gubisch, S. Capone, *Czechoslovak Journal of Physics*, Vol. 56 (2006), Suppl. B, 1192-1198.

# Multilayered metal oxide thin film gas sensors obtained by conventional and RF plasma-assisted laser ablation

V. Marotta, S. Orlando

*CNR - Istituto di Metodologie Inorganiche e dei Plasmi – Sezione di Potenza,  
Zona Industriale, I-85050 Tito Scalo (PZ), Italy  
orlando@pz.imip.cnr.it*

B. Mitu

*National Institute for Lasers, Plasma and Radiation Physics,  
P.O. Box MG 36 Magurele, Bucharest, 77125 Romania*

## Summary

Reactive pulsed laser ablation has been established as a feasible method for thin film deposition of a large variety of compounds with simple or complex stoichiometry such as oxides, nitrides, semiconductors and superconductors. This technique relies on photoablation of pure elements, or a mixture of materials, with simultaneous exposure to a reactive atmosphere. The reactivity of the plasma plume can be enhanced if the ambient gas is excited, for example by an additional RF discharge. In the case of oxides, reactions between the laser vaporized metals and oxygen lead to the formation of intermediate complexes and finally to oxide thin films.

SnO<sub>2</sub>-based multilayered thin films of In<sub>2</sub>O<sub>3</sub>, have been deposited by conventional and RF plasma-assisted Reactive Pulsed Laser Ablation, with the aim to evaluate their behaviour as toxic gas sensors. The depositions have been carried out by a frequency doubled Nd-YAG laser ( $\lambda = 532$  nm,  $\tau = 7$  ns) on Si(100) substrates, in O<sub>2</sub> atmosphere. The thin films have been characterized by X-Ray Diffraction and Electrical Resistance measurements. A comparison of the electrical response of the simple (indium oxide, tin oxide) and multilayered oxides to toxic gas (nitric oxide) has been performed. The influence on the structural and electrical properties of the deposition parameters, such as substrate temperature and RF power, is reported.

## 1 Introduction

Studies on semiconductor oxides are growing very fast due to the successful involvement of these materials as detecting devices. Metal oxide coatings are widely used as transparent resistive heaters, electrical electrodes for flat panel display and electrochromic devices, antireflecting and high refraction index materials for optical applications, and gas sensors. These thin films are usually produced by Chemical Vapor Deposition [1], Microwave discharge, Molecular Beam Epitaxy [2], sputtering [3] and sol-gel process [4]. Another attractive choice for the preparation of these films is the reactive pulsed laser ablation and deposition (RPLAD) [5]. In our laboratory, pulsed laser deposition (PLD) has been already applied successfully in the past to deposit many materials such as semi- and super-conductors, nitrides and oxides [6-8]. This technique relies on photoablation of pure elements, or a mixture of materials, with simultaneous

exposure to a reactive atmosphere. Neutral and ionized species are formed in the laser ablated plume. In the case of oxides, reactions between the laser vaporized metals and oxygen lead to the formation of intermediate complexes [9,10] and finally, when collected on suitable substrates, to oxide thin films. Gas sensors based on semiconducting oxide thin films present some advantages with respect of other types of gas sensors. To detect small amounts of a reactive gas in air, the surface reactions are much more relevant than the bulk changes, so that the specific surface of sensitive elements must be as large as possible. The RPLAD technique is adequate for satisfying such a primary requirement. In addition to high sensitivity, thin film sensors have high stability combined with simple construction at low cost. In this paper, the RPLAD deposition of indium oxide and tin oxide thin films, and multilayers of these two compounds, has been performed in order to evaluate the behaviour of such films as toxic gas (NO) sensors. The deposited films have been characterized by Electric Resistance measurements to understand the influence of physical parameters such as the substrate temperature and the RF power applied to generate reactive oxygen plasma.

## 2. Experimental

The experimental set-up has been described in detail elsewhere [7]. In the experiments here reported, the multi-port stainless steel chamber has been pumped down to  $10^{-3}$  Pa, whereas the depositions were performed in static  $O_2$  atmosphere (pressure 100 Pa). Commercial metallic targets of indium and tin have been mounted to the rotating holder (2 rpm). The Quantel Nd:YAG 581 laser ( $\lambda=532$  nm,  $\tau = 7$  ns, repetition rate = 10 Hz, fluence =  $8$  J/cm<sup>2</sup>) was impinging on the target at  $45^\circ$  with respect to the normal at constant fluence of  $8$  J/cm<sup>2</sup>. The gaseous species were collected on heated Si (100) substrates (temperature up to 1000 K) positioned 5 cm far away from the target in the on-axis configuration. The PLD set up has been improved by employing a RF generator (13.56 MHz ENI Model OEM-6A). The substrate holder is surrounded by an isolated stainless steel ring concentric to the substrate holder and connected to the RF generator through a customized matching unit [6,8]. Thin films of indium oxide and tin oxide, and two-layered films (Sn - In) have been deposited on Silicon (100) substrates by reaction of laser ablated metallic targets of indium and tin in presence of oxygen, at different substrate temperatures [7]. X ray spectra were detected by a *Rigaku Miniflex* diffractometer using the  $K\alpha$  line of a Cu target ( $\lambda= 0.154056$  nm) as an X ray source; step scan  $0.02^\circ$ /sec. A four-contact probe, based on a *Keithley 224 Programmable Current Source* and a *Keithley 182 Sensitive Digital Voltmeter*, has been utilized to evaluate the resistance variation of thin films when exposed to 1000 Pa of 5% NO in He gas

mixture after evacuation. The resistance measurements have been performed at room temperature and in the dark to avoid any influence due to the light [11].

### 3. Results and discussion

The improvement of the film surface smoothness has been achieved either by increasing the deposition temperature or by assisting the conventional PLD with the RF plasma. These evidences had been reported in a previous paper [12].

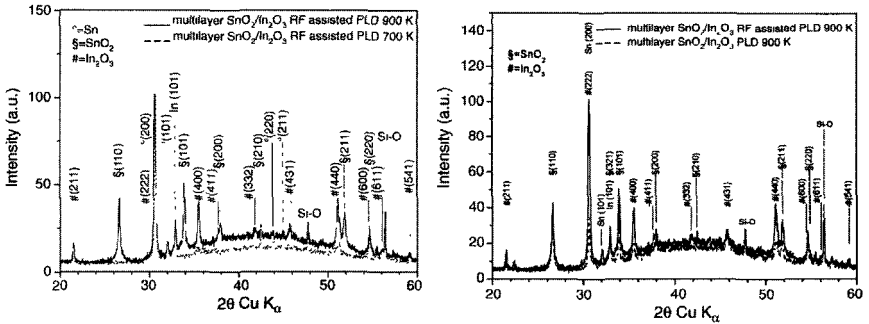


**Figure 1.** Comparison of the XRD patterns of  $\text{SnO}_2\text{-In}_2\text{O}_3$  bilayers deposited: (left) by RF plasma assisted PLD at 700K and 900K substrate temperature respectively; (right) at 900K substrate temperature by conventional PLD and RF plasma-assisted PLD.

X-Ray Diffraction (XRD) analysis showed polycrystalline structures either in indium oxide and tin oxide single layer depositions and in bi-layered films [9,10]. XRD data of samples deposited by conventional PLD, at low deposition temperature (below 600 K), show predominant diffraction peaks corresponding to metallic phases for both indium and tin thin films, and also for multilayers ( $\text{In}_2\text{O}_3\text{-SnO}_2$  and  $\text{SnO}_2\text{-In}_2\text{O}_3$ ). Increasing the deposition temperature, the oxidation becomes more evident but some "metallic" peaks still testify a further uncomplete oxidation. Only at 900 K deposition temperature almost all the peaks connected to metal phases disappear. Analogous behaviour has been found in the samples produced with the RF oxygen plasma. Comparing the two sets of samples the peaks enhancement due to the RF plasma is evident, even if the major effect is due to the deposition temperature. We summarize the results in Figure 1: on the left are reported the patterns of multilayered ( $\text{SnO}_2\text{-In}_2\text{O}_3$ ) samples produced at two different substrate temperatures (700 and 900 K) by employing the RF oxygen plasma. The diffraction peaks corresponding to  $\text{In}_2\text{O}_3$  and  $\text{SnO}_2$  are much more evident when the deposition temperature is higher. Also some metallic peaks, in particular corresponding to tetragonal tin - which is the first layer onto the substrate - become negligible. Even if the In (101)

metallic peak does not seem to be very much affected by the temperature, the great enhancement of almost all the oxide diffraction peaks reveal a huge improvement of the oxidation also for the indium oxide top layer.

The effect of the presence of the RF plasma during the deposition is shown in Figure 1 (right): the XRD spectra of multilayered ( $\text{SnO}_2\text{-In}_2\text{O}_3$ ) samples deposited at 900 K substrate temperature are compared in order to evidence the improvement of the oxides' formation induced by the RF plasma. The crystallinity enhancement is noteworthy especially for the indium oxide top layer considering that often is quite difficult to grow the second layer in a well oriented crystalline phase. In particular, the enhancement of the  $\text{In}_2\text{O}_3$  (222) peak is considerable, even if it is overlapping the Sn (200) peak. The relative intensity of the last one should be a little bit higher than the Sn (101) diffraction peak, close to it. Unfortunately, the In (101) diffraction peak of the conventional PLD sample cannot be evaluated because of the overlap to another diffraction peak related to the superficial silicon oxides present on the substrate.

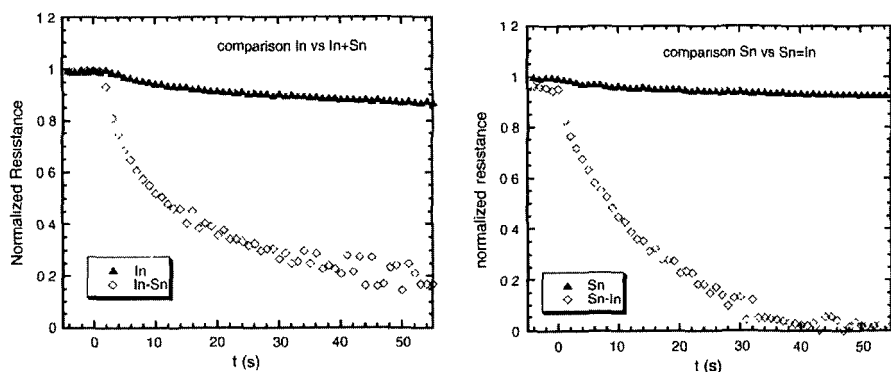


**Figure 2.** Comparison of the normalized resistances, as function of time after exposure to NO toxic gas, of: (left) indium oxide single layer and bilayered  $\text{In}_2\text{O}_3\text{-SnO}_2$ ; (right) tin oxide single layer and bilayered  $\text{SnO}_2\text{-In}_2\text{O}_3$ .

When the toxic gas is adsorbed by the film, the surface resistance changes depending upon the variation of the free carriers involved in the adsorption. In Figure 2, the normalized resistance variations of the films produced by RF plasma assisted PLD at high deposition temperature (900 K) have been shown when exposed to NO toxic gas. On the left (Figure 2) are reported the behaviours of the single layer indium oxide film and of the indium oxide - tin oxide bilayer. Analogous behaviours are shown, on the right, for the tin oxide single layer film and for the tin oxide - indium oxide bilayer.

#### 4. Conclusions

In this paper we report preliminary results on the resistance variation, when exposed to NO toxic gas, of thin films (indium oxide, tin oxide, and bilayers  $\text{SnO}_2\text{-In}_2\text{O}_3$  and  $\text{In}_2\text{O}_3\text{-SnO}_2$ ). The “sensors” were grown on Si (100) substrates by reactive pulsed laser ablation and deposition of metal targets (indium and tin) in presence of oxygen also activated by a RF generator. The XRD characterization has shown the structural correlation with the deposition temperature and with the presence of oxygen plasma, generated by a RF source. Both the single layers of indium oxide and tin oxide work well as toxic gas detectors. An improvement due to the multilayered deposition has been ascertained because the bilayered films have shown a faster time response velocity and a larger resistance variation with respect to single oxide thin films. Work is in progress to better understand the influence of other deposition parameter, such as laser fluence and wavelength.

#### Acknowledgments

One of the authors (B. M.) gratefully acknowledges NATO-CNR Advanced Fellowships Programme 2002 (Grant n. 215.35S) for financial support. This work was partially supported by the Italian research ministry MIUR under the project MIAO.

#### References

- [1] E. N. Eremin, L. I. Nekrasov, E. A. Rubtsova, M. V. Belova, V. L. Ivanter, L. N. Zacharov, L. N. Petukhov, *Russ. J. Phys. Chem.*, **56** (1982) 788.
- [2] S. Nakamura, Y. Harada, M. Seno, *Appl. Phys. Lett.*, **58** (1991) 2021.
- [3] G. Sberveglieri, P. Benussi, G. Coccoli, S. Groppelli, P. Nelli, *Thin Solid Films*, **186** (1990) 349.
- [4] R. Rella, P. Siciliano, L. Vasanelli, C. Gerardi, A. Licciulli, *J. Appl. Phys.*, **83** (1998) 2369.
- [5] D. B. Chrisey, G. K. Hübner (Eds.), *Pulsed Laser Deposition of Thin Films*, John Wiley & Sons, Inc., New York, 1994.
- [6] A. Giardini, V. Marotta, S. Orlando, G. P. Parisi, *Surf. and Coat. Technol.* **151-152** (2002) 316.
- [7] V. Marotta, S. Orlando, G.P. Parisi, and A. Giardini, *Appl. Surf. Sci.*, **154-155** (2000) 640.
- [8] V. Marotta, S. Orlando, G.P. Parisi, A. Giardini, *Appl. Phys. A*, **69** [Suppl.] (1999) S675.
- [9] R. Teghil, V. Marotta, A. Giardini Guidoni, T. M. Di Palma, C. Flamini, *Appl. Surf. Sci.*, **138-139** (1999) 522.
- [10] A. Mele, D. Consalvo, D. Stranges, A. Giardini Guidoni, R. Teghil, *Int. J. Mass Spectrom. Ion Process*, **95** (1990) 359.
- [11] A. Giardini Guidoni, V. Marotta, S. Orlando, G. P. Parisi, *Int. J. of Photoenergy* **3** (2001) 213.
- [12] V. Marotta, S. Orlando, G. P. Parisi, A. Santagata, *Appl. Surf. Sci.*, **208-209** (2003) 575.

# **A new competitive technique for the production of porphyrin thin films: the Glow Discharge induced Sublimation (GDS)**

M. Tonezzer, A. Quaranta, G. Della Mea

*Dipartimento di Ingegneria dei Materiali e Tecnologie Industriali, Università di Trento, via Mesiano 77, 38050 Povo(TN), Italy*  
*tonezzer@lnl.infn.it*

G. Maggioni, S. Carturan

*Università di Padova, c/o INFN-LNL Viale dell'Università, 2- 35020 Legnaro, Italy*

## **Summary**

Thin porphyrin assemblies, widely used as sensing materials in different kinds of transducers, are usually produced through chemical deposition techniques. In this work a new physical technique named Glow-Discharge-induced Sublimation (GDS) has been employed for the first time for the production of cobalt 5,10,15,20 meso-tetraphenyl porphyrin (CoTPP) thin films. For the sake of comparison, CoTPP coatings have been also produced by vacuum evaporation and spin coating procedures. The inspection of the surface morphology with a Scanning Electron Microscope evidenced a higher surface roughness of GDS samples with respect to films deposited by means of conventionally used procedures. Optical measurements performed in atmospheres containing ethyl alcohol vapours highlight that GDS films yield more than ten times intense responses in comparison with the films deposited through the commonly used techniques, very fast response times ( $t_{50} = 12$  sec and  $t_{90} = 72$  sec) and fast and complete recovery.

## **1 Introduction**

Porphyrins are widespread compounds in nature, where they play essential functions for life [1]. A great number of features makes porphyrins eligible as good “sensing material” able to detect the volatile organic compounds (VOCs) present in the environment [2]. Porphyrins are stable compounds and their properties can be finely tuned by simple modifications of their basic molecular structure increasing thus the versatility of these molecules. In order to be exploited as sensing materials, porphyrins compounds are usually deposited as thin solid films through chemical techniques (solvent casting, Langmuir-Blodgett, spin coating) [3]. Fewer efforts have been carried out to produce thin solid films by means of physical technique in spite of the fact that these techniques assure several advantages as great reproducibility, more uniformity and stricter control of the film thickness in comparison with standard chemical techniques. Moreover physical techniques, producing thin solid films without using any extraneous compound, allow to produce samples characterized by very



high purity. The material purity is expected to play a very important role in gas sensing field because the traces of retained solvent can partially hinder the interaction between the film and the analyte molecules. Recent optical measurements demonstrated that vacuum evaporated thin porphyrin films exhibit higher responses towards analyte molecules than the chemically deposited ones [4]. This paper reports the employment, for the first time, of a new physical technique developed at LNL and named Glow-Discharge-induced Sublimation (GDS) for the deposition of thin cobalt 5,10,15,20 *meso*-tetraphenyl porphyrin (CoTPP). GDS technique is based on the use of a weakly ionized glow discharge produced in a standard radio frequency magnetron sputtering equipment: low energy ( $E < 1\text{keV}$ ) He ions impinge on solid organic powder leading to the sublimation of the organic molecules and to their condensation onto the substrate. GDS has recently showed to place as an attractive deposition technique for the production of thin organic films for gas sensing applications allowing to produce samples characterized both by high purity and especially by extraordinarily large surface area to bulk ratios [5,6]. It is worth to note that this last feature represents a very important characteristic in gas sensing field because a large surface area improves the interaction between film and analyte molecules and therefore the sensing capability of the films. Thin CoTPP films were also deposited through spin coating (SPIN) and vacuum evaporation (VE) techniques, for the sake of comparison. In order to study and compare the behaviours of the different samples, optical measurements in presence of various atmospheres of ethyl alcohol (EtOH) were performed.

## Experimental

CoTPP compound is commercially available (Acros Organics) and was used directly without some further process.

This material was deposited in the form of thin films onto clean quartz substrates by means of GDS technique. GDS set-up consisted of a vacuum chamber evacuated by a turbomolecular pump to a base pressure of  $10^{-4}$  Pa. The glow discharge was sustained by a 1-in. cylindrical magnetron sputtering source connected to a radio frequency power generator (600 W, 13.56 MHz) through a matching box. The CoTPP powder was put on the surface of an aluminum target and placed on the sputtering source. The glow discharge feed gas was helium (99.9999 %), whose pressure inside the chamber was measured through a capacitance gauge. Typical values of rf power, target DC self-bias, and working pressure were in the ranges  $10 \div 20$  W,  $-20 \div 300$  V, and  $20.0 \pm 0.1$  Pa, respectively. CoTPP thin films were also deposited through vacuum evaporation and spin-coating techniques.

Optical absorbance spectra were acquired utilizing an experimental apparatus in which the measure chamber, placed inside a Spectrophotometer V-570 Jasco,

is connected to two mass flow controllers suited to assure an accurate real-time control of the vapour concentrations into the chamber during the spectra collections. This apparatus allows to record both dynamic behaviours at a fixed absorbance wavelength and complete absorbance spectra in different vapour concentration atmospheres.

## Results and discussion

SEM pictures of SPIN, VE and GDS samples of CoTPP compounds, reported in Figure 1, point out three different morphologies depending on the three different deposition techniques.

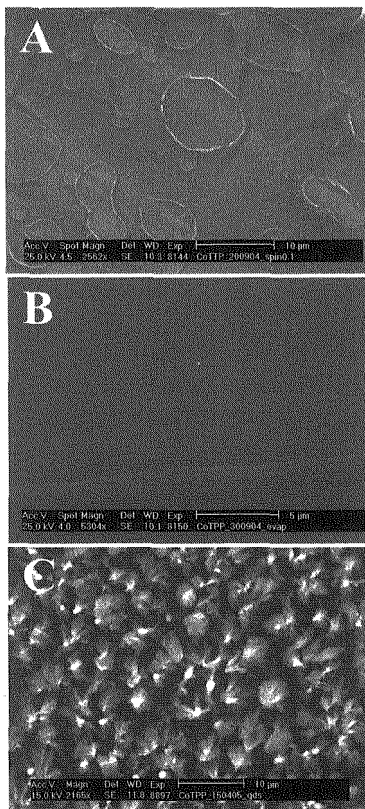


*Fig.1: SEM images of SPIN (A), VE (B) and GDS (C) films of CoTPP.*

In particular VE and SPIN samples show surfaces characterized by flat morphology and very low surface area to bulk ratios; GDS sample, on the

contrary, is characterized by extraordinary rough surfaces and by very large surface area/bulk ratios.

In order to study and compare the responses of the three CoTPP samples (SPIN, VE and GDS) upon exposure to various ethyl alcohol (EtOH) atmospheres, the absorbance variation  $\Delta A$  was utilized:

$$\Delta A = A_t - A_o$$

where  $A_t$  and  $A_o$  are respectively the Soret band ( $\lambda = 440$  nm) absorbance intensities of the samples under EtOH and nitrogen atmospheres.

A comparison of the evolution of the B band ( $\lambda = 440$  nm) intensity of the three CoTPP samples upon exposure to 1000-4500 ppm of EtOH as a function of time is shown in Fig. 2.

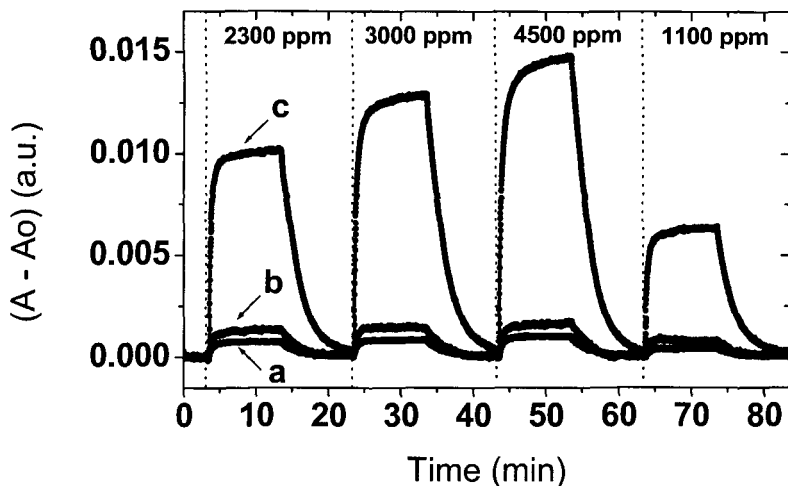


*Fig.2: Concentration dependence of SPIN (a), VE (b) and GDS (c) films of CoTPP compound upon exposures to EtOH atmospheres over the range 1100 – 4500 ppm.*

As can be seen, the kinetics of the gas exposure are characterized by a fast increase of the band intensity followed by a slow increase of this intensity until saturation values are reached. As the ETOH vapour stream is switched off, a dry nitrogen flush is activated. This rapidly initiates recovery and after few seconds the original Soret band intensities have been restored.

It is worth to point out that the optical behaviours of all the samples are characterized by a complete and fast recovery: this experimental result becomes particularly interesting taking into account that all the measurements have been

performed at room temperature.

Fig. 2 points out the more than ten times sensing capability of the GDS sample in comparison with the SPIN and the VE ones in the EtOH detection: these larger GDS intensities can be attributed both to the high purity and especially to the extraordinarily high surface area to volume/ratio of GDS assemblies.

In order to characterize the speed of the response the parameters  $t_{50}$  and  $t_{90}$  (defined, respectively, as the time taken for the signal intensity to reach the 50% and the 90% its final saturated value) are usually used. These parameters, respectively  $t_{50}$  in the order of ten seconds and  $t_{90}$  in the order of one minute, reflect that the GDS films of CoTPP behave as fast sensors. In particular  $t_{50}$  has been found to be at least half of those measured for similar chemically deposited porphyrin assemblies (for SPIN sample of CoTPP compound  $t_{50} = 23$  sec) and considerably smaller than those values typically reported for different molecular systems.

From these preliminary tests it is possible to hold that GDS places itself as a very promising technique for the deposition of thin CoTPP solid film for gas sensing applications allowing to produce samples characterized by very fast responses, complete recovery and extraordinarily larger intensity and sensitivity in comparison with the samples deposited by means of the standard deposition techniques.

## Acknowledgements

This research was financially supported by the Fifth Commission of Istituto Nazionale di Fisica Nucleare (DEGIMON project).

## References

- [1] D. Dolphin (Ed.), *The Porphyrins*, VI(a), VII(b), Academic Press, New York, **1978**.
- [2] N.A. Rakow et al. - *Nature*, **406** (2000) 710.
- [3] A. D'Amico et al. *Sens. Actuators B* **65** (2000) 209.
- [4] M. Tonezzer et al - presented at Eurosensor XIX, 11th – 14th September **2005**, submitted *Sens Actuators B*.
- [5] G. Maggioni et al. *Chem. Mater.*, **17** (2005) 1895.
- [6] G. Maggioni et al. *Surf. Coat. Technol.*, **200** (2005) 476.

# Optical Sensing to Organic Vapors of Fluorinated Polyimide Nanocomposites containing Silver Nanoclusters

S. Carturan, M. Bonafini, G. Maggioni,

*I.N.F.N. – Laboratori Nazionali di Legnaro, Viale dell'Università 2, 35020  
Legnaro, Italy, carturan@lnl.infn.it*

A. Quaranta, M. Tonezzer, G. Della Mea

*University of Trento, Department of Materials Engineering and Industrial  
Technologies, via Mesiano 77, 38050 (TN), Italy*

G. Mattei, C. de Julián Fernandez, P. Mazzoldi

*University of Padova, Department of Physics, Via Marzolo 8, 35123 Padova,  
Italy*

## Summary

Polyimide-silver nanocomposite films were prepared by surface modification with KOH aqueous solution followed by K-assisted Ag doping and thermal reduction in hydrogen-containing atmosphere. The film porosity was controlled by dispersing into the polymer the compound azodicarbonamide, which decomposes and desorbs during thermal treatment, thus generating a more porous structure. After heat treatment in reducing atmosphere, the films present mono-dispersed metallic nanoparticles with average size of about 5 nm and a narrow size distribution. The exposure to water, acetone and ethanol vapors causes absorbance changes of the plasmon absorption peak of silver, which are ascribed to the changes of the refractive index of the embedding medium. The reversible absorbance changes and the fast response (40-160 s) over a concentration range from 800 to 88000 ppm make these nanocomposite films useful for optical detection of organic vapors.

## 1 Introduction

Optical gas sensors have been attracting growing interest owing to several advantages over the conventional electrical gas sensors [1,2]. In fact, they are unaffected by electromagnetic noise and fire ignition and can be used for remote control and information through an optical fibre network. In particular, materials whose optical absorption properties reversibly change in the presence of atmospheric gases and moisture are considerably attractive for use as optochemical sensors.

As known, dielectric materials containing nanoclusters of Cu, Ag and Au present optical absorption bands, named plasmon absorption bands, which depend both on the particle size and on the refractive index of the surrounding medium. Since the adsorption of gas molecules modifies the dielectric properties of the nanoparticle-surrounding medium, the optical absorption change can be correlated to the kind and amount of adsorbed gas.

This paper deals with a study of the sensing capability towards organic vapors of nanocomposite materials constituted by Ag nanoparticles embedded in transparent polyimide thin films obtained by ion-exchange technique followed by annealing in reducing atmosphere [3,4].

## 2. Experimental

The chemical structures of the starting polyimides 6FDA-DAD and BPDA-3F are sketched in Fig. 1. The synthetic procedure for their preparation and their physical properties have been reported elsewhere [5]. Thin films about 1  $\mu\text{m}$  thick were obtained by spinning a solution of each polyimide (10% wt. solids) in N-methylpyrrolidone on silicon and silica substrates. Azodicarbonamide (ADC) was mixed to the polyimide-containing solution at two different concentrations: 5 wt. % and 15 wt. %. The samples were heated in air up to 250  $^{\circ}\text{C}$  for 1 hour in order to effect the thermolysis and removal of ADC compound. Afterwards the films were immersed in KOH 5M for time intervals ranging from 5 s up to 1 min at 45 $^{\circ}\text{C}$ . Both polyimides react with KOH to give the salt potassium polyamate, as reported in Fig. 1. Subsequently, the samples were immersed in a solution of  $\text{AgNO}_3$  50mM at 45 $^{\circ}\text{C}$ , thus undergoing the ion-exchange process between potassium and silver ions. Thermal reduction of silver and particles aggregation were attained by annealing the samples in reducing atmosphere ( $\text{H}_2$  12% - Ar) at 350 $^{\circ}\text{C}$  for 30 min.

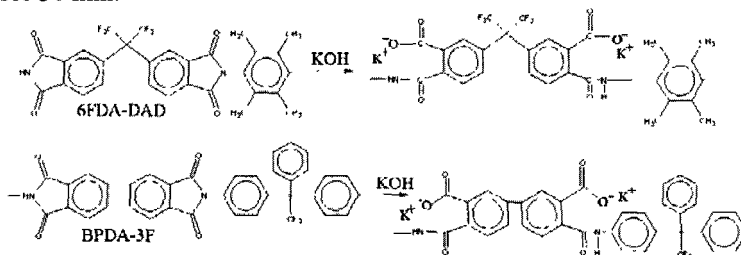


*Fig.1 Chemical structures of 6FDA-DAD and BPDA-3F polyimides and alkaline hydrolysis reaction scheme.*

Optical UV-Vis absorption spectra were recorded by using a Jasco V530 spectrometer. Nitrogen physisorption experiments were carried out on polyimide films with and without ADC at 77 K on an ASAP 2020 Micromeritics sorptometer. The specific surface area was calculated by the BET equation. The silver cluster dimension and distribution were investigated by cross sectional transmission electron microscopy (TEM), carried out with a field emission gun FEI TECNAI F20 (S)TEM microscope operating at 200 kV.

## 3. Results and Discussion

A strong increase of the films porosity is achieved by including ADC into the two polyimides, as evidenced by nitrogen physisorption measurements. In fact,

the 6FDA-DAD doped with 5 % of ADC exhibits an increase of effective surface area from  $1.7 \text{ m}^2/\text{g}$ , for the undoped polymer, to  $21.7 \text{ m}^2/\text{g}$ .

As to the optical transparency of polymer films, after the ion-exchange procedure the samples are still transparent, but after the heat treatment in reducing atmosphere they exhibit an intense yellow colour. The optical absorption spectra, shown in Fig. 2, exhibit an absorption peak at 430 nm for 6FDA-DAD and at 440 nm for BPDA-3F. As can be observed, the intensity of the plasmon peak increases at increasing ion exchange time duration. On the other hand, 6FDA-DAD thin film treated in KOH for 1' and  $\text{AgNO}_3$  for 2' exhibits a plasmon absorption feature of lower intensity with respect to shorter treatment times. This deviation from the expected trend can be ascribed to the thinning of the pristine film during the prolonged KOH treatment.

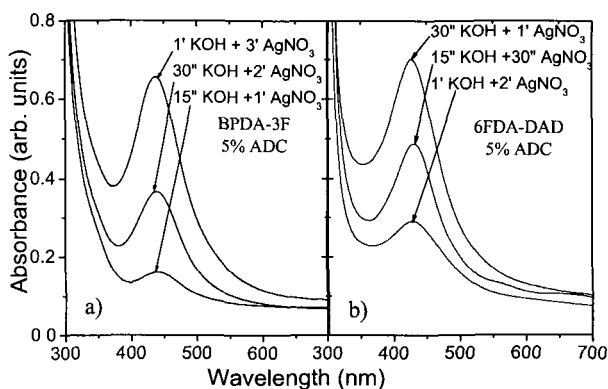
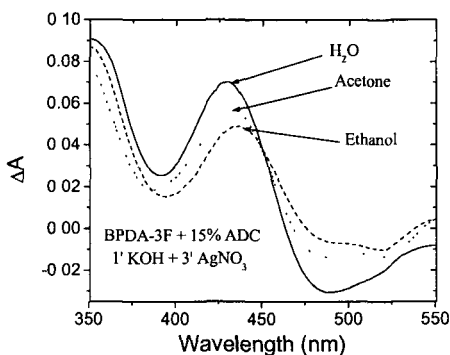


Fig.2 Optical absorption spectra of the BPDA-3F and 6FDA-DAD thin films treated at different times in KOH and  $\text{AgNO}_3$  aqueous solutions.

The presence of silver clusters is confirmed by TEM measurements, not reported. Along the doped layer a uniform distribution of spherical silver clusters has been observed, whose mean size was evaluated to be  $\langle D \rangle = 5.1 \text{ nm}$ . By fluxing saturated vapors of water, ethanol and acetone, the plasmon absorption peak exhibits a change of both intensity and position, induced by the local change of the refractive index of the medium surrounding the nano-sized metal clusters. Figure 3 displays the absorbance changes  $\Delta A$  defined as  $A_{\text{analyte}} - A_{\text{nitrogen}}$  of the sample BPDA-3F doped with 15 % ADC and treated for 1' and 3' in KOH and  $\text{AgNO}_3$  aqueous solutions, respectively. As can be observed the variation is more pronounced in the presence of water saturated vapors and decreases with acetone and ethanol.



**Fig.3** Absorbance variation  $\Delta A$  in presence of saturated vapors of water, ethanol and acetone for the BPDA-3F thin film. The treatment parameters are detailed in the graph.

For a better evaluation of the sensing capability of the nanocomposites towards the different analytes, a kinetic response study has been performed, by exposing the samples to the vapors at concentrations ranging from 800 to 88000 ppm. The maximum available concentration depends on the vapor pressure of the different analytes at room temperature. Figure 4 displays, as an example, the kinetic responses to the three analytes of the 6FDA-DAD thin film doped with 5 % ADC and treated for 30'' in KOH and for 1' in  $\text{AgNO}_3$  aqueous solutions.

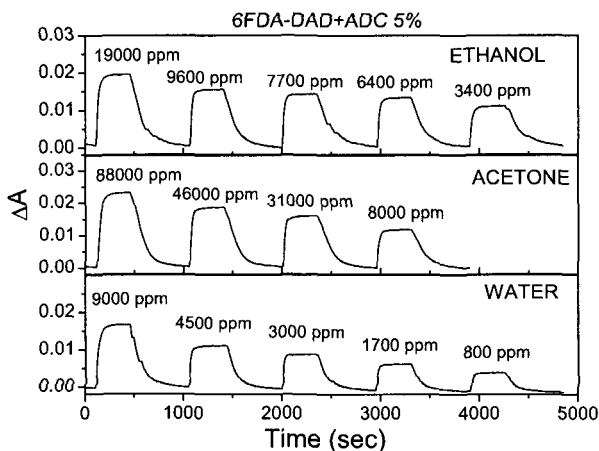


**Fig.4** Dynamic absorbance variation in presence of vapors at different concentrations of the 6FDA-DAD thin film doped with 5 % of ADC and treated for 30 seconds and 1 minute in KOH and  $\text{AgNO}_3$  aqueous solutions, respectively.

The data have been collected by measuring the absorbance changes at 422 nm, with a bandwidth of 5 nm, every 5 seconds. From the kinetic response curves the response and recovery times have been also calculated. The response times range from 40 to 160 s and the recovery times from 140 to 460 s. These



relatively low values point out the fast permeation of analyte molecules through the polyimide matrix, which easily reach the cluster proximity.

#### 4. Conclusions

Silver-nanoclusters-containing fluorinated polyimide films have been produced by using the ion exchange procedure followed by thermal treatment. The porosity of the polymer matrix has been enhanced by adding to the solved polyimide small amounts of azodicarbonamide, which thermally decomposes thus increasing the free surface area of the polymer films up to more than tenfold. The distribution of silver nanoclusters in the film is homogeneous, as shown by TEM micrographs, and the average nanocluster size is 5.1 nm.

The optical sensing capability of silver-polyimide nanocomposite materials have been tested upon exposure to vapors of water, ethanol and acetone. The analyte/film interaction produces a change of the nanoparticle plasmon absorption peak owing to a change of the average refractive index of the environing medium. Measurements of the absorbance changes at a fixed wavelength show that the nanocomposite films respond to all the analytes at concentrations ranging from 800 to 88000 ppm. Response times ranging from 0.7 to 2.0 min and recovery times in the order of few minutes have been obtained for all the nanocomposite films.

#### Acknowledgements

This research was financially supported by the Fifth Commission of Istituto Nazionale di Fisica Nucleare (DEGIMON project).

#### References

- [1] K. Eguchi, Optical gas sensors, in: G. Sberveglieri (Ed.), Gas sensors, Kluwer Academic Publisher, Dordrecht, 1992, pp. 307-328.
- [2] W.R. Seitz, Chemical sensors based on fiber optics, *Anal. Chem.* 56 (1984) 16A-34A.
- [3] K. Akamatsu, K. Nakahashi, S. Ikeda, H. Mawafune, Fabrication and structural characterization of nanocomposites consisting of Ni nanoparticles dispersed in polyimide films, *Eur. Phys. J. D* 24 (2003) pp. 377-380.
- [4] S. Ikeda, K. Akamatsu, H. Nawafune, T. Nishino, S. Deki, Formation and growth of copper nanoparticles from ion-doped precursor polyimide layers, *J. Phys. Chem. B* 108 (2004) pp. 15599-15607.
- [5] S. Carturan, A. Quaranta, A. Vomiero, M. Bonafini, G. Maggioni, and G. Della Mea, Polyimide-Based Scintillators studied by Ion Beam Induced Luminescence, *IEEE Trans. Nucl. Sci.* 52(3) (2005) 748-751.

# SOLID STATE DIRECTIONAL ANEMOMETER FOR HARSH ENVIRONMENTS

P. BRUSCHI, N. NIZZA

*Dipartimento di Ingegneria dell'Informazione, via G. Caruso 16, 56122 Pisa, Italy.  
[p.bruschi@iet.unipi.it](mailto:p.bruschi@iet.unipi.it)*

M. PIOTTO

*IEIIT-Pisa CNR, via G. Caruso 16, 56122 Pisa, Italy.*

M. SCHIPANI

*STMicroelectronics, via Tolomeo 1, 20010 Cornaredo (MI), Italy.*

An anemometer consisting in two silicon chip pairs glued to a thin ceramic plate is presented. The four chips include a precise temperature sensor and a polysilicon heater and the two pairs are positioned along orthogonal axes in order to measure both the modulus and the direction of the wind. The ceramic plate protects the chips from contamination maintaining, at the same time, the thermal contact between the wind and the sensors. Preliminary characterisation of the device is presented and discussed.

## 1. Introduction

The knowledge of wind distribution is a key information in many application fields including meteorology, aeronautics, energy conversion, controlling systems and environmental monitoring. The dispersion of a poisonous agent after a catastrophic leakage from an industrial plant or simply after a period of intense traffic in a town can be predict more accurately if the real distribution of the wind flows is known. Simple numerical models, in fact, begin to fail in urban environments with a complex geometry of building structures and street configuration [1,2] or in a forest with an irregular geometry [3]. Therefore, experimental measurements of the wind intensity and direction are necessary both to validate the existing numerical models and to generate new ones. In particular, the complicated nature of wind distribution inside an urban area requires a dense network of sensors to provide a knowledge of the wind distribution. The sensors should be (i) miniaturized to both reduce the visual impact and increase the network density, (ii) low power demanding to decrease the routine maintenance operations of the network and (iii) suitable for harsh environments.

In this work we present a thermal anemometer based on a silicon chip, previously used in innovative single sensor flow-meters [4], which is equipped with a precise temperature sensor and a polysilicon resistor, used as a heater. The

device is made up of (i) two chip pairs to sense the orthogonal components of the wind and (ii) a thin ceramic plate that protects the chips from the air stream.

## 2. Device design and simulation

### *Operating principle*

In order to understand the operating principle of the sensor the simple configuration of Figure 1 (a) can be considered. The two elements, represented as squares in the figure, are composed of a heater and a temperature sensor, measuring the element temperature.

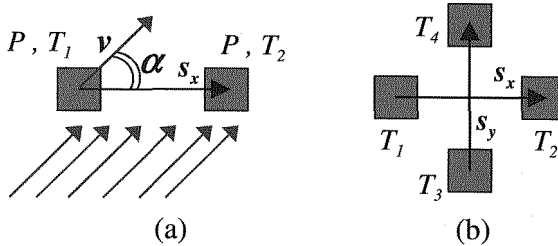


Figure 1. Two element (a) and four element (b) anemometer configuration.

The temperature of the elements are indicated by  $T_1$  and  $T_2$ , while  $P$  is the power delivered to the heaters, identical for the two elements. Let us start by assuming that mismatch errors are not present. In this condition, if both elements are fed by the same heating power and the wind speed is zero, than  $T_1=T_2$ . Conversely, if a wind speed component along the  $s_x$  direction is present, than heat transfers from the upwind to the downwind element through forced convection. Experiments performed with similar arrangements [5] showed that the temperature difference created by the air flow is nearly proportional to the cosine of the angle  $\alpha$  between the wind direction and the  $s_x$  axis. Unfortunately, the dependence on the modulus of the wind speed is more complicated and non linear so that an empirical calibration is generally required. In order to detect both the wind modulus and direction, two one-dimensional structures with orthogonal axes  $s_x$  and  $s_y$  can be combined to form the four element sensor of figure 1 (b). For such an arrangement the following equations can be reasonably hypothesized:

$$T_2 - T_1 = A(v)\cos(\alpha); \quad T_4 - T_3 = A(v)\cos(\alpha - 90^\circ) \quad (1)$$

where  $A(v)$  is a function of the wind speed  $v$ .

The proposed device is built according to this four element configuration.

The elements consist in silicon chips including a precise temperature sensor based on the  $\Delta V_{BE}$  principle (sensitivity 3.3 mV/K) and a polysilicon heater. The chips have been fabricated using the Bipolar-CMOS-DMOS process BCD3s of STMicroelectronics. More details about these elements are given in Ref. [4]. The chips are glued to a ceramic-epoxy laminate (RO 4003), 0.25 mm thick, characterized by a  $0.6 \text{ WK}^{-1}\text{m}^{-1}$  thermal conductivity, roughly six times the conductivity of standard laminates for printed circuit boards. The laminate is provided with a copper layer (35  $\mu\text{m}$  thick) the geometry of which was defined with standard photolithographic process to obtain the interconnects for the chips. The laminate is mounted on top of a stainless steel cylinder as shown in figure 2(a). In this way the four chips, forming the structure of figure 1(b), are in thermal contact with the air stream through the thin laminate, which, at the same time, protects the chips from contamination, dust or moisture. A photograph of the laminate taken from the chip side is shown in figure 2 (b).

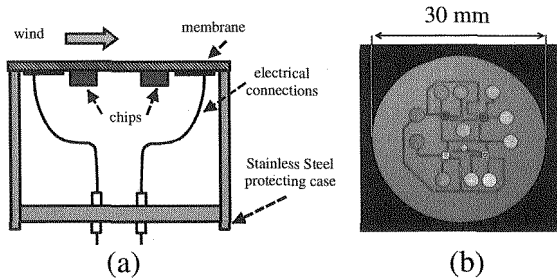


Figure 2. Final configuration of the sensor probe (a) and optical photograph of the laminate with the chip and copper interconnect layer(b).

### *Driving and Readout circuit*

The interface circuit for the sensor described in the previous section has been designed on the basis of simulations performed using the finite element environment FEMLAB<sup>TM</sup>. A particularly relevant result is shown in figure 3, representing the case of wind direction along the  $s_x$  axis ( $\alpha=0$ ). The upwind and downwind temperatures,  $T_{up}$  and  $T_{down}$ , respectively, and their difference is reported. It can be observed that, as the wind speed increases from zero,  $T_{down}$  actually increases and  $T_{up}$  decreases, in conformity with the considerations of previous section. However, this trend stops just for very low wind speeds and also  $T_{down}$  begins to decrease (overall cooling). The result is a non monotonic behaviour of the output signal ( $\Delta T=T_{down}-T_{up}$ ) that reduces the valid wind speeds to a range clearly unsuitable for most applications. In order to solve this problem, a driving strategy that stabilizes the average temperature of the 4 sensor elements has been adopted. In this way, considering a simpler two elements configuration, if one sensor temperature decreases, the other one should necessarily increase.

This result has been obtained by means of the circuit of figure 4. The four voltages  $V_{1-4}$ , linearly dependent on the corresponding sensor element temperatures, are amplified by the four blocks indicated with A (based on the quad op-amp LT1114) and their average is computed by resistors R. The average temperature signal ( $V_{CM}$ ) is compared with the desired set-point ( $V_{SET}$ ) and the difference, amplified by the instrumentation amplifier IC1 (AD620), is used to drive the heaters of the four chips, connected in parallel. IC2 is a power op-amp (L272M). The diode D1 is necessary to prevent the heater voltage from getting negative and cause instability.

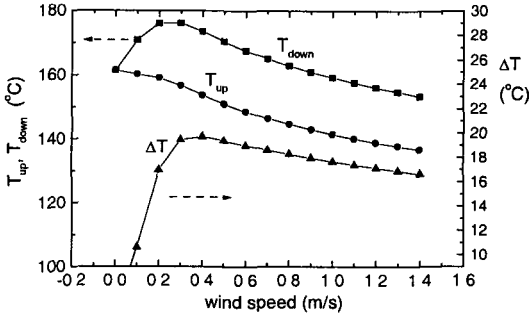


Figure 3. Finite element simulations showing the overall cooling phenomenon.

The average temperature signal ( $V_{CM}$ ) is compared with the desired set-point ( $V_{SET}$ ) and the difference, amplified by the instrumentation amplifier IC1 (AD620), is used to drive the heaters of the four chips, connected in parallel. IC2 is a power op-amp (L272M). The diode D1 is necessary to prevent the heater voltage from getting negative and cause instability.

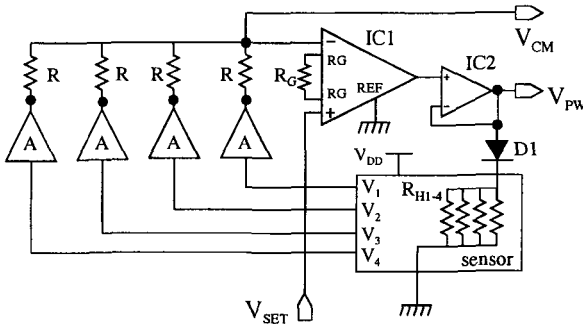


Figure 4. Circuit used to implement the constant average temperature method.

### 3. Experimental results

The effectiveness of the proposed driving strategy is shown in figure 5 (a) where the sensor responses, obtained with the constant average temperature and the traditional constant power methods, are compared. The experiments were performed in a purposely built wind tunnel consisting of a pipe (diameter 120 mm) equipped with a fan and a reference anemometer. The output signal  $V_X$  is proportional to the temperature difference  $T_2-T_1$  (see figure 1) while the offset

$V_X(0)$  has been subtracted. We note that in conditions of constant power, the sensor output actually saturates and tends to invert slope as predicted by the simulations, while with the constant average driving the saturation does not occur.

The effect of varying the angle is represented in figure 5 (b), where the signals  $V_X$  and  $V_Y$ , proportional to the temperature differences  $(T_2-T_1)$  and  $(T_4-T_3)$ , respectively, are shown for a fixed wind speed. A large offset (not cancelled in these curves) can be observed for the  $V_X$  data. The offset is mainly due to non symmetrical thermal conductivities deriving from the uncertainty on the glue layer thickness between the chips and the laminate and the non symmetrical copper interconnection layout. The presence of offsets is typical of these systems and has to be acquired during calibration in order to be cancelled by signal processing. Solid lines represent the best fit operated using sinusoidal functions. A good agreement with the prediction of Eq. (1) can be observed.

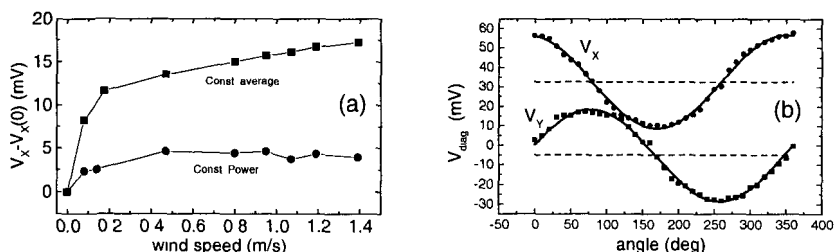


Figure 5. Sensor response with constant power and constant average heater driving (a) and dependence of the output signals on wind direction for  $v = 1.4$  m/s (b).

## Acknowledgments

The authors thank STMicroelectronics of Cornaredo (Milan, Italy) for fabricating the chips used in this work.

## References

1. A. Dobre, S. J. Arnold, R. J. Smalley, J. W. D. Boddy, J. F. Barlow, A. S. Tomlin and S. E. Belcher, *Atmospheric Environment* **39**, 4647 (2005).
2. J. W. D. Boddy, R. J. Smalley, N. S. Dixon, J. E. Tate and A. S. Tomlin, *Atmospheric Environment* **39**, 31477 (2005).
3. M. Molder, L. Klemetsson and A. Lindroth, *Agricultural and Forest Meteorology* **127**, 203 (2004).
4. P. Bruschi, D. Navarrini and M. Piotta, *Sensors and Actuators A* **110**, 269 (2004).
5. B. W. Van Oudheusden and A. W. Van Herwaarden, *Sensors and Actuators A* **21-23**, 425 (1990).

# A Focal Plane Array based on CMOS Uncooled Thermoelectric Infrared Detectors

C. Calaza, N. Viarani, G. Pedretti, M. Gottardi, V. Zanini, A. Simoni  
ITC-irst, via Sommarive, 16, 38050 Povo (TN), Italy. [carlos@itc.it](mailto:carlos@itc.it)

## Summary

This paper describes an uncooled infrared thermal imager fabricated with a standard CMOS process (AMS 0.8 $\mu$ m) and a compatible front-side bulk micromachining post-process based on a TMAH solution. The fabrication approach does not involve any material deposition, lithography step or particular etch-stop technique after the CMOS process flow, so that the imager cost is almost equal to that of the CMOS chip cost. The infrared imager is composed of a focal plane array (FPA) with 16x16 thermopile pixels monolithically integrated with the addressing and readout electronics. The optical measurements performed with the fabricated devices have shown a responsivity  $S$  of 15.0 V/W, a noise equivalent power  $NEP$  of 1.37 nW/Hz<sup>1/2</sup> and a normalized detectivity  $D^*$  of 1.05·10<sup>7</sup> cm·Hz<sup>1/2</sup>·W<sup>-1</sup> for the infrared pixel. The readout channel features a maximum gain of 85dB with an equivalent input noise of 22 nV/Hz<sup>1/2</sup>. An infrared imager based on the FPA has been build and thermal imaging has been demonstrated.

## 1 Thermopile pixel

Figure 1 shows a micrograph of the fabricated FPA. Each pixel consists of a thermally-isolated micromachined membrane suspended by two arms that contain an embedded thermopile temperature sensor made up of polysilicon/aluminium thermocouples. The absorbed infrared radiation heats up this membrane causing a temperature rise that is measured by the thermopile sensor. The thermal isolation is attained by etching away the silicon substrate under the pixel structure by means of a front-side bulk micromachining post-process based on a TMAH solution [1]. This etching process has been carried out with the single CMOS dies and does not require a particular etch stop technique. The etch openings are readily obtained with the CMOS photolithographic steps, by arranging the several opening masks (active area, via, contact and pad) on top of each other.

The thermopile is made up of two 5 thermocouple series connected between them by an additional thermocouple shared by the two support arms. The pixel output voltage  $V_T$  is given by  $V_T=N\cdot\alpha\cdot\Delta T$ , where  $N$ ,  $\alpha$  and  $\Delta T$  denote the number of thermocouples, the Seebeck coefficient of the materials and the temperature difference between hot and cold junctions. The optimization of the performance achievable with this CMOS-MEMS approach for a given pixel

pitch has been carried out using the finite element method. A FEM model of the pixel has been used to calculate the temperature distribution caused by a heat load that emulates the absorption of infrared radiation. The different performance parameters can be derived using this temperature to evaluate the thermopile output voltage using the previous equation.

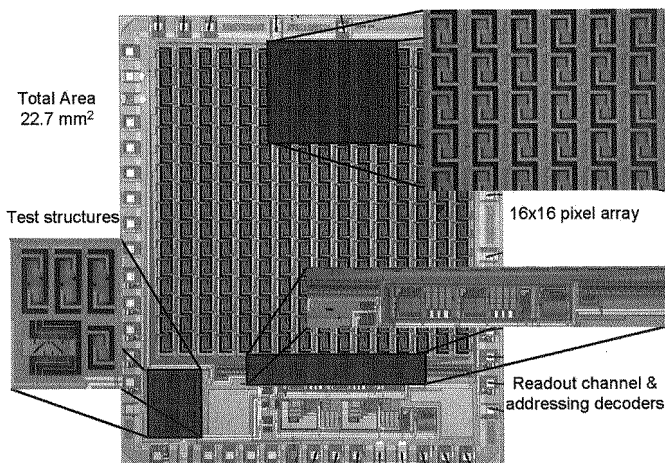


*Fig.1 Micrograph view of the fabricated FPA*

The geometry selected improves the responsivity attainable with a certain pixel size by increasing the absorbing membrane area while preserving a good thermal isolation between the thermopile hot and cold junctions. The pixel structure is outlined by two etching openings with two different sections: the main one ( $20\mu\text{m}$  width) is intended to expose the silicon substrate during the etching process, while the narrow one (only  $2\mu\text{m}$ ) is intended to lengthen the support arms with a minimum loss of absorbing area. The use of only two support arms also allows the arrangement of the pixels in the same column on a shared etched cavity increasing the overall FPA fill factor. Table 1 summarizes the main parameters that characterize the FPA pixel. The pixel includes a heating resistor intended to implement a self-test function that allows an electrical test of the FPA without need of specific infrared equipment [2].

## 2 Readout channel

Since the voltage levels self-generated by the thermopile pixels are in the range of few  $\mu\text{V}$  the implemented readout channel consists of a low-noise voltage amplifier with high gain that can be tuned for different operation conditions (from 50dB to 85dB). The readout circuit makes use of the chopper principle and the correlated double sampling technique to reduce the amplifier offset level and the noise floor [3]. The addressing of the FPA is carried out by



means of two independent decoders (rows and columns) that control the set of MOS switches integrated in the silicon rims between adjacent columns to connect the thermopile and the heater ends of the selected pixel to the associated column lines. The addresses are externally supplied so that the pixels can be randomly accessed or can be sequentially scanned to obtain an infrared frame.

FPA pixel characteristics	
Active area	$20.6 \times 10^3 \mu\text{m}^2$
Fill factor	0.56
Pixel pitch	$228 \times 220 \mu\text{m}$
Arm length / width	$173 \times 31 \mu\text{m}$
Structure thickness	From 3.2 to 4.1 $\mu\text{m}$
Thermocouple number	11
Thermopile resistance	40.1 k $\Omega$
Seebeck coefficient	143 $\mu\text{V/K}$

*Table 1 Main characteristic parameters of the FPA pixel*

### 3 Experimental results

A specific test structure [4] has been included into the FPA chip in order to obtain a measurement of the Seebeck coefficient of the n-polysilicon/metal thermocouples ( $\alpha=143\mu\text{V/K}$ ). The system (pixel and readout channel) has been electrically assessed using the embedded pixel self-test capability, which allows the emulation of the infrared radiation absorption by dissipating a known power with the embedded heating resistor. The voltage generated by the thermopile can be calculated from the measured readout output and together with the applied heating power provides an estimation of the ideal pixel responsivity (100% absorptance), 26.7 V/W. This output voltage allows the estimation of the temperature difference between the hot and cold junctions,  $\Delta T = V_{\text{th}}/N \cdot \alpha_{\text{ab}}$ , that can be used to estimate the thermal conductivity of the pixel, which is found to be  $5.88 \cdot 10^{-5}$  W/K.

The FPA has been optically characterized in the 8-14  $\mu\text{m}$  band, usually used for infrared thermal imaging. A rather high absorptance is expected in this band due to the presence of the Si-N bonds in the passivation layer molecules, which have vibrational and rotational states with associated wavelengths in this band. The optical measurements have been carried out using a Scitec IR-21V infrared emitter as source, an Oriel pyroelectric sensor as calibrated reference detector and two equal band pass filters to restrict the wavelength range in both detectors. A reflected image of the infrared emitter has been projected onto the detectors measuring plane using a gold coated parabolic mirror. Figure 2 shows the infrared beam profile measured by the fabricated 16x16 FPA. The output signal obtained with both detectors has been used to evaluate the pixel optical responsivity, 15.0 V/W, which corresponds to a mean absorptance of 56% in the

band between 8 and 14  $\mu\text{m}$ . The noise equivalent power NEP is measured to be  $1.37 \text{ nW/Hz}^{1/2}$ , which corresponds to a normalized detectivity  $D^*$  of  $1.05 \cdot 10^7 \text{ cm}\cdot\text{Hz}^{1/2}\cdot\text{W}^{-1}$ . The relative spectral responsivity has been measured including a monochromator into the optical setup. The pixel shows a regular absorption in this band with an absorption peak at  $8.8\mu\text{m}$  due to the presence of polysilicon and metal layers in the support arms.

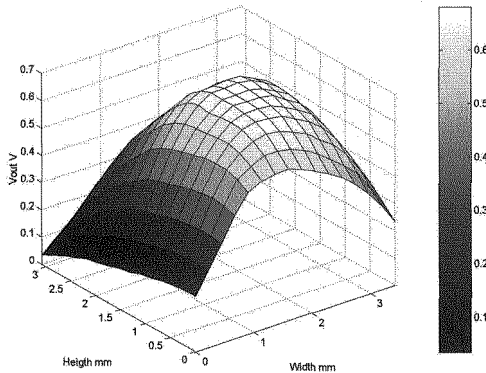


*Fig. 2 Profile of the test infrared beam measured with the fabricated 16x16 FPA*

#### 4 Thermal imager

A thermal imager has been created using one of the fabricated FPA chips together with a housing that includes the infrared imaging optics and a computer that is used to control the operation of the demonstrator (address generation) and to acquire and display the image data. The housing is basically an aluminium holder that contains an IR lens casting the image of the thermal scene onto the sensor array. The lens has a diameter of 7.25 mm, a focal length of 8.7 mm, an f-number  $n_f$  of 1.2 and is covered by an antireflection coating that provides a transmission of 94% in the infrared band between 8 and 12  $\mu\text{m}$ .

The signals from the individual pixels are multiplexed and amplified by the FPA on-chip circuitry. The integrated row and column decoders are controlled through the pixel address supplied by the computer. For the acquisition of a complete image all pixel addresses are sequentially supplied and the respective pixel signals are synchronously converted with the computer acquisition hardware. The A/D converter in the acquisition hardware measures the output value by integrating the signal during 20 ms, discarding its values during the first 5 ms after an address change in order to let the amplifier output signal settle to the new value. This integration scheme is used to suppress the noise and signal components with frequencies above 50 Hz. With this timing method the pixel acquisition lasts for 25 ms, while the acquisition of a complete image

frame with 256 pixels requires 6.4 s, which corresponds to a frame rate of 0.16 Hz. This frame rate can be increased by reducing either the delay or the integration time, however, a shorter delay will increase the electrical cross-talk between pixels, and a decreased integration time will deteriorate the NETD due to the larger signal bandwidth and increased noise.

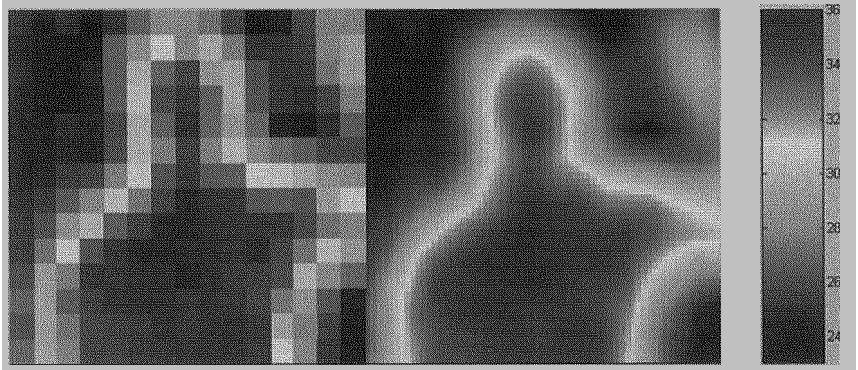


*Fig. 3 Thermal image of a person, acquired with the thermal imager developed at ITC-irst: (a) Unprocessed image, 16x16; (b) the image after a bilinear interpolation between pixels, 64x64.*

Figure 3 shows an image acquired with the thermal imager based on the CMOS FPA and the previously described setup. The picture shows a person, head and chest with one arm up, at a distance of approximately 2 meters. The blue region corresponds to the cold background at ambient temperature, while red regions correspond to the hottest parts, 13°C above this ambient temperature. The NETD achieved with this setup is 490 mK, for a signal bandwidth of 50 Hz.

## References

1. TIMA laboratory, CMP Multi-Project Circuits Service. <http://cmp.imag.fr>
2. B. Charlot, F. Parrain, S. Mir, B. Courtois, *Proceedings DTIP'2001*, Cannes-Mandelieu, France, April 2001, 96
3. D.A. Johns, K. Martin, *Analog Integrated Circuit Design*, John Wiley and Sons, 1997
4. M. von Arx, O. Paul, H. Baltes, *IEEE Trans. Semiconductor Manufacturing*, Vol. 10 201 (1997)

## Acknowledgments

This work has been supported by the Provincia Autonoma di Trento, through the funded project DIRMI.

# A 2-D PLANAR MICROFLUXGATE WITH SPUTTERED CORE

Andrea Baschirotto

Dept. of Innovation Engineering, University of Lecce, 73100 Lecce – Italy

Enrico Melissano, Pietro Siciliano

Microelectronics and Microsystems Institute of the National Council of Research (IMM-CNR), 73100 Lecce – Italy

Enrico Dallago, Piero Malcovati, Marco Marchesi, Giuseppe Venchi

Power Electronics Laboratory, Department of Electrical Engineering, University of Pavia, 27100 Pavia - Italy

## Summary

In this paper a double axis planar micro-Fluxgate magnetic sensor is presented. The ferromagnetic core material, the Vitrovac 6025 X, has been deposited on top of the coils with the DC-magnetron sputtering technique, a new type of procedure with respect the existing solutions in the field of Fluxgate sensor. This procedure allows us to obtain a core with the good magnetic properties of the amorphous ferromagnetic material, typical of a core 25  $\mu\text{m}$  thick, but with a thickness of only 1  $\mu\text{m}$ , typical of a core electrodeposited. The micro-Fluxgate has been realized in a 0.5  $\mu\text{m}$  CMOS process using copper metal lines to realize the excitation coil and aluminum metal lines for the sensing coils. Applying a triangular excitation current of 18 mA peak at 100 kHz the magnetic sensitivity achieved is about 0.45 mV/ $\mu\text{T}$ , suitable for detecting the Earth's magnetic field ( $\pm 50 \mu\text{T}$ ), while the linearity error is 1.15% of the full scale. The maximum angle error of the sensor, evaluating the Earth magnetic field, is 3.4°. The power consumption of the sensor is about 13.7 mW.

## Introduction

Many applications require low-cost and low-power highly sensitive miniaturized magnetic sensors to locally and accurately measure weak magnetic fields in a plane [1, 2]. For this task integrated devices appear to be the best solution. Unfortunately, none of the existing integrated magnetic sensors, such as magnetoresistive [3] or Hall sensors [4], fulfils simultaneously all the desired requirements due to their poor magnetic field measurement accuracy. Innovations are expected in the integrated sensors based on the Fluxgate principle.

Following the experience in [5, 6], the sensor presented in this paper is a micro-Fluxgate, developed in a CMOS process, where the ferromagnetic core is realized as a post processing step with the DC-magnetron sputtering technology. This technique allows us to realize a core with the good magnetic properties of the amorphous ferromagnetic material and with a very small thickness (about 1  $\mu\text{m}$ ). At this time, in literature it is possible to find solutions with

electrodeposited magnetic

### The basic sensor structure

Fig. 1 shows a photo of the micro-Fluxgate sensor, realized in a  $0.5\ \mu\text{m}$  CMOS integrated circuit process. The planar excitation coil, which has been realized in copper, is characterized by  $5.5\ \mu\text{m}$  thickness, 71 turns and  $12\ \mu\text{m}$  pitch ( $8\ \mu\text{m}$  metal width and  $4\ \mu\text{m}$  of spacing between two metals). The total area for the excitation coil is  $1760 \times 1760\ \mu\text{m}^2$  and its resistance is about of  $123.4\ \Omega$ .

The geometrical parameters of the sensing coil, realized in aluminum, are:  $1\ \mu\text{m}$  thickness,  $1.4\ \mu\text{m}$  metal width and  $1.6\ \mu\text{m}$  of spacing between two metals. The total area for the sensing coils, consisting of 66 turns, is  $650 \times 650\ \mu\text{m}^2$  and their resistance is about of  $1.84\ \text{k}\Omega$ .

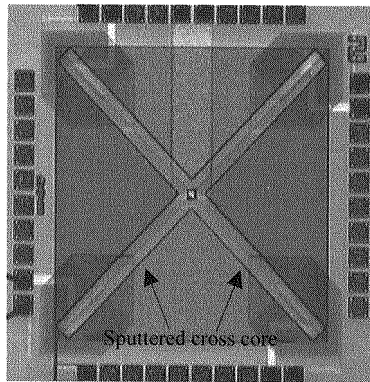


*Fig. 1 Photograph of the micro-integrated Fluxgate realized (with the sputtered ferromagnetic core of  $1\ \mu\text{m}$  thick).*

The ferromagnetic cross-shaped core (Fig. 1), realized with the Vitrovac 6025 X [7], has been obtained with the DC-magnetron sputtering technique. The thickness of the sputtered core, of about  $1\ \mu\text{m}$ , has been evaluated with a SEM microscope.

In order to optimize the DC-magnetron sputtering process and to verify that the material is not degraded by the deposition process, we performed several measurements of the magnetic properties of the deposited material, with a system of coils similar to the loop tracer reported in [8]. A comparison between the sputtered and the as-cast ferromagnetic material hysteresis is shown in Fig. 2. It is evident that the two measured loops are different from the loop given by the supplier (Vacuumschmelze). These differences can be explained as follows:

1. In our system the magnetic circuit is open (the sputtered core is not a toroid)

and therefore the demagnetization field must be taken into account.

- The secondary coils are not strictly wrapped around the sputtered core therefore a flux leakage exists.

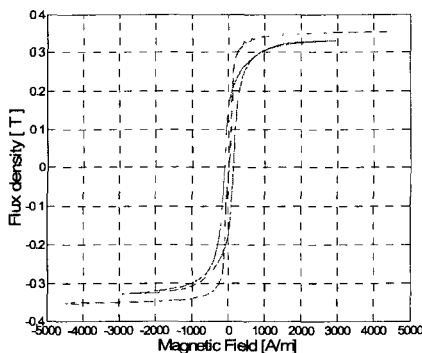


Fig. 2 Comparison between the hysteresis loops of the Vitrovac sputtered and as-cast (dashed line).

Because of this only a comparison between the B-H loop of the sputtered material and the as-cast material is possible. From this point of view, the two loops look similar, resulting in nearly equivalent magnetic properties. The fundamental difference is the coercivity field, that for the deposited core is greater, about 100 A/m. This difference is in agreement with the results described in [9]. The increase of the coercivity after deposition of the material will result in a slight increase of the current required in the excitation coil to achieve the saturation of the core. The measured magnetic properties of the deposited material are anyway suitable for the correct operation of the Fluxgate sensor with only a slight increase of the power consumption.

## Measurement and results

The characterization of the sensor has been realized using a universal source (HP3245A) to supply the excitation coil. The frequency of excitation has been fixed to 100 kHz and the excitation current has been set to 18 mA<sub>peak</sub>, which is the value necessary for the core saturation.

The fundamental component of the differential output voltage, after an amplification of about 33 dB, and imposing an external magnetic field with a pair of Helmholtz coils, has been evaluated using a spectrum analyzer (HP3589A). This voltage is plotted in Fig. 3 against the external magnetic field. The sensor shows a linearity error of about 1.15% of the full scale in the range of  $\pm 50 \mu\text{T}$  with a sensitivity of about 0.45 mV/ $\mu\text{T}$ .

To evaluate the possibility of using this integrated micro-Fluxgate sensor as a compass, the voltage output has been measured while rotating the sensor in a

horizontal plane. Fig. 4 shows the output voltage for each axis of sensitivity exposed to a magnetic induction of about 20  $\mu\text{T}$ . The angle error is smaller than  $3.4^\circ$  and includes signal non-linearity, hysteresis and noise. The power consumption of the sensor, considering the resistance of the excitation coil of 123.4  $\Omega$  and 18  $\text{mA}_{\text{peak}}$  of triangular current excitation, is about 13.7 mW. At the moment this power consumption is not comparable with the other existing solutions because it is evaluated for the sensor alone. In this case the circuitry has not been realized yet and therefore its power dissipation was not taken into account.

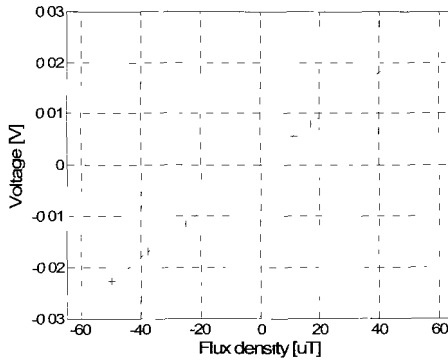


Fig. 3 Voltage output form the sensor imposing different value for the external magnetic field.

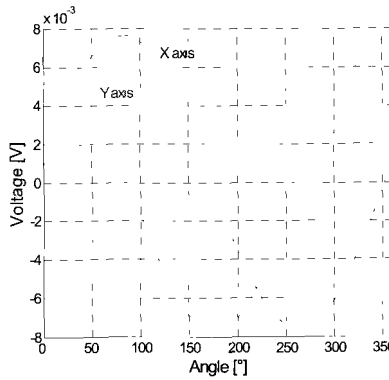


Fig. 4 Angle response for the two measurement axes (X and Y).

### Conclusions

In this work a micro-Fluxgate with ferromagnetic core sputtered has been presented. This technique allows us to reduce the thickness of the core and

therefore the power consumption maintaining the good magnetic properties of the amorphous ferromagnetic material, the Vitrovac 6025 X, used as target.

The experimental results presented show that the sensor has good sensitivity, 0.45 mV/ $\mu$ T, and linearity, with an error of about 1.15%, in a range of  $\pm 50$   $\mu$ T. The measurement error when measuring the magnetic field angle is smaller than 3.4° and includes signal non-linearity, hysteresis and noise. The power consumption, referred only to the sensor, is actually about of 13.7 mW. The magnetic properties of the sputtered core could be improved with suitable treatments, e.g with an annealing after its deposition; hence we also expect a reduction of the power consumption.

### Acknowledgment

The authors would like to thank ing. Marco Morelli (STMicroelectronics) for the support in the micro-integrated coils realization and Vacuumschmelze, Hanau Germany, for Vitrovac® samples and support.

### References

- [1] Pavel Ripka, "Magnetic Sensors and magnetometers", Artech House Boston, London (2001).
- [2] M. Vopálensky, P. Ripka, A. Platil, "Precise magnetic sensors" Sensors and Actuators A 106 (2003) pp. 38 – 42.
- [3] C.H. Smith, R.W. Schneider, "Magnetic field sensing utilizing GMR materials", Sensor Review 18 1998 230–236.
- [4] R. Popovic, W. Heidenreich, Magnetogalvanic sensors, In: R. Boll, K.J. Overshott, Eds., "Magnetic Sensors", vol. 5, Sensors, A Comprehensive Survey, VCH, 1989, pp. 43–95.
- [5] A. Baschiroto, E. Dallago, P. Malcovati, M. Marchesi, G. Venchi, "From a PCB Fluxgate to an integrated micro Fluxgate magnetic sensor", Proceeding of Instrumentation and Measurement Technology Conference (IMTC-2005), Ottawa (Canada) 17 – 19 May 2005, pp. 1756-1760;
- [6] A. Baschiroto, F. Borghetti, E. Dallago, P. Malcovati, M. Marchesi, E. Melissano, G. Venchi and P. Siciliano, "Fluxgate magnetic sensor and front-end circuitry in a micro-integrated system", EUROSENSORS XIX, Barcelona (Spain) 11-14 September 2005;
- [7] Vacuumschmelze Hanau Germany, Amorphous metals VITROVAC [www.vacuumschmelze.de](http://www.vacuumschmelze.de);
- [8] P.T. Squire, S.M. Sheard, C.H. Carter and M.R.J. Gibbs, "Digital M-H plotter for low-coercivity metallic glasses", J.Phys. E: Sci Instrum. 21 (1988), pp. 1167-1172.
- [9] M. Ali "Growth and Study of Magnetostrictive FeSiBC Thin Films for Device Applications", University of Sheffield (1999) Ph.D thesis



# **An optical probe for RF electric field**

Lucio Ciccarelli, Mario Medugno

*I.M.M. - C.N.R., Naples, Italy*

[Lucio.Ciccarelli, Mario.Medugno]@na.imm.cnr.it

## **Summary**

Electromagnetic field (EMF) sensors are widely used in several industrial, scientific and medical applications and for measurements of fields yield by a huge set of communication devices. We focuses on some experiences on the use of an integrated optical device which implements a Mach-Zehnder interferometer, and on its further development as an electromagnetic field sensor. The probe is mainly made by non conductive materials, making such device suitable for experimental measurement of electromagnetic fields in near field region (or Fresnel's one) of transmitting antennas. Here no simple theory is available in order to evaluate the fields and mutual coupling between antennas and standard probes strongly affect the measurements: the optical probe avoids the coupling of the fields with metallic structures and the loss of antenna calibration which typically yield measurement errors.

## **1 Introduction**

Standard expensive sensors probes for electric and magnetic field measurements [1], also in the Fresnel region, are often equipped with optical transmission lines to avoid coupling with the measuring field. Their heads generally need both power source and electronics for: i) conditioning and processing of the signals received by an external antenna; ii) electro-optical (EO) conversion to eventually drive an optical link with the measure equipment.

The mutual coupling of EMF with the standard probe scheme is the source of precision loss, which can strongly be reduced by a completely optical probe. Recently have been developed new EMF sensors made by dielectric materials to overcome this problem.

## **2 The principle of an optical EMF**

The probe is an optical driven device with input-output optical fibers connecting it to a laser source and a photodetector. A very tiny resistively loaded antenna with a flat response in a wide band, yields the electric input for an integrated Mach-Zehnder interferometer. The optical probe is implemented on a LiNbO<sub>3</sub> substrate as sketched in the Figure 1.

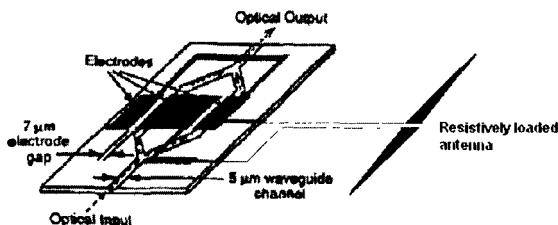


Figure 1: Optical EMF probe scheme

Applying an electric field to the electrodes, a phase shift  $\Gamma$  arises in the arms of the interferometer yielded by the electro-optic effect of the  $\text{LiNbO}_3$  underlying the waveguide channels; this produces an amplitude modulation in the optical output. Optical probes result in small dimension devices mainly made by non metallic parts, thereby dramatically less invasive than standard EMF probes.

## 2.1 The optical interferometer

The base component of the optical probe is a symmetric Mach-Zehnder interferometer. It was developed on a  $\text{LiNbO}_3$  substrate in order to exploit the Pockel effect which results in a linear change of the refractive index due to an external E-field. The substrate has X-cut, Y-propagating waveguides, as the extraordinary index of the Z axis  $n_e$  is lower than the ordinary index  $n_o$  of the X axis, where the relatively large electro-optic coefficient is  $r_{33} = 32,2 \text{ pm/V}$ . The phase shift is  $\Gamma = -\pi V r_{33} L n_e^3 / \lambda G_{EL}$ , where  $L$  is the electrodes length and  $G_{EL}$  their spacing. Planar and channel optical waveguides (green ellipses in the Figure) were manufactured by using high energy ion implantation technique of oxygen ions at 5 MeV [2].

## 3 Optical EMF probe characterization and experiments

In this section we characterize electrically and optically the integrated optical device, and we propose a model suitable for implementing non-invasive probe in a range of several Gigahertz.

The Mach-Zehnder interferometer is used as an optical modulator of the input laser source, therefore the device can be modeled by the electric equivalent circuit shown in Figure 2. Here the generator is the antenna (which voltage equals the field  $E$  times the antenna effective length  $h_e$ ) with two series

impedances: the antenna impedance  $Z_a$  and antenna loading  $Z_l$ . The modulator impedance has an optical input port and an output optical port both characterized by two efficiency parameters  $\eta_i, \eta_o$ , therefore it converts the electric signal at the electrodes into an optical signal according to the Thevenin complex equations and the optical power budget.

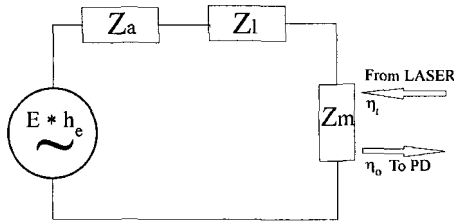


Fig. 2 Equivalent circuit of the EMF probe

The interferometer electrodes have a “push-pull” configuration such that a dual phase change is induced in the arms, yielding a doubled Pockel effect. The electrodes, which parameters are in Table 1, are supplied with the signal induced by a suitable resistively loaded dipole antenna, implementing a progressive wave in order to suppress the typical resonance of metal dipoles. The design of a such tapered antenna is derived according to the Wu-King approximation [3,4] and is characterized by an impedance distribution:

$$Z(x) = 60 g(h, k, a) / (h/2 - |x|) \quad \text{where:}$$

$$g(h, k, a) = 2 \{ [ \sinh^{-1} h/a - Ci(2ka, kh) ] + j [ 2(1 - e^{-jkh}) / hk - Si(2ka, kh) ] \}$$

and  $h$  is the dipole length,  $\lambda$  is the wavelength,  $k = 2\pi/\lambda$  is the wavenumber,  $a$  is the thickness of the antenna,  $C_i$  is the cosine integral and  $S_i$  is the sine integral.  $Z(x)$  can be realized as a pure resistance because when  $a < l$  the imaginary part of  $g(h, k, a)$  is smaller than the real part of  $g(h, k, a)$ . For this kind of antenna  $|Z_a|$ , the module of the antenna impedance at the gap, is a monotone decreasing function of the frequency and can be shown that the peak corresponding to the resonance frequency are smoothed with respect to one occurring in an ordinary metal dipole.

Using this approximation we realized a triangular shaped resistively loaded antenna  $8 \times 0.35\text{cm}$ , increasing the frequency range of linearity for the EMF probe. The antenna elements are made by the following process: 1) Deposition of a  $1.4 \mu\text{m}$  film of ITO by sputtering on the substrate (1 mm glass); 2) Deposition by spinning of reversible photoresist; 3) Lithography of the ITO film

by the antenna element mask; 4) Subsequent development of photoresist (negative process); 5) Wet etching of ITO elements by HCl.

<i>Electrodes length</i>	5,0 e-02 [m]
<i>Electrodes thickness</i>	1,4 e-06 [m]
<i>Modulator capacity</i>	2,2 e-11 [F]
<i>Modulator resistance</i>	1,0 e+8 [ohm]

*Table 1* Optical probe electrical characterization.

The MZ based optical probe has been preliminary tested with different laser source: a 2 mW in fiber laser diode (LD) at 1300 nm, a 150 mW in fiber LD at 980 nm, a 100 mW in fiber LD at 830 nm and an He-Ne in fiber coupled laser at 630 nm; the optical power was variable for each LD. After several measurements in laboratory and in anechoic chamber with an open-ended wave guide, we experimented a random power loss frequently dependent on optical device and fibers stress. Such power loss fluctuations were due to damages in fiber lines which were optically detected next to the pigtails of the interferometer.

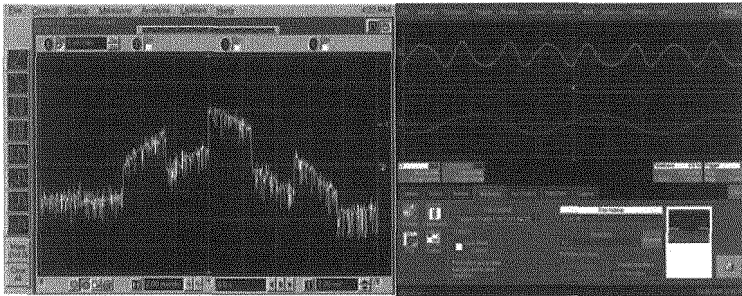


*Fig. 3* Probe response for ELF and VHF band

The measured total loss was greater (63 dB) than the calculated one by the optical power budget below; new fibers have been soldered and the power fluctuations were reduced at all. Photodetectors suitable for the sources spectrum and power were tested. We used at first a Thorlabs DET 410 photodetector electrically terminated with different RF shielded resistive loads  $R_L$  for probe exposition in the range ELF to VHF band (30 Hz-150 MHz). We experienced several critical problems with such device: the conversion slope was not constant vs frequency with upper limit at few MHz (dependent on  $R_L$ ), the battery charge state was critical for interferometric and  $V_\pi$  measurements (i.e. the voltage yielding the  $\lambda/2$  phase shift). In order to resolve these problems we used a

Newport amplified photodetector with a wider band (up to 1,5 GHz) and a conversion gain of 200 V/W, necessary to match the optical power budget used in this experimental phase, that is:

$$L_T = L_{MZ} + L_{FC} + L_S = 3 \text{ dB/cm} \times 7 \text{ cm} + 2 \times 3 + 2 \times 0,5 = 28 \text{ dB}$$

where  $L_T$  is the sum of losses due to Mach-Zehnder interferometer, the two Fiber Coupling and the two Solderings of optical fibers.

In the Figure 3 is shown electrical outputs of the probe exposed to Extremely Low Frequency (ELF) composed by the fields of power supply at 50 Hz and an additive electrical field supplied by an square wave at 200 Hz (on the left). The environmental 50 Hz field was measured with a standard probe (PMM mod.8053A) and it was 300 mV/m. A small exposition cell has been realized in order to generate stronger fields at higher frequencies and to mitigate the external noise. In this way we obtained cleaner interference figures as showed in Figure 3. Sensitivity was estimated in order of 100mV/m.

#### 4 Conclusions

The proposed EMF probe configuration is suitable for implementing low cost optical chips for Industrial, Medical, Scientific applications e.g. antenna radar systems for geophysical applications which have to reach tens of meters under the soil, spatial applications where integrated optical devices are suitable, and biomedical applications which requires non invasive sensors. As further development, the antenna probe must be integrated into the interferometer substrate in order to a) optimize the implementation process, b) minimize the electrical coupling with the field.

#### 5 References

- [1] Kanda M 1993 Standard probes for electromagnetic field measurements *IEEE Trans. Antennas and propag.* **41** 10 1349-64
- [2] Bentini G G, Bianconi M, Chiarini M, Corra L, Macagnani P, Tamarri F and Guzzi R 2002 Theory and design of an integrated optical sensor based on a Mach-Zehnder interferometer *Sensors and Microsystems Proceedings of 7th italian conference*, World Scientific 318-25
- [3] Wu T T and King R W P 1965 The cylindrical antenna with nonreflecting resistive loading *IEEE Trans. Antennas and propag.* **AP-13** 3 369-73
- [4] Shen L C and King R W P 1965 Corrections to The cylindrical antenna with nonreflecting resistive loading *IEEE Trans. Antennas and propag.* **AP-13** 6 998.

# Coated Fiber Bragg Grating As High Sensitivity Hydrophone

Salvatore D'Addio, Andrea Cusano, Antonello Cutolo

*Engineering Dept., University of Sannio, Corso Garibaldi 107 82100 Benevento  
Italy*

[a.cusano@unisanio.com](mailto:a.cusano@unisanio.com)

Stefania Campopiano

*Department for Technologies, University of Naples Parthenope, Napoli, Italy*

Michele Giordano

*Institute for Composite and Biomedical Materials, National Research Council  
Piazzale Vincenzo Tecchio, 80 - 80125 Napoli, Italy*

Mario Balbi, Sergio Balzarini

*Whitehead Alenia Sistemi Subacquei, via Monteruscello 75, Pozzuoli, Italy*

## Summary

In this work, a new fiber optic hydrophone based on the intensity modulation of the laser light in an FBG (Fiber Bragg Grating) under the influence of the sound pressure is presented. In order to increase the sensitivity, the FBG has been coated with a proper material. The minimum detectable acoustic pressure is found to be about 10Pa. In comparison with conventional fiber optic hydrophones based on bare FBGs, an increase of sensitivity of three order of magnitude is obtained. In addition, the developed FBG hydrophone detects an acoustic field in water with excellent performances: linear response and wide dynamic range. Thanks to the simplicity of its operating principle, geometry and interrogation scheme, this type of hydrophone can provide a practical alternative to the current state of the art in piezoelectric hydrophone technology.

## 1 Introduction

In the last years, fiber optic hydrophones have been attracting considerable interest due to their potential advantages, such as immunity to electromagnetic interference, remote sensing, stability in harsh environments, wide dynamic range. Several fiber optic sensing schemes have been reported, including interferometric techniques [1-3], polarimetric techniques [4-6] and fiber grating techniques [7-9]. While a conventional fiber optic hydrophone is composed by an ordinary optical fiber and relies on the phase shift of the laser light propagating through the sensing fiber under the influence of the sound pressure, the operating principle of a FBG-based hydrophone is typically based on the intensity modulation of the laser light due to the shift of transmission power spectrum curve of the sensing element under the influence of the acoustic field.

The important feature of the intensity-modulated FBG-based hydrophone is its simplicity. Since the detection is carried out by the measurement of light intensity, which is generally easier than that of a shift in wavelength or phase, the structure of an FBG-based hydrophone is expected to be more compact and simpler compared to a conventional optical fiber hydrophone. Unfortunately, the low sensitivity to acoustic pressure of this class of sensors will limit their use in underwater applications, where piezoelectric transducers are widely used despite their dimensions, complex signal processing and electronic front-end and difficult multiplexing. In this work, a novel fiber optic hydrophone that uses a fiber Bragg grating embedded in a material of low elastic modulus is presented.

For a given acoustic pressure, the basic effect of the FBG coating is to enhance the dynamic strain experienced by the sensor of a factor given by the ratio between the fiber and the coating elastic modulus.

## 2 Principle of operation

In this section, the interaction between a uniform Bragg grating of length  $L$ , written into the core of a standard single-mode fiber, and an incident acoustic wave is presented. For a spatial uniform sound pressure  $P(t)=p \cdot \sin(\omega_S t)$  around the FBG (where  $p$  and  $\omega_S$  are the amplitude and angular frequency of the sound pressure, respectively), the corresponding normalized Bragg wavelength shift  $\Delta\lambda_B/\lambda_B$  is given by ref. 9:

$$\frac{\Delta\lambda_B}{\lambda_B}(t) = \left[ -\frac{(1-2\nu)}{E} + \frac{n^2}{2} \frac{(1-2\nu)}{E} (2p_{12} + p_{11}) \right] P(t) \quad (1)$$

where  $n=1.465$ ,  $E=70\text{GPa}$ ,  $\nu=0.17$  and  $p_{11}=0.121$  and  $p_{12}=0.270$  are the effective refractive index of the guided mode, the Young's modulus, Poisson ratio and the elasto-optic coefficients of the optical fiber, respectively. Thus, the spectral response of the FBG moves without changing its shape at the same frequency of the applied acoustic pressure. For a GE-doped FBG at 1550 nm,  $\Delta\lambda_B/\Delta P$  was measured as  $-3 \times 10^{-3}$  nm/MPa over a pressure range of 70Mpa [10]. This means that with interrogation units able to perform wavelength shift measurements with a resolution of 0.1ppm in the investigated acoustic frequency range, an acoustic pressure limit of detection of tens of KPa can be obtained.

When the optical fiber is coated with plastic material, it exhibits some order of magnitude increase in its pressure sensitivity [11-12].

Indeed, according to the Hocker analysis [13], if the FBG is coated with a thick layer of polymer, the normalized wavelength pressure sensitivity is given by:

$$\frac{\Delta\lambda_B}{\lambda_B}(t) = \left[ -1 + \frac{n^2}{2} [p_{12} - \nu(p_{11} + p_{12})] \right] \frac{(1 - 2\nu_{coa})}{E_{coa}} P(t) \quad (2)$$

where  $E_{coa}$  and  $\nu_{coa}$  are the Young's modulus and the Poisson ratio of the coating, respectively.

Therefore, it can be seen from eq.(2) that for coatings with small Young's modulus compared with the fiber one, the wavelength pressure sensitivity of the FBG can be increased significantly. This means that by a proper choice of the coating elastic properties, shape and dimension, excellent pressure sensitivity gain is possible.

### 3 Experimental set-up

As mentioned in the previous section, the wavelength shift of the spectrum curve of the FBG is directly related to the incident sound pressure. Based on this line of argument, a low cost intensity based demodulation technique that relies on the use of a narrowband source and a broadband FBG is used. In the transmission mode and by working on the edge of the grating spectrum, the transmitted optical power  $P_t$  is directly related to the sound pressure according to the following expression:

$$P_t(t) = P_i \left[ T_0 + \frac{\partial T}{\partial \lambda_0} \frac{\partial \lambda_0}{\partial p} P(t) \right] \quad (3)$$

where  $P_i$  is the incident optical power,  $T_0$  is the transmission value at FWHM,  $\partial T/\partial \lambda_0$  and  $\partial \lambda_0/\partial p$  represent the edge slope of the grating spectral response and the wavelength sensitivity to the pressure, respectively. Yet, in order to achieve the maximum sensitivity and dynamic range, the laser wavelength should be set in correspondence of the full width at half maximum (FWHM), on either the longer or shorter wavelength side of the spectrum curve. It is seen from eq.(3) that the ac component of the transmitted light power is proportional to the sound pressure experienced by the FBG. Thus, the detection of the light with a photodiode provides an electrical output directly proportional to the acoustic field in the water. From the resulting temporal waveform, the amplitude, the frequency and the phase of the field can easily be measured after a proper calibration procedure.

The experimental set-up is shown in Figure 1. The acoustic field is generated by a PZT acoustic transducer, immersed in a water tank of 11m long, 5m large and 7m deep together with the reference PZT hydrophone and the hydrophone under test, at a distance of 1m and 2.2m from the PZT transducer, respectively. A computer-controlled scanning stage that allows independent translations in X, Y, and Z directions and rotations about the vertical axis is used to place the optical fiber hydrophone. The utilized fiber Bragg grating (characterized by a



central wavelength of 1547.62nm and a FWHM of 0.45nm) was embedded in a material, the Damival 13650 Gecalsthom, of spherical geometry of diameter of  $D=4.4$  cm exhibiting a lower value of elastic modulus than the fiber. The optical source was a stable narrowband wavelength tunable laser, its output wavelength is tuned to the center of the slope of the transmission spectrum curve of the FBG, at 1547.85nm, in order to achieve the better performance of the interrogation system. The power of light is selected at the value of 8mW. The wavelength stability was less than 1pm. The laser light intensity modulated by the FBG subjected to the sound pressure is detected by a photodiode. Two optical isolators, the first at the output of the laser, the latter at the input of the photoreceiver, are inserted in order to stabilize the sensor output signal. The resolution of the system was estimated to be slightly less than 1pm in the frequency range of interest. The outputs of the optical fiber and electric hydrophone were collected in a PC by an A/D acquisition board.

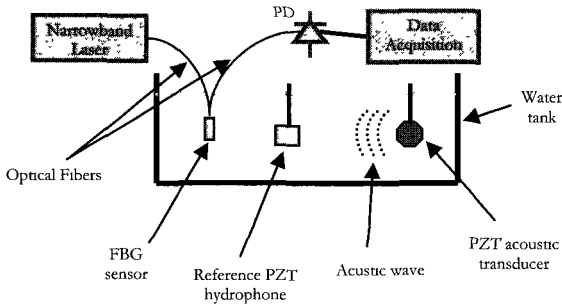


*Fig.1 Lateral view of the experimental set-up*

#### 4 Results and discussion

In this section, we report the results of measurements carried out to evaluate the performances of the new optical fiber hydrophone and to compare the obtained performances with a reference PZT hydrophone. In particular, in figure 2-left, a comparison between the typical temporal response of the sensor FBG under test and the reference hydrophone PZT to a sound pressure pulse at the frequency of 4.6KHz is shown. It can be seen that the FBG hydrophone operates as good as the piezoelectric technology. The phase difference between the two responses is due to the different distance from the acoustic source. Using the measured signal-to-noise ratio from the FFT of sensor response, the minimum detectable pressure level was estimated to be about 10Pa. In figure 2-right, the sensitivity curve of the FBG sensor as function of the the sound pressure frequency is plotted. It can be seen that the FBG hydrophone presents a decreasing response in the range from low frequencies up to about 16KHz. For

upper frequencies the signal to noise ratio approaches the unity around the value of  $-235\text{dB re V}/\mu\text{Pa}$ .

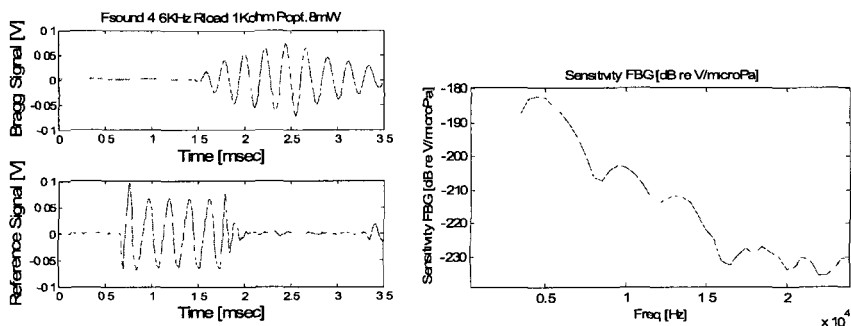


*Fig.2 Left: Typical temporal response of the sensor FBG under test (upper) and the reference hydrophone PZT (lower) to a sound pressure pulse of 2KPa at the frequency of 4.6KHz  
Right: the calculated sensitivity curve of the FBG hydrophone*

In conclusion, preliminary results demonstrate performances that could be really competitive with conventional and widely used piezoelectric based hydrophones for underwater applications.

## References

- [1] J. A. Bucaro et al., Appl. Opt., vol. 16, no. 7, pp. 1761, Jul. 1977.
- [2] P. C. Beard et al., Electron. Lett., vol. 33, no. 9, pp. 801, Apr. 1997.
- [3] C. Koch, Appl. Opt., vol. 38, no. 13, pp. 2812, May 1999.
- [4] R. P. De Paula et al., IEEE J. Quantum Electron., vol. 18, n. 4, pp. 680, 1982.
- [5] H. L.W. Chan et al., J. Appl. Phys., vol. 66, no. 4, pp. 1565, Aug. 1989.
- [6] NK. S. Chiang et al., J. Lightw. Technol., vol. 8, no. 8, pp. 1221, 1990.
- [7] E. Fisher et al., Applied Optics Vol. 37, No. 34, Dec. 1998
- [8] N. Takahashi et al., Ultrasonics 38, 581 (2000)
- [9] D.C. Betz et al., J.I of Smart Materials and Structures, vol.12, pp.122, (2003).
- [10] Xu M.G. et al., Electron. Lett. 29 398–9 (1993)
- [11] J. A. Bucaro et al., Applied Optics, Vol. 18, Issue 6, pp. 938-941 (1979)
- [12] G. B. Hocker, Applied Optics, Vol. 18, Issue 21, pp. 3679-3681 (1979)
- [13] Hocker G.B Appl. Opt. vol.18 pp.1445 (1979)

## Strain Measurements in Porous Silicon by Raman Scattering

M. A. FERRARA<sup>1,2</sup>, L. SIRLETO<sup>1</sup>, G. MESSINA<sup>2</sup>, M. G. DONATO<sup>2</sup>,  
L. ROTIROTI<sup>1</sup> AND I. RENDINA<sup>1</sup>

<sup>1</sup>*Istituto per la Microelettronica e Microsistemi – CNR  
Via P. Castellino 111 - 80131 Napoli*

<sup>2</sup>*DIMET - Università “Mediterranea” Reggio Calabria,  
[antonella.ferrara@na.imm.cnr.it](mailto:antonella.ferrara@na.imm.cnr.it)*

### Summary

Strains produce a modification of the vibration properties of materials, which can be observed by Raman scattering: a compressive stress results in an increase of the Raman frequency shift, while tensile stress results in a decrease. On this line of arguments, in this work, we investigate adsorption strains in porous silicon by Raman spectroscopy.

The adsorption of chemical species induces a compressive strain in the porous silicon due to the action of the molecular forces, as a consequence a reversible blue-shift of the Raman spectra of the sample has been observed.

### Introduction

Porous silicon (PS) is a material of great interest for the study of adsorption phenomena. The structure of PS may be spongelike, moreover, the high specific area and the great reactivity of the porous layer allow its use as a base for detection of vapors and liquids [1,2].

For sample of porous silicon, strain depends on various parameters, like the porosity of the porous silicon layer, the doping type and the level of the silicon substrate. Measurements of strain have been carried out with high resolution X-ray diffraction apparatus [3]. Due to the large internal surface, the strain is also very sensitive to oxidation, and the presence of the fluid or to impregnation of various substance. For example in Ref. [4] has been proved that when a p<sup>+</sup> type porous silicon layer is filled by a liquid, a small increase of strain is observed for pentane and ethanol. On the contrary, for vapour adsorption a small decrease of strain has been observed when capillary condensation occurs in the pores [5]. In both cases X-ray diffraction has been used in order to measure strains induced by vapour adsorption in porous silicon.

Raman scattering can be used to measure strain induced in substrate, in fact an increase of the Raman frequency shift is observed when a compressive stress is applied, while tensile stress results in a decrease [6].

In this paper, we study adsorption strains in porous silicon by using spontaneous Raman scattering. We prove that when the PS structure is exposed to saturated vapor of isopropanol or ethanol, a reversible blue shift of the Raman spectra is observed.

### Spontaneous Raman Emission

Porous silicon is composed of wires and/or dots of nonuniform dimensions. If the size of the particle reduce to the order of nm, the wave function of optical phonons will non longer be a plane wave. The localization of wave function leads a relaxation in the selection rule of wave vector conservation. Not only the phonons with zero wave vector  $q=0$ , but also those with  $q>0$  take part in the Raman scattering process, resulting in the red shift of the peak position and the broadening of the peak width. The line-shape asymmetry increases as the incident photon energy is increased [7-15].

A quantitative model, developed by Campbell and Fauchet, calculates that the peak position mainly depends on the number of atoms included in a cluster, while the width of spectra depends on the shape of crystallites [13,14]. If PS is modeled as an assembly of quantum wires, the phonon confinement is assumed to be two dimensional, while if the PS is modelled as an assembly of quantum dots, the confinement is three dimensional. The weight factor of the phonon wave function is chosen to be a Gaussian function as follows:

$$W(r, L) = \exp\left(-\frac{8\pi^2 r^2}{L^2}\right) \quad (1)$$

where  $L$  is the correlation length related with the size of dots. Square of Fourier transform is given by:

$$|C(q)|^2 = \exp\left(-\frac{q^2 L^2}{16\pi^2}\right) \quad (2)$$

The first-order Raman spectrum  $I(\omega)$  is thus given by:

$$I(\omega) \cong \int \exp\left(-\frac{q^2 L^2}{4}\right) \frac{d^3 q}{[\omega - \omega(q)]^2 + \left(\frac{\Gamma}{2}\right)^2} \quad (3)$$

where  $q$  is expressed in units of  $\frac{2\pi}{a}$  and  $a=0.54$  is the lattice constant of silicon,  $\Gamma$  is the natural line width for c-Si at room temperature ( $3.5 \text{ cm}^{-1}$ ) and  $\omega(q)$  is the dispersion relation for optical phonons in c-Si [12] which can be taken according to:

$$\omega(q) = \omega_0 - 120 \left( \frac{q}{q_0} \right)^2 \quad (4)$$

where  $\omega_0 = 520 \text{ cm}^{-1}$  and  $q_0 = 2\pi/a_0$ .

## Experimental Results

The PS sample used in this experiment is a porous silicon monolayer obtained by electro-chemical etching on  $p^+$  type ( $\rho=8\text{-}12\text{m}\Omega \text{ cm}$ ) standard silicon wafer. The total porous silicon sample thickness is 20 micron and the porosity is 70%.

The Raman scattering measurements were carried out, at room temperature, by using a Jobin Yvon Ramanor U-1000 double monochromator, equipped with a microscope Olympus BX40 for micro-Raman sampling and an electrically cooled Hamamatsu R943-02 photomultiplier for photon-counting detection. A Coherent Innova 70  $\text{Ar}^+$  laser, operating at 514.5 nm wavelength was utilized as excitation source. In order to prevent laser-annealing effects, the laser power was about 2 mW at the sample surface. Using a 50X objective having long focal distance, the laser beam was focused to a diameter of about 1  $\mu\text{m}$ . Its position on the sample surface could be monitored with a video camera. All components of the micro-Raman spectrometer were fixed on a vibration damped optical table.

The location of the Raman peaks and the shape of crystallites are obtained fitting the experimental results by a curve obtained with the model proposed by Campbell and Fauchet formulated in (3). We start our investigation measuring the normalised Raman spectra in unperturbed porous silicon monolayer. The results are shown in Fig. 1; the measured Raman peak is at about  $519.7 \text{ cm}^{-1}$ , corresponding to a red-shift of 15.7 THz with respect to the pump wavelength. We note that the observations are in excellent agreement with the value of the optical phonon frequency in porous silicon [12,15]. The estimated crystal size is of  $6.0\text{E-}7 \text{ cm}$ .

In Fig. 2 are shown the experimental Raman spectra in PS sample after exposure to isopropanol (a) and ethanol (b). Fitting the experimental results

with the model developed by Campbell and Fauchet [13,14], Raman peaks are obtained at about  $520,2 \text{ cm}^{-1}$  both for isopropanol and for ethanol. Therefore, we measure a shift of Raman spectra with respect to the unperturbed case of about  $0.5 \text{ cm}^{-1}$  both for isopropanol and for ethanol. These shifts are in agreement with the compressive strain obtained by Dolino *et al.* by X-rays diffraction [3]. We note that the Raman shift is reversible.

In both cases, the strain is compressive because an increase of the Raman frequency shift is observed.

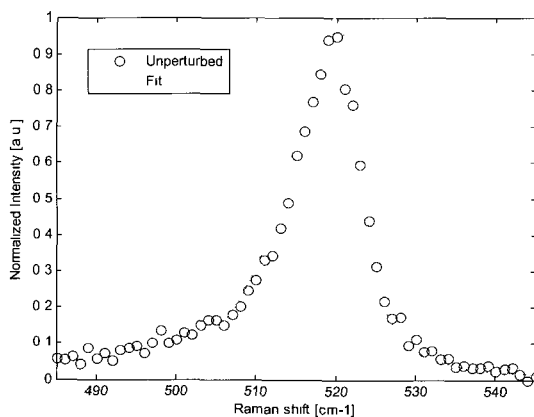


**Figure 1:** Unperturbed Raman spectra in porous silicon sample.

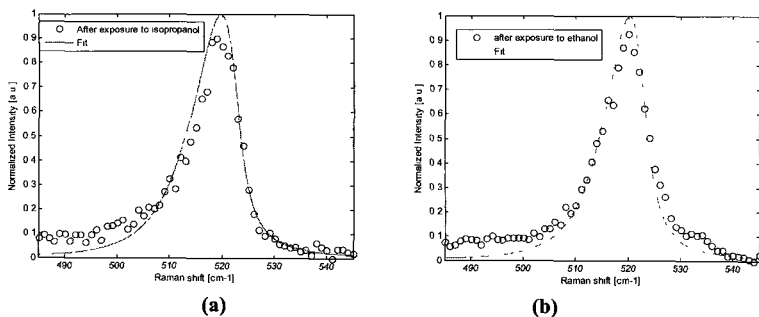


**Figure 2** Spontaneous Raman spectra in porous silicon sample after exposure to (a) isopropanol and (b) ethanol.

## Conclusions

In this paper, adsorption strains in porous silicon by Raman measurements has been investigated. The experimental results prove that when the porous

silicon structure is exposed to isopropanol or ethanol a reversible increase of the Raman frequency is observed.

### References

- [1] A. G. Cullins, L. T. Canham and P. D. J. Calcott, *J. Appl. Phys.* **82**, 909-965, 1997.
- [2] W. Thei B., *Surf. Sci. Report* **29**, 91-192, 1997
- [3] D. Bellet, G. Dolino, *Thin Solid Films* 276, 1-6 (1995)
- [4] D. Bellet, G. Dolino, *Phys. Rev. B* **50**, 17162-5 (1994)
- [5] G. Dolino, D. Bellet, C. Faivre, *Phys. Rev. B* **54**, 17919-30(1996)
- [6] I. De Wolf, *Spectroscopy Europe* 15/2 (2003)
- [7] J. M. Perez., J. Villalobos, P. McNeilll, J. Prasad, R. Cheek and J. Kelber, J.P. Estrera, P.D. Stevens and R. Glosser, *Appl. Physics Lett.* **61** (5), 563-565, 1992.
- [8] G. Mariotto, F. Ziglio, F. L. Freie Jr., *Journal of non cristalline solids* 192 - 193, 253-257, 1995.
- [9] Z. Sui., P. P. Leong, and I. P. Herman, *Appl. Physics Lett.* **60** (17), 2086-2088, 1992.
- [10] S. L. Zhang, Y. Hou and K. S. Ho, B. Qian and S. Cail, *J. Appl. Phys.* **72** (9), 4469-4471, 1992.
- [11] J. D. Moreno, F. Agullo-Rueda, E. Montoya, M. L. Marcos and J. Gonzales-Velasco, R. Guerrero-Lemus and J. Martinez-Duart, *Appl. Phys. Lett.* **71** (13), 2166-2168, 1997.
- [12] F. Kozlowski, W. Lang, *Appl. Phys. Lett.* 5401-5408, 1992.
- [13] H. Ritcher, Z. P. Wang and L. Ley, *Solid State Communications* **39**, 625-629, 1981.
- [14] I. H. Campbell and P. M. Fauchet, *Solid State Communications* **58**, 739-741, 1986.
- [15] R. Tsu, H. Shen and M. Dutta, *Appl. Physics Lett.* **60** (1), 112-114, 1992.

# Fiber Bragg Gratings and Magnetic Shape Memory alloys: a Novel High Sensitivity Magnetic Sensor

C. Ambrosino, P. Capoluongo, D. Davino, C. Visone, A. Cutolo, A. Cusano  
*Eng. Dep. of the Univ. of Sannio, Benevento ITALY*

S. Campopiano

*Dept. for Techn. of the Univ. of Naples Parthenope Naples ITALY*  
stefania.campopiano@unisannio.it

M. Giordano

*Inst. for Composite and Biomedical Materials, Nat. Res. Council, Naples ITALY*

## Summary

In this work a novel magnetic field sensor based on Fiber Bragg Gratings (FBG) is demonstrated. Up to now, FBGs based magnetic sensors have been proposed by using Terfenol, metallic alloy as transducer. Here, a different configuration is proposed employing a new class of magnetic active materials, Magnetic Shape Memory alloys (MSMs) with a very giant magnetostriction coefficient. A FBG has been bonded on a MSM sample and sensor characterization has been carried out. Experimental results and comparison with Terfenol based FBG sensor performances are reported, showing, for MSM, a sensitivity  $(\Delta\lambda_B/\lambda_B)/(\Delta H/H_m)$  of  $1.81 \cdot 10^{-4}$ , where  $\lambda_B$  is the Bragg wavelength and  $H_m$  the mean magnetic field in the considered range.

## 1 Introduction

In last years a great number of applications of magnetic sensors, spreading from electrical power industry to control engineering and robotics have gained great interest [1-3]. For all these applications optical current sensors are a winning choice, due to their many advantages compared to conventional iron-core current transformers, including their immunity to electromagnetic interference, high dynamic range, easily integration within structures and competitive costs [4]. In particular, among optics devices, FBGs exhibit good features in terms of sensitivity, resolution and bandwidth [5]. In general, the common FOSs used to detect magnetic field are based on the Faraday effect, but due to the low value of the Verdet coefficient, they showed very low sensitivity. In order to overcome this drawback, FBGs based sensors exploit different transducers. Recently, FBG based magnetic field and current sensors have been demonstrated [6,7], exploiting Terfenol-D magnetostrictive rod as elasto-magnetic transducer. Unfortunately, Terfenol-D works for low magnetic field achieving a non linear range of response already around few tens of kA/m and a maximum strain of 0.24% [8]. Along this line of argument, here, a novel FBG based sensor is proposed employing a new class of magnetic active material, Magnetic Shape Memory alloys (MSMAs) [9-12]. This material presents a

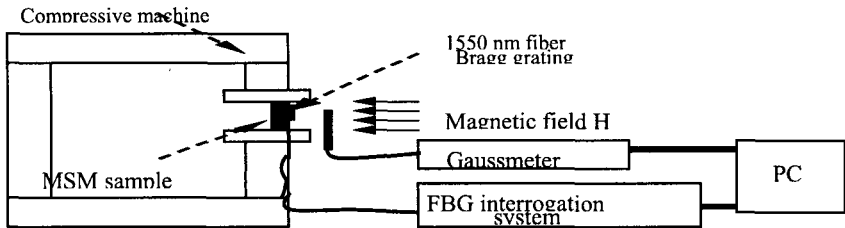


magnetostriction coefficient that is almost two order of magnitude higher than Terfenol one (up to 10%) [9] and so it can reach a very high sensitivity. The sensor is formed by a FBG bonded on the MSMA stick. When the active material is subjected to magnetic field there is a redistribution of its internal martensitic twin variants, resulting in the change of the element shape. This change in the active material produces strain that is transferred to the bonded FBG, which in turn changes its resonance wavelength. The FBG interrogation system used for this sensor relies on a low cost ratiometric technique based on the use of a broadband light source and an in fiber grating optical filter, able to convert wavelength shifts in amplitude modulation [13,14]. In the following, experimental results of magnetic fields detection in the range of 0-200 kA/m are reported.

## 2 Experimental set-up

All reported tests have been performed on a sample of  $3 \times 5 \times 20 \text{ mm}^3$  stick of MSMA in martensitic state. The elasto-magnetic characteristics of such types of materials are reported in [9] with a threshold field value around 250 kA/m and a saturation value of 500 kA/m. After a suitable bonding protocol choice, a FBG has been bonded with cyanoacrilate glue oriented along the principal axis of the transducer. In addition, in order to obtain the reversibility of the magnetic -field-induced strain, the material was pre-stressed by springs or in other way [9-11].

*Fig. 1. A schematic diagram of the set up*



In this case, the sample was placed in a tension-compression testing system (Lloyd Instruments LRXPlus 5kN) between two aluminium rods. The compressive stress was applied along the [100] crystallographic direction while the magnetic field was successively applied perpendicular to the stress using a custom electromagnet opportunely fed. With this actual configuration, however, a maximum magnetic field approaching the threshold value can be obtained. So the performances retrieved are referred to the worst case. Improved performances would be available if higher magnetic fields are involved in. Magnetization was measured in the direction of the applied magnetic field using a Hall effect based gauss-meter (Lakeshore 475 DSP), while the strain induced on the fiber optic sensor was measured by using the technique based on the

optical filtering combined with broadband interrogation described in [13,14]. In particular, the optoelectronic setup used for the proposed magnetic sensor relies on the interrogation optic sensor system described in [13,14], with an optic filter with a nominal linearity range of 10nm (centered at 1550nm), a super luminescent diode with 40nm FWHM bandwidth (at 1550nm) and a FBG with a central wavelength,  $\lambda_B$ , free at 1548 nm and a 0.736 nm FWHM bandwidth. Previously, a proper calibration procedure has been carried out, in order to obtain the FBG response expressed directly in terms of wavelength shift. The schematic diagram of the whole set up described above is represented in Figure 1.

### 3 Results and discussion

#### 3.1 Magnetic field sensor and sensitivity

In order to characterize the sensing system, several tests have been performed. The magneto-elastic active material's response also depends on the compressive stress applied to it. Infact, the higher is the level of pre-stress and the lower is the occurred strain. So several tests with different pre-stress levels have been performed. For each one, a sinusoidal magnetic field with amplitude around the threshold value for MSM sample has been applied to the structure in order to explore the range [0-300] kA/m.

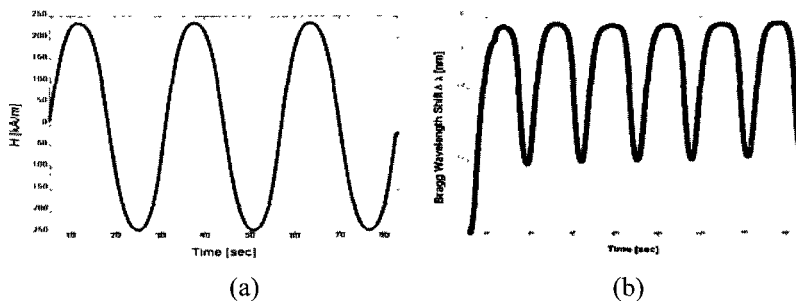


*Fig. 2. (a) Gaussmeter signal (b) Fiber Bragg wavelength shift*

Related Gauss-meter and FBG responses have been acquired using a data acquisition (DAQ) system. Here, results for a 15N of pre-stress for which the best results have been obtained limited by the limited magnetic field range used, are showed.

In Figure 2 are reported the time history of the gaussmeter and the FBG response expressed directly as wavelength shift. It is worth to note from FBG response that the MSM sample acts always in a tensile stress state. Even though, before magnetic field applications, the FBG was initially in a compressive state (due to

the 15 N pre-stress) this state has been chosen as baseline. Indeed, the curve in Figure 2 (b) starts from the point  $\Delta\lambda_B = 0$  and the first path represents the first magnetization curve for the material.

In Figure 3. the sensor characteristics has been reported. From the figure, it can be noticed that the sensor response results linear almost up to 100 kA/m and a sensitivity  $(\Delta\lambda_B/\lambda_B)/(\Delta H/H_m)$  of  $1.81 \cdot 10^{-4}$  for applied fields smaller than 100 kA/m has been estimated. Here,  $H_m$  is the mean magnetic field in the considered range. The minimum detectable value for  $\Delta H/H_m$ , under these conditions, is  $3.56 \cdot 10^{-2}$ .

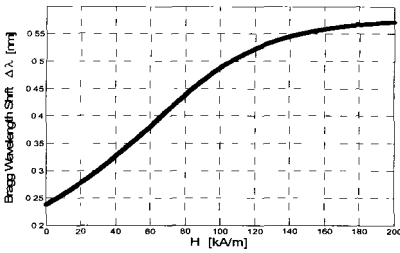


Fig.3. Magnetic sensor characteristic

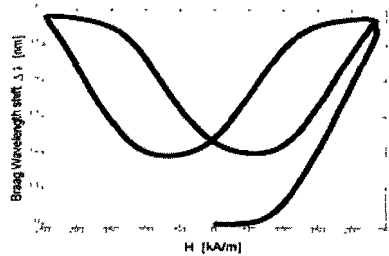


Fig. 4. System strain field characteristic

### 3.2 System characterization

Furthermore, the same setup has been used for the whole system characterization. In Figure 4, the system strain-field characteristic is shown.

The curve starts from the point  $\Delta\lambda_B = 0$ ,  $H=0$  and the first path represents the first magnetization curve for the material, then follows the typical butterfly closed-loop shape of a hysteretic material. It is worth noting that the first path is outside of the closed-loop because the latter is a minor-loop of the limit-cycle.

### 4 Comparison with Terfenol-based sensor

Using the same interrogation sensor system exploited for MSM characterization, tests have been also carried out in the case of Terfenol D rods. Also Terfenol needs a pre-stress and in this case, a maximum magnetic field of approximately 12 kA/m was applied. In fact Terfenol works correctly for lower magnetic field than MSM achieving a saturating response for few tens of kA/m. Several tests have been performed with different level of pre-stress even if the maximum strain was obtained and showed for a level of pre-stress of 43N. A sensitivity  $(\Delta\lambda_B/\lambda_B)/(\Delta H/H_m)$  of  $5.1 \cdot 10^{-5}$  has been estimated. The results are in agreement with data previously reported in literature [8]. Comparing the obtained characteristics and relative sensitivities of MSM and Terfenol based sensors, it's worth to note that similar sensitivity can be achieved by using MSMA magnetic materials but with a significantly extended dynamic range. Moreover it can be seen that forcing higher magnetic fields, a great improvement

in the magnetostriction coefficient and thus in the sensor sensitivity can be achieved.

## 5 Conclusion

The exploitation of a FBG magnetic field sensor has been demonstrated. The FBG has been bonded to a pre-stressed MSM sample. The interrogation optoelectronic system used for the proposed magnetic sensor relies on a low cost ratiometric technique based on optical filtering combined with broadband interrogation. With this set up, a sensitivity  $(\Delta\lambda_B/\lambda_B)/(\Delta H/H_m)$  of approx.  $2 \cdot 10^{-4}$  has been achieved even if MSM material has not been exploited up its real possibilities. Comparing results obtained using also Terfenol D, it appears that despite working in the worst case for MSM with magnetic field values lower than 300 kA/m, MSM and Terfenol have similar performances. But increasing magnetic field values the situation change overworking for MSM a magnetostriction coefficient two order of magnitude higher than Terfenol one. Therefore, in order to further increase the MSM sensitivity and exploit all the linear range, a development of magnetic set up with magnetic field up to 500kA/m has been planned.

## References

- [1] J. E. Lenz, Proc. of the IEEE, Vol 78, No 6, p. 973 - 989, 1990.
- [2] T. Bosselmann, Proc. SPIE Vol. 5855 pp 188-193, 2005
- [3] K. Bohnert et al. Proc. of SPIE Vol. 5855 pp 210-213, 2205
- [4] T. Wang, et al., IEEE Trans. on Instr. and Meas., vol. 50, no. 3, 2001.
- [5] B. Culshaw and J. Dakin, Artech House inc., Norwood, 1997.
- [6] J. Mora et al. IEEE Phot. Techn. Letters, Vol. 12, No. 12, pp. 1680 - 1682, 2000.
- [7] D. Satpathi et al. IEEE Sens. Journ., Vol. 5, No. 5 Oct. 2005 pp. 1057-1065
- [8] M.Pasquale, Sens. and Act., 2003 pp 142-148
- [9] J. Tellinen et al., 8th Intern. Conf. ACTUATOR'02, Bremen, Germany, 2002.
- [10] O. Heczko, Journ. of Magnetism and Magnetic Materials (2005) 787-794
- [11] A. A. Likhachev et al. Mat. Science and Eng. 378 (2004) 513-518
- [12] O. Heczko, L. Straka, Materials Science. and Eng. A 378 (2004) 394-398
- [13] A.Cusano et al. Sensors and Actuators, 110 (1-3) 276-281, 2003
- [14] A. Cusano et al. Optical Engineering, (accepted)

# A COMPUTATIONALLY EFFICIENT MODEL FOR THERMAL SENSORS SIMULATION<sup>1</sup>

F. MANCARELLA, A. RONCAGLIA, M. PASSINI,  
G. C. CARDINALI, M. SEVERI

*IMM Bologna, CNR, Via Gobetti 101  
Bologna, I-40129, Italy*

Thermal sensors based on silicon micromachining have many applications in the MEMS field. In order to design such devices for an optimized performance a flexible simulation model is needed. We propose here a computationally efficient modeling technique for computer aided design of micro thermal sensors.

## 1. Introduction

Realizing thermal microsystems, such as micro hotplates, bolometers, thermopiles and so on, typically requires several design and fabrication cycles until the specifications are fulfilled. An accurate thermal model, that permits to estimate the temperature distribution on the structures, could appreciably reduce the fabrication and test time, and, consequently, the overall realization cost. On the other hand, thermal simulations of complex three-dimensional devices are usually very time-consuming. However, for devices realized on thin membranes, it is possible to introduce proper approximations that permit to treat the problem by a two-dimensional PDE model.

In the following, this modeling approach is described and validated on measurements performed on polysilicon-based thermopiles, realized on a thin dielectric suspended membranes.

## 2. PDE model

For thin-film microstructures, like those presented in this work, the ratio of lateral extent to thickness exceeds unity by at least one order of magnitude. Hence, temperature gradients perpendicular to the membrane plane can be neglected resulting in a two-dimensional thermal model.

The two-dimensional thermal model adopted is the following:

$$\frac{\partial^2(T - T_e)}{\partial x^2} + \frac{\partial^2(T - T_e)}{\partial y^2} - \frac{h}{\lambda d}(T - T_e) - 4\sigma T^3(\epsilon_u + \epsilon_l)(T - T_e) + \frac{1}{\lambda d}P_0 = 0 \quad (1)$$

---

<sup>1</sup> This work is supported by Netgas project- EC V framework program, proposal IST-2001-37802

where  $T(x,y)$  is the unknown temperature distribution on the device,  $T_e$  the room temperature,  $h$  the heat transfer coefficient through air,  $\epsilon_u$  and  $\epsilon_l$  the emissivities of the upper and lower faces of the device respectively,  $\sigma$  the Stephan-Boltzmann constant,  $P_0$  the heating power surface density,  $d$  the thickness of the membrane and  $\lambda$  its average thermal conductivity calculated as:

$$\lambda = \sum_s \frac{\lambda_s t_s}{d}$$

being  $\lambda_s$  the thermal conductivity of the  $s$ -th membrane component layer and  $t_s$  its thickness.

### 3. Finite element simulations and results

For simplified geometries, Eq. (1) can be analytically solved, however for the cases in which the analytical method fails due to more complicated geometries, like for instance the device reported in Figure. 1, a finite element (FEM) simulation is needed. To this purpose, the simple model expressed by Eq. (1) has been implemented in a commercial FEM simulator (FemLab [1]).

In order to validate the 2-d model, the simulated results have been compared with the electrical measurements performed on infrared detectors, realized by a CMOS-compatible technology [2]. In these devices,

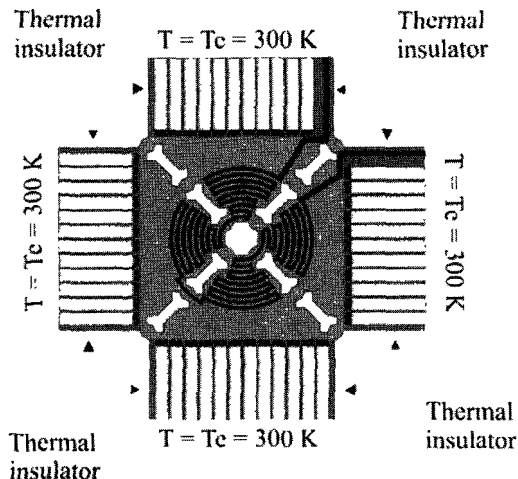


Figure 0. Thermopile layout for Finite Element Simulation

thermocouples fabricated with heavily doped polysilicon and aluminum thin films are employed, disposed on a dielectric suspended membrane for thermal isolation from the substrate. The device response has been measured at the wafer-level by emulating the incoming infrared radiation with a polysilicon heater placed on the membrane center.

The thermal PDE problem expressed by Eq. 1 has been solved together with a model of the electrical field and current (Laplace equation with ohmic electrical transport). In doing this, the two differential equations turn out to be coupled by means of the polysilicon resistivity temperature dependence  $\rho(T)$ , and by the heat source  $P_0$  generated on the polysilicon heater by Joule effect, expressed as

$$P_0 = \frac{\|\nabla V\|^2}{d\rho_0(1 + \beta(T - T_e))}$$

where  $\nabla V$  is the electrical potential gradient in the heater structure,  $\beta$  the temperature coefficient of the polysilicon resistance (TCR),  $\rho_0$  the resistivity at the room temperature  $T_e$  and  $d$  the membrane thickness .

As far as the model boundary conditions are concerned, it has been assumed that the cold junctions of the thermocouples are at the same constant temperature of the silicon bulk  $T_e$ . The effect of the air surrounding the 2-d boundary of the thermopile has been neglected. This assumption is reasonable, since air thermal conductivity is at least one order of magnitude lower with respect to that of the other materials. Therefore, the device boundary is supposed to be thermally isolated where in contact with air.

Table 1. Thermal, electrical and geometrical parameters used in the FEM simulations.

<b>THERMAL CONDUCTIVITIES <math>\lambda</math> (W/mK)</b>			
ALUMINUM	MEMBRANE	N-POLY	P-POLY
150	1,61	27	13
<b>THERMOPOWERS <math>\alpha</math> (<math>\mu</math>V/K)</b>			
N-POLYSILICON		-205	
P-POLYSILICON		239	
<b>THICKNESSES</b>			
N-POLY		160 nm	
P-POLY		320 nm	
THIN ALUMINUM		50 nm	
THICK ALUMINUM		1100 nm	
MEMBRANE		2500 nm	
<b>SHEET RESISTANCES (<math>\Omega</math>/sq)</b>			
N-POLY		120	
P-POLY		200	

The electrical, thermal and geometrical parameters used in the simulations are reported in Table 1. All have been measured using specific test structures on

the samples employed in the experiments, except the convective coefficient  $h$ , treated as a fitting parameter.

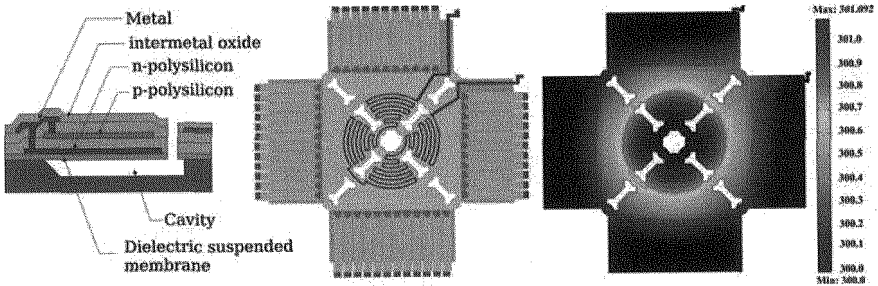


Figure 2. Double-polysilicon thermopile: thermocouple cross-section (left), thermopile layout (center) and estimated temperature distribution (right).

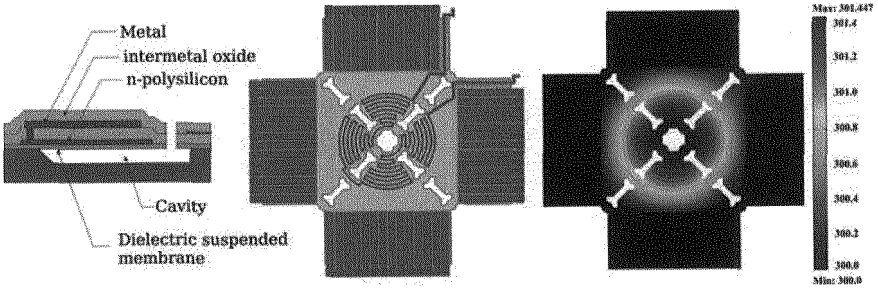


Figure 3. Al/n-poly thermopile: thermocouple cross-section (left), thermopile layout (center) and estimated temperature distribution (right).

The value of  $h$  was estimated by matching simulation and measurement results on a double-polysilicon thermopile, chosen as a reference device (see Figure 2). Subsequently, the extracted  $h$  value has been used to simulate other devices with different kind of thermoelements (Figure 3 in example), but having the same membrane geometry and, consequently, the same features concerning heat exchange through air.

In these simulations, the radiative heat loss has been linearized, since the peak temperature difference typically reached on the membrane center during both the test and the normal operation of the devices is a few hundreds mK above the room temperature. It is rather clear that this approximation is not correct if a high temperature device (such as a hotplate) has to be simulated.

In Figures 2, 3 the simulated thermopile layouts and the temperature distribution obtained on the membrane using the proposed model may be observed. The best match between the measured and simulated results for the device in Figure 2 has been obtained for a value the convective coefficient  $h$  equal to  $325 \text{ W/m}^2\text{K}$ . By using this value, we also calculated the temperature



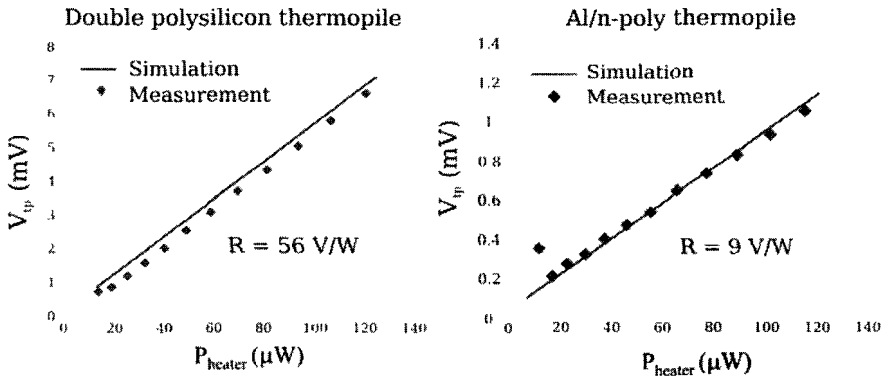


Figure 4. Comparison between measured and simulated responsivity for a double polysilicon (left) and Al/poly (right) thermopile.

distribution and the responsivity of an Al/polysilicon thermopile (Figure 3). The comparison of simulation and measurements for the latter case yielded the result reported in Figure 4 (right side), in which the good agreement observed seems to confirm the appropriateness of both the model and the parameters employed.

#### 4. Conclusions

A simulation model useful for designing thermal microsensors based on thin membranes has been proposed and validated with measurements performed on micromachined IR detectors. A good agreement between measurements and simulations has been achieved on different device types using a unique value of the fit parameter employed to describe the heat exchange through air.

#### References

1. <http://www.femlab.com>
2. A. Roncaglia, F. Mancarella, G. C. Cardinali, F. Tamarri, M. Severi, *Euroensors XIX Proceedings*, Barcelona, Spain, Sept. 11-14, p. MC13, (2005).

# Characterization of a Point-Wise Close Electric Field Sampling System exploiting the Electro-Optic Effect

Lucio Rossi, G. Breglio, A. Irace, P. Spirito

*Dept. of Electronic Engineering and Telecommunications, University "Federico II", Napoli, Italy*

[l.rossi@unina.it](mailto:l.rossi@unina.it)

## Summary

The linear (Pockels) electro-optic effect that many bi-refracting crystals show can be exploited to realize sensing devices that investigate the intensity and shape of the electric field close to integrated circuits and devices. Non-invasiveness, wide bandwidth, linearity and small spatial resolution are the main features that a sensor based on such a principle can achieve. In this work we aim to give a first characterization of a step-by-step electro-optical probe which measures the variation of light polarization induced by a lithium niobate crystal (realized by SELEX S.I.) immersed in the electric field provided by a high frequency Integrated Circuit.

## 1 Introduction

The modern design of RF and Microwave devices is constantly driven by the pushing need of smaller dimensions, light weight and reduced power consumption, but with the shrinking dimensions the devices testing becomes an issue as the design feedback itself. To overcome these difficulties and considering that modern day automatic network analyzers are, if not bandwidth limited, at least lacking flexibility since measurement is restricted to some particular ports only, a near electric field point-wise measurement system with peculiar features of non-invasiveness and wide bandwidth is proposed.

This system is based on the Electro-Optic effect which, being caused by a distortion in the electrons motion inside the atoms or molecules of a substance, is very fast and can be used for sensing purposes in the GHz bandwidth. Another advantage beyond doubt is the non-invasiveness of the system due to the fact that the crystals (or the polymers) used have a low permittivity and interfere as little as possible with the field to be measured.

## 2 Theory behind the instrument: The Electro-Optic Effect

Some anisotropic crystals which are lacking a centre of symmetry exhibit the linear electro-optic effect which can be explained as a modification either in the form or the orientation of the optic indicatrix when an electric field is applied

across them. When this happens, some additional terms appear in the index ellipsoid equation:

$$\left(\frac{1}{n^2}\right)_1 x^2 + \left(\frac{1}{n^2}\right)_2 y^2 + \left(\frac{1}{n^2}\right)_3 z^2 + 2\left(\frac{1}{n^2}\right)_4 yz + 2\left(\frac{1}{n^2}\right)_5 xz + 2\left(\frac{1}{n^2}\right)_6 xy = 1 \quad (2.1)$$

The Pockels (linear) electro-optic effect modifies the value of the coefficients in the above equation. An electro-optic tensor  $\underline{r}$  (6x3) can be introduced to relate each one of the coefficients with the applied electric field:

$$\Delta_i = \sum_{j=1}^3 r_{ij} E_j \quad \Delta_i = \Delta \left( \frac{1}{n^2} \right)_i \quad i \in (1, \dots, 6) \quad (2.2)$$

Consider for example the LiNbO<sub>3</sub> crystal in the conventional reference system. The values of the non-zero elements in the electro-optic tensor are given in Table 2.1

	LF (pm/V)	HF (pm/V)
r <sub>33</sub>	32	30.8
r <sub>13</sub>	10	8.6
r <sub>22</sub>	6.8	3.4
r <sub>42</sub>		28

Table 2.1 Electro-optic coefficients for the LiNbO<sub>3</sub> crystal. LF and HF stand for low and high frequency respectively

If we have a reference system in which x is orthogonal to m and apply the electric field along the y axis the index ellipsoid changes as follows:

$$x^2 \left( \frac{1}{n_o^2} - r_{22} E_y \right) + y^2 \left( \frac{1}{n_o^2} + r_{22} E_y \right) + \frac{z^2}{n_e^2} + 2yz \cdot r_{42} E_y = 1 \quad (2.3)$$

This is the so-called transverse configuration which can be exploited for modulation and with some additional element for sensing purposes.

To understand how this is possible, consider the light propagating along the z direction, the indexes of refractions of the two allowed polarizations after developing in series up to the linear term are:

$$n_x = \left( \frac{1}{n_o^2} - r_{22} E_y \right)^{\frac{1}{2}} \approx n_o + \frac{1}{2} n_o^3 r_{22} E_y$$

$$n_y = \left( \frac{1}{n_o^2} + r_{22} E_y \right)^{\frac{1}{2}} \approx n_o - \frac{1}{2} n_o^3 r_{22} E_y$$
(2.4)

This means that the two polarizations of a wave propagating along the z axis undergo the following total phase difference:

$$\Delta\phi_{TOT} = \pi \frac{V}{V_\pi} \quad V_\pi = \frac{\lambda d}{2Ln_o^3 r_{22}}$$
(2.5)

Inserting two polarizing plates one before and the other after the crystal and 90° rotated with respect to the other, the light intensity at the output is the one showed in Figure 2.1

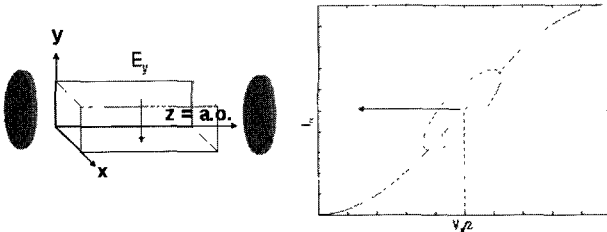


Figure 2.1 Modulation with the electro-optic effect

For sensing purposes this characteristic has to be moved left in order to obtain to have the linear region around the 0 V point. This can be performed using a couple of retarding plates as showed in the next section.

### 3 The Optical Chain

The Optical chain is showed in Figure 3.1. An 835 nm pulsed laser goes through a polarizing beam splitter to obtain a linear polarization and probe the input power. Thanks to two retarding plates we gain two degrees of freedom to adapt

the polarization of the light to the crystal features in order to obtain maximum linearity and signal swing from the electro-optic effect.

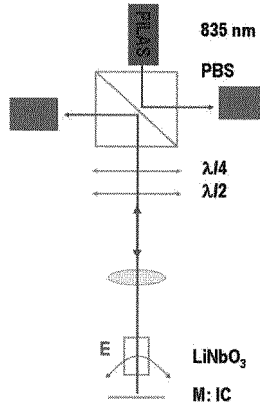
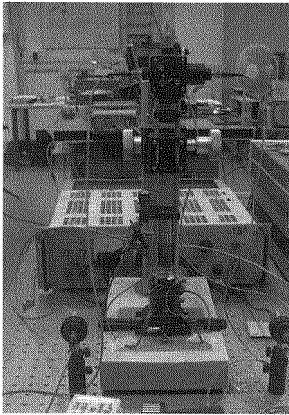


Figure 3.1 The optical chain

The beam then crosses the electro-optic crystal and is focused on top of the DUT where is reflected back in the optical chain. The light finally reaches the beam splitter again, where the component reflected by 90° is probed by a second photodiode PD2.

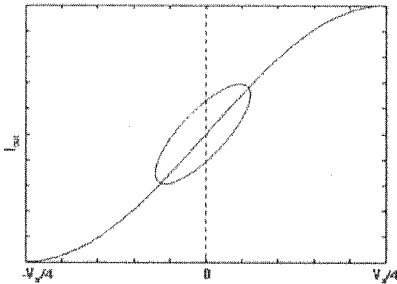


Figure 3.2 Input/Output characteristic of the optical chain

The effect of inserting the two retarding plates can be calculated using the Jones formalism and is showed in Figure 3.2.

As it is possible to notice from Figure 3.2 not only the Input/Output characteristic is now centered around the 0 V point, but the periodicity is also reduced by a factor two which results in a steeper slope in the linear range so that a better sensitivity is achieved.

## 4 Measurements

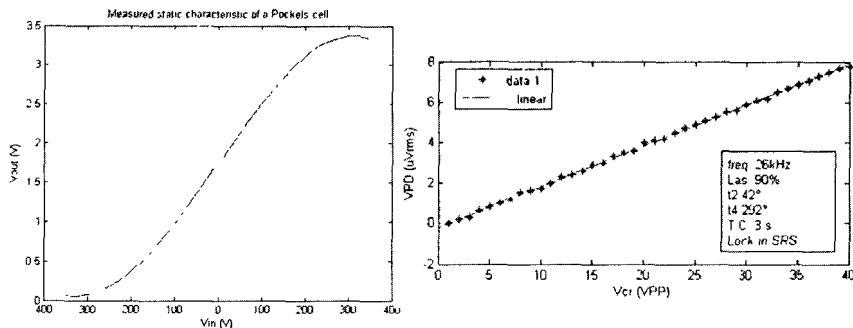


Figure 4.1 Measured I/O characteristic with a Q-switching Pockels cell and small signal characteristic of x-cut 2x2x1 mm crystals

The first lithium niobate crystal that was used inside the optical chain was a Pockels cell meant for laser Q-switching (C1041 Dorotek) with considerable dimensions. The static characteristic has been measured in this case and it is showed in figure 4.1. A  $V\pi$  of around 1.2 kV was measured and it is in good agreement with the theory. The  $V\pi$  periodicity is also in agreement with the fact that light crosses the LiNbO<sub>3</sub> crystal two times.

Some other smaller (2x2x1 mm) crystals have (realized by Selex S.I.) have been characterized in this system. They were x-cut and their “small signal” behavior in the range of 0-40 V<sub>PP</sub> applied to the crystal at a frequency of 26 kHz was measured. In order to retrieve the noisy signal a Lock-in amplifier (Stanford Research SR844) tuned at the frequency of the laser pulses was used. The results of these measurements are showed in Fig. 4.1.

## REFERENCES

- [1]. R. Hofmann, H.-J. Pfeleiderer "Electro-optic Sampling System for the Testing of High-speed Integrated Circuits Using a Free Running Solid-state Laser" JOURNAL OF LIGHTWAVE TECHNOLOGY, VOL. 14, NO. 8, 1788-1793 (AUGUST 1996)
- [2]. J. Allam, C. L. Yuca and J. R. A. Cleaver "Quantitative electro-optic sampling for high-speed characterization of passive and active devices" 0-7803-5298-X/99 IEEE (1999)
- [3]. K. S. Giboney, S. T. Allen, M. J. Rodwell, J. E. Bowers "Picosecond Measurements by Free Running Electro-Optic Sampling" IEEE Photonics Technology Letters Vol. 6, No. 11, (Nov. 1994)
- [4]. G. R. Lin, Y. Chang "A Novel Electro-Optic Sampling system by Using Delay-Time Tunable Pulsed Laser Sources" 0-7803-5947-X/00/\$10.00©2000 IEEE
- [5]. R A Dudley, A G Roddie, D J Bannister "ELECTRO-OPTIC PROBING OF MICROWAVE CIRCUITS" TH3A-2

# On The Realization Of Chromium Silicide Stress Sensor

D. Caputo, G. de Cesare, A. Nascetti, R. Scipinotti

*Department of Electronic Engineering, University of Rome "La Sapienza",  
via Eudossiana, 18 00184 Rome (Italy)*

## Summary

In this paper, a very thin and high conductivity chromium silicide film, formed on a n-type amorphous silicon layer, is utilized as active material in a stress sensor. The sensor can be deposited directly on the stressed materials without additional packaging, avoiding the use of the adhesive resin which usually affects the device performances.

Details of fabrication and characterization of sensors grown on different kind of substrates (glass, metal, ceramic and plastic) suitable for mechanical stress and pressure measurement are reported.

## 1 Introduction

Mechanical stress is an important physical parameter in various areas of application, such as industrial automation, mechanics, automotive and medical engineering [1][2]. In particular, strain gauges are used in a number of advanced applications such as non destructive manipulation of the objects with robotic hands [3].

The common approach to stress measurement is essentially based on the use of piezoresistors realized in different technologies. This approach has different limitations: large area, small sensitivity and high temperature drift. On the other hand the use of silicon thin film technology at low deposition temperature (<150 °C) using novel substrates, like plastic, has recently received great attention due the new large area applications.

Here, we present a thin film stress sensor where the active material is a very thin and high conductivity chromium silicide film formed on a n-type amorphous silicon layer. An important advantage of our device with respect to the existing approaches is due to the low temperature fabrication process, which can be lower than 100°C for all the technological steps. Furthermore, the sensor element can be deposited directly on the stressed materials without additional packaging, avoiding the use of the adhesive resin which usually affects the device performances. The presented sensor has been used in two different applications: to measure a force applied on glass or metal substrates and a vacuum pressure induced on ceramic or plastic membranes.

## 2 Device fabrication and operation

Figure 1 shows the structure of the sensor element.

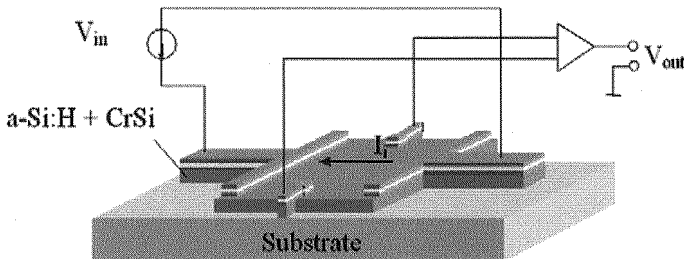


Fig. 1: Structure of the stress sensor

The first step of the sensor fabrication process is the deposition of a 500 nm n-type amorphous silicon film by PECVD in a high vacuum deposition system, with the following recipe: gas flow of pure silane 40 sccm; silane diluted phosphine 10 sccm; pressure 300 mTorr; power density 40 mW/cm<sup>2</sup>; deposition temperature 100 °C.

A three-layer chromium-aluminum-chromium (15/300/15 nm) is then vacuum evaporated and patterned by photolithographic process and chemical etching, in order to form the metal contacts. At the interface between amorphous silicon and chromium, a chromium silicide (CrSi) layer is formed.

The CrSi acts as active layer by shunting the resistance of the amorphous layer in the sensor structure. In fact its electrical conductivity is about two orders of magnitude higher than the n-doped a-Si layer ( $2.5 \times 10^{-2} \Omega^{-1} \text{cm}^{-1}$ ) [4].

Finally, a reactive ion etching (RIE) has been performed, in an O<sub>2</sub>(10sccm)/CF<sub>4</sub>(100 sccm) gas mixture, to define the active area of the sensor.

The presented sensor has been deposited on different substrates: glass, metal, ceramic and plastic and has been utilized for force and pressure measurements.

From an electrical point of view, the sensor can be considered as a simple bridge of resistances between four metal contacts, where the resistances are due to the conductivity of the amorphous silicon/chromium silicide stacked films. In the operating condition, two contacts of the bridge are used to apply the bias current to the sensing element, while the other two, orthogonal to the previous ones, provide an output voltage proportional to the anisotropic modification of the resistivity induced by the mechanical deformation. The output voltage of the sensor has been monitored by a very high input impedance CMOS amplifier (LMC6032 National Semiconductor), with a gain equal to 100.



### 3 Force measurement

In order to generate shear stresses the substrate on which the sensor is fabricated has been clamped at one side and a vertical force has been applied to other side. Figure 2 reports the output voltage of two sensors, fabricated on Corning Glass 7059, with different orientation of the sensor contact with respect to the direction of applied stress  $\sigma_x$ . As expected, the slope of the output voltage vs the bending momentum of the sensor A is much lower of the output voltage of sensor B, whose bridge resistances are rotated by  $+45^\circ$  with respect to the applied strain (see inset in Figure 2). Sensor B shows a sensitivity around  $0.4\text{V}/(\text{Nm})$ . For both devices we observe an excellent linearity in the investigated range. This property is due to the deposition of the device directly on the substrate, since the linearity in the sensor response is usually affected by the adhesive resin used to fix the sensor element [5].

For the sensor grown on the metal substrate, we deposited a 500 nm thick silicon nitride film as isolation layer between metal and amorphous silicon layer, because the very low transverse resistivity of the doped amorphous silicon directly connects the electrodes with the substrate. Two different substrate thicknesses (0.8 mm and 1.5 mm) have been used. Equal applied forces determine different deformations of the two substrates. Results are reported in Figure 3, where as expected we observe a much higher sensitivity of the sensor grown on the thinnest substrate. In particular, in agreement with theory, we found that the ratio of the two slopes is very close to the ratio of the cube of the thicknesses of the two substrates and equal to 1.1 and  $8\ \mu\text{V}/\text{g}$  for the 1.5 and 0.8 mm substrates, respectively.

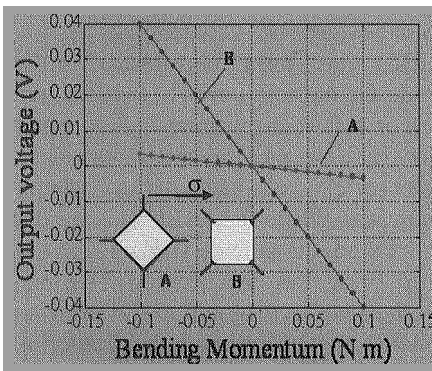


Fig. 2: Output voltage vs the bending momentum of two sensors, with different orientation of the contacts with respect to the applied stress.

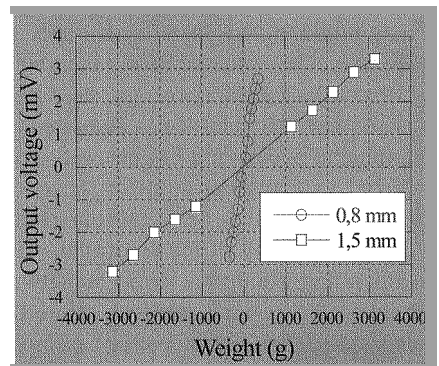


Fig. 3: Output voltage of the sensor vs weight applied on steel substrates with different thicknesses.

#### 4 Pressure measurement

Two sensors ( $1 \text{ mm}^2$  area) have been fabricated on a ceramic membrane, with 9 mm diameter and 0.6 mm thickness. One sensor is close to the center, the second is positioned at half radius of the diaphragm (see inset in Figure 4). The ceramic membrane has been positioned as a cap of a volume that has been emptied by a rotary vacuum pump. The membrane deformation, proportional to the pressure, has been monitored measuring the sensor output voltages, which are reported in Figure 4. The gains of the two sensors are equal to  $14.5 \text{ mV/mBar}$  and  $3.75 \text{ mV/mBar}$ . The different slopes are, obviously, ascribed to the different deformations of the membrane at the sensor positions.

As a final application as pressure sensor, we report in Figure 5 the output voltage of a sensor ( $1 \text{ mm}^2$  area) fabricated on Kapton tape. As shown in the inset, the tape has been attached to a glass substrate to avoid plastic deformation during fabrication steps. We observe that, the output voltage of the sensor shows good linearity as a function of vacuum pressure in the investigated range.

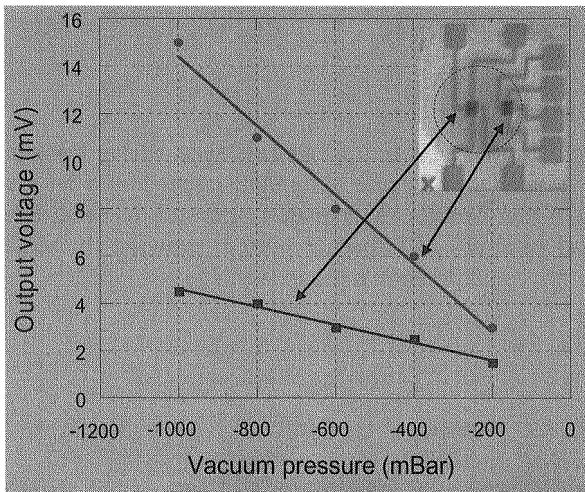
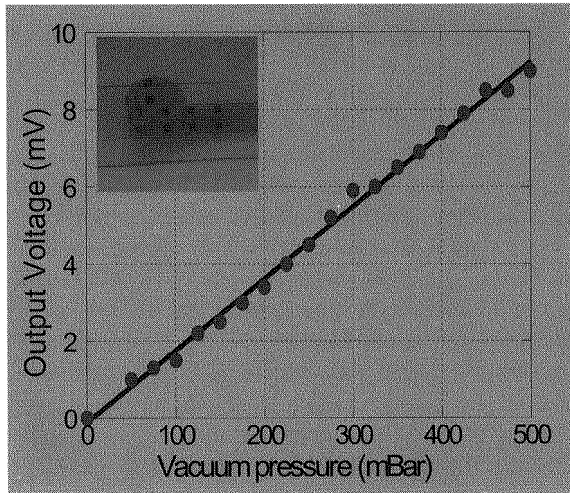


Fig. 4: Output voltage vs pressure of two sensors, with different position on the ceramic membrane



*Fig. 5: Output voltage vs pressure of a sensor deposited on Kapton membrane.*

## 5 Conclusions

Different applications of a thin film stress sensor have been presented. The active layer is a very thin silicide chromium layer grown on a n-type a-Si:H region. Details of fabrication and characterization results on different substrates (glass, steel and ceramic) have been reported, showing the suitability of our sensor for both force and pressure measurements.

## References

- [1] A. Bicchi, J.K. Salisbury, D. L. Brock; A. I. Memo No. 1262, MIT Cambridge, MA, Oct 1990.
- [2] A. Cicchetti, A. Eusebi, C. Melchiorri, G. Vassurra; 7th Int. Conf. On Adv, Robotic, ICAR'95, Spain, Sept, 1995.
- [3] J. Butterfass, M. Grebenstein, H. Liu, G. Hirzinger; ICRA'01, IEEE Int. Conf. On Robotic and Automation, Korea, May 2001.
- [4] R.A. Street, in "Hydrogenated amorphous silicon" Cambridge University Press, (1991)
- [5] L. Biagiotti, M. Gavesi, C. Melchiorri and B. Riccò; Proceedings of IEEE International Conference on Robotics and Automation 2 (2002) 1655.

## Nanogravimetric Immunodetection of Gliadin by $\mu$ Libra Balance

F. Olimpico, M. Pighini, S. Bernardi, A. Scarpa and S. Greco,  
*Technobiochip Srl, Via Carrara 12/A 04100 Latina (Italy)*  
[s.greco@technobiochip.com](mailto:s.greco@technobiochip.com)

### Summary

A nanogravimetric piezoelectric crystal-based immunoassay for the detection of gliadin is here described. Gliadin is the ethanol-soluble fraction of gluten, the protein content in wheat, barley, rye and oats, and it is responsible for gluten intolerance called Coeliac Disease, an autoimmune disease, characterised by damage to all or part of the *villi* lining the small intestine. The method for gliadin detection utilized a nanogravimetric balance (Technobiochip's  $\mu$ Libra), where the piezoelectric crystal quartzes were functionalized with antibodies specific to gliadin. We functionalized the quartzes surface by using different strategies, alone or in combination (e.g.  $\gamma$ -aminopropyltriethoxysilane (APTES)+3,3'-Dithiodipropionic acid di (N-succinimide ester) (DTSP), Poly-L-Lysine or Protein A). Moreover, we have compared the binding of two anti-gliadin antibodies, Sigma and PN3, against both standard IRMM or Sigma purified gliadin APTES+DTSP and Poly-L-Lysine treatments were the best functionalization methods for Sigma or PN3 antibody binding, respectively. In conclusion, obtained data revealed that the nanogravimetric method is able to detect gliadin with a good sensitivity, so providing a useful test for the presence of toxic gluten.

### Introduction

Coeliac disease (CD) is an inflammatory disease of the upper small intestine, characterised by villous atrophy resulting from gluten ingestion in genetically susceptible individuals, where association with particular HLA-DR and DQ types is well established [1,2]. Gluten represents the cereal storage proteins found in wheat, barley rye and oats. These proteins fall into four groups: albumins, globulins, glutenins and prolamins. Wheat, barley rye and oats prolamins (known respectively as gliadins, hordeins, secalins and avenins) represent the alcohol-soluble fraction of storage proteins and are responsible for triggering the disease. Gliadins may be subdivided according to their relative electrophoretic mobility into  $\alpha$ ,  $\beta$ ,  $\gamma$  and  $\omega$  subfractions [3,4]. Interaction of these proteins with the intestinal mucosa leads to permanent mucosal damage and causes an immune reaction in several tissues and organs, leading to a large number of complications, such as anaemia, osteoporosis, infertility, neurological disorders and skin disorders [5]. WHO/FAO CODEX ALIMENTARIUS has not yet produced a guidelines concerning the definitive acceptable levels and methods for gluten measurement, due

to the current lack of a golden standard method for the detection of CD-toxic gluten suitable for all types and states of foods.

This study was aimed at the design and production of an immunonanogravimetric sensor. The nanogravimetric method is based on piezoelectric quartz device, which offers most of the properties required for an ideal immunosensor in a wide range of applications, such as in clinical diagnostics, food quality control and environmental monitoring. The potential of piezoelectric devices is based on the relationship between mass deposited on quartz surface and the resonant frequency changes accordingly to the Sauerbrey' and Kanazawa's formulas [6,7]. Detection of purified gliadin has been achieved by immobilizing anti-gliadin antibodies onto gold electrodes of quartz crystals surface. We functionalized the quartzes surface by using different strategies, alone or in combination, (e.g. APTES+DTSP, Poly-L-Lysine or Protein A). Moreover, we have compared the binding of both two anti-gliadin antibodies, Sigma and PN3, and standard IRMM or Sigma purified Gliadin from wheat.

## Materials and Methods

### *Reagents*

Mouse Polyclonal anti-Gliadin Antibody (Ab) was obtained from SIGMA (Milan, Italy) and Mouse Monoclonal Anti-Gliadin PN3 Ab was kindly provided by KCL (King's College London). Other reagents were purchased from Sigma (Milan, Italy). The quartz crystals, 10 MHz AT-cuts, gold electrodes, were obtained from International Crystal Manufacturing Company (Ohio, USA).

### *Apparatus*

$\mu$ Libra is a Quartz Crystal Microbalance (QCM) produced by Technobiochip Srl (Latina, Italy), composed by a Main Unit and a Cell Base Unit which contains two oscillators and equipped with two low-volume flow-through cells for real-time measurements.  $\mu$ Libra output data are elaborated by the LibraVIEW software.

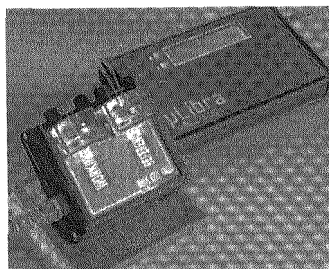


Fig. 1: Quartz Crystal Microbalance  $\mu$ Libra

### *Experimental protocol*

After cleaning with piranha solution ( $\text{H}_2\text{SO}_4:\text{H}_2\text{O}_2$  7:3 v/v) and functionalizations, quartzes were placed in a static flow-cell when basal frequency oscillation ( $\Delta f$ ) was stabilized by buffer adding (Phosphate Buffered Saline, PBS, 10mM pH 7.4), the antibody solution (SIGMA or PN3 0.1 mg/ml) was flown and the surface saturated with a BSA solution (0.1 mg/ml). After PBS washing, gliadin solutions (SIGMA or IRMM 0.1 to 0.05 mg/ml in PBS) were flown and  $\Delta f$  of antigen-antibody interaction recorded. All the experiments were performed as triplicates.

### *Strategies of Antibodies Immobilization*

Different strategies in order to firmly stabilize antibody onto quartzes surface were used:

1. *Lipoic Acid deposition by Langmuir-Blodgett techniques*: APTES quartzes were functionalized with 10 layers of lipoic acid with a commercially available KSV LB-5000 instrument. Formed films were compressed at 10 mm/min to produce surface pressure of 11 mN/m.

2. *Traut's reagent*: antibody solution was incubated for 1 hour with Traut's reagent, which reacts with primary amines to introduce sulfhydryl groups. After purification using a Sephadex 25G column, the fractions showing maximum absorbance at 280 nm have been pooled and the free sulfhydryl groups produced have been titrated by Ellman's method.

3. *APTES + DTSP-SAM (self-assembled monolayer)*: quartzes were dipped in 2% APTES solution for 20 minutes, baked at 120°C, sonicated in a water bath for 2 minutes and finally washed with ultra pure water. After silanization, they were dipped into 10 mM DTSP in DMSO and incubated for 30 minutes at room temperature and then washed with distilled water.

4. *Poly-L-lysine+DTSP-SAM*: quartzes were dipped into a poly-L-Lysine solution (poly-L-lysine: $\text{H}_2\text{O}$  1:1 v/v) for 15 minutes, placed in oven at 60°C for 20 minutes and air dried. Thus, modified quartzes were dipped into a 10 mM DTSP solution in DMSO for 30 minutes and washed with distilled water.

5. *APTES)+DTSP-SAM+Protein A*: APTES-DTSP-modified quartzes were placed in a static flow-cell and incubated with Protein A (1mg/ml).

### **Results and Discussion**

Several approaches for achieving firmly and/or oriented antibody immobilization have been studied and applied to piezoelectric immunosensor development.

First approach used was a Langmuir-Blodgett deposition. This technique is useful for the preparation of solid-supported highly organized films assembled at the

liquid-gas interface, and enables the precise control of the monolayer thickness. A very low oscillation frequency decrease of  $18 \pm 2.2$  Hz was observed subsequently to the interaction between gliadin and Ab bound to ten layers of lipoic acid deposited by LB technique (data not shown). Secondly, an oscillation frequency decrease of  $25 \pm 3.2$  Hz was observed after interaction with thiolated antibody (data not shown). The very low antigen binding results previously obtained, aimed us to perform SAM covalent strategies.

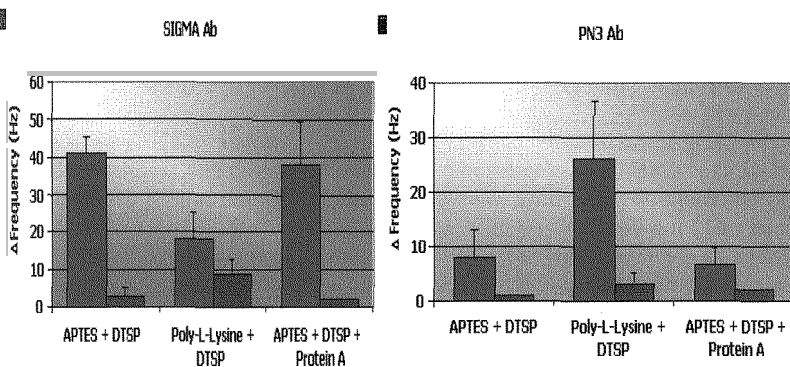


Fig. 2 Means of difference of oscillation frequency ( $\Delta F$ ) after SIGMA (A) or PN3 (B) anti-gliadin Ab binding to quartz by using SIGMA (purple bars) or IRMM (red bars) gliadins are represented as histograms. Experiments were performed in triplicates and standard deviations shown.

As shown in Figure 2, an overall high affinity of SIGMA antibody for gliadin (Sigma>>>IRMM) than the PN3 antibody, was observed, and among the different immobilization methods, a better binding of SIGMA antibody was observed on the APTES+DTSP-modified quartz surface rather than on the Poly-L-lysine one. Conversely, PN3 antibody showed a greater affinity for the Poly-L-lysine modified quartz surface rather than for the other two methods.

These preliminary experiments have shown that nanogravimetric sensor might be useful for the detection of gliadin in foods and SAM strategies are the best methods to bind the antibody onto crystal surface.

### Acknowledgments

The present study is part of the CD-Chef FP5 EC project, which regards the development of a disposable microsystem with integrated optimal extraction and

detection for precise and accurate quantitation of coeliac disease toxic gluten in all types of foods.

### References

- [1] Sollid LM, Markussen G, Ek J, Gjerde H, Vartdal F, Thorsby E. Evidence for a primary association of celiac disease to a particular HLA-DQ alpha/beta heterodimer. *J Exp Med*, 1989; 169:345-350.
- [2] Lundin KE, Scott H, Hansen T, Paulsen G, Halstensen TS, Fausa O. Gliadin-specific, HLA-DQ(alpha 1\*0501,beta 1\*0201) restricted T cells isolate d from the small intestinal mucosa of celiac disease patients. *J Exp Med*, 1993; 178:187-196
- [3] Ejllnckd AJC. N-terminal amino acid sequencing of prolamins of wheat and related species. *Nature*, 1979; 282:527-529.
- [4] Peter R Shewry ASTDDK. Cereal proteins and coeliac disease. In: Michael N Marsh, *Coeliac Disease*. Oxford: Blackwell Scientific Publications, 1992; 305-348.
- [5] Van de Kamer JH WHDW. Coeliac Disease IV. An investigation into the injurious constituents of wheat in connection with their action on patients with coeliac disease. *Acta Paediatr*, 1953; 42:223-231.
- [6] Sauerbrey GZ. Use of quartz crystal vibrator for weighting thin films on a microbalance. *Z Phys* 1959; 155:206-222.
- [7] Kanazawa KK, Gordon JG. Frequency of a quartz microbalance in contact with liquid. *Anal Chem* 1985; 57:1770-1771.



# INTEGRATED SILICON MICRO FLOW CYTOMETER BASED ON HOLLOW ARROW WAVEGUIDES

R. Bernini

*IREA-CNR, Via Diocleziano 328, 80124 Napoli, Italy*  
[bernini.r@irea.cnr.it](mailto:bernini.r@irea.cnr.it)

E. De Nuccio, A. Minardo, L. Zeni

*DII, Seconda Università di Napoli, Via Roma 29, 81031 Aversa, Italy*

P. M. Sarro

*ECTM-DIMES, TUDelft. NL-2600 GB Delft, The Netherlands*

## Summary

An integrated silicon micro flow cytometer based on hollow core AntiResonant Reflecting Optical Waveguide (ARROW) is proposed. The hollow core ARROW permits to confine both the cells to be analysed and the excitation light to carry out fluorescent measurements. This solution permits to design the device in order to enhance the pump source/cells interaction. In this paper, the operation principles, the main fabrication steps and some experimental tests are shown.

## 1 Introduction

The flow cytometer is a device that realises multi-parametric measurements on single cells or particles [1]. Typically, the cells are forced to travel in line by the hydrodynamic focussing effect. In this way, the cells arrive at the detection region, where multi-parametric analysis is carried out by observing both the scattered light and the emitted fluorescence. The conventional bench top flow cytometer presents an optical detection instruments arranged in delicate optical alignment methods and apparatus. Moreover, by using bulk optical device, the flow cytometer is expensive and not portable instrument[1].

Recently, the integration of optical waveguides with microfluidic devices for optical detection has been widely investigated. In this line of argument, the capability of AntiResonant Reflecting Optical Waveguides (ARROWs) to confine the light in media with low refractive index and their possibility to be realized with hollow core appear an optimal starting point toward the realization of the micro flow cytometer. In fact, the hollow core ARROW offers the possibility to confine both the light and the liquids in the core region. In this way, it is possible to couple the light directly inside the probe liquid, so as to enhance light-cells interaction.

In this paper, a integrated micro flow cytometer is proposed. The device is realised using standard silicon technology and offers the possibility to integrate the microfluidic part with the microelectronic devices necessary for the detection.

In order to validate the correct behaviour of the device, the hydrodynamic focussing phenomenon investigation and the fluorescence measurements are carried out.

## 2 Principle and design

The scheme of the proposed integrated micro flow cytometer is shown in Figure 1(a). The sample liquid, containing the cells or particle under analysis, is injected into the central inlet. By tuning opportunely the flow rates of the sheath liquid, the hydrodynamic focusing effect reduces in diameter the central sample flow, forcing the cell to travel in line. The marked cells/particles intercept the pump light source which travels collinearly along the path, so the fluorochromes are excited to a higher energy state. This energy is released as a photon of light with specific spectral properties unique to different fluorochromes. The fluorescent emission light is collected by the two arms placed orthogonally to the flow, so as to increase the signal/noise ratio. The collected light is coupled into the optical fibers in order to be analysed.

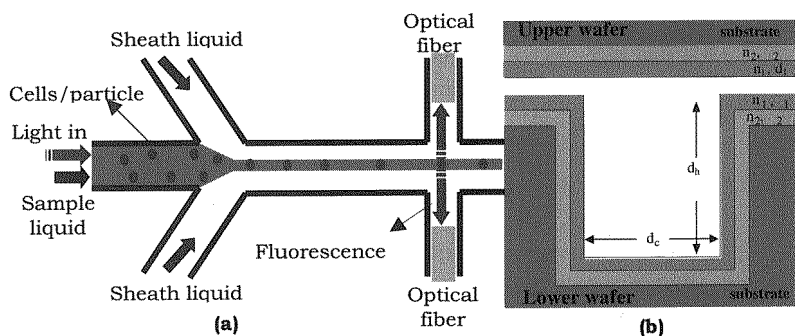


Fig.1 Scheme of the proposed flow cytometer (a).Section of the hollow core ARROW waveguide (b)

The structure is based on integrated hollow core ARROW waveguide (Figure 1(b)), that presents a low refractive index  $n_c$  core region and two cladding layers designed to form a high reflectivity Fabry-Perot antiresonant cavity. This solution permits to confine both pump source and the liquid with the cells under analysis, so as to reduce in complexity the detection system by using the same channel to excite and to focus the cells.

In order to minimize the optical losses, the antiresonant condition has to be achieved. For a fixed core width  $d_c$  and core refractive index  $n_c$ , in the equivalent one-dimensional vertical structure, this condition is guaranteed for the cladding layers thicknesses [2]:

$$d_{1,2} = \frac{\lambda}{4n_{1,2}^2} \left[ 1 - \left( \frac{n_c^2}{n_{1,2}^2} \right) + \left( \frac{\lambda}{2n_{1,2}^2 d_c} \right)^2 \right]^{-1/2} (2N+1) \quad N = 0,1,2,\dots \text{ (eq. 1)}$$

where  $\lambda$  is the operating wavelength.

### 3 Device fabrication

The micro flow cytometer is realised in standard silicon technology by using two silicon wafers bonded together (Figure 1(b)). By photolithography, the pattern of the structure is impressed on the bottom wafer. The anisotropic dry etching permits to realize the channels (the depth is set to 150 $\mu$ m and the width is 200 $\mu$ m). The channel dimensions are chosen to permit easily the insertion and consequently the alignment of both the excitation and collection fibers. The used materials are silicon dioxide (SiO<sub>2</sub>) as second cladding that presents a refractive index  $n_2=1.457$  at the wavelength  $\lambda=633$ nm, and silicon nitride (Si<sub>3</sub>N<sub>4</sub>) as first cladding with a refractive index  $n_1=2.227$ . By using the core refractive index  $n_c=1.333$  (water) and  $d_c=150\mu$ m in eq. 1, the thickness values are  $d_1=266$ nm for  $N=1$  and  $d_2=266$ nm for  $N=0$ . The interferometric layers are deposited by LPCVD at 800°. After that, the bottom and the upper wafers are joined together by direct wafer bonding. Finally, the excitation and collection fibers are inserted in the respective locations and there sealed by optical glue.

### 4 Results and discussion

The hydrodynamic focusing effect is achieved by tuning the flow rate of the sheath liquid respect to the sample liquid flow rate. Finite Elements Method (FEM) has been used to solve the fluidodynamics equations of the structure, with the aim of finding the optimal ratio between core flow rate and shield flow rate (FRR).

In Figure 2, the concentration profile of an aqueous solution in diffusing water shows the hydrodynamic focussing phenomenon simulated by solving the Navier-Stokes and Diffusion-Convection coupled equations. The values for the flow rates at the inlets are 5ml/h for the central liquid and 15ml/h for the focusing liquids (FRR=3). In this case we have a Flow Rate Ratio, the physical effect is clear and the calculated width of the focused stream is about 20 $\mu$ m.

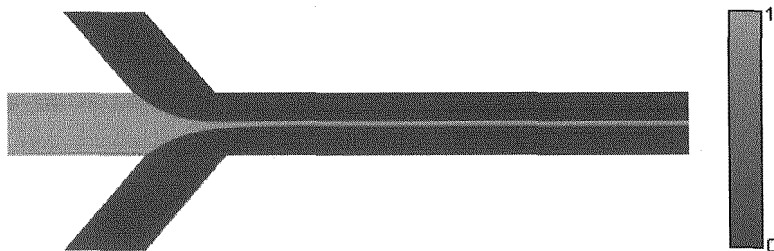


*Fig.2 The simulated hydrofocussing phenomenon by calculation of the concentration profile of an aqueous solution in water diffusing*

An experimental observation of the hydrofocussing effect was conducted by injecting a fluorescent dye (a water solution of resorufin) into the core of the structure, while using de-ionized water as the sheath liquid. Results are shown in Figure 3. In this case, the silicon top wafer was substituted by a thin glass slide in order to observe the emitted fluorescence by a fluorescence microscope. By setting  $FRR=3$ , with a central liquid flow rate equal to 5ml/h, the focussed stream width value is about  $24\mu\text{m}$ , that is the typical dimension of the cell of interest, finding a good agreement with the numerical simulation.

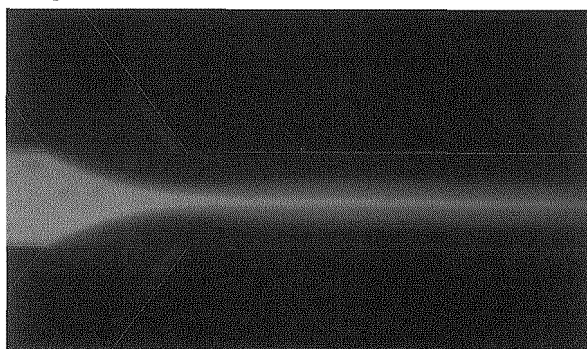


*Fig.3 Experimental results for the hydrofocussing process*

The testing of the detection system has been carried out by considering the device realised by silicon wafer/silicon wafer bonding. The measurements were performed by using a pump source laser ( $\lambda=532\text{nm}$ ), an optical filter stopping the wavelengths lower than 532nm, a femtowatt photodiode and an oscilloscope. Due to the low-pass band behaviour of the photodiode, the absolute velocities of the liquids have been reduced, so to be reduced the cells occurrence. By setting the sample flow rate to 1ml/h and the  $FRR=3$ , the results of the test are shown in Figure 4. The intensity's peaks of the collected emitted fluorescence represent the

cell event. It is to underline that at low flow rates, the sample stream becomes unstable due to the large pressure difference between the sample and sheath flows near the channel inlets, resulting in discontinuous liquid motion. The discontinuous sample flow causes particles to become trapped in the inlet reservoir, which is one of the major reasons for the low cell rate in the capturing [3].

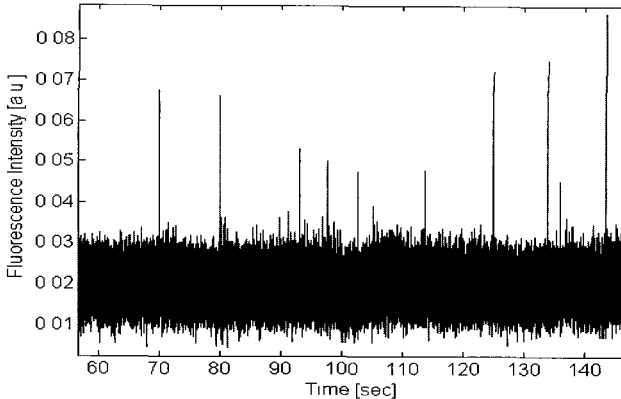


*Fig. 4 Collected fluorescence intensity of the marked cells*

In conclusion, a novel micro flow cytometer has been proposed. The device is based on the hollow core ARROW waveguide, realised in standard silicon technology. The correct behaviour of the device has been investigated, showing good results. The technological choices are motivated observing the capability of the hollow core antiresonant optical waveguides to confine both the sample liquid and the pump source, and the possibility to integrate microelectronic devices with standard IC process.

### References

- [1] Gwo-Bin Leea, Che-Hsin Linb, Guan-Liang Changc, *Sensors and Actuators A*, 103, (2003), 165–170.
- [2] R. Bernini, S. Campopiano and L. Zeni, *IEEE J. Selected Topics in Quantum Elect.*, 8, 106, (2002).
- [3] Yi-Chung Tung a, Min Zhang a, Chih-Ting Lin b, Katsuo Kurabayashi a,c, Steven J. Skerlos, *Sensors and Actuators B*, 98, (2004), pp. 356–367.

### Acknowledgments

The authors would like to thank the IC Process Group of DIMES for technical assistance.

# Properties of heme *c* containing enzyme layer self-assembled on planar metallic electrodes

S. Kaciulis, A. Mezzi

*Istituto per lo Studio dei Materiali Nanostrutturati ISMN-CNR,  
P.O. Box 10, I-00016 Monterotondo Stazione (RM), Italy  
[mezzi@mlib.cnr.it](mailto:mezzi@mlib.cnr.it)*

A. Galdikas, V. Bukauskas, A. Mironas, A. Šetkus  
*Semiconductor Physics Institute, A. Gostauto 11, Vilnius, Lithuania*

V. Laurinavičius, R. Meškys, J. Razumienė  
*Institute of Biochemistry, Mokslininku 12, Vilnius, Lithuania*

## Summary

Electrical properties of symmetric metal-enzyme (pyrroloquinoline quinone-dependent and heme *c* containing alcohol dehydrogenase) junctions were experimentally investigated in planar structures in gaseous surrounding. Two types of the ADH molecules (type II and III) have been used in the experiments. Gas sensitive state in the junctions is induced by temporal connection of an external dc-voltage to the electrodes. The properties of the structures, determined by a relationship between the electron transfer and chemical processes in metal-ADH junction, have been analyzed. Alcohol sensitive characteristics and the XPS chemical composition of molecular layers, consisting of pure ADH-II and ADH-III, have been compared.

## 1 Introduction

In the most developments, the biosensors are based on electron transfer from enzyme to electrode stimulated by enzyme catalyzed biochemical reaction [1-3]. Practically applicable devices are frequently developed long before comprehending their functioning mechanism. Nevertheless, the understanding of these processes can be valuable for the description of the biosensor's principal limitations and also for its further improvement.

Present study is focused on an original family of the sensors based on dry enzyme layer that respond to vapours in air. This report presents novel results of the study focused on the two forms of alcohol dehydrogenase (ADH) and describes the formation and the properties of a pure molecular layer.

## 2 Experimental

Soluble quinohemoprotein ADH type (QH ADH-II) from *Pseudomonas Putida* HK 5 and membrane-bound quinohemoprotein ADH type (QH ADH-III) from *Gluconobacter* sp 33 were used for dry molecular layers in our study. The two proteins contain heme c and pyrroloquinoline quinine cofactor (PQQ). The dry layers with QH ADH-II and QH ADH-III were deposited from individual colloidal solutions based on tris-HCl and potassium phosphate buffers, respectively. A layer has self-assembled on a substrate with planar metallic electrodes after drying at ambient temperature in air. Planar strip-like electrodes were shaped from thin films of different pure metals by standard photolithography on an insulating base-plate (e.g., glass). Pt, Au, Ag and Ni have been used for the electrodes. The typical gap between the electrodes was of about 50  $\mu\text{m}$ .

DC-voltage drop was measured on the load resistance connected in series to the Me/ADH/Me structure after the ADH-layers were dried in ambient atmosphere. During the dc-electrical tests, an original method was used for the activation of the ADH molecules. The method is analogous to an electrical shock and was proposed by us recently [4]. For the activation, the planar Me/ADH/Me structures were temporary (100-300 seconds) connected to an external power source. After the activation, the signal proportional to the current was measured in the circuit without an external power source. The sequence of the procedures was cycled for a long time and analogous results were obtained in each cycle.

XPS investigations were carried out by means of an VG ESCALAB Mk II spectrometer equipped with Al  $K\alpha$  source and five-channeltron detection system. In order to avoid the X-ray damage, the sample holder during the measurements was cooled with liquid nitrogen.

## 3 Results and Discussions

After the activation, the junctions generated an electric signal in response to alcohol vapour in air. Typical variation of the signal in response to a pulse of ethanol and 1,2-propanediol is illustrated in Fig. 1. The activation voltage was  $U_{e0} = 4.24$  V at  $T = 22$  °C and relative humidity of air of 43 %. This response was recorded in unlimited number of the cycles, each of which consisted of four periods, namely the activation, waiting, responding and restoring. The sequence of the measured signals was described in detail in our previous report [4]. It follows from Fig. 1 that the kinetics of the response signal is individual in the ADH-II (2) and ADH-III (1) dry-layers. The difference between the signals is described by  $\Delta_1$  and  $\Delta_2$  that are a delay between the rises and the falls of response signals respectively in the two ADH types. Another distinctive characteristic of the signal is a spike in the response signal of ADH-III layers

after the clean air was let to flow through the sensor chamber. The origin of the differences in Fig. 1 is not clear at present state of our investigations.

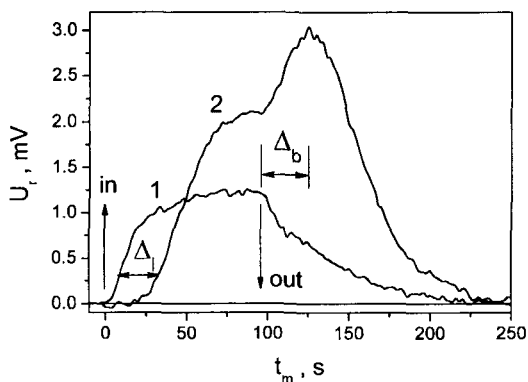


Fig. 1. Time dependence of the electrical signal measured for ADH-III (1) and ADH-II (2) in response to a pulse of ethanol vapour (4.4 %) in air.

The responses of the Me/ADH/Me structures were proportional to the partial pressure of ethanol vapour in air. The proportionality is illustrated in Fig. 2 by typical dependences of the response of the ADH-II dry-layers (two sensors) on the amount of 1,2-propanediol (1) and ethanol (2) vapour in air ( $T_a = 21\text{ }^\circ\text{C}$ ; RH = 43 %) after the activation with external voltage  $U_{e0} = 4.2\text{ V}$ .

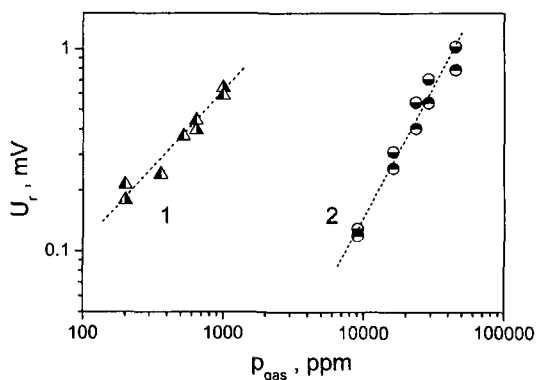
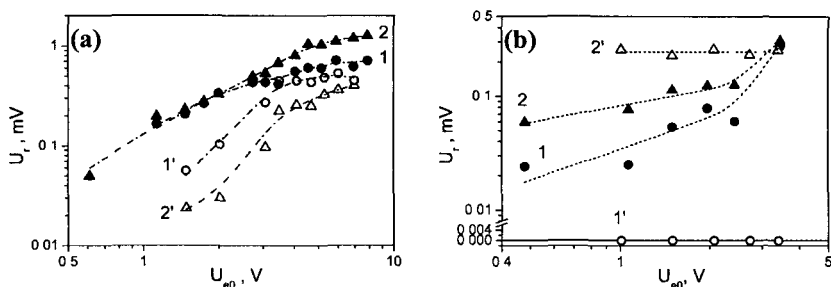


Fig. 2. Dependences of the response signal of ADH-II based structures to 1,2-propanediol (1) and ethanol (2).



The dependences in Fig. 2 can be described by a power law  $U_r \sim p^b$  with  $b \approx 0.8$  (line 1) and 1.5 (line 2). Analogous results were obtained for ADH-III layers.

It was ascertained that the response of a dry enzyme layer is dependent on the residual compounds from the buffer. An influence of these compounds on the response of the dry enzyme layers is illustrated in Fig. 3. The dependences of the response on the activation voltage are plotted in the figures. It was found that the effect of the residual compounds is significant at low  $U_{e0}$ .



**Fig. 3** The response at various activation voltages  $U_{e0}$  temporary applied to the ADH-III (1,1') and ADH-II (2,2') layers before (1,2) and after (1',2') washing: (a) to ethanol vapour (34500 ppm); (b) to 1,2-propanediol vapour (1000 ppm).

From the sensitivity tests it was concluded that the selectivity of the pure ADH based dry layers is higher than those containing residual compounds from the buffer. The most evident change in the selectivity is shown in Fig. 3b. There was no response to 1,2-propanediol in pure ADH-II dry layers, while the removal of the residual compounds from ADH-III layers increased significantly the response signal to 1,2-propanediol (see 2' in Fig. 3b).

As it was mentioned in our previous publication [5], the enzymes can be characterized by spectral fingerprints, when they are investigated by XPS. Therefore, the shape of C 1s signal is typical for ADH-II and ADH-III dry layers, composed from the three components, positioned at BE = 285.0, 286.5 and 288.1 eV and assigned to C - C, C - OH and C = O, C - NO, respectively (Fig. 4). The differences in the C 1s spectra of two enzymes can be explained by the presence of buffer residuum and some non-controllable contaminants. When the buffer residuum was removed by washing the samples in distilled water, the C 1s spectra of both enzymes became identical. The complete removal of the residuum from the ADH-III layer is demonstrated by the K 2p signal detected in the as-deposited sample, while it was absent in the washed sample (spectra 1 and 2 in Fig. 4a). At the same time, the C 1s spectrum was unchanged, what indicates that the buffer removal was performed without the modification of the enzyme's structure.

In addition, the XPS analysis proved that the metal electrodes are still completely covered by enzyme layer after rinsing the samples with distilled water.

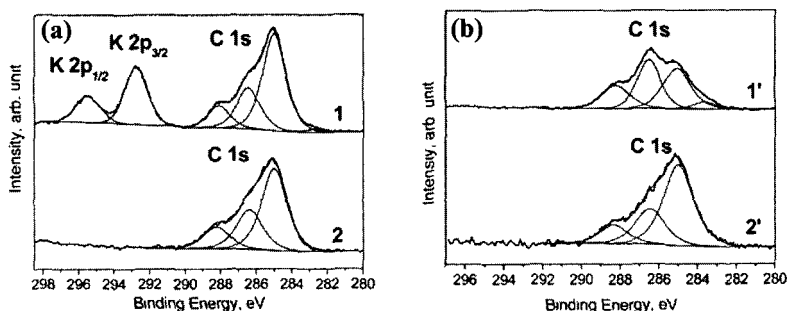


Fig. 4. XPS spectra registered before (1,1') and after (2,2') the removal of buffer residuum from ADH-III (a) and ADH-II (b) layers by washing in distilled water.

### Acknowledgments

The work in the Semiconductor Physics Institute and the Institute of Biochemistry was carried out in the frame of the joint project "BIOHEMAS" supported by the Lithuanian State Science and Studies Foundation.

Dr. A. Mezzi acknowledges the support of the European Center of Excellence "PRAMA".

### References

1. W. Schuhmann, *Rev. Molecular Biotechnology*, 82 (2002), p. 425.
2. M. Aslam, N.K. Chaki, J Sharma, K. Vijayamohanam, *Current App. Phys.*, 3 (2003). p. 115.
3. B. Bhushan, D.R. Tokachichu, M.T. Keener, S.C. Lee, *Acta Biomaterialia*, 1 (2005), 327.
4. A. Šetkus, J. Razumienė, A. Galdikas, V. Laurinavičius, R. Meškys, A. Mironas, *Sens. Actuators B: Chem.*, 95 (2003), 344.
5. A. Curulli, A. Cusmà, S. Kaciulis, G. Padeletti, L. Pandolfi, F. Valentini, M. Viticoli, *Surf. Interface Anal.*, 38 (2006), 478.

# Detection of labelled DNA based on amorphous silicon devices

D. Caputo, G. de Cesare, A. Nascetti, R. Scipinotti

*Department of Electronic Engineering, University of Rome "La Sapienza", via Eudossiana, 18 00184 Rome (Italy)*

R. Negri, A. Tarquini

*Laboratory of Functional Genomics and Proteomics of Model Systems, University of Rome "La Sapienza", via dei Sardi, 70, Rome (Italy)*

## Summary

In this paper, we present an alternative fluorochrome labeled DNA detection system based on the use of an amorphous silicon photosensor. The sensor is an n-i-p stacked structure whose photo-response has been optimized by using a numerical device simulator. The optimization process was performed as a trade off between the spectral selectivity and the dark current of the device in order to increase the signal-to-noise ratio.

It has been observed that the system detection limit lies around 3 nmol/l. Taking into account the specific activity of labeled DNA in the solution, it corresponds to a minimal surface density of fluorochrome around 50 fmol/cm<sup>2</sup>. This result is very encouraging because it is obtained with a low cost system, where the use of optics for focusing and filtering of both exciting and emitting radiation is avoided.

## 1 Introduction

Microarray technology (or DNA chip) allows the parallel study of many different DNA sequences in a single hybridization experiment [1] [2] [3]. The quantification of the hybridization is mainly based on the detection of fluorescent molecules bound to the DNA target [2]. Fluorescence is detected by laser scanners, CCD cameras, or microscopy [4], which produce an image of the microarray [4][5]. However, most of these systems are quite expensive and need complex optics for focusing and filtering of the emitted light.

Recently [6][7], amorphous silicon (a-Si:H) sensors have been developed as alternative detectors in order to take advantage of its on-chip integration possibility. In this paper, we present an alternative fluorochrome labeled DNA detection system based on the use of an amorphous silicon (a-Si:H) sensor, where the need of complex optics is overcome.

## 2 Labeling the DNA

The DNA molecules have been labeled with the fluorochrome Alexa Fluor 350, whose excitation (open squares) and emission (open circles) spectra are reported in Fig. 1. We observe that this fluorochrome is excited by UV radiation

with an excitation peak at  $\lambda_{\text{ex}}=340$  nm and re-emits visible spectra with an emission peak at  $\lambda_{\text{em}}=442$  nm.

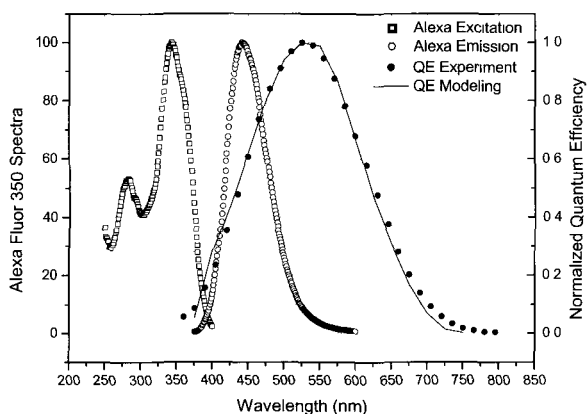


Fig. 1: Emission (open circles) and excitation (open squares) spectra of the fluorochrome Alexa 350. Measured (solid circles) and modeled (solid line) QE of the sensor are also reported.

24 bases long DNA oligonucleotides, carrying an amine group at the 5' extremity were labeled by reacting them with a succinidyl ester of Alexa Fluor 350. As an alternative, a double stranded molecules, produced by Polymerase Chain Reaction (PCR), were labeled using a substrate of labeling reaction solution containing 1  $\mu$ l of aminoallyl mix 100x composed by 25mM dATP, 25mM dCTP, 25mM dGTP, 10mM dTTP, 15mM dUTP. The 3-aminoallyl-dUTP has the function to replace the Thymine bases in the new DNA chain and to make a coupling point with the labeling fluorochrome.

Labeled molecules were purified by electrophoresis method and analysed by spectrophotometry in order to determine DNA concentration and specific activity. In the different experiments specific activities in the range of 0.5÷1.5 molecules of fluorochrome/molecule of DNA have been estimated. Labelled DNA preparations of known specific activity were subsequently used to test the sensitivity of the detection system.

### 3 Photodetector fabrication and characterization

The sensor is an n-i-p stacked structure, deposited on a glass substrate covered by a transparent conductive oxide (TCO). In order to detect the light emitted by the fluorochrome, the detector's quantum efficiency should match the emission spectra of the Alexa Fluor 350 as much as possible. The optimization of the spectral selectivity, however, should take into account the photocurrent as

well as the dark current of the device in order to achieve the actual signal-to-noise ratio.

Modeling of device performances has been carried out by a numerical device simulator [8]. In the optimization process we considered the optical properties of the glass and the TCO. The spectral transmittance of a TCO covered glass substrate is like to a high-pass filter for the wavelengths of the incident light. The cutoff wavelength occurs at 390 nm, wavelength positioned between the peaks of the excitation and emission spectra of the fluorochrome. This has an important consequence in the detection system, because the sensor detects only the light emitted by the Alexa Fluor 350 and not the UV excitation radiation, filtered by the TCO covered glass.

Basing on simulation results and taking into account the growth rate in the chambers of our Plasma Enhanced Chemical Vapor Deposition (PECVD) system, we deposited a n-i-p device with the deposition parameters reported in Table 1 corresponding to the following optimized layer thicknesses: 25, 100 and 25 nm for the n, i and p zones, respectively.

Layer	SiH <sub>4</sub> (sccm)	CH <sub>4</sub> (sccm)	PH <sub>3</sub> (sccm)	B <sub>2</sub> H <sub>6</sub> (sccm)	P <sub>D</sub> (Torr)	P <sub>RF</sub> (mW/cm <sup>2</sup> )	T <sub>D</sub> (°C)	t <sub>D</sub> (sec)	Thickness (Å)
n <sup>+</sup>	40	--	10	--	300	30	200	120	250
i	40	--	--	--	300	30	180	600	1000
p <sup>+</sup>	40	--	--	3	300	30	160	180	250

Table 1-Deposition parameters of the a-Si:H sensor.

In Fig. 1 the normalized quantum efficiency (QE) curve (solid line) as obtained from simulations and the normalized measured QE (solid circles) of the device are shown. Even though the peak of the device QE does not occurs at  $\lambda_{em}$ , the thickness of the deposited layers ensures a good trade-off between photogenerated carrier collection and the requirement of a low dark current.

Circle shaped samples with area equal to 3.14 mm<sup>2</sup> have been characterized measuring dark current and photocurrent at  $\lambda_{em}$ . The lamp intensity at 440 nm was 15.7  $\mu$ W. The device dark current in operating condition ( $V_{bias} \sim 100 \mu$ V) was in the order of  $5 \cdot 10^{-10}$  A/cm<sup>2</sup> and its responsivity around 145 mA/W.

#### 4 Discussion

The detection system where our detector is included is depicted in Fig. 2. UV radiation is incident on the labeled DNA, dropped on the same glass substrate but on the other side with respect to the sensor.

Spatial confinement of the DNA solution has been achieved by manufacturing a Kapton microtrap 350  $\mu$ m deep. The radiation re-emitted by the

fluorochrome passes through the substrate and is absorbed by the sensor, which is aligned with the DNA solution.

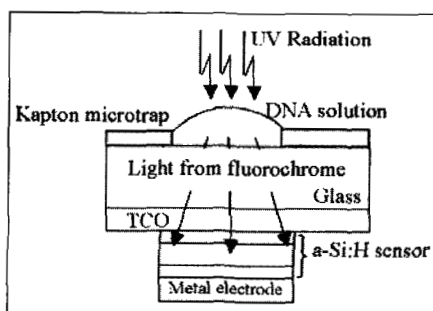


Fig. 2: Experimental set-up of DNA detection system. The light is impinging on the solution containing DNA dropped on the top of substrate.

The selected excitation wavelength for fluorochrome excitation was  $\lambda_{em}=253.4\text{nm}$ , because this wavelength ensures a good excitation efficiency and is very well filtered by both glass substrate and TCO. The UV lamp intensity at 253.4 nm was in order of  $3\ \mu\text{W}$ . The photo-detector is therefore illuminated only by the emission wavelength and the photocurrent generated inside the sensor is directly proportional to the amount of labeled DNA.

Sensor photocurrent due to fluorochrome fluorescence is reported as solid circles in Fig. 3 versus DNA concentration.

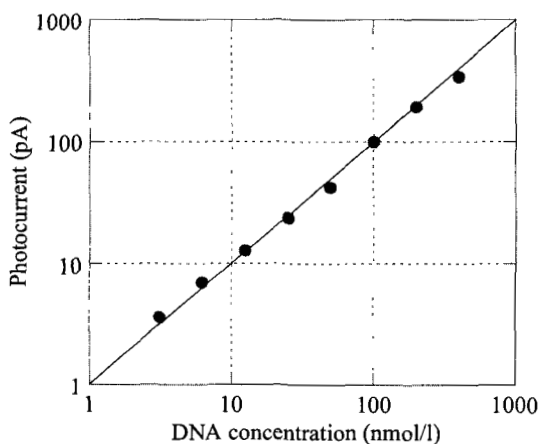


Fig. 3. Measured sensor photocurrent (symbols) as a function of DNA concentration. The offset correction allows to obtain the excellent linearity shown by the solid line.

These data have been calculated performing the correction of the photocurrent offset due to glass substrate fluorescence when the UV radiation is impinging on a solution without DNA. The slope-1 solid line in the double logarithmic plot of Fig. 3 serves as guide for the eyes to show the excellent linearity of the detector response over more than two orders of magnitude. We also observe that the detection limit of our system lies around 3 nmol/l. From the measured values of dark and photo current, we deduce that this limit can not be ascribed only to the current shot noise, but has to be related to the experimental set-up.

Finally, taking into account the specific activity of labeled DNA in the solution, we calculated a minimal detectable surface density of fluorochrome around 50 fmol/cm<sup>2</sup>.

## 5 Conclusions

An alternative fluorochrome labeled DNA detection system based on the use of an amorphous silicon sensor has been presented. The sensor has been deposited on a glass substrate avoiding the use of optics for focusing and filtering of both exciting and emitting radiation. The photodiode has been optimized by using a numerical device simulator taking into account both the spectral selectivity and signal-to-noise ratio. The detector response has been measured as a function of DNA concentration. An excellent linearity has been found over more than two orders of magnitude. DNA concentrations as low as 3 nmol/l have been measured and a minimal surface density of fluorochrome of 50 fmol/cm<sup>2</sup> has been estimated.

## References

- [1] M. Schena, D. Shalon, R.W. Davis, P.O. Brown, *Science* 270 (1995) 467.
- [2] D. Meldrum, *Genome Res*, 21 (1999) 20.
- [3] S.K. Moore, *IEEE Spectrum*, 3 (2001) 54.
- [4] R.M. Ostroff, D. Hopkins, A.B. Haeberli, W. Baouchi, B. Polisky, *Clin. Chem.*, 45 (1999) 1659.
- [5] J.B. Lamture, K.L. Beattie., B.E: Burke, M.D. Eggers, D.J. Ehrlich, R. Fowler, M.A. Hollis, B.B. Kosicki. R.K. Reich. S.R. Smith, *Nucleic Acids Res.* 22 (1994) 2121.
- [6] F. Fixe, V. Chu, D. M. F. Prazeres, J.. P. Conde, *Nucleic Acids Research* 32 (2004) e70.
- [7] T. Kamei, B.M. Paegel, J.R. Scherer, A.M. Skelley, R.A. Street, R.A. Mathies, *Anal. Chem.* 75 (2003) 5300.
- [8] D. Caputo, U. Forghieri, F. Palma, *Journal of Applied Physics* 82 (1997) 733.
- [9] D. Caputo, *Solar Energy Materials and Solar Cells* 59 (1999) 289.

# Carbamate, triazinic and benzotriazinic pesticide analysis using an inhibition tyrosinase organic phase enzyme sensor

Luigi Campanella, Elisabetta Martini, Dalina Lelo, Mauro Tomassetti

*Department of Chemistry, University of Rome "La Sapienza", P.le A. Moro 5, 00185 Rome Italy*

luigi.campanella@uniroma1.it; mauro.tomassetti@uniroma1.it

## Summary

Tyrosinase enzyme inhibition has recently been used with increasing frequency to determine different types of pesticides, in particular those of the triazinic type. Starting from this premise, the present authors, who originally developed inhibition biosensors based on the enzymes butyrylcholinesterase + choline oxidase to determine organophosphorus and carbamate pesticides, also as OPEE devices (i.e. organic phase enzyme electrodes), more recently suggested a new tyrosinase inhibition OPEE suitable for determining triazinic pesticides. In the present research several triazinic pesticides have been tested using this inhibition OPEE. In addition they indicated how, using this biosensor, also benzotriazinic and carbamate pesticides can be detected up to a concentration of the order of  $10^{-8}$ - $10^{-9}$  mol l<sup>-1</sup>.

## 1 Introduction

Several inhibition biosensors have been constructed for pesticide determination [1-3]. The majority are based on the inhibition of the enzyme acetylcholinesterase or of the enzyme butyrylcholinesterase. Also our research group on several occasions has undertaken the development of this type of inhibition biosensor [4-6].

Moreover, the recent development of OPEEs (Organic Phase Enzyme Electrodes) [7, 8] has provided a way of working round one of the greatest difficulties often found in the biosensor analysis of pesticides which is related to the poor solubility in water shown by many of these compounds. In this context we recently showed how [9, 10], in its inhibition OPEE configuration, the tyrosinase biosensor allows triazine pesticides to be determined when operating in organic solvent (chloroform), in which the pesticides tested are much more soluble than in water.

This reduces the risk of underestimating the concentration of these pesticides due to the difficulty of dissolving them completely in the aqueous phase. The method was first optimized [9], and then some triazine pesticides (Atrazine, Atrazine-desethyl, Atraton, Propazine) were tested [9, 10]. The method has been extended to other triazines (Simazine and Ter-buthylazine) and to another important class of pesticides, i.e. benzotriazines; one of these 1, 2, 3-



benzotriazinic pesticides which also have a phosphorodithioate group, i.e. azinphos-methyl, has been tested by tyrosinase inhibition OPEE.

Since bibliographic references [11] show that also carbamates exert an inhibiting action on the tyrosinase also a carbamate pesticide (Pirimicarb) was tested.

## 2 Methods

In practice the enzymatic inhibition tyrosinase biosensor operating in non-aqueous solvent (OPEE) described in detail in previous papers [7-9] was used in order to determine several phytopharmaceuticals having a triazinic, benzotriazinic or carbamate structure (Fig.1).

The inhibition biosensor calibration curve at growing pesticide concentrations is obtained by recording the percentage inhibition of biosensor response as a function of the pesticide concentration in the solution in which the biosensor has been immersed for a given period of time (incubation time) before substrate (phenol) addition. This response is then compared with the biosensor response to the phenol in the absence of pesticide. For the calibration curves, as required, standard solutions of pesticides in water-saturated chloroform from  $2.0 \times 10^{-6}$  mmol l<sup>-1</sup> to 10 mmol l<sup>-1</sup> are usually used.

In practice, in order to perform each measurement, the biosensor is dipped into a thermostated cell containing 10 ml of organic solvent (water-saturated chloroform) kept under constant magnetic stirring and the signal is allowed to stabilize. Then 200 µl of a solution of phenol  $2.5 \times 10^{-2}$  mol l<sup>-1</sup> in water-saturated chloroform (i.e. concentration previously optimized [9]) is added and the signal variation measured. The measuring cell is rinsed and dried and a new measure performed by washing and then dipping the biosensor in 10 ml of one of the various water-saturated chloroform atrazine-containing solutions prepared to build the calibration curve, then waiting for a period of time equal to the incubation time of 20 min (time optimized in previous research [9]), while the enzyme and the inhibitor remain in contact, before adding 200 µl of a phenol solution  $2.5 \times 10^{-2}$  mol l<sup>-1</sup> in chloroform.

After adding the phenol solution the signal variation is recorded and compared with the one previously obtained. In constructing the calibration curve the final pesticide concentration is placed on the X-axis and the following ratio on the Y-axis:

$$\Delta i\% = \frac{(S_c - S_d)}{S_c} \times 100$$

Where:

$\Delta i\%$  = percent inhibition value

$S_c$  = signal variation due to the addition of phenol in the absence of pesticide in solution.

Sd = signal variation on addition of phenol after the biosensor has been "incubated" in the presence of pesticide.

All the triazine, benzotriazine and carbamate pesticides tested were determined using this operating procedure.

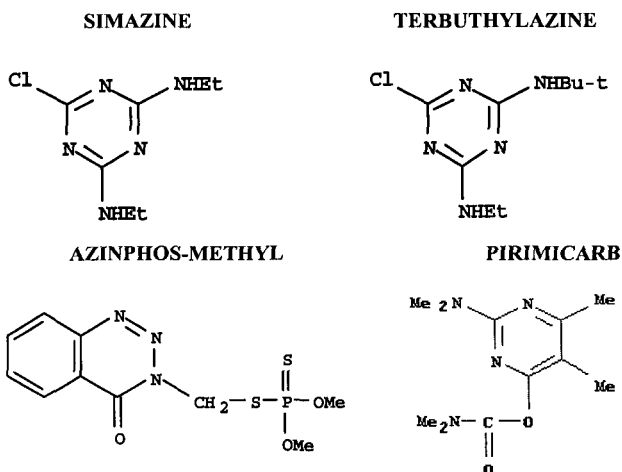


Fig. 1 – triazinic, benzotriazinic and carbamate pesticides analyzed

### 3 Results

The calibration curves of several triazine and benzotriazine pesticides tested in water-saturated chloroform are shown in graphic form in figures 2(a), 3(a) and 4(a). As can be seen, in all cases a logarithmic trend is obtained that is typical of an inhibition biosensor response, which may thus be converted into a linear trend by transferring the data to a semilogarithmic diagram (see figures 2(b), 3(b) and 4(b)). Tables 1, 2 and 3 show the equations referring to the straight lines obtained by transferring the data to a semilogarithmic diagram, as well as the main analytical data found.

Figures 5(a) and 5(b) respectively show calibration curves (both logarithmic trend and trend converted into linear form using a semilogarithmic diagram) of a typical carbamate pesticide, while the relative equation and analytical data are summarized in table 4.

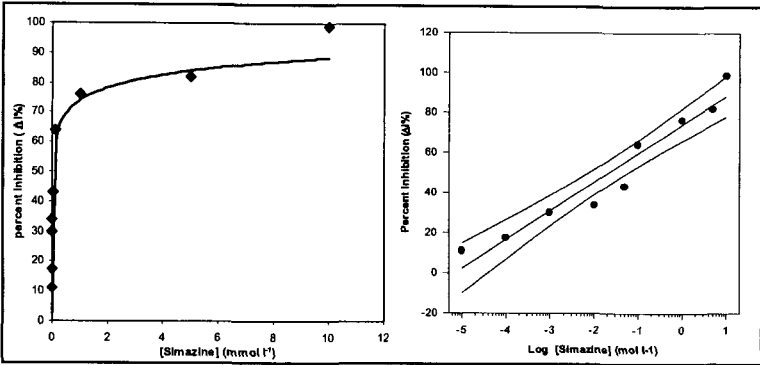


Fig. 2 (a) Calibration curve (Simazine) in water-saturated chloroform, and (b) the same calibration curve data as in (a) transferred to a semilogarithmic scale.

$$y = (5.8 \pm 2.3) \text{Log}(x) + (71.6 \pm 8.9)$$

$$r^2 = 0.9483 \quad (1 - \alpha) = 0.90 \quad t = 2.365$$

x = concentration (mmol l<sup>-1</sup>) ; y = percent inhibition (ΔI%)  
 Linear range from 2.0 x 10<sup>-5</sup> mmol l<sup>-1</sup> to 10 mmol l<sup>-1</sup>.  
 LOD = 1.0 x 10<sup>-5</sup> mmol l<sup>-1</sup>  
 "Pooled SD%" = 12 %

Tab 1: Analytical data relative to the calibration curve of fig. 2 (b)

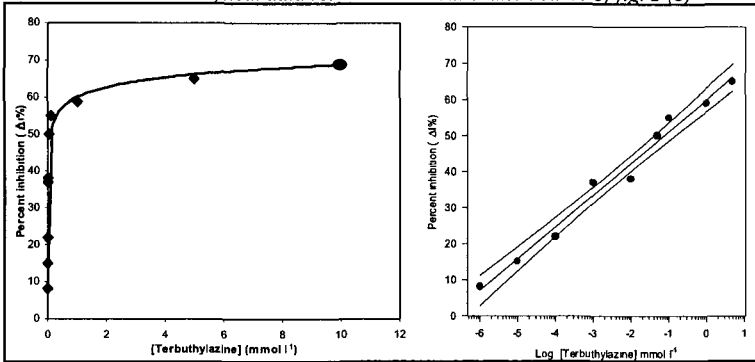


Fig. 3 - (a) Calibration curve (terbutylazine) in water-saturated chloroform, and (b) the same calibration curve data as in (a), transferred to a semilogarithmic scale.

$$y = (4.2 \pm 2.1) \text{Log}(x) + (62.3 \pm 8.8)$$

$$r^2 = 0.9527 \quad (1 - \alpha) = 0.90 \quad t = 2.447$$

x = concentration (mmol l<sup>-1</sup>) ; y = percent inhibition (ΔI%)  
 Linear range from 2.0 x 10<sup>-6</sup> mmol l<sup>-1</sup> to 10 mmol l<sup>-1</sup>.  
 LOD = 1.0 x 10<sup>-6</sup> mmol l<sup>-1</sup>  
 "Pooled SD%" = 8 %

Tab 2. Analytical data relative to the calibration curve of fig. 3 (b)

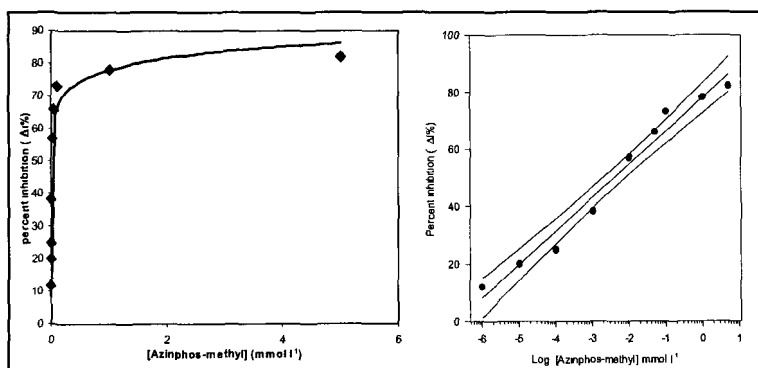


Fig. 4 - (a) Calibration curve (Azinphos-methyl) in water-saturated chloroform, and (b) the same calibration curve data as in (a), transferred to a semilogarithmic scale.

$$y = (4.9 \pm 1.3) \text{Log}(x) + (108.1 \pm 10.9)$$

$$r^2 = 0.9797 \quad (1 - \alpha) = 0.90 \quad t = 2.446$$

$x = \text{concentration (mmol l}^{-1}\text{)} ; y = \text{percent inhibition } (\Delta I\%)$   
 Linear range from  $2.0 \times 10^{-6} \text{ mmol l}^{-1}$  to  $5 \text{ mmol l}^{-1}$ .  
 LOD =  $1.0 \times 10^{-6} \text{ mmol l}^{-1}$   
 "Pooled SD%" = 9 %

Tab 3: Analytical data relative to the calibration curve of fig. 4 (b)

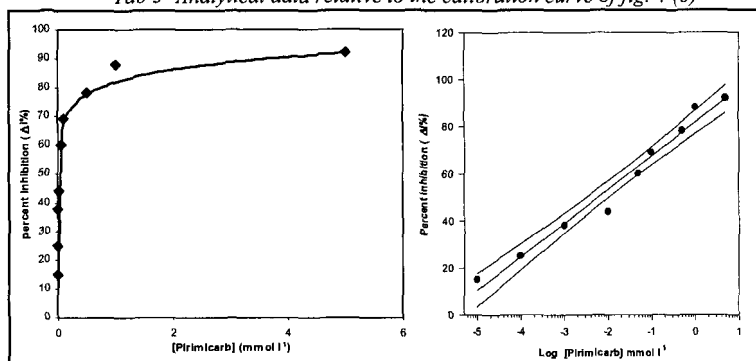


Fig. 5 - (a) Calibration curve (Pirimicarb) in water-saturated chloroform, and (b) the same data of calibration curve in (a), transferred in a semilogarithmic scale.

$$y = (6.2 \pm 0.5) \text{Log}(x) + (81.8 \pm 8.6)$$

$$r^2 = 0.9739 \quad (1 - \alpha) = 0.90 \quad t = 2.356$$

$x = \text{concentration (mmol l}^{-1}\text{)} ; y = \text{percent inhibition } (\Delta I\%)$   
 Linear range from  $2.0 \times 10^{-5} \text{ mmol l}^{-1}$  to  $5 \text{ mmol l}^{-1}$ .  
 LOD =  $1.0 \times 10^{-5} \text{ mmol l}^{-1}$   
 "Pooled SD%" = 11 %

Tab 4: Analytical data relative to the calibration curve of fig. 5 (b)

#### 4 Conclusion

The results obtained indicate the complete validity of the method. The tyrosinase biosensor, in the inhibition OPEE configuration, allowed triazine, benzotriazine and carbamate pesticides to be determined when operating in organic solvent (chloroform), in which the pesticides tested are much more soluble than in water.

Also in this case the results using the same operating procedure as in the case of the inhibition OPEE based on the bienzymatic pair butyrylcholinesterase + choline oxidase [12, 13] were completely positive, while as solvent, instead of the water-saturated chloroform/hexane mixture (50% v/v), previously used for the butyrylcholinesterase + cholinase oxidase OPEE, this time only water saturated chloroform was used in view of the good solubility of the substrate (phenol) in this solvent.

#### References

- [1] Besombes J.L., Cosnier S., Labbé P., Reverdy G. (1995), *Anal. Chim. Acta* 311: 255-263.
- [2] McArdle A., Persaud K.C. (1993), *Analyst* 118: 419-423.
- [3] Mazzei F., Botrè F., Lorenti G., Simonetti G., Porcelli F., Scibona G., Botrè C. (1995), *Anal. Chim. Acta* 316: 79-82.
- [4] Campanella L., Cocco R., Sammartino M. P., Tomassetti M. (1992), *Sci. Tot. Environ.*, 123/124: 1-16.
- [5] Campanella L., Achilli M., Sammartino M. P., Tomassetti M. (1991), *Bioelect. Bioenerg.*, 26: 237-249.
- [6] Campanella L., Colapicchioni C., Favero G., Sammartino M. P., Tomassetti M. (1996), *Sens. Act. B* 33: 25-33.
- [7] Campanella L., Favero G., Sammartino M. P., Tomassetti M. (1994), *Talanta* 41: 1015-1023.
- [8] Campanella L., Favero G., Sammartino M. P., Tomassetti M. (1998), *Talanta* 46: 595-606
- [9] Campanella L., Bonanni A., Martini E., Todini N., Tomassetti M. (2005), *Sens. Act. B* 111-112: 502-514.
- [10] Campanella L., Dragone R., Dalina L., Martini E., Tomassetti M. (2005), *Anal. Bioanal. Chem.* (in press).
- [11] Lee K.H., Koketsu M., Choi S. Y., Lee K.J., Lee P., Ishihara H., Kim S.Y. (2005), *Chem Pharm. Bull.*, 53(7): 747-749.
- [12] Campanella L., De Luca S., Sammartino M. P., Tomassetti M. (1999), *Anal. Chim. Acta* 385: 59-71.
- [13] Campanella L., Persi L., Sammartino M.P., Tomassetti M., Zannella S. (2000), *Ann. Chim.* 90: 35-49.

#### Acknowledgments

This work was funded by FIRB (Fondi di Investimento per la Ricerca di Base) - Bando 2001 "Microsensori e nanofiltri per il controllo di aggregati di molecole e di microrganismi in fase liquida: applicazione alla potabilizzazione dell'acqua".

# **DNA-BASED PIEZOELECTRIC BIOSENSOR FOR Human Papilloma Virus (HPV) DETECTION**

D. Dell'Atti, M. Minunni\*, S. Tombelli, M. Mascini  
*Università degli Studi di Firenze, Dipartimento di Chimica, e-mail  
corresponding author: [minunni@unifi.it](mailto:minunni@unifi.it)*

A. Cavazzana, M. Zavaglia, G. Bevilacqua  
*Università degli Studi di Pisa, Dipartimento di Oncologia, dei trapianti  
e delle nuove tecnologie in medicina*

## **Summary**

HPV infection is one of the most common diseases sexually transmitted. HPV DNA is present in all the lesions associated to cervical cancer.

The aim of this work is the development of piezoelectric DNA biosensors to detect viral DNA as an alternative method respect to traditional diagnostic techniques based on cytological screenings (PAP TEST) or on molecular biology tests.

## **1 Introduction**

The carcinoma of the uterine cervix is the second most common type of cancer worldwide among women [1]. In the European Union more of 25000 new cases are diagnosed each year (3.8% of all women neoplasia) with a mortality rate near to 50% [2]. Molecular and epidemiologic studies have provided unequivocal evidences of a tight link between the cervical carcinoma and the infection with Human Papilloma Virus (HPV).

HPV is a double-strand DNA virus that belongs to the papovavirus family. More than 200 HPV types have been identified and at least 80 different HPV genomes have been sequenced. Moreover 30 HPVs are associated at cancer and they are subdivided in low and high risk to develop the uterine cervix carcinoma. Low-risk HPVs (6, 11) generate benign lesions or warts and high-risk HPVs (16, 18) have potential to progress into cancer. Traditionally, the conventional method to detect the presence of the virus is the PAP TEST, but this cytological screening has some limitations such as reading errors of cytological preparation. Moreover it is a prognostic method since it supplies only a data of the actual situation of the organ. Today it is common to support the cytological screening

with techniques of molecular biology in order to detect directly the viral DNA (PCR ELISA assay, HPV DNA test, Hybrid Capture assay).

The aim of this work was to develop DNA piezoelectric biosensors to detect HPV and its genotypes. DNA piezoelectric biosensors are rapid, inexpensive, label free analytical methods and they could represent a promising alternative to current HPV DNA screening technologies. Three DNA biosensors have been developed and optimized. Two biosensors were designed in order to obtain a device for simultaneous detection of different HPV genotypes. The target sequences mapped into the gene for L1 region (viral protein) of the viral capsid. The first biosensor was developed using a 11-mer probe common to all the genotypes. The second one has a 31 bases probe which consists of a conserved region coincident with the 11-mer probe and a “degenerated” region. This latter consists in a mixture of probes differing only in few bases, able “to catch” and hybridise to different HPV genotypes. In particular the 31-mer probe was chosen aiming to the detection of: 6, 11, 16, 18 and 33 strains, the most interesting strains for screening. The last developed biosensor was specific for HPV 18, that is considered a high risk genotype. The hybridisation reaction was first studied with synthetic oligonucleotides and biosensors were optimised in the main analytical parameters.

## 2. Materials and methods

9.5 MHz AT-Cut quartz crystals (14 mm) with gold evaporated (42.6 mm<sup>2</sup> area) on both sides were purchased by International Crystal Manufacturing (USA). The measurements were conducted in a methacrylate cell where only one side of the crystal was in contact with the solution. The quartz crystal analyser used for the measurements was the QCMagic analyser by Elbitech (Marciana, Livorno, Italy).

The reagents for the probe immobilisation are: 11-mercaptoundecanol from Sigma (Milan, Italy), Dextran 500 from Amersham Biosciences (Uppsala, Sweden), (+)/-epichlorohydrin and *N*-hydroxysuccinimide from Fluka (Milan, Italy). Ethanol and all the reagents for the buffers were purchased from Merck (Italy).

Two different buffers were used: immobilisation buffer (NaCl 300 mM, Na<sub>2</sub>HPO<sub>4</sub> 20 mM, EDTA 0.1 mM, pH 7.4) and hybridisation buffer (NaCl 150 mM, Na<sub>2</sub>HPO<sub>4</sub> 20 mM, EDTA 0.1 mM, pH 7.4). Oligonucleotides were purchased from MWG Biotech (Milan, Italy). The base sequences of the 5'-biotinylated probes and of the complementary targets are shown in the table 1.

<i>PROBE</i>	<i>SEQUENCE</i>
HPV 18 "20bases"	5'biotin-TTC TAC ACA GTC TCC TGT AC-3'
HPV31 deg "31bases"	5'-biotin- ttt gtt act gt(gt) gt(at) gat ac(ct) ac (at) cgc agt a-3'
HPV11 "11bases"	5'-biotin -ttt gtt act gt-3'
<i>TARGET</i>	<i>SEQUENCE</i>
HPV 18 "20bases"	5'-GTA CAG GAG ACT GTG TAG AA-3'
HPV31 deg "31bases"	5-tac tgc g(at)g t(ag)g tat c(at)a c(ac)a cag taa caa a-3'
HPV11 "11bases"	5'- aca gta aca aa -3'

*Tab1.*

***Probe immobilisation:*** Before the immobilisation of the probe, the crystals were washed in a boiling solution of H<sub>2</sub>O<sub>2</sub> (30%), NH<sub>3</sub> (30%) and milliQ water in a 1:1:5 ratio for ten minutes and then rinsed with milliQ water. The biotinylated probe was immobilised via biotin-streptavidin binding on the gold sensor surface previously modified with thiol/dextran/streptavidin as reported in Tombelli et al. [3].

***Hybridisation reaction:*** Once the probe was immobilised on the gold surface, the hybridisation reaction with synthetic oligonucleotides in hybridisation buffer solution was conducted by adding to the sensor cell 100 µL of the oligonucleotide solution at different concentrations in the range 0.06-1 µM. The reaction was monitored for 10 minutes, the solution was then removed and the surface washed with the same hybridisation buffer to eliminate the unbound oligonucleotide. After each cycle of hybridisation, the single stranded probe on the crystal surface was regenerated by 1 min treatment with HCl 1 mM solution.

### 3. Results and discussion

The biotinylated probes were successfully immobilised on the sensor surfaces and this was in agreement with our previous work conducted with different biotinylated probes [3, 4].

Three calibration curves with synthetic oligonucleotides were obtained using respectively the 31-mer probe and 11-mer probe, able to detect the HPV presence.



The results are shown in figure 1. It is clear that the highest signal was recorded when the 31-mer probe hybridises the target with higher molecular weight, 31-mer target (calibration curve A). The lowest signals were observed when the 11-mer probe hybridises the target with lower molecular weight, 11-mer (calibration curve C). In between the hybridisation signals obtained with 11-mer probe and target 31-mer (calibration curve B) were found.

Moreover a calibration curve was also obtained for biosensor HPV18, using the HPV 18 probe (calibration curve D). (Figure 2).

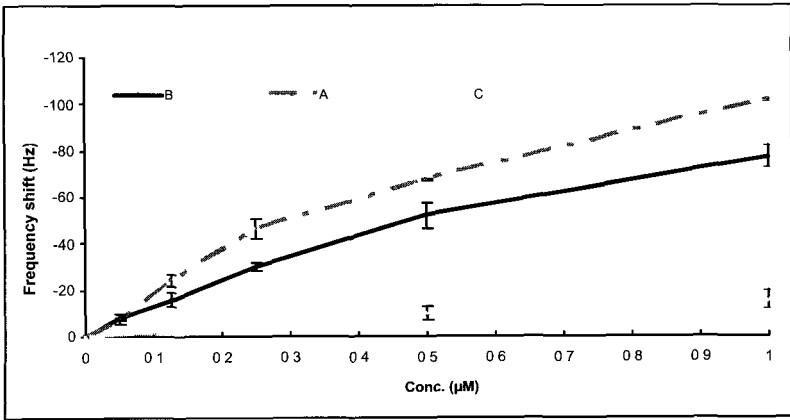


Fig. 1: Calibration curves obtained respectively with: A) probe 31mer- target 31mer, B) probe 11mer-target 31mer; C) probe 11mer-target 11mer

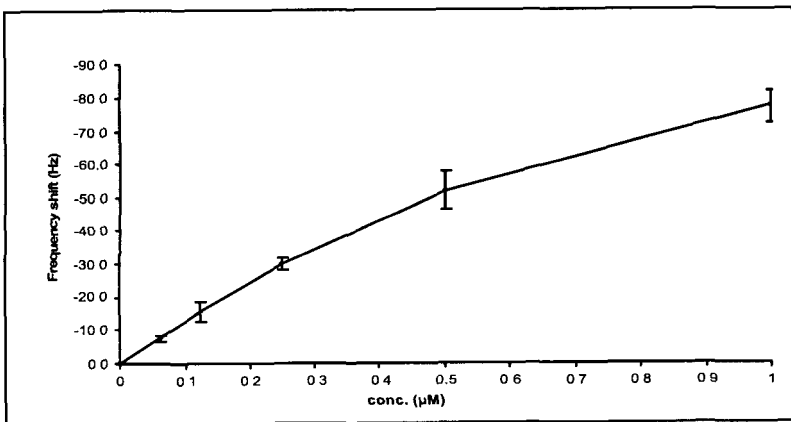


Fig. 2: D) Calibration curve obtained with probe specific for HPV 18 and its complementary target. Concentration range: 0.06-1µM.

For each sensor the specificity was tested adding 1  $\mu\text{M}$  26-mer solution of non-complementary sequence, used as negative control. No remarkable hybridisation signal was obtained, in accordance with the specificity of the sensors (shift  $<3$  Hz). Reproducibility, expressed as average coefficient of variation ( $\text{CV}\%_{\text{av}}$ ), was evaluated for the different sensors. The  $\text{CV}\%$  values are respectively: calibration curve A 10%, calibration curve B 20%, calibration curve C 28%, calibration curve D 11%. The measurements were always repeated in triplicates.

As the best results were obtained when the 31mer probe was immobilised (calibration curve A,  $\text{CV}\%_{\text{av}}$  10%), this biosensor was chosen for the simultaneous detection of different HPV genotypes.

#### 4. Conclusion

The developed sensors optimised with synthetic oligonucleotides demonstrated the possibility to obtain an HPV biosensor able to detect the virus presence and, eventually to biosensor to perform also the relative genotyping, by coupling it to a second biosensor specific for HPV 18 genotype.

Future work will be directed in testing these biosensors with real samples such as amplified DNA (by polymerase chain reaction) extracted from scraping, aiming to demonstrate the potentialities of these devices as an alternative method with respect to screening technologies currently in use. The application of such devices will be first as qualitative screening for the virus presence (yes or not HPV) by using the degenerated 31-mer probe common to all the genotypes; then if the first answer is positive for the virus presence, further HPV genotyping with the relative specific biosensor to apply in series to the first one will be performed. We have here shown the HPV 18 successfully applied. Biosensor development for the second high risk genotype for cervical cancer (HPV 16) is in progress.

#### References

- [1] Parkin DM, Bray F, et al. *Int J Cancer* 2001, 94:153-156
- [2] Black RJ, Bray F, et al. *Eur J Cancer* 1997 33: 1075
- [3] Tombelli, S., Mascini, M., Braccini, L., Anichini, M., Turner, A.P.F., 2000. *Biosens. Bioelectron.* 15 (7–8), 363–370.
- [4] Minunni, M., Tombelli, S., Scielzi, R., Mannelli, I., Mascini, M., Gaudiano, C., 2003. *Anal. Chim. Acta* 481 (1), 55–64

# User Friendly Electrochemical Hand-Held Device For Durum Wheat Safety

Michele Del Carlo, Marcello Mascini,  
Dario Compagnone  
*Department of Food Science, University of Teramo, Teramo*  
mdelcarlo@unite.it

Angelo Visconti  
*Institute of Sciences of Food Production, ISPA-CNR, Bari*

## Summary

In this report we describe the development of an integrated device for different analytes threatening durum wheat safety. Particularly we have developed diverse electrochemical biosensors, based on screen printed electrodes for the detection of organophosphate pesticides (dichlorvos and pirimiphos methyl), toxins (ochratoxin) and PCR amplified DNA from *Fusarium culmorum*. All the analytes were detected below the maximum residue level, when established by the European Union. A dedicated software was also developed to simplify the implementation of the procedure and data interpretation.

## 1 Introduction

Durum wheat safety is affected by different threats comprising both abiotic and biotic agents. Organophosphorus compounds (OP) are widely used in agricultural practices. They inhibit acetylcholinesterase (AChE) [1]. This can lead to clinical implications and high acute toxicity [2]. Among OPs Dichlorvos and Pirimiphos methyl are important for the durum wheat industry [3]. European Union regulation foresees a maximum residue limit (MRL) for dichlorvos in durum wheat at 2.0 µg/g [4-5]. Among biotic agents fungi that produce toxins are a widespread threat. *Fusarium* species, (e.g *Fusarium culmorum*) are universal fungal contaminants of cereals [6]. Their early identification is crucial in order to avoid crop losses and protect consumer health. Other fungi belonging to *Aspergillus* and *Penicillium* species can contaminate cereals resulting in a possible contamination with ochratoxin A (OTA). Recently, the European Commission fixed the maximum levels for OTA at 5 µg/kg in cereals.

In this report we describe the application of biosensors to the determination of such contaminants in durum wheat samples. All the reported applications have been developed using a PalmSens hand-held potentiostat (PalmSens, Amsterdam, The Netherlands). Finally, a dedicated software was also developed in order to enable the end user to carry out the different analysis regardless his technical training and skills.

## 2 Detection procedures

### *Screen printed electrochemical sensors for dichlorvos and pirimiphos-methyl*

Both the determination reported rely on the inhibition activity of OPs pesticides towards AChE combined with the electrochemical detection of choline at a modified screen printed choline oxidase biosensor. Standard and sample extract solutions were analyzed: first, a blank sample extract was measured, and then the current of either the standard or the sample extract was measured. The inhibition was calculated as:  $I(\%) = 100 \cdot (I_0 - I_i)/I_0$ .

### *Screen printed electrochemical sensors for the detection of ochratoxin*

Competitive electrochemical enzyme-linked immunosorbent assays based on disposable screen printed electrodes have been developed for quantitative determination of ochratoxin A (OTA).

Indirect and direct format of immunosensors based assay were developed. 6  $\mu$ l of OTA-BSA in buffer (indirect) and 6  $\mu$ l of goat IgG (anti-mouse IgG) (direct) in buffer were dispensed on the screen printed working electrodes, PVA solution was used to block the surface. 6  $\mu$ l of OTA monoclonal antibody were added to the electrode surface for 30 min at room temperature. Binding or competition was run with 6  $\mu$ l of OTA-AP conjugate or conjugate + standard for 30 min at room temperature. Washing was then carried out. The activity of the label enzyme was measured electrochemically by addition of 100  $\mu$ l of substrate solution (5 mg/ml 1-naphthyl phosphate in DEA buffer; prepared daily), for 2 min at room temperature. The product, 1-naphthol, was detected by DPV.

### *Screen printed electrochemical sensors for the detection of Fusarium sp DNA*

DNA electrochemical sensors were developed for the detection of specific sequences of *Fusarium Culmorum*. The sensing principle of the application was based on the affinity interaction between complementary strand of nucleic acids: the probe was immobilised on the sensor surface and the target was free in solution. The hybridisation was measured using square wave voltammetry (SWV). The label-free detection was done by monitoring the guanine oxidation peak. This approach rely on the use of inosine-modified (guanine-free) probes. In fact, the non electroactive base inosine still forms a specific base-pair with the cytosine residue. This results in a flat baseline for the probe-modified electrode. The hybridisation was detected by the appearance of the guanine oxidation peak of the target sequence. The specificity of the genosensors was tested.

## 3 Results

Two different extraction approaches have been optimised for dichlorvos: the former using whole wheat kernels and aqueous extraction and the latter using

grounded samples and hexane extraction. A typical electrochemical signal as obtained by the instrument is shown in figure 1.

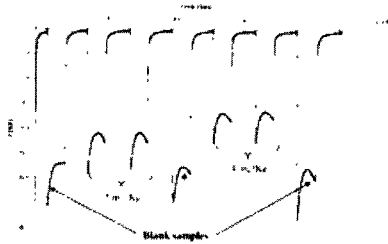


Figure 1: typical chronoamperogram obtained in the inhibition assay

In the first approach, the method was calibrated both in buffer and durum wheat extract. The detection limits in durum wheat samples were 0.45 mg/kg for the eeAChE and 0.07 mg/kg for rAChE. These characteristics allowed the detection of contaminated samples at the legal maximum residue limit, which is 2 mg/kg. Moreover fortified samples of durum wheat were obtained with both dichlorvos and the commercial product Didivane, which contains dichlorvos as active molecule. At all the tested levels, the occurrence of contaminant was detected with an average recovery of 75%. The total assay time, including the extraction step, was 30 min. Samples (n=55) fortified at different levels (4, 2, 1, and 0.5 mg/kg) were extracted and analyzed with the proposed electrochemical assay using both eeAChE and rAChE. The incomplete recovery (75%) may be due to concurrent causes, such as the use of whole kernels as sample, water-based extraction solvent, and adsorption exerted by the matrix.

In order to apply the electrochemical method to ground wheat samples, as generally required in food analysis, a nonaqueous extraction solvent was required. To perform electrochemical analysis with the choline oxidase biosensor, dichlorvos needed to be transferred to PBS solution, thus avoiding any electrochemical interference by organic solvents. Therefore, the filtered hexane extract was submitted to liquid-liquid partitioning with PBS and the upper organic layer was removed by evaporation. Dichlorvos was easily measured in ground wheat by electrochemical bioassay at levels as low as 0.05 µg/g. The mean recoveries of dichlorvos ranged from 97 to 108%, RSDr values ranged from 5.5 to 7.8%, and RSDR values ranged from 9.9 to 17.6%. A good correlation between dichlorvos concentrations obtained by electrochemical biosensor and GC analysis was also found ( $r=0.9919$ ).

The electrochemical assay for the detection of AChE inhibitors above outlined has been also optimised for the detection of pirimiphos methyl in durum wheat. A procedure for the oxidation of pirimiphos methyl via N-bromosuccinimide (NBS) and AChE inhibition was optimised in buffer solution for reagents concentration and inhibition time. As a compromise, between

analytical performance and overall assay length, a 10 min. incubation of NBS and AA and 30 min. AChE incubation was selected. Calibration were performed both in buffer and in sample extract. The intra electrode CV was between 1.6 and 15.0, the inter electrode CV% was between 4.6 and 15. The detection limit (LOD) was 38 ng/mL, and the I50% was 360 ng/ml. The calibrations were slightly affected by the sample matrix resulting in a increased LOD (65-133 ng/ml) and I50% (640-1650 ng/ml). Spiked samples were prepared at the EU regulated level (5 mg/Kg) and analysed resulting in a recovery of 70.3%. Competitive electrochemical enzyme-linked immunosorbent assays based on disposable screen printed electrodes have been developed for quantitative determination of ochratoxin A (OTA). The assays were calibrated using monoclonal antibodies in the direct and indirect format. OTA working range, I50 and detection limits were 0.05-2.5  $\mu\text{g L}^{-1}$  and 0.1-7.5  $\mu\text{g L}^{-1}$ , 0.35  $\mu\text{g L}^{-1}$  and 0.93  $\mu\text{g L}^{-1}$ , 60  $\mu\text{g L}^{-1}$  and 120  $\mu\text{g L}^{-1}$  in the direct and indirect assay format, respectively. The immunosensor in the direct format was selected for the determination of OTA in wheat. Samples were extracted with aqueous acetonitrile and the extract analyzed directly by the assay without clean-up. The I50 in real samples was 0.2  $\mu\text{g L}^{-1}$  corresponding to 1.6  $\mu\text{g/kg}$  in the wheat sample with a detection limit of 0.4  $\mu\text{g/kg}$ . Within- and between-assay variability were less than 5 and 10%, respectively. A good correlation ( $r = 0.9992$ ) was found by comparative analysis of naturally contaminated wheat samples using this assay and an HPLC/immunoaffinity clean-up method based on the AOAC Official Method 2000.03 for the determination of OTA in barley.

As long as concern DNA detection 4 different probes were used to obtain 4 sensors that were tested for selectivity and specificity with synthetic sequences and PCR samples. The DNA biosensors were used to test PCR samples. The results exhibited a dose dependent response up to 7  $\mu\text{g/mL}$ , for higher concentrations an hook effect was observed. In order to avoid false negatives a control procedure was introduced. The PCR samples were split in two aliquots, one of which was thermally denatured, for the analysis. It was evaluated that if the denatured/non denatured was higher than 3, the sample were to be considered as positive.

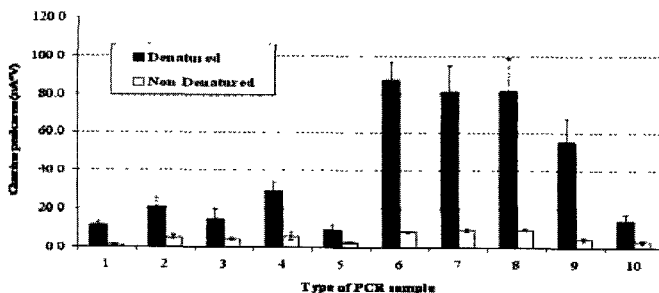


Figure 2: results obtained with one of the selected DNA probes with PCR samples

Particularly, interesting results were obtained using the probes complementary to the region 3 and 4. The screen printed electrode modified with the probe complementary to region 3 exhibited good repeatability (CV within 20% on 3 consecutive measurements) with no measurable analytical signal in the presence of different amounts of non-complementary PCR sample.

#### 4 Dedicated software

The software has an user friendly interface that inform the user on the procedural steps that must be performed (e.g “add 20  $\mu$ l of Vial A to Vial B, mix and transfer on the sensor surface”) allowing the realisation of the measurement even to not-trained personnel. All the internal controls result in a “pass or fail” message as well as all the incubation times are controlled by the software. At the end of every protocols the user receive a screen message that contains an self explanative result via a colour code according to a ‘traffic light scheme’ (Figure 3).

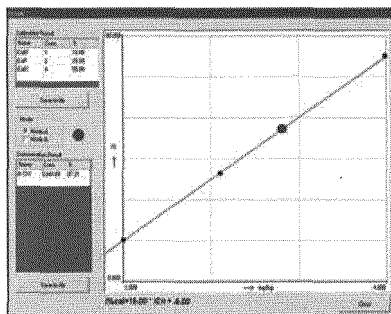


Figure 3: typical software frame obtained with a dichlorvos positive sample

#### References

- [1] U.S. FDA. Pesticide Monitoring Database 1996-1999; <http://www.cfsan.fda.gov/>
- [2] Council Directive 80/778/EEC (OJ L229, p 11, 30/08/1980) of 15 July 1980.
- [3] H. Kidd, D. Hartley, J. Kennedy, Insecticides and Acaricides. In European Directory of Agrochemical Products, 2nd ed.; The Royal Society of Chemistry: London, U.K.,; 3 (1986) 99-247
- [4] Commission Directive 2001/57/EC of 25 July 2001.
- [5] W.J. Donarsky, D.P. Dumas, D.P.Heitmeyer, V.E. Lewis, F.M. Raushel, Archives of Biochemistry and Biophysics, 227 (1989) 4650-4655
- [6] A. Bottalico, G. Perrone, European Journal of Plant Pathology, 108 (2002) 611 –624

#### Acknowledgments

This research was supported by MIUR project no. N12792 472 (SINSIAF)

# Determination of immunoglobulin G in human serum by means of an immunosensor fitted with an enzymatic probe as detector and a Clark electrode as transducer

Luigi Campanella, Elisabetta Martini, Mauro Tomassetti

*Department of Chemistry, University of Rome "La Sapienza", P.le A. Moro 5, 00185 Rome Italy*

luigi.campanella@uniroma1.it;mauro.tomassetti@uniroma1.it

## Summary

A new immunosensor is developed to measure human immunoglobulin G. The method is competitive in the heterogeneous phase and separative. The greatest novelty lies in the use of a tyrosinase biosensor as detector and a Clark electrode as transducer. The enzymatic marker is alkaline phosphatase. Using this new immunosensor it was possible to determine anti-HIgG up to a concentration in the order of  $10^{-11}$  mol l<sup>-1</sup>. The present note makes a detailed analytical comparison between this new immunobiosensor and a similar potentiometric detection immunosensor proposed by us in a previous work.

## 1 Introduction

In previous work [1] we constructed and characterized an electrochemical immunosensor for the determination of antibodies of human immunoglobulin G, i.e. anti-HIgG (human anti-immunoglobulin G). This immunosensor was based on a potentiometric gaseous diffusion electrode for NH<sub>3</sub> as transducer and a polymeric membrane overlapping the head of the electrode, on which human immunoglobulin G (HIgG) was immobilized. Furthermore, urease was used as enzyme marker for the antibody (anti-HIgG). The immunosensor was characterized by a limit of detection (LOD) of  $5 \times 10^{-8}$  mol l<sup>-1</sup> and by a linearity interval between  $9 \times 10^{-8}$  and  $6.5 \times 10^{-6}$  mol l<sup>-1</sup> of anti-HIgG. We are currently continuing this investigation, above all by developing a measuring system with a lower limit of detection. For this purpose a pre-concentration system by immunoprecipitation was initially developed, which, although tedious, successfully attained the goal set with an LOD of  $10^{-11}$ - $10^{-12}$  mol l<sup>-1</sup>. The potentiometric immunosensor method was then used to determine immunoglobulin G in human serum. It was found however that the presence of urea in the serum can be the cause of a small but non negligible interference, especially at low immunoglobulin G concentrations. To overcome this problem we then constructed a completely different and highly innovative immunosensor that used the alkaline phosphatase enzyme as marker, sodium phenylphosphate as substrate and a tyrosinase biosensor as detector. In this case the transducer was a Clark type amperometric electrode. Clearly the construction geometry of



this kind makes the immunosensor extremely selective. After optimizing the 'competitive' measurement procedure also in this case, it was used to determine the anti-HIgG, with a LOD comparable to the one described above for the potentiometric measurement using the preconcentration method.

## 2 Experimental

### *Materials and Apparatus*

The amperometric measurements were performed in a 25 ml thermostatted glass cell kept under constant stirring. The Clark electrode was supplied by Amel (mod.332) and the amperometric measures were performed using an oximeter (Amel model. 360), connected to a recorder (AMEL mod. 868). Anti-HIgG phosphatase alkaline conjugated, Anti-HIgG, HIgG and tyrosinase enzyme were supply by Sigma-Aldrich, Immobilon membrane by Millipore, UK.

## 3 Methods

*Method 1 (determination of anti-HIgG with potentiometric immunosensor) (Figure 1)*

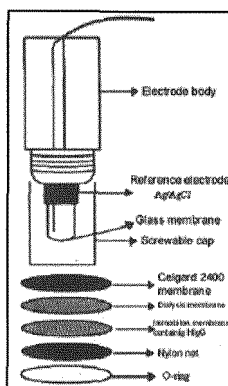


*Fig. 1 – Diagram of potentiometric immunosensor used*

The Immobilon membrane, on which the HIgG was immobilized, was fixed onto the head of potentiometric gas diffusion electrode for  $\text{NH}_3$ . Before measurement, the potentiometric immunosensor was immersed in  $0.1 \text{ mol l}^{-1}$  (pH 8.0), containing 0.05 % Tween-20 by weight and 2.5% BSA by weight (bovine albumin was used to minimize non specific adsorption on the membrane). The anti-HIgG to be determined, together with a fixed concentration of the anti-HIgG urease conjugated in  $0.1 \text{ mol l}^{-1}$  Tris-HCl buffer solution, pH 8.0 was then incubated. The labelled and unlabelled antibody competed to bond with the HIgG present on the membrane. Urea (the enzyme

substrate) was added to the renewed solution, after washing all the anti-HIgG not bound to the HIgG out of the immunosensor using the same buffer. A calibration curve was used to determine the concentration of the unknown anti-HIgG. The sequence followed in measuring the anti-HIgG by this 1st method is schematized in figure 2.

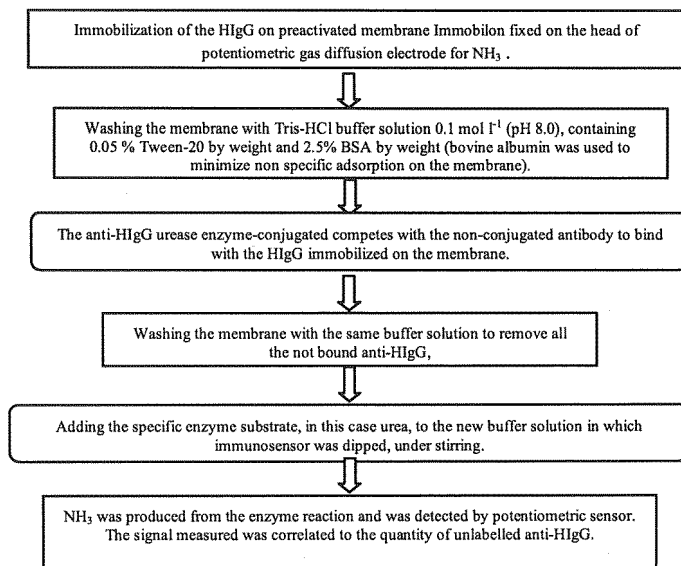


**Fig.2** - Determination of antibody (anti-HIgG) by potentiometric immunosensor, using a  $\text{NH}_3$  electrode as transducer. Test geometry: competition for HIgG immobilized on Immobilon membrane, between anti-HIgG urease conjugated and anti-HIgG non conjugated.

*Method 2 (determination of anti-HIgG with immuno-biosensor) (Figure 3)*

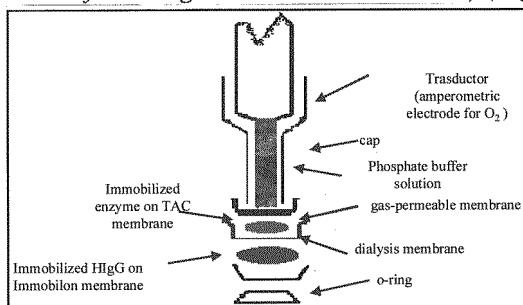


**Fig. 3** – Diagram of immuno-biosensor used

In practice, three membranes were mounted on the head of the electrode, in the following order: gas-permeable membrane, dialysis membrane, TAC membrane with tyrosinase enzyme and Immobilon membrane with HIgG alkaline phosphatase immobilized on it. The membranes were kept in place by a nylon net and an O-ring. Prior to measurement the immuno-biosensor was

dipped into a Tris-HCl buffer solution,  $0.1 \text{ mol l}^{-1}$  (pH 8.0), containing 0.05 % Tween-20 by weight and 2.5% BSA by weight (bovine albumin was used to minimize non specific adsorption on the membrane). The anti-HlgG to be determined was then added together with a fixed concentration ( $0.1 \text{ mol l}^{-1}$ ) of alkaline phosphatase conjugated anti-HlgG to the Tris-HCl buffer solution, pH 8.0. The enzyme-conjugated antibody competes with the non-conjugated antibody to bind with the HlgG immobilized on the membrane. After washing with the same buffer solution to remove all the unbound anti-HlgG, the specific enzyme substrate, in this case sodium phenyl-phosphate, was added to the new buffer solution in which the immunosensor was dipped, under stirring. The measured signal correlates inversely with the quantity of anti-HlgG to be measured. A calibration curve was constructed and used to determine the unknown concentration of anti-HlgG contained in the sample. The sequence for measuring the anti-HlgG by this 2nd method is schematized in figure 4.

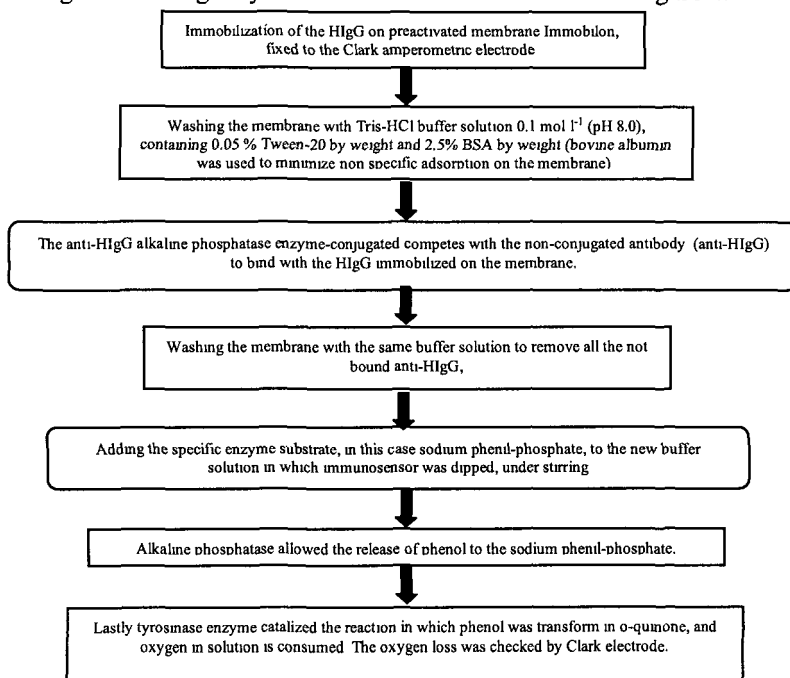


**Fig. 4** - Determination of antibody (anti-HlgG) by immuno-biosensor, using a Clark electrode as transducer and a tyrosinase biosensor as detector. Test geometry: competition for HlgG immobilized on Immobilon membrane, between anti-HlgG alkaline phosphatase conjugated and anti-HlgG non conjugated.

#### 4 Results and discussion

Figures 5 and 6 respectively show the semilogarithmic diagram calibration curves obtained for the determination of the anti-HlgG with the potentiometric immunosensor (fig. 1) and the immuno-biosensor (fig. 3). Table 1 compares the

principal analytical data for anti-HlgG determination obtained using both the potentiometric immunosensor developed in the preceding work [1] and the amperometric immunosensor that uses a tyrosinase biosensor proposed in the present research. The linearity range is about two decades for the potentiometric immunosensor and one and a half decades for the immuno-biosensor. The limit of detection is shifted three decades lower for the immuno-biosensor compared with the potentiometric immunosensor.

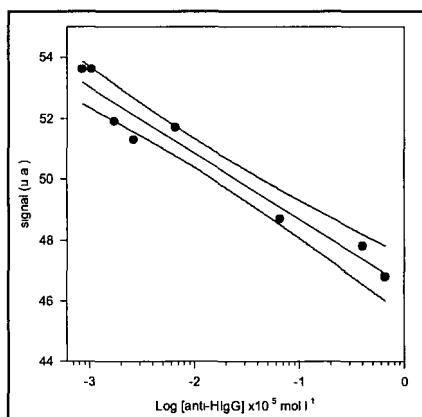


Fig. 5 - Calibration curve and confidence interval for the anti-HlgG. Potentiometric immunosensor response as a function of growing anti-HlgG concentrations using the Immobilon membrane.

Methods	Determination of Anti-HlgG by means of potentiometric immunosensor. Geometry of the test: competition between free anti-HlgG, conjugated with urease and not conjugated, for the HlgG immobilized on the membrane of immunosensor	Determination anti-HlgG by means of immuno-biosensor, that uses as detector a tyrosinase enzyme sensor. Geometry of the test: competition for the HlgG, immobilized on the membrane, between the anti-HlgG conjugated with the alkaline fosfatase and not conjugated, both free in solution.
Employed Membrane	Immobilon	Immobilon
Regression equation ( $Y = a.u.$ , $X = mol\ l^{-1}$ ) level of confidence ( $1 - \alpha = 0.95$ ;	$Y = -0.99 (\pm 0.06) \log X + 46.2 (\pm 0.7)$ ( $n - v = 6$ ; ( $t = 2.26$ ))	$Y = -0.86 (\pm 0.04) \log X + 1.33 (\pm 0.02)$ ( $n - v = 7$ , ( $t = 2.36$ ))
Linear range ( $mol\ l^{-1}$ )	$(0.08 - 6.6) \times 10^{-6}$	$(0.26 - 13) \times 10^{-10}$
Correlation coefficient	0.9510	0.9831
Repeatability of the Measurement (as pooled SD%)	5.9	4.2
Low detection limit (LOD) ( $mol\ l^{-1}$ )	$0.04 \times 10^{-6}$	$0.13 \times 10^{-10}$
Instrumental response time (minutes)	50	20
Lifetime (number of successive measures)	3	2-3

Table 1 - Analytical characterization and comparison of immunosensor methods for determining anti-HlgG which respectively use as transducer a potentiometric sensor for  $NH_3$  and an amperometric gas diffusion sensor for  $O_2$  (i.e. tyrosinase biosensor as detector).

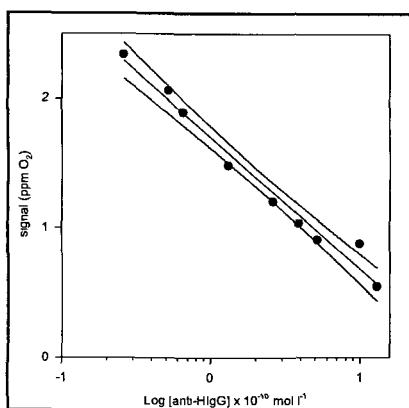


Fig. 6 - Calibration curve and confidence interval for the anti-HIgG. Immuno-biosensor response as a function of growing anti-HIgG concentrations using the Immobilon membrane.

## 5 Conclusions

With the new amperometric immunobiosensor, which uses a tyrosinase biosensor as detector, the limit of detection is about three decades lower than the potentiometric immunosensor. Immunoglobulin G detection using the immunobiosensor also displays a better precision  $RSD\% = 4.2$  instead of 5.9 and an enhanced correlation coefficient for the calibration curve.

Human serum	Found immunoglobulin G concentration ( $\text{mol l}^{-1}$ ), without urea addition	Experimental $\Delta\%$ after 0.5 ml urea $10^{-2} \text{ mol l}^{-1}$ addition (using immunobiosensor)	Experimental $\Delta\%$ after 0.5 ml urea $10^{-2} \text{ mol l}^{-1}$ addition (using potentiometric immunosensor)
Diluted 1:1000	$1.3 \times 10^{-9}$	+2.76	-25.60
Diluted 1:10000	$1.8 \times 10^{-10}$	+1.10	-22.63
Diluted 1:100000	$1.7 \times 10^{-11}$	-0.25	-28.26

Table 2 - Determination of immunoglobulin G in human serum using two different immunosensors and urea interference (as  $\Delta\%$  of immunoglobulin G found before and after urea addition to human serum at different dilution level).

Above all it became possible to determine immunoglobulin G in human serum without the slightest interference by urea or other species contained in the human serum, also at low immunoglobulin G concentration level (see table 2).

## References

- [1]. L. Campanella, R. Attioli, C. Colapicchioni, M. Tomassetti; *Sensors and Actuators B* 55 (1999), 23.

## Acknowledgments

This work was financed by FIRB (fondi di Investimento per la Ricerca di Base)- Bando 2001 "Microsensori e nonofltri per il controllo di aggregati di molecole e di microorganismi in fase liquid: applicazione alla potabilizzazione dell'acqua".

# SPR IMAGING TECHNIQUE: A STUDY ON DNA-DNA BIOLOGICAL INTERACTIONS

*M.G. Manera<sup>1,2</sup>, J. Spadavecchia<sup>1</sup>, R. Rella<sup>1</sup>, A. Leone<sup>1</sup>,*

*<sup>1</sup>IMM - CNR, Via Provinciale per Arnesano, 73100 Lecce,  
mariagrazia.manera@le.imm.cnr.it*

*<sup>2</sup>ISUFI-Istituto superiore di formazione interdisciplinare, Università degli studi  
di Lecce, Viale Gallipoli, 73100 Lecce*

*D. Dell'Atti<sup>3</sup>, M. Minunni<sup>3</sup>, M. Mascini<sup>3</sup>*

*<sup>3</sup>Dipartimento di Chimica, Università degli studi di Firenze, Via della Lastruccia  
3, 50019 Sesto Fiorentino ( Fi)*

## Summary

Surface Plasmon Resonance (SPR) imaging is a label free method that can be used in an array format for the detection of biomolecular interactions. In this work the interaction between oligonucleotide DNA probes, immobilized onto suitable photolithography patterned gold substrates and their complementary strands was monitored by means of changes in the optical properties of the surface. The investigation involved the DNA probe specific for the 35S promoter, a marker of the presence of genetically modified organisms (GMOs).

## 1 Introduction

Surface Plasmon Resonance (SPR) technique is a surface sensitive optical method for the characterization of ultra thin films adsorbed onto gold or other noble metal surfaces [1]. The interaction processes taking place between oligonucleotides immobilised onto suitable photolithography patterned gold substrates and their complementary strands are beginning to assume an important role in biotechnological applications and in particular in the realization of biosensors for specific applications like food control, medicine, environmental control [2]. The possibility to monitor the nucleic acids hybridisation process by a specific experimental set-up allows the detection of a complementary sequence in a sample of unknown DNA, by immobilising a suitable probe [3,4]. Traditional techniques for the analysis of specific hybridisation require the use of

labels, such as radioactive isotopes or fluorescent molecules. They make use of dangerous and expensive reagents, consequently, great attention has been devoted to the development of new, simpler and faster, label free biosensors. Specific variations in mass, generated at the surface of a sensing layer and due to the hybridisation reaction, have been detected by using a quartz crystal microbalance (QCM) as a transducer [5]. Also changes in surface optical properties due to unlabeled DNA hybridisation have been observed by using the surface plasmon resonance technique (SPR) [6]. Our work deals with the use of this latter approach for DNA sensing applications. The surface plasmon resonance phenomenon is the result of the interaction between electromagnetic waves of the incident light and the free electron systems in a conducting surface layer like a metal. The use of SPR technique to probe surface interactions is advantageous, since it is able to monitor any dynamic process occurring at the metal surface, such as adsorption or degradation, rapidly. It can give information on the rate and the extent of adsorption, enabling the determination of dielectric properties, the association/dissociation kinetics and affinity constants of specific interactions.

Two different experimental systems for the excitation of surface plasmons were developed by Otto and Kretschmann. The latter is generally used in the designs of most SPR instruments and it is adopted in this work. The position of the resonance angle is sensitive to the refractive index immediately adjacent to the metal surface. A change in the refractive index of the surface generates different SPR responses. In this paper we describe the preparation of specific substrates for SPR imaging experiments suitable to host sequences of DNA in array configuration. The details of the adopted SPR experimental set-up were already described elsewhere [7]. We have investigated the presence of a target analyte, the P35S oligonucleotides, specific for the 35S promoter, a marker of the presence of genetically modified organisms (GMOs) inserted in the host genome to regulate the transgene expression. The probe 35S was thiolated in 5' and immobilized by self-assembling monolayer technique (SAM) onto gold surfaces. Notwithstanding we are interested in the realization of a specific SPR imaging experimental set-up suitable to observe DNA hybridisation, the DNA sequences adopted in this work being significant in the control of GMOs.

## **2 Experimental**

*Preparation of patterned substrates:* Gold patterned substrates were prepared starting from 25x25 mm<sup>2</sup> SF10 slabs. A Cr/Au (2nm / 50nm) metallic multilayer was deposited on the slabs by e-beam evaporation. An accurate deposition system calibration has been previously performed by using test samples in order to obtain a strict control on the deposited metal thickness to improve SPR evidence. A bright field mask having arrays of circles with different diameter

(from 50 to 200  $\mu\text{m}$ ) has been used to expose a positive photoresist. A 7.5 nm Cr film has been successively deposited on the sample surface and with good arrays have been obtained by the classical lift-off technique. Thiolated oligonucleotide probes (HS-ssDNA) used in our work are 25 mer for GMO (5'-HS-(CH<sub>2</sub>)<sub>6</sub>-GGC CAT CGT TGA AGA TGC CTC TGCC-3'). The oligonucleotide probes were immobilised onto each single gold trap (150  $\mu\text{m}$  in size) by the self assembling monolayer formation (SAM). For this purpose a 5  $\mu\text{l}$  of 1  $\mu\text{M}$  HS-ssDNA solution was prepared (in Na<sub>2</sub>HPO<sub>4</sub> 0,02mM Tris-10mM NaCl buffer, pH 7,2) and droplets of this solution were spotted onto the surface of the realised substrate and left for 2h at room temperature in a humid environment to prevent the spots from drying out. Then the substrate was immersed into a solution of MCH( mercaptoethanol 10<sup>-4</sup>M) for 1h to eliminate the non specific adsorption of the oligonucleotide bases on the gold surface; successively the substrate was soaked in deionised water for some minutes and rinsed with water to remove unbound probes.

*SPR-Imaging apparatus:* SPR studies were performed on a specially designed system exploiting the Kretschmann configuration. In order to obtain SPR images, a collimated beam generated by a LED source ( $\lambda=660$  nm, spectral width  $\Delta\lambda=20$  nm) illuminates the functionalized gold sensor surface which is in contact with the solution, through a coupling prism and under a variable incident angle controlled by a rotating platform. The reflected light is detected at a fixed angle with a CCD camera which produces an "SPR image", then transferred to a computer for analysis. The data could be plotted as spatial intensity maps of the SPR substrate surface, where an increase in intensity indicates an increase in SPR response. SPR image arises from variations in the reflected light intensity from different parts of the sample. These variations are created by changes in the dielectric at the interface with the metal layer; specifically binding of organic matter to the transducer surface increases the local refractive index, allowing to quantify interactions between an immobilised and a free molecular species. The images presents 480x512 raw resolution at 8bpp (grey-scale levels) and were acquired by using a commercial software package (Spiricon Laser Beam Diagnostics). All experiments were carried out at room temperature. The in situ investigated region of the gold surface was about 2x2 mm<sup>2</sup>, which was large enough to monitor several immobilised oligonucleotide probe traps simultaneously.

### 3 Results and Discussion

Figure 1a shows the pseudo-colours SPR image corresponding to a magnification of the region of the sample containing each gold traps after immobilization of the thiolated probes.



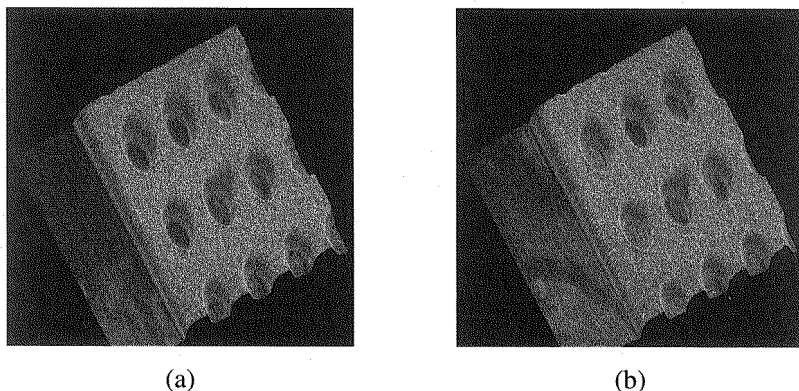


Figure 1: Pseudo-colours SPR-Image of the gold traps after immobilization (a) of the P35S probe and after hybridization of the target sequence with the immobilized P35S probe (b).

Our aim was to obtain SPR images of the array and to monitor the immobilization and hybridisation processes in real time. Consequently, the experimental set-up demonstrates the potentiality of the proposed technique to detect the DNA-DNA interaction and to test a preliminary threshold of sensitivity of this interaction.

An array consisting of the same thio-oligonucleotides probes were immobilized onto all the different gold traps. After the immobilization of the oligonucleotide probes, the biochip was placed in a suitable cell (75  $\mu$ l in volume). The efficiency of the immobilized active probes was tested in dynamic liquid phase in order to demonstrate the hybridization process taking place with the complementary strand present in the injected solution. Figure 1b puts in evidence the variation in the SPR image morphology (variation in the grey-scale levels inside the gold traps) of the investigated region of the sample after twenty minutes from the immersion in a flow of buffer solution containing the DNA target.

Each step involved in the biosensing process has been followed by SPR measurements in conventional scanning angle configuration and by imaging methods.

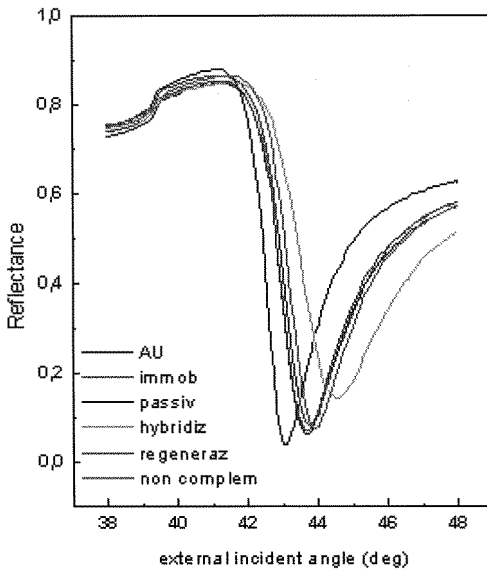


Figure 2: Scanning-angle SPR measurements of each step of the biosensing process.

Figure 2a reports the scanning-angle SPR measurements related to each step; the immobilization of the probes onto the Au substrates results in a shift toward higher angles of the minimum of the SPR curve as predicted by the SPR theory, when a layer is adsorbed onto the metal film. A second step, is the surface passivation, conducted with the mercapto-ethanol solution to eliminate any possible aspecific adsorption onto the gold surface. The passivation step gave a negligible shift in the SPR curve reported in Figure 2. Finally the hybridisation reaction with complementary target was performed and, in this case, it results in a shift of the resonance minimum toward higher values, demonstrating that the surface binding between the probe and its complementary sequence causes an increase of the refractive index and thickness of the layer above the metal film. Afterwards, the regeneration process performed to dissociate the hybrid proba-target allowing a second measurement cycle on the same surface, causes the dissociation of the target leaving the surface and then, consequently, the return of the SPR minimum to smaller angles. Finally a negative control, consisting in non complementary DNA oligonucleotides, was injected into the cell. No significant signal was observed in this case as shown in Figure 2 and in Figure 3.

Figure 3 shows the SPR images relative to the mentioned steps (immobilisation, hybridisation, regeneration, negative control injection). The change in reflectance (represented by a change in colours), can be observed at each step; the variations are due to the different chemical processes occurring at the gold metal surfaces, demonstrating that different events can be monitored by this SPR imaging technique.

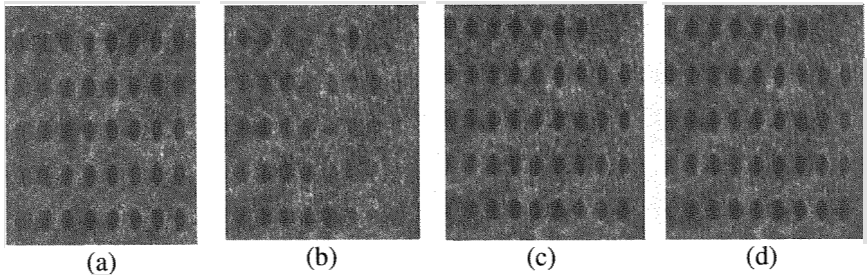


Figure 3: SPR images acquired after: (a) probe immobilization in buffer solution; b) hybridisation in buffer solution; c) regeneration; d) negative control with a non complementary target.

Figure 4 reports the Absolute Difference image at grey-scale levels of the images recorded after and before the hybridisation reaction, in order to roughly evaluate how the hybridisation process occurs. In other words, the activity is performed to estimate the binding of the target sequence and its distribution in each well. In order to improve the qualitative process of measurement of the hybridisation effect, an automatic procedure has been used to align the input images allowing the correct evaluation of the absolute difference. On the other hand, by using the proposed automatic calibration tool, a generic pixel at location  $(i,j)$  in the image obtained before hybridisation is exactly related to the corresponding pixel in the image evaluated after the hybridisation. This step is crucial since just one offset pixel in the absolute difference gives rise to apparent faults during the interpretation of the output image. The code for the evaluation of the absolute difference image has been developed in MathWorks Matlab<sup>®</sup> 7 (Figure 4) with Image Processing Toolbox 5.2.

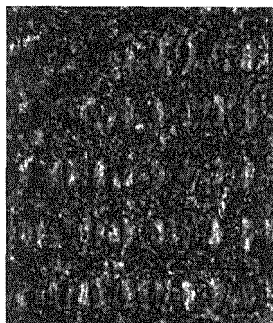


Figure 4: SPR difference image :  $\text{abs}(\text{post binding image} - \text{after binding image})$ .

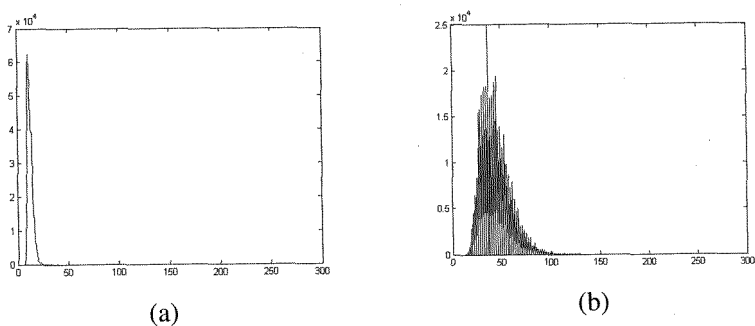


Figure 5: Histogram at gray-scale levels of the (a) immobilization image and (b) hybridization image.

Figure 5 shows histograms of grey-levels (a global operator) related to images acquired before (a) and after (b) hybridization. We can note that the image acquired after hybridization presents a shift in the grey-levels distribution demonstrating the occurrence of the binding event. The presence of variations in the distribution of the images demonstrates that the reflectance of the surface increases; this phenomenon is due to the binding events of the target sequence to the immobilized probe according to the previous qualitative considerations.

## Conclusions

A SPR- based platform has been used in order to obtain images of self assembled thio-oligonucleotides onto suitably patterned gold surfaces. The detection of hybridization events of complement DNA (target) onto the surface-immobilized DNA (probes) has been realized. The hybridization resulted in an increase in the local index of refraction, which in turns led to a change in the reflectivity from the surface that is monitored by a CCD camera. This work demonstrated the potentiality of the SPR imaging technique, complementary to the scanning SPR apparatus, in monitor in situ DNA adsorption onto noble metal surfaces. Important controls are included to test for non-specific binding of target DNA to the substrate and to verify that the observed DNA/DNA interactions are sequence specific.

## Acknowledgments

The authors are grateful to F. Casino and C. Martucci for technical assistance during the realization of the experimental set-up.

## References

- [1] J. Homola, S.S. Yee, G. Gauglitz, *Sens.Actuators B* 1999, 54, 3-15.
- [2] K. L. Beattie, W. G. Beattie, L. Ming, S. L. Turner, R. Coral-Vazquez, D.D. Smith; P.M. McIntre, D.D Dao., *Clin Chem.*1995, 41(5), 700-706.
- [3] V. Dugas, G. Depret , Y. Chevalier, X. Nesme, E. Souteryand, *Sensors and Actuator B: Chemical*(2004) B101(1-2),112-121
- [4] T. Livache, E. Maillart, N. Lassalle, P. Mailley, B. Corso, P. Guedon, A. Roget, Y.Lavy *Journal of Pharmaceutical and Biomedical Analysis*, 32 (2003) 687,
- [5] F. Caruso, E. Rodda, D. N. .Furlong, K., Niikura, Y. Okahata, *Anal. Chem.* 69 1997, 2043-2049.
- [6] Christina Boozer, Qiuming yu, Shengfu Chen, Chi-Ying lee, Jiri Homola, Sinclair S.Yee, Shaoyi Jiang, *Sensors and Actuators B* 90 2003, 22-30.
- [7] R. Rella, J. Spadavecchia, M.G. Manera, P. Siciliano, A. Santino, G. Mita. *Biosensors and Bioelectronics*, 20(2004) 1140-1148.

# LAB-ON-CHIP INTEGRATED GENETIC ANALYSIS

R.Aina, G.Barlocchi, M.Cattaneo, P.Corona, A. Fischetti, M.Marchi,  
U. Mastromatteo\*, M. Palmieri, M. Pesaturo, F. Villa, A. Vinay

*STMicroelectronics, Via Tolomeo, 1- 20010 Cornaredo (MI)*

## Abstract

STMicroelectronics has leveraged its long-standing experience in microfluidics and silicon integration of miniaturized components to address the growing demand for fast, convenient and low cost DNA analysis: the result is the *In - Check* product platform, the first commercial chip that combines the capability of different common laboratory instruments into a single, self-contained unit. The ST platform is based on a silicon chip that integrates all the functions needed to identify given oligonucleotide sequences in a sample, including microfluidic handling, a miniaturized PCR reactor and a custom microarray. The chip is mounted on a plastic slide that provides the necessary mechanical, thermal, electrical and fluidic connections. In addition to the slide itself a dedicated set of instruments is provided: users outside the traditional lab setting can easily be trained and operate the platform to generate molecular diagnostic information where it is most useful. Due to a fast time-to-answer, portability and panel of probes, the *In-Check* platform is particularly suited for diagnostic applications in which it is useful to simultaneously screen a number of sequences. Additional pathogens can be added to a panel without any additional cost.

## 1. Introduction

Genetic assay have an enormous scope of applications in biotechnology and medicine, ranging from agriculture and farming to the detection of pathogens in foods to genetic diagnostics on human subjects. Recently, there has been much interest in the implementation of microfluidic devices for genetic tests. Genetic analysis, in fact, are powerful technology drivers and excellent candidate applications for miniaturization technologies because the demand for inexpensive genetic information is essentially unlimited, and the cost and time for the diagnostic decrease with sample volume. In addition, since manufacturing techniques are similar to those used for conventional integrated circuits it is

possible to leverage four decades of know-how and use existing production facilities; besides genetic assay can benefit from the automation and control provided by miniature electronic devices.

To address the growing demand for fast, convenient and low cost DNA analysis STMicroelectronics has leveraged its long-standing experience in microfluidics and silicon-based integration of miniaturized components: the result is the *In-Check* product platform, the first commercial chip that combines the capabilities of different common laboratory instruments into a single, self-contained unit.

Here in the following a full description of *In-Check* product platform is given.

## 2. *ST In -Check Platform Technology*

The heart of “In-Check platform” is a **silicon chip** that integrates all the functions needed to identify given oligonucleotide sequences in a sample, including microfluidic handling, a miniaturized PCR reactor consisting of a bank of twelve triangular channels, each 150-by-200  $\mu\text{m}$ , buried in silicon and a custom microarray. The chip is mounted on a 1”x 3” plastic slide that provides the necessary mechanical, thermal, electrical and fluidic connections. The chip is designed to handle small sample volumes (2-8  $\mu\text{l}$ ), and does not require highly trained personnel to be operated.

The PCR processor can be loaded directly and sealed to prevent evaporation during temperature cycles. Acting as a *fully integrated PCR reactor*, the chip allow users to run fully customized amplification processes. All chemical reactions occur on the biochip and, because the cartridge that carries it is disposable, this technique is free of the cross-contamination risk of conventional instruments. The In-Check platform, based on a silicon lab-on-chip device, *accelerates the PCR speed by at least 3 times*, compared to the same protocol running on a conventional thermocycler. Besides, thanks to the outstanding temperature control of the PCR solution, the In-Check platform ensures an extremely high specificity of the amplified products compare to a conventional thermocycler.

The surface in contact with the fluid are biocompatible and do not inhibit polymerase.

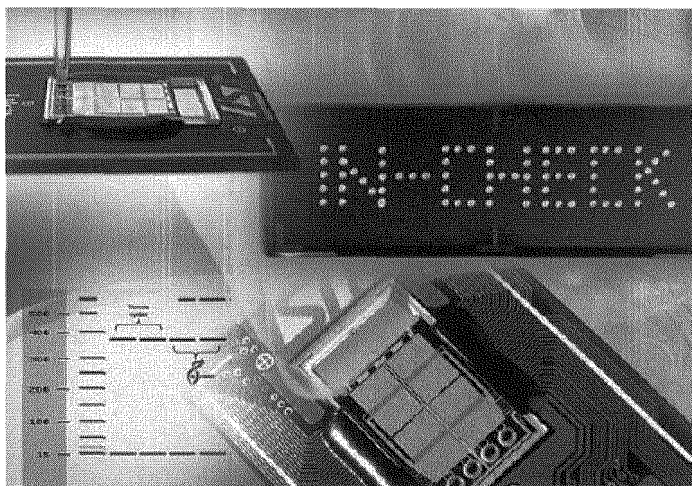


Fig. 1 – Sample is loaded on a chip using a standard micropipette tip. On – Chip PCR results are equivalent to thermocycler in less than 30% of the time and on-board microarray delivers superior contrast and spot definition for reliable data interpretation.

The In-Check chip comprise a **microarray** that is used to **hybridize and detect the amplicons**. Users receive a pre-spotted product ready to perform a given analysis, or can alternatively spot oligos of their choice. The detection is based on standard fluorescent labelling. Up to 200 individual spots allow even some of the most complex diagnostic applications to be placed on the microarray, including control probes and duplicates for redundancy and statistical reliability of data. Single nucleotide mismatches can be detected and will result in a negative outcome on a given spot.

### 3. *ST* In – Check Platform Instruments

The platform Instruments include a Multiplex Thermal Control System and a Compact Optical Reader. The first one is an integrated



compact high precision **Temperature Control System (TCS)** which drives and fully controls the In-Check chip. The TCS is a completely independent modular system that manages up to five different tests and protocols simultaneously.



Fig. 2- LC02 Disposable Card and Compact Optical Reader

Compared to a conventional thermocycler and hybridization station, the user can start the tests independently without having to wait to collect the complete set of samples. Thanks to the ST microcontroller based embedded architecture the temperature accuracy is within  $\pm 0.1\%$ . An interesting feature permits to control the ramping speed during the temperature transition to fully optimize PCR protocols. The system is modular and can be scaled to accommodate the need of both large diagnostic setting and point-of-care applications. The second instrument is a Compact Optical Reader which detects and analyzes the microarray in a few seconds. Autofocus, automatic optics setting and microarray tool analysis make this instrument particularly suited for non trained personnel and point-of-care applications. At the same time, the advanced mode option allows to change the hardware parameters and automatically collect the complete set of spots data to satisfy the most demanding expert user.

#### **4. ST In – Check Platform: The Present Applications and Next Evolution**

Today due to a fast time-to-answer, portability and panel of probes, the In-Check platform is particularly suited for diagnostic applications in which it is useful to simultaneously screen a number of sequences. Additional pathogens can be added to a panel without any additional cost. Moreover, the simplification of operations needed, the self-contained nature of the chip and the reduced footprint of the instrumentation make it an ideal platform to develop Point-of-care applications.

For the future the goal is to integrate in the current platform the functional block for sample preparation. In order to include in a silicon Lab On Chip this functional block it has been developed a device based on dielectrophoresis (DEP) able to sort, isolate and burst target cells from clinically relevant samples. Although the physics may appear complex, the technology needed to accomplish DEP is straightforward and relatively inexpensive.

Because the DEP force is proportional to two independent terms, it is possible to exploit this versatility applying appropriate electrical signals to the electrodes and so optimize each application in accordance to the dielectric characteristic of the particles. The developed device has been designed for the separation of white blood cells in a diluted row blood sample and then lead these cells in an electroporation section to perform lysis for the genetic information extraction.

#### **References**

- K.B.Mullis et al. “ The Polymerase Chain Reaction “ Boston, MA: Birkhauser,1994.
- G.Barlocchi, P. Corona, U. Mastromatteo, F.F.Villa : “ *Silicon Micromachining for Lab On Chip* “ .Sensors and Microsystems 5<sup>th</sup> Italian Conference - Lecce, Italy, 12-16 February 2000.

# Use of Cavitands as Selective Adsorbing Materials in GC-like Air Quality Monitoring Microsystems

S. Zampolli, I. Elmi, G.C. Cardinali, M. Severi  
CNR – IMM Bologna, Italy, [zampolli@bo.imm.cnr.it](mailto:zampolli@bo.imm.cnr.it)  
E. Dalcanale, P. Betti

*Dipartimento di Chimica Organica e Industriale, Università di Parma, Italy*

## Summary

The use of cavitands as innovative pre-concentration materials for outdoor air quality monitoring applications was studied. With respect to conventional adsorbing materials, cavitands feature lower desorption temperatures and a selective pre-concentration behaviour due to the specificity of the host-guest interactions. These characteristics make them particularly suitable for integration in simplified GC-like gas sensing systems based on micromachined components. The detection limit of a miniaturized GC system with a MOX sensor used as detector will be reported.

## 1 Introduction

Lack of selectivity of Metal Oxide Semiconductor (MOX) gas sensors is one of the major issues in applications where single compounds within complex mixtures must be detected and quantified. Some of the compounds typically found in air quality samples, like e.g. water vapour, though being harmless to population, are present at high concentrations and can vary rapidly with time, producing significant shifts in the response of MOX sensors. Other compounds, like e.g. benzene, are toxic or even carcinogenic at ppb concentrations. Optimization of sensing materials and sensor operating conditions to be used in arrays often allows to reach the selectivity necessary for classification purposes, but quantitative analyses of mixtures are generally not possible.

In previous works [1, 2], the authors have shown how the use of miniaturized silicon micromachined gas-chromatographic (GC) separation columns, combined with innovative injection procedures, can be exploited to increase the selectivity of MOX sensors for quantitative monitoring of ppb-level VOC concentrations in indoor air samples.

For outdoor air quality monitoring applications, the concentrations of benzene, toluene, ethylbenzene and xylene to be quantified are in the sub-ppb range, at least one order of magnitude lower than for indoor air quality. In classical GC analyses, purge-and-trap pre-concentration procedures are often used to increase the quantity of pollutants injected into the analyzing systems, allowing to reach the necessary sensitivities. However, the materials typically used in purge-and-trap configurations (e.g. Tenax®) have several constraints which do not allow their use in simplified micromachined GC systems, like e.g.

the high temperatures necessary for desorption and trap purging and the need for inert desorption carrier gases.

In this work, the use of quinoxaline-bridged cavitands as innovative, selective pre-concentration materials for miniaturized GC-like applications is proposed. Used in purge-and-trap configuration, benzene, toluene, ethylbenzene and xylene are desorbed in air at temperatures lower than 100°C, allowing for the use of simplified injection procedures without the need for carrier gas bottles. The selectivity of the pre-concentration eliminates non-aromatic compounds from the sample mixture, enhancing the effectiveness of the GC separation procedure. Furthermore, by optimizing the desorption kinetics, cavitands are expected to provide selective release of the target analytes at different temperatures, allowing for the combination of pre-concentration and separation effects in a single device.

## 2 Experimental

### 2.1 Cavitands

For this work we have chosen a quinoxaline-bridged cavitand (QxCav) having a cavity of 8.3 Å depth which completely engulfs aromatic guests, providing additional weak CH- $\pi$  interactions with the cavity walls. In particular the complexation properties of QxCav towards aromatic compounds have been demonstrated both in solution [3] and in the gas phase [4].

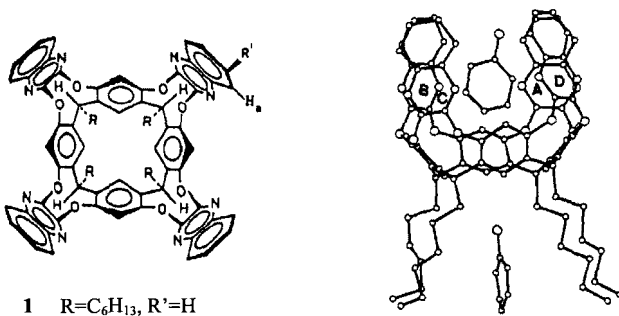


*Fig. 1: sketch and X-ray structure of QxCavC6(1)•PhF (side view)*

Cavitand **1** (see fig. 1) has been prepared following a published procedure [3]. To be used as a trap for purge and trap gas chromatography analysis, the cavitand has been crystallized from acetone and the resulting crystalline powder has been passed through 35-60 mesh sieves to obtain a material having homogenous granulometry.

## 2.2 Characterization of cavitands

The experimental setup used for the characterization of the cavitands is shown in figure 2. A gas distribution system comprising several mass flow controllers connected to certified bottles provides a calibrated mixture of aromatic volatile organic compounds at different concentrations eluted in synthetic air, which is sampled by the cavitands in a purge and trap configuration.

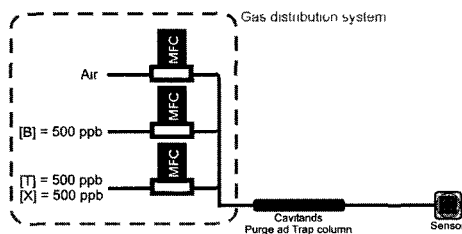


Fig. 2: Characterization system used for cavitand testing

During sampling the cavitands are kept at room temperature. A MOX sensor is mounted in a low-volume chamber and connected to the outlet of the cavitand cartridge. The absorption efficiency of the cavitands is measured by comparing the sensor response in case of a cartridge filled with cavitands with the response in case of an empty cartridge. After a certain sampling time (15 or 20 minutes), the cavitands are heated with a linear temperature ramp from room temperature to 80°C in 25 minutes, and a MOX sensor is used as detector of the released volatiles.

In figure 3a the typical sensor response during absorption of benzene is shown. In red the sensor response in case of an empty cartridge is reported, representing the sensor response to the injection of 20 ppb of benzene for 15 minutes. The black plot represents the sensor response when the cartridge is filled with 54 mg of QxCav in a mesh 35-60. The comparison of these responses clearly shows the high absorption efficiency of the considered cavitands.

In figure 3b the sensor responses during the desorption temperature ramp are compared. The black plot shows the sensor response to the compounds released after a 20 minutes absorption of 20 ppb of benzene, while the red plot refers to the release of a mixture of 5 ppb of toluene and 5 ppb of m-xylene.

As can be disclosed from these plots, in both cases the release has a maximum peak at around 70°C, which is a temperature low enough to be easily implemented in a miniaturized and portable purge and trap system. On the other hand, the temperature at which the release occurs is very similar for all of the considered compounds, therefore the selectivity needs to be enhanced for a reliable quantification of the single aromatic compounds.

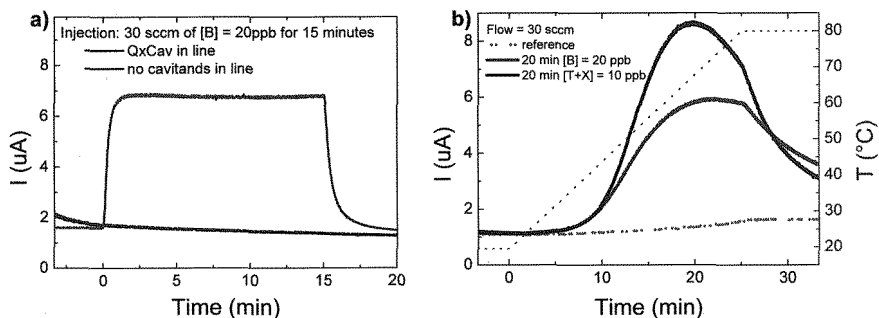


Fig. 3: Cavitants absorption efficiency (a) and desorption kinetics (b)

### 2.3 Increase of selectivity: GC system architecture

To increase the selectivity, a GC-like approach is proposed, as shown in recent publications [1,2]. After the cavitants cartridge, a micromachined GC separation column is inserted before the MOX sensor used as detector (fig. 4). After sampling and release of the volatile organic compounds by the cavitants, the pre-concentrated mixture is separated in time by the stationary phase of the GC column.

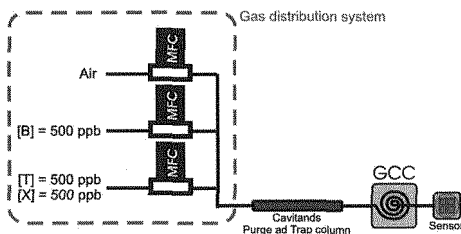


Fig. 4: Selectivity increase: GC separation column

In figure 5a) the chromatograms relative to different concentrations of benzene, toluene and xylene sampled for 25 minutes are shown. While the short GC column used in this case does not allow for a sufficient separation of the toluene peak, the different peak heights for benzene concentrations as low as 1 ppb can be easily disclosed, as shown in the calibration curve in figure 5b.

### 3 Conclusions

The use of cavitants as selective pre-concentration materials in a miniaturized GC like outdoor air quality monitoring was studied. The results show the feasibility of ppb level benzene monitoring using a MOX sensor as detector and a micromachined GC separation column for selectivity

enhancement. The absorption efficiency and desorption kinetics of cavitands are compatible with the integration in a miniaturized system, and micromachining of a cavitand purge and trap cartridge will be investigated. Furthermore the use of new bridging groups for the cavitands will be studied, aiming at selective desorption kinetics of the different aromatic compounds in order to reach a temperature-selective desorption technique without the necessity of a GC separation column.

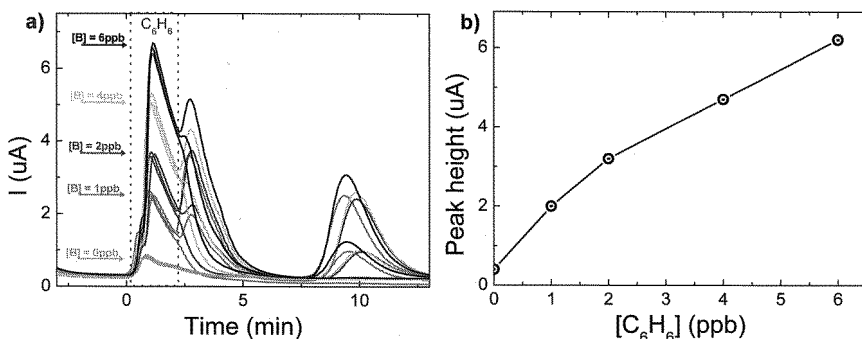


Fig. 5: Chromatograms of different concentrations of benzene in a mixture with toluene and xylene (a) and calibration curve for benzene (b)

## References

- [1] S. Zampolli, S. Nicoletti, I. Elmi, G.C. Cardianali, L. Dori, 9th Italian Conference on Sensors and Microsystems AISEM 2004, Trento, Italy
- [2] S. Zampolli, I. Elmi, J. Stürmann, S. Nicoletti, L. Dori, G.C. Cardinali, *Sensors and Actuators B*, 105 (2005) 400–406
- [3] P. Soncini, S. Bonsignore, E. Dalcanale and F. Ugozzoli, *J. Org. Chem.* 1992, 57, 4608
- [4] M. Vincenti, E. Dalcanale, P. Soncini and G. Guglielmetti, *J. Am. Chem. Soc.*, 1990, 112, 445

## Acknowledgments

This work was funded by the MIUR projects FISIR “Microsistemi per applicazioni ambientali ed agroalimentari” and FIRB RBNE019TMF.

# Fast optical detection of chemical substances in integrated silicon-glass chip

L. DE STEFANO, I. REA, L. ROTIROTI, K. MALECKI AND I. RENDINA

*Institute for Microelectronics and Microsystems – National Council of Research*

*Via P. Castellino 111 - 80131 Napoli*

L. MORETTI, F. G. DELLA CORTE  
*DIMET "Mediterranea" University of Reggio Calabria*

*Località Feo di Vito, Reggio Calabria, Italy*

*[luca.destefano@na.imm.cnr.it](mailto:luca.destefano@na.imm.cnr.it)*

## Summary

In this communication, a silicon-glass microfluidic chip for the realization of optical sensing components in lab-on-chip applications has been demonstrated. The technology of Anodic Bonding, of great importance for the integration of microfluidic functions, has been used for the fabrication of chemical microsensors. A cross injection valve has been integrated with the porous silicon optical transducer on the prefabricated glass wafer with microchannels, so ensuring sample injection into the stream of carrier gas. A pneumatic actuation has been used for the valve control.

The porous silicon (PSi) is the optical transducer material. Due to its porous structure it has a very large specific surface area of the order of  $200\text{-}500\text{ m}^2\text{ cm}^{-3}$ , so that an effective interaction with several substances is assured. The optical read out of the PSi layer has been realized by means of an external optical system. The obtained preliminary results show that very short response time allow to classify this simple analytic opto-chemical chip in the area of advanced sensors for chemical analyzers

## Introduction

There is a compelling need for fully integrated and networked environmental sensor solutions that provide for both early warning type detectors, coupled with sample collection, and confirmatory detectors that can provide accurate species identification. In addition to environmental sensors, the development of easily deployable medical instruments capable of determining whether an individual has been exposed to a biological pathogen and the specific nature of the pathogen are equally critical to the health monitoring. Micro-opto-electrical-mechanical systems (MOEMS) and micro-total-analysis systems have unique features fulfilling these critical needs. The fast and intensive development of lab-on-chip for sensing application is due to several factors essential for routine analytical determinations, such as very limited sample consumption and the short analysis time which can be obtained by measuring a transient signal in a flow-through detector.



The AB technique easily allows the encapsulation and sealing of three-dimensional microfluidic structures, such as channels, chambers, cavities and other complex gas or liquid routes on silicon chips [1-2]. Additionally, glass transparency at optical wavelengths enables simple, but highly accurate, alignment of pre-patterned or structured glass and silicon wafers.

On the other hand, porous silicon (PSi) can be employed as a transducer element due to its sponge-like nanostructure: it is able to effectively interact with several chemicals and biological molecules. On exposure to bio-chemical substances, several physical quantities of the PSi, such as refractive index, photoluminescence, and electrical conductivity, change drastically. In environmental monitoring applications, optical read-out techniques are of particular interest mainly because they do not require electric contacts that may cause explosions or fire in dangerous environment, and also allow wireless remote interrogation. We have recently proposed several PSi optical sensors with monolayer as well as multilayer structure, based on the refractive index change induced in different ways by chemicals (such as hydrocarbons, flammable substances, pesticides, etc.) and biological species (DNA and enzymes) [3-5].

In this work we have joined some typical microelectronic fabrication technologies together with the PSi transducer features and the microfluidic injection of the analytes to realize a new microminiaturized opto-chemical analyzer. The Flow Injection technique is commonly exploited to perform different chemical and biological diagnosis in a wide range of sensing applications. On the other hand, porous silicon is receiving great attention due its sponge-like structure allowing a very effective interaction with several chemicals and biological molecules. Moreover, we have characterized the sensor dynamic by time-resolved measurements on exposure to several volatile organic compounds.

## Experimental results

The scheme of the complete optical microsystem and the read-out experimental set-up is shown in Figure 1.

The reaction micro chamber with the PSi on the bottom was produced by a two-step electrochemical etch of a  $\langle 100 \rangle$  silicon wafer,  $p^+$  type, using an HF/EtOH (30:70) solution. The first step creates a thick sacrificial layer of high porosity PSi which has been completely removed by rinsing the samples in a NaOH solution. The result is an empty chamber into the silicon substrate with depth of 150  $\mu\text{m}$ .

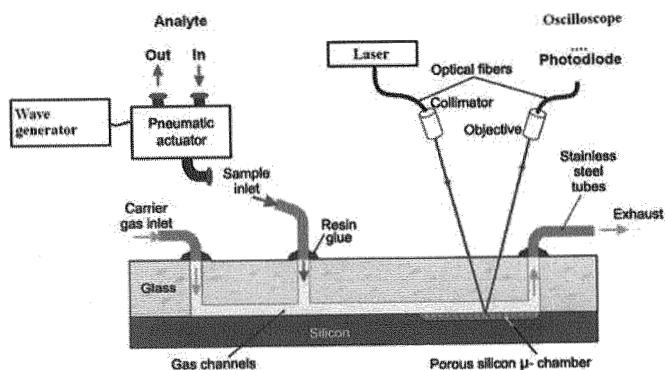


Fig. 1 Scheme of the complete optical microsystem and of the read-out experimental set-up.

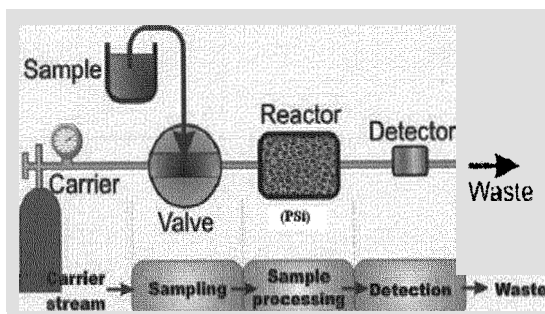


Fig. 2 Scheme of the flow injection analysis principle.

Since the diameter of the porous silicon area is always about 1 cm, the total volume of the analysis chamber is 12  $\mu\text{L}$ . By using a fresh etching HF/EtOH (30:70) solution, without moving the chip from the electrochemical cell, a second etch step (150  $\text{mA}/\text{cm}^2$  for 45 s) produces PSi monolayer on the bottom of approximately 6  $\mu\text{m}$  thickness and a porosity of 70 %.

A Borofloat 33 type glass has been chosen as a chip cover. In order to feed gas or liquid substances, inlet and outlet channels have been mechanically drilled in the top glass wafer, on the opposite sides of the porous region.

In Figure 2 the principle of the flow injection analysis, which is a widespread microfluidic technique in the lab-on-chip world, is shown: a continuous flow of nitrogen carriers the analyte from the tank source into the PSi microchamber which acts both as the reaction chamber, since it allows the capillary condensation of the analyte, and as the detector, since it allows the optical transduction of the gas-material interaction. A pneumatic actuator has been used for the injection valve control. We have optimised the frequency of the valve opening (100 mHz) and the pressure of the carrier searching for the fastest time response of the sensor device.

We have performed time-resolved measurement in order to characterize the sensor dynamic: using the laser beam from an IR source, we have measured, as a function of time, the signal of a receiving photodetector before, during and after the exposure to some organic volatile compounds (Isopropanol, Ethanol and

Methanol). On exposure to the vapours, due to the phenomenon of capillary condensation, the average refractive index of the layer increases, and, as a consequence the optical thickness of the porous silicon layer also increases. The result of a time-resolved measurement is shown in Figure 3: in the case of Isopropanol, we have obtained a response time to the solvent presence which is 156 ms, while the signal returns to its original value in shorter time but always in the order of milliseconds ( $\tau_{\text{rec}}=24$  ms).

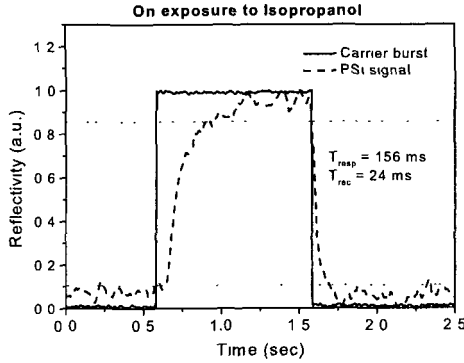


Fig. 3 Time resolved measurement in case of Isopropanol. The optical response and the time reference of the carrier have been shifted for the sake of clarity.

The response time depends not only on the physical phenomena involved (i.e., equilibrium between adsorption and desorption of each substances in the PSi layer) but also on the geometry of the test chamber and on the measurement procedure. In the same experimental way, we have verified the stability and repeatability of the sensor on several pulses of the gas analyte (Fig. 4)

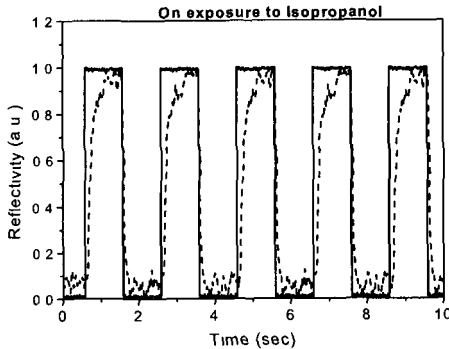


Fig. 4 Repeatability and reversibility of the gas sensing measurements.

## Conclusions

The integration of a PSi sensor element and the micromechanical technologies led to a compact microsystem capable to discriminate very small amount of pure organic compound. A very fast response signal has been observed when a short injection time has been applied to introduce solvents vapors into the system. We have characterized the sensor dynamic by time-resolved measurement during exposure to Isopropanol. The data reveal fast analysis time and the complete reversibility of the sensing mechanism.

## References

- [1] B. Puers, E. Peeters, A Van Den Bossche, A. Sansen, *Sens. Actuat. A*, 21-23 (1990), pp 108-114.
- [2] Ljibisa Ristic, *Sensors Technology and Devices*, pp. 207, 1994.
- [3] L. De Stefano, I. Rendina, L. Moretti, A.M. Rossi, S. Tundo, *Applied Optics*, 43/1, 167-172, 2004.
- [4] L. De Stefano, I. Rendina, L. Moretti, A.M. Rossi, A. Lamberti, P. Arcari, O. Longo, M. Rocchia, *IEEE Trans. on Nanotech.* 3/1, 49-54, 2004.
- [5] L. Rotiroti, L. De Stefano, L. Moretti, A. Piccolo, I. Rendina, A. M. Rossi, *Biosen. Bioelec.* 20/10, 2136-2139, 2005.

# CMOS SINGLE PHOTON AVALANCHE DIODE FOR IMAGING APPLICATIONS

M. Scandiuzzo, D. Stoppa, A. Simoni  
*ITC-irst, via Sommarive, 18, 38050 Povo di Trento, Italy*  
[scandiuzzo@itc.it](mailto:scandiuzzo@itc.it)

L. Pancheri, G.-F. Dalla Betta  
*DIT, Università di Trento, Via Sommarive 14, 38050 Povo di Trento, Italy*

## Summary

This paper reports on a novel distance sensor employing an avalanche photodiode (APD) operating in a single photon counting configuration for Time-Of-Flight 3D imaging applications. An active pixel containing a single photon detector and a read-out channel has been designed. A 64 pixel linear array has been fabricated in a conventional industrial high-voltage 0.8- $\mu\text{m}$  CMOS technology, together with an APD test structure. The pixel size is  $38 \times 180 \mu\text{m}^2$  and the power consumption is  $15 \mu\text{W}$ . A characterization of the sensor is reported.

## 1 Introduction

Recently, three dimensional (3D) measuring systems, known also as range finders, have emerged in many application fields, like safety, surveillance and robotic guidance, where specific patterns obstacles and moving elements should be recognized in real time by using small and cheap systems. Several scannerless range finders based on the time of Flight (TOF) technique have been recently proposed [1,2,3,4]. In order to employ the direct TOF with accuracies in the cm range, high detector sensitivities and picosecond time discrimination capability are needed. Due to its high sensitivity, a Single Photon Avalanche Diode (SPAD) can be a suitable device for direct TOF range finding.

A SPAD is basically an APD biased beyond its breakdown voltage to be operated in the Geiger mode. In this configuration, single photon detection can be achieved, provided that a suitable quenching mechanism is implemented. The feasibility of SPADs in conventional CMOS and BiCMOS technology, as demonstrated in the past few years [5-6], opens the way to the realization of low-cost and high-performance fully integrated systems for high sensitivity imaging.

In this paper a pixel which includes a SPAD and a readout circuit for photon arrival time estimation is proposed. The pixel contains a SPAD, a quenching

circuit, a comparator, an arrival-time estimation circuit and an averaging circuit to increase the distance measurement resolution.

In order to validate the operation principle, a test chip consisting of 64-pixel linear array has been fabricated in a high-voltage 0.8- $\mu\text{m}$  CMOS technology. An electro-optical characterization of the test structures and of the array has been carried out and is presented here. The sub-Geiger responsivity and the dark count rate in the Geiger mode have been measured, assuring the suitability of the device for the application here proposed. Moreover experimental results of 3D images are reported with a precision better than 2mm with only 100 frames averaging.

## 2. Pixel Architecture

The block diagram of the proposed pixel is sketched in Fig. 1a. It consists of a SPAD, a quenching resistor  $R_{\text{quench}}$  to limit the avalanche current, a voltage comparator for the avalanche event detection and an analog time counter, which measures the arrival time of the received light pulse. To reduce the influence of jitter noise and to limit the effect of thermally-generated spurious events, the measurement is repeated many times and the arrival-time information is averaged by means of two circuits dedicated to the count of low and high numbers of events, respectively. In this way the time resolution of the system is increased by a factor  $N_p^{1/2}$ , where  $N_p$  is the number of pulses spread on the scene, but the overall measurement time is kept low because the read-out of the pixel array is not performed at every measurement cycle. This solution becomes of paramount importance as the number of pixels increases.

To avoid the use of high-voltage transistors, expensive in terms of area occupation, the cathode of the SPAD is connected through the quenching resistor to  $V_{\text{dd}}$ , and the biasing above the breakdown voltage  $|V_b| \approx 27\text{V}$  of the SPAD is assured by means of the external line  $V_{\text{spad}}$  biased at a very negative voltage (about -25 V).

## 3. SPAD

A schematic cross section of the fabricated Avalanche Photodiodes is shown in Fig. 1b. In order to avoid edge breakdown, a guard-ring surrounding the p+ implantation has been implemented using a p-tub layer inside a deep ntub available in this fabrication processes. The active area is defined by means of an optical window opened in the metal light shield only in correspondence with the region where avalanche multiplication occurs. The SPADs implemented in the pixels have a circular active area with a diameter of 5  $\mu\text{m}$ .

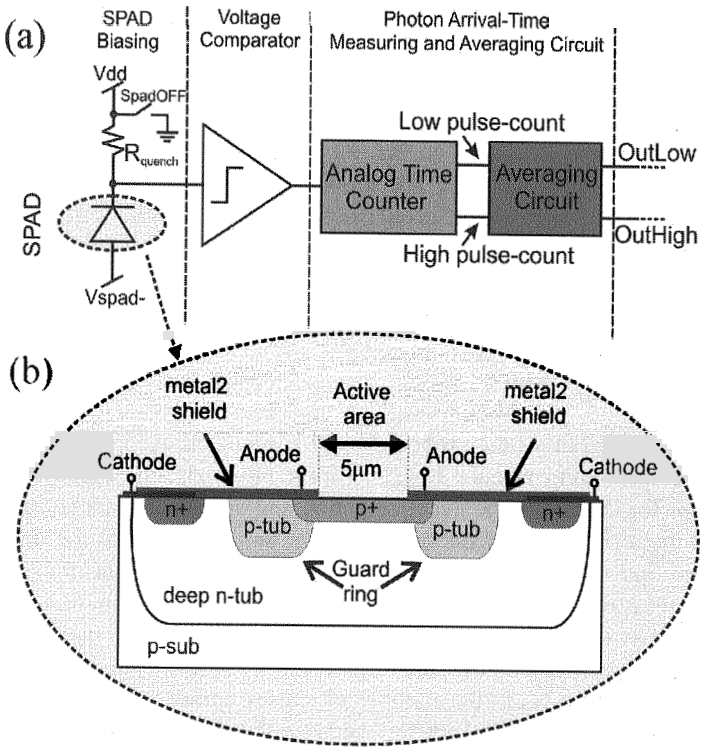


Fig. 1. (a) Pixel block diagram and (b) APD cross section

An APD test structure, having a circular active area with 100  $\mu\text{m}$  diameter, has been fabricated in the same chip, in order to test the characteristics of the device. An electro-optical characterization of the APD test structure has been carried out. The device has a breakdown voltage of 26.8 V at ambient temperature. The spectral responsivity has been measured at room temperature and is shown in Fig. 2 at 0V bias and with a reverse bias just below breakdown voltage. The multiplication gain is about 15 with a 26 V reverse bias voltage at the light wavelength  $\lambda = 550 \text{ nm}$

In order to measure the dark count rate, the APD has been biased with a 200 kOhm quenching resistor, thus obtaining a passively quenched SPAD with about 1  $\mu\text{s}$  dead time. The dark count rate was measured at different temperatures and different excess bias voltages, and its value normalized for the area of the SPAD included in the pixels is shown in Fig. 3. The dark count rate approximately doubles every 10  $^{\circ}\text{C}$ , indicating an SRH dominated dark count.

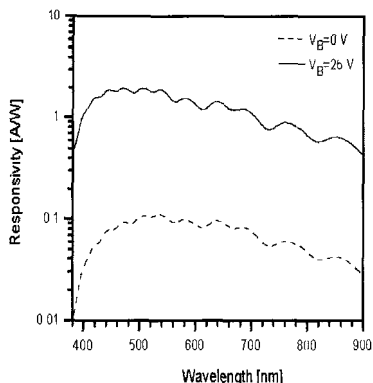


Fig. 2. APD spectral responsivity

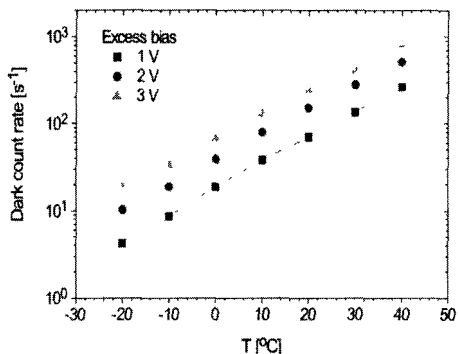


Fig. 3. Dark count rate as a function of the temperature for different excess bias voltages

The reported results indicate that the 5- $\mu\text{m}$  diameter SPAD included in the pixel should have a dark count rate of about 100 Hz at room temperature with 3 V excess bias voltage. This is a very good value, since in a measuring time-window, some tens of nanoseconds long, the probability of having spurious events caused by thermally generated dark counts will be very low.

#### 4. Experimental Results

The distance measurement of a cooperative target in the 2m-5m range, obtained after pixel calibration, exhibiting a precision better than  $\pm 0.75\%$ . This value could be further improved, at the expense of a reduced frame rate, if an external averaging operation is implemented. Extrapolating the achieved experimental results for a 64x64-pixel array would give a resolution of 1mm with a real time operation (30fps) capability.

Preliminary examples of 3D scene acquired through a vertical scanning (64 frames), and illuminated using an uncollimated, 905-nm, 100-ns pulsed laser source having a mean power of about 250mW, is illustrated in Fig. 4. The insets (a-b) shown the intensity map (2D image), while the measured 3-D data, coded both in the z-axis and in grey-level intensity, are represented in the insets (c-d) with two different perspective views. The two objects are placed in front of plane at 50cm from the sensor. It is worth noting that the resolution of the reported 3D images is mainly limited by the preliminary optical setup.



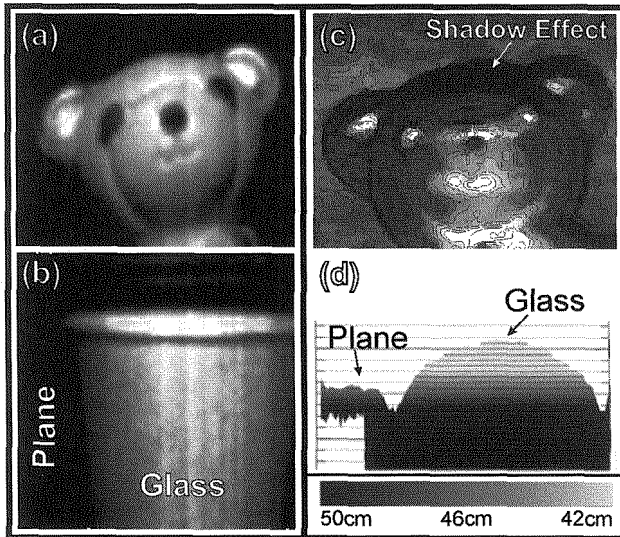


Fig. 4: Examples of 2D and 3D images.

## Conclusion

A novel pixel architecture has been presented, which includes a SPAD and a read-out channel in the same pixel. Besides the SPAD, a dedicated quenching circuit, a voltage comparator for the avalanche detection, a time-to-voltage converter and a filtering stage for the extraction of the mean time value are integrated in each pixel. Experimental results confirm the validity of the design approach. The measurement of non-cooperative targets has been successfully performed with a precision of some millimetres and a pixel-to-pixel uniformity of few centimetres mainly limited by the optical setup used for preliminary tests

## References

- [1] R. Lange, P. Seitz, *IEEE Journal of Quantum Electronics*, 37 (2001), 390
- [2] D. Stoppa, L. Viarani, A. Simoni, L. Gonzo, M. Malfatti, G. Pedretti, *Proc. of European Solid-State Circuit Conference*, (2004), 419.
- [3] R. Jeremias, W. Brockherde, G. Doemens, B. Hosticka, L. Listl, P. Mengel, *ISSCC Digest of Technical papers*, (Feb 2001), 252.
- [4] C. L. Niclass, A. Rochas, P. A. Besse, E. Charbon, *ISSCC Digest of Technical papers*, (Feb. 2004), 120.
- [5] A. Rochas, A. R. Pauchard, P.A. Besse, D. Pantic, Z. Prijic and R. S. Popovic, *IEEE Trans. on Electron Devices*, 49 (2002), 387.
- [6] A. Biber, P. Seitz, H. Jäckel, *IEEE Trans. on Electron Devices*, 47 (2000), 2241.

# Design of a MEMS Test-Structure for Stress Characterization by Capacitive Read-out

Marco Bellei, Roberto Gaddi, Antonio Gnudi

*ARCES-DEIS University of Bologna, viale Risorgimento 2, 40136 Bologna, Italy*  
[mbellei@dcis.unibo.it](mailto:mbellei@dcis.unibo.it)

## Summary

A MEMS (Micro-ElectroMechanical System) test-structure for the characterization of the planar stress induced in structural layer deposition of a surface micromachining process is here presented. A classical rotating needle design has been adopted and extended with electrical capacitive transduction of the rotation angle, in order to allow automated measurements. Moreover, stress extraction is performed by digital fashion, leading to a potential improved robustness versus capacitive parasitics effects. Electromechanical design aspects and preliminary results obtained by finite element simulations are discussed. An average device resolution of  $\pm 18$  MPa has been obtained for the extracted planar stress in a gold structural layer.

## 1 Introduction

It is well-known from planar microelectronics that process steps induce a mechanical stress in deposited layers. Although the film deposition should be stress-controlled for all the layers, in a micromachining process the knowledge of the in-plane stress induced by fabrication is a key aspect especially in structural parts, such as suspended plates and beams. The parasitic effects of an unexpected stress can affect the device performances and sometimes dramatically impair its electromechanical behavior. Several characterization techniques have been proposed. Electrical measurements could be generally less accurate than their alternative counterparts [1,2,3,4,5], but they do not need non standard instrumentations and they are suitable for automated measurements, if an automatic prober is available. Among electrical techniques, three challenging categories have been proposed: electrostatically actuated microstructures [6, 7]; resonating beams (the operation principle of which can be found in [8]); comb-drive microstructures with in-plane displacement and analog capacitive read-out [9]. These methodologies exhibit potential drawbacks due to a quite complex modeling for achieving high accuracy and they are sensitive to process parameters. In addition, the first and the second can be exploited for tensile stress only, while the third extracts the stress in an analog fashion by transducing the strain into small capacitance variations. Moreover, since it exploits sidewall capacitances, it generally requires fabrication process with high-aspect ratio and the structural parts could be sensitive to processes featuring high residual stress gradients.

In this work we would like to introduce a novel methodology for stress estimation based on electrical measurements by avoiding the above-mentioned potential problems. The more interesting potential benefit of the presented test-structure is the digital read-out since good accuracy and precision in the measured capacitance values are not relevant: the fundamental requirement is to discriminate about a threshold value, as in digital electronic circuits.

From a mechanical point of view, it should be noted that the presented device is properly a strain sensor. Nevertheless, since we assume the knowledge of the strain-stress relation under elastic regime, generally we will refer directly to the stress as the unknown parameter.

## 2 Design aspects

We present a test-structure design in which the stress-induced rotation of a classical lancet or needle [10] is measured by digital capacitive detection instead of traditional optical inspection. Figure 1 shows the layout image of the device. After the release step, the residual stress in the suspended structure will induce a strain in the stress beams and thus a clockwise (negative) or counter-clockwise (positive) rotation for compressive or tensile stress respectively. The relationship between rotation angle and planar stress can be extracted by employing a non-linear finite element analysis (FEA) or, for rough estimation, by analytical physical models based on Hooke's law.

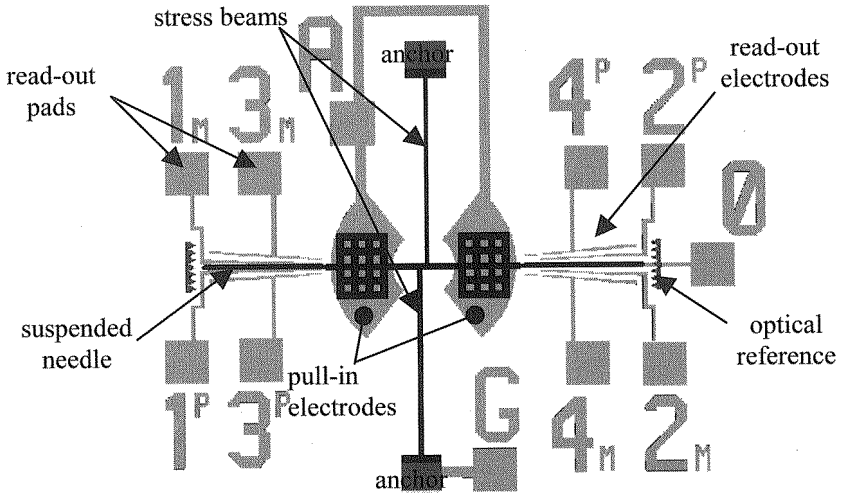


Figure 1 Layout image of the designed test-structure (black: suspended structure; grey: probe pads and underlying electrodes).

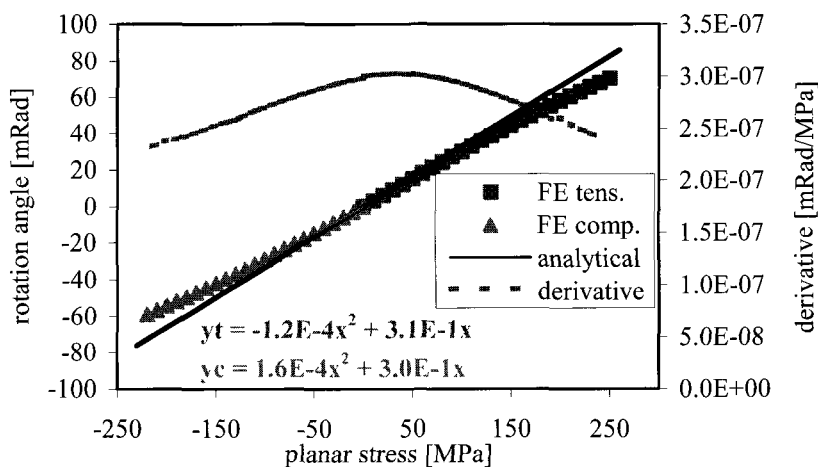


Figure 2 Mechanical response of the test-structure and its derivative. Parabolic fitting functions are also shown both for tensile ( $y_t$ ) and compressive ( $y_c$ ) stresses.

Figure 2 shows the above-mentioned relationship together with its derivative. The decreasing derivative magnitude for increasing values of the stress magnitude is mainly due to the non-ideal hinges which connect the stress beams to the suspended needle. Its stiffness induces an unwanted increased bending of the stress beams for increasing rotations. Thus, the total force induced by stress will have a component also in the lateral direction, which does not contribute to rotation. The structural layer is made of gold and we assume a nominal Young's modulus of 80 GPa and Poisson's ratio of 0.42. For further aspects on the fabrication process, refer to [11]. The stress beams are 265  $\mu\text{m}$  long and 10  $\mu\text{m}$  wide.

The rotation angle has been quantized thanks to  $N$  radial adjacent electrodes alternatively placed under the suspended needle on the left and on the right, as shown in Figure 1. For lowering the quantization error, the electrodes width and distance must be chosen at the minimum size allowed by the fabrication process. By taking into account the maximum rotation angle of  $\pm 80$  mRad consequently obtained given the stress range of interest, a number  $N=9$  can be used. Thus, the discretized rotation angle can be obtained by measuring the nine capacitances between the G pad (connected to the needle) and each of the pads  $\{0, 1^P, \dots, 4^P, 1_M, \dots, 4_M\}$  connected to the read-out electrodes. These capacitances assume a high (H) value for the electrodes located just underneath the needle and a low (L) value for all remaining pads. If a threshold between H and L capacitance values is defined as  $C_{th}=0.25 \times C_{max}$ , where  $C_{max}$  is the maximum capacitance corresponding to the perfect superposition between the suspended needle and a read-out electrode, either one or at most two measured capacitances can assume

the H-state. In the former situation the suspended needle is basically overlapped with one electrode only, while in the latter it features a partial overlap with two adjacent electrodes (left- and right-side placed respectively). In this preliminary design, the capacitance has been modeled as a parallel plate capacitor.  $C_{\max}$  and  $C_{\text{th}}$  must be measured by appropriate reference capacitive structures. After device fabrication, a more efficient methodology for L-H discrimination could be studied and thus adopted.

In order to obtain the best swing between L and H value, a larger capacitance signal in H-state can be obtained by removing the extra air-gap through electrostatic actuation of the suspended structure. For this purpose, two actuation electrodes are introduced (see A pad in Fig. 1). In this situation, a  $C_{\max}$  value of 300 fF has been obtained by FEA. Moreover, we observe that this operation becomes necessary if the suspended layer is affected by high positive stress gradient, since the distance between the long needles and the underlying electrodes could lower the capacitive signal below the parasitics threshold. By finite element electromechanical simulations on the actuated structure affected by stress gradient up to 5 MPa/ $\mu\text{m}$ , we observed a  $C_{\max}$  value down to 90 fF, which is widely acceptable.

### 3 Resolution and read-out table

In the considered stress range, the corresponding rotation angle range is nearly  $80+80=160$  mRad (see fig. 2). Since 8 (+1 for zero stress) electrodes have been used for discretization and partial overlap of two electrodes is also exploited, the angle resolution is  $160/(8 \times 2) = 10$  mRad. By employing the approximated linear characteristic, an average value of nearly  $\pm 18$  MPa can be estimated.

By taking into account the capacitance-discretized angle configurations and the stress-angle non-linear relationship  $\theta = \theta(\sigma)$ , a truth/read-out table can be obtained (Table 3). Since the derivative of the mechanical characteristic is not constant, it is not possible to express the resolution in a compact form and thus stress corresponding to rotation angles has been written as a set of intervals.

Finally, by measuring the nine capacitance values on the read-out pads, we expect to find only one of the considered configurations which corresponds to the unknown planar tensile stress within a certain error.

The maximum rotation angle is imposed by the expected stress magnitude range, with a theoretical limit value here assumed to be approximately  $[-250, 250]$  MPa. Although the stress range observed by wafer curvature is smaller for the gold-alloy deposited by previous electroplating setup of the process [12], a potential wider range could be observed through this structure, if required.

4 <sub>M</sub>	3 <sub>M</sub>	2 <sub>M</sub>	1 <sub>M</sub>	0	1 <sup>P</sup>	2 <sup>P</sup>	3 <sup>P</sup>	4 <sup>P</sup>	$\theta$ [mRad]	$\sigma$ [MPa]
L	L	L	L	H	L	L	L	L	0 ±5	-17÷16
L	L	L	L	H	H	L	L	L	10 ±5	16÷48
L	L	L	L	L	H	L	L	L	20 ±5	48÷79
L	L	L	L	L	H	H	L	L	30 ±5	79÷109
L	L	L	L	L	L	H	L	L	40 ±5	109÷138
L	L	L	L	L	L	H	H	L	50 ±5	138÷167
L	L	L	L	L	L	L	H	L	60 ±5	167÷195
L	L	L	L	L	L	L	H	H	70 ±5	195÷222
L	L	L	L	L	L	L	L	H	80 ±5	222÷248

Table 3 Truth/read-out table of the designed test-structure for the case of tensile stress.

## 4 Conclusions

A test-structure design for residual tensile/compressive planar stress characterization by electrical measurements has been presented. The potential benefits are the robustness of digital extraction, the electromechanical model/design simplicity and thus the reduced sensitivity to technology parameters. Moreover, the possibility of optical inspection can be also exploited. The main drawback is the intrinsic low resolution. Nonetheless, a more complex design based on mechanical amplifications [13,14] can lead to a better resolution. In addition, whenever data on plastic regime will be available after a full characterization of the gold layer, a new study including non-elastic deformation should be performed.

## References

- [1] H.Guckel, etAl., IEEE Trans. on Electron Dev., 35 n. 6 (1988), 800
- [2] W.Fang, J.A.Wickert, J. Micromech. Microeng., 6 (1996), 301
- [3] Y.-H.Min, Y.-K.Kim, J. Micromech. Microeng., 10 (2000), 314
- [4] M.W.Denhoff, J. Micromech. Microeng., 13 (2003), 686
- [5] X.Y.Ye et Al., Sensors and Actuators A, 54 (1996), 750
- [6] K.Najafi, K.Suzuki, IEEE Int Workshop on MEMS '89 (Jan. 1989), 96
- [7] P.M.Osterberg, S.D.Senturia, J. of Microelectromechanical Systems, 6 n.2 (1997), 107
- [8] A.Prak, et Al., J. of Microelectromechanical Systems, 1 (1992), 179
- [9] L.L.Chu et Al., J. of Microelectromechanical Systems, 11 n.5 (2002), 489
- [10] L.B.Wilner, IEEE Solid State Sens. and Act. Workshop (June 1992), 76
- [11] F.Giacomozzi et Al., Workshop on Millimeterwave Comm. MEMSWAVE (July 2004), C25
- [12] B.Margesin et Al., Proc. of DTIP of MEMS&MOEMS (May 2003), 402
- [13] Y.B.Gianchandani, J.Najafi, J. of Microelectromechanical Systems, 5 n.1 (1996), 52
- [14] A.Bagolini, B.Margesin, et Al., Sensors and Actuators A, 115(2004), 494

# Controlling sensing properties of composite polymers using different conductive nanoparticles

Anna Castaldo, Ettore Massera, Luigi Quercia, Girolamo Di Francia

*ENEA Centro di ricerche di Portici Via vecchio Macello, Loc. Granatello, Portici (Na)  
80055*

[Anna.Castaldo@portici.enea.it](mailto:Anna.Castaldo@portici.enea.it)

## Summary

We report on a new class of polymeric sensors based on a properly selected polysilsesquioxane filled with different conductive powders obtained by ball milling. These sensors exhibit excellent sensing properties with respect to both polar and apolar analytes and do not base their operating mechanism on the swelling. In fact, exposure to water molecules or hexane vapours determines an increase of conductivity. In particular the response in the full RH% range for devices obtained with different filler (Zn-Graphite, Zn, Cu) is of four magnitude orders variation between 0% and 100% RH in the conductivity of the sensors.

## 1 Introduction

In the past many papers have appeared in literature describing the use of electronic nose based on array of sensors, each one showing low selectivity, used to characterize analyte mixtures [1]. Often in such devices polymer-carbon black composites have played a very important role in spite of their simple manufacture and cheapness [2]. The mechanism of response in polymer carbon-black composite sensing films is, at its simplest level, based on film swelling. Vapours sorbed in the film cause the film to swell, disrupting conductive pathways by pushing carbon particles apart, thus increasing the electric resistance of the film itself. For the first polymers used in electronic nose applications, chemical functionality was very rarely considered. Clearly, polymer selection greatly depends on the suite of target compounds. If target compounds represent a broad distribution of chemical functionalities, then a broad distribution of polymers should be necessary. Unfortunately the use of a single filler, i.e. carbon black, could preclude the possibility to treat given classes of polymers, due to possible incompatibilities with solvents and dispersing agents for that kind of filler. For this reason we are at present investigating various conductive fillers, e.g. noble metals or alloys intermetallic

compounds, whose processing is compatible with polymers, designed to sense specific analytes, as thioles, or amines.

In this work we consider various different nanometric fillers obtained by mechanical ball milling (BM), starting from graphite, copper, silicon [3] and their alloys. It is important to note that BM permits to obtain nanocrystalline metal alloys with properties that are undoubtedly quite different from equilibrium intermetallics. Moreover, nanoscale in the sensors is known to have an high impact on the performance [4]. Polymers investigated as matrix in this study belong to an emerging class of three-dimensional polyhedral silicon polymers, named polysilsesquioxanes, containing nanosized cages. Such hybrid amphiphilic materials with nano-size interfaces between organic and inorganic domains may offer good opportunities to create composites with unique properties [5], [6], [7]. In particular in this study we use the Poly [(propylmethacryl-heptaisobutyl-POSS)-*co*-(*n*-butylmethacrylate)] shown in Figure 1, whose functionality classification in base to a definition of Ryan and colleague reported in a NASA bulletin on composite for electronic-nose [8] is WD-HBB. Heptaisobutyl and butyl chains grant for a weak dipolar (WD) character, while siloxane and methacrylic group furnish hydrogen-bond basic (HBB) properties. This, in general, makes such a polymer a versatile matrix for polymer composite sensors and, as a matter of fact, excellent sensing properties of a polysilsesquioxane with respect to hydrogen and methane have been already reported [9]. Here, we have investigated the effects of alternative fillers in the same POSS polymer matrix. In particular nano-fillers have been fabricated by ball milling starting from both *n*-type and *p*-type doped crystalline silicon also as graphite-silicon alloys while as far as metallic fillers are concerned, we have already obtained interesting results with copper and zinc submicrometric conductive powders that we have tested vs ammonia and apolar vapours.

### 3 Results and Discussion

The incorporation of the polyhedral oligomeric silsesquioxanes or POSS into polymeric matrices by covalent bonds has received a considerable amount of attention. POSS have a compact hybrid structure with an inorganic core made up of silicon and oxygen  $(\text{SiO}_{1.5})_n$  externally surrounded by organic tails. The interaction between the organic tails and the polymeric matrix controls the POSS degree of dispersion in the medium, i.e. its compatibility and thus the final properties. The feasibility of controlling the arm number, arm length, the arm functionality makes POSS topologically ideal for the preparation of nanocomposite materials. Hybrid materials, second generation composite, have excellent properties, high porosity, very good thermal and mechanical properties, low dielectric constant. Promising candidates for sensor materials, in our opinion, are methacrylate based POSS, versatile matrix for the sensing of



both polar and apolar analytes. On the base of the above reported physico-chemical properties we assumed as starting hypothesis for this work that a similar polymer could swell when exposed to analytes while selectivity could be conferred to the sensor by dispersing in the polymer secondary fillers home made by ball milling techniques, tailored for the best dispersion in the polymer itself.

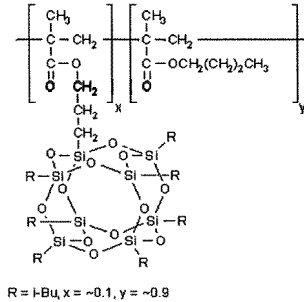


Fig.1 Poly [(propylmethacryl-hepta-isobutyl-POSS)-co-(n-butylmethacrylate)]

We excluded carbon black for the difficulty to obtain good dispersion in the polymer solvent and worked to synthesize carbonaceous nanofillers, like graphitic powder or nanostructured metals like zinc and copper. Figure 2 shows SEM images of some of the fillers used in this study. They are graphite, zinc, copper-graphite. We have synthesized also silicon, silicon-graphite, zinc-graphite submicrometric powders.

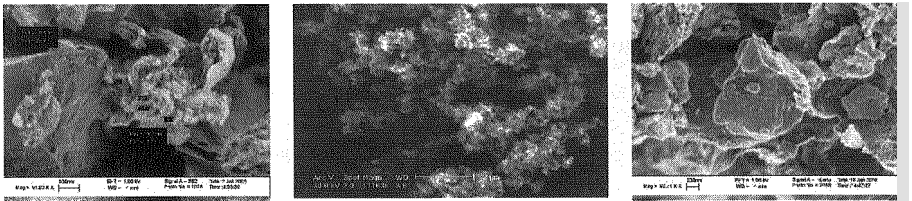


Fig.2 Graphite, zinc, copper-graphite.

Several POSS based nanocomposites with a graphite content ranging between 10% to 20 % in weight were obtained and sensor devices were fabricated by means of spinning deposition on Alumina substrates with interdigitated Au contacts. In Fig.3 the response to water vapour in the 30%-70% range of relative humidity of the device based on a 20% graphite nanocomposite film is reported.

As it is possible to observe, the device response is quite high and the sensor rapidly and reversibly follows RH% variations, increasing its conductivity in presence of water molecules.

This unusual behaviour suggests that sensor device does not work on the swelling mechanism (decrease of conductivity in presence of the analyte). It is important to note that we also tested the POSS without any fillers and even in this case we observed a small increase of its conductivity in presence of water molecules. This furthermore points towards a more complicated mechanism involving POSS cages. In our opinion secondary fillers ameliorate the charge transfer between the cages as it is suggested by the fact that we note that even with metallic filler performance with respect to relative humidity is very good (see Fig.4).

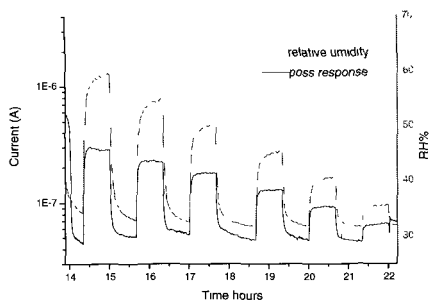


Fig. 3 Device response to RH of the graphite filled POSS

Another interesting aspect of POSS based device is the very large amount of conductivity variation. In Fig. 4 is reported the response in the full RH% range for devices obtained with different filler (Zn-Graphite, Zn, Cu) where the four magnitude orders variation between 0% and 100% RH in the conductivity of the sensors is shown. Sensors devices have been also tested in presence of apolar vapours, like hexane, to verify the versatility of the matrix. In Fig. 5 response to hexane in anhydrous ambient of different devices is reported.

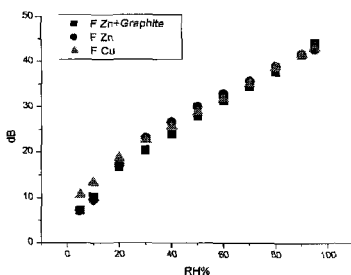


Fig 4 Performance in the humidity sensing of devices in logarithmic scale.

It is possible to observe, even in this case the increase of the conductivity in presence of the analyte.

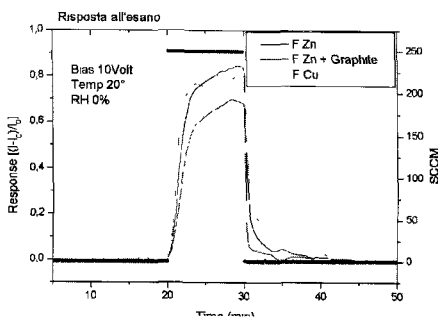


Fig.5 Response to hexane of various devices.

Work is in progress to comprehend operating mechanism of such new class of polymeric sensors.

#### 4 Conclusions

In this work we present polymeric nanocomposite sensors, based on a POSS matrix properly selected and nanostructured compatible fillers, that exhibit excellent sensing properties and could be used in the sensing of both polar and apolar analytes. In particular we obtain new RH% devices with different filler (Zn-Graphite, Zn, Cu), whose conductivity varies of four magnitude orders between 0% and 100% RH.

#### References

- [1] Deisingh A.K., Stone D.C., Thompson M., Intern.J. Food Science and Tech. 39, (2004) 587-604.
- [2] Quercia L.; Loffredo F.; Di Francia G.; Sensors and Actuators B, 109, (2005),153.
- [3] Castaldo A., Di Francia G., Massera E., Quercia L., Fameli G., Delli Veneri P., Book of Abstracts AISEM 2005 p. 53.
- [4] Di Francia G., Quercia L., Rea I., Maddalena P, Lettieri S., Sensors and Actuators B, 111-112, (2005), 117-124.
- [5] Patel RR, Mohanraj, Pittmann CU, Journal of Polymer Science Part B Polymer Physics 44 (1) (2006) 234-248.
- [6] Striolo A., McCabe C, Cummings PT, Journal of Physical Chemistry B 109 (30), (2005), 14300-14307.
- [7] Zheng L., Waddon A. J, Farris R. J., Bryan Coughlin E. Macromolecules, 35, (2005) 2375-2379.
- [8] Ryan M. A. Shevade, A.V., Zhou H., Homer M.L. NASA Bulletin oct.2004 714-719.
- [9] Fujimoto, C. H.; Hickner, M. A.; Cornelius, C. J.; Loy, D .A. Macromolecules (2005) in Press.

# BIOSENSORS BASED ON NANO ELECTRODE ENSEMBLE AND SCREEN PRINTED SUBSTRATES

W.VASTARELLA<sup>a</sup>, M.DE LEO<sup>b</sup>, J.MALY<sup>a,c</sup>, A.MASCI<sup>a</sup>,

L.M.MORETTO<sup>b</sup>, R.PILLOTON<sup>a\*</sup>

<sup>a</sup> *ENEA, SP061, Via Anguillarese 301, 00060 Santa Maria di Galeria, Rome (I)*

<sup>b</sup> *Dipartimento di Chimica Fisica, Università Ca' Foscari, Venice (I)*

<sup>c</sup> *Dep. of Biology, University of J.E.Purkyne, 40001 Usti nad Labem (CZ)*

\* [pilloton@casaccia.enea.it](mailto:pilloton@casaccia.enea.it)

## Summary

Metal nanowires were synthesized according to an electroless deposition method in polycarbonate template, obtaining nano electrodes ensembles with specific features and well defined diameter size. Nano electrode ensembles were coupled with disposable screen printed substrate in order to increase the sensitivity of the commonly used carbon graphite working electrode for electrochemical sensing. Furthermore, working surface modification provided the basis for original protein immobilization procedures that otherwise would not be allowed.

*Abbreviations. ADS: physical adsorption; Au: gold; CA: chrono-amperometry; CYS: cysteamine; FIA: flow injection analysis; GA: glutaraldehyde, GOx: glucose oxidase; l.o.d.: limit of detection; PB: phosphate buffer 0.1M (pH=6.8); PC: polycarbonate; RE: printed Ag/AgCl pseudo-reference electrode; RSD: relative standard deviation, SAM: self-assembled monolayer; SPE: screen printed electrode; SPS: screen printed substrate, WE: working electrode.*

## 1. Introduction

Nanostructured materials have proven as one of the most powerful tools in new technologies and research, due to their absolutely peculiar properties at nanometer size scale. Many studies have shown that optical, mechanical, photo-catalytic and transport properties drastically changes, depending on quantum size effect, as the mean diameter of the particles is in the exciton size regime (i.e. 10nm) [1-6]. Both metallic and semiconductor nanosized materials have found large applications in biochemistry, bioanalytical techniques as well as luminescence, catalysis, optoelectronics and photochemistry [7-10]. The unique chemical and physical properties of metal, oxide and semiconductor nanoparticles make them extremely suitable also for designing new and improved sensing devices, especially electrochemical sensors and biosensors. The important functions of nanostructured particles include the immobilization of biomolecules, the catalysis of electrochemical reactions, the enhancement of electron transfer mechanism between electrode surfaces and proteins, labeling of biomolecules and even acting as reactant. The topic task is still the capability to assemble the biochemical recognizing system on such sensors, by controlling at the same time the surface activation (i.e. using SAM), the chemical-physical modification of the substrate and the immobilization of biomolecules [11-20].

Recently, nanoelectrode ensembles (NEEs) with specific features were synthesized in PC template, according to an electroless deposition method [21-23]. Nanowires of Au were obtained with the expected diameter size (Fig.1) and coupled with carbon SPE. The association of Au NEE with graphite SPS is aimed to couple the high electroanalytical sensitivities, deriving from the nanosized properties, with the feasibility and versatility of screen printing technology in easy to be used sensor fabrications. NEE based sensors and biosensors were electrochemically compared to unmodified carbon or conventional Au SPEs.

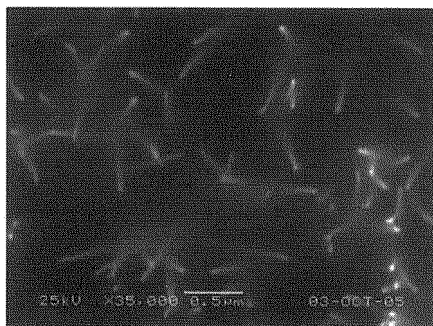


**Figure 1:** Scanning electron microscopy (SEM) image of Au nanowires deposited into nanoporous PC membranes (nominal pore size: 30 nm)

## 2. Experimental

### 2.1- Preparation of Screen Printed Substrates

Conducting and insulators inks were printed on 0.3–0.5 mm thick polyvinyl-chloride (PVC) substrate using a HT10 Fleischle™ screen printer (Brackenheim, Germany). Silver and carbon-graphite pastes for the conducting paths and WE, Ag/AgCl for RE and insulator pastes were all from GWENT Electronics Materials Inc™. New templates for an optimized planar concentric lay-out and specific three-electrode probes were previously designed. SPEs based on conductive pastes from GWENT were shown to be useful for batch or flow-through measurements where a high quality of the electrochemical response is required.

### 2.2- Synthesis of Au nanowires

Amongst the plenty of methods to synthesize nanosized materials, the formation of metal, semiconductor, oxide and polymer nanowires or nanotubules via templates represents one of the most simple and rapid one, especially when using nanoporous PC or alumina membranes as template system. Electroless deposition of Au was performed into track etched PC membrane (Unipore™, nominal pore size 30 nm, thickness 10  $\mu\text{m}$ ) according to Menon et al. [21]. Track-etched polymer membranes are preferred for NEE fabrication over alumina membranes because of their smaller pore densities and their lower fragility. The original synthetic route was slightly varied, by immersing the membrane 40 minutes for the surface activation by Sn (tin chloride solution was from Sigma Aldrich™), 15 minutes for Ag nanoparticles deposition (silver nitrate from Sigma Aldrich™) and using  $\text{AuCl}_4^-$  solution (Sigma Aldrich™) for final Au deposition by means of galvanic displacement [22,23]. SEM observations, as the one reported in figure 1, show the successful formation of 30 nm diameter Au nanowires with a good size distribution, after removing the front side of the membrane from the Au layer grown on the template surface.

### ***2.3- Nanoelectrode ensembles on screen printed substrate***

Au nanowires modified PC membranes can be either used as platform for immobilization of biomolecules or as free standing NEEs, i.e. a large assembly of very small ultramicroelectrodes confined in a rather small space. In each case, NEEs can exhibit three distinct voltammetric response regimes, depending on the scan rate and reciprocal distance between the nanoelectrode elements, which is a function of the pore density of the template [24]: total overlap regime, pure radial regime and linear regime.

It was demonstrated that for electroanalytical applications the total overlap regime is the most advantageous one because of the higher faradaic-to-capacitive current ratios [21]. Without giving a detailed description of theoretical equations supporting the electrochemical behaviour of NEEs, it should be sufficient to know that total overlap regime, usually observed at NEEs fabricated from commercial track-etched membranes, presents a signal to noise ratio in the order of  $10^2$  respect to a conventional Au macro electrode with the same geometrical area [21,24].

In order to assemble our nanoelectrodes based membrane with SPS (obtaining NEE/SPS), Au NEE membrane was one side peeled and soaked only on the rear side into a wet graphite ink pad. Either a vacuum pen or a vacuum-controlled silicone rubber tube were conveniently used for placing the inked membrane on the graphite WE. Afterwards, the device was completed by printing insulator and RE layers as in common screen printing procedure. In each case, the active WE area is defined by the insulator geometry ( $2.53 \text{ mm}^2$ ).

### ***2.4- Analytical procedure for NEE/SPS characterization***

A home made flow cell was used for the characterization of NEE/SPS and successively, for the amperometric detection of glucose with a Glucose oxidase (GOx) based biosensor. The microcell was tailored with appropriate dimensions and inner electrical connections, in order to tightly lodge the screen printed substrate on the bottom surface of the Perspex block. The NEE/SPS was screwed between these two polymer blocks, leaving two holes in the upper side equipped for connection to the sample loop ( $125 \mu\text{L}$ ) via Teflon tubing. The peristaltic pump (Minipuls-3 from Gilson<sup>TM</sup>) was used to propel solution along a FIA system. PB was used as a carrier in all the following experiments. Amperometric experiments performed under batch and FIA conditions were conducted with the Autolab<sup>TM</sup> potentiostat PGSTAT10 and GPES electrochemical analysis system (ECOchemie).

## **3. Results**

### ***3.1- Assays on NEE/SPS glucose sensor***

The aim of this preliminary work was to evaluate the FIA response to a substrate sample after immobilization of a specific enzyme on NEE/SPS. GOx immobilization was used as a model system to test feasibility of the sensing probe and analytical performances of nanoelectrodes assembled at a SPE. The preparation of NEEs, was followed by the SAM formation and subsequent covalent attachment of the enzyme. A well experimented methodology which has been used in our laboratory, was chosen as immobilization method of GOx on Au element:

a) cysteamine was assembled on Au nanodisks either electrochemically (20 s of 21 mM CYS growth at +700 mV vs. RE) or chemically (immersing for 16 hours the NEE/SPS in a solution of 21 mM CYS);

b) glutaraldehyde (GA) was chosen as a coupling agent; SAM/NEE/SPS was immersed for 1 hour in a 12.5 % v/v solution of GA;

c) GOx buffered solution ( $6 \text{ mg mL}^{-1}$ ) was dropped on GA/SAM/NEE/SPS and left to be covalently attached thanks to the primary amine groups of the enzyme. The non-

covalently bound enzyme as well as the excess of GA was easily removed by a three-fold washing process with buffer solution. Figure 2 shows the signal to background ratio (dots) as well as the response of current (squares) and background (triangles) at different applied potential, due to the oxidation/reduction of the produced  $\text{H}_2\text{O}_2$ , when multiple injections of  $10^{-4} \text{ M}$  glucose sample were performed on the same GOx/SAM/NEE/SPS.

The unmodified NEE/SPS did not respond to glucose,

confirming that non-specific oxidation of glucose at the Au surface does not take place. The best signal to noise ratio was achieved in this sensor within the range +500 and +600 mV.

The response of the biosensor to various glucose concentration was investigated between  $7.5 \cdot 10^{-6} \text{ M}$  and  $3.1 \cdot 10^{-2} \text{ M}$  ( $R^2=99.3\%$ ), which is within the analytical range for blood monitoring. At higher glucose concentration, where saturation of enzymatic active sites takes place, the response is no more linear. The glucose injection led to well defined peaks with a response time of approximately 20 s, and return time of 50 s. The sensitivity for GOx/SAM/NEE/SPS was calculated from the slope of the calibration curve and was  $34.6 \text{ nA mM}^{-1}$  glucose, limit of detection (l.o.d.) of  $1.5 \cdot 10^{-4} \text{ M}$  calculated by Zund Meier method [26]. The linear response can be estimated by using a Michaelis Menten analysis of the calibration plot: an apparent constant of 14.9 mM was obtained after extrapolation of the Lineaweaver-Burk relation and the value was significantly lower than that of the native enzyme (33 mM) [27]. High operational stability was also achieved within 48 hours of continuous glucose injection. These analytical data were compared with those available from literature in similar enzyme systems based on Au NEEs [28]: our sensors are valuable in their features at least for some of these parameters, such as linear range (up to 30mM), RSD (3.9%), l.o.d. (0.15 mM).

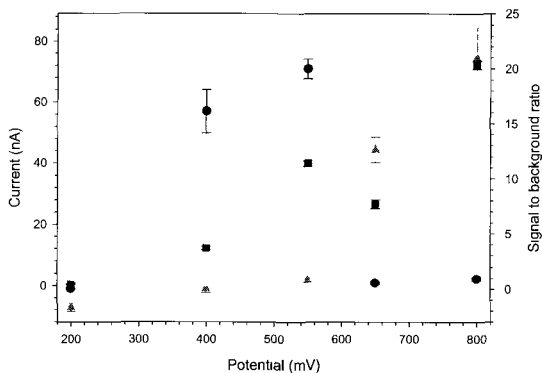


**Figure 2:** Hydrodynamic voltammogram under FIA conditions of GOx modified NEE/SPS. Flow rate:  $0.4 \text{ mL min}^{-1}$ , applied potential: +600 mV. Grey triangles: background signal; squares: current signal, black dots: signal to background ratio

#### 4. Conclusions

Using an electroless procedure for the deposition of Au nanowires into nanoporous PC template membrane, nanoelectrodes ensembles (NEEs) with interesting mechanical, electrical and optical properties, as well as unique surface chemistry were prepared. Fabrication of SPS in association with these nanosized component resulted in an original system of NEEs/SPS for biosensor applications. NEEs/SPS were tested in a glucose oxidase based sensor under FIA. High sensitivity, stability, and linearity of the electrochemical response of the overall system were successfully achieved. According to this novel approach, the advantage of nanostructured material properties (such as higher signal to background ratio than conventional electrode, capability to control the property depending on the nanoparticles diameter size) was further enhanced by the typical features of thick film technology in screen printing production (such as disposability, flexibility, durability of the product).

#### Acknowledgements

These experiments have been supported by FIRB, the Italian Fund for Fundamental Research and by CoSMiC, the ENEA target Project on Biosensors and Bioelectronics - [www.biosensing.net](http://www.biosensing.net)

#### References

- 1) M. Nirmal, D.J. Norris, M. Kuno, M.G. Bawendi, A.L. Efros, M. Rosen, *Phys. Rev. Lett.*, **75** (1995) 3728–3731.
- 2) A.P. Alivisatos, *Science*, **271** (1996) 933.
- 3) C.M. Lieber, *Solid State Commun.*, **107** (1998) 607.
- 4) V. Albe, C. Jouanin, D. Bertho, *J. Cryst. Growth*, **185** (1998) 388.
- 5) R.E. Smalley, B.I. Yakobson, *Solid State Commun.*, **107** (1998) 597.
- 6) A.J. Williamson, A. Zunger, *Phys. Rev. B-Condens Matter*, **59** (1999) 15819.
- 7) M. Bruchez, M. Moronne, P. Gin, S. Weiss, A.P. Alivisatos, *Science*, **281** (1998) 2013.
- 8) V.L. Colvin, A.N. Goldstein, A.P. Alivisatos, *J. Am. Chem. Soc.*, **114** (1992) 5221.
- 9) H. Henglein, *Chem. Rev.*, **89** (1989) 1861.
- 10) I. Kleps, A. Angelescu, M. Miu, *Materials Science and Engineering*, **C 19** (2002) 219.
- 11) N. Dharmaraj, H.C. Park, B.M. Lee, P. Viswanathamurthi, H.Y. Kim, D.R. Lee, *Inorganic Chemistry Communications*, **7** (2004) 431.
- 12) S. Valizadeh, J.M. George, P. Leisner, L. Hultman, *Electrochimica Acta*, **47** (2001) 865
- 13) I. Willner, E. Katz, *Angew. Chem. Int. Ed.*, **39** (2000) 1180.
- 14) R.A. Kamin, G.S. Wilson, *Anal. Chem.*, **52** (1980) 1198.
- 15) C.A. Koval, F.C. Anson, *Anal. Chem.*, **50** (1978) 223.
- 16) T. Nakanishi, B. Ohtani, K. Uosaki, *Jpn. J. Appl. Phys.*, **36** (1997) 4053.
- 17) S. Ogawa, F.F. Fan, A.J. Bard, *J. Phys. Chem.*, **99** (1995) 11182.
- 18) C.J. Zhong, W.X. Zheng, F.L. Leibowitz, *Electrochemistry Communications*, **1** (1999) 72.
- 19) F.C. Meldrum, J. Flath, W. Knoll, *Langmuir*, **13** (1997) 2033.
- 20) A. Badia, L. Cuccia, L. Demers, F. Morin, R.B. Lennox, *J. Am. Chem. Soc.*, **119** (1997) 2682.
- 21) V.P. Menon, C.R. Martin, *Anal. Chem.*, **60** (1995) 1920
- 22) B. Brunetti, P. Ugo, L.M. Moretto, C.R. Martin, *J. Electroanal. Chem.*, **491** (2000) 166.
- 23) L.M. Moretto, N. Pepe, P. Ugo, *Talanta*, **62** (2003) 1055
- 24) J.C. Hulteen, V.P. Menon, C.R. Martin, *J. Chem. Soc. Faraday Trans.*, **92** (1996) 4029.
- 25) F. Cheng, L.D. Whiteley, C.R. Martin, *Anal. Chem.*, **61** (1989) 762.
- 26) P.C. Meier, R.E. Zund, *Statistical Methods in Analytical Chemistry*, J.D. Winefordner (Ed.), J. Wiley & Sons Inc., New York (1993) 87.
- 27) B. Swoboda, V. Massey, *J. Biol. Chem.*, **240** (1965) 2209.
- 28) M. Delvaux, S. Demoustier-Champagne, A. Walcarius, *Electroanalysis*, **16/3** (2004) 190.



# Buried Microchannels by Electrochemical Etching of Silicon

G. Barillaro, A. Nannini

*Dipartimento di Ingegneria dell'Informazione: Elettronica, Informatica, Telecomunicazioni, Università di Pisa, via G. Caruso 16, 56126 Pisa-Italy*  
[g.barillaro@iet.unipi.it](mailto:g.barillaro@iet.unipi.it)

## Summary

In this work, a simple, *one mask* process for the fabrication of buried microchannels into silicon substrates is presented. The process flow consists of two main technological steps: 1) fabrication of high aspect ratio meander-shaped structures into a n-type silicon substrate by using a photo-electrochemical etching technique; 2) thermal oxidation to merge the top of grooved structures and leave a buried channel at the bottom. The fabrication process is detailed and experimental results are reported and discussed.

## 1 Introduction

In last years, a number of processes for the fabrication of microchannels into different substrates (i.e. silicon, quartz, plastic) has been proposed. Microchannels, besides from being essential components of any microfluidic system, in which they act as connection parts between pumps, valves, etc., are used as separation columns for gas and liquid chromatography, as heat exchangers in microreactors or electronic chip cooling.

Three main approaches are today employed for microchannel fabrication: 1) wafer-to-wafer bonding techniques (i.e. anodic or fusion bonding) [1]; the main drawbacks of such processes are the wafer-to-wafer misalignment and micro voids introduced during the bonding process. 2) Surface micromachining techniques, which use a thin film as a structural part, deposited upon a suitable sacrificial layer which is dissolved to obtain the microchannel [2]. The limits of such an approach are the dimension of fabricated channels, usually restricted to few microns by the maximum thickness of the sacrificial layer. 3) Bulk micromachining, exploiting both dry and wet (anisotropic and isotropic) silicon etching techniques to obtain microchannels grooved into the silicon substrate [3]. The channels are usually sealed by means of thermal oxidation. This approach is, however, quite complex requiring both dry and wet etching steps.

In this work an original process for the fabrication of buried silicon microchannels with high aspect ratio is reported. The process exploits the electrochemical etching of silicon to fabricate high aspect ratio meander-shaped trenches, that are then sealed by thermal oxidation. The fabrication process is straightforward and requires only one mask.

## 2 Fabrication process

A schematic view of main technological steps of the buried microchannel fabrication process is reported in Fig. 1.

The starting material was a *n*-type silicon wafer with resistivity of 2.2–4  $\Omega\cdot\text{cm}$ , 550  $\mu\text{m}$  thick,  $\langle 100 \rangle$  oriented, single-side polished. A 100 nm thick silicon dioxide layer was grown by means of a thermal dry oxidation (1 h at 1050  $^{\circ}\text{C}$ ). A standard lithographic step was used define in the oxide layer several meander-shaped patterns with different pitch and dimension. A KOH etching was then employed to transfer the pattern into the silicon, producing in this way the notches which were exploited as seed for the next silicon electrochemical etching.

Photo-electrochemical etching in a HF-based solution [4] was then performed and high aspect ratio trenches were fabricated (Fig.1a). The etching current was properly changed during the electrochemical process from a given initial value

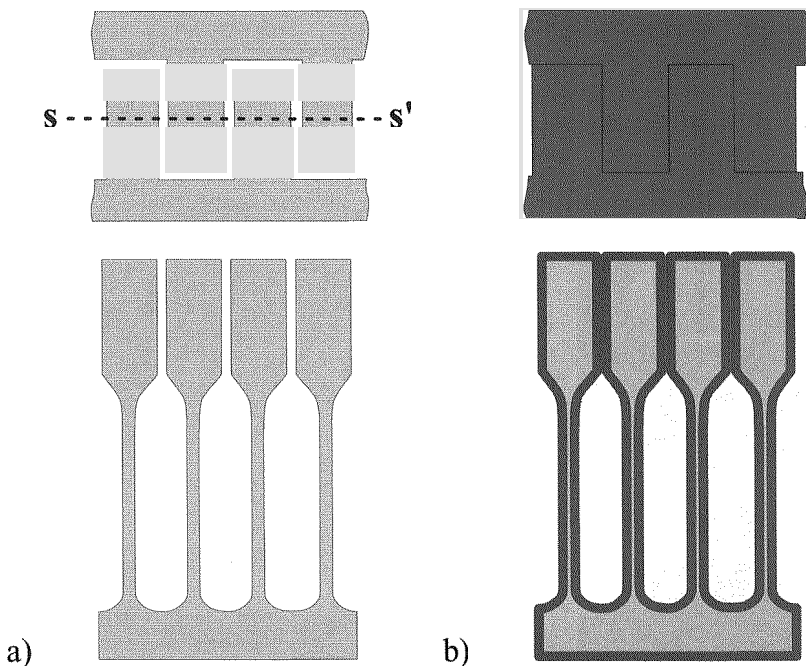


*Fig.1 Main technological steps of the buried microchannel fabrication process: a) fabrication of meander-shaped trenches by electrochemical etching of silicon; b) sealing of the top of etched trenches by thermal oxidation.*

to a higher one in order to increase the channel size over a given depth. Actually, varying the etching current is a feasible way to change the porosity (i.e. the ratio between the etched silicon mass and the total silicon mass) and in turn the lateral size the etched structure.

A wet thermal oxidation was finally employed to seal the top of fabricated trenches and leave a buried pipe at the bottom. In fact, as the lateral size of trenches changes perpendicularly to the wafer surface, the outgrowing oxide layer only seals the top part of the structure, where the gap between adjacent silicon walls is thinner, and a buried path is obtained at the bottom (Fig. 1b).

### 3 Experimental results and discussion

The buried microchannel fabrication process is mainly based on the photo-electrochemical etching (PEE) of a n-type silicon substrate in a HF-based solution

Since 1990, the PEE of a n-type silicon wafer is a well known method for fabricating deep regular macropore array with high aspect ratio (over 200) and pore diameter in the range of the micrometer [5, 6]. An array of pre-defined notches on the substrate surface, produced by standard lithography and subsequent KOH etch, is in this case required to restraint the macropores growth in pre-determined positions during the etching process.

Recently, it has been demonstrated that the PEE can also be employed to etch

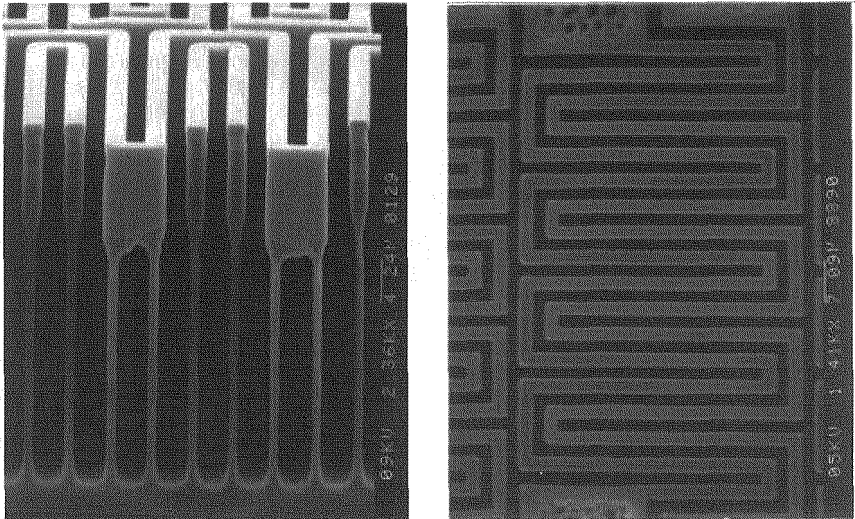


*Fig. 2 SEM cross-section (left) and top view (right) of the meander shaped trenches fabricated by electrochemical etching. It is visible the change in the lateral size of the structure over a given depth (left image).*

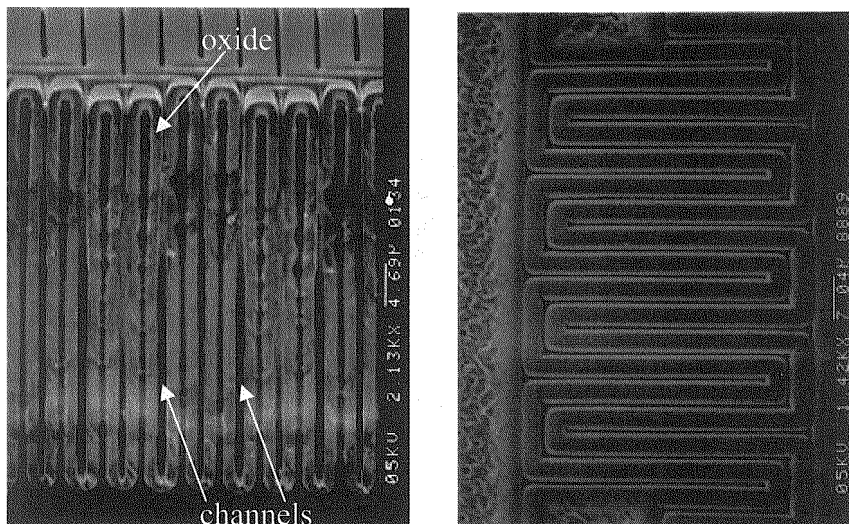


*Fig. 3 SEM cross-section (left) and top view (right) of the buried microchannels obtained at the end of the thermal oxidation step. It is clear that while the top of the structure is sealed by the outgrowing oxide, a buried pipe is left at the bottom (left image).*

silicon microstructures with a high degree of freedom about the shape, size, porosity and pitch [4, 7]. In fact, changing the pre-defined geometry on the substrate surface it is a feasible way to vary the shape of the microstructure resulting from the PEE. In this way, squared and circular spirals, pillars, tubes, walls, and other structures with high aspect ratio, were fabricated on the same silicon die.

In this work, by defining a meander-shaped pattern on the silicon surface, meander-shaped trenches were grooved into the chosen substrate by using PEE. A SEM top view and the cross-section of a typical sample after the electrochemical etching step are shown in Fig. 2. In this case, an etching current of 30 mA, corresponding to a porosity of 50%, for 5 minutes was used to etch the top part of the structure; the current was then increased to a value of 42 mA for 15 minutes to obtain a porosity of 70% at the bottom. According to the etching current variation, the lateral size of the etched structure increases over a given depth, as can be seen from the cross-section of Fig.2: trenches are about 2  $\mu\text{m}$  wide at the top and about 3  $\mu\text{m}$  at the bottom.

Fig. 3 shows a SEM top view and the cross-section of a typical sample after the thermal oxidation sealing step. The steam oxidation process was performed at 1050  $^{\circ}\text{C}$  for 4 h. It is clear that while the top part of the structure (low porosity region) is completely sealed by the outgrowing oxide layer, a buried path is

obtained at the bottom (high porosity region). The resulting buried pipe is about 20  $\mu\text{m}$  high and 1  $\mu\text{m}$  wide, corresponding to an aspect ratio of 20.

#### 4 Conclusions

An original, *one mask* process for the fabrication of buried microchannels into silicon substrates was reported in this work. The process is based on the photo-electrochemical etching of the silicon, used to produce high-aspect ratio meander-shaped trenches with a size variation along the direction perpendicular to the wafer surface. This variation allows to seal the top part of trenches by means of thermal oxidation, while leaving a buried channel at the bottom. Future work will be devoted to the optimisation of the channel geometry, definition of inlet and outlet of the channel, and filling tests.

#### References

- [1] G. Perret, J. Boussey, C. Schaeffer, M. Coyaud, IEEE Trans. on Components and Packaging Technologies, **23**, 665 (2000).
- [2] W. J. Nam, S. Bae, A. K. Kalkan, S. J. Fonash, J. Vac. Sci. Technol. A, **19** (4), 1229 (2001).
- [3] C. Rusu, R. van't Oever, M. J. de Boer, H.V. Jansen, J.W. Berenschot, M.L. Bennink, J.S. Kanger, B.G. de Grooth, M. Elwenspoek, J. Greve, J. Brugger, A. van den Berg, J. of Microelectromechanical Systems, **10**, 238 (2001).
- [4] G. Barillaro, A. Nannini, M. Piotta, Sens. Act. A, **102**, 195 (2002).
- [5] V. Lehmann and H. Föll, J. Electrochem. Soc., **137**, 653 (1990)
- [6] V. Lehmann, J. Electrochem. Soc., **140**, 2836 (1993).
- [7] G. Barillaro, P. Bruschi, A. Diligenti, A. Nannini, Physica status solidi (C), **2** (9), 3198 (2005).

# Gas Sensing Properties of Metal-oxide/Organic Hybrid Materials grown by Supersonic Beam Deposition

F. Siviero, N. Coppedè, L. Aversa, M. Nardi, A. Pallaoro, T. Toccoli, R. Verucchi, and S. Iannotta

*IFN-CNR Istituto di Fotonica e Nanotecnologie – Sezione ITC di Trento, Via Sommarive 18, 38050 Povo di Trento, Italy.- [iannotta@itc.it](mailto:iannotta@itc.it)*

A.M. Taurino, P. Siciliano

*IMM-CNR Istituto per la Microelettronica e Microsistemi - Via per Arnesano 73100 Lecce. Italy*

## Summary

Hybrid organic-inorganic gas sensing devices have been developed by means of supersonic beam co-deposition of titania clusters and copper phthalocyanine. This technique allows controlling the cluster size and structure as well as the kinetic properties of organic precursors, thus enabling both the room-temperature growth of nanocrystalline TiO<sub>2</sub> and its functionalization. Particularly the high kinetic energy transferred to the organic molecules is exploited to enhance reactivity at the interface between the two counterparts, resulting in the synthesis of a new material with interesting gas sensing properties. The hybrid devices show improved performances as to stability and sensitivity towards oxidizing and even non-oxidizing gases, which is a remarkable result for metal-phthalocyanine based sensors. The role of the organic-inorganic interface in the development of such characteristics is briefly discussed.

## 1. Introduction

The synthesis and characterization of new functional hybrid nanomaterials is a rapidly evolving field of research, which is constantly enlarging its range of applications [1]. Particularly for gas sensing, the functionalization of inorganic materials with organic species is a very promising approach to produce new generations of devices overcoming the limits due to the limited selectivity of metal oxides and to the low stability of organic molecules. Among different techniques for the synthesis of nanostructures, the supersonic beam deposition of molecules [2] and clusters [3] allows unique control on the properties of the precursors, on their mutual interaction and the formation of interfaces. This is achieved by controlling key parameters as the kinetic energy and momentum of the particles, as well as cluster size and crystalline structure.

We report here about the development and the response characterization of hybrid devices made of alternating layers of copper phthalocyanine and cluster-assembled titania. The results point out how this original approach to the synthesis of such hybrid nanostructures brings to the development of novel sensing properties.

## 2. Experimental

The deposition of the sensing layers was performed in an UHV apparatus equipped with two supersonic molecular beam sources (the one for the organics and the cluster source), a quartz microbalance and a Jobin-Yvon in-situ ellipsometer. The deposition chamber is connected via an UHV transfer line to the analysis one, which hosts facilities for electron spectroscopy and surface characterization (XPS, UPS, Auger, LEED). This experimental setup allows the co-deposition and the in situ characterization of hybrid thin films and interfaces.

The source for organic species consists of a quartz tube ending with a nozzle (50-100  $\mu\text{m}$ ) in which powders of organic species are sublimated by Joule heating and carried out of the source in the supersonic expansion of the carrier gas. Acting on gas inlet pressure and source's temperature we tune the kinetic energy of the precursors: in the case of CuPc, helium is used and the kinetic energy gained by the molecules is about 18 eV, as measured by time-of-flight mass spectrometry. The  $\text{TiO}_2$  cluster deposition is performed with the Pulsed Microplasma Cluster Source [4], which is based on the ablation of a titanium rod by means of a pulsed plasma discharge, followed by condensation of clusters from the gas phase in helium plus 0.1% oxygen. Aggregates dispersed in the supersonic beam show a mass distribution ranging from a few to several hundreds of atoms: the maximum and the relative abundance of heavier and lighter species of such distribution can be controlled by changing the operation parameters (mainly discharge timing), or by aerodynamic separation effects. Mass selection is a very powerful tool in order to determine the properties of the nanostructured film, since a correlation between size and crystalline phase has been observed.

The sensors were prepared using alumina substrates with 7 pairs of interdigitated gold electrodes (200  $\mu\text{m}$  spacing) and platinum heaters on the back. The test of gas sensing devices was carried out with small concentrations of high-purity methanol and  $\text{NO}_2$ , which were diluted in dry air with precision MKS mass flow controllers. The current flowing in the films at the fixed voltage of 4 V was measured by a Keithley 6517A sourcemeter.

## 3. Results and discussion

We have explored two kinds of different device architectures: the deposition of copper phthalocyanine on  $\text{TiO}_2$  (CuPc/ $\text{TiO}_2$  sensor) and vice versa ( $\text{TiO}_2$ /CuPc). The thickness of the layers was estimated by measuring the deposition rate with the quartz microbalance to be about 80 nm for the oxide and 60 nm for the organic film. The performances of the hybrid sensors have been compared with the ones of pure CuPc devices deposited with the same technique. Figure 1 shows the response to 10 ppm of methanol, defined as the ratio between the change in current  $\Delta I$  and the current value  $I_g$  reached in presence of the gas.

At the temperatures of 155°C for CuPc and CuPc/TiO<sub>2</sub> sensors and 130°C for TiO<sub>2</sub>/CuPc, we observe a p-type response typical of organic materials and the baseline currents  $I_0$  in pure dry air are reported in Table 1. It can be noted how the hybrid films show a similar conductivity, which is roughly one order of magnitude lower than that of the pure organic film. At this temperature the conductivity of the hybrids is due to the organic layer, since the oxide has a much higher resistance. In the case of CuPc deposited on the oxide, the organic film has a very defected structure induced by the high surface roughness of nanostructured TiO<sub>2</sub>, which has a granular structure with grains typically in the 5-30 nm range and peak to peak corrugation of several tens of nm [5]. On the other hand for the opposite architecture the cluster deposition is likely to damage the soft organic layer causing a decrease in its overall conductivity.

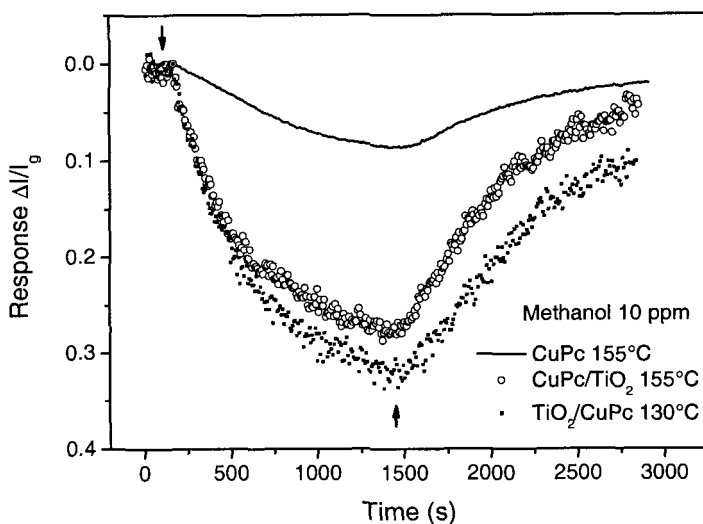


Fig. 1 Response of pure CuPc and hybrid sensors to 10 ppm of methanol. Arrows indicate the beginning and the end of gas exposure.

Organic devices are found to have a low sensitivity to methanol as usually reported in literature for reducing gases [6], while the hybrid sensors show a much higher response. This result can be explained envisaging a large contribution to the response from the interface region between CuPc and the oxide. We have strong indications that the kinetic energy supplied to the precursors is able to enhance the reactivity at interfaces, overcoming large



activation barriers, for this kind of material [7] and for different systems [8]. Anyhow the presence of chemical interactions between the organic and inorganic counterparts is likely to be the origin of the sensitivity of hybrids to the reducing gas, by virtue of a charge transfer mechanism from  $\text{TiO}_2$  to CuPc.

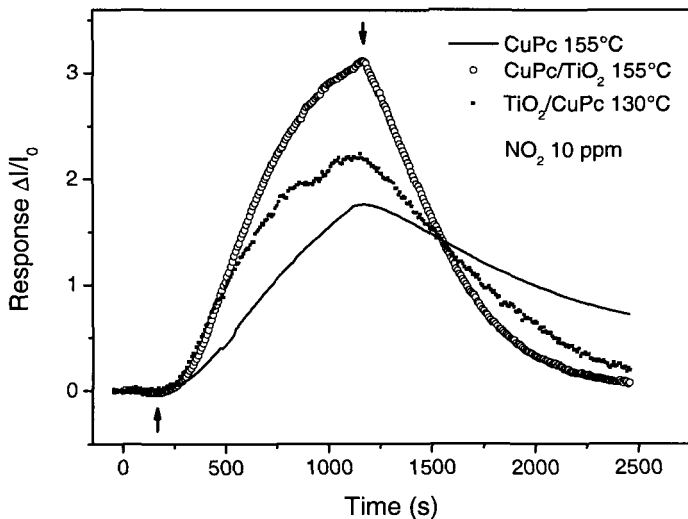


Fig. 2 Typical sensors response to 10 ppm of nitrogen dioxide.

Upon interaction with an oxidizing specie such as  $\text{NO}_2$ , the response of the pure CuPc sensors is clearly not as low as in the previous case, anyway the hybrids still show higher response (defined as  $\Delta I/I_0$ ), as reported in Figure 2. In this case hybrid devices demonstrate also better recovery performances with respect to the pure organic, for which the “poisoning” effect of  $\text{NO}_2$  is evident. Table 1 reports the percentage of the current change recovered in a period equivalent to that of gas exposure (about 22 min). For methanol we don’t observe such a significant difference in the recovery properties of the different sensors as in the case of nitrogen dioxide, also taking into account that the  $\text{TiO}_2/\text{CuPc}$  device is operated at a lower temperature.

**Table 1.** For each type of sensor we report the current  $I_0$  flowing in the films in pure dry air and the percentage of the change in current recovered after about 22 min from the exposure to methanol and  $NO_2$ .

<i>Sensor</i>	$I_0$ (A)	<i>Recovery % Methanol</i>	<i>Recovery % NO<sub>2</sub></i>
CuPc	$9.44 \times 10^{-8}$	73	59
CuPc/TiO <sub>2</sub>	$8.2 \times 10^{-9}$	83	98
TiO <sub>2</sub> /CuPc	$6.0 \times 10^{-9}$	68	91

### Conclusions

Novel hybrid nanotitania-copper phthalocyanine resistive gas sensors have been developed by jointly using supersonic beams of molecules and clusters. The properties of the interface between the two materials as synthesized by this technique are at the basis of the development of novel sensing properties, such as the ability to respond to reducing gases at low operating temperatures, where pure TiO<sub>2</sub> has no sensing activity and pure CuPc shows quite poor performances. We envisage new classes of gas-sensing devices could be developed on the basis of these results.

### Acknowledgments

This work is financially supported by MIUR - FIRB Program - project SQUARE (RBNE01Y8C3\_007) and FUR - Provincia Autonoma di Trento - projects RASO2 and NanoCOSH<sub>y</sub>.

### References

- [1] C.Sanchez, B.Julian, P.Belleville, M.Popall, J. Mater. Chem., 15 (2005) 3559.
- [2] S. Iannotta and T. Toccoli, Journal of Polymer Science B 41, 2501, 2003.
- [3] P.Milani, S.Iannotta, "Cluster beam synthesis of nanostructured materials", Springer-Verlag, Berlin-Heidelberg, 1999.
- [4] E. Barborini, P. Piseri, P. Milani, J. Physics D: Appl. Phys. 32, L105, 1999.
- [5] T.Toccoli, S.Capone, L.Guerini, M.Anderle, A.Boschetti, E.Iacob, V.Micheli, P.Siciliano and S.Iannotta, IEEE Sens.J., 3 (2003) 199.
- [6] C.Maleysson, M.Passare, J.P.Blanc, V.Battut, J.P.Germain, A.Pauly, V.Demarne, A.Grisel, C.Tiret, R.Planade, Sens. and Act. B, 26-27 (1995) 144.
- [7] N.Coppedè, L.Aversa, M.Nardi, A.Pallaoro, F.Siviero, T.Toccoli, R.Verucchi, E.Iacob, V.Micheli, M.Anderle, A.M.Taurino, P.Siciliano and S. Iannotta, X AISEM Conference Proceedings, World Scientific Publications, 2005.
- [8] L.Aversa, R.Verucchi, G.Ciullo, P.Moras, M.Pedio, L.Ferrari, A.Pesci and S.Iannotta, App. Surf. Sci., 184 (2001) 350.

# Focused Ion Beam in Gas Sensor Technology

Vera La Ferrara, Ivana Nasti, Ettore Massera, Brigida Alfano and  
Girolamo Di Francia

*ENEA, Centro Ricerche Portici Località Granatello 80055 Portici (NA)*  
[vera.laferrara@portici.enea.it](mailto:vera.laferrara@portici.enea.it)

## Summary

Focused Ion Beam is used to realize two gas sensing devices machining as substrate a silicon/Si<sub>3</sub>N<sub>4</sub> wafer and using single walled carbon nanotube ropes as sensitive element. Ionic beam is applied both for milling substrate and for platinum deposition. Sensors are characterized at room temperature introducing NH<sub>3</sub> and NO<sub>2</sub> gases in test chamber. A well defined resistance change is observed

## 1 Introduction

Recently, nanoparticles and nanowires are receiving an increasing attention in the field of chemical sensors. High surface to volume ratio and enhanced reactivity of nanosensors [1] improve device response, even at room temperature, and limit the device power consumption. It has been reported that when metallic nanowires or nanoparticles are exposed to specific analyte molecules, a change in their electrical resistance is recorded [2]. Analogous effects have been observed for single walled carbon nanotubes [3,4] and for metal oxide semiconducting nanostructures [5-7].

In order to overcome the obvious complexity related to nanodevice fabrication, several special tools have been, and still are, under investigation.

In this respect, one of the most promising apparatus is the Focused Ion Beam (FIB). The use of high energy FIB is an already well established technique in microelectronics and micro-fabrication for mask-less patterning. Moreover milling and deposition by FIB have already found applications in micro-electromechanical and micro-optomechanical systems, micro-sensors and actuators [8,9]. Dual Beam (FEI - Quanta 200 3D) system, located at ENEA laboratory, is composed of an electron column (Scanning Electron Microscopy - SEM), a Ga ions column (Focused Ion Beam - FIB) and a gas injector system (a Pt organometallic precursor). By means of this apparatus imaging, patterning deposition and etching of both conductive or isolating materials is possible.

In this work we report first results on the realization of gas sensing devices obtained fabricating by FIB patterning Si/Si<sub>3</sub>N<sub>4</sub> substrate and using single walled carbon nanotube (SWCNT) ropes as chemical sensitive interfaces. Sensors are analyzed at room temperature using NH<sub>3</sub> and NO<sub>2</sub> as testing gases.

## 2 Experimental

The first gas sensor device is realized starting with a silicon substrate coated with a  $\text{Si}_3\text{N}_4$  layer (200 nm deposited by PECVD). By e-beam evaporator, one pad, 200  $\mu\text{m}$  width, is deposited on silicon substrate placing on two metallic layers of Cr (20 nm thickness) and Au (280 nm thickness). By means of FIB, under 30 KeV accelerating voltage, 30 pA emission current, 1  $\mu\text{s}$  dwell time without overlap for the digitised ion beam position, a 1  $\mu\text{m}$  wide channel milling Cr/Au pad has been realized obtaining two separated microelectrodes on which SWCNTs have been subsequently deposited.

At this aim, SWCNTs have been dispersed in dimethylformamide (DMF) to debundle nanotubes and form an uniform suspension of nanotube ropes with average diameter of 50 nm and 3–4  $\mu\text{m}$  length. Few drops of the suspension have been deposited between two Cr/Au electrodes. One single nanotube is found by SEM and contacted by FIB depositing platinum using injector of organometallic precursor (figure 1).

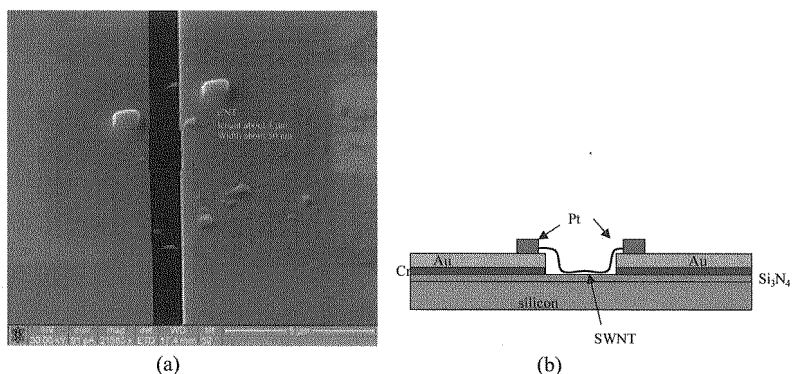


**Fig. 1:** (a) SEM image of carbon nanotubes on a FIB milled channel (1  $\mu\text{m}$  width) (b) Scheme of device: silicon substrate coated with  $\text{Si}_3\text{N}_4$  on which two Cr/Au electrodes are realized. One single rope, placed on it, is contacted by platinum deposited by FIB

The second gas sensing device has been fabricated depositing SWCNTs ropes on silicon substrate coated with a 100 nm  $\text{Si}_3\text{N}_4$  layer, PECVD deposited.

The substrate surface has been explored by means of FIB, selecting one CNT rope, suitable for the subsequent fabrication process. Under 30 KeV accelerating voltage, 10 pA emission current and 0.1  $\mu\text{s}$  dwell time with 50% overlap for the digitised ion beam position, the CNT rope has been contacted realizing a platinum electrode at each of the rope ends. Each electrode, about 300

nanometer in diameter, have a length of a few microns, ending in contacting gold pads ( $0.25 \text{ cm}^2$ ), previously deposited by e-beam evaporation. In figure 2 we show the nanotube device fabricated according to the above process.

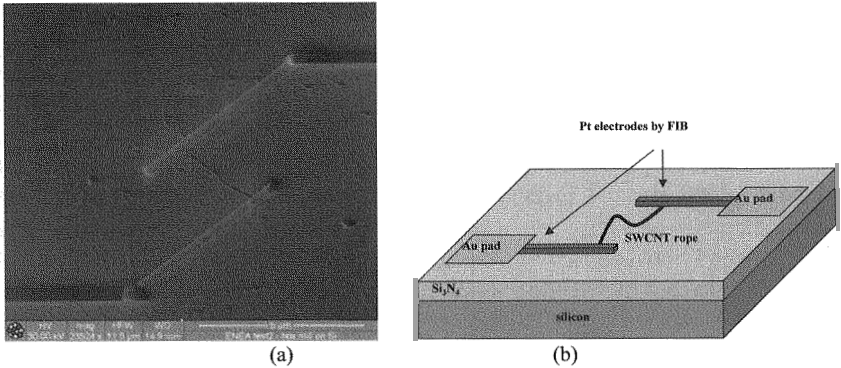


**Fig. 2:** (a) Ion image of carbon nanotube on silicon/ $\text{Si}_3\text{N}_4$  device. Single nanotube has been contacted by two Pt wires deposited by FIB using Pt organometallic precursor (b) Device scheme

### 3 Results and discussion

After FIB micro-machining, a volt-amperometric technique, at constant bias, is employed for sensor dc electrical characterization in a controlled gas-flow environment, pre-mixed with dry carrier in the desired percentage by mass flow meters and continuously controlled by means of an in-line FTIR. Total gas flow is set to 500 sccm. For the measurements here reported, certified bottles containing mixtures of 30 ppm of nitrogen dioxide in synthetic air and 500ppm of ammonia in synthetic air, have been used [10].

Results are reported in figures 3 and 4. Devices have been DC biased at 0,1Volt. Graphs show that both the sensor devices respond to  $\text{NH}_3$  via an increase of resistance while  $\text{NO}_2$  results in a decrease of their resistance. Such a different behavior in reducing and oxidizing environments has been already reported for similar materials [11] and claimed to be due to the interaction between nanotube devices and gas molecules, via nanosized local defects on CNT. Although it is evident a resistance change when devices are in presence of gas, current doesn't recover when synthetic air is again introduced in the test chamber.

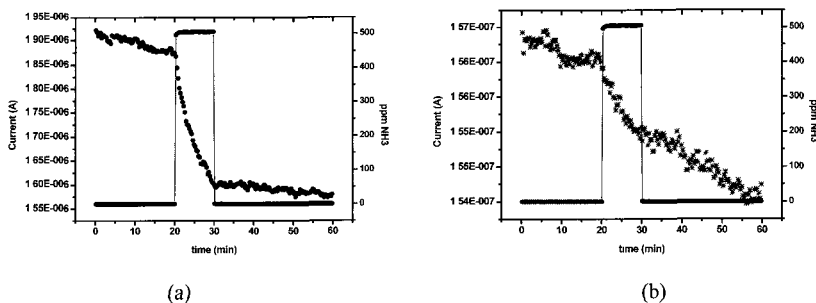


**Fig. 3:** Sensor output current is reported versus the measurement time under 500ppm of NH<sub>3</sub> in synthetic air. (a) Gas sensor device response (see scheme reported in figure 1); (b) Gas sensor device response (see scheme reported in figure 2)

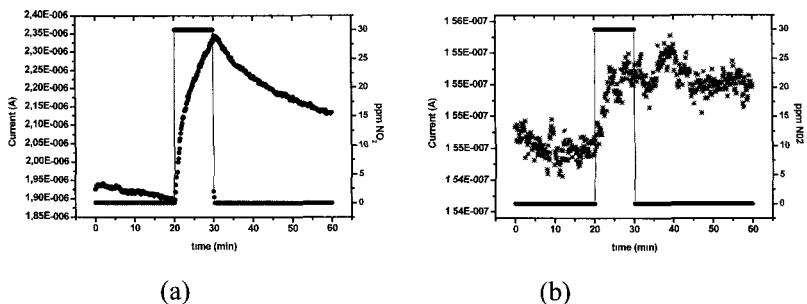


**Fig. 4:** Sensor output current is reported versus the measurement time under 30ppm of NO<sub>2</sub> in synthetic air. (a) Gas sensor device response (see scheme reported in figure 1); (b) Gas sensor device response (see scheme reported in figure 2)

In table 1 the relative current variations is reported in order to compare devices behaviour.

<i>device</i>	<i>variation in NH<sub>3</sub> (%)</i>	<i>variation in NO<sub>2</sub> (%)</i>
First type	16	20
Second type	1	0.6

**Table 1:** Current relative variation of two devices respect to gas environment

Gas sensor response is more evident for the first device type with respect to the second one, probably because even if one single CNT wire is effectively contacted by FIB, the concomitant effect of other CNT wires deposited between

two Cr/Au electrodes cannot be ruled out. On the contrary the second sensor response is certainly due to just one SWCNTs rope as it is evident in figure 2.

#### 4 Conclusions

We have shown our first attempts to use FIB as a tool to fabricate nanosensing devices. Both for patterning and for soldering, suitable operating conditions have been found for the realization of two sensing devices based on CNT wires. The devices respond both to  $\text{NH}_3$  and to  $\text{NO}_2$  although not reversibly. Further investigations are necessary to enhance desorption mechanism.

#### References

- [1] G. Di Francia, L. Quercia, I. Rea, P. Maddalena, S. Lettieri, *Sensor and Actuators B*, 111-112 (2005) 117
- [2] F. Favier, E.C. Walter, M.P. Zach, T. Benter, R.M. Penner, *Science*, 293 (2001) 2227
- [3] P.G. Collins, K. Bradley, M. Ishigami, A. Zettl, *Science* 287 (2000) 1801
- [4] J. Kong, H.J. Dai, *J. Phys. Chem. B*, 105 (2001) 2890
- [5] E. Comini, G. Faglia, G. Sberveglieri, D. Calestani, L. Zanotti and M. Zha, *Sensor and Actuators B: Chemical* 111-112 (2005) 2.
- [6] E. Comini, G. Faglia, G. Sberveglieri, Z. Pan, Z.L. Wang, *Applied Physics Letters*, 81 (2002) 1869
- [7] X.Y.Kong, Y. Ding, R.S. Yang, Z.L. Wang, *Science*, 303 (2004) 1348
- [8] R. Puers, S. Reyntjens, D. De Bruyker, *Sensors and Actuators A*, 97 (2002) 208
- [9] A.A.Tseng, *J. Micromech. Microeng.*, 14 (2004) R15
- [10] L. Quercia, F. Cerullo, V. La Ferrara, G. Di Francia, C. Baratto, G.Faglia, *Phys. Stat. Sol. (a)* 182, (2000) 473
- [11] R.S. Lee, H.J. Kim, J.E. Fischer, A. Thess and R.E. Smalley, *Nature*, 388 (1997) 255.

# PROCESS DEPENDENCE OF DOPED POLYSILICON THERMAL CONDUCTIVITY FOR THERMAL MEMS APPLICATIONS<sup>1</sup>

F. MANCARELLA, A. RONCAGLIA, S. CRISTIANI,  
G. C. CARDINALI, M. SEVERI

*IMM Bologna, CNR, Via Gobetti 101  
Bologna, I-40129, Italy*

Thermal conductivity measurement by micromachined test structures permits to evaluate the microscale variations of thermal conductivity on different devices. We used this technique to measure polysilicon thermal conductivity with particular concern to investigating its dependence on annealing temperature and doping type.

## 1. Introduction

Doped polysilicon layers are widely employed in fabricating thermal microsystems such as bolometers, micro hotplates or thermopiles thanks to their thermal and electrical properties. Since the performances of such devices are strongly influenced by heat conduction, a precise characterization of polysilicon thermal conductivity is of paramount importance.

In order to determine the thermal conductivity ( $\kappa$ ) of thin films, microstructures like those proposed in [1] can be adopted. In this work, such microstructures have been adopted in order to investigate the dependence of polysilicon thermal conductivity on the type of doping adopted (p or n-type) and the annealing conditions.

## 2. The test structure

The device consists of a dielectric cantilever micromachined on a silicon substrate by anisotropic etching. It is 200  $\mu\text{m}$  wide and 150  $\mu\text{m}$  long. The tip of the cantilever can be heated by a heavily-doped polysilicon resistor and its temperature measured by the variation of a second resistor with different geometry. Both are connected to bonding pads by platinum or aluminum interconnections, placed over the suspended dielectric arms. The cantilever-type membranes employed in the test structures have been released from the underneath silicon substrate by anisotropic etching using a TMAH solution.

---

<sup>1</sup> This work is supported by Netgas project- EC V framework program, proposal IST-2001-37802



Figure 1 reports a microphotograph of a released device and a layout detail in which the two resistors used for heating and temperature monitoring (needed for the measurement as explained in section 3) are highlighted.

The measurement principle relies on the fact that, when a Joule power  $P$  is dissipated on the heater, the temperature of the cantilever tip is increased by  $\Delta T$  with respect to the substrate. At the steady-state, this phenomenon depends on the balance between the heat produced and the one dispersed towards the colder surrounding environment along the cantilever, the four arms, and the air. The heating power  $P$  and the temperature difference  $\Delta T$  are thus related by:

$$G = G_a + G_c + G_h = \frac{P}{\Delta T}$$

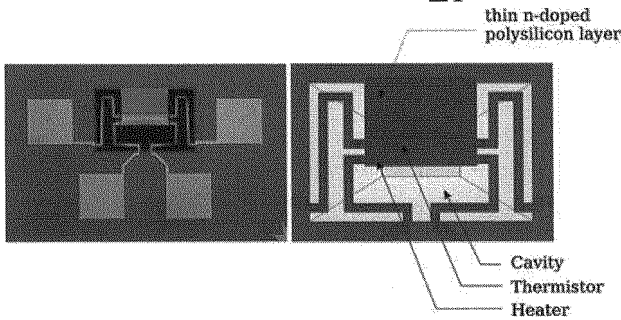


Figure 1. Micrograph of a released micromachined test structure for thermal conductivity measurement (left) and a detail of the cantilever (right).

where  $G$ ,  $G_a$ ,  $G_c$  denote the thermal conductances of the whole structure, the four arms and the cantilever respectively, while  $G_h$  is the one due to heat exchange through air.  $G_c$  is given by

$$G_c = \sum \frac{\kappa_i d_i w}{L}$$

where the summation runs over the component layers of the cantilevers, and  $\kappa_i$ ,  $d_i$ ,  $w$  and  $L$  indicate their respective thermal conductivity, thickness, width and length.

As proposed in [1], the thermal conductance of a particular layer is obtained by subtracting the overall measured conductance of the corresponding cantilever from a reference one. In order to do that, different structures have been realized like those represented in Figure 2, which differ in the cantilever composition. Structure (a) is the reference one, composed by a plain supporting membrane (a stack of LPCVD silicon oxide/nitride). In the other devices, a layer of p- or n-type polysilicon is added to the supporting membrane (see the cross sections of the different cantilevers reported in Figure 3).

Since the presence of an additional film increases the thermal conductance of the cantilever sandwich, the  $\kappa$  value of the layer considered can be calculated by subtraction of the reference structure from the modified structure as described in the following.

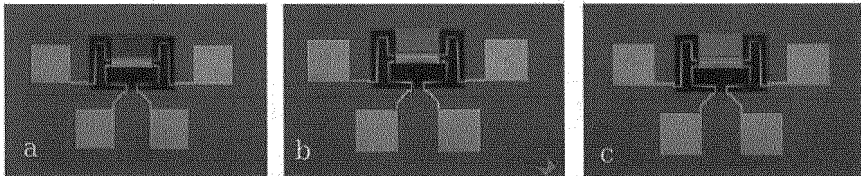


Figure 2. Micromachined test structures for thermal conductivity measurement: reference cantilever (a), n-polysilicon (b), p-polysilicon (c).

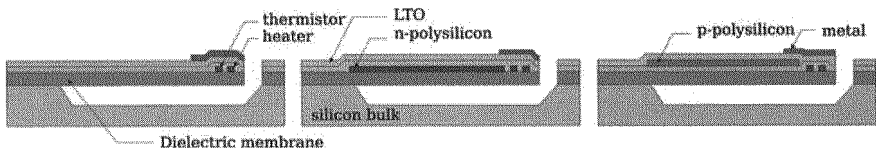


Figure 3. Schematic cross-sections of microcantilevers used to determine the thermal conductivities of thin films. Reference structure (left), modified structures for n-polysilicon (center) and p-polysilicon (right) thin films.

Once the thermal conductances of the two structures have been determined with the method described in Section 3, the thermal conductivity of the added layer is calculated as

$$k_{\text{poly}} = \left| G_{\text{poly}} - G_{\text{ref}} \right| \frac{L}{d_{\text{poly}} w_{\text{poly}}}$$

where  $d_{\text{poly}}$ ,  $w_{\text{poly}}$  and  $L$  are the thickness, width and length respectively of the layer of interest.

In both cases, the measured overall thermal conductance also includes a contribution due to heat convection, than can be cancelled thanks to the method used, provided it is maintained constant from one measurement to another.

### 3. The measurement method

A scheme of the measurement setup is reported in Figure 4. The reference cantilever is heated biasing the resistor, placed over the free end of the structure, by imposing a current  $I_h$ . In this way a temperature difference  $\Delta T$  is created between the tip of the cantilever and the silicon bulk.

This  $\Delta T$  is estimated by measuring the resistance change of the thermistor (fabricated with polysilicon, as well). In order to eliminate the offset due to the instrumentation, that can be deleterious due to the low temperature difference measured, the following procedure has been adopted. For a fixed value of the heater current  $I_h$ , the thermistor current is ramped up from  $I_{th}-\Delta I_{th}$  to  $I_{th}+\Delta I_{th}$  (indicated as  $I_{ramp}$  in the figure),  $I_{th}$  being a reference value. From the slope of the resulting  $V_{th}(I_{th})$  curve, an offset-compensated  $R_{th}$  value is obtained for different  $I_h$  values, and the temperature difference  $\Delta T$  is extracted from the previously calibrated TCR (temperature coefficient of resistance) value for the polysilicon thermistor.

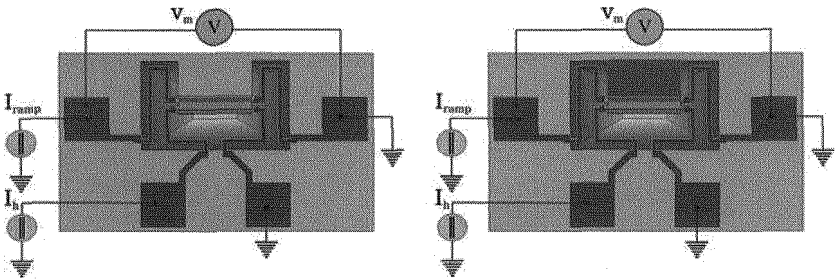


Figure 4. Electrical probe setup used in the thermal conductivity measurement.

Consequently, the thermal conductance can be calculated by the following expression:

$$G = \frac{P_h}{\Delta T}$$

where  $P_h = I_h^2 R_h$  is the power dissipated by the heater.

Typical results obtained on a reference cantilever ( $G_{memb}$ ) are reported in Table 1.

Table 1. Measurement results obtained on the reference cantilever.

HEATER	THERMISTOR ( $\mu A$ )	$\Delta T$ ( $^{\circ}C$ )	$G_{memb}$ ( $\mu W/mK$ )
0	10-15	-	-
125	10-15	1.63	34.92
250	10-15	7.32	34.98
375	10-15	16.58	34.76
500	10-15	29.52	34.70

The described technique has been applied to measure the thermal conductivity of heavily doped polysilicon layers implanted with boron and phosphorus respectively, and annealed at different temperatures. The

corresponding calculated thermal conductivities  $\kappa$  are shown in Table 2. From the results it is apparent that n-type polysilicon thermal conductivity does not depend strongly on annealing, differently than p-type polysilicon. This can be probably ascribed to the different grain growth kinetics in the two layers. In fact phosphorus enhances grain growth even at low temperatures, and this would explain the higher thermal conductivity of n-type polysilicon even for the 900 °C temperature annealing.

Table 2. Measured thermal conductivities on polysilicon samples annealed at different temperatures.

LAYER	implant dose ( $\text{cm}^{-2}$ )	anneal. temp. (°C)	$\rho$ ( $\mu\Omega\text{cm}$ )	$\kappa$ (W/mK)
n-poly	$3.3 \times 10^{15}$	900	2.15	23.44
		1000	1.71	25.33
		1100	1.56	26.17
p-poly	$6.6 \times 10^{15}$	900	6.46	9.14
		1000	3.90	10.46
		1100	1.79	16.88

#### 4. Conclusions

Test microstructures have been used to estimate the microscale variation of n- and p-type heavily doped polysilicon thermal conductivity as a function of the annealing temperatures. The results point out that n-type polysilicon thermal conductivity does not depend strongly on annealing, differently than p-type polysilicon, probably due to the different grain growth kinetics in the two layers.

The microstructures and measurement method described could also be adopted to estimate the thermal conductivity of other microelectronic materials, such as silicon dioxide, nitride and metal films.

#### References

1. M. von Arx, O. Paul, H. Baltes, *Journal of Microelectromechanical Systems* **9**, 136 (2000).
2. A. McConnell, S. Uma, K. E. Goodson, *Journal of Microelectromechanical Systems* **10**, 360 (2001).

# **GAS SENSING SYSTEM CONSISTING IN MOX-BASED MICROSENSORS INTERFACED TO A NOVEL INTEGRATED 5-DECADE DYNAMIC RANGE FRONT-END**

Marco Grassi, Piero Malcovati

*Department of Electrical Engineering, University of Pavia*  
marco.grassi@unipv.it

Simonetta Capone, Luca Francioso, Pietro Siciliano

*Research Center IMM-CNR, Lecce*  
simona.capone@le.imm.cnr.it, luca.francioso@le.imm.cnr.it

Andrea Baschiroto

*Department of Innovation Engineering, University of Lecce*

## **Summary**

Research on gas sensors aims to improve the performance, minimize size, power consumption and cost of such devices. For implementing gas sensing microsystems with the above mentioned features, the micromodule approach, where the sensors and the read-out electronics are manufactured on different chips and mounted in the same package or on the same substrate, appears well promising and versatile. The proposed system, realized for environmental monitoring purpose, consists of an integrated tin-oxide SnO<sub>2</sub> resistive sensor over micromachined substrate followed by a 0.35 $\mu$ m CMOS auto-scaling read-out circuit. The interface circuit, which is actually a trans-resistance variable gain amplifier connected to an incremental A/D converter, after the initial calibration procedure, required to minimize offset and gain inter-scale error, achieves a worst case accuracy of about 0.1% over a range of more than 5 decades (100 $\Omega$ -20M $\Omega$ )

## **1. Introduction**

Gas sensors are widely used for several applications, ranging from environmental and air-quality monitoring to automotive and industrial control. Recently, especially in view of legislative initiatives aimed to the reduction of pollution and of human exposure to dangerous gasses, hand-held systems for gas sensing are becoming quite important, thus pushing in the direction of improving the performance, minimizing size, power consumption and cost of such systems[1][2]. A gas-sensing microsystem consists of three main parts that are subject to continuous development from researchers: an array of gas sensors, an electronic read-out circuit and a pattern recognition data processor. The improvements in the overall gas-sensing microsystem are obtained by improving the single parts and/or their coordination. Micro-membrane resistive gas sensors have been recently developed[3] and appear to be the most promising sensing devices for portable applications, since their thermal time constant is small

enough to reach the operating temperature by means of a low-power integrated heater, and to operate the device at different temperatures in time and in space[4][5]. On the other hand, the research is also concentrated on developing read-out electronic circuits in IC form, which are mandatory for realizing portable gas sensing systems. Their compactness is extremely interesting since it is possible include in the same IC both the conditioning of the signal coming from the sensor and the signal digitalization. In this way the read-out electronic circuit can be directly connected with the block implementing the pattern recognition digital signal processing algorithms for the final detection of the target gases. These digital blocks are the objective also of important research activity. For instance, recently developed dynamic pattern recognition techniques extract important information also from the derivative of the sensor response[6]. Therefore they require an electronic interface circuit sufficiently fast to preserve the transient data, i.e. that provides at least 10 accurate samples of the resistance value of every element of the array per second. Thus both the sensor micromodule and the IC-interface, reported in Fig. 1 should be fast enough to grant sufficient dynamic data for this kind of feature extraction method.

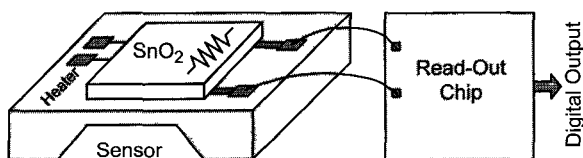


*Fig. 1. Block diagram of the proposed gas sensing Microsystem.*

## 2. Gas sensor development

According to the main guidelines of research on gas sensors, miniaturized and low power consumption microsensors have been designed and fabricated. These are chemoresistive gas sensors based on Metal Oxide thin films (MOX) acting as gas sensing elements, realized with the sol-gel technique and deposited by spin coating on silicon micromachined substrates equipped with integrated heater/thermometer and interdigitated electrodes. Since these types of gas sensors are based on chemiadsorption and charge transfer processes between the gas molecules and MOX film causing a simple electrical resistance variation of the gas sensing element, they are characterized by a real functioning easiness. To this important feature, they join enhanced gas sensing properties due to the nanocrystalline sol-gel MOX films, small size and reduced power consumption due to the use of Si-micromachined substrates[3]. The developed substrates are Si micro-hotplates ( $2 \times 2 \text{ mm}^2$  sized) with a central area consisting of a thin dielectric membrane of silicon nitride ( $\text{Si}_3\text{N}_4$ ) ( $\sim 0.8 \text{ }\mu\text{m}$  thick and  $\sim 700 \times 700 \mu\text{m}^2$  lateral sized), suspended and supported by a silicon bulk rim. Inside the central area, a smaller region ( $\sim 300 \times 300 \mu\text{m}^2$  sized), the “active area”, on which the sensing element is deposited, was realized. Following a vertical approach, a

buried platinum heater/thermometer and IDC electrodes have been integrated in the active area in different layers of the dielectric membrane. The implementation of a thermometer in the Pt heater structure allows the simultaneous measurement of the working temperature of the sensor. The Pt interdigitated electrodes, deposited by RF sputtering, consist of  $n=5$  fingers  $50\mu\text{m}$  spaced,  $20\mu\text{m}$  wide and  $300\mu\text{m}$  long; the use of interdigitated electrodes with a large length-to-width ratio allows even the evaluation of sensing films with very high sheet resistivity. The dielectric membrane provides the thermal insulation between the active area, heated up to the high working temperatures of the sensor ( $200\div 400^\circ\text{C}$ ), and the external Si-bulk frame, that remains at room temperature. In such a way the low thermal conductivity and inertia of the micromembrane allows a low power consumption (in the range of  $20\div 50\text{mW}$ ) and the possibility to operate not at constant but periodically variable temperature (pulsed or oscillating), being the latter a measurement methodology which improves the sensor selectivity. Fig. 2 shows a cross section scheme of the designed Si-micromachined substrates.

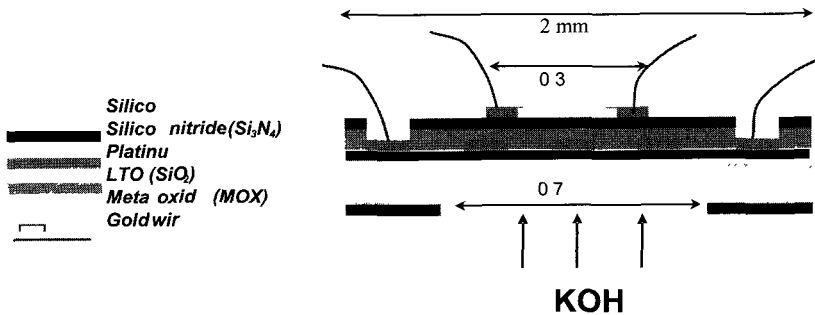


Fig. 2. Cross section scheme of the designed Si-micromachined substrates.

### 3. The IC interface

The read-out circuit[10] is composed of a single-ended continuous-time programmable trans-resistance amplifier that converts the current  $I_{\text{sens}} = V_{\text{REF}}/R_{\text{sens}}$  flowing through the sensor into a voltage and of a fully-differential switched-capacitor oversampled 13-bit incremental A/D converter that digitizes the output of the first stage. In addition two 8-bit DACs and a DSP section allow us to reconfigure the input stage features to match sensor specifications. The gas sensor, modeled as a resistance  $R_{\text{sens}}$ , is connected between a reference voltage  $V_{\text{REF}}$  and the operational amplifier (opamp) virtual ground, biased at  $V^+$ . A current  $I_{\text{sens}}$  is then flowing across the sensor given by:  $I_{\text{sens}} = (V_{\text{REF}} - V^+)/R_{\text{sens}}$ , being the nominal voltage drop across the sensor  $50\text{mV}$ . The sensor resistance possible values range in the 5.2-decade extremely large interval [ $100\Omega$ - $20\text{M}\Omega$ ], that would give a comparable and, then, extremely large dynamic range at the opamp output voltage. This would result to be impracticable. In order to

accommodate this large  $R_{\text{sens}}$  range, the feedback resistance  $R_f$  is adjusted in order to be comparable to  $R_{\text{sens}}$ . In this way the output swing is comparable to  $V_{\text{REF}}$  and can be managed by the opamp. This  $R_f$  programming is done by splitting the resistance values into 10 scales, each of them covering about half decade. These different scales are generated by realizing the feedback resistor with an array of different possible  $R_f$  to be properly connected for each scale. The use of different scales requires to face the problems arising from the mismatches (mainly in terms of offset and gain error) between consecutive scales. A calibration technique is used for this purpose, which exploits a partial overlap of adjacent scales of about a quarter of decade. Notice that the above approach of adjusting the  $R_f$  value to match the  $R_{\text{sens}}$  value does not give a full resistance matching, due to quantized values of  $R_f$ . Any mismatch between  $R_f$  and  $R_{\text{sens}}$  corresponds to a deviation of the output voltage and then limits the accuracy. Fig. 3 shows the complete read-out schematic. In this circuit, the regulated current source used to compensate inter-scale system offset mismatch is realized with an 8-bit buffered resistive DAC (DAC1 in the schematic) and a programmable resistor  $R_{\text{DAC}}$ , that also needs to be selected from an array. In this design we decided to have always  $R_{\text{DAC}}=R_f$  in order to keep the opamp working with gain and feedback factors of the same order of magnitude over the entire dynamic range and to guarantee a good integrated component matching for  $R_{\text{DAC}}$  and  $R_f$ . Notice that  $I_{\text{cal}}$  and  $I_{\text{sens}}$  may range from 25nA to 5mA. Furthermore, by regulating the sensor voltage reference ( $V_{\text{REF}}$ ) through an additional buffered DAC (DAC2), it is possible to correct separately the gain-error of each of the 10 scales available in the circuit. As shown in Fig. 3, the two 8-bit D/A converters (DAC1, DAC2) and the two selector circuits for  $R_f$  and  $R_{\text{DAC}}$  (SEL1, SEL2) are all controlled by a common digital unit, whose tasks are of course the choice of the current measurement range and the actual correction of offset and gain error for each scale using the “calibration words” determined during initial setup phase.

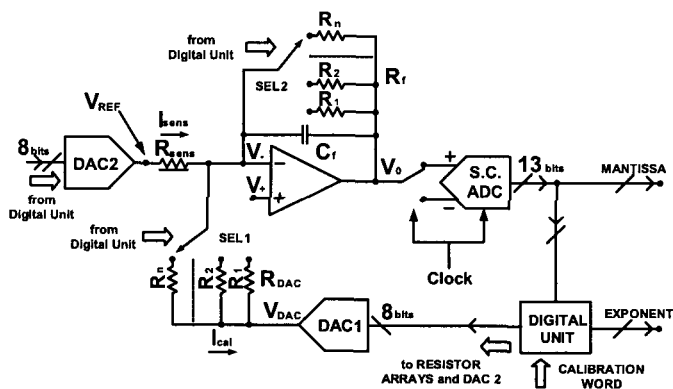


Fig. 3. Integrated re-configurable front-end channel.



#### 4. Electrical and chemical measurements

The electrical characterization of the interface circuit accuracy has been performed testing separately every single one of the ten available partially overlapped scales and then by re-constructing the full system transfer function by canceling inter-scale offset and gain error mismatch. Thus in Fig. 4, the relative error in the resistance value measurement, performed over the complete 5.3 decades dynamic range, may be plotted. These data underlines that the accuracy of the front-end circuit in terms of relative precision of resistance value measurement is better than 0.1% for almost the whole input dynamic range, while the root mean square (RMS) electrical error in resistance sensing is better than 250ppm. Several chemical measurements with different gas types (as methane and ethanol) by using the designed micromodule system were performed. A calibration gas sensing test-bench for electrical-conductance measurements in controlled atmosphere is used for the experiments. In particular, the microsensor is introduced into a stainless-steel-made cylindrical test cell, connected to a multichannel mass flow programmer/display (MKS mod.647B) driving three separate gas-channels connected to four distinct analog mass flow controller (MFCs of MKS mod.1179A). Dry air is used both as reference gas and as diluting gas to obtain gaseous mixtures in air at different concentrations. Certified bottles of synthetic air and methane (2000 ppm in dry air) are used; whereas, for ethanol, different vapor concentrations were obtained by diluting in air the saturated vapors coming from a ethanol bubbler. The electrical characteristics of the developed microsensors are obtained measuring by prototype front-end circuit connected to the sensor device. A photo of the instrumentation setup is reported in Fig. 5. For the gas sensing tests, undoped and Pd-doped (with 5% weight of palladium) tin oxide based microsensors are used. Fig. 6 shows the system transient response varying ethanol concentration, from 4000ppm<sub>vol</sub> to 6400ppm<sub>vol</sub>. The coating used in these particular measurements is a Pd-doped SnO<sub>2</sub> thin layer with a working temperature of the hotplate of 350°C.

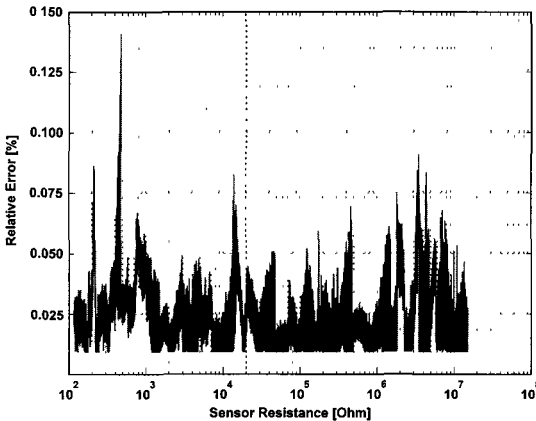


Fig. 4. Relative error of  $R_{sens}$  measurement [100Ω-20MΩ].



Fig. 5. Complete instrumentation used for chemical measurements.

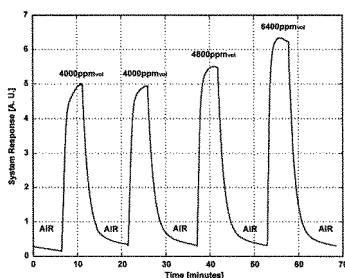


Fig. 6. System transient response to ethanol.

## 5. References

- [1] "Portable system for ambient gas monitoring with smart A/D front-end improving sensors resolution and accuracy", PRIN 2003091427, [<http://ims.unipv.it/prin03>], funded by Italian Government.
- [2] D. Barrettino, M. Graf, S. Hafizovic, S. Taschini, C. Hagleitner, A. Hierlemann, H. Baltes, "A single-chip CMOS micro-hotplate array for hazardous-gas detection and material characterization", IEEE ISSCC proceedings, pp. 312-313, 2004.
- [3] S. Capone, P. Siciliano, "Gas Sensors from Nanostructured Metal Oxides", Encyclopedia of Nanoscience and Nanotechnology, Vol. 3, pp. 769-804, 2004.
- [4] G. Ferri, N. Guerrini, V. Stomelli, "A temperature control system for integrated resistive gas sensor arrays", SPIE VLSI Circuit and Systems II, Vol. 5837, pp. 972-982, 2005.
- [5] General Olfaction and Sensing on a European Level, "GOSPEL" Network, [<http://www.gospel-network.org>], funded by European Community.
- [6] E. Martinelli, G. Pennazza, C. Falconi, A. D'Amico, C. Di Natale, "Comparison between two alternative feature extraction methods for chemical sensor array", World Scientific AISEM proceedings, pp. 334-339, 2003.
- [7] M.Grassi, P.Malcovati, G. De Iaco, A.Baschirotto, "An Integrated Wide-Range Resistance-to-Time Converter With Decoupled Oscillator", AISEM book of abstracts, pp.172, 2005.
- [8] A. Flammini, D. Marioli, A. Taroni, "A low-cost interface to high value resistive sensors varying over a wide range", IEEE IMTC proceedings, pp. 726-731, 2003.
- [9] D. Barrettino, M. Graf, W. H. Song, K. Kirstein, A. Hierlemann, "Hotplate-based monolithic CMOS microsystems for gas detection and material characterization for operating temperatures up to 500/spl deg/C", IEEE Journal of Solid State Circuits, vol.39, n. 7, pp. 1202-1207, 2004.
- [10] P. Malcovati, M. Grassi, F. Borghetti, V. Ferragina, A. Baschirotto, "Design and Characterization of a 5-Decade Range Integrated Resistive Gas Sensor Interface with 13-Bit A/D Converter", IEEE Sensors proceedings, in press, 2005.

# **Polymeric Replicas from Porous Silicon Template (and Its Response to Vapour)**

Vera La Ferrara, Ivana Nasti, Ettore Massera, and Girolamo Di Francia  
*ENEA, Centro Ricerche Portici Località Granatello 80055 Portici (NA)*  
[vera.laferrara@portici.enea.it](mailto:vera.laferrara@portici.enea.it)

## **Summary**

Polystyrene replica is realized preparing polystyrene and depositing the polymer onto a nanostructured porous silicon matrix used as a template. The thin polymer film is peeled off from the substrate and exposed to organic vapours. Swelling affects the optical reflectance and, by a specially adjusted set-up, the kinetic of the vapour desorption is measured in order to investigate replicas as drug delivery systems.

## **1 Introduction**

Nanometer sized structures are emerging for the development of future devices in several different fields. Polymeric materials have, in fact, many characteristics that make them ideally suited for defining nano-electromechanical structures even with low-cost processes such as replication and templating. Flexible polymers have been actually used as replicas of nanostructured template to fabricate sensors, deformable and tunable opticals fibers and biocompatible materials. They have good mechanical property (Young's modulus can be tuned over two orders of magnitude), are cheap and have the property to tight with silicon and glass permitting to design hybrid devices that could contain silicon electronics, light sources and detectors [1]. Moreover porous polymers are quite attractive due to their porous size related tunable diffusion kinetic . As a matter of fact, swelling-controlled release systems are actually used as drug release systems in a wide range of applications from simple nasal to buccal to more complex bioadhesive uses [2]. Recently, porous polymer nanostructures produced from an oxidized porous silicon template have demonstrated their effectiveness for drug delivery applications [3]. Because of the tunability of porous silicon surface, it is possible to fabricate several polymer replicas. In this way, it is possible to transfer the mechanical properties of porous silicon to a variety of organic polymers, tuning their drug release time.

In this work we have realized porous polystyrene replicas using as a template a nanostructured porous silicon (PS) matrix. To investigate the feasibility of such replicas as drug delivery systems, the thin polymer film has been peeled off from the substrate and exposed to organic vapours. A new optical measurement

method based on the modification of the optical reflectance induced by the polymer swelling is also proposed in order to measure the desorption kinetic.

## 2 Experimental

To fabricate the porous silicon masters, PS samples have been prepared by anodic etch of n-type <100>-oriented Si with 1 ohm\*cm resistivity in a solution 50% aqueous HF:isopropilic alcohol (7:3 by volume) with a current density of 40 mA/cm<sup>2</sup> for 10 minutes. Samples have been partially oxidized in ambient air for about one month. Polymer has been prepared using a solution of polystyrene in toluene obtained on a rotating plate at 25°C for about 1 hour. The porous polymer replica has been prepared by means of polystyrene/toluene solution cast into oxidized porous silicon and dried in ambient air for two days.

The porous silicon template has been immersed in HF for 1h. Resulting composite porous silicon/polystyrene has been mechanically peeled off from the porous substrate and then washed in 10% NaOH to remove nanoporous phase on polymeric replica surface. Porous polystyrene replica, so obtained, has a thickness of 300 nm. A polystyrene film, with the same thickness, peeled off from silicon substrate, has been fabricated and measured to compare the chemical and morphological properties with porous polystyrene replica ones. In figure 1 we show a SEM image of the porous polystyrene replica.

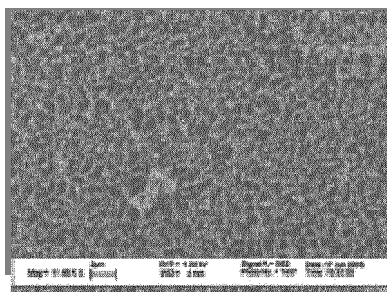


**Fig. 1** SEM image of porous polystyrene replica after removal from porous silicon template and washing in NaOH.

In order to characterize polystyrene replicas as controlled release devices, polystyrene films have been put in a test chamber where acetone saturated vapour (20%) mixed with nitrogen has been introduced as swelling agent.

Optical reflectance has been measured by means of an optical fiber (illuminating samples with an halogen lamp) and collecting data at a fixed wavelength (631 nm) with a CCD spectrometer (figure 2). Total gas flow has been set to 500 sccm in all the performed tests.

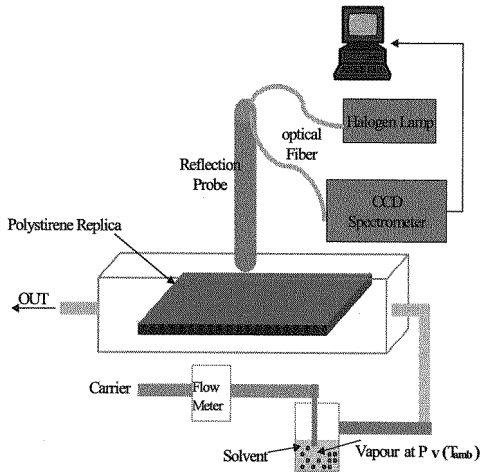


**Fig. 2** Experimental set up for optical measurements. Acetone saturated vapour mixed with nitrogen has been introduced in the test chamber controlling total gas flow by a mass flow meter. An optical fiber illuminates samples and its optical reflectance is collected by a CCD spectrometer.

### 3 Results and discussion

Optical reflectance dynamic response of polymeric replica has been recorded switching from nitrogen to acetone saturated vapour for both the polystyrene film and the porous polystyrene replica (figure 3).

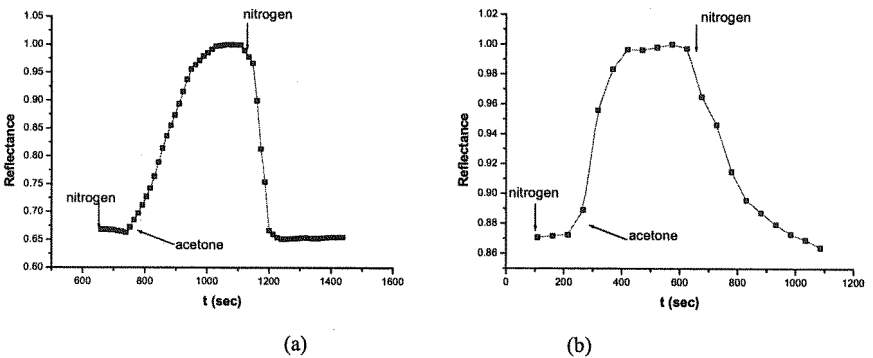


**Fig.3** Reflectance measurement of (a) the polystyrene film and (b) the porous polystyrene replica switching from nitrogen to acetone saturated vapours.

Measurements show that the mechanism of acetone release of polystyrene replicas is different respect to polystyrene one.

At this aim, the desorption kinetic has been investigated analyzing reflectance decreasing, obtained when nitrogen is introduced in test chamber. Results are shown in figure 4.

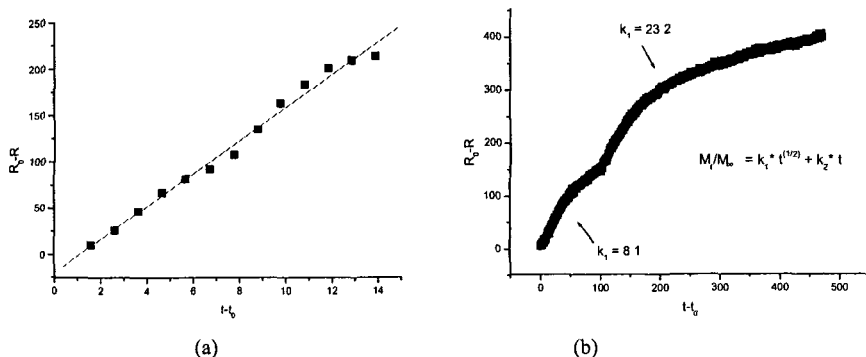


Fig. 4 Reflectance data  $R_0-R$  and time  $t-t_0$ , reported as axis, have been extracted from figure 3 when nitrogen is introduced after samples have adsorpted acetone saturated vapour. In particular  $R_0$  and  $t_0$  are respectively reflectance and time values in presence of nitrogen at the initial time. Acetone release data have been fitted: (a) linear fit for polystyrene film (b) Peppas' model [4] for porous polystyrene replica

As expected, measurements show that mechanism of acetone release is strictly Fickian only for porous polystyrene replica. In figure 4a it is reported linear behavior of acetone release for polystyrene film. In figure 4b it is evident a Fickian behavior for acetone release kinetic. Peppas' equation [4] reported in figure and used for data fit, describes the fractional drug release. Different constant  $k$  are probably due to morphology of porous polystyrene replica.

#### 4 Conclusions

We have shown how it is possible to transfer porous silicon morphology onto polystyrene and obtain polymeric replicas capable to tune the kinetic of chemical release when exposed to organic vapour.

#### References

- [1] S.R.Quake and A. Scherer, Science, vol 290 (2003) 1536-1540
- [2] N.A. Peppas and P. Colombo, J. of Controlled Release, 45 (1997) 35
- [3] Y. Y. Li, F. Cunin, J. R. Link, T. Gao, R. E. Betts, S. H. Reiver, V. Chin, S. N. Bhatia, M. J. Sailor, Science 299 (2003) 2047
- [4] N.A. Peppas, P. Bures, W. Leobandung and H. Ichikawa, Europ. J. of Pharmaceutics and Biopharmaceutics, 50 (2000) 27

# **A Software Tool for the Simulation of IPMC Actuators and Sensors**

C. Bonomo, L. Fortuna, P. Giannone, S. Graziani, S. Strazzeri  
*Dipartimento di Ingegneria Elettrica Elettronica e dei Sistemi*  
*University of Catania*  
*Viale A. Doria, 6 – 95125 – Catania, ITALY*  
*Tel. +39 095 7382327- Fax: +39 095 330793*  
[pietro.giannone@diees.unict.it](mailto:pietro.giannone@diees.unict.it)

D. Harvey, G.S. Virk  
*School of Mechanical Engineering*  
*University of Leeds*  
*Woodhouse Lane, Leeds, West Yorkshire, UK. LS2 9JT*  
*Tel. +44 113 343 2156- Fax: +44 113 343 2150*

## **Summary**

Ionic Polymer Metal Composites (IPMCs) are emerging materials made of an ionic polymer membrane metallized on both sides with a noble metal. They can work either as a low-voltage-activated motion actuator or as a motion sensor. When an electric field is applied across the IPMC thickness a deformation occurs, while if they are deformed they generate a detectable voltage.

IPMCs have the additional benefits of being pliable lightweight, soft and so forth. These benefits make IPMCs suitable for applications in very different fields including robotics, aerospace, biomedical, etc.

In this paper the authors introduce a software tool to simulate the behaviour of both IPMC sensors and actuators working in air. The software tool is completed by a graphical user interface (GUI) developed in Matlab®. The GUI has been developed in order to give a useful tools that allow the user to understand the behaviour and the parameters involved in the phenomena. In the GUI, parameters affecting the sensing and the actuating properties of IPMC-based transducers are taken into account together with their dynamic characteristics

## **1 Introduction**

Ionic Polymer Metal Composites (IPMCs) are emerging materials used to realize motion actuators and sensors [1],[2]. In the former case a voltage input is able to cause the membrane to bend while in the latter case by bending an IPMC membrane, a voltage output is obtained. Figures 1a and 1b show the basic working principles of an IPMC respectively as actuator and as sensor.

Several applications can be found in the literature regarding these materials [3],[4],[5].

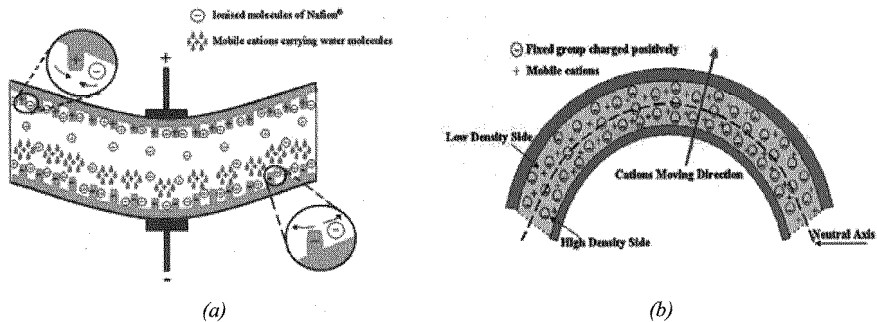


Fig.1 (a) The IPMC working as actuator and (b) as sensor.

Based on the analytical models introduced in [7] and [8], a software tool for the simulation of the IPMC behaviour, both as motion actuator and sensor, has been implemented. The models, on which the software tool is based, are organized into blocks. As far as the IPMC actuator is concerned, the model is divided into a cascade of two sub-blocks, the first is devoted to predicting the absorbed current as a function of the input voltage, and the second that transduces the absorbed current either to a deflection or in a force, as requested by the user.

As for the sensor model, the software for the sensor simulation has been implemented by a single block able to convert the mechanical stimulus into an electrical signal.

## 2 The IPMC working as actuator

As largely reported in the literature [1], [5], [6], the IPMC mechanical behaviour is produced basically from the charge accumulation. Starting from this assertion, the solution to adopt two sub-blocks allowed the estimation of the current absorbed by applying a voltage across the electrodes. The current is then converted to a mechanical reaction by using an electromechanical model.

The electrical transduction was obtained by using an equivalent nonlinear circuit in order to estimate the non-linear behaviour between the applied voltage and the absorbed current [7]. The electromechanical transduction is obtained by using the well-know Euler-Bernoulli theory of the pinned beam and an adaptation of the theory of the piezoelectric coupling effect. A scheme of the model to implement the proposed software is reported in Figure 2.

The first step to carry out is the identification of the parameters  $\bar{P}$  in the model for different IPMC samples, in order to create a database. The



identification is performed by testing the samples, acquiring the necessary data and optimising the parameters so that the model matches the response.

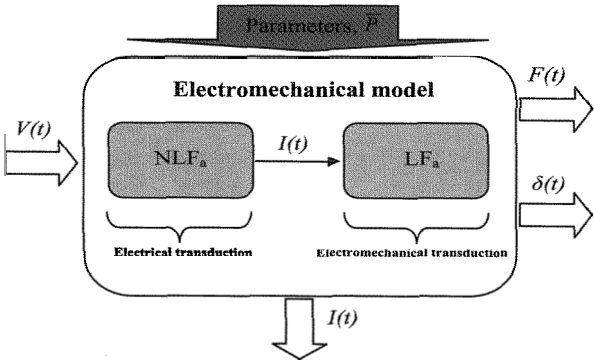


Fig.2 Scheme of the electromechanical model.

### 2.1 The actuator software

The software tool is very easy to use: the GUI appears clear, and each parameter is well explained. The graphic interface shown in Figure 3 gives the reader an idea on how it is possible to predict the nonlinear behaviour of the IPMC at low frequency.

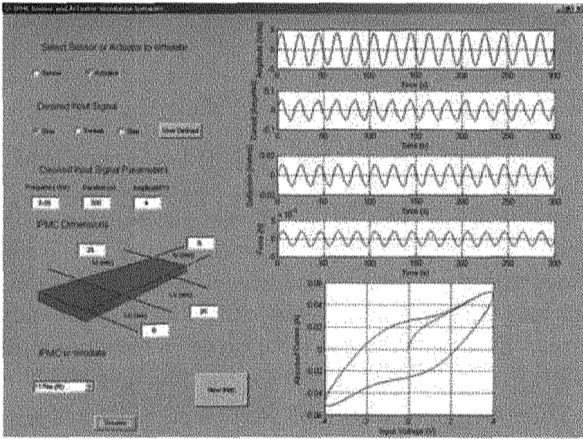


Fig.3 The GUI of the software tool proposed for the actuator.

The software interface requires both the dimensions of the IPMC, which desired behaviour is to be simulated and the applied voltage signal. On the right

hand side of the panel the signals involved in the simulation process are shown. Those signals are respectively: the applied voltage, the absorbed current, the free deflection, the blocking force and the voltammogram.

If a voltage sweep frequency is selected as input, the software is able to estimate also the resonance frequency and the amplitude of the deflection at that frequency.

### 3 The IPMC working as sensor

As far as the IPMC working as sensor is concerned, a linear model was suggested based, as previously mentioned, on the Euler-Bernoulli theory of the pinned beam and on an adaptation of the theory of the piezoelectric coupling effect [8]. The scheme of the electromechanical model used to implement the simulation software, together with the involved quantities, is reported in Figure 4.

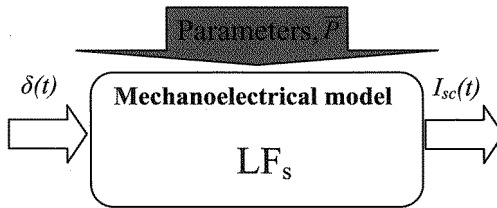


Fig.4 Scheme of the mechano-electrical model.

#### 3.1 The sensor software

The GUI of the sensor can be opened directly by the window shown in Figure 3, in particular it is sufficient to select the *sensor* button to switch in the sensor simulation mode. Figure 5 shows the software interface to simulate the IPMC sensor behaviour. In this case the input signal is not a voltage but a deflection.

A typical simulation phase is also reported in Figure 5 where the input signal is a frequency sweep deflection. As it can be seen from the same figure, the sensor response depends on the frequency of the input signal. In particular, the sensor shows a typical band pass behaviour.

#### Acknowledgments

The research activity presented in the paper is supported by the EU under the VI Framework project ISAMCO NMP2-CT-2003-505275; the membranes used in the mentioned measurement surveys were supplied by CCR (Consorzio Catania Ricerche), as part of the project collaboration activity.

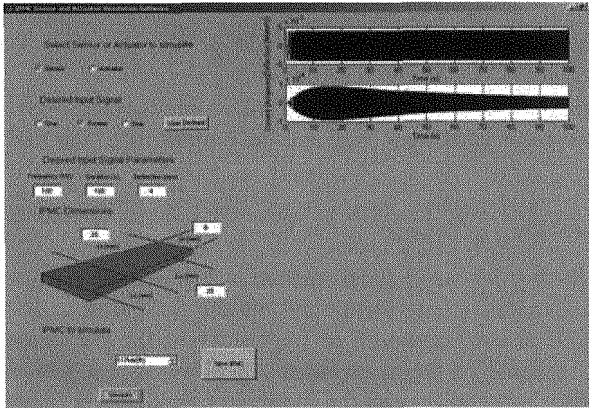


*Fig.5 The GUI of the software tool proposed for the sensor.*

## References

- [1] M. Shahinpoor and K. J Kim, Ionic polymer–metal composites: I. Fundamentals, *Smart Materials and Structures* 10, 2001, pp 819–833.
- [2] M. Shainpoor, Y. Bar-Cohen, J.O. Simpson, and J. Smith, Ionic Polymer-Metal Composites (IPMC) as Biomimetic Sensors, Actuators, and Artificial Muscle - A Review, *Int. J. Smart Materials and Structures*, Vol. 7, 1998, pp. R15-R30.
- [3] Shahinpoor M., Kim J. K., S., IV. Industrial and medical applications, *Smart Materials and Structures* 14 (2005) 197–214
- [4] Tung S., Witherspoon S. R., Roe L. A., Silano A., Maynard D. P., Ferraro N., A MEMS-based flexible sensor and actuator system for space inflatable structures, *Smart Materials and Structures* 10 (2001) 1230–1239
- [5] Bar-Cohen, Electroactive Polymers As Artificial Muscles-Capabilities, Potentials And Challenges, *HANDBOOK ON BIOMIMETICS*, Yoshihito Osada (Chief Ed.), Section 11, in Chapter 8, “Motion” paper#134, publisher: NTS Inc., Aug. 2000.
- [6] S. Nemat Nasser, J. Y. Li, Electromechanical response of Ionic Polymer Metal Composites, *Journal of Applied Physics*, Vol. 87 (2000), n° 7, pp.3321-3331.
- [7] C. Bonomo, L. Fortuna, P. Giannone, S. Graziani, An Electric Circuit to model Ionic Polymer-Metal Composites as Actuator, *IEEE Transactions on Circuits & Systems* Vol. 53 No. 2 2006.
- [8] C. Bonomo, L. Fortuna, P. Giannone, S. Graziani and S. Strazzeri, A model for ionic polymer metal composites as sensors, *Smart Materials and Structures* 2006, Vol. 15, pp.749-758.

# Synthesis and Characterization of Imprinted TiO<sub>2</sub> Nanoparticles. Preliminary results

Rosaria Anna Picca, Cosimino Malitesta  
*Laboratorio di Chimica Analitica, Dipartimento di Scienza dei Materiali,  
Università di Lecce, Via Arnesano, 73100 Lecce  
rosanna.picca@unile.it*

Daniela Manno  
*Laboratorio di Microscopia elettronica, Dipartimento di Scienza dei Materiali,  
Università di Lecce, Via Arnesano, 73100 Lecce*

## Summary

The synthesis of TiO<sub>2</sub> nanoparticles (TiO<sub>2</sub>-NPs) in the presence of a target analyte (*l*-tyrosine) has been developed to prepare imprinted nanostructured materials. The effective growth of TiO<sub>2</sub>-NPs and their size distribution in stable dispersions has been evaluated by HRTEM analysis. UV-Vis spectroscopic characterization has been performed to study interactions between TiO<sub>2</sub>-NPs and *l*-tyrosine.

## Introduction

Molecular imprinting [1] has spread out as a viable technique to realize high selective recognition sites for a target molecule. Imprinted polymers (MIPs) are employed for several analytical applications as they can mimic bioreceptor behavior while improving stability and reducing costs [1]. In particular, they were also proposed as active layers in sensors to detect different analytes such as drugs, amino acids, toxins, pesticides [2]. However, conventional MIPs suffer of some disadvantages: heterogeneous site affinity (non-covalent approach), incomplete template removal, reduced number of active sites and difficult access to them [3, 4]. Thus, alternative imprinting methodologies and materials have been developed to overcome these limitations [4, 5].

Inorganic oxides appear suitable candidates for imprinting procedures: in fact, they possess rigidity, high surface area and porosity [6]. Among them, SiO<sub>2</sub> and TiO<sub>2</sub> 3-D matrices are easily realized via sol-gel process. In last years, other techniques have been applied to prepare imprinted thin films directly on a substrate (for example, the surface of a transducer): surface sol-gel process [7], liquid phase deposition [8], spin coating [9]. As a result, recognition sites are present in a high number and located near or at the surface, thus mass transport is favored enhancing sensor performances.

Nanoparticles (NPs) possess these properties in even higher degree leading to the development of sensors based on  $ZrO_2$ -NPs [10] and even on single-nanoparticle [11]. On the basis of these considerations, it appears very attractive to conjugate the selectivity conferred by imprinting technology and the sensitivity of NPs in sensors.

To our best knowledge, no work has been presented on imprinting of  $TiO_2$ -NPs. In this paper it is reported for the first time the synthesis of imprinted  $TiO_2$ -NPs. The selected template is *l*-tyrosine and growth of  $TiO_2$ -NPs is performed by room temperature hydrolysis of titanyl oxalate complex as illustrated in our previous work [12]. In fact, adding Ti (IV) salt to an *l*-tyrosine (Tyr) solution could lead to the formation of colloidal titania imprinted by this amino acid. This target molecule was chosen as it plays a central role in biological systems because it is not only the precursor of dopamine, etc. but its metabolism is also involved in some diseases (Parkinson's, atherosclerosis, etc.) [13]. HRTEM and UV-Vis spectroscopy characterizations are presented to assess NPs formation and to evaluate occurrence of imprinting effects.

## Experimental

$K_2TiO(C_2O_4) \cdot 2H_2O$  and *l*-tyrosine were purchased from CARLOERBA Analytical Grade, while phenol (> 99%),  $HClO_4$  and NaOH from Sigma. All chemicals were used as received. All solutions were prepared in ultrapure water (Milli-Q, Millipore,  $18.2 M\Omega \cdot cm$ ).

UV-Vis measurements were performed with a Varian Cary 50 UV-VIS spectrophotometer computer-controlled by CaryWin-UV software.

A JEOL 2010 microscope was used at an acceleration voltage of 160 kV for HRTEM analysis.

## Results and discussion

HRTEM analysis (Figure 1) was carried out to assess NPs growth in the presence of Tyr. and their size distribution. A mean diameter of 2 nm was found.

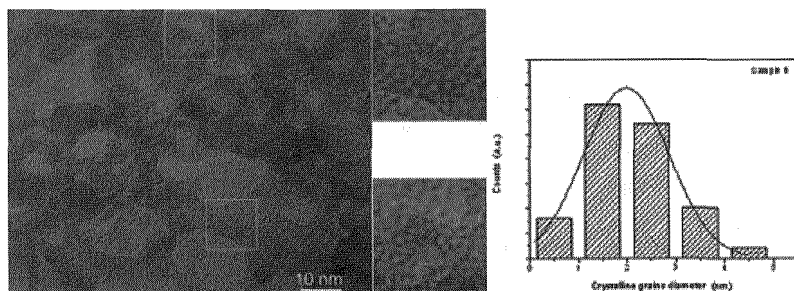
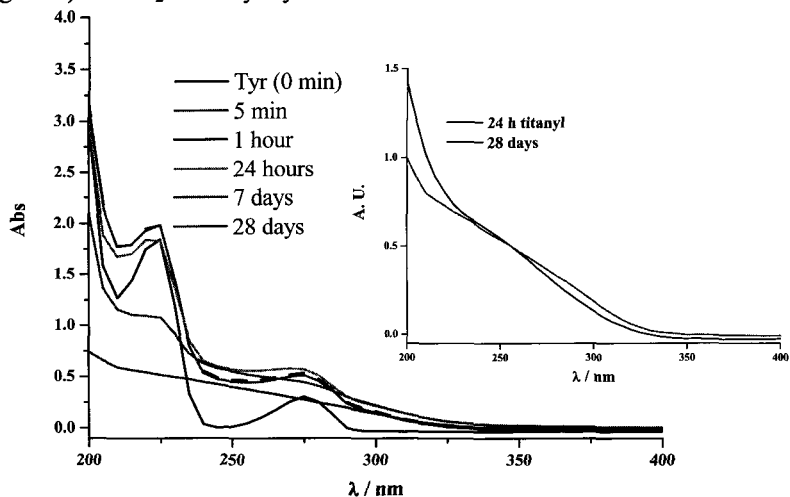


Fig.1 HRTEM micrographs and size distribution of NPs grown from Tyr  $2.5 \cdot 10^{-4} M$  with titanyl oxalate  $10^{-4} M$

As already shown [12],  $\text{TiO}_2$ -NPs growth in titanyl aqueous solutions can be followed by UV-Vis spectroscopy as they present an absorption band between 250-350 nm.

As also Tyr shows two absorption peaks (Figure 2 – Tyr (0 min)) at 225 and 275 nm, spectroscopic characterization was employed to record time evolution (Figure 2) of  $\text{TiO}_2$ -NPs-Tyr system.



**Fig.2** UV spectra of  $2.5 \cdot 10^{-4}$  M Tyr solution with titanyl oxalate  $10^{-4}$  M.  $\text{TiO}_2$  spectrum after 24 hours growth and  $\text{TiO}_2$ -NPs-Tyr spectrum after 28 days in the inset

As it can be noticed, the usual appearance of  $\text{TiO}_2$  band is observed, while Tyr absorption disappears after 28 days, leaving a spectrum quite similar to  $\text{TiO}_2$  alone (see the inset). This evidence supports the hypothesis of tyrosine inclusion in  $\text{TiO}_2$ -NPs during their growth. The possible interactions of tyrosine carboxylic moieties with  $\text{TiO}_2$  surface [14] are not evident in this case, because a 350 nm red shift in the  $\text{TiO}_2$  band did not occur.

It was also evaluated if pH environment can influence the formation of  $\text{TiO}_2$ -NPs (in titanyl and/or titanyl/tyrosine systems).

Extremely acidic or basic media ( $\text{HClO}_4$  2 M,  $\text{NaOH}$  1 M) cause inhibition of nanoparticle nucleation in both systems. No change is observed when titanyl is added to acid (see figure 3) or basic (data not shown) solutions of Tyr. On the other hand, acidification (or alcalinization) of  $\text{TiO}_2$ -Tyr samples (3 hours aged) does not alter UV spectra evolution confirming that NPs nucleation, not growth, is inhibited by extreme pHs.

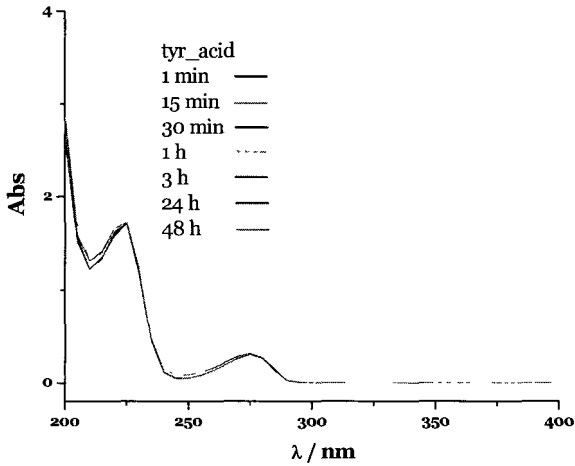


**Fig.3** UV spectra of  $2.5 \cdot 10^{-4}$  M Tyr solution in  $\text{HClO}_4$  2 M before and after adding  $10^{-4}$  M titanyl

As  $\text{TiO}_2$  photocatalytic effects [15] are well known, it is important to estimate sunlight influence on  $\text{TiO}_2$ -NPs formation. Thus, some aliquots, both for titanyl and titanyl/Tyr systems, were stored in the dark and exposed to light only during UV measurements. The recorded UV spectra indicate that radiation does not affect colloids.

Formation of  $\text{TiO}_2$ -NPs in presence of phenol was investigated to assess the role of  $-\text{OH}$  phenolic group in imprinting by Tyr. Figure 4 shows that increasing in absorption occurs within 24 h and it depends on  $\text{TiO}_2$ -NPs growth as no significant modification of phenol spectrum is evident.

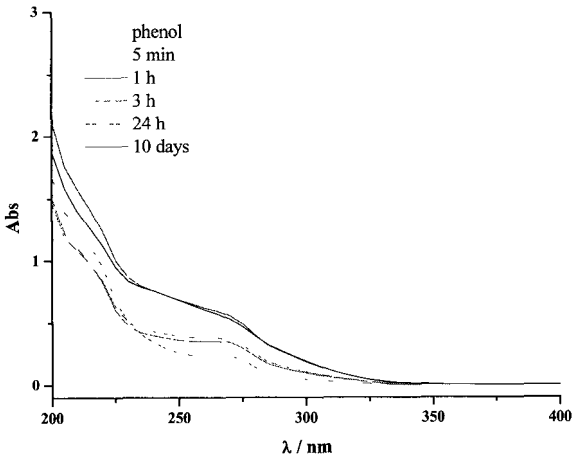


**Fig.4** UV spectra of  $2.5 \cdot 10^{-4}$  M phenol solution before (yellow) and after addition of  $10^{-4}$  M titanyl oxalate

As a result, it can be concluded that phenolic hydroxyl group is likely not responsible for binding with titania.

## Conclusions

The first example of synthesis of TiO<sub>2</sub>-NPs imprinted for *l*-tyrosine has been proposed, based on hydrolysis of a titanyl complex in Tyr aqueous solutions. HRTEM characterization has been developed to confirm TiO<sub>2</sub>-NPs formation. Spectroscopic investigation of TiO<sub>2</sub>-Tyr system has revealed that recorded spectra are not the sum of single species absorption profiles but there is a significant time evolution. In particular, while TiO<sub>2</sub>-NPs grow also in this case, Tyr absorption decreases during time until disappearing after almost one month. Extreme pH conditions inhibit NPs nucleation also in the titanyl/Tyr system. The use of phenol as “template” has demonstrated that phenolic moiety does not interact with titania. These preliminary results on spectroscopic analysis indicate that inclusion (hopefully imprinting), rather than adsorption, of amino acid molecules into TiO<sub>2</sub>-NPs occurs. Further characterizations (Resonance Raman Spectroscopy, ATR-IR) will be performed to fully understand interactions and separative techniques (Flow Field Fractionation) will be applied to isolate imprinted NPs for the preparation of nanostructured thin films as recognition elements in piezoelectric sensors.

## References

1. K. Haupt, *Chemical Communications*, (2003), 171
2. S.A. Piletsky, S. Subrahmanyam, A.P.F. Turner, *Sensor Review*, 21 (2001), 292
3. N. Sallacan, M. Zayats, T. Bourenko, A.B. Kharitonov, I. Willner, *Analytical Chemistry*, 74 (2002), 702
4. S.C. Zimmerman, M.S. Wendland, N.A. Rakow, I. Zharov, K.S. Suslick, *Nature*, 418 (2002), 399
5. A. Katz, M.E. Davis, *Nature*, 403 (2000), 286
6. D.Y. Sasaki, *Molecularly Imprinted Polymers Man-made mimics of antibodies and their applications in analytical chemistry*, B. Sellaergren (Editor), Elsevier (2001) Amsterdam (The Netherlands) 213
7. S.-W. Lee, I. Ichinose, T. Kunitake, *Langmuir*, 14 (1998), 2857
8. L. Feng, Y. Liu, J. Hu, *Langmuir*, 20 (2004), 1786
9. M. Hashizume, T. Kunitake, *Langmuir*, 19 (2003), 10172
10. G. Liu, Y. Lin, *Analytical Chemistry*, 77 (2005), 5894
11. S.-K. Eah, H.M. Jaeger, N.F. Scherer, G.P. Wiederrecht, X.-M. Lin, *Applied Physics Letters*, 86 (2005), 031902/1
12. C. Malitesta, A. Tepore, L. Valli, A. Genga, T. Siciliano, *Thin Solid Films*, 422 (2002), 119
13. G.G. Huang, J. Yang, *Biosensors and Bioelectronics*, 21 (2005), 408
14. T. Rajh, J.M. Nedeljkovic, L.X. Chen, O. Poluektov, M.C. Thurnauer, *Journal of Physical Chemistry B*, 103 (1999), 3515
15. T. Cassagneau, J.H. Fendler, T.E. Mallouk, *Langmuir*, 16 (2000), 241



# A SINGLE CHIP GENERAL PURPOSE CIRCUIT FOR SENSOR INTERFACING AND CHARACTERIZATION

M. Schipani, T. Ungaretti  
*STMicroelectronics, via Tolomeo 1, 20010 Cornaredo (MI) - Italy,*  
*e-mail: monica.schipani@iet.unipi.it*

P. Bruschi, N. Nizza  
*Dipartimento di Ingegneria dell'Informazione, Università di Pisa,*  
*via G. Caruso, 56122 Pisa - Italy*

## Summary

A single-chip general purpose interface for MEMS sensors has been introduced. The capacitive readout circuit, consisting in a fully differential switched capacitor circuit implementing CDS and Chopper Stabilization Techniques is designed and illustrated. The circuit can be tuned to work with sensors of nominal capacitance values ranging from 200fF to 3pF, with a maximum differences between the two sensor elements of 500fF. The effectiveness of the input common mode stabilization circuit is demonstrated by means of electrical simulations.

## Introduction

MEMS sensors are very interesting devices thanks to their microscopic dimensions, high sensitivity and low power consumption. The mechanical sensor can be integrated with its electronic readout interface, obtaining a complete system on chip (or system in package), the capabilities of which make MEMS suitable for a wide range of application areas such as, for example, automotive industry, consumer electronics and industrial processes.

For each particular application, requiring a specific sensor, the electronic readout interface is designed according to the sensor characteristics and this increases the costs to produce a complete system. A valid solution to this problem is represented by a general purpose interface, capable of reading out different type of sensors. Such an interface represents also a good platform to quickly validate a new sensor architecture, reducing time to market.

A large variety of integrated sensors falls within the two main categories of capacitive and resistive sensors. Examples are accelerometers, pressure sensors and microphones. In this work, an interface with flexible read out channels for both capacitive and resistive sensors is presented.

A general overview of the whole chip is introduced, describing the various specifications of interest and how to meet them in terms of block diagram. Then we focus on the capacitive readout circuit that is a discrete-time (switched

capacitor) circuit, implementing a  $C/V$  (capacitance-to-voltage) conversion. This solution, differently from other techniques such as capacitance-to-time or capacitance-to-frequency conversion, allows to have both analogue and digital output, increasing the versatility of the interface. In this paper, the switched capacitor front end is presented in details, with particular emphasis on the input common mode control circuit. In particular the beneficial effect in terms of offset and sensitivity to parasitic capacitance mismatches reduction is shown.

### Description of the general purpose interface

The schematic block diagram of the general purpose interface is represented in Fig. 1. Different readout channels can be multiplexed to ensure the compatibility with the different type of sensor. Sigma-delta and SAR analog-to-digital converters for either precision and velocity performance, respectively, will be included. The interface is equipped with the testing and trimming circuitry, the voltage and current references and the generators of all the required clock signals. The interface has been designed to be able to communicate with low cost microcontroller with no need of external components so also the circuitry implementing SPI and I<sup>2</sup>C protocols will be included.

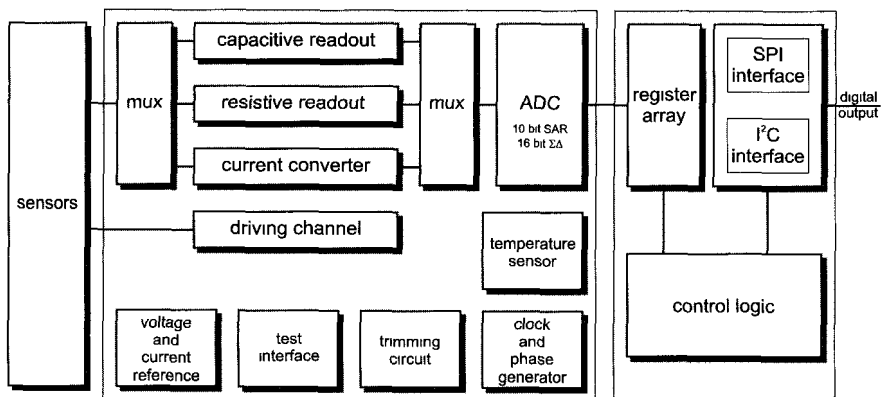


*Fig. 1 Schematic block of general purpose sensor interface*

The capacitive readout channel is a fully differential switched capacitor circuit implementing Correlated Double Sampling (CDS) [1] [2] and Chopper Stabilization Techniques. This system, represented in Fig. 2, works with a three phase clock in order to cancel offset and  $1/f$  noise. Careful design of the fully differential amplifier has been carried out to minimize the thermal noise. This is required since thermal noise represents the main source of uncertainty in CDS systems because of the foldover mechanism.

An internal trimming circuit provide for sensor capacitance mismatch calibration.

The gain and the bandwidth of the system are widely programmable to better meet applications requirements.

According with common MEMS sensors characteristic, the nominal value of input capacitances  $C_{S1}$  and  $C_{S2}$  can vary from 200fF to 3pF with a maximum difference of 500fF (absolute value).

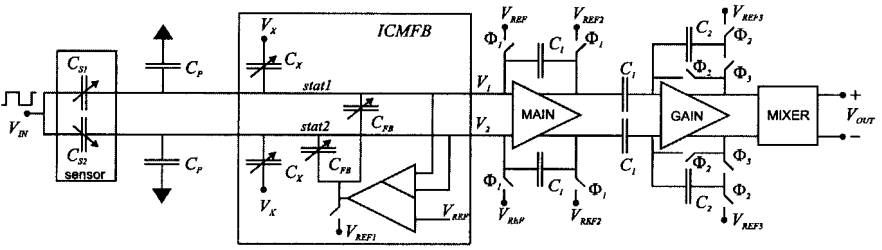


Fig. 2 Capacitive readout circuit

The chosen architecture requires the input common mode (ICM) to be constant to avoid gain, offset and non linearity errors, thus an input common-mode feedback (ICMFB) circuit has been included. The values of  $C_X$  and  $C_{FB}$  have to be chosen satisfying the equation

$$C_S V_{IN} + C_X V_X + C_{FB} V_{ICMFB} = 0$$

where  $C_X$  is the mean value of the two sensor capacitances.

In order to make ICMFB efficient for the whole sensor capacitance range, all capacitor used in ICM control circuit has to be opportunely programmable. Therefore, capacitive networks similar to that represented in Fig. 3 are used.

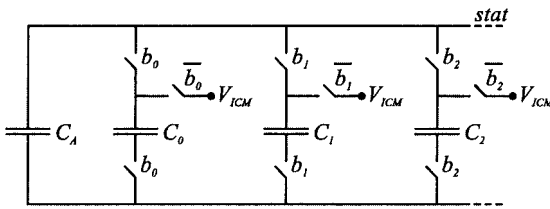


Fig. 3 Programmable capacitive network

The amplifier used in ICMFB is a folded cascode with an input differential pair (see figure 4) that senses the variation of input common mode voltage with respect of a voltage reference.

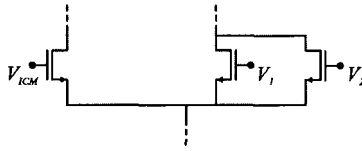


Fig. 4 Input differential pair of the amplifier used in ICMFB

### Simulation results

Fig. 4 shows the output waveform of the main blocks of the circuit. The input signal is a 3V square wave. The mean value of sensor capacitances  $C_S$  is 300fF with a difference of 1fF. An offset of 10mV has been introduced by means of a voltage source in series with the GAIN amplifier inputs.

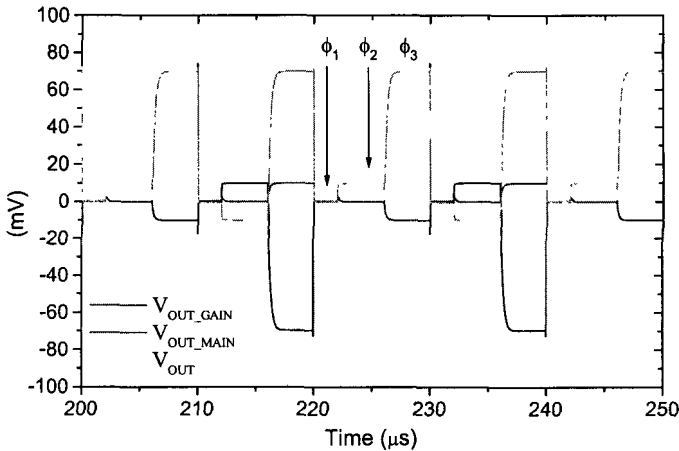


Fig. 4 Output waveform of the main block of the circuit

In the figure, the three working clock phases are highlighted. After the reset phase  $\phi_1$ , offsets and low frequency noise are stored during the phase  $\phi_2$  and then the input signal is amplified during the phase  $\phi_3$ . The valid output value is the sampled at the end of phase  $\phi_3$ .

The effect of programming the ICMFB capacitors is shown in Fig.5. The sensor capacitances  $C_{S1}$  and  $C_{S2}$  are set either to 1.3pF (so there is no input signal) and unbalanced parasitic capacitance are placed at the input nodes *stat1* and *stat2*. Under this conditions an undesired output signal is due to the input common mode voltage variation.

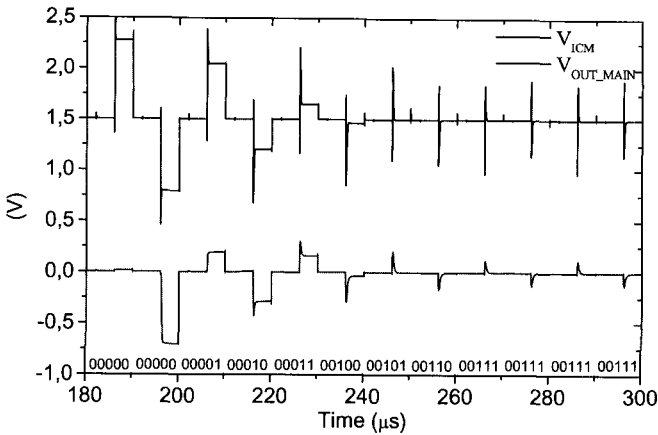


Fig. 5 The effect of programming ICMFB capacitors

The progressive variation of the code that sets the capacitors towards the optimum value is shown on the bottom. The upper plot represents the input common mode voltage while the lower plot is the output voltage. As expected, for the correct code value the input common mode voltage is constant and there is no output error, so the ICMFB works properly.

## References

1. Baschiroto, A. Gola, E.Chiesa, E. Lasalandra, F. Pasolini, M. Tronconi and T. Ungaretti, "A  $\pm 1g$  Dual-Axis Linear Accelerometer in a Standard  $0.5\mu m$  CMOS Technology for High-Sensitivity Applications" IEEE Journal of Solid State Circuits, vol. 38, no. 7, July 2003.
2. M. Lemkin, B.E. Boser, "A Three-Axis Micromachined Accelerometer with a CMOS Position-Sense Interface and Digital Offset-Trim Electronics" IEEE Journal of Solid State Circuits, vol. 34, no. 4, April 1999.
3. J. Zhang, K. Zhang, Z. Wang, and A. Mason, "A Universal Micro-Sensor Interface Chip with Network Communication Bus and Highly-Programmable Sensor Readout", Midwest Symposium on Circuits and Systems, vol. 2, pp. 246-249, August 2002.

# **A Three-Axis Low-g Ultracompact Linear Accelerometer**

F. Dalena, G. Roselli, P. Flora

*STMicroelectronics*

*c/o Distretto Tecnologico, via per Arnesano Km 5, 73100 Lecce, Italy*

[francesco.dalena, giuditta.roselli, pasquale.flora]@st.com

## **Summary**

This paper describes a three-axis low-g ultracompact linear accelerometer that includes a sensing element and IC interface processing the information from the sensing element and providing an analog signal to the external world. The ultracompact accelerometer has been designed for consumer market where the chip size becomes smaller and smaller. The proposed device is a three-axis accelerometer with a LGA package of 5x3x1mm. Thanks to the very small size of the device its main applications are: gaming, virtual reality, free-fall detection, mobile terminals, appliance and robotics.

## **1 Introduction**

As with any technology, certain market demands must to be attained prior to widespread adoption in a broad range of end applications. In the case of MEMS (Micro Electrical Mechanical System) technology, low cost and higher sensitivities (new awareness of position and movements detected with higher accuracy) had to be achieved.

Today, communication, consumer and industrial markets are considered emerging markets for MEMS devices and will be the key drivers for their success.

Capacitive accelerometers, and in general capacitive microsensors, have the main advantages of low-power, high-sensitivity, relatively simple structure, inherently low temperature sensitivity, and is easily integrated with CMOS.

This paper describes a new three axis linear accelerometer in a LGA 3x5x1 mm package. Thanks to the ultracompact dimension it is possible the use of this accelerometer in various consumer market application like: gaming, virtual reality, free-fall detection for data protection, picture browsing, mobile terminals, appliance and robotics [1].

The device contains two dies: 1) sensing element; 2) IC interface.

The electrical signal generated by mechanical part is very small so the IC interface must have very low noise and no offset.

The IC interface is factory-calibrated for sensitivity, Zero-g level, internal oscillator, current/voltage references, output resistor and the trimming values are stored inside the device by a non volatile structure.

The three axis accelerometer works with a power supply from 2,16V to 5,5V with a current consumption of 640  $\mu\text{A}$  at 2,4V; it is able to sense  $\pm 2\text{g}$  at full scale with an acceleration noise density of  $50\mu\text{g} / \sqrt{\text{Hz}}$ .

## 2 Mechanical Sensor

Fig. 1 shows the sensor equivalent electrical circuit: it consists of two sensing capacitors  $C_{s1}$  and  $C_{s2}$  between the single rotor and each of the two stators. Some additional parasitic capacitors are present between each stator and ground. These capacitors are due to the mechanical die, IC interface and interconnections between two dies.

When acceleration is applied to the sensor the proof mass displaces from its nominal value, causing an imbalance in the capacitive half-bridge Fig.1.

So an external acceleration causes a reduction in the value of one capacitance and improves the value of the other capacitance. This differential capacitive sensor has the important property of reducing the entire common mode signal that the mechanical part could sense. This imbalance is measured using charge integrator in response to a voltage pulse applied to the sense capacitor.

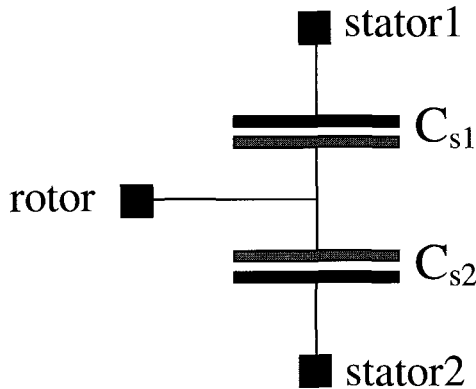


*Fig.1 Electrical schematic of the mechanical part*

### 3 ASIC

Interface circuitry is an important part of integrated inertial sensors. The design of interface circuits with high sensitivity, low noise and large dynamic range is very challenging. Prior interface circuit designs for capacitive sensing were mainly focused on high sensitivity and low electronic noise, but low power consumption has not been achieved. However, in consumer applications, low power operation is always a predominant requirement.

The differential capacitive sensor needed a fully differential IC interface to take advantage of the differential capacitive sensor structure. This means a bigger chip area but also a lot of advantages like: power supply

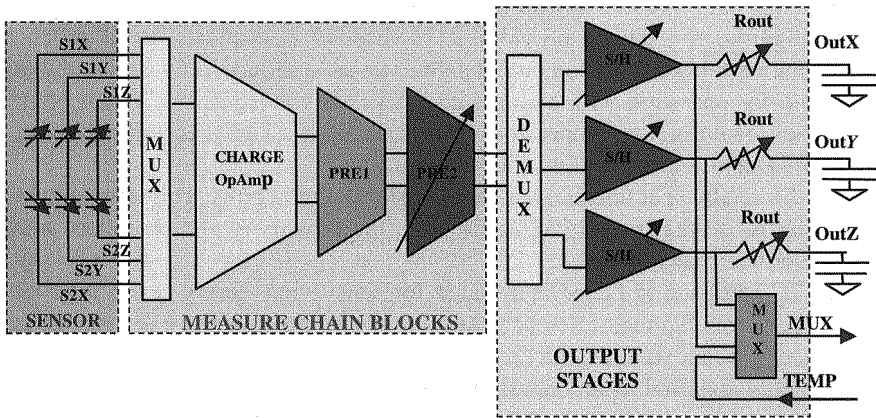


Fig.2 ASIC Block Diagram

The accelerometer measures changes in a capacitive half-bridge to detect deflections of a proof mass, which result from the acceleration input [2]. When an acceleration is applied to the sensor, the proof mass displaces from its nominal value, causing an imbalance in the capacitive half-bridge. This imbalance is measured using charge integrator in response to a voltage pulse applied to the sense capacitor. This capacitive position sensing has a low intrinsic temperature coefficient, can be highly sensitive, and is easily integrated with CMOS [3]. The sensing element is manufactured using a dedicated process called THELMA developed by ST to produce inertial sensors and actuators in silicon. The IC interface is manufactured using a CMOS process that allows high level of integration to design a dedicated circuit, which is trimmed to better match the sensing element characteristics.



The “measure chain blocks” Fig.2 realize a low-noise capacitive amplifier that implements a Correlated Double Sampler (CDS) at its output to cancel the offset and 1/f noise.

A fully differential structure [4] is used to read the charge difference which flows through the sense capacitors in response to a voltage step. The differential structure has several other important advantages, including improved power-supply rejection ratio and first-order rejection of common-mode errors, such as switch charge injection and substrate noise. The “output stage” is composed of a multiplexer, controlled by three different digital phases necessary for the TDM (Time Division Multiplexing) technique, and three S&H, working in the same manner for X, Y, Z, channels and converting the differential signal into a single-ended one, compatible with the external world.

In addition, the device provides an embedded multiplexer to allow the redirection of either the analog output signals or an auxiliary input signal onto a single pin for operation with a single channel A/D converter. For instance, an application could be the temperature measurement if a signal is applied to the TEMP PAD and it is redirect on MUX output PAD.

All the analog parameters are ratiometric to the supply. This allows that increasing or decreasing the voltage supply, the sensitivity and the offset will increase or decrease linearly.

The IC interface is factory-calibrated for sensitivity, Zero-g level, internal oscillator, current/voltage references and the trimming values are stored inside the device by a non volatile structure.

The only external components are the capacitors at the output pins to implement low-pass filtering for antialiasing and noise reduction. The cut-off frequency ( $f_t$ ) of the external filters is:

$$f_t = \frac{1}{2\pi \cdot R_{OUT} \cdot C_{load}(x, y, z)}$$

The internal filtering resistor ( $R_{OUT}$ ) has a nominal value of 32k $\Omega$  and it is factory-calibrated at 10%. The cut-off frequency is function of the external capacitance:

$$f_t = \frac{5\mu F}{C_{load}(x, y, z)} [Hz]$$

This means that large capacitor values correspond to high measurement resolution.

A very useful feature to test the sensor mobility and the front-end has been included in the ASIC. It is called “self-test” and it is governed by ST pad. The ST pad is put to gnd in normal mode. When the ST pad is put to Vdd an actuation force is applied to the sensor simulating an input force. This produces a change in the DC level of the analog output of the device.

The microsystem [1] exhibits a  $\pm 2g$  full-scale, operates from a minimum power supply of 2,16V and with a current consumption of  $650\mu A$ . It is capable of measuring accelerations over a maximum bandwidth of 2.0 kHz on a temperature range of  $-40\text{ }^{\circ}\text{C}$  to  $+85\text{ }^{\circ}\text{C}$ . The acceleration noise density is equal to  $50\mu g / \sqrt{\text{Hz}}$ .

#### 4 Conclusion

In this paper a complete fully-integrated three-axis linear accelerometer in a LGA  $3 \times 5 \times 1$  mm package has been presented. The accelerometer has three ratiometric analog outputs and one multiplexed output to interface the sensor with a single channel A/D converter. The device match three power supply standard: 2,4V; 3,3V; 5V.

Thanks to the ultracompact dimension it is possible the use of this accelerometer in various consumer market application like: gaming, virtual reality, free-fall detection for data protection, picture browsing, mobile terminals, appliance and robotics

#### Acknowledgments

The authors would like to thanks F. Guglielmo and A. Castelfranco for the careful design of the device layout, and G. Tripoli for the contribution in order to realize the ASIC design.

#### References

- [1] LIS302ALB Data Sheet.
- [2] M.Lemkin, "*Micro Accelerometer Design with Digital Feedback Control*", doctoral dissertation, Univ. of California at Berkeley, 1997.
- [3] C. Contiero, B. Murari, B. Vigna, "Progress in Power IC and MEMS, "analog" Technologies to interface the real world", 2004 Proceedings of IEEE.
- [4] N.Yazdi, H.Kulah, K.Najafi, "Precision Readout Circuits for Capacitive Microaccelerometers", Sensor, 2004 Proceedings of IEEE.
- [5] M.Lemkin, B.E.Boser, "A Three-Axis Micromachined Accelerometer with a CMOS Position-Sense Interface and Digital Offset-Trim Electronics", IEEE Journal of solid state circuit, vol. 34, no. 4, April 1999.

# Vehicle Health and Comfort Level Measurement: A Preliminary Study

Fabio Lo Castro, Arnaldo D'Amico  
Electronic Department, University of Rome Tor Vergata,  
Via del Politecnico 1, 00133 -Rome, Italy  
[Lo.castro@ing.uniroma2.it](mailto:Lo.castro@ing.uniroma2.it)

Giovanni Brambilla  
CNR, Istituto di Acustica "OM Corbino".  
Via del Fosso del Cavaliere 100, 00133 -Rome, Italy

## Summary

In this paper is presented a system able to measure the vibrations inside the car, formed by a PC, an acquisition board and two MEMS tri-axial accelerometers as sensors. We tested the device on a vehicle measuring the acceleration, driving along different types of street as highway and street. Subsequently the accelerations have been weighted with curves given by the normative in order to evaluate the comfort and the risk level.

## 1 Introduction

The fatigue is a problem in all 24-hour operations, especially during driving. Our biological clocks switch the brain automatically to low levels of alertness after an heavy workload or during the night to induce sleepiness.

Vehicle accidents due to driver error and fatigue are a significant cause of death, accident and injury. The studies on the safety drive, specially by the automotive industry, try to reduce these accidents acting on different ways that can be divided in three safety levels: prevention, warning and alert.

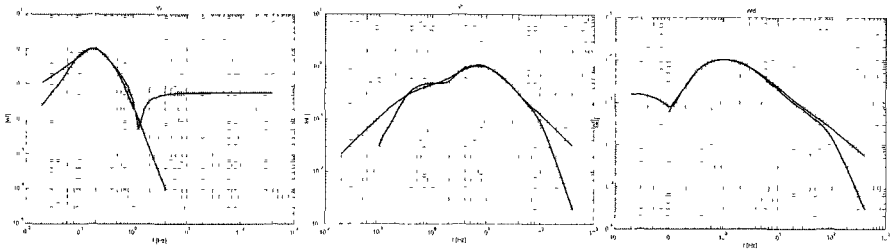
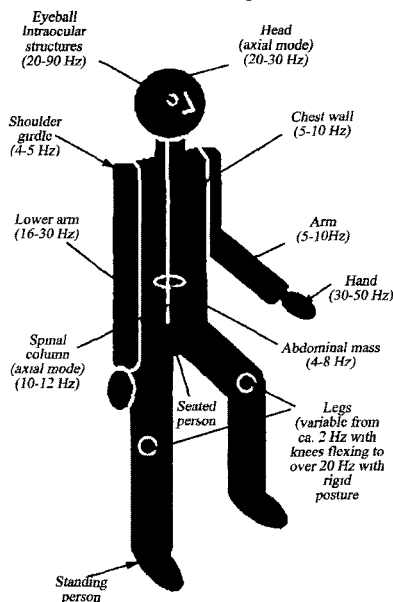


Fig.1 Frequency weight filters:  $W_b$ ,  $W_d$  and  $W_f$

This paper has been focused on the prevention, studying the vehicle health and comfort levels, related to vibrations inside the car. Analyzing the frequency spectrum of the vibration it is possible to find the cause of discomfort.

In the literature it is explained how the human sensitivity to vibration is highly frequency-dependant, as shown in figure 2. The effect of frequency is reflected in the principal frequency weightings labelled  $W_k$ ,  $W_d$  and  $W_f$ , that are used to evaluate the comfort and the sickness levels.

Table 1 resume the corresponding acceleration weighting values to the risk levels, normalized to eight hours, and the comfort levels.



**Fig.2** Simplified human body sub-systems. Each body sub-system has a resonance frequency band.

#### Directive 94/C230/03 on physical risk

Threshold Level rms	$A(8) = 0,25 \text{ m/s}^2$
Action Level rms	$A(8) = 0,5 \text{ m/s}^2$
Limit value rms	$A(8) = 0,7 \text{ m/s}^2$
High risk level rms	$a_w \text{ eq} = 1,25 \text{ m/s}^2$

Comfort levels	
$a_w < 0.315 \text{ m/s}^2$	not uncomfortable
$0.315 < a_w < 0.63 \text{ m/s}^2$	a little uncomfortable
$0.5 < a_w < 1 \text{ m/s}^2$	fairly uncomfortable
$0.8 < a_w < 1.6 \text{ m/s}^2$	uncomfortable
$1.25 < a_w < 2.5 \text{ m/s}^2$	very uncomfortable
$a_w > 2.5 \text{ m/s}^2$	extremely uncomfortable

**Table 1** Normalized acceleration values to eight hours versus risk levels and r.m.s. acceleration values corresponding to the comfort Levels

## 2 Experimental

We have developed a hardware prototype (see figure 3), driven by a Personal Computer, that is able to evaluate the Health Level and the Comfort Level of the vehicle expressed as weighted RMS acceleration value, according to the European directive ISO 2631-1.

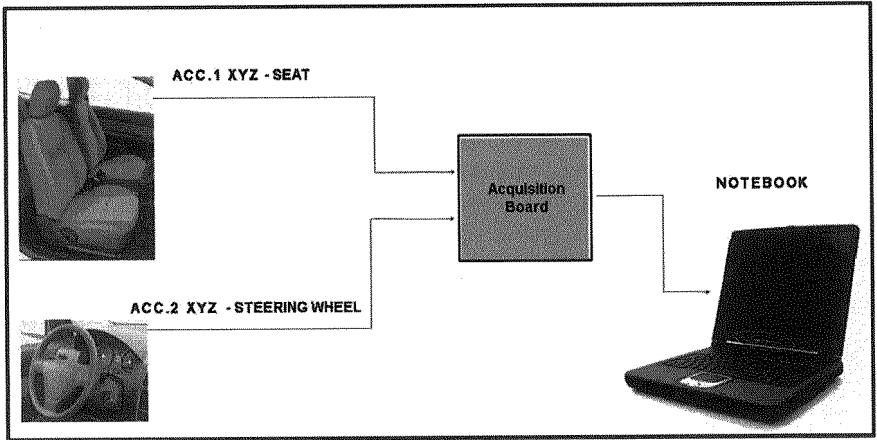


*Fig.3 Acquisition system installed on the car*

The ISO 2631-1 directive gives only tables with values for the  $W_k$ ,  $W_d$ ,  $W_f$  so we have used an approximation function of the third order quasi-least-square which has an r.m.s. errors at the one-third octave frequencies less than 0.08 [1], as shown in figure 1.

The following vertical acceleration filter  $W_k$  and horizontal acceleration filter  $W_d$  have been used to evaluate the comfort level:

$$W_k = \frac{80.03s^2 + 989.0s + 0.02108}{s^3 + 78.92s^2 + 2412s + 5614}$$

$$W_d = \frac{14.55s^2 + 6.026s + 7.725}{s^3 + 15.02s^2 + 51.63s + 47.61}$$

In order to evaluate the motion sickness the following filter has been used:

$$W_f = \frac{0.05726s^3 + 3.876s}{s^3 + 4.263s^2 + 4.777s + 4.396}$$

The frequency ranges considered are:

- 0.5 Hz to 80 Hz for health, comfort and perception;
- 0.1 Hz to 0.5 Hz for motion sickness;

Different paths as highway, road and street, have been chosen to study the vehicle vibrations due both to the ground and to the vehicle speed.

Two Tri-axial accelerometer (LIS3L02AS4) with a range of  $\pm 2g$  as maximum acceleration have been used to test the vibration levels inside a car. The first accelerometer was placed on the dashboard and the second one was placed on the driver seat.

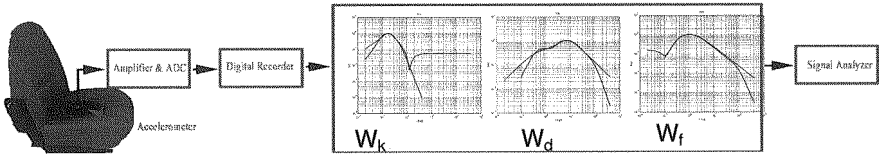


Fig.4 Acquisition system used to evaluate the Comfort and Health level of the vehicles.

### 3 Results and discussion

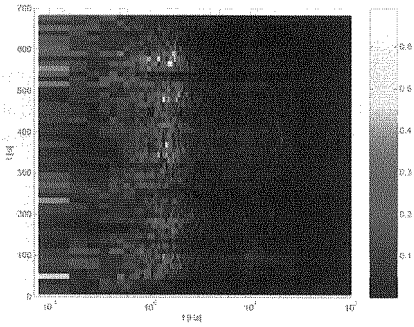
Table 2 shows the frequency responses of the vehicle used, captured along a highway and a street. The Sensor was a tri-axial capacitive accelerometer model STM LIS3L02AS4 mounted in a deformable pad that follows the seat contour place on the seat surface. The data recorded by the PC have been filtered to evaluate the comfort and sick level, as shown in figure 4. Both levels show that the vibration on the highway are higher than street vibration due to the speed and the state of the shock absorbers.

Seat comfort Level Measurement [ $m/s^2$ ]		
RMS $a_w$	street	highway
$a_w$	0.55	0.72

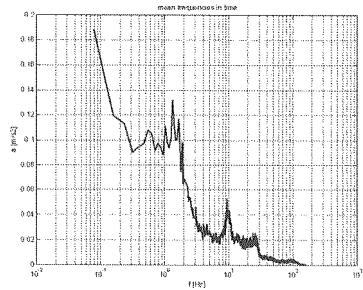
Sickness Level Measurement [ $m/s^2$ ]		
RMS $a_w$	street	highway
$a_w$	0.31	0.41
A(8)	0.16	0.21

Table 2 Comparison of the different sensors versus time need to damp vibrations

Figure 5 shows the frequency spectrum versus time during a test along the highway where two peaks are always visible, one centred between 1Hz and 2 Hz and the other at around 10 Hz. The temporal mean of the spectrum is shown in figure 6.



*Fig.5 Spectrogram of a test performed along a highway.*



*Fig.6 Mean frequency spectrum of a test performed along a street.*

## 4 Conclusions

Two single tri-axial accelerometer, placed on the seat surface and on the dashboard, have been used to measure the vibrations inside the vehicle. The data, recorded by the PC, have been filtered by a third order approximation equation of the ISO 2631-1 acceleration frequency weight curves to estimate the Comfort and Sickness Levels of a car.

## References

1. L. Zuo, S.A. Nayfeh , Journal of Sound and Vibration 265 (2003), 459–465.
2. Magnus Wollström, TRITA - FKT Report 1998:44, ISSN 1103 - 470X, ISRN KTH/FKT/FR--98/44--SE
3. Börje Rehn, Umeå University Medical Dissertations - New Series No. 852 – ISSN 0346-6612 – ISBN 91-7305-517-4
4. F. Benvenuti, S. Giambattistelli, O. Nicolini, I. Pinto, E. Cini, etc , ISPESL-“Linee guida per la valutazione del rischio da vibrazioni negli ambienti di lavoro”.

# Forced Damping Vibration of a Cantilever Beam

Fabio Lo Castro

*Electronic Department , University of Rome Tor Vergata  
Via del Politecnico 1, 00133 -Rome, Italy  
[Lo.castro@ing.uniroma2.it](mailto:Lo.castro@ing.uniroma2.it)*

Paolo Bisegna

*Department of Civil Engineering, University of Rome Tor Vergata  
Via del Politecnico 1, 00133 -Rome, Italy*

## Summary

Forced damping vibration strategies have a paramount relevance in all those cases where surface vibrations represent disturbances.

Knowing that surfaces show different resonant modes of vibration related to their geometry we have selected a cantilever beam that has only one principal resonant frequency. Therefore we have developed a circuit that, using the opposite phase signals technique, reduces the oscillation time of the cantilever beam.

Different sensors as accelerometer, piezoelectric, infrared proximity detector have been used to read out the vibration of the cantilever.

## 1 Introduction

The system under study has been a steel cantilever beam (250mm length, 40mm width and 1.5mm thick) with two identical piezoelectric wafers, model number QP15W made by ACX, applied on both sides close to the constraint. One piezoelectric wafer has been used to detect the vibration and the second one to generate the vibrations or to damp the cantilever oscillation, respectively when driven by a sine wave or when the control system is enabled.

A Labview program controlled the beginning and the end of the solicitation and acquired the signal read out by the sensor. To compare the efficiency of the piezoelectric wafer we have been used other types of sensors, as infrared, model OPB704W made by OPTEK, and quartz/shear accelerometer, model K-SHEAR number 8702B100 (8614) made by Kistler .

## 2 Experimental

The block diagram in figure 1 shows the architecture of the experiment. The PC generates a sine wave that drives the actuator, the sensor detect the vibrations, that are shifted and amplified by the control board, and applied to the actuator in order to damp the oscillation.



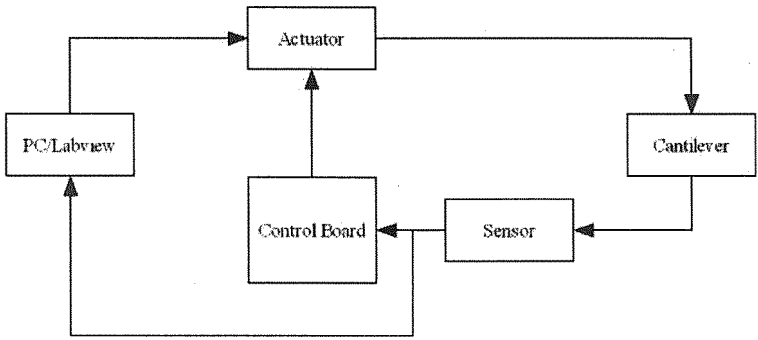


Fig.1 System block diagram

The pictures in figure 2 and 3 show the cantilever beam with the piezoelectric wafers near the constraint while the accelerometer or the IR sensor is placed on the end of the free edge of the cantilever beam.

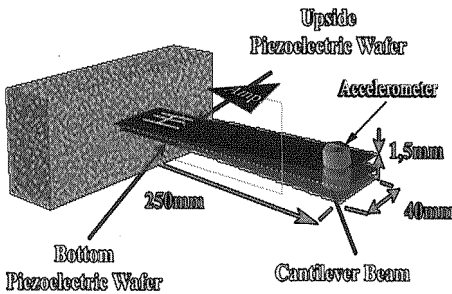


Fig.2 The cantilever under test

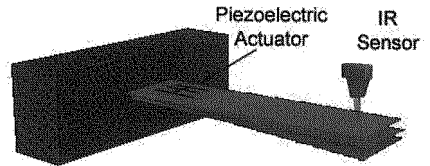


Fig.3 The IR sensor placed on the end of the free edge

The principle used to reduce the vibrations (see figure 4) is that the sum of opposite phase sine waves, with the same amplitude, is a null signal.

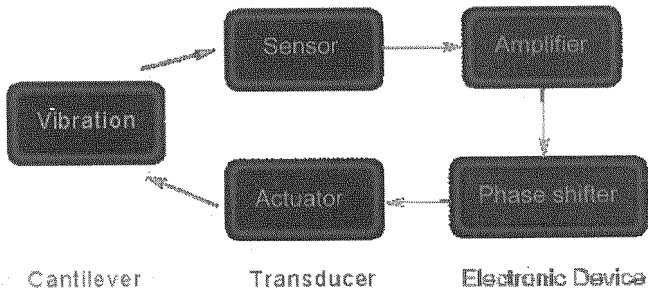


Fig.4 The closed loop system

It is necessary to shift the phase of the signal read out by sensor because it changes according to the position of the sensor, respect to the origin of the oscillation, and the gain of the amplifier.

In this way a PID control has been designed with the possibility to select the single parameters of the controller.

### 3 Results and discussion

In this experiment has been measured the time need to damp the vibration until the 95% of the initial amplitude, value established by our limit of detection under which noise and signal was unrecognised.

Four sensor/actuator couples have been tested, called NULL, ACC, IR and PIEZO:

- NULL: Free damping oscillation; the cantilever was first excited by first piezoelectric wafer (actuator) and then left free to oscillate. No control loop was applied. The sensor was the second piezoelectric wafer.
- ACC: damping circuit realized with the couple accelerometer/piezoelectric wafer with the piezoelectric used as actuator
- IR: damping circuit realized with the couple IR sensor/piezoelectric wafer with the piezoelectric used as actuator.
- PIEZO: damping circuit realized with two piezoelectric wafers, the first used as sensor and the second as actuator .

In the last experiment the actuator was first driven by the Pc to excite the cantilever and then it was switched to the control board to damp the oscillation. The results of the tests are shown on table 1 while figure 5 and 6 shows respectively the transient of a free oscillation and of a damping oscillation of the PIEZO couple.

Sensor Type	Damping factors		
	50% [s]	90% [s]	95% [s]
NULL	2.7	10	14
ACC	0.06	0.20	0.26
IR	0.04	0.16	0.23
PIEZO	0.08	0.30	0.40

*Table 1 Comparison of the different sensors versus time need to damp vibrations*

During the experiment the inconvenience of the accelerometer used was the low sensitivity, in fact it was been placed near the end of the free edge of the cantilever where there was the maximum displacement of the cantilever beam.

The sensitivity of the infrared system was better than the accelerometer one, even though changing its distance from the constraint,.

The only requirement of the IR sensor respect to the other sensors is that it has to be placed on another system stand respect the cantilever.

This is an advantage for a very small cantilever, or where the mass of the accelerometer is heavy.

In fact we have measured a change in the resonance frequencies of the cantilever with and without the accelerometer from 21.1 Hz to 18.7 Hz for the first resonance frequency and from 127.7Hz to 123.0 Hz for the secondary resonance frequency.

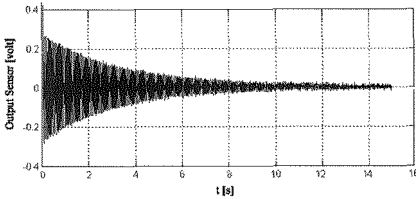


*Fig.3 Free damping vibration*

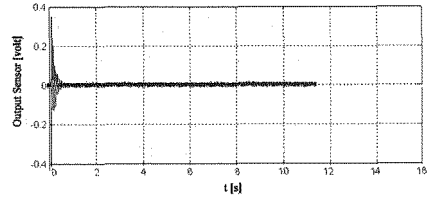


*Fig.4 Forced damping vibration*

During the development of the control circuit of the IR Emitter and Receiver to make the IR sensor, particular attention has been made to reduce the interference with other light sources, so that the sensor could be able used in a open environment.

#### 4 Conclusions

In this paper a cantilever has been considered as a single dimension system so that only one sensor, as an accelerometer or a piezoelectric wafer or an infrared device, has been used to drive a single piezoelectric actuator to damp the vibration.

A PID control unit has been developed to drive the actuator, changing the parameters according to the sensors characteristics.

Furthermore it has been developed an IR sensor as vibration sensor to be tested with the accelerometer and the Piezoelectric wafer.

All couples sensor/actuator have worked properly as shown in the table 1.

**References**

1. E.F. Crawley and J. de Luis - *AIAA Journal*, vol. 25, 1987, 1373--1385.
2. G. Caruso - *Smart Materials and Structures*, vol. 10(5), 2001, 1059--1068
3. F. Lo Castro, G. Caruso, P. Bisegna - *AISEM 2004*, 257-261
4. "Vibration Control of Plates using Periodically Distributed Shunted Piezoelectric Patches.": Mohammad Tawfik AboElSooud, Ph.D. Proposal
5. "Structural vibration suppression by concurrent piezoelectric sensor and actuator.": S M Yang and C A Jeng - 1996 *Smart Mater. Struct.* 5 806-813

# IMPROVED CAPILLARIES CONNECTION TO A CONTINUOUS FLOW GLASS MICROMACHINED MICRO-CELL

W. VASTARELLA<sup>a</sup>, M.ILIE<sup>a,b</sup>, L. NARDI<sup>a</sup>, A. MASCI<sup>a</sup>, R. PILLOTON<sup>a</sup>

<sup>a</sup>*ENEA, Via Anguillarese, 301, 00060 Santa Maria di Galeria, Rome, Italy*

<sup>b</sup>*Univ. Politehnica Bucuresti, LAPI, P.O. Box 15-135, Bucharest, Romania*

*e-mail corresponding author [Mihaela.Ilie@casaccia.enea.it](mailto:Mihaela.Ilie@casaccia.enea.it)*

E. CIANCI, S.QUARESIMA, A. COPPA, V. FOGLIETTI

*CNR/IFN, Via Cineto Romano 42, Rome, Italy*

## SUMMARY

Long term-functional tests of previously developed fluidic connections to a continuous flow micro-cell revealed troubles such as bubble formation and analyte loss. In order to overcome these drawbacks alternative technical solutions are investigated concerning both the materials and the flow-pattern transferring as well as the assembly technique. Thus, the sand blasting of borofloat glass -as well as the lithography of photosensitive glass (FOTURAN)- are used for generating the openings, araldite is used as a glue and a sandwich technique is approached in order to obtain the reservoir with openings for the capillaries. Functional tests are in progress with in-house built borosilicate glass adaptors.

## 1 Introduction

An important step towards total analysis systems miniaturization is represented by the appropriate fluidic connections. A continuous flow micro-cell has been previously obtained by the authors and tested<sup>1</sup> in an analytical system. The micro-cell consisted of a planar array of Au working electrodes, covered by a glass reservoir (600 nl capacity), connected with perpendicular capillaries and provided with a reference electrode (Ag/AgCl wire). The micro-reservoir has been micromachined in borofloat® glass by means of optical lithography combined with wet etching<sup>2</sup>. The fluidic connections aim to insure the turbulence free fluid flow and the reliability while assembling /disassembling the capillaries. The first technical solution adopted<sup>1</sup> for these fluidic connections was based on the use of elastic silicone materials, for both adaptors and gluing; the seal was made liquid-proof by using additional conical adaptors. Long term tests at 10 µl/min showed the accumulation of bubbles in the reservoir as well as a low reliability of the connection and its dependency on the position of the pump (either at the entrance

or at the exit of the reservoir). Each constructive part was analysed and morphologically characterized from the point of view of surface smoothness and contact surface compatibility.

A second technical solution is presented in this work, in order to minimize the drawbacks of the first one. Other methods and materials are investigated to obtain the openings: a) sand blasting of borofloat® glass and b) optical lithography & wet etching of photosensitive glass (Foturan®), respectively. The openings and the reservoir are obtained on different slides of glass, having a thickness of 0.4 mm; the necessary parts are assembled only after the capillaries are fixed on the cover provided with in- house-made glass adaptors. Polyimide and respectively araldite have been used as adhesive.

## 2 The analysis of the previously obtained device

The parts of the connection have been investigated: surface and walls of the adaptors, openings, gluing material, reliability of the adhesion of silicone adaptors on glass. As it was previously shown<sup>2</sup>, the wet etching of glass has been optimized to obtain a very low roughness and an isotropic process. In these conditions the diameter of the opening has a minimum value in the middle of its transversal section thus deviating the flow lines. The coupling of the capillaries has been performed<sup>1</sup> using a multi-part silicone adaptor made of components with different shapes (Fig.1a). The cutting of these adaptors generated radial (Fig.1b) or coiled (Fig.1c) micro-channels that enabled the glue (silicone) to advance towards the functional opening down to the analyte flow zone, and to act as an additional irregularity resulting in a further deviation of the flow lines.

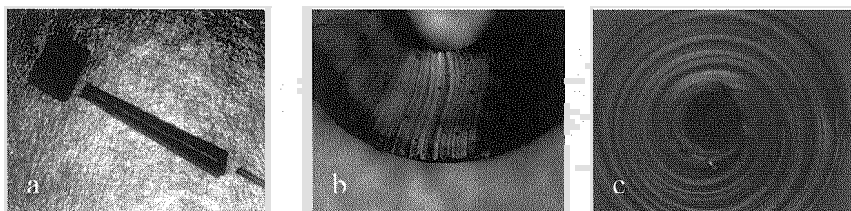


Fig.1 a) multi-part adaptor (mag. X2); b) radial and c) coiled channels on the adaptors surfaces ( X20)

We suppose the lowering of the connections reliability is due to the mechanical aging of the gluing material. Thus, two main causes have been identified for bubbles formation and connection reliability: on one side the surface irregularities of both adaptors and openings and on the other side the glue aging.

### 3. Improving technical solutions

A simpler rhombus shape of the reservoir showed better results than the previous one. The profile of the transversal section of the openings has been drastically improved by means of the anisotropy of the new involved technological processes: wet etching of photosensitive glass Foturan®<sup>3</sup> and, respectively, sand blasting of borofloat® glass. Besides, a sandwich solution has been approached for obtaining the reservoir (Fig. 2.a): the electrodes array (1) is covered with the pool (2) and the openings (3) that are obtained on different glass slides (each of 8x8x0.4 mm<sup>2</sup>). The double side isotropic etching of borosilicate glass in HF 10% vol. is replaced by the double side etching of Foturan® glass (previously exposed with 100 J/cm<sup>2</sup> UV radiation at a wavelength of 310 nm and cured one hour at 500°C and then at 600°C) (detail of the opening in Fig.2.b). This anisotropic process provides an aspect ratio of 1:30 on each of the two slides. Thus, as can be seen in the exploded image (Fig.2.c), the reservoir consists of two pieces (2,3) glued together meanwhile the multipart assembly has been replaced by only one piece of borosilicate glass capillary (4), micromachined using small scale glass blowing.

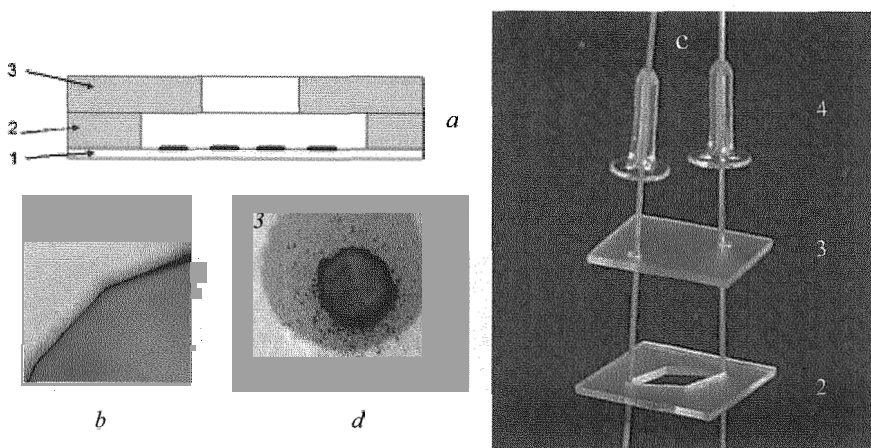
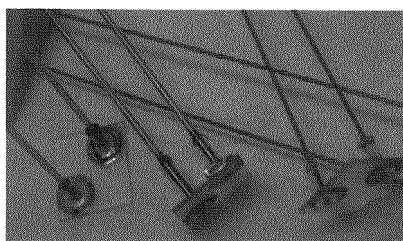


Fig.2 The sandwich solution a) transversal section of the microcell b) detail of the opening; (x500); c) exploded image of the reservoir; d) sandblasted opening (X10)

Differently from other proposed solutions<sup>4</sup> the additional structure does not belong to the reservoir body. The main problem was the global and local roughness of the photosensitive glass due to thermal induced stress in the

unexposed areas. An improvement has been obtained when dehydrating<sup>5</sup> the glass at 250°C for one hour immediately after the etching. Higher temperature treatment<sup>6</sup> at 570°C eliminated the micro-strains induced in the bulk of the material but induced macro strains at global level.

The openings in borofloat® glass were also performed by one side sand blasting 2 min at 6 bar with FEPA P120 Al<sub>2</sub>O<sub>3</sub> particles. The masking layer was the RapidMask HD™ dry processing , self adhesive photo resist film with a dry thickness of 50µm optically patterned, exposed in a mask aligner with 2J/cm<sup>2</sup> at a wavelength of 436 nm. Although the high anisotropy of the process one can notice the roughness of the surface around the border (Fig.2.d). The polyimide coated capillary has been inserted in the adaptor and the parts have been glued over the



a



b

*Fig.3. Capillaries connections: a) polyimide coated capillaries with external diameters of 400µm respectively 700µ are glued inside the adaptor using polyimide; b) the teflon tubes inserted over the adaptors*

opening by means of fast-cured polyimide that renders them fix and sealed (fig.3.a). The fixed capillaries have a length of several centimeters in order to avoid bending stress of the glued zone and in the same time to allow a safe connection to the external pipes by means of additional house-made conical couplers. There is practically no danger of blocking either the capillary or the opening with the adhesive material because the capillary is cut after the gluing. Several tens of capillaries with inner diameters in the range 0.4mm-0.7mm have been assembled and tested at low bending stress. Half of them were stripped off. Higher stress-resistance has been obtained when araldite has been used to glue the adaptors on the covers and teflon tubes were used instead of capillaries. The tubes were not glued at all but simply heated and inserted over the adaptors (fig. 3.b) .



#### 4. Conclusions

Previously obtained fluidic connections have been tested by means of long term continuous flow functioning during which bubbles formation and analyte loss have been noticed due to irregular profile of the openings obtained by double-side isotropic etching of borosilicate glass (aspect ratio 1:1). The profile has been smoothed and the aspect ratio became 1:30 when using double-side etching of photosensitive glass Foturan®. The pool and the openings have been obtained separately and glued after etching. In order to increase the reliability of the connection the couple of silicone adaptors has been replaced by one single glass adaptor traditionally micromachined by glass blowing. Flexible teflon tubes were mounted over the glass adaptors in order to enable the analyte flow and this connection ended to be more reliable than the previous one obtained with fused silica capillaries inserted and fixed with polyimide inside of the glass adaptors. Araldite and polyimide have been experimented as gluing materials and the first one showed a higher reliability. An increasing of the local and global roughness has been noticed in both sand blasting and photosensitive glass processing. In the first case the resist /process has to be improved, while in the second one the dehydrating of glass<sup>4</sup> at 250°C has been performed with pretty good results. Further efforts are dedicated to improve the surface quality of the micromachined glass and the alignment of the cover with respect to the reservoir. The functional tests are in progress.

#### Acknowledgements

The authors acknowledge "Progetto 5% Nanotecnologie" of MURST, Italian Found for Research (FISR), Theme 4"Optical and Electro-Optical Sensors", Italian Found for Fundamental Research (FIRB) and Cosmic (ENEA target project on Biosensors and Bioelectronics) for financially sustaining this work. Special thanks are addressed to Mrs. Emilia Castagna (ENEA-International Relation Office) for her efficient logistic support.

#### References

1. J. Maly, M. Ilie, V. Foglietti, E. Cianci, A. Minotti, L. Nardi, A. Masci, W. Vastarella, R. Pilloton, *Sensors and Actuators B* 111-112 (2005) 317-322
2. M. Ilie, V. Foglietti, E. Cianci, A. Minotti, *Advanced Topics in Optoelectronics, Microelectronics and Nanotechnologies*, Proceedings of SPIE Vol.5227 (2003), pp. 318-321
3. M. Ilie, V. Foglietti, E. Cianci, A. Minotti, E. Vasile, L. Nardi, J. Maly, R. Pilloton, A. Masci, *Sensors and Microsystems*, Ferrara, Italy 2004, 72-77
4. B. L. Gray, D. Jaeggi, e.a., *Sensors and actuators* 77(1999) 57-65
5. K. Grob, *Making and Manipulating Capillary Columns for Gas Chromatography*, Huethig Heidelberg 1986, ISBN 3-7785-1312-5, pp.105-120
6. Y. Cheng, K. Sugioka, et al., *RIKEN REVIEW* no.50, Jan. 2003

# SIMULTANEOUS DETECTION OF POLYCHLORINATED BIPHENYLS (PCBS) BY MEANS OF AN ELECTROCHEMICAL DISPOSABLE MULTIARRAY SENSOR

Sonia Centi, Serena Laschi, Ilaria Palchetti, Marco Mascini  
*Dipartimento di Chimica, Università degli Studi di Firenze, Via della  
Lastruccia 3, 50019 Sesto Fiorentino, Firenze, Italia,  
e-mail corresponding author: [sonia.centi@unifi.it](mailto:sonia.centi@unifi.it)*

## Summary

Polychlorinated biphenyls (PCBs) constitute a well-known ecological problem. In addition to the conventional techniques used for the analysis of PCBs, generally based on gas chromatography coupled with mass spectrometry (GC/MS), alternative methods based on immunoassays provide inexpensive and rapid screening techniques for both laboratory and field analysis. In this work disposable antibody-coated magnetic beads coupled to disposable screen-printed electrochemical arrays were used to develop an immunosensor for detection of some coplanar PCB congeners. Compared to single electrodes, arrays have the advantage of testing many samples simultaneously. The advantage of using screen-printed arrays (based on four-working electrodes and a reference electrode) is that they can be mass-produced at a low cost and thus be disposable. The proposed immunosensor is based on a direct competitive immunoassay scheme involving magnetic beads as solid phase and screen-printed arrays as transducers for the evaluation of the extent of the immunochemical reaction. Alkaline Phosphatase (AP) is used as enzyme label and the detection of the reaction product is performed by using Differential Pulse Voltammetry (DPV). This immunoassay format could be easily applied to the detection of PCBs in many matrices such as food or sediment/soil.

## 1 Introduction

Polychlorinated biphenyls (PCBs) are among the 16 chemicals designated as persistent organic pollutants (POPs). They are highly stable compounds that persist in the environment, accumulate in the fatty tissues of most living organisms since they are lipophilic, and are toxic to humans and wildlife. Their chemical stability makes PCBs one of the most widespread environmental pollutants.

There are 209 PCB congeners, which are divided into three classes based upon orientation of the chlorine molecules, i.e., coplanar, mono-ortho coplanar, and non-coplanar. Some of the them (the so-called coplanar congeners), in addition to be stereochemically similar to the planar 2,3,7,8-tetrachlorodibenzo-p-dioxin

(2,3,7,8-TCDD), show also a biochemical activity and toxicity similar to these compounds, for this reason they are indicated as “dioxin-like” molecules.

A disposable electrochemical immunosensor based on magnetic beads and carbon array is proposed as a screening device for the rapid detection of coplanar PCBs. Antibody-coated magnetic beads used as solid phase for the immunochemical test, coupled with carbon screen-printed arrays as electrochemical transducers were reported as new interesting tool in affinity-based biosensors [1,2].

## 2. Materials and Methods

Electrochemical measurements were performed using CHI 1030 multichannel potentiostat coupled with CHI 5.5 software (CH Instrument inc.). Carbon screen-printed electrochemical array were printed in house using a High Performance Multi Purpose Precision Screen Printer DEK 245 (DEK, Weymouth, UK), using different thermoplastic inks. The cell consisted of four graphite working electrodes with a diameter of 2 mm, a graphite counter electrode and a silver pseudo-reference electrode. A connector for the array was used coupled to a magnetic bar. Differential Pulse Voltammetry (DPV) was used as electrochemical technique with the following parameters: range potential 0/+600 mV, step potential 7 mV, modulation amplitude 70 mV, interval time 0.1 sec..

A competitive assay was developed, following the scheme reported in figure 1. Magnetic beads protein G coated were modified by immobilisation of antibodies against PCB169. The beads obtained were incubated with a optimised dilution of the tracer (PCB169-AP) and PCBs present in the sample. After molecular recognition, the extent of the affinity reaction was evaluated by addition of an enzymatic substrate, which was transformed in a electroactive product and oxidized at the electrode surface using a useful potential value.

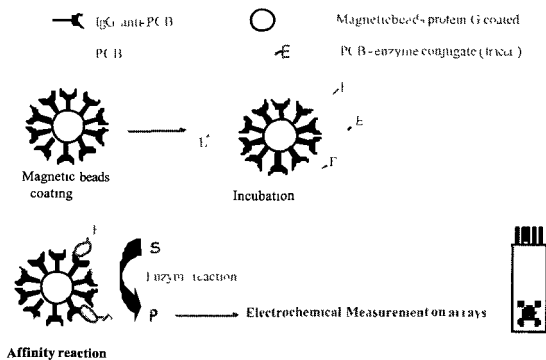


Figure 1: Schematic representation of a competitive assay and of the electrochemical measurement on carbon screen-printed array.

### 3 Procedure

#### 3.1 Beads preparation and antibody immobilisation

The magnetic beads coupled with protein G were washed with 0.1 M sodium-phosphate solution pH= 5 before use to remove the  $\text{NaN}_3$  preservative. A suspension of 10  $\mu\text{L}$  of the beads was introduced in a tube containing 500  $\mu\text{L}$  of antibody (IgG anti-PCB169) solution 100  $\mu\text{g}/\text{mL}$  prepared in 0.1 M sodium-phosphate solution pH= 5. After 20 minutes incubation time, the tube was positioned on a magnet holding block, the supernatant was removed and the beads were washed twice with 500  $\mu\text{L}$  of washing solution (0.1 M sodium-phosphate solution pH= 5). Antibody-coated beads could be prepared in advance and kept at  $+4^\circ\text{C}$ .

#### 3.2 Affinity reaction and electrochemical measurement

50  $\mu\text{L}$  of suspension containing antibody-coated beads were mixed with 940  $\mu\text{L}$  of sample solution; 10  $\mu\text{L}$  of the tracer solution (PCB169-AP) was added to this mixture. After 20 minutes incubation time, the beads were magnetically separated and the supernatant was removed. After two washing steps, the beads were re-suspended in 100  $\mu\text{L}$  of working assay buffer and 10  $\mu\text{L}$  of the suspension were transferred onto the surface of each working electrode of the array. To better localise the beads onto the electrode, the magnet holding block was placed on the bottom part of the electrode. Then 300  $\mu\text{L}$  of the enzymatic substrate solution ( $\alpha$ -naphthyl phosphate 1  $\text{mg}/\text{mL}$  in DEA buffer) were deposited on the screen-printed array, closing the electrochemical cell. After 5 minutes, the enzymatic product was finally determined by DPV.

The results were reported as  $B_x/B_0$  percentage units, where  $B_x$  is the signal in presence of competitor and  $B_0$  is measured without competitor.

### 4. Samples analysis

1 g of non contaminated marine sediment samples (collected and characterised by GC-ECD in Fisheries Research Service-Marine Laboratory, Aberdeen, Scotland) were spiked before the extraction by addition of 1 mL of a standard congener solution and kept in contact for 16 hours. Then a sonication assisted extraction was carried out [3].

#### 4.1 Extraction procedure

0.5 g of marine sediment sample were added to 10 mL of methanol and after a short mixing time (5 minutes), the mixture was sonicated for 2 minutes using an ultrasonic probe. After 2 minutes to allow for the sedimentation of the solid, the sample was filtered using a nitrocellulose 0.45  $\mu\text{m}$  filter and then was diluted 100

times by addition of a solution containing magnetic antibody-coated beads and the tracer at the optimised dilution. Then, the competition reaction was performed as described in section 3.2.

## 5. Results and Discussion

### 5.1 Immunosensor application to PCB standard solutions analysis

The immunosensor developed using the antibody against PCB169 (IgG anti-PCB169) and the tracer PCB169-AP was applied to the detection of the coplanar congeners PCB169 and PCB126. Calibration curves are shown in Figure 2: they exhibited sigmoidal shapes typical of a competitive immunoassay. The different sensitivities measured were due to the different affinities of the antibody against the two coplanar congeners. This consideration was demonstrated by the  $IC_{50}$  values of each congener (0.2 ng/mL for PCB169 and 2.6 ng/mL for PCB126) and by the different values of detection limit ( $6.8 \cdot 10^{-2}$  ng/mL for PCB169 and  $7.6 \cdot 10^{-1}$  ng/mL for PCB126).  $IC_{50}$  is defined as the target analyte concentration which inhibits the assay by 50% and detection limit has been calculated by evaluation of the mean of the blank solution response (in absence of competition) minus two times the standard deviation.

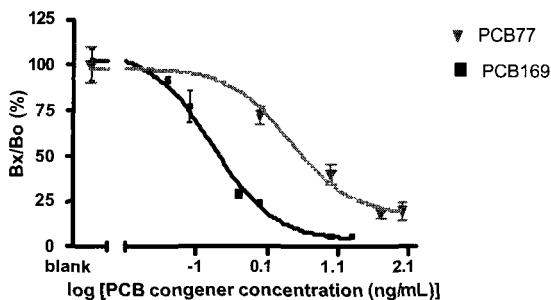


Figure 2: Calibration curves for PCB169 and 126 performed by the electrochemical immunosensor using IgG anti-PCB169 as antibody and PCB169-AP as tracer. IgG anti-PCB169 100  $\mu$ g/mL.

### 5.2 Analysis of marine sediment samples

The results obtained from the analysis of marine sediment samples are reported in Table 1. The  $B_x/B_0$  values were calculated by considering the responses of the spiked marine sediment samples and that of the corresponding un-spiked sample (blank). The same PCB solutions were also prepared by spiking the buffer and also in this case the responses were compared with the corresponding blank (un-spiked buffer). As it can be seen in table 1, a similar behaviour was obtained for both extracted samples and samples prepared in buffer, all solutions gave a decrease of signal with respect to the corresponding blank. For both cases the

signal percentage obtained for R, S and T samples, which contained the same congener (PCB169) but at different concentrations (0.1, 1 and 5  $\mu\text{g/Kg}$ ) was different. The signal percentage measured for the sample T was lower than the value obtained for the sample S and R, which contained the same congener (PCB169) but a lower concentration (respectively, 0.1 and 1  $\mu\text{g/Kg}$  versus 5  $\mu\text{g/Kg}$ ). Different signal percentages were measured for the S and U samples, containing different congeners (PCB169 and PCB126) but at the same concentration.

Table 1: Results obtained from the analysis of marine sediment samples, extracted by the sonication assisted method. A comparison with the signal obtained in the buffer for the same concentrations is reported.

Sample code	Spiked congener	Spiked concentration ( $\mu\text{g/Kg}$ )	Buffer $B_x/B_0$ (%)	Marine sediment $B_x/B_0$ (%)
R	PCB169	0.1	$75 \pm 2$	$74 \pm 2$
S	PCB169	1	$21 \pm 4$	$28 \pm 2$
T	PCB169	5	$8 \pm 1$	$6 \pm 2$
U	PCB126	5	$44 \pm 4$	$40 \pm 6$

## 6 Conclusions

A sensitive and reproducible immunosensor for the detection of some coplanar PCB was developed. The assay scheme was based on magnetic beads coupled to disposable and low cost sensor. Different dioxin-like congeners could be detected in short time at ppb level. The possibility to perform a screening measurement that allows to know in short time if a sample is contaminated or no, is important when a big number of samples have to be analysed; therefore these experiments could be a valid analytical tool to carry out a fast screening of many samples, analysing only positive samples with traditional methods in order to have a exact quantification of PCB concentration.

## References

- [1] Palecek E., Fojta M., Jelen F., *Bioelectrochemistry*, 56, 2002, 85-90.
- [2] Centi S., Laschi S., Fránek M., Mascini M., *Anal. Chim. Acta*, 538, 2005, 205-212.
- [3] H. Okuno, B. Yim, Y. Mizukoshi, Y. Nagata and Y. Maeda, *Ultrasonics Sonochemistry* 7 (2000), 261-264.

# Integrated Microgravimetric Set-up for Chemical Sensing

G. Pioggia

*Centro Interdipartimentale di Ricerca "E. Piaggio", Università di Pisa*

F. Di Francesco

*Istituto di Fisiologia Clinica, CNR, Pisa*

G. Campobello, G. Cannatà, N. Donato

*Dip. di Fisica della Materia e Tecnologie Fisiche Avanzate, Univ. di Messina*

A. Bonavita, G. Micali, G. Neri

*Dip. di Chimica Industriale ed Ingegneria dei Materiali, Università di Messina*

## Summary

It is a well known fact that stability and reproducibility of measurement are crucial topics for chemical sensing. Most problems are intrinsically associated with the sensor chemico-physical characteristics and with the fabrication techniques, but often the measurement set-up must carefully be designed. In this paper we addressed the development of an integrated microgravimetric set-up able to perform fast and accurate measurements with an array of quartz crystal microbalances (QCMs). In order to guarantee measurement accuracy, reliability and repeatability, the sampling system was designed to control and optimise factors capable of influencing the generation of sensor transduction signals. The system comprises a dedicated electronic interface for measuring the QCM resonance frequency by using a novel technique. This technique allows reducing the measurement time while maintaining a high frequency resolution. The system was simulated in the range of frequencies covered by prototypal PVA-coated QCMs. The resonance frequency was estimated for a six elements sensor array with a resolution lower than 0.2Hz when the input signal presents a SNR near 40dB at a 1sec scan rate.

## 1 Introduction

The piezoelectric effect in coated quartz crystals can be exploited as a sensing mechanism for the direct monitoring of organic compounds in gaseous and liquid phase. A quartz sensor, also known as quartz crystal microbalance (QCM), consists of a quartz disc with electrodes patterned on the opposite sides, one of which covered with a sensing layer capable of suitable interactions with the analyte of interest. The application of an oscillating electric field across the electrodes triggers mechanical vibrations, whose frequency is related to the acoustic load of the sensor. A one-dimensional transmission-line model can be used to model the behaviour of such a sensor, by analyzing the effect on wave propagation of the absorption and diffusion of analytes into the viscoelastic coating. The use of QCM in liquids is considerably harder than in gaseous media. This happens because the observed frequency shift is caused not only by the mass effect, but also by the viscous coupling with liquid at the quartz surface, that depends on the surface roughness, the surface stress and possible changes in the

liquid properties. Moreover, changes in the viscoelastic properties of the sensing layer (swelling and/or softening, cross linking or phase transitions) may generate additional contributions to frequency shift which cannot be easily distinguished from those related to mass changes. The low sensitivity and the insufficient specificity can be considered drawbacks of microgravimetric measurements, but the ongoing research on new materials and dedicated processing architectures continues to offer solutions to these problems, widening the application field of QCM sensor arrays.

In this paper authors addressed the development of an integrated microgravimetric set-up able to convey in optimal conditions the analyte of interest and perform fast and accurate measurements of the minimum detectable mass change with QCM sensor array. In order to guarantee measurement accuracy, reliability and repeatability, the sampling system was realised to control and optimise factors capable of influencing the generation of sensor transduction signal, and a new method proposed by Campobello et al. [1] for fast and accurate frequency shift estimation was adopted.

## **2 The microgravimetric set-up**

The microgravimetric set-up was composed of a hydraulic and an electronic section, the former consisting of a sampling system and an exposure chamber, the latter of an oscillator and sub-section for resonance frequency estimation. The sampling system was composed of a line of chromatographic air with a controlled flow and an in-line humidity generator. Inert PTFE tubing and fittings were used to send different concentrations of water vapour into the exposure chamber, where QCMs were housed. A valve allowed to switch the system between state 1 (QCMs flushed with chromatographic air, baseline acquisition and cleaning) and state 2 (exposure of QCMs to humid air). The measurement protocol consists of three phases for each experiment: baseline acquisition; exposure; desorption and cleaning.

### *2.1 The exposure chamber*

To expose the array of QCMs to a chemical mixture in optimal conditions, the chamber was designed to:

- to simultaneously expose all the sensors under the same conditions
- to accurately reproduce the shape of the input concentration signal
- to obtain the same concentration profile in repeated measurements
- to obtain short analyte concentration rise/fall times
- to avoid memory effects and sample dilution
- to use only a small amount of sample

A homogeneous flow with low speed gradient, no recirculating zones or stagnant regions and the same local concentration of volatiles over each sensor



was obtained by choosing a radial geometry for the chamber, whose dedicated deflector allowed homogeneous flow conditions with low velocity gradients (figure 1).

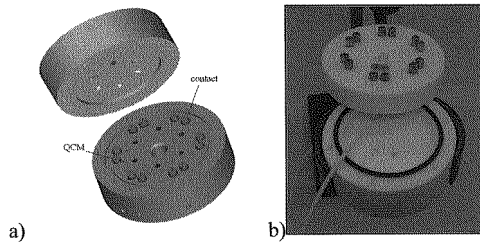


Figure 1 – Exposure chamber for QCM sensor array; a) 3D drawing, b) a photo

## 2.2 The electronic section

In order to study the response of quartz crystal resonators, the complete frequency response in a range centered on the resonance frequency can be monitored. As an example, 10MHz AT-cut quartz were spin-coated by polyvinyl alcohol (PVA), a highly hydrophilic polymer. The surface wettability and easiness of functionalization make it of great interest for chemical and biological sensing. The frequency response of such PVA-coated quartz crystals at different humidity levels was investigated. If a purely gravimetric changes occurred, a frequency shift with no change in peak admittance would result. This case is limited to thin coatings rigidly coupled to the underlying crystal and not for polymers. Prototypal PVA-coated crystals show a viscoelastic behaviour resulting in changes in peak admittance, as a consequence of an energy loss (damping) (figure 2a). In particular, humidity induces a swelling and softening in the material. Figure 2b shows the resonance frequency shift at different humidity levels.

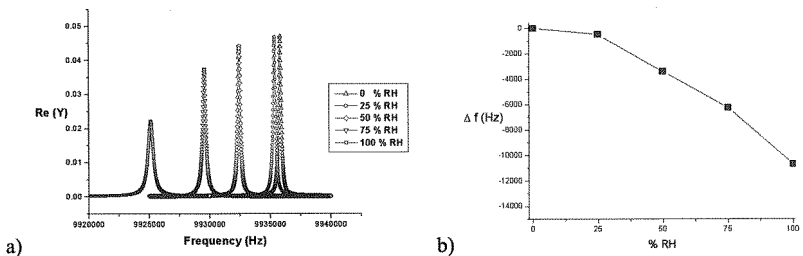


Figure 2 – a) Changes in peak admittance and b) resonance frequency shift of prototypal PVA-coated crystals at different humidity levels

A network analyzer was used to acquire the complete frequency response. Such instruments are interesting for laboratory use and research but are expensive

and voluminous. An oscillating circuit is more practical, since the crystal can be incorporated into the circuit with a quasi-digital output signal and a frequency counter can be employed to estimate the resonance frequency. In case of pure mass accumulation, if the mass variation is uniformly distributed throughout the crystal (uniform thickness and density of the film) and the shear velocity is identical in the film and in the crystal, the Sauerbrey equation [2] is valid and quantifies the frequency shift due to a variation of the deposited mass. Factors such as mechanical clamping, damping in the electrical circuit, temperature variations are not considered, hence calibration methods are needed. In case of pure mass accumulation, the oscillator circuit must work at a constant phase of the quartz resonator and sensor resolution and accuracy depend on the device and method for frequency estimation. Let  $A$  be the area of the quartz crystal in  $\text{cm}^2$ ,  $M$  the mass attached on the crystal surface and  $f_q$  the resonance frequency; considering the density of quartz ( $2.648 \text{ g cm}^{-3}$ ) and the propagation rate of the acoustic wave ( $3.336 \times 10^5 \text{ cm s}^{-1}$ ), it can be obtained:

$$\Delta f = -2,26 \cdot 10^{-6} f_q^2 \frac{\Delta M}{A}$$

A frequency shift of 1 Hz corresponds to  $40 \text{ pg/mm}^2$  of mass variation. Commercial systems are designed to reliably measure mass changes up to  $100 \mu\text{g}$ , whereas the minimum declared detectable mass change is around  $10 \text{ pg/mm}^2$ , which corresponds to a frequency shift of  $0.25 \text{ Hz}$ . Viscoelastic coatings on hydrophilic or hydrophobic surfaces may be difficult to model, and the change in their properties cannot be distinguished in a simple way from the mass effect within the sensor response. Furthermore, until recently, it was generally perceived that viscoelasticity would result in such a severe damping to prevent oscillation of the crystal, until Kanazawa and Gordon [3] and Bruckenstein and Shay [4] showed that the energy loss is not so severe as to preclude oscillation.

In general the sensor transfer function can be determined by a one-dimensional transmission-line model and in particular by the acoustic load concept (ALC) [5], even though on the basis of a number of calibration measurements. In the ALC model the acoustic load impedance carries all the changes in the sensitive coating, i.e. pure mass accumulation, mass accumulation accompanied by material property changes, or material property changes induced by chemical or physical effects. Furthermore, the ALC model directly relates the acoustic load impedance to the resonance frequency shift,  $\Delta f$ , and the motional resistance change,  $\Delta R$  or similar values representing acoustic energy dissipation. In particular, Lucklum et al. [6] have found that the resonance frequency is to be measured at the maximum real part of quartz admittance and the motional resistance at the reciprocal of the maximum real part of quartz admittance. The maximum of the real part of quartz admittance does not coincide with a constant quartz phase. Borngraber et al. [7] have solved this issue realising an automatic gain-controlled oscillator, by modifying a well proven oscillator circuit [8]. It

follows that high efficient and accurate electronic oscillating circuits and methods for resonance frequency shift estimation are mandatory.

Frequency estimation is a wide studied problem and several methods exist in literature [9]. In particular, as regards the accuracy, a lower bound was proved in the case of Additive White Gaussian Noise, known as Cramer-Rao lower bound, by means of it, the accuracy can be related on three key factors: sampling frequency, Signal-to-Noise Ratio (SNR) and number of available samples [10]. However, other parameters can be taken into account in QCM measuring, i.e. the elaboration time and the bandwidth.

In this work a new method proposed by Campobello et al. [1] for fast and accurate frequency shift estimation was adopted. The method can estimate the frequency starting from samplings of a sinusoidal signal. An oscillator circuit with a sinusoidal signal at the resonance frequency as the only output was adopted. The main characteristic of such a method is its intrinsic low complexity and use which enable an easy setting of the right balance between speed, accuracy and bandwidth relating to the particular QCM sensor under test. The output sinusoidal signal is processed by a dedicated electronic interface (figure 3) composed of the following main subsections:

- Reference signal (white quartz or signal generator)
- Mixer (for down conversion)
- Filter (for noise reduction and anti-aliasing)
- ADC (acquisition board)
- DSP (elaboration implemented by hw or sw algorithm)

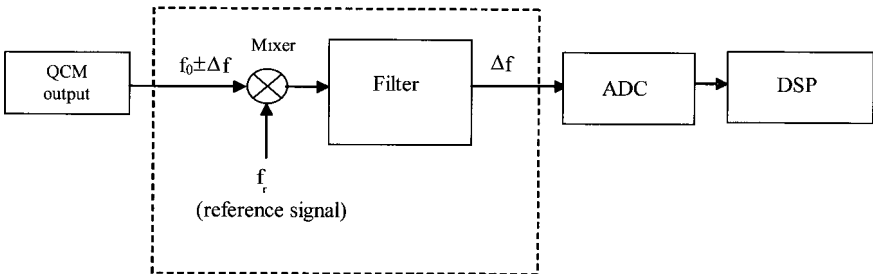


Figure 3 – The electronic interface

The use of a white quartz as reference allows the frequency shift caused by temperature variations to be compensated placing inside the measurement chamber both crystals. The system was simulated in the range of frequencies covered by six prototypal PVA-coated QCMs (40kHz) at a scan rate of 1sec. In figure 4 the maximum absolute error is reported. It can be noticed the frequency is estimated with a resolution lower than 0.2Hz when the input signal presents a SNR near 40dB. These results are very interesting for biomedical applications, where the analyte concentrations are extremely small.

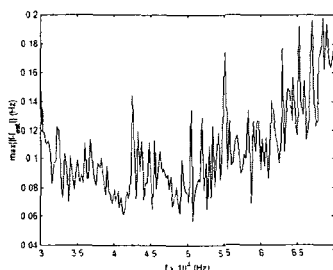


Figure 4 – The maximum absolute error in frequency estimation

## Conclusions

In this paper we proposed and discussed an instrument for fast and accurate measurements with an array of quartz crystal microbalances (QCMs). The sampling system, the exposure chamber and the dedicated electronic interface were detailed. A novel method for frequency estimation allows the measurement time to be reduced while a high frequency resolution is maintained. Taking into account prototypal PVA-coated QCMs, the resonance frequency was estimated with a resolution lower than 0.2Hz with an input signal SNR near 40dB at a 1sec scan rate for a six elements sensor array. These results are promising for the application of such a system in biomedical research where measurements at very low concentrations are mandatory.

## References

1. G. Campobello, N. Donato, A. La Corte, G. Pioggia, "A New Method for Fast and Accurate Frequency Estimation", *IEEE Transactions on Signal Processing*, submitted.
2. C.K. O'Sullivan, G.G. Guilbault, "Commercial quartz crystal microbalances – theory and applications", *Biosensors & Bioelectronics* 14 (1999) 663–670.
3. K.K. Kanazawa, J.G. Gordon, "Frequency of a Quartz Crystal Microbalance in Contact with Liquid", *Anal. Chem.* 57 (1985) 1770-1771.
4. S. Bruckenstein, M. Shay, "Dual quartz microbalance oscillator circuit", *Anal. Chem.* 66 (1994) 1847-1855.
5. R. Lucklum, P. Hauptman, "The generalized acoustic load concept for QCM-Mass sensitivity, Viscoelasticity, and other phenomena", *Proceedings of Eurosensors XVI* (2002) 7-8.
6. R. Lucklum, C. Behling, R.W. Cernosek, S.J. Martin, "Determination of complex shear modulus with thickness shear resonators", *J. Phys D: Appl. Phys.* 30 (1997) 346-356.
7. R. Borngraber, J. Schroder, R. Lucklum, P. Hauptmann, "Is an oscillator-based measurement adequate in a liquid environment?", *IEEE Transactions on Ultrasonics, Ferroelectrics and Frequency Control*, 49(9) (2002) 1254-1259.
8. F. Eichelbaum, R. Borngraber, J. Schroder, R. Lucklum, P. Hauptmann, "Interface circuits for quartz-crystal-microbalance sensors", *Review of Scientific Instruments*, 70(5) 1999.
9. S. Kandeepan, S. Reisenfeld, "DSP Based Frequency Estimation Techniques and Their Relative Performance", *CSNDSP*' (2002).
10. D.C. Rife, R.R. Boorstyn, "Single-Tone Parameter Estimation from Discrete-Time Observations", *IEEE Transactions on Information Theory*, IT-20 (5) (1974).

# **In-Situ monitoring of Volcanic Gases at Solfatara crater with hybrid e-nose**

S. De Vito, E. Massera, L. Quercia, G. Di Francia

*ENEA – C.R. Portici, Via Vecchio Macello s.n.c., 80055, Portici (NA), Italy,  
saverio.devito@portici.enea.it*

## **Summary**

The analysis of fumarolic gases, released in high activity volcanic areas, can provide significant information on the status of these areas. Variation in composition of these gases can, in fact, be correlated with volcanoes' dynamics. These variations are typically due to chemical interactions between magma and the different layers of rocks and aquifers with which it came in touch during its movements toward surface. In this work, we propose the use of an hybrid e-nose, hosting both commercial and ENEA developed gas sensors, for the analysis of fumarolic gases within the solfatara crater. This approach has shown to be capable to provide both qualitative and quantitative information that by the use of pattern recognition techniques and neural regression schemes could be used to extract significant indexes on undergoing volcano dynamics.

## **1. Introduction**

Understanding volcanoes dynamic has always fascinating researchers in the effort to model and forecast dangers of high activities periods. These events pose relevant threats to human beings, since they produce severe impact on human settlements. Given the impossibility to control volcanoes dynamics, prediction capabilities are the only way to effectively contain damages. As such, these capabilities are highly needed especially when high population density settlements are located in the nearside of an high activity volcanic area. Here, surveillance networks typically rely, at present, on the predominant use of geophysical methods of analysis. During the last decade, geochemical methods have been studied and the analysis of fumarolic gases, released in high activity volcanic areas, revealed capable to provide significant information on the status of these areas. Variation in composition of these gases, in fact, seems to be correlated to volcanoes dynamics. These variations are typically due to changes in chemical interactions between magma and the different layers of rocks and aquifers it can find in its movement toward the surface and the ratio between particular species (e.g H<sub>2</sub>O to CO<sub>2</sub> ratio) is considered an important fingerprint

of the volcanic activity [1]. Increase in H<sub>2</sub>O concentration is in fact considered to be related to the heat flow caused by magma movements, whether the CO<sub>2</sub> concentration, although relatively high in volcanic gases, can have limited relation with magma movements being less reactive than other magma components [2]. Furthermore, some fumarolic gases can have a relevant impact on local climate and also on life conditions of human. For this reasons, volcanic gases are periodically monitored, usually with analysis carried out ex-situ with laboratory scale equipment using techniques such as mass spectrometry and gas chromatography. Unfortunately, for such methodologies the characteristic time, that recently showed up as an important feature for fumarolic gas analysis [3], is very coarse. Furthermore, direct spring sampling in this harsh environment can be very dangerous for humans and measurements systems or, in some cases, even impracticable. In the last few years, the need for on-site and continuous monitoring with unattended operation has been constantly growing and some application of remote sensing techniques have been developed for use in this scenario [4]. Optical methods, for example, seems to offer a practicable way, but they are affected by some disadvantages such as beam scattering due to high water vapour content and beam position change due to temperature fluctuation of fumarolic gases.

In this paper we propose the use of a portable e-nose for the analysis of fumarolic gases at Solfatara crater. Solfatara crater is located within Campi Flegrei area, probably the most complex volcanic structure on the earth surface. We believe that e-Noses could represent a valid answer to these needs thanks to the abilities to discriminate between different mixture patterns [5] or to actively determine single analyte concentrations in complex mixtures such as volcanic gases [6][7]. When equipped with the right sensor array and coupled with an opportune data analysis subsystem e-noses can, in fact, easily meet any significative time resolution constraint in this applicative scenario.

## **2. The proposed system**

During last years, we designed and developed a portable e-nose prototype, named NASECANE™, based on a high modular three stage architecture. The first stage host a ten slots sensor array. The developed prototype can host an array of sensors with different transducing mechanism both commercial or developed on purpose at the ENEA laboratories. Sensors can be feeded with a pump based subsystem or let operate in open air. The second stage host a precision electrometer while the third stage includes data processing subsystem, communication subsystem and a battery providing power to the entire system. The MCU based data processing subsystem has been chosen to be capable, in the near future, of running dedicated sensor fusion algorithms in order to make the e-nose capable to work out classification/regression schemes as a standalone unit.

Furthermore the modular design allows for replacement of the communication subsystem at the moment based on RS-232, with a wireless module either Bluetooth or WiFi.

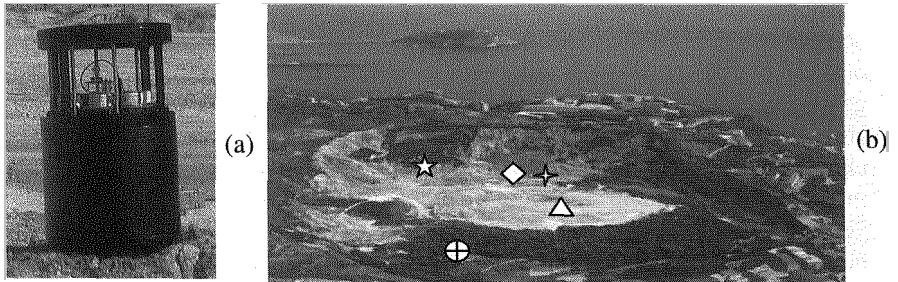


Figure 1: NASECANE prototype e-nose (a). Sampling locations within Solfatara crater : "Bocca Grande"  $\star$  $\diamond$ , "Sauna"  $\star$ , "Fangaia"  $\triangle$  and the control site  $\oplus$ . (b)

### 3. Experimental

Located inside the Campi Flegrei volcanic district, the Solfatara crater is the site of the most conspicuous superficial thermal anomaly in the area; volcanic gases are emitted within the entire crater, by means of several fumaroles surrounding the main one, called "Bocca Grande". If sufficiently accurate the analysis of such gases may provide information on the temperature and pressure conditions in the hydrothermal reservoir feeding the fumaroles and its relationship with the underlying magma body [2]. In table 1, we report type and characteristic of the selected sensors.

Table 1. The sensors array selected for the fumarolic gases analysis.

	Range	Resolution	Manufact.
CL2	0,2-20 ppm	0,02	COTS <sup>1</sup>
CO	1-1000 ppm	1	COTS <sup>1</sup>
H2S	0,3-100 ppm	0,05	COTS <sup>1</sup>
NO	3-250 ppm	0,2	COTS <sup>1</sup>
NO2	0,2-20 ppm	0,02	COTS <sup>1</sup>
SO2	5-2000 ppm	2	COTS <sup>1</sup>
ENE1	-	-	ENE1 <sup>2</sup>
ENE2	-	-	ENE1 <sup>3</sup>
RH	5-95% RH	3%	COTS <sup>1</sup>
TEMP	(-10)-50°C	0,2	COTS <sup>1</sup>

<sup>1</sup> Elect. Cell.

<sup>2</sup> Porous Silicon Membrane

<sup>3</sup> Inverse Diode Porous Silicon Heterojunction

The selection of the sensor array has been driven by the known composition of fumarolic gases and by the need to combine both commercial and ENEA developed sensors so to obtain a deeper insight on their dynamic. We conducted our investigations using the e-nose, analyzing the gas emitted at several locations within the Solfatara crater (see Fig.1), positioning the prototype at a maximum distance of 5 meters from the fumaroles (“Bocca Grande”, “Sauna”) or inside the areas interested by diffuse degassing (“Fangaia”). Previously a short campaign had been conducted in order to assess the influence of weather conditions, measurements sites selection etc.

#### 4. Results

Data analysis has been performed on sampled data by means of statistical (PCA) and pattern recognition techniques. The e-nose detected significant differences among fingerprints of the different sources within the Solfatara crater and between in-Solfatara samples and the control site. A clear separation of site-specific clusters is achievable by means of a PCA plot using two or three principal components. Responses analysis has shown the presence of near-constant characteristic ratios between many couples of specific sensor responses, regardless of the variable measurement conditions (wind intensity and direction). Some of these ratios are site specific while some others are specific of the entire Solfatara crater with respect to the control site.

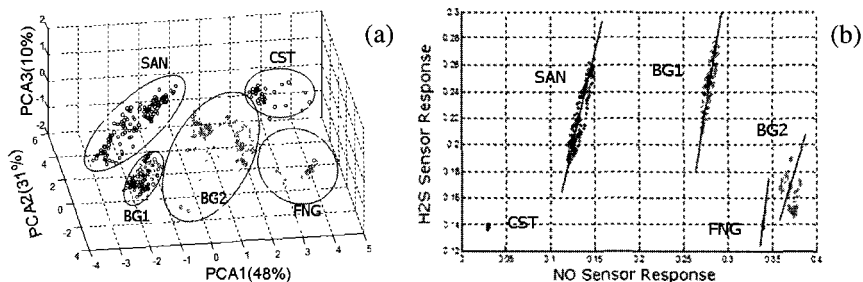


Figure 2: 3D-PCA scatter plot of normalized data (a); NO versus H2S sensors responses plot (b) (V). BG1= Bocca Grande 1, BG2= Bocca Grande 2, SAN = Sauna, FNG= Fangaia, CST = Control Site

As an example, in Fig. 2 (b) we show the presence of a site specific x-axis intersection of regression line and very similar angular coefficient over the entire crater when looking at H2S and NO COTS sensors responses. Analyzing different couples of sensor responses, we also found specific angular coefficient for each of the 4 Solfatara measurement sites.

Furthermore, we performed regression analysis by the use of neural networks (3 layer Back Propagation Networks) in order to highlight the capability of the



two ENEA sensors to predict the response of specific COTS sensors and ultimately estimate specific gas concentration by means of neural sensor fusion<sup>4</sup>. The ENEA developed sensors revealed to be extremely good at estimate the commercial NO sensor response reaching values of less than 1% when evaluating both MAE (Mean Absolute Error) and STD (Error Standard Deviation) with respect to the range of sensor responses. We also evaluated the same performance indexes for different BPNs trained to estimate any other commercial sensor response when feeded with couple of other sensor instantaneous response. A subset of obtained results is presented in table 2. All BPNs have been trained using 75% of samples set and tested on the remaining 25% adopting a 4-fold cross-validation scheme.

<i>Estim.</i>	<i>S1</i>	<i>S2</i>	<i>MAE</i>	<i>STD</i>
NO2	ENE A1	ENE A2	0.045	0.07
<b>H2S</b>	<b>CO</b>	<b>SO2</b>	<b>0.095</b>	<b>0.08</b>
H2S	ENE A1	ENE A2	0.045	0.055
CO	ENE A1	ENE A2	0.09	0.10
CL2	ENE A1	ENE A2	0.045	0.055
SO2	ENE A1	ENE A2	0.05	0.04
RH	ENE A1	ENE A2	0.06	0.05
<b>NO</b>	<b>ENE A1</b>	<b>ENE A2</b>	<b>&lt;0.01</b>	<b>&lt;0.01</b>
NO	CO	CL2	0.07	0.095
NO	H2S	RH	0.055	0.055
NO	H2S	ENE A1	0.06	0.05
NO	H2S	CO	0.06	0.095

Table 2: Performance of BPN based regression estimating COTS sensor response using a subset (actually two) of the remaining sensor responses.

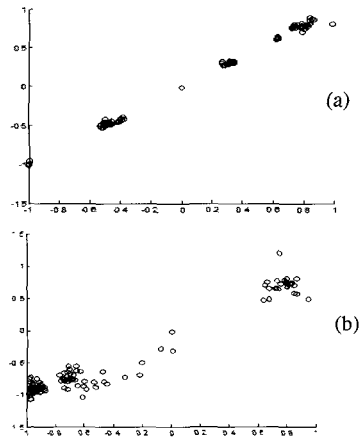


Figure 2: Normalized regression plot for the estimation of NO (a) and CL2 (b) using ENEA1, ENEA2 sensor responses. On the X axis the commercial sensor outputs is reported, Y axis shows the BPN response estimation .

As it can be observed,, performance indexes reach values that can be considered sufficient for the implementation for the e-nose of an instrument fault accommodation scheme (IFA). IFAs can provide graceful performance degradation instead of a catastrophic one, when one of the sensor of a sensing apparatus became faulty, see for example [8]. This scheme can be implemented by means of multiple sensor fusion subsystems trained to operate on a subset of working sensor responses for the estimation of the faulty sensor response. In this

<sup>4</sup> Network has been feeded with Enea developed sensors instantaneous response. 15 sigmoidal tangent units have been used in the hidden layer, a single linear unit represented the output layer.

case, we show that a set of BPN properly trained can estimate a faulty sensor response by knowing the instantaneous response of only two of the working sensors set.

## 5. Conclusions and Further works

We have tested a prototype e-nose in a complex operative scenario such as the Solfatara crater. The response quality allows for the extraction of interesting features with respect to the geochemical point of view. Further works are required in order to exploit e-nose fingerprint relationships with other significant geochemical and geophysical parameters, and so effectively extend classic methods of geochemical analysis.

We have also obtained significative information about ENEA developed sensors array subset. ENEA sensors, when coupled with a sensor fusion subsystem, have proven to be very effective in estimating commercial NO sensor response. The intrinsic nature of Solfatara fumarolic gases emission, characterized by known species correlations, and the properties of selected hybrid sensor array made possible to reach a very significant robustness to sensor faults, the response of a faulty sensor being guessed with sufficient accuracy by the use of a neural based IFA subsystem.

## Acknowledgments

The authors wish to thanks Vulcano Solfatara s.r.l. for the precious collaboration and kindness.

## References

1. D. Tedesco, JC Sabroux, Bull. Volcanol. 49, 381-387. (1987).
2. G. Chiodini, M. Todesco et al. Geophys. Res. Lett. 30, 1434 (2003).
3. M. Zimmer, J. Erzinger, J. Volcanol. Geotherm. Res. 125, 25-38 (2003).
4. A. Rocco, et al., Appl. Phys. B 78, 235-240 (2004).
5. T. C. Pearce, et al., Eds., Wiley, (2002) (ISBN: 3-527-30358-8).
6. M. Pardo et al., Sensors and Actuators B 65 267-269, (2000).
7. S. De Vito et al., Proc. of Eurosensors XIX, (2005). EA available on CD.
8. D. Capriglione et al., Proc. of 13<sup>th</sup> ICIAP, LNCS 3617, 1117-1125 (2005).

# Monitoring of Airborne Fine Particles and NO<sub>x</sub> Beside a Major Road

M. C. Carotta, E. Ferrari, S. Gherardi, C. Malagù, M. Piga, G. Martinelli and A. Rosignoli  
*CNR-INFN- Physics Department, University of Ferrara, via Saragat 1, Ferrara, 44100, Italy*  
[ferrari@fe.infn.it](mailto:ferrari@fe.infn.it)

## Summary

In this paper a correlation between nitrogen oxides (NO<sub>x</sub>), and diesel particles was performed. New monitoring units constituted by an array of chemoresistive gas sensors capable of detecting CO, NO<sub>x</sub> e O<sub>3</sub> were located at two different heights to study the gas vertical distributions. Diesel particles were sampled directly from the exhaust pipe of diesel car to assess the structure, dimension and shape of fresh particles. While a second sampling was carried out close to a busy road in the centre of the city to assess the contribution at the airborne urban particulate of particles exhausted by the diesel vehicles. The particles were sampled by a multistage cascade impactor and characterized by different analytical methods (SEM, EDS).

## 1 Introduction

In the last 20 years, in Italy, fleet of cars has increased of 60%, and nowadays the diesel cars represent the 58% of the vehicles sold in comparison with the 40% of gasoline powered vehicles. The reason of the diesel powered vehicles booming market is that the diesel engine use up about less then 10-15% of energy per kilometre with respect to gasoline and the fuel is cheaper than gasoline. The pollution from vehicles arises from the by-products of combustion process (emitted via exhaust system) and from evaporation of the fuel itself. These emissions are composed from volatile organic compounds (VOCs) and they are produced because the fuel is not completely burnt (oxidized) during the combustion. NO<sub>x</sub> result from the oxidation of nitrogen at high temperature and pressure in the combustion chamber. CO occurs when carbon in the fuel is partially oxidized rather than fully oxidized to CO<sub>2</sub>. PM is produced from the incomplete combustion of fuels, additives in fuels and lubricants, worn material that accumulate in the engine lubricants and those coarse particles brakes, tires and dust emission from road. [1]

Despite the significant improvement in diesel engine design and efforts made to reduce emissions in general, heavy duty diesel fuelled vehicles in average emit the half of CO but 6 and 8 times of particle mass and NO<sub>x</sub>, respectively, more than a gasoline fuelled vehicles. Therefore the diesel vehicles are one of the most important producers of PM and NO<sub>x</sub> in urban environment.

The diesel particle exhaust are constituted by carbonaceous particles (soots) and inorganic particles (ashes), that are generated by mechanisms such as molecular growth, condensation, coagulation, agglomeration and oxidation of molecular precursors in the combustion chamber. Traditionally, the assessment of diesel exhaust particles has been based on mass concentration, but this may not give an accurate valuation of the diesel aerosol exposure. By number count, most diesel aerosol is found in nuclei mode with a particle diameter less than 50 nm and a number median diameter between 15 and 20 nm when measured under atmospheric conditions. However, most of the aerosol mass lies in the accumulation mode with particle size ranging from 50 nm to 1  $\mu\text{m}$  and the median aerodynamic diameter between 100 to 200 nm.[2]

NOx play an important role in photochemical reaction cycles, leading to smog in the urban troposphere, depletion of stratospheric ozone and acid rain. In photochemical smog formation certain gas phase reactions are promoted by ultraviolet light.

Aim of this work is to correlate the NOx and diesel particle sources through a set of local measurements performed with portable and versatile devices: small gas monitoring units based on solid state gas sensors to measure NOx concentrations and portable multistage cascade impactor to collect particulate matter.

## 2 Experimental

The experiment was divided in two parts: in the first one diesel and airborne particulate matter were sampled and in the second one NOx concentrations were measured. The results were compared to assess the correlation between the gas and diesel particles. The diesel particles were sampled directly from the exhaust pipe of a diesel car (Opel Astra, 2002, Euro III) at a distance of 30 cm, the engine was operated at idle condition. The airborne particle sampling point was close to a busy interception and located at the heights of 3 and 8 meters above the street on the windowsill and about 10 meters from the crossroads.

The particles were sampled with a Portable Cascade Impactor Sampler (PCIS), that separates the particulate in five granulometric fractions and at every stage it was placed a polycarbonate filter where particles were collected. The stage cut-off diameters are 10-2.5, 2.5-1.0, 1.0-0.5, 0.5-0.25, <0.25  $\mu\text{m}$ , respectively, for the five stages of the impactor. The two final stages particles (<0.5  $\mu\text{m}$ ) are interesting for this work because they are mostly generated by primary combustion sources and are characteristic of relatively fresh emissions such as those dominating in a typical urban area [3]. The particle composition and the morphology were determined by scanning electron microscope (SEM) equipped with energy electron spectrometry (EDS). The voltage for the energy dispersive X-Ray analysis was 20 KeV and the time of X-Ray collection was 100 s. Each filter was covered with gold before SEM observation.

Near the particle collection points units for gas pollutants monitoring were located. They consisted of an array of chemoresistive gas sensors capable of detecting CO, NO<sub>x</sub> and ozone. The thick-film gas sensors were developed and fabricated by the Sensor and Semiconductor Laboratory of the University of Ferrara.

### 3 Particle Sampling and Analysis

The soot particles appear as agglomerates composed of small, basic particles that are spherical or nearly spherical with varying diameter from 10 to 80 nm. The primary particles are constituted of graphite. During the agglomeration of soot, inorganic ultrafine particles are included into the growing clusters, while condensable unburned hydrocarbons along with water-solved inorganic precursors easily adsorb onto the extended surfaces of porous clusters [1b].

The SEM observations revealed the heterogeneity, in dimensions and shape, of airborne particles. However, the particles collected in the last two filters of the impactor seem to belong to two species: nanometric sphere agglomerates and single spheres with diameter ranging from 100 up to 300 nm. The agglomerate particles (see Figure 1a) were similar in structure and dimensions to those observed in diesel engine samples (see Figure 1b). Single spherical particles, as in Figure 1c, were found only in the airborne particles; their origin could be ascribed to a different combustion source. The microanalyses carried out on this particles revealed a high content of carbon (about 78%), oxygen and, in some, a small amounts of Zn and Na.

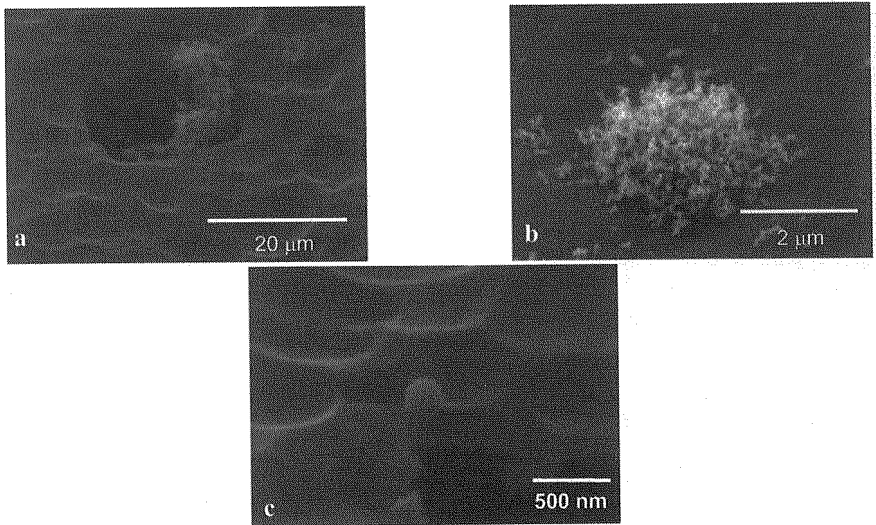


*Fig. 1 a) Soot airborne particle; b) Soot particle exhausted by diesel car; c) Ash airborne particle*

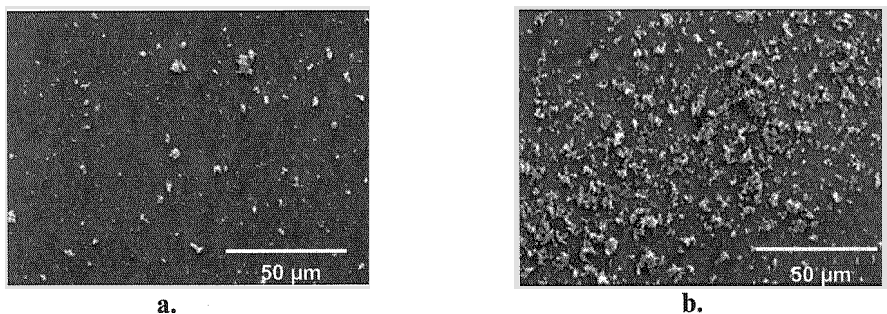


*Fig.2 Airborne collected on filter D at 8m (a) and 3m (b).*

The vertical distribution was studied sampling the airborne particles for 15 minutes at two levels (3 and 8 m). The particles number was greater at lower level with respect to the upper level (see Figure 2). This fact was due to vehicular source and the break up of road surface that contribute to the generation of fine and coarse particles, respectively, at road level, while finest particles fraction, lighter than coarse fraction, can reach greater heights before deposition.

### Monitoring of NO<sub>x</sub> concentrations

The concentrations of NO<sub>x</sub> was measured in January, at the same time of particulate samplings. NO<sub>x</sub> was detected by a WO<sub>3</sub> sensor doped with manganese. The sensors were calibrated on the concentrations measured with chemiluminescent spectroscopy device located in the monitoring unit of the regional environment protection agency (ARPA). The NO<sub>x</sub> concentration, measured at the two levels during the first 19 days of January 2006, showed higher values at lower level, nearest to the vehicular source of the pollutant, as for particulate.

The gas concentration follows a vertical as a daily dispersion, showing low concentrations at night or at dawn and high concentrations at diurnal hours, with peak values that correspond to moments of intense traffic. This it clearly seen in Figure 3, in which the daily hourly concentrations, of two subsequent weeks were compared: the first was a holiday week, characterized by low traffic except Friday, Epiphany day, hence low NO<sub>x</sub> concentrations; during the second the concentrations were higher because the normal activities (school, works, etc.) restarted, so the vehicular traffic increased whit NO<sub>x</sub> concentration. Especially at 8.00 am, 14 pm and 20 pm higher values were recorded nearest to the road. During the nigh time the vertical difference of concentrations was slight, except when an inversion of concentration sometimes occurs for short time intervals. Such an inversion is probably due to dispersion of pollutants from the bottom to the top or the lack of vehicular sources during the night revelled the presence of

pollution sources at highest level, usually covered by traffic, as domestic and industrial chimney emissions.

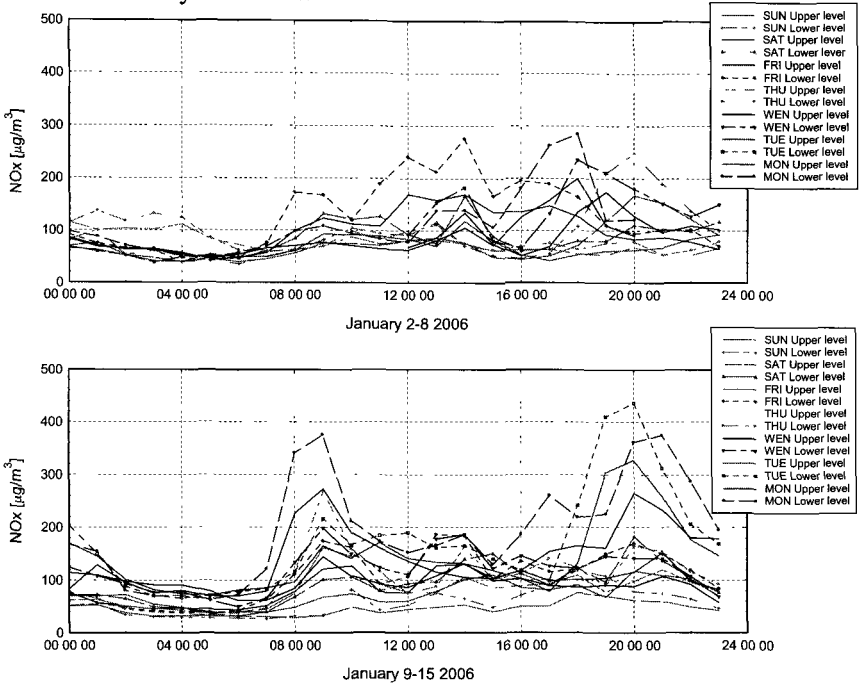


Fig.3 Comparison of daily NOx concentrations measured in two consecutive weeks

It turns out from previous observations that the finer fraction of particulate matter (with diameter less than  $1\ \mu\text{m}$ ), collected near the street, is composed mainly by soot particles recognized as diesel particles.

The vertical distribution of particulate matter highlighted greater concentrations of soot particles at lower level, near the pollution source. This fact represents a strong evidence that the source is traffic; in this situation, the dependence on height of finer particles and NOx can be related.

## References

1. M. Yip Wong, *Exposure assessment in a bus way canyon*, pp27-28 <http://www.sbg.ac.at/ipk/avstudio/pierofun/exotica/thesis-mari.pdf>.
2. Health Effect Institute, Research Directions to Improve Estimates of Human Exposure and Risk from Diesel Exhaust, p.154.
3. C. Misraa, M. Singha, S. Shena, C. Sioutasa, P. M. Hall, Development and evaluation of a personal cascade impactor sampler (PCIS), *Aerosol Science* 33 (2002) 1027–1047.

# A DYNAMIC-ELEMENT MATCHED CCII FOR SMART SENSORS

Giuseppe Ferri, Vincenzo Stornelli, Andrea De Marcellis, Christian Falconi\* and Arnaldo D'Amico\*

*Dipartimento di Ingegneria Elettrica, Università dell'Aquila, Monteluco di Roio, 67100 L'Aquila, Italy, e-mail: [ferri@ing.univaq.it](mailto:ferri@ing.univaq.it)*

*\*Dipartimento di Ingegneria Elettronica, Università di Tor Vergata, Rome, Italy*

## Summary

In this paper the dynamic element matching (DEM) technique is applied to a second generation current conveyor (CCII) in order to compensate the input offset and  $1/f$  noise voltages. Apart from a residual clock-feedthrough error, a significant reduction in the offset voltage between CCII X and Y nodes is achieved with a slight increase in circuitry complexity. As an example, the dynamic-element matched CCII has been used for the design of a resistive sensor interface. Simulation results confirm theoretical results.

## 1 Introduction

Smart sensors have both the sensing element and the electronic interface integrated in the same chip, resulting in many advantages, such as low cost, high performance, low power dissipation, low susceptibility to interference, small size and weight. For low cost reasons, CMOS smart sensors are generally preferable; unfortunately CMOS amplifiers exhibit rather high input offset and noise voltages, especially in low-voltage low-power applications. Consequently, in CMOS interfaces for smart sensors it is often essential to compensate the input offset and  $1/f$  noise voltages of the amplifiers; since static offset compensation techniques require calibration and may not compensate time varying errors (such as drift and  $1/f$  noise), only dynamic techniques are suitable for CMOS smart sensors. Circuits using dynamic techniques may be grouped in three main classes [1]: autozero circuits (AZCs), chopper circuits (CHCs) and circuits which use dynamic element matching (DEM). In AZCs the error sampled in a first phase is used to reduce the error during the second phase. CHCs modulate the signal twice and the input offset voltage only once; as a consequence, the signal is modulated to higher frequency and then demodulated back to the base band, while the input offset voltage is only modulated to higher frequency and may be removed by averaging (low pass filtering in continuous time systems or digital averaging in non continuous time systems). However, since in symmetric (or "quasi-symmetric") circuit topologies offset is (mainly) due to mismatch of a few components, it may also be reduced by dynamically interchanging those components; this strategy is known as dynamic element matching (DEM). In this



paper we have applied the DEM technique to a second generation current conveyor (CCII) [2], which can be used as an active element in resistive sensor interface [3-5].

**2 Second Generation Current Conveyor (CCII)**

Second generation current conveyors (CCII) are current-mode basic blocks [2-5] which, in numerous applications, can favourably replace operational amplifiers, both in linear and nonlinear contexts. In an ideal CCII device (see Figure 1), if a voltage is applied at Y node, an equal voltage is produced at X node and the current flowing into X node is equal or opposite to the current flowing into Z node. Moreover, Z and Y nodes show infinite impedances and X node shows zero impedance. Positive (CCII+) and negative (CCII-) current conveyors are respectively obtained for  $I_Z = I_X$  and  $I_Z = -I_X$ .

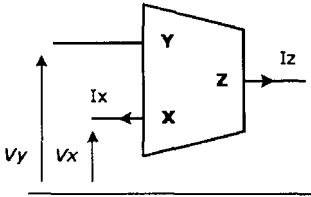


Fig.1 Ideal CCII block scheme

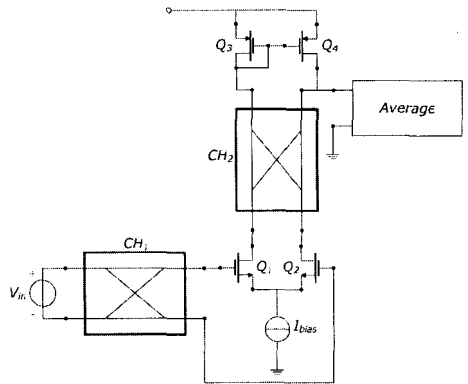


Fig.2 CCII-DEM input stage block scheme

Typically, in CCII, a unity voltage transfer function  $V_X/V_Y$  is ensured by implementing a differential transistor input pair, but a residual offset due to components mismatch affects the follower operation.

**3 Dynamic-element matched CCII**

We have applied the DEM technique to a second generation current conveyor (CCII) resulting, to the best of our knowledge, in the first ever reported offset (and 1/f noise) compensated CCII. In Figure 2 the input stage of the dynamic-element matched CCII is shown: the DEM technique is applied by means of the

chopper switches ( $CH_1$ - $CH_2$ ). Figure 3 shows the complete transistor level schematic of the proposed CCII-DEM.  $Q_1$  and  $Q_2$  are the input transistor pair, biased by  $I_{ref}$ .  $Q_5, Q_6$ . Transistors  $Q_3, Q_4$  constitute the active load of the input pair, while  $Q_7, Q_8$  and  $Q_9, Q_{10}$  are the output stages ( $X, Z$  nodes respectively). Finally, transistors  $Q_{s1}$ - $Q_{s8}$  form the dynamic switches clocked by two opposite non-overlapping phases.

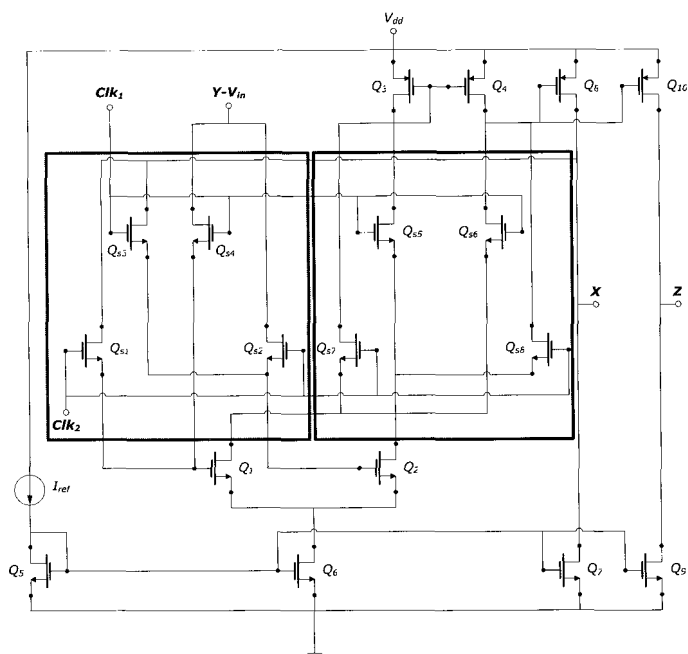


Fig.3 CCII-DEM at transistor level

Figure 4 shows the input offset voltage of the proposed CCII-DEM as a function of the X-node load resistance. The systematic offset of the designed CCII is about  $40 \mu\text{V}$ ; a random offset has been simulated through the insertion of a DC voltage between the gate of the transistor  $Q_1$  and the correspondent terminal of the block  $CH_1$  (see Figure 2).

Figure 5 shows a typical CCII offset behaviour vs. time domain when a systematic offset of  $2 \text{ mV}$  has been applied at Y node: as shown CCII offset has been reduced to  $120 \mu\text{V}$ .

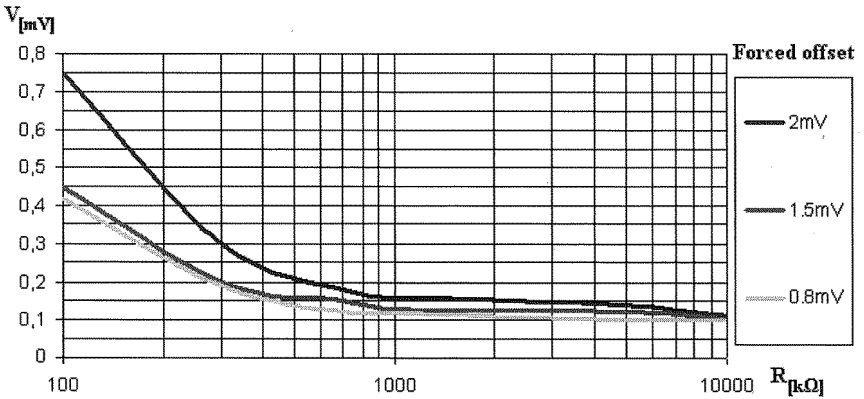


Fig.4 CCII-DEM offset simulation results: a forced offset has been applied after compensation of the input switch

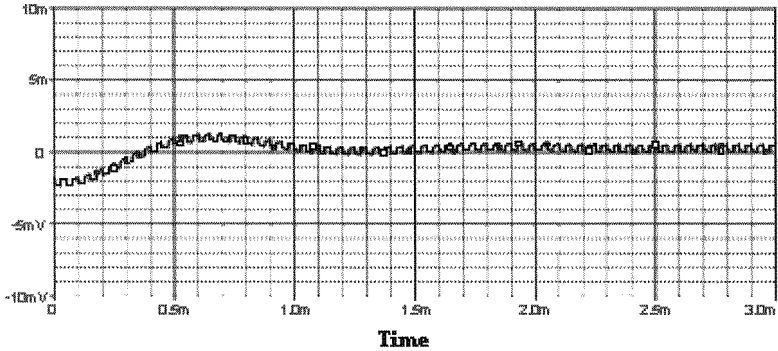


Fig.5 Offset compensated CCII when a systematic offset of 2mV is applied at Y node

**4 CCII DEM for sensor interface applications**

In Figure 6 a CCII resistive sensor interface is depicted [4-5]. This scheme utilizes two CCII+ and one CCII- . The sensor is modelled by the resistance  $R_p$ ; if we call  $x$  its relative variation, the output voltage  $V_{out}$  is directly proportional to  $x$  plus components due to the offset of the implemented CCII's ( $V_{OFF-i}$ , where "i" indicates the  $i$ -th CCII); eq.(1), obtained designing  $V_{REF2}=V_{REF}R_p/R_1$  and  $R_2=R_3=R_{23}$ , shows how low CCII offset values give a better sensor estimation by eliminating the related terms. This interface has been both simulated with a classical second generation CCII and with the here proposed CCII-DEM. In both solutions a random offset has been introduced in the current conveyors. Simulation results has shown, as expected, a significant improvement in  $R_p$

estimation accuracy, when a CCII-DEM is used, due to the quasi-cancellation of the offset terms in eq(1).

$$V_{out} = \left( \frac{R_4 R_{p0}}{R_{23} R_l} V_{REF} \right) x + \left( \frac{R_4 R_{p0} (1+x)}{R_{23} R_l} V_{REF} \right) V_{OFF1} + (V_{OFF2} + V_{OFF3}) \frac{R_4}{R_{23}} \quad (1)$$

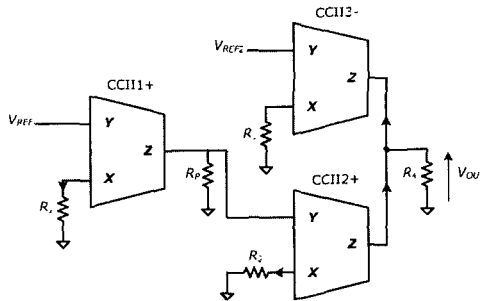


Fig.6 CCII sensor interface

## 5 Conclusions

In this paper we have applied the DEM technique to a second generation current conveyor (CCII). Simulation results, apart from residual clock-feedthrough error, show a significant reduction in the offset voltage between CCII X and Y nodes with a slight increase in circuitry complexity. The DEM-CCII has been applied in the design of a CCII based resistive sensor interfaces, significantly improving its accuracy.

## References

1. C. Falconi, C. Di Natale, A. D'Amico, M. Faccio, "Electronic interface for the accurate read-out of resistive sensors in low voltage-low power integrated systems", *Sensors and Actuators A*, 2004.
2. G. Ferri, N. Guerrini, "Low voltage low power CMOS current conveyors", Kluwer Academic Publisher, Boston, 2003, 226 pp., ISBN 1-4020-7486-7.
3. J.Samitri, M. Puig-Vidal, S. A. Bota, C. Rubio, S. K. Siskos, T. Laopoulos, "A Current-Mode Interface Circuit for a Piezoresistive Pressure Sensor", *IEEE Trans. on Instrumentation and Measurements*, Vol. 47, No.3, June 1998, pp.708-710.
4. C. Cantalini, G. Ferri, N. Guerrini, S. Santucci, "A low voltage low power current mode gas sensor integrated interface", *ICM Proc. 2004, Tunisia*.
5. G. Ferri, N. Guerrini, S. Del Re, F. Mancini "CCII-based integrated gas sensor interfaces", *Sensors And Microsystems, Proc. AISEM (Italian Conference on Sensors and Microsystems)*, 2004, pp. 424-429.

## Multisensor Layout for Robots in Hostile Environments

Claudio Moriconi, Marco Santoro

*Department of Robotics, ENEA Research Center "Casaccia", Via Anguillarese  
301, 00060 Rome, Italy  
[marco.santoro@casaccia.enea.it](mailto:marco.santoro@casaccia.enea.it)*

### Summary

Robots operating in harsh and hostile environments need reliable multisensorial systems able to automatically acquire as much information as possible. Sensory data from a range of disparate and independent multiple sensors have to produce an improved model or estimate of the domain of interest. Therefore the automated intelligent combination of data from multiple sensors can derive less ambiguous/uncertain information about the desired state.

ENEA, the *Italian National Agency for New Technologies, Energy and the Environment*, is developing a multisensorial layout for robots operating in such environments.

### Introduction

A multisensorial distributed unit contains several discrete sensors over a definite surface area/volume (Fig. 1).

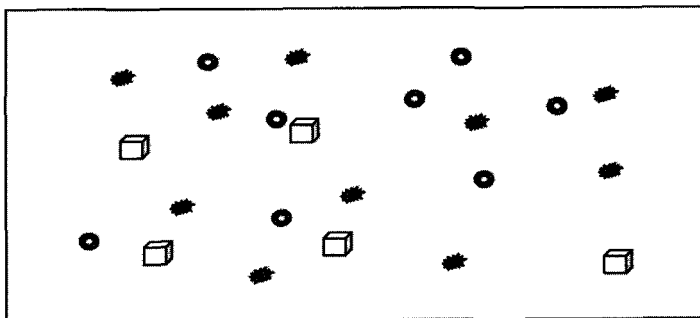


*Fig. 1 General layout of a multisensorial distributed unit*

The Department of Robotics (<http://wwwrob.brindisi.enea.it/>) at ENEA Research Center "Casaccia" is currently developing a multisensor device able to measure and acquire different physical quantities in order to allow pattern recognition of the gathered observations i.e. their classification and description. The sensor system currently contains

- 30 Platinum Resistance Temperature Detectors of  $100\Omega@0^{\circ}\text{C}$  nominal resistance (PT100);
- 30 Silicon PIN Photodiodes sensitive to visible and infrared radiation (peak sensitivity at 900nm and spectral bandwidth range  $\lambda_{0.5}=600 \dots 1050\text{nm}$ );
- Pressure Pad based on a foam material whereby light introduced to the foam is scattered in a manner dependent on the force applied to the surface of the foam.

### How the multisensor device works

60 pressure sensors are spaced evenly (Fig. 2) throughout the area of the touchpad (210mm X 350 mm). Each individual pressure sensing element consists of a tiny light source and a tiny detector imbedded in a thin cellular elastomer (Fig. 3). As pressure is applied to the elastomer in the region of the sensor, the cell size distribution is altered along with the bulk optical scattering properties of the material in that area. The light detector measures the change in scattered light intensity at the sensor, and interprets this as a change in pressure.

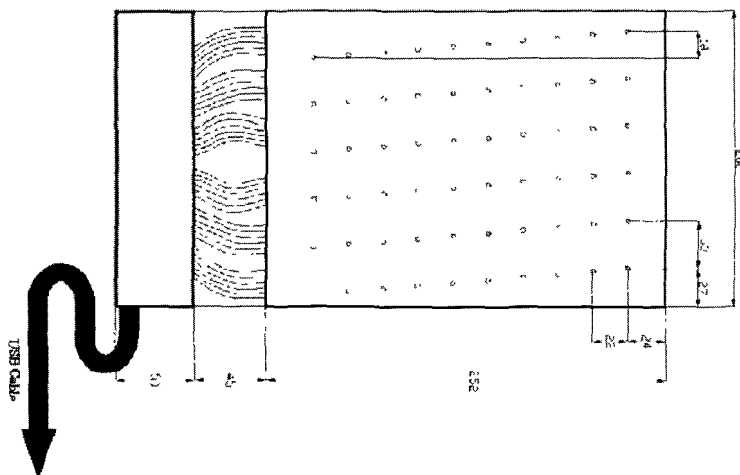
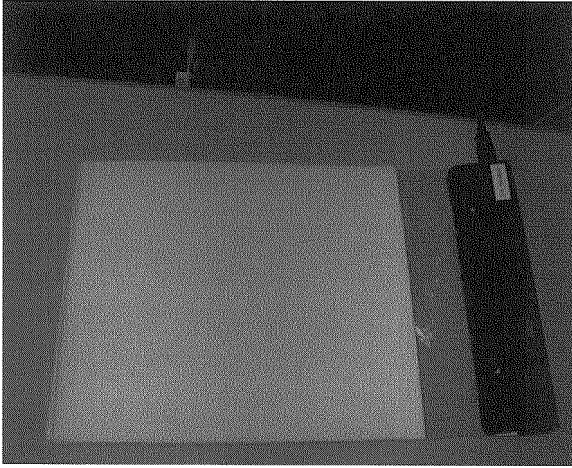


Fig.2 Layout of the pressure pad



*Fig. 3 The pressure pad*

Optical fibers laminated into the structure are used as the “nervous system”, to deliver transmitted light to the location of the sensors, and to deliver received light back from the sensor. It is convenient and less expensive to use these fibers rather than individual light sources and detectors actually located within the material.

The light source is a light emitting diode (LED) connected to a bundle of fibers, and the light detector is an array of photodiodes connected to a second set of fibers. A microcontroller converts the signals from the detectors to digital signals, conditions those signals, and computes the required pressure information or decision data using a set of algorithms implemented in firmware. This pressure system is unaffected by electromagnetic interference, since light intensity is used for measuring the pressure applied, but the foam layers have to be protected by an outer covering material (Nylon New Perlite) that avoids outer light to enter the optic fibers (Fig. 4).

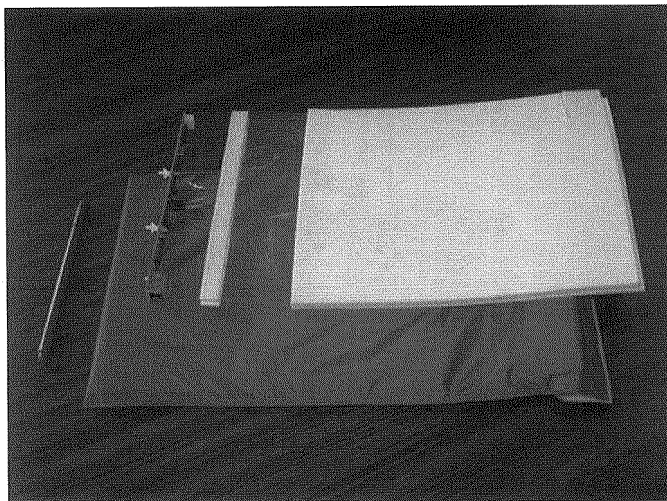


*Fig. 4 Nylon cover, beneath the pressure pad. It completely covers the pad when pressures are being detected*

This layout is being completed by further sensor layers. 30 evenly spaced Platinum Resistance Temperature Detectors of  $100\Omega@0^\circ\text{C}$  nominal resistance (PT100) and 30 evenly spaced Silicon PIN Photodiodes (Fig. 5) are being placed over the pressure pad. These additional layers allow the detection of temperature and visible and infrared radiation.

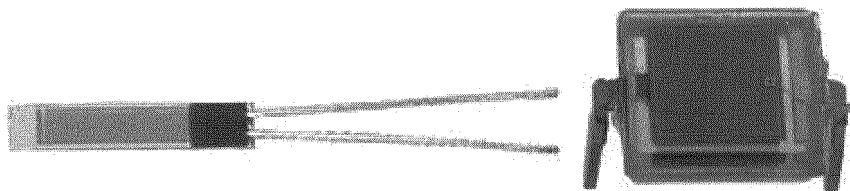


*Fig. 5 Platinum Resistance Temperature Detector (Pt 100), range  $-50 \div +600^\circ\text{C}$  (left) and Silicon PIN Photodiode, range  $\lambda_{0.5}=600 \dots 1050\text{nm}$  (right)*



Some inertial sensors (Fig. 6) will be inserted inside the pad in order to detect low-frequency vibrations.

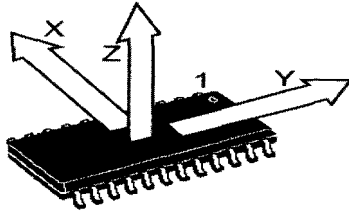


*Fig. 6 INERTIAL SENSOR: 3-Axis 2g/6g Linear Accelerometer*

Partitioned data clustering algorithms are being developed with the aim of classifying detected data. A complete pattern recognition system allows improving the understanding of the information acquired.

# WIRELESS SENSOR NETWORKS OVERVIEW, LOOKING AT THE ZIGBEE ARCHITECTURE

Danilo Blasi, Vincenzo Cacace, Luca Casone, Marco Rizzello  
*STMicroelectronics c/o Distretto Tecnologico-ISUFI (Pal.B, p.t.)*  
*Via per Arnesano 16, 73100 - Lecce – Italy*  
*{danilo.blasi, vincenzo.cacace, luca.casone, marco.rizzello}@st.com*

## Summary

The Wireless Sensor Networks (WSN) are an emerging application field that promises wide support to the interaction between people and their surroundings. Because of the extremely variable nature of this interaction, the WSN topic is still in its stage of development and rises several challenges, which span from the design of a smart device that allows easy and reliable access to the environmental characteristics, to the creation of a wireless network of such devices that cooperate to perform complex tasks. Besides, the pressing market request for low cost/power/dimension products emphasizes the need for standards against the use of expensive proprietary solutions adopted so far. In this paper, we will discuss the most important features of WSN, introducing the IEEE 802.15.4 and ZigBee architecture, showing how their key aspects fit the WSN requirements.

## 1 Introduction to WSN

In the recent years, improvements in embedded systems and integrated radio circuits have made available a new kind of applications: the Wireless Sensor Networks.

The potential of the WSN concept [1] simply lays in the three words composing the acronym itself: ‘*Wireless*’ puts the focus on the freedom that the elimination of wires gives in terms of mobility handling and ease of the system installation; ‘*Sensor*’ reflects the capability of micro-/nano-technology to provide means to perceive and interact – in a wide sense – with the world; ‘*Networks*’ gives emphasis on the possibility to build up systems whose functional capabilities are given by a plurality of devices possibly distributed over large areas.

WSN are usually characterized by a high number of very low cost devices, densely deployed, with limited energy and computational resources. A possible simplified functional architecture of a generic WSN device is shown in Fig. 1. Five basic components are illustrated: the transducing unit (XDCR, including multiple sensors and/or actuators), the micro controller unit (MCU), the memory unit, the radio interface and the power unit. The device may also integrate two additional components such as a location finding system (LOC) and a mobilizer (MOB): they are special sub-systems providing information about the device’s position and allowing the device’s mobility, respectively.

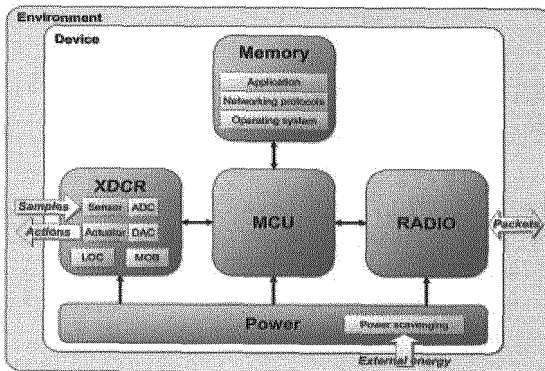


*Fig.1 - The functional architecture of a WSN device*

Altogether, the network's members are able to monitor and/or control a wide variety of environmental conditions that include, but are not limited to, temperature, humidity, vehicular movement, lightening conditions, pressure. In effects, the great interest WSN are gaining is essentially related to the nearly 'infinite' range of their applications. In the simplest form, a WSN may include devices/nodes exchanging data with a single base station, which is in charge of synchronizing and managing all the network transmissions. In such an 'infrastructured' network organization, however, the covered area and the manageable number of members are respectively limited by the wireless link range and the base station's elaboration capabilities. Clearly, a larger area may be monitored by deploying multiple base stations and making them interconnected (through either wired or wireless links), but this is an expensive solution due to the infrastructure's implementation. An alternative, challenging approach – which would also potentially boost the system scalability – is to manage communications in a distributed and infrastructureless way (otherwise said "ad hoc" mode). Such networks are composed by nodes only, possibly with different kind of functionalities and capabilities (i.e., heterogeneous networks) not including base stations. Nodes are required to be self-configuring and self-organizing to participate in distributed and multi-hop communications, where fixed infrastructure are unnecessary. This way, distributed measurement and control systems can be more easily built up, even over wide geographic area. It has to be pointed out that the realization of such systems has to deal with low-cost nodes: this implies limited energy and scarce processing resources. The multihop communications well fit with the first constraint, as they are expected to consume less energy than the traditional single hop ones; conversely, multi-hopping requires a higher number of nodes that execute advanced networking protocols to face the topology changes mainly due to nodes' failures. On the

other side, the high number of devices favours both the robustness (if a node got failed, another would take its place) and information reliability (the same information can be gathered from multiple, different sources). The redundancy of correlated information (i.e. produced by multiple sensor devices that are reporting of a common phenomenon) is usually considered also in the relaying process: in particular, rather than separately propagating high correlated data items towards their intended consumers, they may be aggregated, depending on the target application, as they are flowing through the network, so that considerable energy and bandwidth savings can be achieved. This is the main idea behind a well-know data centric technique called *in-network aggregation* [2, 3].

## **2. Many applications, few standards: IEEE 802.15.4 and ZigBee**

As already said, WSN may effectively support many new application areas. For example, given their characteristics of rapid deployment, self-organization and fault tolerance, they are very valuable in emergency scenarios (e.g., search and rescue, battlefield, etc.). Other typical application scenarios include industrial and building automation, environmental control, health care, urban traffic control, interactive museums, and so on.

This variety of WSN domains may make very hard the design of a unique *general-purpose HW/SW platform*. In spite of producers' and vendors' concrete actions aiming at developing largely reusable and interoperable components and/or devices, the 'sensor and control arena' is still mostly composed by many proprietary solutions that are almost incompatible.

However, one of the proposed standards well suited for WSN is the IEEE 802.15.4 [4] for Low-Rate Wireless Personal Area Networks. It belongs to the IEEE 802.x family and, such as, defines specifications for the ISO/OSI Medium Access Control (MAC) sub-layer and the Physical Layer (PHY) (see Fig. 2). Its main target is low data rate wireless connectivity (up to 250 Kbps, in 27 channels of ISM band) among low power, low cost, low dimension devices, typically operating in a personal operating space (POS) within tens of meters. The specifications establish a rough classification of devices, distinguishing between *Reduced Function Devices (RFD)* and *Full Function Devices (FFD)*. The former identified as the network's 'users' or 'leaf nodes', are meant to be devices with poor resources. The latter, implementing the full set of networking functionalities (e.g. coordination, addresses assignment, packet relaying, etc.), can be identified as the WPAN coordinators and are supposed to have higher resources. Following this classification, devices are allowed to establish communications, according to two possible network configurations: "star" (RFD/FFD devices can communicate through a FFD intermediate central coordinator) and "peer-to-peer" (FFD devices can directly communicate,

without mediators). To manage networks deployed over wider areas (e.g. multi-hop relaying), protocols above layer two of ISO/OSI stack (see Fig. 2) have to be defined. The ZigBee Alliance [5] is just carrying out this definition process atop the IEEE standard.

The ZigBee Alliance is an association of Companies working together to enable reliable, cost-effective, low-power, wirelessly networked, monitoring and control products based on an open global standard. The Alliance is not pushing a technology itself; it is rather providing a standardized base set of solutions for sensor and control systems. The ZigBee membership includes promoters (like Philips, Motorola) and participants (like STMicroelectronics).

The ZigBee specifications concern the networking and security protocols, the application framework and services for different application profiles. Other addressed functionalities relate to (i) discovery and management of multi-hop paths, (ii) reliable transfers (based on handshaking procedures), (iii) devices description according to supported application profiles, (iv) wide support to application layer (e.g. devices and services discovery).

ZigBee was ratified in December 2004; since then, a growing number of companies interested in integrating ZigBee technology within their products has appeared on the market: so that a steady growth in ZigBee-compliant devices availability is expected in the near future. Nevertheless, different issues are still either not clarified or not solved at all. Just a new ZigBee version is under definition to cope with, among all, (i) devices mobility support, (ii) datagrams fragmentation, (iii) multicast traffic management. Other topics are still not faced up to, such as mechanisms for knowing nodes' physical locations and

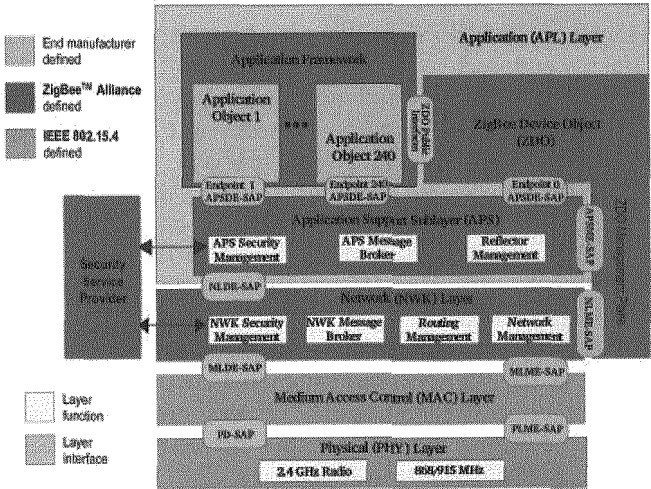


Fig.2 - The IEEE 802.15.4 and ZigBee protocol stack

position-aware protocols.

Together with IEEE 802.15.4 standard, ZigBee was expected – by its promoters – to become a fully defined protocol stack for WSN, leaving to system developers the realization of the application software only. However, ZigBee already does not appear to be able to support all WSN possible applications, even if the definition of new application profiles is in progress. For example, the address centric ZigBee/IEEE 802.15.4 framework does not seem to well match with data centric WSN, like those considered in the well known “Smart Dust” Project [6]. Moreover, the production and deployment costs are still too high. All in all, there is still room for R&D activities in the field of WSN.

#### 4 Conclusion

According to recent marketing reports on the factors influencing the WSN market [7, 8], the success of competing WSN solutions will be based on customer demand for reliability, simplicity, price and availability, with the risk to obtain too slow standardization efforts and many prompt proprietary solutions. On the other side, experience demonstrated that an accepted industrial standard is better than no standard at all but, in its turn, it will be always determined by wide industrial and market consensus. For sure, even in the absence of consolidated standards, there will be an explosive and pervasive adoption of WSN and their applications in the near future!

#### References

- [1] I.F.Akyildiz, M.C. Vuran, O. B. Akan, W. Su, “Wireless Sensor Networks: A Survey Revisited”, *Computer Networks Journal* (2005)
- [2] B. Krishnamachari, D. Estrin, and S. Wicker, “Modelling Data-Centric Routing in Wireless Sensor Networks”, *Proc. of IEEE Infocom*, 2002.
- [3] C. Intanagonwiwat, R. Govindan, D. Estrin, J. Heidemann, and F. Silva, “Directed Diffusion for Wireless Sensor Networking”, *Proc. of IEEE/ACM Transactions on Networking*, 11(1), 2003.
- [4] <http://standards.ieee.org/getieee802/download/802.15.4-2003.pdf>
- [5] <http://www.zigbee.org>
- [6] J.M. Kahn, R.H. Katz, and K.S.J. Pister, “Next century challenges: mobile networking for smart dust”, *Proc. of the ACM MobiCom*, pp. 271-278, 1999.
- [7] K. West, “Wireless Sensor Technology and Market Tracking Service: ZigBee, Zwave, Insteon, RFID, IEEE 802.15.4 and their Competition”, Report abstract WTRS, 2005.
- [8] J. Dexheimer and Dr. R. Hannemann, “Investment Opportunities in Sensor Networking: Dust, Hype, Fuzz, and Reality, First Analysis with Physical Sciences Inc. and D13 Partners”, 2004.

# MOTES SENSOR NETWORKS IN DYNAMIC SCENARIOS: A PERFORMANCE STUDY FOR PERSVASIVE APPLICATIONS IN URBAN ENVIRONMENTS

M. CONTI, E. GREGORI AND G. VALENTE

*Institute for Informatics and Telematics, Italian National Research Council,  
Via G. Moruzzi 1,  
56124, Pisa, Italy  
E-mail: {firstname.lastname}@iit.cnr.it*

G. ANASTASI AND C. SPAGONI

*Information Engineering Department, University of Pisa,  
Via Diotisalvi 2,  
56122, Pisa, Italy  
E-mail: {firstname.lastname}@iet.unipi.it*

The use of mobile agents for data collection tasks in sensor networks may have significant advantages over traditional ad hoc sensor networks. Such agents, also known as Mobile Ubiquitous LAN Extensions (MULEs), have already been described and evaluated in literature by the means of simulation and numerical analysis. In this paper we investigate the performance of the data MULE model and its ability to support sensor-based applications in a real urban environment through an experimental analysis. Specifically, we use a testbed based on Berkeley motes, and analyze the impact of parameters like the MULE's speed and the distance between the static node and the MULE's line of motion on the contact time. The results obtained are very promising and show that the MULE architecture is really suitable for a large set of sensor-based applications in urban environments.

## 1. Introduction

As discussed in<sup>1</sup>, in a delay-tolerant scenario a three-tier MULE architecture provides the benefits of both the infrastructure and the infrastructure-less approach to connectivity, in terms of sensor energy consumption, data success rate and infrastructure cost. It comprises of a three-tier layered abstraction that can be adapted to different situations and needs: (i) a top tier for WAN connection; (ii) a middle tier of MULEs; (iii) a bottom tier of static wireless sensor nodes.

The top tier (i) is composed of Access Points and is meant to be set

up at convenient locations, where reliable network connectivity and power are guaranteed. Access Points should communicate with a central data warehouse to synchronize the data they collect.

The intermediate layer of mobile MULE nodes (ii) is characterized by large storage capacities (relative to sensors), renewable power, and the ability to communicate with both sensors and networked Access Points. As a result of their motion, MULEs collect and store data from the sensors.

The bottom tier (iii) normally consists of randomly distributed wireless sensor nodes. In our case however, the placement is strategic depending on the purpose of the application. Anyway, the work performed by sensor nodes has to be minimal, as their constraint on resource usage is the highest of all tiers.

The three-tier architecture supports increased reliability as the redundant Access Points and multiple MULEs create a fault-tolerant system where failures can only lead to reduced data success rate and increased latency<sup>2,3</sup>.

## 2. Experimental Environment and Methodology

Our experimental testbed is based on Mica2 Motes with the TinyOS operating system and MIB510 sinks.

We ran our experiments in a big parking area at the CNR campus at Pisa: the actors were a mobile sensor node (the MULE), trying to collect the data packets sent by a static sensor node (see Fig. 1).

In our experiments we measured the system's performance in terms of *contact time*.

In many papers the radio range  $R$  of the static node is assumed to be fixed. Hence, the packet loss experienced by the mobile MULE is assumed to be 100% when the distance between the mobile and the static node is greater than  $R$ , and immediately drops to 0% as soon as the MULE enters the radio range of the static node. Under this hypothesis, the contact time

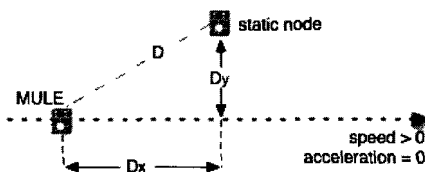


Figure 1. Testbed environment



is defined in<sup>4</sup> as the time interval during which the mobile node is within the radio range of the static node. The contact time can be derived analytically in terms of the radio range  $R$ , the distance between nodes, and the MULE's speed<sup>4</sup>. Accordingly, the number of packets  $N_{rx}$  correctly received by the MULE can be easily derived based on the contact time and the bit rate of the wireless link (which is assumed constant as well).

The above communication model is simple and analytically tractable. However, it is not completely realistic. We considered a different, more realistic, definition of contact time. In our analysis the contact time is defined as the total time during which the packet loss experienced by the MULE is below a given threshold (e.g., 15%). The contact time thus gives an indication of the amount of time during which the MULE is able to receive data from the static node with a given communication quality (expressed in terms of packet loss).

We evaluated the effect of the MULE's speed and the perpendicular distance between the static node and the MULE's line of motion ( $D_y$  in Fig. 1) on the contact time. We replicated all the experiments several times to increase the accuracy of the results. The results presented below are averaged on all the replicas. A more detailed view of the results is available in<sup>5</sup>.

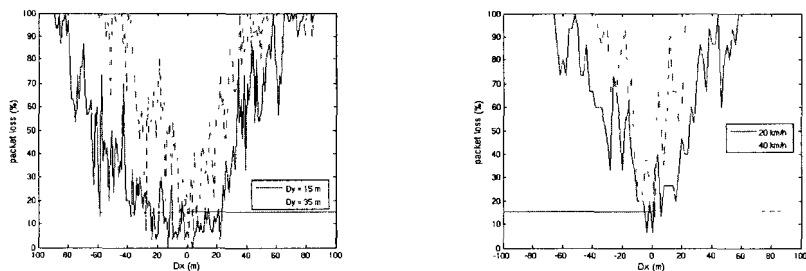
### 3. Experimental Results

As mentioned above, in an urban environment the role of MULE may be played by different actors (e.g., persons, buses, cabs) and, hence, MULEs may have different speeds. Therefore, we decided to divide our analysis into two parts. First, we considered a *low mobility* scenario assuming that MULEs are pedestrians and, hence, their speed is limited in the range [1, 2] m/s. In the second part, we considered a *high mobility* scenario where MULEs are buses (or cabs) and their speed varies in the range [20, 40] km/h.

#### 3.1. Low Mobility Scenario

The low mobility scenario is characterized by a limited range of speeds (from 1 to 2 m/s). In a such a scenario, in addition to the MULE's speed, the distance between the nodes, and the duty cycle of the static node may impact both the contact time and the total number of packets received by the MULE. Fig. 2(a) shows the packet loss as a function of the distance between the nodes. In our experiments we considered three different val-

ues for the perpendicular distance,  $D_y$ , between the static node and the MULE's line of motion: 15, 25 and 35 m. For the sake of clarity in Fig. 2(a) the curve at 25 m is omitted (the results for 25 m are in between those for 15 and 35 m, respectively). From the packet loss curve we can easily derive an estimate for the contact time. Assuming a threshold value for the packet loss of 15% we have approximately the following values for the contact time: 61 s (15 m), 36 s (25 m), and 12 s (35 m).



(a) Impact of distance in low mobility scenarios.

(b) Impact of the MULE's speed in high mobility scenarios.

Figure 2. Packet loss and contact time in low and high mobility scenarios.

From the above results it emerges that the perpendicular distance  $D_y$  has a strong impact on the contact time.

### 3.2. High Mobility Scenario

A MULE scenario in an urban environment can theoretically involve mobile nodes attached to anything. For example we can think of buses acting as MULEs, as they are intrinsically characterized by coordination and attitude to "full coverage" of a zone. Based on the above remarks, we extended our analysis to a high mobility scenario where the MULE moves at speeds typical of vehicles in residential areas (20 to 40 km/h).

By the time we were planning those experiments we observed that, at these speeds, when  $D_y > 15$  m the communication becomes very difficult and unreliable. Therefore, we decided to run this second set of experiments at a distance  $D_y = 15$  m.

Figure 2(b) shows the packet loss as a function of the distance  $D_x$  measured along the MULE's line of motion, for different MULE's speeds. As expected, the contact time becomes shorter and shorter as the MULE's

speed increases (Fig. 2(b)). With a MULE moving at 20 km/h, the two nodes are able to communicate with a packet loss lower than 15% for no more than 10 meters ( $-4 < D_x < 6$ ), resulting in a contact time reduced to around 2 s. In the case of a MULE moving at 40 km/h the contact time is approximately 0 s. However, even with such low values of the contact time, the number of packets successfully transferred to the MULE is not negligible.

#### 4. Conclusions

Based on the above results we can conclude that the MULE architecture is really suitable for a rich set of environmental monitoring applications in urban environments, both in low and high mobility scenarios. Our analysis was based on Mica2 Berkeley motes. We can reasonably expect that with future advancements in sensor networks technology, it will be possible to achieve even better results than those presented in this paper.

#### Acknowledgments

This work has been carried out under the financial support of the FET-IST HAGGLE project and the Italian Ministry for Education and Research (MIUR) in the framework of the FIRB-PERF and FIRB-VICOM projects.

#### References

1. R. C. Shah, S. Roy, S. Jain, and W. Brunette. Data MULEs: Modeling and Analysis of a Three-tier Architecture for Sparse Sensor Networks. *Elsevier Ad Hoc Networks Journal*, vol. 1, issues 2-3, 2003.
2. M. Ho and K. Fall. Poster: Delay Tolerant Networking for Sensor Networks. In *Proc. First IEEE Conference on Sensor and Ad Hoc Communications and Networks (SECON)*, Santa Clara, CA, USA, 2004.
3. D. Jea, A. Somasundra, and M. Srivastava. Multiple Controlled Mobile Elements (Data Mules) for Data Collection in Sensor Networks. In *Proc. IEEE International Conference on Distributed Computing in Sensor Systems (DCOSS)*, Marina del Rey, CA, USA, 2005.
4. S. Jain, R. C. Shah, G. Borriello, W. Brunette, and S. Roy. Exploiting Mobility for Energy Efficient Data Collection in Sensor Networks. In *Proc. Modeling and Optimization in Mobile, Ad Hoc and Wireless Networks (WiOpt)*, Cambridge, UK, 2004.
5. G. Anastasi, M. Conti, E. Gregori, C. Spagoni, and G. Valente. Motes Sensor Networks in Dynamic Scenarios: an Experimental Study for Pervasive Applications in Urban Environments. *Journal of Ubiquitous Computing and Intelligence (American Scientific Publishers)*, vol. 1, issue 1, 2006.

# PORTABLE SOFTWARE TOOLS FOR CONFIGURING A IEEE 802.15.4 WSN WITH MOBILE DEVICES

Marco Rizzello

*STMicroelectronics, SST Advanced System Technology, WSN platform team  
Via per Arnesano 16, c/o Complesso Garrisi, Building B, 73100 Lecce, Italy  
[marco.rizzello@st.com](mailto:marco.rizzello@st.com)*

Anna Gentile, Federico Vergori

*Università degli Studi di Lecce, DII, Facoltà di Ing. Informatica, Lecce, Italy  
[anna.gentile@unile.it](mailto:anna.gentile@unile.it)*

## Summary

This paper presents a framework for setting up a Wireless Sensor Network (WSN) by means of a mobile device like a PDA, through an IEEE 802.15.4 wireless link. This problem of installing a network of small sensing devices in a general environment is often referred to as “Commissioning practice”, especially in the industrial world. In order to setup such a network, there is the need to face firstly with the network connections establishment, and when the topology is well formed, then it turns the time to setup the application related parameters, as the trigger levels, policy rules for actuators, timers and so on. A serial communication protocol has been designed and introduced between an IEEE 802.15.4 node and a PDA, in order to allow to the PDA to enter in the WSN and to tune the network and application’s knobs. Once setup is done, the application could be started and the status of sensors and actuators is updated on the PDA. The protocol supports only star topology. A small demo has been succeeded by using few nodes, a commercial PDA and prototypal IEEE 802.15.4 boards.

## 1 Introduction

Wireless Sensor Networks are the new frontier of computing; typically we suppose they are built up with hundreds or even thousands of small, battery-powered devices, scattered throughout a target environment that can be indoor as for Home/Building/Industrial Automation/Monitoring, or outdoor as for Military or Environmental applications.

To make feasible the actual deployment of these systems, there is the need to lower the costs both of the single device and of the overall network infrastructure; the former is primarily a problem of technology maturity but requires also a general design of the single node; the latter is a question about the smartness of the network.

Our work focuses on the second aspect, experiencing the design and the realization of a software tool that can ease the creation of compelling applications for WSN, facing the problems tied to initial setup both of the networking layer, the core of the operation, and of the applications related issues; all in all, trying to generalize these setup procedures, despite the several

scenarios that can be imagined for each application field. In particular, we implemented these tools upon an IEEE 802.15.4 compliant WSN, facing problems related to this architecture and protocol stack, briefly described here.

## 2 IEEE 802.15.4/ZigBee

ZigBee is today the only standard-based technology that addresses the needs of a great part of WSN applications and it was designed to satisfy the markets needs for a cost-effective, standard-based low-data-rate wireless network, supporting low power consumption, security and reliability [1][1]. To this aim, the ZigBee Alliance, an industry-based working group ([www.zigbee.org](http://www.zigbee.org)) to which STMicroelectronics adheres, is developing standardized application software on top of the IEEE 802.15.4-2003 wireless standard [2], by working closely with the IEEE to ensure an integrated, complete, and interoperable network, providing interoperability certification testing of 802.15.4 systems that include the ZigBee software layer. It may be helpful to think of IEEE 802.15.4 as the physical radio specifications and ZigBee as the logical network and application software, as Fig 1 illustrates.

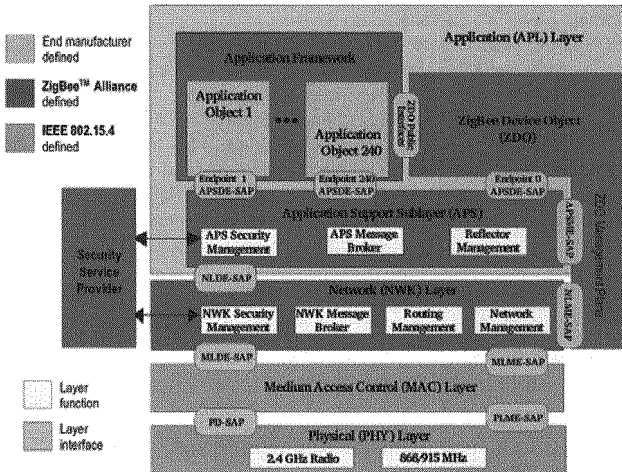


Fig 1 The ZigBee protocol stack

ZigBee-compliant products operate in unlicensed bands, including the worldwide 2.4GHz (16 channels), with a maximum raw data-throughput rates of 250Kbps, and an achievable transmission distance expected to range from 10 to 75m, depending on power output and environmental characteristics.

ZigBee networks are typically built with a combination of three device types:

- the network coordinator (PAN - Personal Area Network – Coordinator), the most sophisticated device, that requires the greatest amount of memory and computing power in order to maintain overall network knowledge;

- the full function device (FFD), that supports all 802.15.4 features; it is responsible for network router functions, but it could also be used in network-edge devices;
- the reduced function device (RFD), that carries limited functionality to lower cost and complexity. It's generally found in network-edge devices (where the network touches the real world, by means of sensors), as slave of an FFD.

Ultra-low power consumption is the way ZigBee technology promotes a long lifetime for devices with non-rechargeable batteries, trying to conserve the power of the slave nodes. For most of the time, a slave device is in deep-sleep mode and wakes up only for a fraction of a second to confirm its presence in the network (the transition time from sleep mode to active state is around 15ms and new slave enumeration typically takes just 30ms). ZigBee networks can use beacon or non-beacon operation modes, while security and data integrity are key benefits of the ZigBee technology, leveraging the security model of the IEEE 802.15.4 MAC sub-layer which specifies four security services, and implementing a special cross-layer in the ZigBee protocol stack.

A general ZigBee device/node is essentially made of a MCU with memory, a low-power Radio, a battery and one or more transducers that determines the functional behaviours of each node; but, despite their simple and low-count element composition, the nodes have to perform complex functionalities, given that the strength of the system has to be put in the network and not in the single device, so a tool to configure this sort of distributed engine is needed.

In the scientific community a general property of WSN is that often named "self-healing" or "self-organization", borrowed and inherited by the Ad Hoc Networks studies, where it is intended that the network must be able to operate under very dynamic conditions in an unattended mode, referring especially to the network layer functions (topology management, addressing, routing and so on).

From the point of view of the system integrator and of the end user, that is our main interest in this work, the network will operate in three different states, specifically start-up, steady, and failure state.

### **3 Our Software Tool**

With this software tool we address the first two stages, ignoring the maintenance of the network and failure issues. In practice, it has been designed by defining procedures to setup and manage a ZigBee network, providing for network topology control, node addressing and application properties (user entered description, location/tagging information and grouping) and node binding, ignoring for the moment security-related issues, as well as network management support (reconfiguration, change of topology and device roles, network diagnosis).

The services offered by this software will aim to make ZigBee-WSN quickly programmable (initial setup), checkable and usable (steady state). Initial setup

includes both network and application parameters (e.g. sampling time, standby time).

Functionalities offered by this tool are divided into three levels: NWK, ZDO and AF. NWK level includes network scanning and associations; services of ZDO level allow user make device and service discovery (e.g. number, address, type and features of all devices of the network); AF level includes all functionalities that allow monitoring and control of a Home Automation environment.

We developed our software upon the Java 2 Micro Edition Platform, following the Connected Device Configurations (CDC) guidelines, as we think it will be useful to deploy this tool on mobile devices (cell phones and PDA), without worrying of the different platforms, being the Java technology portable and more common in these types of devices. We used a commercial PDA and the Chipcon CC2420 Development Board Kit for tests, in a Building Automation scenario, realizing the monitoring of the environment in our laboratories as shown in Fig 2.

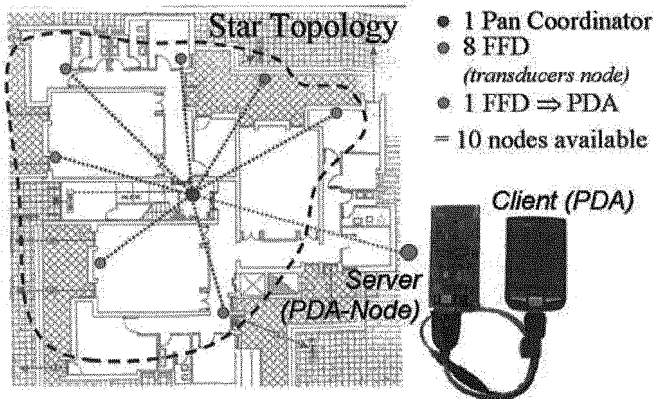


Fig 2: Home Automation testbed for the development tool

#### 4 Communication Protocol

The communication between PDA and PDA-Node is based on a client-server model through a RS232 link. Client is represented by PDA, by which the user can make requests to PDA-Node that is the server; PDA-Node is a kind of proxy between the PDA and the coordinator of the ZigBee network. Communication is performed using a variable length packet consisting of the fields shown in Fig 3.

The packet is made of a SOP byte used to characterize the incoming data transmission, a Header of a fixed length, a variable length Payload and a FCS that is used for checksum.

SOP <sub>□</sub>	HEADER <sub>□</sub>				PAYLOAD <sub>□</sub>	FCS <sub>□</sub>	
Start of packet <sub>□</sub>	Seq. num <sub>□</sub>	Command ID Field <sub>□</sub>			Length <sub>□</sub>	Data <sub>□</sub>	Checksum <sub>□</sub>
		(2-byte) <sub>□</sub>					
1-byte <sub>□</sub>	1-byte <sub>□</sub>	Cmd-Type <sub>□</sub>	Cmd-Level <sub>□</sub>	Cmd-ID <sub>□</sub>	1-byte <sub>□</sub>	Variable <sub>□</sub>	1-byte <sub>□</sub>
		4-bit <sub>□</sub>	4-bit <sub>□</sub>	1-byte <sub>□</sub>			

Fig 3 The packet frame

The Header field is made of 3 sub-fields: Seq num, Command Id Field and Length. The 'Seq-num' sub-field, 1 byte long, specifies the sequential number of each packet, allowing to link each request with the corresponding response. The 'Command Id Field' sub-field, 2 bytes long, is made of 3 sub-fields: Cmd Type, Cmd Level and Cmd Id. The 'Cmd Type' sub-field, 4 bits long, specifies if the command is a request, a response, a subscription or a debug message; the 'Cmd Level' sub-field, 4 bits long too, defines the application domain (AF, ZDO or NWK Level); the 'Cmd Id' sub-field, 1 byte long, specifies the command type as regards an application domain. The 'Length' sub-field, 1 byte long, expresses the number of bytes of Payload.

The 'Payload' field has both a variable frame and a variable length due to the packet type. The 'FCS' field, 1 byte long, is used for checksum to identify errors in packet transmission.

## Conclusions

The main goal of this work has been the implementation of the IEEE 802.15.4 RF capabilities on a PDA node that could be used to setup and monitor a WSN. To this extent a serial communication protocol has been implemented between the PDA itself and a IEEE 802.15.4 prototypal node. Both network and application parameters could be adjusted in order to control the monitoring application. A small demo with few nodes has been succeeded.

## References

- [1] ZigBee Specification, Version 1.0, 14 December 2004.
- [2] IEEE Std. 802.15.4, Wireless Medium Access Control (MAC) and Physical Layer (PHY) Specifications for Low-Rate Wireless Personal Area Networks (LR-WPAN), 1 October 2003.

## Acknowledgments

This work has been performed within the project FIRB «MiTeTIV - MicroTEchnologies for Virtual Immersive Telepresence» funded by "Ministero dell'Istruzione dell'Università e della Ricerca" under PNR 2001-2003.



# **Low-Power Sensor Front-End Electronics With RFID Communication Capabilities For Food Logistic Datalogging Applications**

M. Cicioni\*, A. Scorzoni, F. Alimenti, P. Placidi, L. Roselli  
*Dipartimento di Ingegneria Elettronica e dell'Informazione, via G.Duranti 93,  
06125 Perugia, Italy*  
michele.cicioni@diei.unipg.it, Ph: +39-075-5853644, Fax: +39-075-5853654

S. Zampolli, I. Elmi, G.C. Cardinali, M. Severi  
*CNR-IMM Bologna, via P. Gobetti 101, 40129 Bologna, Italy*

S. Marco, J.M. Gómez, F. Palacio  
*Universitat de Barcelona, Departament d'Electronica, Martí i Franqués 1,  
08028 Barcelona, Spain*

B. Mazzolai, A. Mondini, V. Raffa, V. Mattoli, P. Dario  
*CRIM - Research Center in Microengineering, Scuola Superiore Sant'Anna,  
Via Rinaldo Piaggio, 34, 56025 Pontedera (PI), Italy*

R. Ingles Bort, J. L. Ramirez, E. Llobet  
*Universitat Rovira i Virgili, Dept. of Electronic Engineering, Avda. Països  
Catalans 26, Campus Sescelades, 43007 Tarragona Spain*

E. Abad  
*Fundación Tekniker, Spain*

T. Becker  
*EADS Deutschland GmbH, München (Germany)*

## **Summary**

In this work, we describe a low-power transponder based on a Texas Instruments MSP430 microcontroller which interfaces both with sensors and with a passive, 13.56 MHz RFID front-end. This prototype features commercial *RH*, temperature light sensors. We tested the correct operation of the transponder using a commercial reader compliant to the ISO-15693 directives. The implemented commands are correctly managed using a pulse position coding 1 out of 4, a 100% ASK modulation from reader to transponder and a high data rate from transponder to reader.

## Introduction

Current and future concerns related to agrofood safety and quality will increasingly require a multidisciplinary and universal approach based on the massive use of simple detection systems able to be used “near to the foodstuff”. The technology used nowadays to assess food safety and quality relies on lab solutions that are bulky, costly, punctual and time consuming. Innovative approaches will comply, through the development of innovative Micro and Nano Technology solutions, with the needs of ubiquity, low cost and low power, fast response, simple use and fully interconnection to the decisional bodies. In the framework of the “GoodFood” FP6 Integrated Project, a flexible transponder gas sensing system with RFID communication capabilities for food logistic applications is being proposed. The transponder, besides storing dynamic traceability information, features physical sensors (relative humidity (*RH*), temperature, light) and, depending on the application scenario, will also feature Metal-Oxide chemical gas sensors. The envisaged GoodFood-WP6 scenario imagines the RFID transponder and the Reader immersed in the so-called Ambient Intelligence (AmI) for ubiquitous sensing in the frame of increased food safety and quality.

In this work, we describe a low-power transponder based on a Texas Instruments MSP430 microcontroller [1] which interfaces both with sensors and with the passive, 13.56 MHz RFID front-end communication electronics. This prototype features a Sensirion SHT15 *RH* and *T* sensor and a commercial light sensor, while low-power MOX sensor readout is planned for the next versions. The transponder is designed to give information on food evolution during transport. After being programmed with data logging parameters at the beginning of the logging phase, it should store information from the various sensors during transport and this information should be read on arrival of the food at final destination.

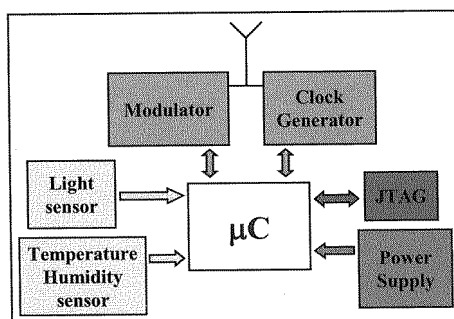


*Fig. 1* Block diagram of the transponder

### Architecture of the transponder

Figure 1 shows a block diagram of the transponder. The microcontroller MSP430F169 is connected to the SHT15 through a two-wire bus which provides temperature and relative humidity measurements in digital form. Data communication is implemented using a proprietary pseudo I<sup>2</sup>C protocol [2].

The light sensor is composed of a visible to IR sensitive diode [3], the electrical current it produces is a function of the amount of incident radiation, then the current signal is converted to voltage signal using a low power operational amplifier. The acquisition is performed using the internal ADC of the microcontroller.

### Communication

In RFID systems, the reader radiates an electromagnetic signal that is also used by the transponder to send the information back to the reader using a load modulation technique. The communication between the transponder and the reader presently uses a subset of ISO-15693 directives. Focusing on the transponder, the reception of incoming commands is based on a ASK modulation with pulse position coding, this signal is demodulated by monitoring the state of a digital signal produced by a counter in the *clock generator* block. This signal is periodic except in the time slot where the modulation is actuated. Conversely, the transmission from the transponder to the reader is based on a FSK load modulation with two subcarriers. A suitable modulation circuit driven by a programmable logic device accomplish this task.

### Antenna

The antenna is built on DuPont™ Pyralux® AP flexible substrate featuring a thickness of 50.8 μm, 3.4 relative dielectric constant, 0.008 dissipation factor. The substrate is bonded to a 18 μm thick copper foil. The antenna works in *near*

field operating region and so the coupling between the devices is mainly magnetic. In order for the RFID transponder to receive the needed energy from the electromagnetic signal, a suitable voltage level should be present at the antenna. To increase this level, the resonance frequency of the antenna must be tuned at the operative frequency. RF simulations were performed using Asitic<sup>TM</sup> and AWR Microwave Office<sup>TM</sup> in order to design the best antenna that could fit a credit card size. In particular, Asitic returned a more correct value of the antenna inductance, while Microwave Office featured was better suited for calculating the complete behavior of this type of structure at the relevant frequencies. The resulting antenna is a five loop planar inductor, featuring a self-resonance frequency higher than 13.56 MHz, due to the presence of embedded parasitic capacitances. Figure 2 shows the equivalent circuit of the designed antenna. To decrease the resonance frequency towards the actual operating frequency we paralleled the inductor with a capacitor  $C_{tune}$  of suitable value. This capacitor was integrated in the antenna, as shown in Figure 3. Because a very precise estimation of the parasitic capacitance requires a very good processing control, we built a modular tuning capacitance (Figure 2) in order to be able to fine tune the resonance frequency after processing.

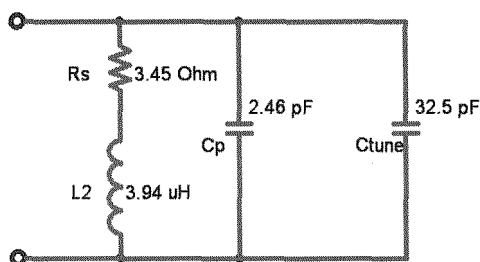


Fig. 2 Equivalent circuit of the designed antenna.

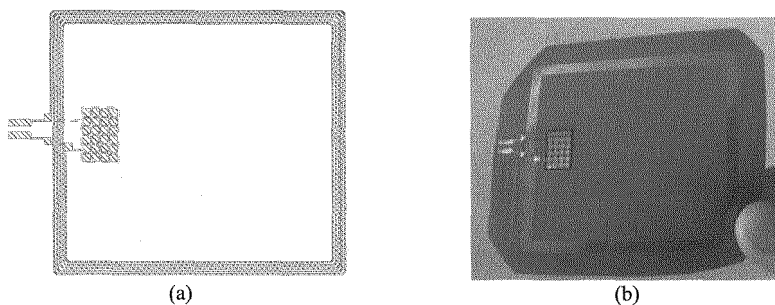


Fig. 3 (a) Layout and (b) physical realization of the flexible antenna

### Transponder operation

The reader-to-transponder and transponder-to-reader communication are managed by a Gate Array Logic (GAL) and by the microcontroller. The reader-to-transponder communication includes a hardware counter which helps the microcontroller to detect the 100% ASK modulations, while the transponder-to-reader communication includes the generation of the frequency  $f_c/28$ , where  $f_c$  is the carrier frequency, the Manchester encoding and the modulation with two subcarriers. Presently the microcontroller code allows the reader to perform ISO-15693 “read single block” and “write single block” operations. We tested the correct operation of the transponder using a commercial reader compliant to the ISO-15693 directives. The implemented commands are correctly managed using a pulse position coding 1 out of 4, a 100% ASK modulation from reader to transponder and a high data rate from transponder to reader.

### Conclusions

In this work we presented a low-power transponder based on a Texas Instruments MSP430 microcontroller interfaced both with sensors and with a passive, 13.56 MHz RFID front-end. This prototype features commercial RH, temperature light sensors. We tested the correct operation of the transponder using a commercial reader compliant to the ISO-15693 directives. The implemented commands are correctly managed using a pulse position coding 1 out of 4, a 100% ASK modulation from reader to transponder and a high data rate from transponder to reader.

### References

1. MSP430x1xx Family user's Guide, Texas Instruments (SLAU049E)
2. SHT1x / SHT7x, Humidity & Temperature Sensor, datasheet
3. SLCD-61N1, Solderable Planar Photodiode, datasheet

### Acknowledgments

We would like to acknowledge Luca Abbati and Marco Gubbiotti for their commitment during their Laurea project.

# A Neural Spectral Classifier for Optical Sensors

Mario Medugno

*I.M.M. - C.N.R., Naples, Italy*

[mario.medugno@imm.cnr.it](mailto:mario.medugno@imm.cnr.it)

## Summary

Multispectral remote sensing devices have the potential for large scale integration and can be successfully used in environmental monitoring; in particular optical sensors could embed microelectronic circuitry in order to perform signal preconditioning and more complex classification tasks for specialized applications. We propose a neural approach for supervised classification of the spectral signature of electrically sensed optical emissions, since the neural networks can be trained for the correct classification without any predetermined logic or programming burden. The software and hardware implementation of a such smart optical sensor for the spectral signature recognition is discussed and the classification results for fire detection are presented.

## 1 Introduction

Automatic surveillance systems on wide territorial areas are infrastructures of growing interest, motivated by natural and anthropic disasters, which “alas” determine huge people injury, ecological and economical losses. Efficient environmental monitoring systems can mainly accomplished by two integrated electronic subsystems, namely sensors and radio communication networks. Monitoring actions are based on environmental remote sensing (over or outside the earth surface) by different optical sensors, usually producing large images made by one or more picture elements for different spectral channels (eg. see Mivis and Modis systems); however each data sensor generally need several processing steps in order to extract the required information among noisy or misleading data.

Depending on the nature of monitoring system, the qualitative and quantitative interpretation of remotely sensed signals requires an ad-hoc choice of computer assisted steps for data pre-processing, feature extraction, classification. Data processing is generally not on-line with the data acquisition process whether in active or passive multispectral image sensors (independently from platform type). Nevertheless real-time data processing aimed to provide the need information is a “must” for special purpose sensors or in applications as motion control, transportation systems, robotics, critical environments monitoring; therefore low cost-definition smart sensors for in-situ, optical detection are investigated.

## 2 Microelectronic Technologies and Sensor Data Processing

Two evolutionary paths are, in my opinion, emerging in the sensor fields due to their integration with embedded processing units: smart sensors and System on Chip (SOC); the former sensor type include procedures for calibration, protocols for automatic interface and setting conforming to the standard proposed in [1] or CMOS sensors with self-contained signal processing circuitry, or VLSI with optically responsive pixel cells as proposed in [2, 3]. The latter sensor type include system integrated sensor with multiple specialized processing units which perform in parallel different tasks on different data (i.e. a MIMD paradigm); several SOC for radio communication, physical, chemical and bio sensing have been recently proposed.

Recent microelectronic advances as the single electron transistors and CMOL technology promise transistors implementation below the 10nm scale, giving therefore a possible path to continue in the next decades the trend of Moore law [4]; as showed therein, such technology is based on a nano-wire crossbar architecture which straightforwardly permits the implementation of high connectivity neuromorphic networks for large pattern classification based on Hopfield model with Hebbian rule. Nevertheless large networks of Hopfield networks were implemented on massively parallel computers [5] showing good pattern learning and noisy auto-association but introducing some drawbacks as spurious states and not yielding any categorized output [6]. Here we propose a data processing approach, oriented to fast and robust pattern classification of generic sensors.

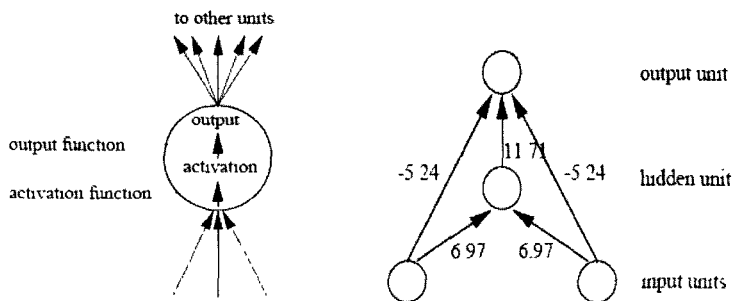
### 2.1 Neural Techniques of Data Processing and Data Classification

We use an Artificial Neural Net (ANN) instead of a statistic approach to data classification because their major advantage is the ability *to generalize*, in the sense that a trained net could classify data from the same class as the learning data set that it has never “seen” before. The implemented ANN is based on robust statistical bases of non parametric techniques proposed by Parzen, which overcome the Hopfield networks drawbacks; our network in fact can be employed as a pattern classifier, and is composed by simple computing node.

### 2.2 Artificial Neural Network

An ANN is a layered network structure made by simple nodes (neurons, in a real NN) processing data (the electric signals of firing neurons) yield by unidirectional interconnection channels (the synapses). The basic structure of a node and of a simple network is sketched in the Figure 1. A node is

characterized by an activation function which describes the combining of input signal, the output function which describes the response to the input stimuli, and the re-configurable channel weights showed by numbers in the Figure 1. Since the first ANN proposal of Mc Culloch and Pitts, a large number of network topologies and learning methods for specific network training have been proposed [7]. In this paper we have considered Probabilistic Neural Network (PNN) for spectral signature classification; a PNN is a three layered network



which differs from Figure 1 as weights only connect two successive layers.

Fig. 1 Basic structure of a Node and ANN

### 3 A Generalizing Classifier by Probabilistic Neural Network

Probabilistic Neural Network (PNN) are able to estimate the unknown probability density functions for each category, and then use it for pattern classification. This method works fine also with multi-modal density by varying a window parameter  $h$ , as complex decision regions  $R_n$  with volume  $V_n$  can be realized by superposition of simple window functions having the form  $\varphi(z) = (1/2\pi)^{1/2} \exp(-z^2/2)$ . If we assume that the region  $R_n$  of the  $n$ -th class is an  $a$ -dimensional hypercube of volume  $V_n = (h_n)^a$ , it can be shown that the  $n$ -th estimate of the density function  $p_n(x)$  for the samples  $x_1 \dots x_b$ , assumed independent and identically distributed, is:

$$p_n(x) = 1/n \sum_i \delta_n(x-x_i), \text{ where } \delta_n(x) = 1/h_n \varphi((x-x_i)/h_n);$$

when  $h_n$  goes to zero,  $p_n(x)$  become a super-position of Dirac delta functions centered at the sample points. Summarizing, the PNN input layer normalize the input pattern, the inner layer computes  $p_n(x)$  and the output layer selects the class with maximum probability. Hardware implementation of PNN



have been suggested in [8] due to their relatively simple computation requirements arising from not stringent space and time complexities.

As first step the PNN has been dimensioned, therefore the number of neurons for each layer has been chosen. This is an application dependent choice, as the number  $a$  of neurons in the input layer depends on the dimension of the input units (the spectral channels), the number  $b$  of neurons in the intermediate layer depends on the number of patterns on which the estimate is based, the number  $c$  of neurons in output layer depends on the number of classes on which a generic patterns can belong. Such application dependency has to be supported by a general purpose re-configurable hardware architecture.

### 3.1 Preprocessing and Feature Extraction for Optical Fire Detection

We need to detect the spectral signature pattern with a “non-imaging” optical sensor. The fire spectrum was early measured in [9] and different reference flames are proposed recently for flame detection. We moreover suppose the optical sensor has to detect the wider possible spectra for fires in natural environment; note that the sunlight reflections can generate strong response in VIS and infrared NIR to TIR bands, i.e. the range 750-10.000nm. Therefore we choose to dispose a setup with single pixel, large FOV multispectral sensors in UV, and two NIR bands able to capture typical CO<sub>2</sub> and flambe spectral peaks. These signals are preprocessed by low noise amplifiers and a converter to translate the typical frequency response of the UV sensors based on gas discharge tube. UV-NIR signals are transformed in digital numbers and are used to compute also a NDVI index; these are the input for the successive supervised classification by PNN.

### 3.2 Classifier Training

The ANN is trained with a reduced set of realized patterns, a subset among all the possible patterns generable in special applications. In order to reach the best generalization, the dataset can be divided in i) a *training set* the user has to issue for the learning phase, during which the error is minimized, ii) a *validation set* the user uses for estimate the classification performance of the ANN over patterns not included in the training set, iii) a *test set* for performance evaluation purposes of the ANN. Some time it could happen that a small training error does not guarantee a low test error.

## 4 System Implementation and Results

The multispectral array sensor has been built by discrete optical sensor and preprocessing board by Hamamatsu; the PNN has been implemented by Matlab

for the preliminary simulated fire tests. A first hardware prototype is based on Microchip PIC 12F675, a versatile MCU with 8-bit ADC and digital output. Preliminary tests show acceptable sensibility and classification for in-situ fire detection, and false alarm rate with butane and propane flames (2 cm diameter size at 40 cm) is less than 10 % in sunlight conditions.

## 5 Conclusions

The proposed neural classifier for multispectral optical sensor has been tested for a fire detection application by optical sensor, and its sensibility and false alarm rate can be increased as further developments. The proposed data process method can be usefully employed as a general tool for the implementation of smart optical sensors. It has been shown its potential for an hardware implementation, integrating optical sensors and the present CMOS programmable technology or the future ULSI devices based on CMOL technologies.

## 6 References

- [1] IEEE 1451.3 Standard for a Smart Transducer Interface for Sensor and Actuators-Digital Communication and Transducer Electronic Data Sheet (TEDS) Form. Dis.Multi.Sys.
- [2] H. Djahanshahi et alii, "Neural-based Smart CMOS Sensor for On-Line Pattern Classification Applications", ISCAS '96 International symposium on circuit & systems, pp. 384-387, 1996.
- [3] Chiu-Hung Cheng et alii, In the blink of a silicon eye, IEEE Circuits and Devices Magazine, vol 17, 3, pp. 20-32, May 2001
- [4] J.H. Lee and K.K. Likharev, "CMol CrossNets as Pattern Classifier", in *IWANN 2005* LNCS3512, pp.446-454, Springer Verlag 2005
- [5] M. Mastroianni, M. Medugno, U. Scafuri, Realizzazione di reti neurali in ambienti paralleli, in *Applicazioni dell'intelligenza artificiale nell'ingegneria*, ed. Liguori (1993) 115-124
- [6] A. Iazzetta, M. Medugno, U. Scafuri, Autoassociative memory simulation on a transputer network, in *Eurosim '92 Simulation Congress*, Capri I 29.9.1992-2.10.1992, ed. North Holland, (1993) 319-324
- [7] J. Hertz, A. Krogh, R.G. Palmer, "Introduction to the theory of neural computation", Addison-Wesley Publishing Company
- [8] D. F. Speckt, "Probabilistic Neural Network", *Neural Networks*, 3(1):109-118, 1990
- [9] A. R. Jones, "Flame Failures detection and Modern Boilers", *J. Phys. E : Sci. Instrum.*, 21, pp. 921-928, 1988.

# Design of a wireless sensor network for urban pollution monitoring

G. Barillaro, P. Bruschi, R.G. Garroppo, S. Giordano, A. Molfese, F. Pieri  
*Dipartimento di Ingegneria dell'Informazione, Università di Pisa, Italy*  
[f.pieri@iet.unipi.it](mailto:f.pieri@iet.unipi.it)

## Summary

Monitoring of air pollution is an essential element for the management of urban areas, and today it is mostly implemented using fixed stations. In this work, we examine the design of an air pollution monitoring solution based on a wireless sensor network, and present some of the issues that must be confronted by the designer. The presented implementation is based on off-the-shelf networking hardware and custom developed sensors. The final system will include a porous silicon based NO<sub>2</sub> sensor, a solid-state, low power anemometer, and temperature sensors. Specific attention is devoted, as is essential in a wireless sensor network, to power consumption issues. It will be shown the power requirements of the sensors often dwarf those of the network connectivity, so that smart sensor sampling strategies are as important as communication strategies for proper power management.

## Introduction

Public monitoring of several different pollutants (NO<sub>2</sub>, CO, ozone, to name the most common) and other environmental variables in urban area is an essential element of the management of modern cities.

Present technical approaches to this task (i.e. sparse, mostly fixed, bulky monitoring stations) lack the desirable pervasiveness and promptness of response. The typical monitoring network of medium/large Italian cities is composed by less than ten stations. As a result, accurate information on the spatial distribution and time evolution of the pollutants, which is important to reduce the disruptive impact of public countermeasures (as is the block of the circulation of private vehicles), is not available. In this respect, the measurement of the wind speed and direction is important to anticipate the pollution evolution. As the wind is strongly influenced by the geometry of surrounding buildings [1], it should be monitored on a very small spatial scale, and not by present-day very coarse networks.

To handle these issues, Wireless Sensor Networks [2] based on many small, autonomous nodes, implementing both the sensing and connectivity functions, are promising. However, extreme care in planning the measurement and communication strategies must be used. Frequently, this aspect is not considered

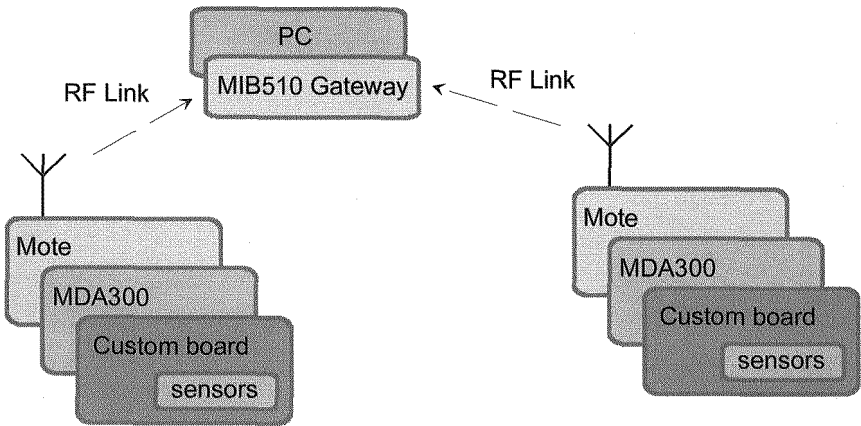
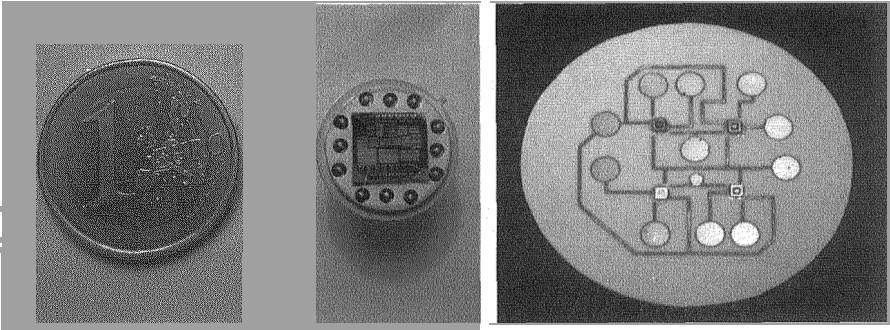


Fig.1 System architecture.

in depth in the literature, that often refers to abstract network models and is more focused on the power optimisation of the communication part [3].

## Architecture

For this project, commercially available hardware – Crossbow Technology MICA2 communication boards (the *motes*), developed at the UCB [4] - (primarily used to implement the connectivity) will be integrated with custom-developed state-of-the-art solid state sensors and their conditioning electronics. Each network node is based on a MPR400 mote, including an RF transceiver (the Chipcon CC1000), working at 915MHz, and an Atmel microcontroller (the Atmega 128L). Each mote can be interfaced with any of several sensor boards (not used in this project), including sensors for temperature, humidity, acceleration, etc. To allow the development of custom sensor boards, an acquisition board (the MDA300), including several 12-bit ADCs and digital I/O channels, is also available. The MDA300 will be used to interface our sensors (described in the following section) with the network. Custom boards, carrying the sensors, will be fabricated and connected to the MDA300 to be used for sensor reading and signal conditioning. The boards are designed to be compact, low-voltage/low-power circuits, with very low idle power consumption. The whole node (mote + MDA300 + sensor board) is powered by two standard AA batteries. A gateway node (the MIB510) is used for interconnection to a PC and mote programming (fig. 1).



*Fig. 2 Photos of the NO<sub>2</sub> PS-based sensors in a standard TO8 package (left), and of the 4-chip anemometer prototype, implemented on a standard PCB (right). The PCD diameter is 35 mm.*

## Sensors

The monitored variables will be NO<sub>2</sub> concentration, wind speed and direction, temperature, and humidity.

Porous silicon (PS) based sensors [5] (fig. 2, left) will be used to measure the concentration of NO<sub>2</sub>. With respect to commercially available NO<sub>2</sub> sensors, our PS-based sensors have the great advantage of ambient temperature operation, which implies reduced power consumption. The effect of humidity, which is a known interfering variable for NO<sub>2</sub> sensors, will be compensated with a humidity sensor, built-in on the MDA300 board.

The anemometer, based on the differential temperature principle, is designed with a standard VLSI technology, already used to fabricate a single sensor flow-meter [6]. The first prototype [7] is based on a 4-chip assembly (fig. 2, right). This prototype suffers of a high power requirements, as heating of the chips is necessary for its operation. However a fully integrated, single chip version (under design), should result in a very compact, low power device.

Finally, the temperature sensor will be a solid-state standard device based on the “ $\Delta V_{be}$ ” principle [9]. Expected energy requirements for the various sensors are summarized in table 1, where the acquisition energy is the total energy required to obtain a valid reading from the sensor. While the prototype anemometer has by far the largest energy requirements, in the final version the NO<sub>2</sub> will be the most important energy user, due to its (relatively) long acquisition time.

Sensor type	required power (mW)	acquisition time (s)	acquisition energy (mJ)
Anemometer (bulk version)	500	35	17500
Anemometer (integrated version)	15	0.200	3
PS-based NO <sub>2</sub> sensor	4	10	40
Solid state temperature sensor	2.5	0.050	0.125
Humidity sensor (built-in)	2.5	4	10

*Table 1 Power requirements of the sensors.*

## Power budget

Extreme care in planning the measurement and communication strategies must be used, especially because the power consumption of the sensors can be a significant part of the total power budget. For estimation of the power requirements, the approach developed in [3] was followed.

The power source is a pair of AA 1.5 V batteries, for which a capacity of 2500 mAh was assumed. The node is supposed to transmit each time the sensors are sampled, with a rate given in the table below. Between transmissions, the node samples the communication channel at a fixed time interval (100 ms for the data in the table), to check for possible transmissions. If a neighbouring node is transmitting, the node receives the data and (possibly) retransmits it to other nodes, depending on the communication strategy. The number of neighbour nodes was set to five. Our data suggests that an important contribution to the overall power consumption is given by the power requirements of the sensors. Therefore, the measurement and communication approaches should be oriented to the reduction of the sample rate of the sensors, implementing dynamic strategies related to the current environmental conditions. Several approaches are possible. A first one can be based on the correlation of pollutant concentration with wind data. As it is known that strong winds reduce the risk of high pollutant concentration, the sensor sample rate (and power consumption) can be reduced when strong winds are present. Another possible approach is to increase the sample rate of pollutant concentration sensors only when the warning threshold concentration is approached. The effectivity of such approaches will be verified with on-field deployment of the network.

Active sensors	sample rate (hr <sup>-1</sup> )	battery life (days)
Bulk anemometer only	10	<7
Integrated anemometer only	10	1580
NO <sub>2</sub> sensor	10	1050
All (int. anemometer, NO <sub>2</sub> , temp., humidity)	10	950
All (int. anemometer, NO <sub>2</sub> , temp., humidity)	20	550

Table 2 Estimated battery life for different sensor sampling scenarios.

### Acknowledgments

This work is financially supported by Fondazione Cassa di Risparmio di Pisa under project RESPIRO. The sensors design is performed by Università di Pisa, while their fabrication is based in part on STMicroelectronics technologies, made available in the framework of the joint Università di Pisa-STMicroelectronics R&D Center.

### References

- [1] J. W. D. Boddy, R. J. Smalley, N. S. Dixon, J. E. Tate, A. S. Tomlin, *Atmospheric Environment*, 39 (2005), 3147.
- [2] W. Tsujita, A. Yoshino, H. Ishida, T. Moriizumi, *Sensors & Actuators B*, B110 (2005), 304.
- [3] J. Polastre, J. Hill, D. Culler, in *Proceedings of the Second ACM Conference on Embedded Networked Sensor Systems (SenSys '04)*, Baltimore, USA, 2004.
- [4] <http://www.xbow.com>
- [5] G. Barillaro, A. Diligenti, A. Nannini, L. M. Strambini, E. Comini, G. Sberveglieri, *IEEE Sensors Journal*, 6 (2006), 19.
- [6] P. Bruschi, D. Navarrini, M. Piotta, *Sensors and Actuators A*, 110 (2004), 269.
- [7] P. Bruschi, N. Nizza, M. Piotta, M. Schipani, *XI Conferenza Annuale dell'Associazione Italiana Sensori e Microsistemi (AISEM 2006)*, Lecce, Italy, 2006.
- [8] R. J. Baker, H. W. Li, D. E. Boyce, *CMOS - Circuit Design, Layout and Simulation*, IEEE Press, New York (1998) 474.

## Application of Multi-sensor Miniaturized System for Olive Oil Evaluation

M. Zuppa, A.M. Taurino, C. Distante, S. Capone, L. Francioso, D. Presicce,  
P. Siciliano

*Microelectronic and Microsystem Institute – CNR Lecce,*  
[Marzia.Zuppa@le.imm.cnr.it](mailto:Marzia.Zuppa@le.imm.cnr.it)

### Summary

The detection of aroma volatile compounds emitted by extra virgin olive oils (EVOOs) is of key importance in the quality control of this product. Physical–chemical techniques (GC, GC/MS, HPLC) and sensory analysis (panel test) are the classical methods used for this purpose, but they are expensive, time consuming, and do not allow on-line measurements.

This work shows the performance of an electronic nose, based on pure and doped SnO<sub>2</sub> sol–gel thin films, used to analyze different “single-cultivar” extra-virgine olive oil samples.

### 1. Introduction

A primary ingredient of the Mediterranean diet is Extra Virgin Olive Oil, which is also one of the most important products of the Italian agricultural industry. Extra Virgin Olive Oils (EVOO) taste and aroma are closely related both to some non volatile compounds and to a number of volatile compounds.

Moreover, many types of EVOO are produced by mixing oils from different “cultivar”, that is, from different variety of tree species coming from different geographical origin area of cultivation. Each type of blend is characterized not only by a different smell but also by different taste and color. The organoleptic properties of oils also depend on the particular blend.

In the Italian region, the presence of typical varieties, the peculiar microclimatic conditions and precise olive orchard management lead to the production of very valuable olive oil with a distinctive taste. Seasonality, water availability and temperatures clearly influencing the ripening process.

Another very important aspect is the ageing of olive oils. In fact, organoleptic properties changes completely during the storage period of olive oils having a strong degradation. Therefore, the detection of aroma volatile compounds emitted by EVOOs is of key importance in the quality control of this product. Physical-chemical techniques (GC,GC\MS, HPLC) and sensory analysis (panel test) are the classical methods used for this purpose, but they are expensive, time consuming and do not allow on-line measurements.

Electronic Nose instrumentation has advanced rapidly during the past ten years with a lot of successful applications in food and drinks industry applications.

This paper reports the performance of a metal oxide sol-gel thin films based Electronic Nose, developed at the sensors laboratory of CNR-IMM Lecce, sensing different “singlecultivar” EVOOs produced by Tuscan producers and



following the ageing of these olive oil samples. So that a technique of classification based on *m*-SOM neural network in combination of the probabilistic neural network was applied to classify the EVOO aroma sensed by the multisensor system.

In order to know the real headspace of olive oil samples sensed by multisensor system, analytical technique like Headspace Solid Phase Micro Extraction \ Gas Chromatography \ Mass Spectrometry (HS-SPME\GC\MS) analysis was applied to the analysis of volatiles compounds in EVOOs samples.

## 2. Experimental set-up

Four samples of different Tuscan single-cultivar EVOOs, labeled *Seggianese*, *Scarlinese*, *Grappolo* and *Mugnai*, were analyzed by means of two different techniques. The complete set of measurement was repeated three times with an interval of 30 days.

The multi-sensor array was composed by six different micro-sensors, which had different sensing layer. They were pure and Ni, Os, Rh, Pd-doped tin oxide sol gel thin films. For the preparation of the pure SnO<sub>2</sub> sols we started from anhydrous SnCl<sub>4</sub> as precursor. For the preparation of the doping solution a prescribed amount of suitable solutions, with an atomic ratio X/N = 0.05 (X= Ni, Os, Rh, Pd respectively), were added to the SnO<sub>2</sub> sols. Details of the preparation of the solution are reported elsewhere [1]. The films were deposited, by means of spin coating, onto Al<sub>2</sub>O<sub>3</sub> substrates pre-arranged for cutting and obtaining (2x2) mm<sup>2</sup> single samples. After the spinning the sensitive layers were thermally annealed at 500°C. The alumina substrates were equipped, on the back side, with Ti/Pt meander as heating element. Moreover, on the front side, onto the sensing layer, inter-digitated Ti/Au electrodes were deposited. Finally, the devices were mounted onto TO39 socket.

During the operation, all the sensors were heated at the operating temperature, which in this case was 250°C, by supplying a given voltage to the heating element. The sensor responses towards the volatile compounds of the different olive oil samples were carried out by applying a constant voltage of 2 V between the electrodes and measuring the current flowing through the sensors by means of an electrometer Keithley 6517A type equipped with a multiplexer module.

Concerning the experimental set-up for the measurements, the baseline was acquired in a dry air -nitrogen atmosphere in a continuous total flow of 100 sccm (standard cubic centimeter per minute) (50 sccm air and 50 sccm nitrogen), while for the measurement 10 ml of sample in a 20 ml vial kept at a temperature of 21°C, was stripped by means of a deviation of the only 50 sccm nitrogen flow for 20 min, maintaining the other 50 sccm of dry air constant. In this way, the volatile compounds were directly transferred by the carrier gas into the sensor chamber. All fluxes were controlled by means of mass flow meters and a mass flow controller (mod. MKS 647B).

All the process was controlled by a PC by means of National Instruments software.

In the case of HS-SPME\GC\MS analysis, SPME 50 $\mu$ m CAR (Carboxen)-PDMS (polydimethylsiloxane) (black code, Supelco) fibers were used and exposed to 10ml of oil sample in 20 ml gastight vials at 21°C. After this, fiber was desorbed in a split/splitless injector, equipped with deactivated SPME glass inserts, and analyses were carried out on a 30m x 250  $\mu$ m ID x 0.25  $\mu$ m HP INNOVAX polyetilenglicole column. A GC system HP 6890 Series, Agilent Technologies, was coupled with HP 5973 mass selective Detector, Agilent Technologies. Injection was split 5:1 with 5 min relay time. GC conditions were: 40°C for 5 min, 150°C at 4°C/min, then 250°C at 15°C/min; injector temperature was 250°C, helium flow was 1ml/min. Transfer line was held at 260°C. Spectra were produced in the electron impact mode at 70 eV. Compounds were identified by comparison with NIST reference spectra. Mass range was 30-350 amu, solvent delay time was 4 min, threshold 150 and scan rate 4,45 scan s<sup>-1</sup>.

### 3. Methods and Results

The Principal Component Analysis was used for the initial examination of the whole dataset. The figure 1 shows the score plot for the first two principal components (PCs), reflecting a not clear clustering in particular for data coming from the third period of maturing. A technique of classification based on *m*-SOM neural network in combination of the probabilistic neural network (PNN) (Figure 2) was applied to classify the EVOO aroma sensed by the multisensor system. The sensor responses were processed by means of the Discrete Wavelet Transform and subsequently Principal Components Analysis to extract useful features [1]. The next step of data analysis was to discriminate different single-cultivar olive oil samples by applying a neural architecture (*m*-SOM) of *m* self-organizing maps, where *m* was the number of single cultivar olive oil groups to be recognized. The processing was mainly made in two phases: training and testing. In the training phase, each map was trained with observations belonging to the same single-cultivar olive oil group. Once the maps were self-organized, a refining process was performed by using Learning Vector Quantisation (LVQ) algorithm to reduce the high uncertainty accumulated at the borders of two or more maps. In the testing phase the unknown measurement vector *x* was presented to the network. The Euclidean distance measure was computed over all neurons of the maps, and the winner map (the one with the nearest neuron or with minimum distance) was considered as the estimated recognized olive oil class [2].

Once the selection of single cultivar olive oil was performed, the single cultivar olive oil samples of different ageing period were discriminated. The codebook vectors of each single map, which were closest to the input vectors, fed up the probabilistic neural network to determinate the period of storage of the oil

sample [3]. In order to test the capability of the classification technique a cross-validation method was performed by selecting randomly a certain number of measurement vectors from whole set as training data of the mSOM-PNN classifier. This procedure was repeated for different times and the average error rate was 8%.

#### 4. Conclusions

In this work four different single-cultivar Tuscan Extra-Virgin Olive Oils were analyzed by means of Electronic Nose. By means of Electronic Nose it was possible to separate among clusters of different EVOOs and of different cultivar, while with the HS-SPME\GC\MS we obtained the chemical map of the different samples.

Even if the PCA clustering results are not completely satisfactory, the mSOM-PNN classifier allows a good classification. The used technique required a small train data set and at the same time it showed a good performance in terms of errors committed in recognizing the given data set in comparison with others supervised technique of classification as kNN or PNN.

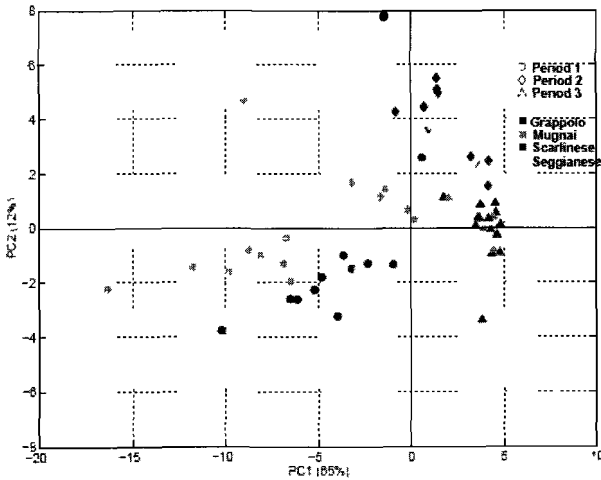
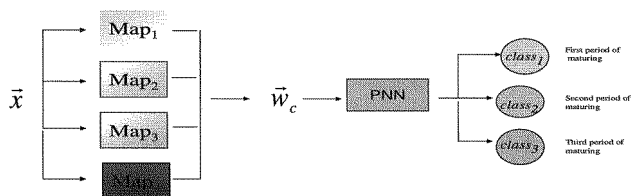


Fig. 1 PCA score plot of whole Electronic Nose data set



**Fig. 2** mSOM-PNN classifier; input vector  $x$  fed up mSom network to assign the single-cultivar olive oil class. The codebook vector of the winner map fed up the PNN algorithm to assign the period of maturing.

## References

- [1] Distanto C., Leo M., Siciliano P., Persaud K.C. *On the study of feature extraction methods for an electronic nose* Sensors and Actuators B 87 (2002) 274–288
- [2] C. Di Natale, A. Macagnano, A. D'Amico, F. Davide, *Electronic nose modelling and data analysis by self organizing neural network*, Meas. Sci. Technol. 8 (1997) 1236–1243.
- [3] Zheng Hai, Jun Wang *Electronic nose and data analysis for detection of maize oil adulteration in sesame oil* Sensors and Actuators B 119 (2006) 449–455

## Acknowledgments

The authors thanks prof. Cimato of CNR - Tree and timber Institute for olive oil samples.

# LOW VOLTAGE LOW POWER IMPROVED CCII BASED INTERFACE FOR MEASURE AND HEATING CONTROL OF RESISTIVE SENSORS

Giuseppe Ferri, Vincenzo Stornelli, Andrea De Marcellis, Fabrizio Mancini  
*Dipartimento di Ingegneria Elettrica e dell'Informazione, Università dell'Aquila, Monteluco di Roio, 67100 L'Aquila, Italy, [ferri@ing.univaq.it](mailto:ferri@ing.univaq.it)*

## Summary

In this paper, we present a low-voltage ( $\pm 0.75\text{V}$ ) low-power ( $200\mu\text{W}$ ) current-mode based integrated interface for the measure and heating control of resistive gas sensors. It is formed by two resistances, two improved CCII, which have been developed to achieve reduced parasitic components at its terminals, and a logic control block which both estimates the resistance sensor value (through a resistance-to-voltage conversion) and controls the temperature of the whole system.

## 1 Introduction

The interfacing of resistive sensors, as sensitive elements, with a suitable integrated circuit is a fundamental characteristic in smart sensors. CMOS technology is widely used, because it allows to match the reduction of costs of the silicon technology with the possibility of designing new low voltage and low power interfaces, typically supplied by a battery. Recently, also the current-mode approach, which considers the current as reference signal, has been applied in sensor interface [1-2]. Second generation current conveyor (CCII) is the current-mode basic block. In this paper, we present a low-voltage ( $\pm 0.75\text{V}$ ) low-power ( $200\mu\text{W}$ ) current-mode based integrated interface, using two improved CCII, which have been developed to achieve reduced parasitic components at their terminals.

## 2 Improved CCII topology

Second generation current conveyors (CCII) are current-mode basic blocks utilized in numerous applications, both in linear and nonlinear contexts, which sometimes can excellently substitute the traditional operational amplifier [3-6]. In fig. 1 the block scheme of a CCII device is reported: if a voltage is applied at Y node, an equal voltage will be obtained at X node while the current flowing into X node is either equal or opposite to the current flowing into Z node.

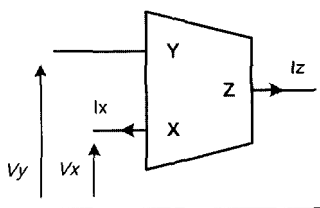


Figure 1. CCII schematic block.

Ideal CCII behaviour is the following:

$$\begin{bmatrix} I_Y \\ V_X \\ I_Z \end{bmatrix} = \begin{bmatrix} 0 & 0 & 0 \\ 1 & 0 & 0 \\ 0 & \pm 1 & 0 \end{bmatrix} * \begin{bmatrix} V_Y \\ I_X \\ V_Z \end{bmatrix} \quad (1)$$

where Z and Y nodes show infinite impedances and X node shows zero impedance. Positive (CCII+) and negative (CCII-) current conveyors are respectively obtained for  $I_Z=I_X$  and  $I_Z=-I_X$ . Non ideal CCIIs present the following relations:

$$V_X = \alpha V_Y \quad (2)$$

$$I_Z = \beta I_X \quad (3)$$

where typically  $\alpha$  and  $\beta$  are very close to 1. Generally, a unity voltage transfer function  $V_X/V_Y$  is ensured by implementing a differential transistor input pair, when large transistors output resistances are required in order to obtain an  $\alpha$  parameter dependent only on the transconductance ratio of the input pair itself. Concerning the current transfer function, unfortunately it is not independent from the load connected to Z node. If this load impedance is negligible with respect to the transistor output resistances,  $\beta$  parameter is very close to its ideal unitary value. In summary, non ideality problems are related to the parasitic impedances at CCII terminals that have to be necessarily taken into account in a large number of low voltage low power applications. For this reason we have developed a novel CCII topology which presents reduced parasitic components at X and Z nodes [1]. Fig. 2 shows the schematic of the improved CCII at transistor level while in fig. 3 its layout is depicted.

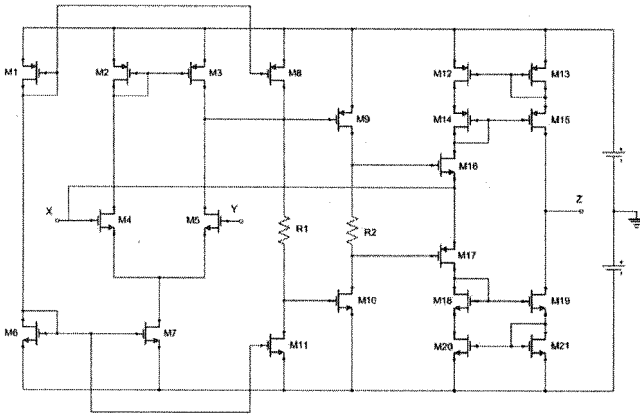


Figure 2: Improved CCII schematic at transistor level.

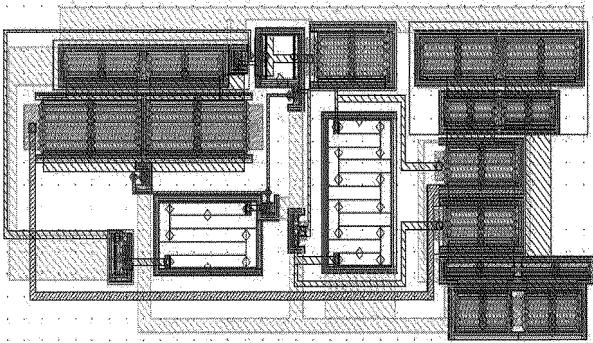


Figure 3: Improved CCII layout.

The parasitic impedance at X node, that is required to be low, is inversely proportional to the input transistors  $g_m$ . A small input resistance requires large values of  $g_m$ , so a trade-off between X node parasitic resistance and power consumption has made. Concerning the Z parasitic impedance, it has been ensured to be high by the transistor output resistances at Z-node. The proposed circuit works at a low supply voltage,  $\pm 0.75V$ , and has a very low power consumption, about  $200\mu W$ . In Tab. 1 the main CCII characteristics are reported.

<i>Data</i>	<i>Value</i>
Voltage supply	$\pm 0.75V$
Power Consumption	$210 \mu W$
3dB Bandwidth	16 MHz
Dynamic Range	-1V/+0.9V
Biasing Currents	$10 \mu A$
Voltage Gain (alfa)	1.00
Current Gain (beta)	1.00 ( $R_X=R_Z=10K\Omega$ )
X Parasitic Resistance	$11.4 \Omega$
Z Parasitic Resistance	$7.2 M\Omega$
Layout area	$0.13 \text{ mm}^2$

Table 1: Improved CCII main characteristics.

### 3 CCII-Based Interface

Fig. 4 shows the considered CCII-based interface where the sensor is modelled by resistance  $R_{sens}$ .

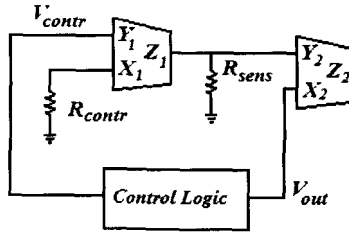


Figure 4 The proposed interface.

The output voltage  $V_{out}$  is linearly proportional to  $R_{sens}$  variations. In fact, considering ideal CCII, we can write:

$$R_{sens} = R_{s0} (1 + X) \quad (4)$$

$$V_{out} = \frac{V_{contr}}{R_{contr}} R_{sens} = \frac{V_{contr}}{R_{contr}} R_{s0} X + \frac{V_{contr}}{R_{contr}} R_{s0} \quad (5)$$

The first term of (5) is linearly proportional to sensor variation and, through the value of  $R_{contr}$ , can be used to maximize circuit sensitivity, while the second one



gives a constant current ( $I_{sens}=V_{contr}/R_{contr}$ ), fixed by a suitable choice of  $V_{contr}$ , through the logic block which is also used for heating the sensor itself. In this way, the problem of the system temperature control and  $R_{sens}$  estimation has been here reduced to the measure of the output voltage dropped across the sensor resistance. This task is made easy thanks to the second CCII that acts as a voltage buffer decoupling the logic block from the system. The delivered current must be such that the temperature has to remain constant. The suitable control logic evaluates the sensor resistance through a resistance to voltage conversion and generates a feedback signal, which maintains the sensor at the desired temperature. Designing improved CCII blocks avoids a bad estimation for  $R_{sens}$ , determined by temperature and power supply variations of the whole system. Fig. 5 shows the heating current variation at different temperatures for  $R_{sens}$  value ranging between  $10K\Omega$  and  $100K\Omega$ . The heating current,  $I_{sens}$ , remains constant enough in the considered range, even if, for high temperature values, the circuit does not maintain this behaviour. Therefore, in the future, a particular attention has to be made to achieve an improved interface, which allows to reduce the sensitivity to the temperature variations of the whole device.

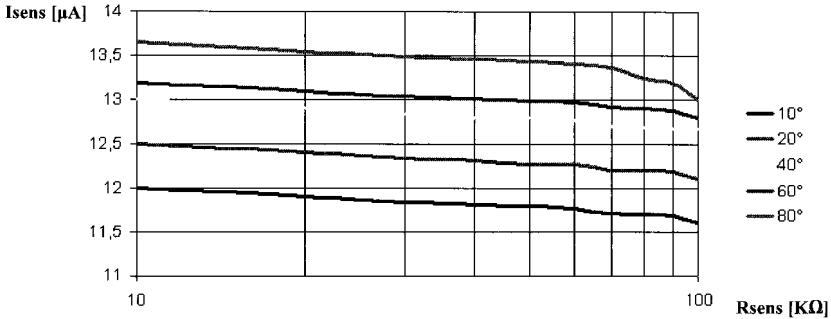


Figure 5.  $I_{sens}$  current vs.  $R_{sens}$  at different temperatures (from the bottom,  $10^{\circ}, 20^{\circ}, 40^{\circ}, 60^{\circ}, 80^{\circ} C$ )

**References**

1. G.Ferri, V.Stornelli, M. Fragnoli, "An integrated improved CCII topology for resistive sensor applications", Analog Integrated Circuits and Signal Processing, accepted for publication, 2006.
2. G.Ferri, N. Guerrini, S. Del Re, F. Mancini "Current Mode Based Integrated Gas Sensor Interfaces", Sensors And Microsystems, Proc. AISEM 2004, pp. 424-429.
3. K.C.Smith, A.Sedra, "The current-conveyor- a new circuit building block", IEEE Proc 56, 1968, pp 1386-1369.
4. A. Sedra, K. Smith, "A Second-Generation Current Conveyor and Its Applications", IEEE Trans. Circuit Theory, 17, 1970, pp. 132-133.
5. G.Ferri, N. Guerrini, "Low voltage low power CMOS current conveyors", Kluwer Academic Publisher, Boston,2003, 226 pp , ISBN 1-4020-7486-7
6. R.Mita, G Palumbo, S.Pennisi, "CMOS CCII+ With High Current -Driving Capability", IEEE Trans. on Circuits and Systems II, Vol 50, Issue 4, April 2003, pp 187 190.

**This page intentionally left blank**

Proceedings of the 11th Italian Conference

# Sensors and Microsystems

This book contains a selection of papers presented at the 11th AISEM (Associazione Italiana Sensori e Microsistemi) National Conference on Sensors and Microsystems. The conference exhibited updated results from both the theoretical and applied research in the field of sensors and microsystems. In an interdisciplinary approach, many aspects of the disciplines related to sensors and microsystems are covered, ranging from physics, chemistry, materials science, biology and applications issues.

**World Scientific**

[www.worldscientific.com](http://www.worldscientific.com)

6759 hc

ISBN-13 978-981-279-338-6  
ISBN-10 981-279-338-0



9 789812 793386